Available online at www.sciencedirect.com

ScienceDirect

Earth and Planetary Science Letters 253 (2007) 429–438

EPSL

www.elsevier.com/locate/epsl

Earthquake scaling, fault segmentation, and structural maturity

Isabelle Manighetti *, Michel Campillo, Sylvain Bouley, Fabrice Cotton

Laboratoire de Géophysique Interne et Tectonophysique de Grenoble, Grenoble, France

Received 28 July 2006; received in revised form 17 October 2006; accepted 2 November 2006
Available online 6 December 2006
Editor: R.D. van der Hilst

Abstract

Slip and length measurements on earthquakes suggest large stress drop variability. We analyze an extended set of slip-length measurements for large earthquakes ($M \geq 6$) to seek for the possible origin(s) of this apparent variability. We propose that such variability arises from earthquakes breaking a variable number of major fault segments. That number depends on the strength of the inter-segment zones, which itself depends on the structural maturity of the faults. We propose new $D_{\max}$–L parameterizations based on that idea of multiple segment-ruptures. In such parameterizations, each broken segment roughly scales as a crack, while the total multi-segment rupture does not. Stress drop on individual segments is roughly constant, only varying between 3.5 to 9 MPa. The slight variation that is still observed depends on fault structural maturity; more mature faults have lower stress drops than immature ones. The new $D_{\max}$–L functions that we propose reduce uncertainties with respect to available relationships. They thus provide a more solid basis to estimate seismic hazard by integrating fault properties revealed by geological studies.

Keywords: Earthquakes osin; Scaling; Slip-length; Fault maturity; Fault segmentation

1. Introduction

A common hypothesis in earthquake mechanics is that earthquakes have a macroscopic behavior of cracks in an elastic medium, with the stress drop being a material property hence being almost constant for crustal earthquakes e.g., [1–5]. From that hypothesis, one expects maximum ($D_{\max}$) or mean displacement (D_{mean}) on earthquakes to scale with rupture length (L) when $L \leq 2W_{\text{seism}}$ (W_{seism} being the thickness of the seismogenic layer), and tapers off for long ruptures ($L > 2W_{\text{seism}}$). While available D–L earthquake data have long been too few to show whether or not that behavior was real (see stormy debate that opposed 'L- and W-model' supporters over 15 yr; [6–12]), it is now generally admitted (exceptions are [13,14]), from examination of denser data sets, that earthquakes more likely follow a 'W-model', hence roughly behave as cracks [15–17]. Shaw and Scholz (2001; later referred to as S&S01) have recently proposed a scale-invariant physical model that includes the two D–L regimes:

$$\begin{aligned} &- \text{ for ruptures with } L \leq 2W,\ D_{\text{mean}} = \alpha * (L/2) \\ &- \text{ for ruptures with } L > 2W,\ D_{\text{mean}} = \alpha * (1/[1/L + 1/2W]) \end{aligned} \tag{1}$$

It is important to note that, in the formulation of that equation, S&S01 postulate that α is proportional to a constant static stress drop, while W represents the width

---

* Corresponding author.
E-mail address: imanighe@obs.ujf-grenoble.fr (I. Manighetti).

0012-821X/$ - see front matter © 2006 Elsevier B.V. All rights reserved.
doi:10.1016/j.epsl.2006.11.004

of the seismogenic layer thus is W_{seism}. The model roughly reproduces the first-order distribution pattern of ~55 earthquake slip-length data (see their Fig. 1). While this suggests that the physical basis of the model is appropriate overall, a closer examination of the data suggests that an additional factor may intervene in the *D*–*L* scaling for actual *D*–*L* data are much more scattered than predicted by the constant stress drop

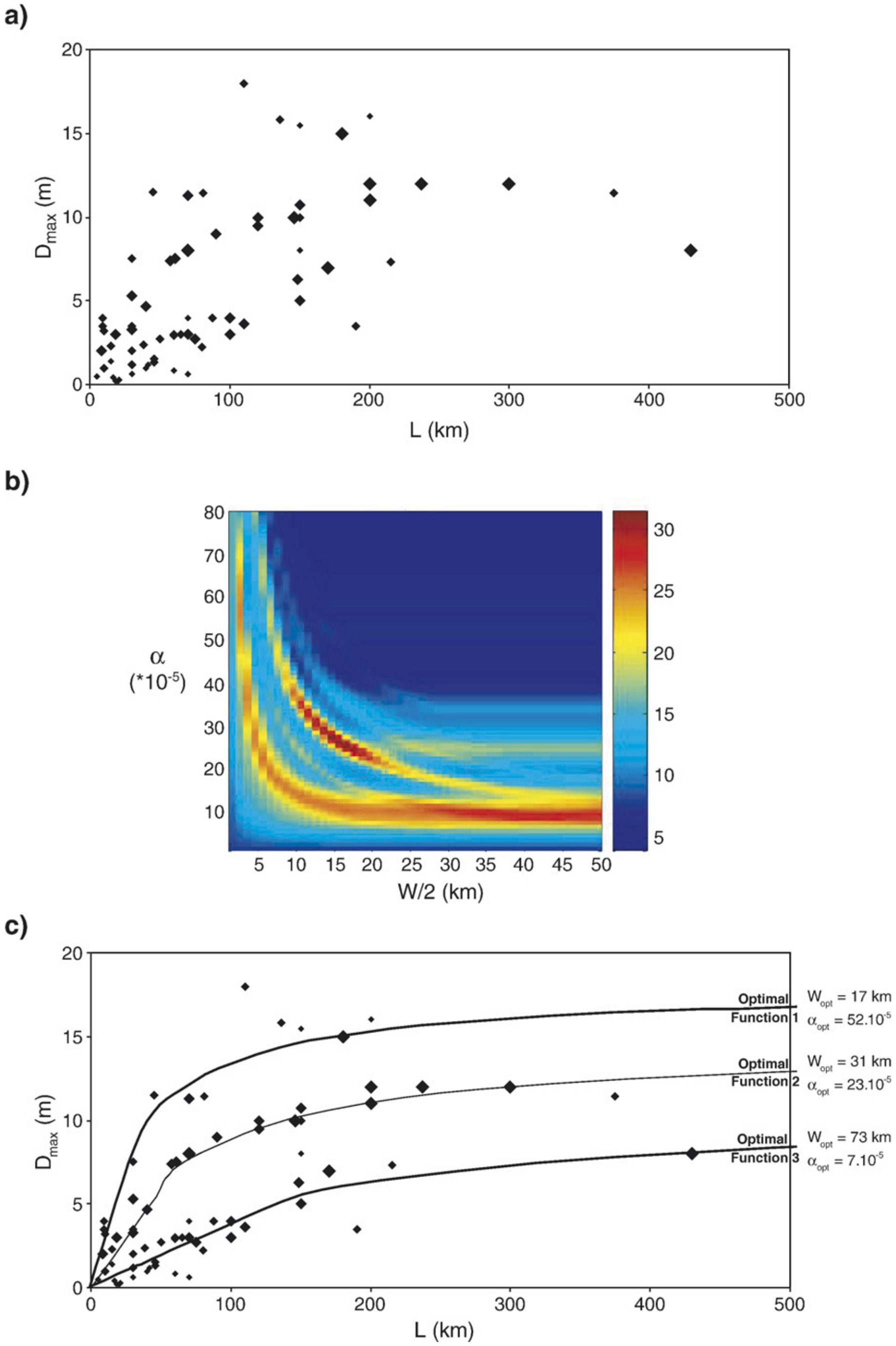

Fig. 1. Displacement-length surface data in Asia (from Table 2). (a) $D_{\max}$ versus *L* plot. Symbol size is proportional to quality weight. (b) Fit quality map resulting from adjusting the data set with one S&S01' function having variable [α,W] values. Three, and possibly fours regions of [α,W] values are found that best-fit distinct data subsets. (c) Data are plotted together with the three optimal S&S01' functions deduced from B. Corresponding optimal [α,W] values are indicated.

model; large earthquakes of similar size (i.e., similar length and width) obviously can produce different slips and stress drops, as it has been pointed out by many authors e.g., [2,17–21]. We focus here on such slip variability and seek for its possible origin(s). We compile all available slip-length measurements for large earthquakes in four seismically active regions of the world. Our data set only includes earthquakes with a magnitude larger than ~6, so that our results are relevant to the largest scale of the earthquake process only. We conduct our analysis using the functional form of Eq. (1). Yet, we give an interpretation of the parameters α and W that is different, though not contradictory, with that of S&S01. We state that the observed slip variability arises from broken geological faults having a variable frictional strength that depends on their long-term slip history (‘structural maturity’) and geometry (large-scale segmentation). While the effect of slip history has already been evoked in earthquake scaling analyses e.g., [18,22–25], that of fault segmentation has never been. We claim that it should be, for it dictates the way earthquakes gain in length, hence strongly governs the relationship(s) between earthquake slip and length.

2. Data sets

We examine displacement-length data for a set of ~250 large ($M \geq \sim 6$), shallow (rupture width ≤40 km, with an average value W_{mean} of 18 km), continental earthquakes of mixed focal mechanisms (strike–slip, reverse and normal), that have occurred in four of the most seismically active regions worldwide: Asia (broad sense), Turkey, West US, Japan. In these regions, long-term active faults are generally well known, with their surface geometry (total length, segmentation, strike variations, associated secondary fault networks), age, maximum slip rate and total cumulative displacement being generally determined. We use these long-term parameters (where available) to qualify the structural maturity of the faults that broke during the analyzed earthquakes, as explained in Table 1 (supporting online material). Doing so, we classify the broken faults in three classes, basically ‘immature’, ‘intermediate’, and ‘mature’ (Table 1). Earthquake slip-length data are compiled from literature (references in Tables 2 and 3; supporting online material). We consider here the maximum displacement ($D_{\max}$), not the mean (D_{mean}), for it is best constrained. Besides, Manighetti et al. [21] have shown that $D_{\max} = 2 * D_{\text{mean}}$ for most large earthquakes worldwide, a property that is found to be scale-independent. Being aware that rupture slip and length measured at surface may be lower than actual maximum slip and length produced at depth, we compile both surface measurements (209 earthquakes; Table 2) and slip-length values inferred at depth from earthquake source models (56 earthquakes; Table 3), and analyze them separately. Surface data are screened for quality, and a ‘quality weight’ assigned to each data from criteria defined in Table 2. Note that, since error bars cannot be properly defined for most data, weighting them with a quality factor is the best we can do to discriminate poor and robust data. While such quality screening is a fundamental step to discuss any scaling law, it has never been done before (in terms of quality weighting of each data). Concerning slip-length data at depth, we did not attempt to ‘qualify’ the quality of the various earthquake source models. Rather we chose to average the different $D_{\max}$–L values proposed for the same earthquakes (Table 3).

3. Data analysis

We start analyzing in detail the Asian data set, for it is the densest. Fig. 1a shows the Asian surface $D_{\max}$–L data, with symbol size proportional to quality weight. The data are rather dispersed, so that a single function cannot be found to adjust them all properly. However the overall shape of the data distribution resembles an asymptotic function similar to that predicted by the S&S01’ model; slip increases with length for short ruptures ($L < 100$–200 km), and seems to saturate for longer ruptures. We note that, while data are dispersed, they do not extend evenly over the plot; there are zones free of data, and zones where data cluster. This suggests the existence of a few specific trends. To check whether or not these trends are significant, we use a figure of merit M to score the adjustment of a couple of [α, W] parameters to the data set, and explore the whole space of the model parameters (Fig. 1b). M is of the form $M = \sum_i (\text{ch}([D_{\text{obs}} - D_{(\alpha,W)}]/D_n))^{-1}$ where D_{obs} is the measured value of slip, $D_{(\alpha,W)}$ is the predicted value of slip, and D_n is an adjustable smoothing parameter (chosen here to be 7 times the standard deviation of D_{obs}). At this stage, we thus assume that α and W are free adjustment parameters. The existence of several, distinct zones of maximum in Fig. 1b indicates that the data cannot be fitted with a single model, but rather include several subsets associated with different models, i.e. different values of [α, W]. Three major zones are identified, whose shape is related to bias between α and W. Since we deal with a limited number of data, we must verify that this multimodal structure is not fictitious. We generated random models having the statistical properties of the data (average and variance of D depending on

L, distribution of *L*) and performed the same test as before. The multimodal structure with respect to the functional form of S&S01 that is exhibited by the data is not produced by sparse random series. We checked a dozen realizations to reach this conclusion. Examples are presented in Fig. A (supporting online material). We can thus conclude on firm ground that the Asian surface data set actually includes at least 3 distinct groups

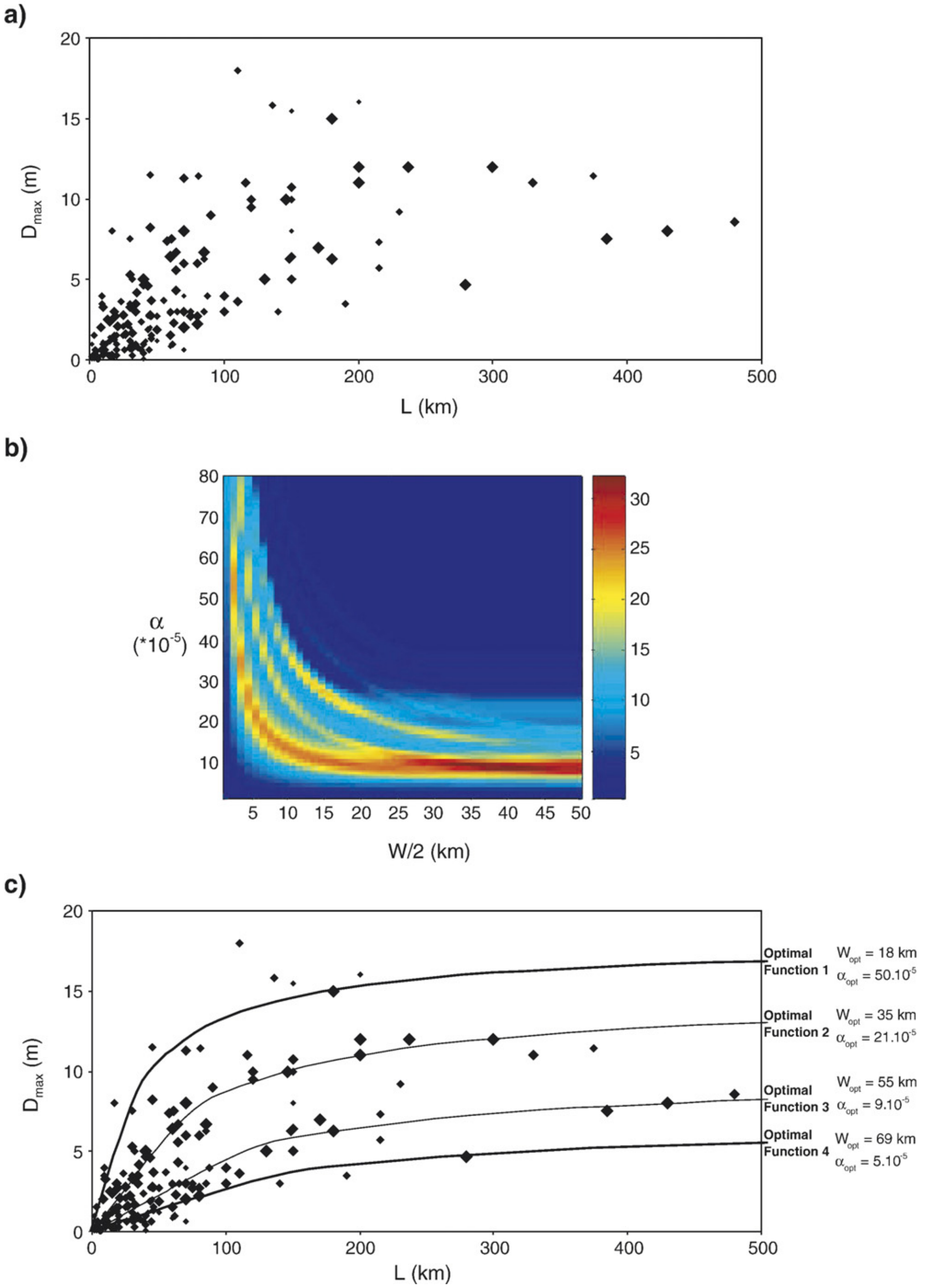

Fig. 2. Displacement-length surface data in the four Asia, West US, Turkey and Japan regions (from Table 2). (a) $D_{\max}$ versus L plot. Symbol size is proportional to quality weight. (b) Fit quality map resulting from adjusting the whole data set (smallest ruptures with $L<50$ km are excluded for clarity) with one S&S01' function having variable $[\alpha,W]$ values. Three, and possibly fours regions of $[\alpha,W]$ values are found that best-fit distinct data subsets. (c) Data are plotted together with the four optimal S&S01' functions deduced from b. Corresponding optimal $[\alpha,W]$ values are indicated.

unambiguously associated with different couples of [α, *W*] parameters. Based on these findings, we searched for the three optimal S&S01' functions that combine to produce the best fit to the entire data set. This is done through an iterative optimization procedure in which each data point is affected to a subset. Fig. 1c shows the results, together with the three couples of optimal [α, *W*] values best adjusting the data. We find that data are properly fitted provided that *W* and α both vary. In the last section of the paper, we discuss statistical tests (using Akaike Information Criterion) that show that the misfit reduction is not due to 'over-fitting' the data with models having a too large number of free parameters. The optimal values of *W* are found to be regularly spaced, the largest being about multiple of the lowest, while α varies irregularly yet decreasing with W. Note that these results are independent of slip mode; strike–slip, reverse and normal ruptures are found in any of the three groups (Fig. B, done for all data; supporting online material).

We applied the same treatment to the other three regional data sets. In all cases the data show a multimodal structure, with at least two or three distinct regions of [α, *W*] values found to adjust distinct data subsets (Fig. C, supporting online material). Fig. D (supporting online material) shows the corresponding optimal S&S01' functions. In all cases, the optimal [α, *W*] parameters vary in a discrete, almost regular fashion. Besides, the optimal [α, *W*] values are roughly similar from one region to the other, so that, on average, 4 recurrent, multiple couple values are suggested, equal to [$(46\pm6).10^{-5}$, 17.5±0.5], [$(20\pm2).10^{-5}$, 32±3], [$(8\pm1).10^{-5}$, 57±4], and [$(5\pm1).10^{-5}$, 71.5±1.5].

Fig. 2a now shows all surface data together. The uneven data distribution appears more clearly, with three main trends distinguishable. Fig. 2b confirms that the whole data set consists of three or four distinguishable data subsets associated with distinct domains of [α, *W*]. Fig. 2c shows the four optimal S&S01' functions that we inferred from this basis. These functions again suggest

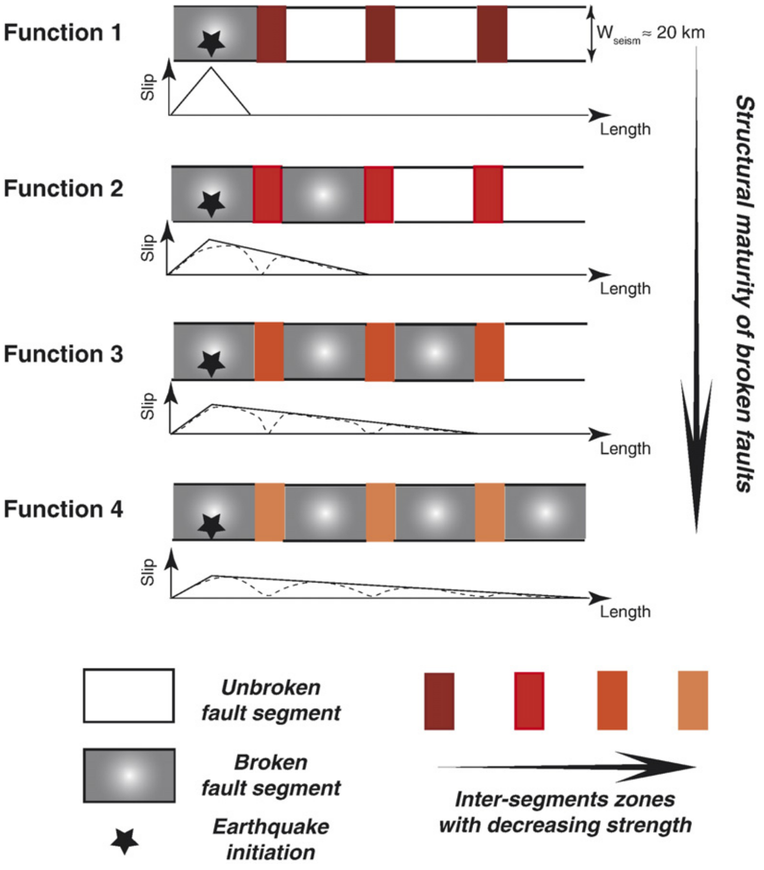

Fig. 3. Proposed scenario. Earthquakes break a variable number of major segments along the faults on which they initiate. That number increases with the degree of structural maturity of the faults, for inter-segments zones have lower strength on mature faults. The shape and amplitude of the resulting slip profiles varies accordingly.

discrete values of W, roughly equivalent to the lowest 18 km value being multiplied by 1 to 4 when one goes from optimal functions 1 to 4. The parameter α is also found to vary in a discrete, yet more irregular fashion.

Finally, Fig. F (supporting online material) shows all slip-length data at depth deduced from inversion models, together with the four optimal S&S01' functions whose existence is inferred, as before, from analysis of Fig. E (supporting online material). Though the data set is different, the optimal W values are similar to those obtained from surface data, while the optimal α values are slightly higher.

Together these results highlight major issues. First, the finding that all data sets contain several distinct data subsets, hence request the combination of several distinct $D_{\max}$–L functions to be adjusted overall, demonstrates that an additional parameter, other than W_{seism} and a constant stress drop, intervenes in the relationship between rupture slip and length (note that this makes that relationship not being strictly speaking a 'scaling law'). Second, the optimal S&S01' functions that are inferred imply variable values of W. Thus, the single crack model does not apply in its simple form. Besides, the range of variation of W is large, while the obtained values are roughly multiple of the lowest. Together these are incompatible with W being the seismogenic thickness. We thus need to admit that W does not represent the width of the seismogenic zone. Rather it is a characteristic length at which slip saturates, to which we will give an interpretation in the following. Finally, the optimal functions that we find also imply variable values of α, thus of stress drop, given by $\Delta\sigma=\mu*(\alpha/2)$ with $\mu=3.10^{10}$ in the original S&S01 interpretation. For instance, when the stress drop is calculated from the inversion model data (total slip values, Fig. F), these variations appear to be quite large, ranging between ~9 and 1 MPa as one goes from optimal functions 1 to 4. Such large variations are incompatible with the constant stress drop hypothesis. This further confirms that the crack model scaling does not apply to earthquakes in its simple form.

4. Interpretation

This led us to seek for a scenario that would retain basic, reasonable ingredients such as the elastic crack behavior and the reality of the seismogenic thickness (W_{seism} ~18 km for our data), while allowing the parameter W in Eq. (1) to take discrete values increasing algebraically. As said before, that fitting parameter W is not W_{seism}, and is unlikely to represent the thickness of anything real for the obtained optimal values do not coincide with any known feature of the Earth structure. We thus hypothesize that W rather is the half rupture length at which slip starts saturating (L_{sat}); we actually observe that slip starts saturating at different lengths along the analyzed ruptures. Some earthquakes would behave as 'simple cracks', having $L_{\text{sat}}=2W_{\text{seism}}$, while some earthquakes would be more complex, with their slip starting to saturate at greater lengths observed to be 2, 3 or 4 times longer than that for a single crack ($L_{\text{sat}}=n*(2W_{\text{seism}})$ with n between 2 and 4). This behavior suggests that those earthquakes are made of several cracks juxtaposed along the rupture strike. This recalls fault segmentation. Indeed, geological faults are segmented, made of a finite number of large-scale segments [26–29]. Note that we are referring here to the segmentation that affects a fault at its largest scale; not to 'slip heterogeneity' on fault planes as commonly described in seismological literature e.g., [30]. The first-order segments that we are evoking thus are of about the same scale than the whole fault they belong to (at most shorter by one order). Generally, only 3–4 such large-scale segments are identified along a fault, independent of its slip mode e.g., [26,27,29,31,32]. As a fault grows with time, linkage between its large-scale segments evolves from 'soft' (i.e., segments are hardly linked) to 'hard' (i.e., segments are fully linked) e.g., [33–36], so that the geometry of the fault zone simplifies and becomes more continuous, more 'through-going' [26,28,37]; inter-segment zones evolve from being wide areas of distributed, disorganized, secondary fissuring and faulting, to becoming narrow zones of localized, through-going faulting. We thus expect the zones that connect the large-scale segments to have an apparent strength that depends on the structural maturity of the overall fault they belong to; high on young, immature faults, and lower on long-lived, mature features [28,29]. Large-scale inter-segment areas may thus behave as more or less 'resistant barriers' to earthquake rupture 'propagation', as has actually been observed in many cases e.g., [21,38–42]. We propose that, depending on the strength of these inter-segment barriers, an earthquake may eventually break a variable number of large-scale segments along the fault on which it initiates. On mature faults, the breakage of a first segment may easily overcome the resistance of the inter-segment barriers, so that it may trigger the cascading rupture of several segments along the fault, resulting in a long, multi-segment rupture. By contrast, on immature faults, the breakage of a first segment is unlikely to overcome the barriers that disorganized, wide inter-segment zones represent, so that only one segment may eventually break, resulting in a short, crack-like rupture. Fig. 3 shows the scenario that we envision. In that scenario, segments have the same length and width (equal to W_{seism} for large earthquakes), while the size of barriers is neglected. Segments behave independently, so that each breaks as an elastic crack. Thus, if only one fault segment breaks, slip starts saturating at $L_{\mathrm{sat}}=2W_{\mathrm{seism}}$. But if the inter-segment barriers are 'weak enough' to allow cascading triggering, two, three or more segments along the fault may break in succession, leading to increase L_{sat} by as many times as there are broken segments (Fig. 3).

5. Facing the model with independent observations

We now test that hypothesis further. A first test consists in facing the actual number of major fault segments broken during earthquakes to the four optimal functions determined earlier (Fig. 4a). We found such information for ~40 earthquakes (details in Table 2). Fig. 4a shows that, overall, earthquakes that have broken one or two major segments pertain to the data subsets that are best fitted by the optimal functions 1 or 2, while earthquakes that have broken 3 to 4 segments pertain to the data subsets that are best fitted by the optimal functions 3 or 4. This is in keeping with the scenario that we propose (Fig. 3).

Another piece of information comes from Manighetti et al. [21]. These authors have studied the generic properties of earthquake slip profiles and shown that these profiles have a self-similar triangular shape that is roughly symmetric when a single major fault segment has been broken, and asymmetric to a various degree

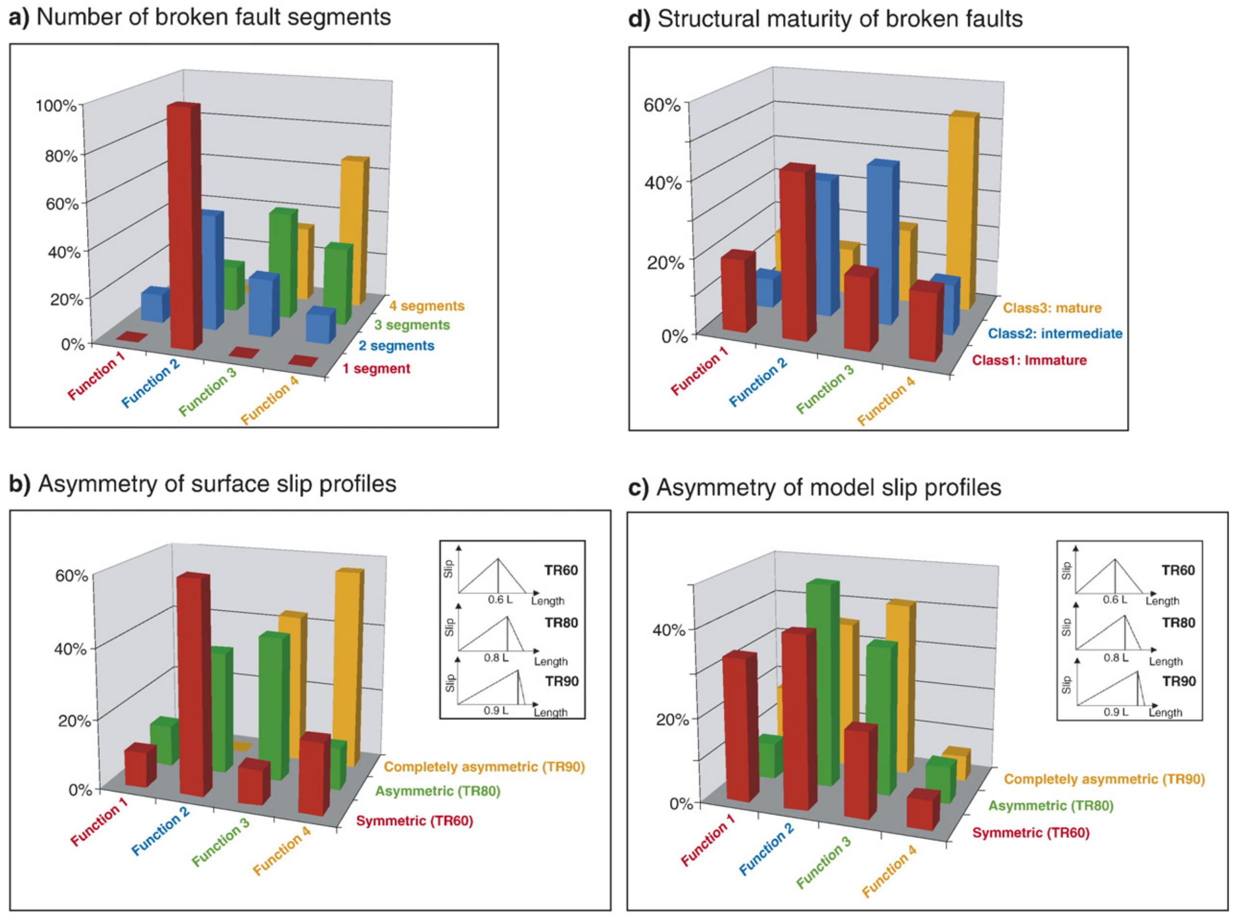
a) Number of broken fault segments

d) Structural maturity of broken faults

b) Asymmetry of surface slip profiles

c) Asymmetry of model slip profiles

Fig. 4. Facing the segmentation scenario with independent data. (a) Number of broken segments as a function of proximity with optimal functions 1 to 4; the number of broken segments is observed to increase as one goes from function 1 to 4. (b) Asymmetry of surface slip profiles (from Table 2; inset recalls the 3 classes of asymmetry depicted by Manighetti et al., 2005) as a function of proximity with optimal functions 1 to 4; asymmetry is observed to increase as one goes from function 1 to 4. (c) Asymmetry of along-strike slip profiles at depth (from Table 3; inset as in b) as a function of proximity with optimal functions 1 to 4; asymmetry is observed to increase as one goes from function 1 to 4. (d) Structural maturity of broken geological faults (from Table 1) as a function of proximity with optimal functions 1 to 4; fault maturity is observed to increase as one goes from function 1 to 4.

a) ALL SURFACE DATA

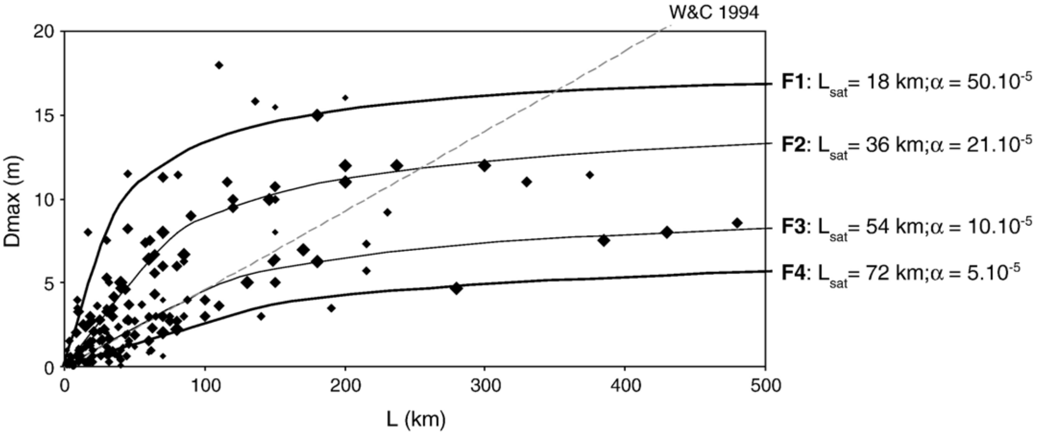

b) ALL MODEL DATA

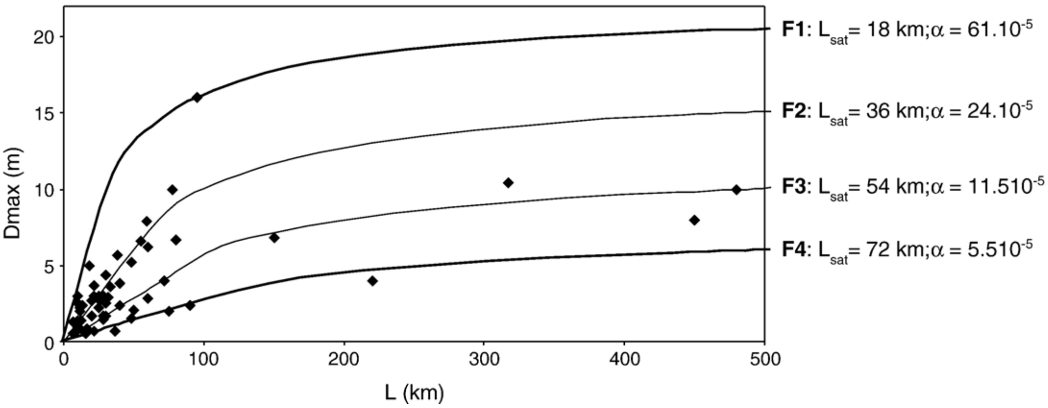

Fig. 5. Modeling the slip-length data. (a) Surface $D_{\max}$–L data (from Table 2). (b) $D_{\max}$–L data inferred at depth (from Table 3). Each global data set is shown with the theoretical functions deduced from the multi-segment rupture model. The regression of Wells and Coppersmith [19] is shown in A for comparison. Apparent stress drops vary from ~9 to 1 MPa as one goes from function 1 to 4 (in b). Yet, actual stress drop on individual crack-like segments only vary from ~9 to 3.5 MPa.

when several segments have been broken; in that later case, the segment with higher slip occupies approximately a third of the total rupture length. Fig. 4b–c report the degrees of asymmetry of ~90 earthquake slip profiles as defined by [21], measured at surface (Fig. 4b) or inferred at depth from inversion models (Fig. 4c). The data are presented with respect to the four optimal functions defined before. Overall, symmetric slip profiles are found for earthquakes pertaining to the data subsets best fitted by the optimal functions 1 or 2, while more asymmetric profiles are found for earthquakes pertaining to the data subsets best fitted by the optimal functions 3 to 4.

We have proposed that the strength of the large-scale inter-segment barriers depends on the structural maturity of the faults to which segments belong, with such barriers being ‘stronger’ on immature faults, and ‘weaker’ on mature faults. Fig. 4d faces the structural maturity (as defined in Table 1) of the faults broken in 140 earthquakes, with the four optimal functions established from surface data. It confirms that overall, earthquakes occurring on immature faults pertain to groups 1 or 2, whereas earthquakes occurring on most mature faults pertain to groups 3 or 4.

6. Discussion and conclusions

Different pieces of evidence thus converge to suggest that the scenario proposed in Fig. 3 represents a valuable basis to interpret the earthquake D–L relationships. An earthquake would break a variable, yet limited number of major segments (or major ‘asperities’) along a fault, depending on whether or not the breakage of the very first segment is 'energetic' enough to overcome the strength of the first encountered major inter-segment barrier, and trigger the rupture of the neighboring major segment(s). That capability of breaking inter-segment barriers would depend on the fault structural maturity; mature faults would be more prone to break in cascading events for their inter-segment barriers are quite narrow and smoothed, whereas more immature faults would more likely break in a single or double event for their inter-segment zones represent much stronger barriers to rupture propagation. The variability in displacement-length earthquake data would result from that multiple event rupturing process. Earthquakes breaking a single segment would behave as a single elastic crack with slip starting to saturate at $L=2W_{\mathrm{seism}}$, while earthquakes breaking several segments would behave as a juxtaposition of several cracks. As a consequence, the minimum rupture size at which slip starts saturating is different from one earthquake to the other, yet in the form $L_{\mathrm{sat}}=n*(2W_{\mathrm{seism}})$ with n the number of broken segments when those are assumed to be similar in length. Intermediate situations with segments of different lengths are likely to exist and result in the scatter of the data points in each subset (in addition to stress drop variability). Yet, it is noteworthy that a model with L_{sat} being multiple of the seismogenic thickness is actually most required by the data. Fig. 5 faces the available $D_{\max}$–L data (surface: Fig. 5a; depth: Fig. 5b) to that theoretical model (defined for $W_{\mathrm{seism}}=18$ km). The adjustment is satisfying: the standard deviation of the residuals $\log(D_{\mathrm{obs}})$–$\log(D_{\mathrm{predicted}})$ calculated as in [19] is only 0.18. The stress drop variations that are suggested by the α variations are not as large as it seems when neglecting segmentation. Indeed, for a data subset corresponding to a n-segment rupture, the stress drop on each segment is $\Delta\sigma=n*\mu*(\alpha/2)$. The inferred stress drops are actually about the same on all broken segments, on the order of 3.5–9 MPa (calculated from inversion model data which are more characteristic of the ruptures at depth; Fig. 5b). The few MPa difference that is still observed obviously depends on fault structural maturity (Fig. 4d); segments on mature, hence weakened faults break in lower stress drop-earthquakes than segments on immature faults, as has been suggested before e.g., [22,29,37]. Note that we verified that this variation in apparent stress drop is not related with the effect of the finite size of the barriers between ruptured segments. Whatever that size (in a realistic range), a change in stress drop is required. The data suggest stress drops ranging from ~9 MPa for single segment-events on immature faults, to ~3.5 MPa for 4 segment-events on mature faults (Fig. 5b). We thus broaden the conclusions of Cao and Aki (1986) and Anderson et al. (1996), stating that fault structural maturity is a major factor, if not the most important, that governs the stress drop of earthquakes, hence the amplitude of ground motions. Careful geological analyses of long-term faults should thus be included in any seismic hazard study. Fig. 5 shows that the maximum length of earthquakes is ~200 km for group 1, ~400 km for group 2, ~500 km for group 3, suggesting that major segments along worldwide faults are ~200 km-long. Together with the observation that stress-drop and segmentation are related, this explains why $D_{\max}$ tends to decrease with total length for large events as pointed out by [30].

Our reappraisal of displacement-length earthquake data has important implications on seismic hazard assessment. First, depending on their structural maturity, faults of similar length may produce significantly different amounts of slip; mature faults obviously break in long ruptures with low slip amplitudes (<4–7 m). By contrast, more immature faults break in shorter, yet more 'energetic' ruptures, on which slip as high as 15 m may be expected.

On the other hand, when one calculates the ratio between maximum slip measured at surface and maximum slip inferred at depth, that one finds that surface slip generally is only a fraction of actual slip at depth, averaging 85% for most large strike–slip ruptures ($M\geq6.5$), 40% for small ($\sim6\leq M<6.5$) strike–slip, reverse and normal earthquakes, and even less than 10% for a few other cases (Fig. G, supporting online material). This suggests that surface measurements of slip cannot be used to calculate an earthquake magnitude unless they are 'corrected' by a certain factor.

Finally, our refined D–L earthquake 'scaling laws' are more accurate than those available (see in Fig. 5a a comparison with regression from Wells and Coppersmith, 1994; later referred to as W&C). We have calculated the standard deviation of the residuals $\log(D_{\mathrm{obs}})$–$\log(D_{\mathrm{predicted}})$ for our data set, using the W&C empirical relation $\log(D_{\mathrm{predicted}})=-1.38+1.02\log(L)$. The standard deviation that we obtain is equal to 0.41, a value similar to the one obtained in the original paper of W&C from a smaller data set. Table 4 (supporting online material) indicates however that the residuals obtained with the W&C relation show a clear bias with earthquake size; the W&C model overestimates slip amplitudes for earthquakes with lengths greater than 200 km (see also Fig. 5a). To further compare our regressions with that of W&C, we have also calculated the residuals that would arise from fitting our entire data set with one single optimal S&S01 relation (that is found to have $W=54.7$ km and $\alpha=12.4\ 10^{-5}$). The variance is similar to the one obtained when using the W&C relation ($\sigma = 0.41$), but the residuals do not exhibit any bias with earthquake size. The residuals also approximately follow a log-normal distribution (Fig. H, supporting online material).

The standard deviation of the residuals obtained when using our best-fitting model with four curves is 0.18 when the entire data set is considered. For the best constrained Asian data set whose modeling requires only three curves, the standard deviation keeps as low (0.17). We checked that this decrease in standard deviation is not an 'artefact' due to the introduction of a too large number of parameters (over-fitting). This was done by computing the Akaike Information Criterion AIC; [43]. This criterion determines the balance between the model improvement and the number of free parameters that contribute to that improvement (increasing the number of free parameters always improves the fit). We computed the AIC for models with n curves and verified that that criterion is decreasing continuously with n, for n between 1 and 4. This test shows that our 4 curve-model significantly improves the residuals without over-fitting. This confirms the potential interest of modelling earthquake slip-length data with a multiple event-model of the form we propose.

In hazard studies where a critical issue is to reduce the uncertainties on seismic hazard assessment e.g. [44], our study may thus have some impact since it produces residues that are twice lower than those associated with available D–L regressions [19]. Our predictive $D_{\max}$–L functions could be used as distinct branches of a logic tree e.g., [45], each with an reduced aleatory variability compared to classical models. Weight assigned to each branch would depend on fault structural maturity (epistemic uncertainty). We are now in the process of refining the 'maturity criteria', so that more accurate functions may be established between earthquake slip and length, and fault structural maturity.

Acknowledgements

We thank M. Cocco, R. van der Hilst and an anonymous reviewer for their comments that helped improving the paper. We thank Y. Delaby, B. Valette and N.A. Abrahamson for their useful suggestions for the data processing.

Appendix A. Supplementary data

Supplementary data associated with this article can be found, in the online version, at doi:10.1016/j.epsl.2006.11.004.

References

[1] K. Aki, Tectonophysics 13 (1972) 423.
[2] H. Kanamori, D.L. Anderson, Bull. Seismol. Soc. Am. 65 (1975) 1073.
[3] J.N. Brune, Seismic Risk and Engineering Decisions, 1976, p. 140.
[4] R. Madariaga, Bull. Seismol. Soc. Am. 66 (1976) 636.
[5] H. Kanamori, E.E. Brodsky, Rep. Prog. Phys. 67 (2004) 1429.
[6] C. Scholz, Bull. Seismol. Soc. Am. 72 (1982) 1.
[7] B. Romanowicz, Geophys. Res. Lett. 19 (1992) 481.
[8] B. Romanowicz, J. Rundle, Bull. Seismol. Soc. Am. 83 (1993) 1294.
[9] C. Scholz, Bull. Seismol. Soc. Am. 84 (1994) 215.
[10] C. Scholz, Bull. Seismol. Soc. Am. 84 (1994) 1677.
[11] B. Romanowicz, Bull. Seismol. Soc. Am. 84 (1994) 1675.
[12] P. Bodin, J.N. Brune, Bull. Seismol. Soc. Am. 86 (1996) 1292.
[13] J.H. Wang, S.S. Ou, Bull. Seismol. Soc. Am. 88 (1998) 758.
[14] T.C. Hanks, W.H. Bakun, Bull. Seismol. Soc. Am. 92 (2002) 1841.
[15] P.M. Mai, G.C. Beroza, Bull. Seismol. Soc. Am. 90 (2000) 604.
[16] B.E. Shaw, C.H. Scholz, Geophys. Res. Lett. 28 (2001) 2991.
[17] B. Romanowicz, L.J. Ruff, Geophys. Res. Lett. 29 (2002) 12.
[18] C. Scholz, C.A. Aviles, S.G. Wesnousky, Bull. Seismol. Soc. Am. 76 (1986) 65.
[19] D.L. Wells, K.J. Coppersmith, Bull. Seismol. Soc. Am. 84 (1994) 974.
[20] D.J. Dowrick, D.A. Rhoades, Bull. Seismol. Soc. Am. 94 (2004) 776.
[21] I. Manighetti, M. Campillo, C. Sammis, M. Mai, G. King, J. Geophys. Res. 110 (2005) B05302.
[22] T. Cao, K. Aki, Pure Appl. Geophys. 124 (1986) 515.
[23] J.G. Anderson, S.G. Wesnousky, M.W. Stirling, Bull. Seismol. Soc. Am. 86 (1996) 683.
[24] C. Marone, Annu. Rev. Earth Planet. Sci. 26 (1998) 643.
[25] S.A. Miller, Geophys. Res. Lett. 29 (2002), doi:10.1029/2001GL014181.
[26] M. Stirling, S.G. Wesnousky, K. Shimazaki, Geophys. J. Int. 124 (1996) 833.
[27] I. Manighetti, G.C.P. King, Y. Gaudemer, C. Scholz, C. Doubre, J. Geophys. Res. 106 (2001) 13667.
[28] Y. Ben-Zion, C.G. Sammis, Pure Appl. Geophys. 160 (2003) 677.
[29] K. Otsuki, T. Dilov, J. Geophys. Res. 110 (2005), doi:10.1029/2004JB003359.
[30] J. Liu-Zeng, T. Heaton, C. DiCaprio, Geophys. J. Int. 162 (2005) 841.
[31] D.P. Schwartz, K.J. Coppersmith, J. Geophys. Res. 89 (1984) 5681.
[32] L.J. An, C.G. Sammis, Tectonophysics 253 (1996) 247.
[33] B. Trudgill, J. Cartwright, GSA Bull. 106 (1994) 1143.
[34] J.J. Walsh, J. Watterson, W.R. Bailey, C. Childs, J. Struct. Geol. 21 (1999) 1019.
[35] M.J. Young, R.L. Gawthorpe, S. Hardy, J. Struct. Geol. 23 (2003) 1933.
[36] N.J. Richardson, J.R. Underhill, G. Lewis, Basin Res. 17 (2005) 203.
[37] S.G. Wesnousky, Nature 335 (1988) 340.
[38] K. Aki, J. Geophys. Res. 84 (1979) 6140.
[39] G. King, J. Nabelek, Science 228 (1985) 984.
[40] R.H. Sibson, Nature 316 (1985) 248.
[41] R.A. Harris, S.M. Day, J. Geophys. Res. 98 (1993) 4461.
[42] R.A. Harris, S.M. Day, Geophys. Res. Lett. 26 (1999) 2089.
[43] H. Akaike, IEEE Trans. Automat. Control 19 (1974) 716–723.
[44] F. Scherbaum, J. Bommer, H. Bungum, F. Cotton, N.A. Abrahamson, Bull. Seismol. Soc. Am. 95 (2005) 1575.
[45] J. Bommer, F. Scherbaum, H. Bungum, F. Cotton, F. Sabetta, N.A. Abrahamson, Bull. Seismol. Soc Am. 95 (2005) 377.

JOURNAL OF GEOPHYSICAL RESEARCH, VOL. 110, B05302, doi:10.1029/2004JB003174, 2005

Evidence for self-similar, triangular slip distributions on earthquakes: Implications for earthquake and fault mechanics

I. Manighetti,[1,2] M. Campillo,[3] C. Sammis,[1] P. M. Mai,[4] and G. King[5]

Received 12 May 2004; revised 26 January 2005; accepted 8 February 2005; published 13 May 2005.

[1] We characterize average slip distributions on earthquakes beyond their individual heterogeneity. For that, we analyze a large number of seismic slip distributions both measured at the surface after earthquakes (44 profiles) and derived from slip inversion models (76 models). Investigating the overall shape of these slip profiles, we find that they are roughly triangular both along strike and dip, and most of them (70–80%) are asymmetric. Long linear slopes and high slip gradients therefore are the key ingredients to describe earthquake slip profiles. The scaling relations between maximum displacement and length (or width) suggest furthermore that the triangular slip profiles are self-similar. Such slip patterns make earthquakes dominated by one major zone of maximum slip hence one major "asperity." Analyzing the position of hypocenters with respect to these "asperities," we find that earthquakes nucleate at a distance from them that averages 20–30% of their total length. Compiling observations on 56 earthquakes, we show that this distance (i.e., the asperity size) is structurally defined. We then compare the earthquake slip profiles to cumulative slip profiles measured on long-term faults of various ages and sizes and find that all profiles have a similar shape, triangular and asymmetric. Hence combining data for a large number of earthquakes leads to point out average, generic characteristics of the coseismic slip that are similar to those that emerge from the accumulation of events with time on a single fault. This suggests that these characteristics result from robust physical properties.

Citation: Manighetti, I., M. Campillo, C. Sammis, P. M. Mai, and G. King (2005), Evidence for self-similar, triangular slip distributions on earthquakes: Implications for earthquake and fault mechanics, *J. Geophys. Res.*, *110*, B05302, doi:10.1029/2004JB003174.

1. Introduction

[2] Our long-term objective is to understand further the processes of earthquakes and fault growth and how they are related. Faults grow through the addition of earthquakes (sometimes associated with creep). This process is not well understood, however, as it cannot be directly observed. Seismic (instantaneous) and cumulative (long term) slip distributions on faults represent two different stages of this process. Recognizing the similarities and differences between these two stages may help to understand better the process of fault growth, i.e., the way earthquakes follow in space and time to make a fault accumulate more slip and lengthen. Here, we address a series of simple questions: Do slip distributions on earthquake faults share any common characteristics? Do they resemble those on long-term faults? Do they provide information on earthquake and fault mechanics?

[3] Cracks in an elastic body have been widely used as a framework to characterize earthquakes with concepts such as stress drop and self-similarity. A first-order implication of this model is that its homogeneous conditions produce elliptical slip distributions on earthquake faults (although it is rarely mentioned that way). Introducing local dissipation at the crack tips make these slip distributions terminating with short tapers, however (so-called "tip tapers" [see *Scholz*, 2002]). In the last 20 years, many studies have combined different data sets acquired during or right after an earthquake to infer (through an inversion procedure) the slip distribution on the rupture plane [e.g., *Hartzell and Heaton*,1983; *Kikuchi and Fukao*, 1985; *Beroza and Spudich*, 1988; *Das and Kostrov*, 1990; *Cotton and Campillo*, 1995]. Hundreds of slip models have been produced (see supporting material[1] (files ES01–ES08)

---

[1] Department of Earth Sciences, University of Southern California, Los Angeles, California, USA.

[2] Now at Laboratoire de Géophysique Interne et Tectonophysique de Grenoble, Grenoble, France.

[3] Laboratoire de Géophysique Interne et Tectonophysique de Grenoble, Grenoble, France.

[4] Institute of Geophysics, ETH-Zurich, Zurich, Switzerland.

[5] Laboratoire de Tectonique, Institut de Physique du Globe de Paris, Paris, France.

0148-0227/05/2004JB003174$09.00

[1] Auxiliary material is available at ftp://ftp.agu.org/apend/jb/2004JB003174.

ES07 for references), each imaging the slip distribution on an earthquake fault. They revealed highly heterogeneous slip distributions, with patches of high slip separated by zones of low to zero slip. Yet, the studies that tried to compare these slip distributions were rare. *Somerville et al.* [1999] and *Mai and Beroza* [2002] did so, but they mainly focused on characterizing the earthquake slip complexity. The overall slip distribution patterns were not considered. In the mean time, surface measurements of seismic slip have accumulated. Many studies used these measurements to seek constraining specific scaling laws for earthquakes [e.g., *Wells and Coppersmith*, 1994; *Shaw and Scholz*, 2001, and references therein]. Studies devoted in the characterization of the slip distributions were rare. Using a few slip profiles, *Sieh* [1996] showed that the slip function could repeat similarly on some faults, but he did not examine these functions in further detail. *Hemphill-Haley and Wealdon* [1999] combined several slip profiles to develop a method for estimating the magnitude of prehistoric earthquakes, but they did not consider their overall shapes either. *Ward* [1997] did pay attention to shape but on the basis of one slip profile only. *Zhang et al.* [1999] analyzed several seismic slip profiles, but they only looked at their termination.

[4] Hence the questions related to the average shape of earthquake slip distributions are still opened. The available amount of data is now large enough to address them. Our approach emphasizes observations. Because earthquake studies lie at the boundary between seismology and tectonics, we combine observations and visions from these two domains. Our aim is to characterize average slip distributions on earthquakes beyond their individual heterogeneity. We use two types of data. First, we compiled (from literature) a large number of slip measurements performed at the surface after earthquakes. Some of these measurements are dense enough to show how slip varies along the whole rupture length. Some others were only done on specific sections of the ruptures (commonly, along major segments within ruptures). Some only consist of maximum displacement-length data. Taken together, however, these measurements allow distribution of surface slip along faults to be examined. Second, to know how total slip varies on entire fault planes, we analyze the slip distribution for 76 slip inversion models whose data have been compiled by P. M. Mai (2004, http://www.seismo.ethz.ch/srcmod). The profiles of maximum and mean slip that we extract from these models allow total slip variations along both fault strike and dip to be studied. We follow the general idea that analyzing many earthquakes together provides a way of smoothing their individual peculiarities (such as specific slip complexities), so that common, general properties, if any, may emerge. With this idea in mind, we successively analyze the overall shape of the slip profiles on earthquake faults, the position of hypocenters with respect to these slip distribution patterns, and the displacement length and width scaling relations for the available earthquakes. In each case, we find some general properties. Another idea is that cumulative slip distributions on long-term faults and systems, which result from the addition of a large number of earthquakes, give an over time-averaged image of earthquakes. Hence general properties of slip distributions should emerge in these cumulative slip distributions as well. We therefore compare our observations on earthquakes to those performed on cumulative faults and systems of various sizes and ages (10^4-10^6 years). This points out similar general properties. We end up discussing the implications of our results for earthquake and fault mechanics.

2. Data Sets

2.1. Surface Measurements of Seismic Slip

[5] From literature, we digitized 23 complete surface slip profiles (i.e., measured along whole length of earthquake rupture) and 20 partial profiles measured along segments within ruptures (Table 1). The retrieved data points have different spacing and precision, depending both on the original spacing and precision of the measurements and on the digitizing process. The corresponding earthquakes are spread worldwide and show various focal mechanisms and magnitudes (6.2–8.3, Table 1). We compiled most of the literature on these earthquakes and compared the various data acquired for each of them. In a few cases (indicated in Table 1), the surface rupture traces were found to extend slightly beyond the length (L_{meas}) along which slip had been measured (because slip at rupture tips is small and difficult to measure). In those cases, we added a point of zero slip to the available slip profiles where the ruptures were observed to actually end (see ES01 for details). The resulting rupture length is called L_{obs} (Table 1).

[6] While many earthquakes break the surface, most of them have no measured slip profile. At best, only their length and maximum slip have been measured. ES02 lists the earthquakes for which we found such measurements.

2.2. Two-Dimensional Earthquake Slip Inversion Models

2.2.1. Slip Models Deduced From Near-Field Data

[7] We use 76 published finite source rupture models that have been compiled by P. M. Mai (2004, http://www.seismo.ethz.ch/srcmod) (Table 2). The large majority are near-field inversion models. They image the overall slip distribution on 43 earthquake fault planes. These earthquakes are distributed worldwide and have various focal mechanisms (mostly strike slip, 45%; mostly dip slip, 55%), and magnitudes (M_w 5.5–8.0).

[8] The slip models were obtained using different data sources (geodetic, strong motion, teleseismic, local P waves, interferometric synthetic aperture radar, or, in best cases, a combination of two or more), inversion techniques, crustal models, methods to stabilize the inversion, and spatial sampling (see *Mai and Beroza* [2002] for details). They are therefore all quite different, and their relative “accuracy” is difficult to estimate. We consequently compare them using only their most basic attributes, i.e., data sources (number, location, quality, nature; Table 2, “data” values), their agreement with complementary observations (surface rupture geometry, distribution of immediate, on-fault aftershocks, etc; see ES01), their agreement with other models generated for the same earthquakes. The models that we eventually regard as being “best constrained” from these considerations are indicated in Table 2.

[9] In order to facilitate their comparison, the models were bilinearly interpolated onto 1 × 1 km grid spacing, so that large differences in spatial sampling could be smoothed

Table 1. Surface Data With Measured Slip Profile[a]

Earthquake	Event	Comments	Date	Kin	Mag	Main References	D_{max}	L_{meas}	L_{obs}
Entire Ruptures									
AL-Denali	S08		11/3/02	SS	7.9	*Eberhart-Philipps et al.* [2003]	9	340	340
AS-Kunlun	S27		11/14/01	SS	8.1	*Lin et al.* [2002]	16.3	400	400
AS-Manyi	S35		11/8/97	SS	7.6	*Peltzer et al.* [1999]	7	170	170
BR-Borah Peak	S03		10/28/83	N + SS	7.3	*Crone and Machette* [1984]	2.7	34	34
BR-Dixie Valley	S44		12/16/54	N	6.8	*Caskey and Wesnousky* [1997]	2.6	46	46
BR-Hebgen Lake	S19		8/17/59	N	7.5	*Zhang et al.* [1999]	5.6	26	26
BR-Pleasant Valley	S45		10/3/15	N + SS	7.7	*Zhang et al.* [1999]	5.8	60	60
IR-Fandoqa	S13		3/14/98	SS + N	6.6	*Berberian et al.* [2001]	3	25	25
IV-Borrego Mountain	S04		4/9/68	SS	6.6	*Wells and Coppersmith* [1994]	0.38	32	32
IV-Imperial Valley	S23		10/15/79	SS	6.6	*Sharp* [1982]	0.75	32	32
IV-Superstition Hill	S47		11/24/87	SS	6.6	*Sharp et al.* [1989]	0.52	25	25
L-Hector Mine	S22		10/16/99	SS	7.1	*Jonsson et al.* [2002]	6.4	60	60
L-Landers[b]	S33		6/28/92	SS	7.3	*Hernandez et al.* [1999] and *Sieh et al.* [1993]	6.7	71	85
PH-Luzon	S34		7/16/90	SS	7.7	*Velasco et al.* [1996]	6.2	130	130
SA-Fort Tejon	S14		1857	SS	7.8	*Hemphill-Haley and Weldon* [1999]	9.5	330	330
SA-San Francisco	S38		1906	SS	8.3	*Thatcher et al.* [1997]	8.6	480	480
TA-Chi Chi[b]	S05	DS motion	9/21/99	R + SS	7.7	*Dominguez et al.* [2003]	7.4	65	80
TA-Chi Chi	S06	SS motion	9/21/99	R + SS	7.7	*Dominguez et al.* [2003]	8.4	65	80
TU-Anatol Sequence	S01		1939–1967	SS		*Barka* [1996]	7.5	840	840
TU-Bolu Gerede	S02		2/1/44	SS	7.3	*Barka* [1996]	3.5	180	180
TU-Duzce	S46		11/12/99	SS	7.2	*Akyuz et al.* [2002]	4.8	40	40
TU-Erzincan	S10		12/26/39	SS	7.9	*Barka* [1996]	7.5	360	360
TU-Mudurnu	S36		7/22/67	SS	7.1	*Barka* [1996]	2	80	80
TU-Tosya	S41		11/26/43	SS	7.3	*Barka* [1996]	4.5	280	280
Segments									
AS-Fuyun[b]	S15	Main ST N	1931	SS	?	*Deng and Zang* [1984]	14.6	60	90
BR-Dixie Valley	S43	Main ST N	12/16/54	N	6.8	*Caskey and Wesnousky* [1997]	2.6	36	36
BR-Dixie Valley	S42	ST very N	12/16/54	N	6.8	*Caskey and Wesnousky* [1997]	2.45	24	24
BR-Dixie Valley	S48	ST S	12/16/54	N	6.8	*Caskey and Wesnousky* [1997]	0.63	7.5	7.5
BR-Fairview Peak	S12	Main ST S	12/16/54	N	7.1	*Caskey et al.* [1996]	3.8	19	19
BR-Fairview Peak	S11	GoldKing N	12/16/54	N	7.1	*Caskey et al.* [1996]	1	12.5	12.5
BR-Pleasant Valley	S37	Main ST S	10/3/15	N + SS	7.7	*Zhang et al.* [1999]	5.8	38	38
IR-Dasht e Bayaz[b]	S07	ST Nimbluk	8/31/68	SS	7.2	*Tchalenko and Berberian* [1975]	4.6	25	34
IV-Elmore Ranch	S09	ST ERF W	11/24/87	SS	6.2	*Hudnut et al.* [1989]	0.13	8	8
IV-Superstition Hill	S39	ST N	11/24/87	SS	6.6	*Sharp et al.* [1989]	0.52	15	15
IV-Superstition Hill	S40	ST S	11/24/87	SS	6.6	*Sharp et al.* [1989]	0.46	13.2	13.2
L-Hector Mine	S20	ST C-S	10/16/99	SS	7.1	*Jonsson et al.* [2002]	6.4	44	44
L-Hector Mine	S21	ST N	10/16/99	SS	7.1	*Jonsson et al.* [2002]	3.5	16	16
L-Landers	S28	ST CAMPROCK	6/28/92	SS	7.3	*Sieh* [1996]	1.2	7	7
L-Landers	S29	ST EMERSON	6/28/92	SS	7.3	*McGill and Rubin* [1999]	6	32	32
L-Landers	S30	ST ES2	6/28/92	SS	7.3	*Zachariasen and Sieh* [1995]	1.47	1.8	1.8
L-Landers	S31	ST ES3	6/28/92	SS	7.3	*Zachariasen and Sieh* [1995]	0.7	1.35	1.35
(L-Landers)	S32	ST Eureka	postslip	SS	7.3	*Peltzer et al.* [1994]	0.15	12.5	12.5
TU-Izmit[b]	S26	Main ST W (S2)	8/17/99	SS	7.4	*Michel and Avouac* [2002]	5.5	70	90
TU-Izmit + Duzce	S25	Main ST E (S3)	8/17and11/12/99	SS	7.4	*Hartleb et al.* [2002] and *Akyuz et al.* [2002]	4.8	68	68
TU-Izmit	S24	ST Sapanca	8/17/99	SS	7.4	*Barka et al.* [2002]	5	27	27

[a] Earthquakes with surface slip profiles analyzed, along entire rupture length and along segments within ruptures. Earthquakes are classified by regions (AL, Alaska; AS, Asia (China and Mongolia); BR, Basin and Range; IR, Iran; IV, Imperial Valley fault system; L, Landers fault system; PH, Philippines; SA, San Andreas fault system; TA, Taiwan; TU, Turkey). Chi-Chi has two profiles, for its lateral and dip-slip motions. Eureka (in parentheses) is only considered in scaling relations. ST, segment; DS, dip slip; SS, strike slip; N, S, W, E, C, north, south, west, east, and center, respectively; S2–S3 (Izmit-Duzce) defined in ES08. Kin, kinematics; SS, strike slip; N, normal; R, reverse. Mag, magnitude is that of corresponding earthquake. D_{max} and L_{meas} are maximum displacement (in m) and rupture length (in km) measured at surface, respectively; L_{obs} is total rupture length at surface, in km.

[b] Earthquakes with $L_{obs} > L_{mes}$ (see ES01).

(see *Mai and Beroza* [2002] for details). This interpolation process added some slip data to the original models. While this lets the overall slip distribution patterns unchanged, it modifies the values of maximum and mean displacements on the ruptures (dubbed D_{maxI} and D_{meanI}, respectively; Table 2). As these modifications are substantial (~10 and 27% for D_{max} and D_{mean}, respectively), we use the original data in our analysis of scaling relations (section 3.3). By contrast, we use the interpolated models in our analysis of slip profile shapes (section 3.1).

[10] The dimensions of the rupture planes used in the models (L_{model}, W_{model}) are generally chosen to be larger than the actual ones to ensure that the entire rupture is imaged. This makes most models having portions of low (often zero) or artifact slip at or close to their edges. Our first step was therefore to remove these artifacts and retrieve the actual length and width of the faults (L_{obs}, W_{obs}, Table 2). So far, this problem has been handled using statistical, systematic treatments. *Somerville et al.* [1999] systematically removed from all models that they analyzed any row or column whose mean slip was less than an arbitrary fraction of the mean slip for the entire model. *Mai and Beroza* [2000] instead used an autocorrelation method that led them to define an effective length at which zones of zero (or small)

Table 2. Models With Tabular Data Analyzed[a]

Earthquake	Event	Date	Kin	Mag	References	Data	L_{model}	L_{obs}	W_{model}	W_{obs}	D_{max}	D_{maxI}	D_{mean}	D_{meanI}	H
Antarctic-main^{b}	59	3/25/98	SS	7.93	*Antolik et al.* [2000]	T	300	280	29	15	35.2	39.5	3	4.4	12
Antarctic-second^{b}	60	3/25/98	N	6.2	*Antolik et al.* [2000]	T	70	70	27.2	15	21.1	22.8	2.8	3.2	12
Borah Peak^{b,c}	16	10/28/83	N-LL	7.3	*Mendoza and Hartzell* [1988]	T	52	52	26	26	1.47	1.56	0.36	0.44	20
Central Chile^{d,e}	20	3/3/85	R	8	*Mendoza et al.* [1994]	LS + SM + T	255	255	165	130	3.3	3.84	0.79	1.05	40
Chi-Chi^{b,c}	73	9/21/99	R-LL	7.68	*Chi et al.* [2001]	SM	112	90	45.5	37	24.3	28.9	2.42	4.62	16
Chi-Chi^{b,c}	74	9/21/99	R-LL	7.66	*Johnson et al.* [2001]	G	104	73	29	29	11.2	14.4	3.35	4.78	
Chi-Chi^{b,c,f}	75	9/21/99	R-LL	7.68	*Ma et al.* [2001]	G + SM + T	80	80	45	45	15.5	20.7	3.6	5.72	17.6
Chi-Ch^{c,d}	76	9/21/99	R-LL	7.62	*Zhang et al.* [2003]	SM	78	60	39	39	8.8	8.8	3	2.8	14
Chi-Chi^{b,c,e}	77	9/21/99	R-LL	7.72	*Wu et al.* [2001]	G + SM	85	85	49	49	25.2	25.2	3.06	3.06	7.5
Chi-Chi^{c,d}	78	9/21/99	R-LL	7.74	*Zeng and Anderson* [2000]	HF	84	84	42	42	4.59	6.71	0.64	2.96	14.5
Colima-Jalisco^{b,e}	53	10/9/95	R	8	*Mendoza and Hartzell* [1999]	T	200	175	100	75	4.77	5.3	1.18	1.32	57.3
Coyote Valley	10	8/6/79	SS	5.69	*Liu and Helmberger* [1983]	SM	10	7	10	7	1.2	1.25	0.26	0.3	8
Duzce^{b,c,e}	83	11/12/99	SS	7.21	*Delouis et al.* [2001]	R + T + Su	60	45	30	30	8	10.9	1.12	2.15	12.5
Duzce^{b,c} (in event 70)	85	11/12/99	SS	7.1	*Delouis et al.* [2002]	G + R + SM + Su + T	65	60	22.5	22.5	6.8	8.8	1.27	2.16	13
Elmore Ranch^{b,c}	28	11/24/87	SS	6.25	*Larsen et al.* [1992]	G	26	26	10	10	2.71	2.9	0.88	1.03	
Gifuken-Chubu^{d}	03	9/9/69	SS	6.41	*Takeo* [1990]	SM	19	19	10	10	1.7	1.87	0.68	0.75	1.4
Hector Mine^{b,c,f}	80	10/16/99	SS	7.22	*Ji et al.* [2002]	G + SM + Su + T	54	54	16	16	8.2	8.9	2.35	2.35	14.8
Hector Mine^{c,d}	81	10/16/99	SS	7.22	*Kavarina et al.* [2002]	G + LS + R + Su + T	68	50	24	17	6.34	6.81	1.37	1.76	6
Hector Mine^{b,c}	82	10/16/99	SS	7.16	*Salichon et al.* [2003]	G + R + T + Su	54	54	18	18	9.46	10.1	1.81	1.99	7.5
Huyga Nada 1^{b}	54	10/19/96	R	6.8	*Yagi et al.* [1999]	G + SM	32	18	32	26	2.92	2.95	0.54	0.49	15
Huyga Nada 2^{b}	55	12/2/96	R	6.7	*Yagi et al.* [1999]	G + SM	29	18	29	20	1.65	1.67	0.42	0.38	21
Imperial Valley^{c,g}	11	10/15/79	SS	6.53	*Archuleta* [1984]	SM	35	35	13	10	1.78	1.75	0.46	0.47	8.5
Imperial Valley^{b,c,e}	12	10/15/79	SS	6.62	*Hartzell and Heaton* [1983]	SM + T	42	42	10.5	10.5	1.8	2.05	0.59	0.62	10
Imperial Valley^{b,c}	13	10/15/79	SS	6.47	*Zeng and Anderson* [2000]	HF	42	37	9	9	2.21	2.15	0.27	0.3	8
Izmit-S1S2^{c,d,e}	68	8/17/99	SS	7.61	*Bouchon et al.* [2002]	SM	135	130	20	20	8.07	7.67	3.3	3.03	17
Izmit-S1S2^{c,g}	69	8/17/99	SS	7.53	*Feigl et al.* [2002]	G + R + Su	128	143	21	21	5.65	6.23	2.07		15
Izmit-S1S2^{b,c,d,f}	70	8/17/99	SS	7.4	*Delouis et al.* [2002]	G + R + SM + Su + T	105	135	22.5	22.5	8	10			13
Izmit-S1S2^{c}	71	8/17/99	SS	7.41	*Segiguchi and Iwata* [2002]	SM	141	140	23.3	23.3	7.17	7.8	1.35	1.9	16
Izmit-S1S2^{c,g}	72	8/17/99	SS	7.38	*Yagi and Kikuchi* [2000]	SM + T	93.6	138	21.6	21.6	6.31	6.23	2.24	1.96	16
(Izmit + Duzce)^{c}	69	8/17/99	SS	7.53	*Feigl et al.* [2002]	G + R + Su	165	180	21	21	5.65	6.23	1.8	1.75	15
(Izmit + Duzce)^{c}	70	8/17/99	SS	7.57	*Delouis et al.* [2002]	G + R + SM + Su + T	172	200	22.5	22.5	8	10	1.85	2.64	13
Izu-Hanto-Oki^{b}	05	5/9/74	SS	6.54	*Takeo* [1990]	SM	25	25	8	8	3	3.1	1.06	1.08	7.5
Izu-Hanto-Oki^{g}	14	6/29/80	SS	6.55	*Takeo* [1988]	SM	19	19	11	11	2.7	2.92	1.06	1.1	7.5
Joshua Tree	36	4/23/92	SS	6.25	*Bennett et al.* [1995]	G	35	30	20	19	0.84	0.84	0.11	0.11	15
Joshua Tree^{b}	37	4/23/92	SS	6.14	*Hough and Dreger* [1995]	T	22	15	20	15	2.05	2.05	0.12	0.12	12.5
Kanto^{c,d}	01	1/9/23	R-RL	7.82	*Wald and Somerville* [1995]	G + T	130	130	70	50	5.2	5.46	1.81	1.8	14.6
Kitamino^{b}	02	8/19/61	R	6.47	*Takeo* [1990]	SM	15	15	11	11	1.6	1.81	0.9	0.74	6
Kobe^{b}	48	1/17/95	SS	6.86	*Ide et al.* [1996]	SM	50	50	19	19	2.8	1.79		0.61	14.5
Kobe^{d,f}	49	1/17/95	SS	6.74	*Sekiguchi et al.* [1996]	SM	64	55	19	19	3.11	3.06	0.73	0.67	16.4
Kobe^{d}	50	1/17/95	SS	6.91	*Yoshida et al.* [1996]	G + LS + T	60	60	17	17	3.3	2.74	0.68	0.89	17
Kobe^{b,e}	51	1/17/95	SS	6.91	*Wald* [1996]	G + SM + T	60	60	16	16	2.42	3.74	0.78	0.73	15
Kobe^{b}	52	1/17/95	SS	6.93	*Zeng and Anderson* [2000]	HF	60	60	19	19	3.7	3.45	0.65	0.72	16.5
Landers^{b,c,e}	38	6/28/92	SS	7.19	*Cohee and Beroza* [1994]	LS	83	100	18	18	6.08	6.62	1.31	1.52	5
Landers^{b,c,e}	39	6/28/92	SS	7.31	*Cotton and Campillo* [1995]	SM	80	100	15	15	6.07	6.32	2.16	2.12	6
Landers^{c,d,f}	40	6/28/92	SS	7.31	*Hernandez et al.* [1999]	G + R + SM + T	80	100	15	15	6.7	7.51	1.95	1.68	6
Landers^{c,d,e}	41	6/28/92	SS	7.28	*Wald and Heaton* [1994]	G + SM + Su + T	78	100	14	14	7.94	8.42	2.4	2.64	6
Landers^{c}	42	6/28/92	SS	7.22	*Zeng and Anderson* [2000]	HF	77	100	14	14	6.77	6.46	1.89	1.89	6.8
Loma Prieta^{b,c,e}	31	10/18/89	R-RL	6.89	*Beroza* [1991]	SM	40	40	14	14	5.87	5.66	1.31	1.42	18
Loma Prieta^{c,e}	32	10/18/89	R-RL	6.95	*Steidl et al.* [1991]	SM	38	38	17	17	4.34	5.56	1.38	1.89	18
Loma Prieta^{c,g}	33	10/18/89	R-RL	6.95	*Wald et al.* [1991]	SM + T	40	40	19	19	5.51	5.68	1.07	1.13	17.3

Table 2. (continued)

Earthquake	Event	Date	Kin	Mag	References	Data	L_{model}	L_{obs}	W_{model}	W_{obs}	D_{max}	D_{maxI}	D_{mean}	D_{meanI}	H
Loma Prieta[b,c]	34	10/18/89	R-RL	6.98	*Zeng and Anderson* [2000]	HF	40	35	18	13	8.92	8.69	1.8	1.86	17.5
Michoacan[g]	21	9/19/85	R	8.02	*Mendoza and Hartzell* [1988]	T	180	150	139	130	7.49	8.3	1.4	1.69	17
Morgan Hill[g]	17	4/24/84	SS	6.24	*Beroza and Spudich* [1988]	SM	30	25	10	10	2.31	2.32	0.26	0.37	7
Morgan Hill[g]	18	4/24/84	SS	6.13	*Hartzell and Heaton* [1986]	SM + T	27	27	12	12	0.79	0.94	0.16	0.23	8.5
Naganoken[g]	19	9/14/84	SS	6.27	*Takeo* [1990]	SM	12	12	9	9	2.2	2.96	1.01	1.12	1.5
Nahanni 1[b]	23	10/5/85	R	6.7	*Hartzell et al.* [1994]	T	40	37	17	12	3.83	4.55	0.53	1.05	8
Nahanni 2[b]	24	12/23/85	R	6.78	*Hartzell et al.* [1994]	SM + T	48	48	21	21	5.16	5.68	0.48	0.92	8
North Palm Spring[d]	25	7/8/86	R	6.11	*Hartzell* [1989]	SM + T	22	20	15.2	12	0.45	0.56	0.14	0.18	11
North Palm Spring[b]	26	7/8/86	R	6.07	*Mendoza and Hartzell* [1988]	SM + T	22	20	15.2	14	0.89	0.96	0.13	0.17	11
Northridge[d]	43	1/17/94	R	6.65	*Dreger* [1994]	T	23	20	27	27	3.31	3.31	0.52	0.52	21.5
Northridge[b,e]	44	1/17/94	R	6.66	*Hartzell et al.* [1996]	SM	19	19	25	25	2.39	2.51	0.66	0.74	17.5
Northridge	45	1/17/94	R	6.81	*Hudnut et al.* [1996]	G		19	19	25	25	2.81	2.81	1.04	0.97
Northridge[d]	46	1/17/94	R	6.7	*Wald et al.* [1996]	G + SM + T	18	16	24	21	3	3.16	0.98	1.13	17.5
Northridge[b]	47	1/17/94	R	6.65	*Zeng and Anderson* [2000]	HF	18	18	24	24	0.89	0.86	0.14	0.15	17.5
Oaxaca[b]	79	9/30/99	N	7.5	*Hernandez et al.* [2001]	SM	90	80	45	37		2.8		0.8	39.5
Oitaken Chubu[b]	07	4/21/75	SS	6.36	*Takeo* [1990]	SM	9	9	9	9	2.5	2.74	1.28	1.07	8.3
Peru 74[e,g]	06	10/3/74	R	7.96	*Hartzell and Langer* [1993]	T	251	251	168	168	4.83	5.66	0.85	1.42	15
Peru 96[b]	56	11/12/96	R	7.89	*Salichon et al.* [2003]	R + T	180	180	120	100	4.37	4.98	0.49	1.09	22
Peru 96	57	11/12/96	R	7.9	*Spence et al.* [1999]	T	300	220	120	120	3.25	3.53	0.77	0.93	21
Petatlan[b]	09	3/14/79	R	7.36	*Mendoza* [1995]	T	120	87	120	120	1.22	1.34	0.29	0.38	15
Playa Azul[b]	15	10/25/81	R	7.23	*Mendoza* [1993]	T	58	54	70	60	4.04	4.72	0.49	1.07	14
San Fernando[b,c]	04	2/9/71	R	6.73	*Heaton* [1982]	SM + Su + T	18	18	19	19	5	5	1.6	1.6	15.4
Sierra Madre[b]	35	6/28/91	R	5.53	*Wald* [1992]	SM + T	6	6	5	5	1.39	1.16	0.17	0.22	3.4
Superstition Hills[c]	29	11/24/87	SS	6.71	*Larsen et al.* [1992]	G	24	24	9	9	3.06	4.08	1.12	1.94	
Superstition Hills[b,c]	30	11/24/87	SS	6.51	*Wald et al.* [1990]	SM	19	19	12	12	4.3	4.5	0.83	0.96	9
Tabas[b,c]	08	9/16/78	R-RL	7.12	*Hartzell and Mendoza* [1991]	SM + T	95	95	45	45	1.44	1.64	0.34	0.39	10.5
Tottori[b]	84	10/6/00	SS	6.79	*Iwata et al.* [2000]	SM	34	33	17.6	17.6	4.03	4.65	0.9	1.23	11
Yamaguchi[d]	58	6/25/97	SS	5.78	*Ide* [1999]	SM	15	12	12	12	0.51	0.52	0.09	0.12	7.6
Zihuatanejo[d]	22	9/21/85	R	7.38	*Mendoza* [1993]	T	90	80	90	75	2.09	2.34	0.43	0.57	20

[a] Earthquake slip models with tabular data analyzed (from http://www.seismo.ethz.ch/srcmod). Earthquakes in parentheses are not included in analysis of slip profile shapes. Event 85 is eastern part of event 70 (S3; see ES08). All abbreviations are as before, plus L_{model}, L_{obs}, model-inferred and "observed" rupture length, respectively (in km); W_{model}, W_{obs}, model-inferred and "observed" rupture width, respectively (in km); D_{max}, D_{maxI}, original and interpolated values of maximum displacement, respectively (in m); D_{mean}, D_{meanI}: original and interpolated values of mean displacement, respectively (in m); H, hypocenter depth (in km). Explanations for L_{obs} (or W) different from L_{model} (or W) are given in ES01. Data entries synthesize the types of data used in models (T, teleseismic; LS, local seismic; SM, strong motions; G, geodetic data, HF, high frequencies only; R, radar; Su, surface measurements). When several models show similar "rating," that with triangular slip profile both along strike and dip is preferred. Models 85, 81, 50, 51, 33, and 46 are not "preferred" although they are based on more data types. Reasons are that 85 is derived from model 70 and is not the best constrained part of the whole model; 81 is based on too few near-field seismic data; 50 and 51 include poorly constrained geodetic data that alter the models; 33 uses poorly constrained teleseismic data that may perturb the solution; and 46 incorporates geodetic data that include significant postslip and consequently alter the model.

[b] Models with slip profiles triangular-shaped along strike and along dip.

[c] Earthquakes with surface data available.

[d] Models with slip profiles triangular-shaped along strike.

[e] Best constrained models.

[f] Better constrained models.

[g] Models with slip profiles triangular-shaped along dip.

Table 3. Other Models With No Tabular Data Available[a]

Earthquake	Date	Kin	Mag	References	L_{model}	L_{obs}	W_{model}	W_{obs}	D_{max}	D_{mean}	H
AL-Alaska[b]	10/23/02	1	6.7	Kikuchi Web site[c]	40	40	20	20			10
AL-Denali[b,d]	11/3/02	1	7.9	Kikuchi Web site	280	280	40	40	14	4.3	15
Aqaba[b]	11/22/95	1	7.3	Kikuchi Web site	50	50	20	20	2.1		10
AS-Kunlun[b,d]	11/14/01	1	8.1	Kikuchi Web site	358	358	40	40			20
Bhuj[b]	1/26/01	2	7.6	*Antolik and Dreger* [2003]	50	60	36	36	12.4	3	22
Biak[b]	2/17/96	2	8.2	*Henry and Das* [2002]	230	230	100	100	12	4	12
Carlsberg[b]	7/15/03	1	7.6	Kikuchi Web site	220	220	39	39	4		15
Fiji[b]	10/14/97	2	7.7	Kikuchi Web site	70	70	70	70			185
FIJI-Tonga	3/9/94	2	7.6	*McGuire et al.* [1997]	80	80	75	75	4		564
Flores Sea[b]	6/17/96	1	7.9	Kikuchi Web site	70	70	70	70			587
GR-Athens[b]	9/7/99	2	5.9	*Roumelioti et al.* [2003]	11	11	13	13	0.95	0.16	8
IR-Iran[b]	5/10/97	1	7.2	Kikuchi Web site	110	110	20	20			15
J-Hokkaido-Nansei[b]	7/12/93	2	7.8	*Mendoza and Fukuyama* [1996]	200	200	70	70	4		20
J-Hokkaido-Toho[b]	10/4/94	1	8.2	Kikuchi Web site	140	140	60	60			50
J-Kushiro-Oki[b]	1/15/93	2	7.5	Kikuchi Web site	50	50	60	60			100
J-Tokachi-Oki	9/26/03	2	7.9	Kikuchi Web site	90	90	70	70	5.5		25
Java[b]	6/2/94	2	7.8	*Abercrombie et al.* [2001]	160	150	70	120	2.5		16
Kamchatka[b]	1/1/96	1	6.6	*Zobin and Levina* [1998]	75	55	60	60	2		10
Kuril	12/5/97	2	7.8	*Zobin and Levina* [2001]	250	250	150	150	2.4		
Mindanao[b]	3/5/02	2	7.3	Kikuchi Web site	60	60	50	50			30
Mindoro[b]	11/15/94	1	7.2	Kikuchi Web site	70	70	24	24			15
New Ireland[b]	11/16/00	1	8.1	Kikuchi Web site	200	200	40	40			35
Petrolia[b]	1992	2	7	*Oglesby and Archuleta* [1997]	28	28	29	29	3		10
Russia[b]	6/28/02	2	7.3	Kikuchi Web site	70	70	50	50			565
Sakhalin[b]	5/27/95	1	7	Kikuchi Web site	44	44	20	20			12
Sanriku	12/28/94	2	7.7	*Tanioka et al.* [1996]	240	240			1.7		
Scotia Sea[b]	8/4/03	1	7.5	Kikuchi Web site	60	60	30	30	6.2	2.7	20
SoAm-Bolivia	6/9/94	2	8.2	*Ihmlé* [1998]	135	135	120	120	4.5		650
SoAm-North Chile[b]	7/30/95	2	8.3	Kikuchi Web site	238	238	102	102			25
SoAm-Peru[b]	6/23/01	2	8.2	Kikuchi Web site	270	270	177	177	4.5	2.8	30
TA-Taiwan[b]	3/31/02	2	7.1	Kikuchi Web site	80	80	60	60			25
USA-New Brunswick[b]	1/9/82	2	5.6	*Hartzell et al.* [1994]	5	5	4	4	0.6		8
USA-Ungava[b]	12/25/89	2	6	*Hartzell et al.* [1994]	13	11.5	4	4	2.2		2.5
Uttarkashi	10/19/91	2	6.8	*Cotton and Campillo* [1996]	48	48	36	36	1.5		12.5
Yonaguni-Jima[b]	12/18/01	1	7.3	Kikuchi Web site	30	30	20	20			10

[a] Other earthquake slip models considered (no tabular data available). Earthquake names, abbreviations, and units as before plus J, Japan; and SoAm, South America. For kinematics, 1, strike slip; 2, dip slip. Explanations for few (L_{obs}, W_{obs}) different from (L_{model}, W_{model}) are given in ES01.

[b] With a slip model analyzed.

[c] Kikuchi Web site http://wwweic.eri.u-tokyo.ac.jp/EIC/.

[d] With surface data available (Table 1).

slip are not contributing, even when localized between slip patches. While these methods are useful to identify the zones that underwent some slip during the earthquakes, they are not appropriate to depict the overall shape of the ruptures. To retrieve the actual dimensions of the ruptures, we instead follow an "observational" approach that favors a "case by case" treatment (see ES01 for details). First, we removed from the models all slip artifacts described by the authors of the models. Then, we compared each model to other observations and data acquired for the corresponding earthquake. A particular attention was paid on the observation of surface breaks, on the geometry of the surface rupture if any (as it allows identifying main segments), and on the distribution of on-fault aftershocks immediately following (by a few days at most) the main shock (as those roughly define the fault dimensions [e.g., *Stein and Thatcher*, 1981; *Pegler and Das*, 1996]). We also compared the different models proposed for a given earthquake and checked for major discrepancies from one to the other. This analysis confirmed that most fault geometries used in inversions overestimate the dimensions of the rupture planes (see ES01 and ES03). A few models, however (i.e., those for Izmit and Landers), underestimate these dimensions. In those cases, it is the length of the modeled ruptures that is shorter than that deduced from surface observation and distribution of immediate, on-fault aftershocks. We handled these cases by adding to the original slip profiles a point of zero slip located where further observations suggest the rupture to actually end. This makes L_{obs} ~20–30% longer than L_{model} for these two earthquakes.

2.2.2. Complementary "Teleseismic" Earthquake Slip Models

[11] We broadened our study by examining 29 additional published slip models (indicated in Table 3). As tabular data were not available for these models, we only could visually inspect them and compile their parameters from the literature. Most of them are built from teleseismic data and hence are quite poorly constrained. The corresponding earthquakes have various focal mechanisms (dip slip, 60%) and magnitudes (M_w 5.6–8.3).

3. Data Analysis

3.1. Characterizing the Overall Shape of the Earthquake Slip Distributions

[12] In order to compare the one-dimensional (1-D) slip profiles measured at surface (along-strike profiles) to the total 2-D slip distributions modeled on fault planes, we analyze the later by depicting how maximum and mean slip vary both

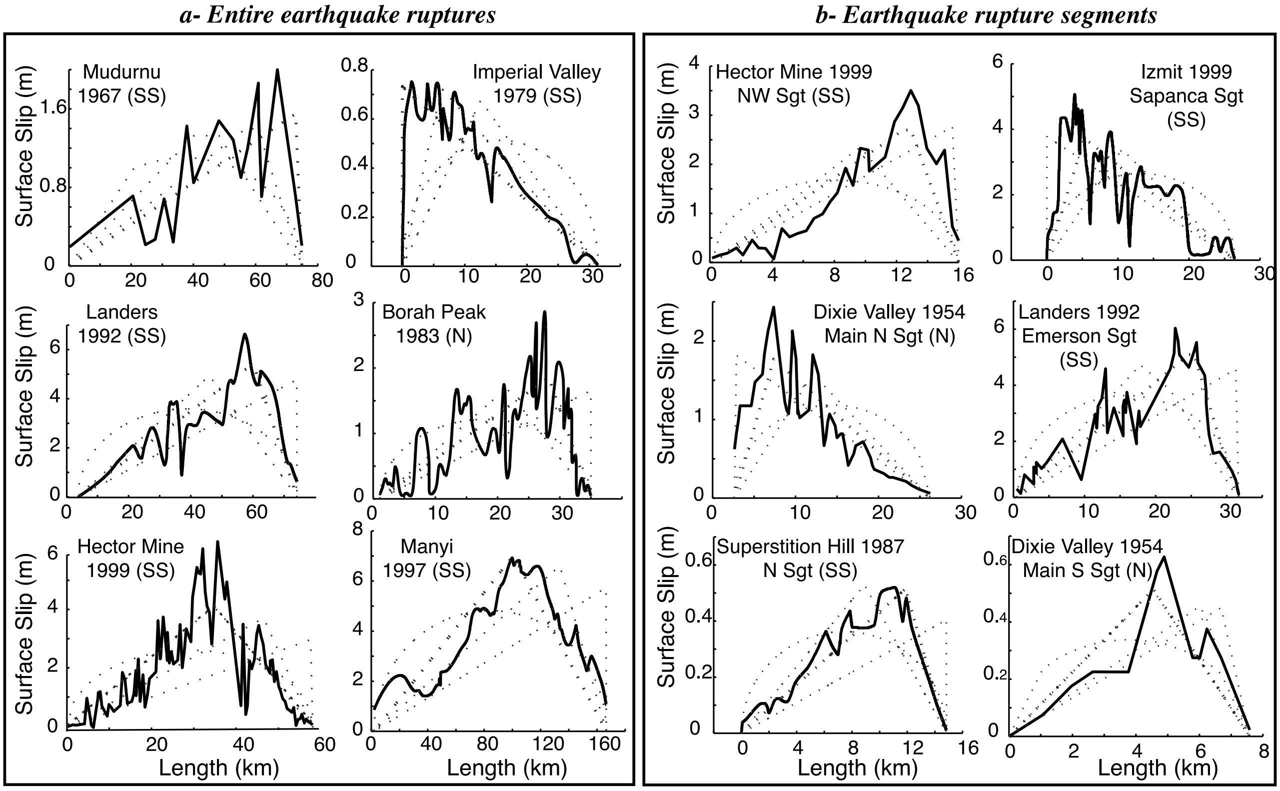

Figure 1. Examples of measured surface slip profiles. (a) Along entire rupture length. (b) Along rupture segments. All profiles are from Table 1. For each, the four attempts of shape correlation are shown in dotted lines, thicker for best fitting function. Sgt, segment; SS and N in parentheses, strike-slip and normal faults; N, S, W, and E, north, south, west, and east segments.

along the length (along-strike profiles) and along the width (along-dip profiles) of the faults. We therefore end up with a collection of one-dimensional profiles, each is given as D(x) (D is displacement or slip, both terms being used similarly; x is position along fault length or width). Hence all profiles are mathematically comparable and can be analyzed similarly, with a general procedure that we describe below.

[13] A visual inspection of the slip profiles having shown that most of them exhibit an overall triangular shape (see examples in Figure 1), we try to constrain this observation. We start by determining the X coordinate (normalized by X_{max}) of the center of gravity of each slip profile (X_{centr}). As the center of gravity of a profile is hardly sensitive to small-scale slip variability, it is a stable parameter that indicates the overall symmetry or asymmetry of the slip function. Any center of gravity located at $X_{centr} > 0.5$ (all X_{centr} are folded onto the [0.5–1] range on the basis of our choice to represent maximum slip always to the right) indicates a slip profile being asymmetric in shape, with an asymmetry more pronounced for higher X_{centr} values. If a slip profile really is triangular in shape, then its X_{centr} coordinate can be used to deduce the X_{apex} position of its apex (i.e., point of maximum slip; in any triangle, $X_{apex} = 3\ X_{centr} - 1$). Knowing this X_{apex} position, a correlation method is used to check how closely a triangle having its apex at X_{apex} approximates the actual slip profile. The coefficient of correlation is then compared to that that one would get from correlating the slip profile with an elliptical function (theoretical predicted pattern). Once the "best correlating" function is determined, the best fitting triangle or ellipse is calculated using a least squares method. In each population of slip profiles, the X_{centr} coordinates were found to more or less cover the full range of possible values ([0.5, 1]). This revealed that the profiles had various degrees of asymmetry. A few of them appeared more represented than others, however (larger number of X_{centr} around some specific values). We chose to use these few dominant degrees of asymmetry as a guide to discriminate the slip profiles otherwise mixed together in each population. From the few dominant X_{centr} values, we determined the corresponding X_{apex} coordinates. Only the few "reference triangles" having their apex at these specific X_{apex} values were then used for correlation to actual slip profiles. This defines a few groups of profiles approximated by the same reference triangle (or ellipse). In each group, profiles are then normalized by both their X_{max} (length or width) and D_{aver} (average slip for each profile). This makes them comparable one to the other regardless of slip variability and scale. The normalized profiles are finally superimposed (with some of them being flipped so that maximum slip is to the right in all cases), and their running average curve is calculated. The latter highlights the similar overall shape of the profiles.

3.1.1. Overall Shape of Seismic Slip Profiles Measured at Surface

3.1.1.1. Individual Earthquake Ruptures

[14] Figure 1a shows a few examples of slip profiles that were measured at the surface along the entire length of the earthquake ruptures indicated in the plots (see Table 1 for

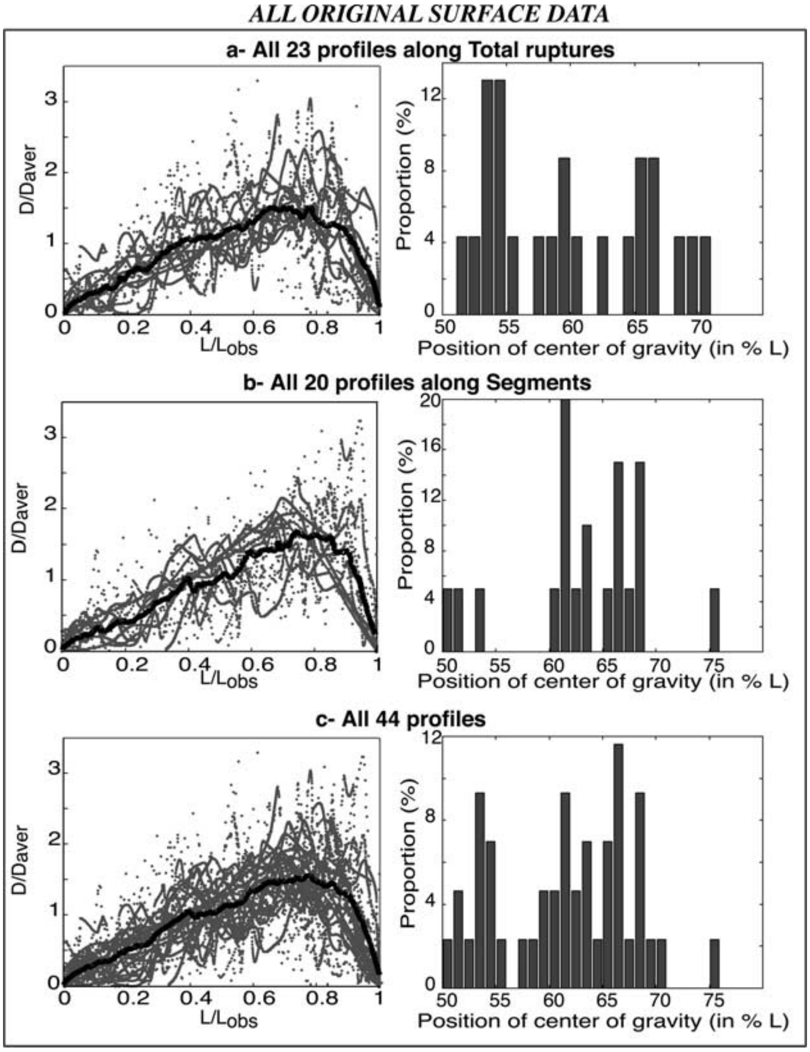

Figure 2. Overall shape of surface slip profiles. (a) All 23 surface slip profiles measured along entire rupture lengths (from Table 1, entire ruptures section). (b) All 20 surface slip profiles measured along rupture segments (from Table 1, segments section). (c) All 44 measured surface slip profiles (from Table 1; the plot includes one additional profile measured on the north Anatolian fault section broken in 1939–1967 sequence). (left) All profiles (dark gray) normalized by L_{obs} and D_{aver} (average slip for each profile) (with some of them being flipped so that maximum slip is to the right), with average curve calculated (black). (right) Histograms of positions of the centers of gravity of the profiles. Positions are reported to half fault length. The few $X_{centr} > 0.66$ result from having added a point of zero slip ahead of some original profiles.

details). Although these earthquakes differ in magnitude, focal mechanisms, location, and timing, the envelope of their surface slip profile looks similar overall, being roughly triangular. These triangular patterns have various degrees of asymmetry, however. Figure 2a (left) shows all 23 surface slip profiles from Table 1, normalized and superimposed as described before. Although all profiles show slip irregularities, their stacking defines an average curve that is roughly triangular and asymmetric. Figure 2a (right) is the histogram of X_{centr} for the 23 profiles. All X_{centr} are >0.51, with ~60% greater than 0.56. This shows that all profiles are asymmetric. This asymmetry is variable, however, so that Figure 2a (left) mixes together profiles being more or less skewed. Although the X_{centr} histogram suggests that a broad range of asymmetries may coexist in the original population, a few peaks are observed (grossly around 0.54, 0.59, and 0.66), which we use as a guide to distinguish the profiles otherwise mixed together in Figure 2a (left). Assuming that the profiles are triangular (Figures 1a and 2a, left), we hypothesize that the functions that best approximate them are triangles having their apex (X_{apex}) at ~60, 80, or 100% of the fault length. ES04a lists the coefficients of correlation (“Corr”) obtained when comparing such reference triangles (dubbed TR60, TR80, and TR100) to the actual slip profiles. The coefficients of correlation obtained when an elliptical function (ELL) is used instead are added for comparison. The four correlating functions are represented in dotted lines for the few examples shown in Figure 1a, with the best fitting one in thicker line. ES04a shows that all but one slip profile are best approximated by a triangle, with

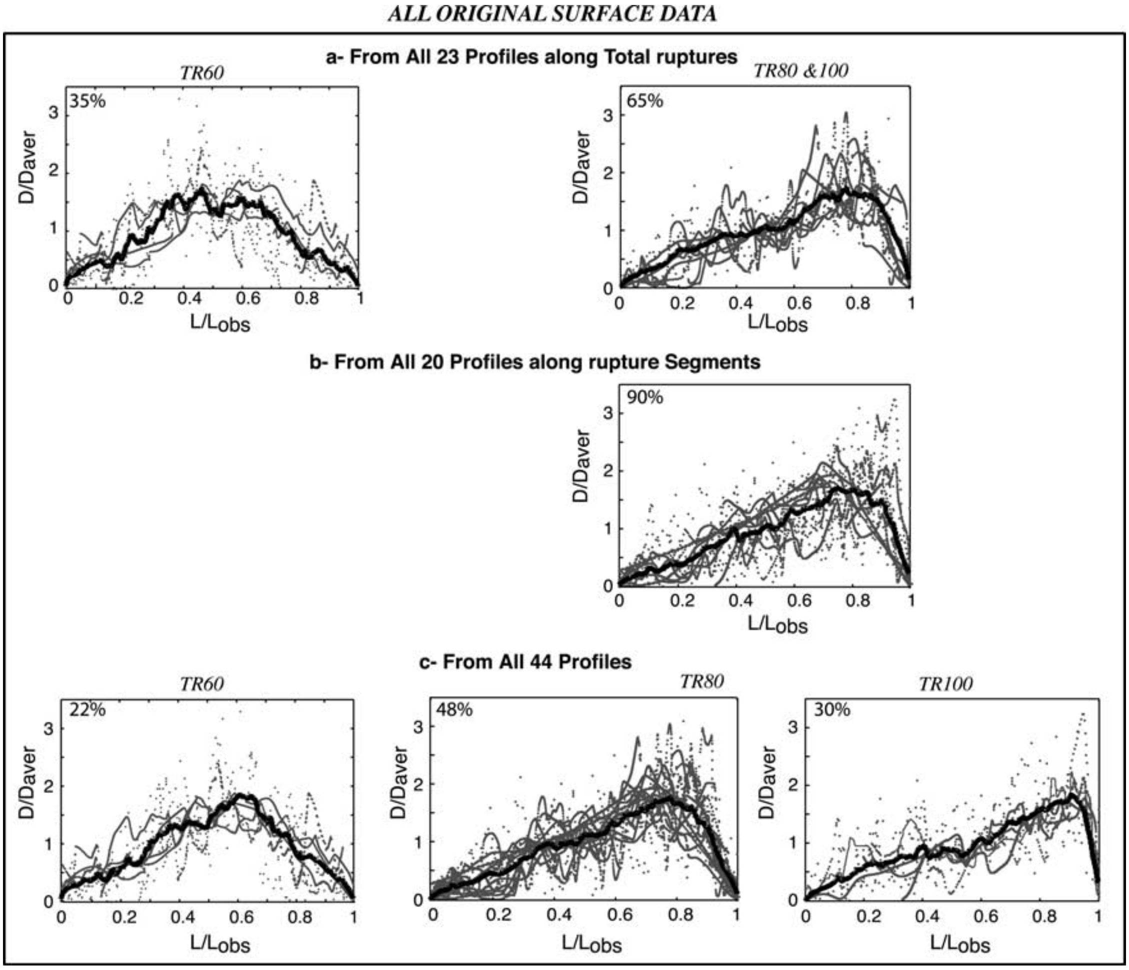

Figure 3. Dominant slip profile shapes identified from Figure 2. (a, b, c) Same populations of profiles as in Figure 2; each plot gathers profiles (percentages indicated) with same best correlating function (average curve in black). TR60, TR80, and TR100 indicate that corresponding reference triangles have their apex at 60, 80, and 100% of fault length, respectively.

Corr > 0.6 for all of them and >0.75 for ~70% of them. Twenty-six percent of the profiles are best approximated by a completely asymmetric triangle (X_{apex} = 1; Corr ~ 0.77), 39% are best approximated by a strongly asymmetric triangle (X_{apex} = 0.8; Corr ~ 0.84), and 30% are best approximated by a more symmetric triangle (X_{apex} = 0.6; Corr ~ 0.77). The slip profiles being best approximated by the same reference triangle are plotted together in Figure 3a (the TR80 and TR100 populations are considered together as data are too few to draw them separately), and their average curve is calculated. The latter highlights the overall similar shape of the profiles. For 65% of them, this shape is that of an asymmetric triangle, with slip decreasing roughly linearly from a maximum value at one rupture tip to zero at the other fault tip (Figure 3a, right). For the remaining 35%, the overall shape is that of a more symmetric triangle, with slip decreasing roughly linearly from a maximum value at about the fault center to zero at both rupture tips (Figure 3a, left). In both cases, the length of the linear sections is on the order of the total size of the event.

3.1.1.2. Segments Within Ruptures

[15] Most large irregularities in earthquake slip profiles are shown to correlate with fault segments within ruptures [e.g., *Segall and Pollard*, 1980; *Schwartz and Coppersmith*, 1984; *Machette et al.*, 1991; *Willemse*, 1997; *Hemphill-Haley and Weldon*, 1999]. Figure 1b shows a few examples of slip profiles measured at surface along such rupture segments. Again, the overall shape of these profiles looks similar, being roughly triangular and asymmetric. Figure 2b (left) shows all available segment profiles superimposed (Table 1). Although each profile is irregular in detail, the average curve calculated from them all again looks triangular and asymmetric. Eighty-five percent of the profiles have X_{centr} > 0.6 and hence are strongly asymmetric (Figure 2b, right). As the peaks in Figure 2b (right) are for X_{centr} values ~similar to those before, we correlate the segment slip profiles to the same TR60, TR80, and TR100 reference triangles (ES04b). We find that 30% of the profiles are best approximated by a completely asymmetric triangle (X_{apex} = 1; Corr ~ 0.67), 60% are best approximated by a strongly asymmetric triangle (X_{apex} = 0.8; Corr ~ 0.80), and 10% are best approximated by a roughly symmetric triangle (X_{apex} = 0.6; Corr ~ 0.88). Figure 3b shows all asymmetric segment profiles superimposed. It shows that slip along earthquake rupture segments generally decreases roughly linearly from a maximum value at one segment tip to zero or some low slip at the other

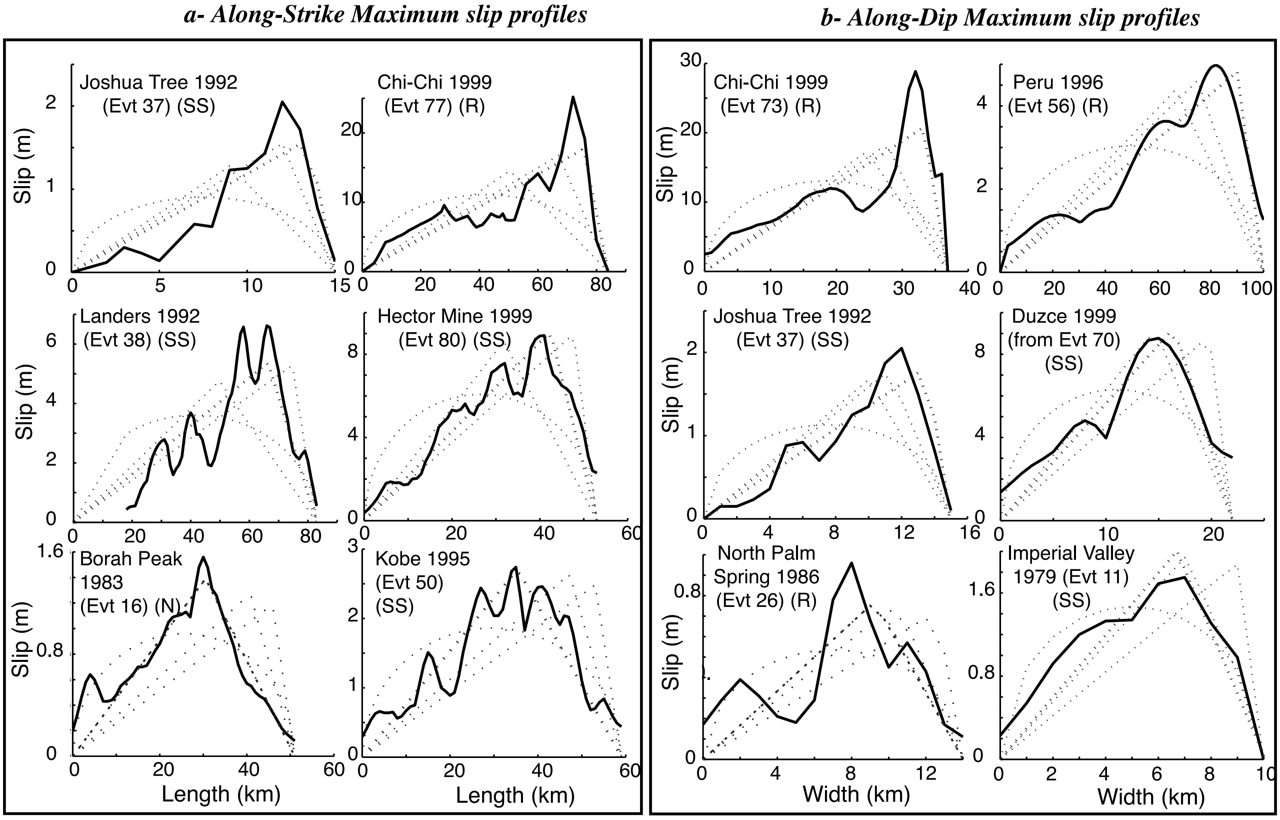
a- Along-Strike Maximum slip profiles

b- Along-Dip Maximum slip profiles

Figure 4. Examples of maximum slip profiles extracted from inversion models. (a) Along strike. (b) Along dip. All profiles are from Table 2. Caption is as for Figure 1 (R, reverse faults).

segment end. In all cases, the peak slip is found at the "interior tip" of the segments, while the linear sections are the "exterior tips" of the earthquake ruptures.

3.1.1.3. Synthesis

[16] Figure 2c (left) shows all analyzed surface slip profiles together (i.e., 44 profiles; details are given in Figure 2 caption), while Figure 3c distinguishes the three dominant patterns. A few profiles are quite symmetric (22%, Figure 3c, left), while the majority of them are strongly (48%, Figure 3c, middle) or completely asymmetric (30%, Figure 3c, right). These similar triangular shapes are found at all scales analyzed, from the smaller segment scale to the larger scale of individual ruptures, and for all focal mechanisms. This suggests that high slip gradients and long linear slopes (length similar to that of the event) are the key ingredients to describe surface slip distributions on earthquake faults.

3.1.2. Overall Shape of Slip Profiles Derived From Slip Inversion Models

[17] From the available slip models (Table 2), we extracted the profiles of maximum and mean slip both along the length (i.e., along strike) and along the width (i.e., along dip) of the fault planes. We ended with four populations of 77 slip profiles (76 + 1, as one model is split into the two distinct planes that it contains; see details in Table 2 and ES01). Since the rupture width is generally not well constrained, the along-strike profiles of mean slip give only a first-order view of the moment distribution on the fault plane. By contrast, zones of maximum slip are the best constrained on a modeled rupture plane. We therefore believe that profiles of maximum slip both along strike and dip give a satisfactory view of the overall slip distribution on the planes.

3.1.2.1. Overall Shape Of Along-Strike Slip Profiles

[18] Figure 4a shows a few examples of along strike profiles of maximum slip that we extracted from the earthquake models indicated. All profiles look triangular in shape and more or less asymmetric. Figure 5a shows all 77 along-strike slip profiles (maximum and mean slip on Figures 5a, left, and 5a, right, respectively). Although all profiles show slip irregularities, the stack draws a homogeneous average curve that looks roughly triangular and asymmetric overall. The histogram of X_{centr} (Figure 5a, middle) confirms that most profiles are asymmetric ($X_{centr} > 0.54$ for ~70% of them) and can be compared to "reference triangles" having their apex at ~60, 80, or 90% of the fault length. The calculation (ES04c) indeed confirms that 23% of the profiles are well fitted by a roughly symmetric triangle (Corr ~ 0.9), 27% are well fitted by a strongly asymmetric triangle (Corr ~ 0.79), and 43% are well fitted by a completely asymmetric triangle (Corr ~ 0.65) (Figure 6a). The remaining profiles (7%) are better approximated by an elliptical function (Corr ~ 0.5).

[19] To further refine our observations, we now consider only the models for earthquakes with a magnitude >6.5, which are the best constrained. This new population includes 63 models over the initial 77. Figures 5b and 6b are done as before for this population. The results are the same: The stacked maximum and mean slip profiles draw a triangular and asymmetric average curve, while the same three dominant degrees of asymmetry are revealed. Figure 5c

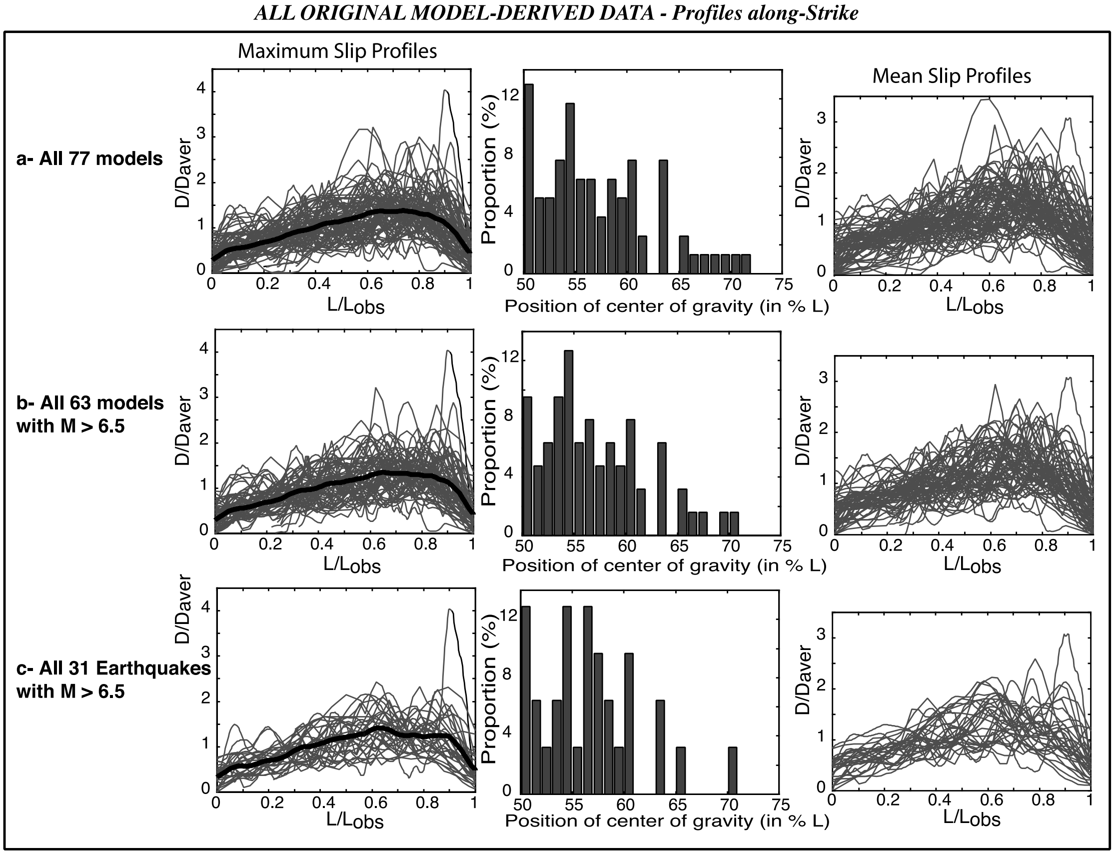

Figure 5. Overall shape of along-strike slip profiles extracted from inversion models (Table 2). (a) All 77 models. (b) All 63 models for earthquakes with M > 6.5. (c) All 31 "earthquakes" with M > 6.5 (i.e., one model only is kept per earthquake, chosen according to Table 2). (left) maximum slip profiles (gray) normalized (by L_{obs} and D_{aver}; D_{aver} is average slip for each profile) and superimposed as before. Average curve is black. Profiles are obtained by extracting the maximum slip value per column and plotting these values as a function of fault length. (middle) Histograms of positions of centers of gravity of maximum slip profiles. (right) Mean slip profiles normalized (by L_{obs} and D_{aver}) and superimposed. Profiles are obtained by calculating the mean slip value per column and plotting these values as a function of fault length. Mean slip therefore directly depends on W (poorly constrained), while maximum slip does not. The few slip profiles that do not end at x = 0 are those with $L_{obs} > L_{model}$. None of the average curves reaches zero at its tips because slip near fault edge is poorly constrained.

now shows the distribution of along-strike slip profiles for a population where only one model is kept per earthquake with magnitude >6.5. This population represents a total of 31 earthquakes. The maximum and mean slip profiles for these earthquake ruptures also are roughly triangular in shape, with most being completely (39%) or strongly asymmetric (26%) and the remaining quite symmetric (32%) (Figure 6c).

3.1.2.2. Overall Shape of the Along-Dip Slip Profiles

[20] We now consider the distributions of slip along the width of the fault planes. As the boundary conditions at the free surface and at the base of the seismogenic zone are different, one may expect the overall shape of the along-dip slip profiles to be different for ruptures at different depths. Yet, if such differences exist, the simple treatments that we apply to the profiles should make them clear.

[21] A few examples of along-dip (maximum) slip profiles are shown in Figure 4b. All show a triangular and more or less asymmetric overall shape. Figures 7a and 8a show the complete population of along-dip slip profiles (represented as before). The stacked profiles draw a homogeneous pattern, suggesting that the individual profiles are not significantly different in shape whether their maximum slip is close to surface or is at depth. Figure 9, on which profiles having their peak slip close to either the fault top or base are distinguished, confirms this point. All profiles have a similar shape, roughly triangular and asymmetric (note, however, that slip does not necessarily go down to zero at surface, while it does at depth). The X_{centr} histogram (Figure 7a, middle) suggests that most profiles can be correlated to reference triangles having their apex at ~66, 75, or 90% of the fault width. The calculation (ES04d) indeed confirms that 43% of the profiles resemble a completely asymmetric triangle (X_{apex} = 0.9, Figure 8a, right; Corr ~ 0.71), 27% resemble a strongly asymmetric triangle (X_{apex} = 0.75; Figure 8a, middle; Corr ~ 0.82), and 14% resemble a roughly symmetric triangle (X_{apex} = 0.66; Figure 8a, left; Corr ~ 0.85). The remaining profiles (15%) are best approximated by an elliptical function (Corr ~ 0.87). Figures 7b and 8b are done as before for the

ALL ORIGINAL MODEL-DERIVED DATA- Profiles along-Strike

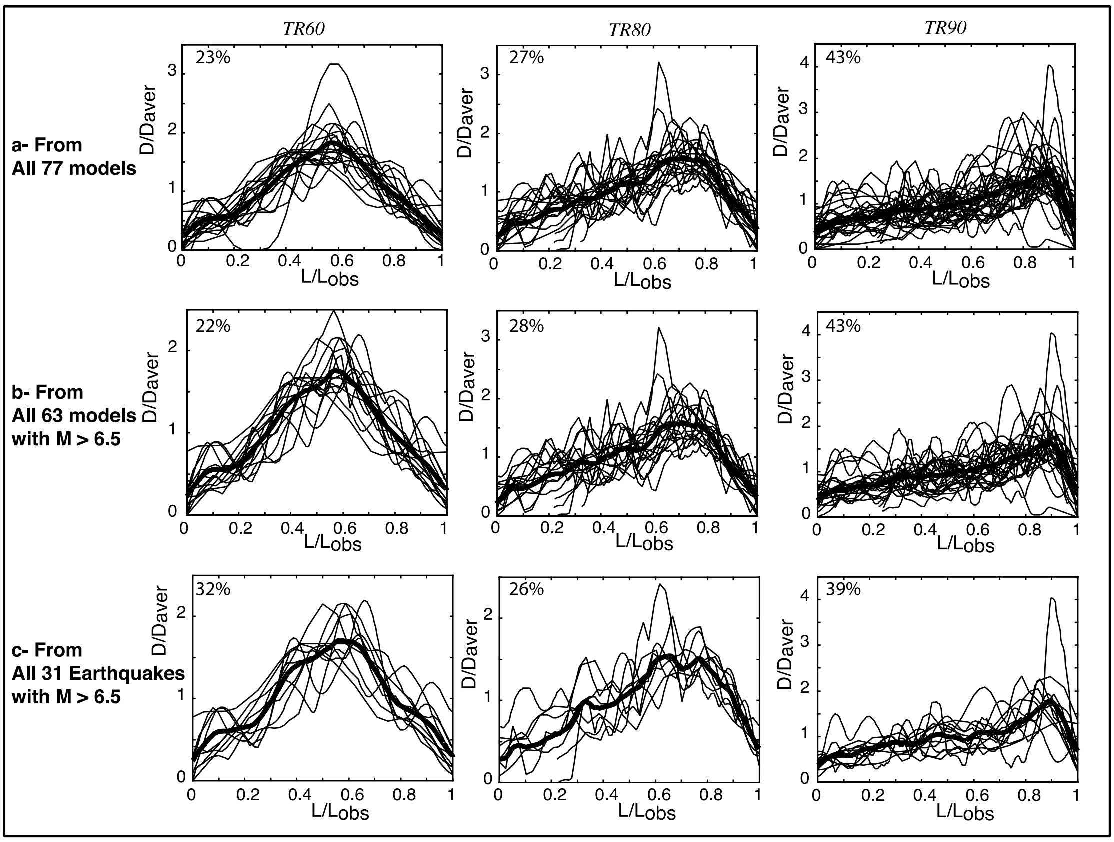

Figure 6. Dominant slip profile shapes identified from Figure 5 (maximum slip profiles only). (a, b, c) Same populations of profiles as in Figure 5. Each plot gathers profiles (percentages indicated) with same best correlating function (average curve black). TRX is as in Figure 3.

63 models performed for earthquakes with $M_w > 6.5$, while Figures 7c and 8c show the along-dip slip profiles for the population of 31 earthquakes with magnitude >6.5. In both cases, results are similar to those found before: Maximum and mean slip profiles are triangular in shape, and most of them are completely or strongly asymmetric.

3.1.2.3. Synthesis

[22] The above analysis shows that most studied earthquake faults have similar triangular-shaped slip profiles, both along strike and dip. Besides, most of these profiles (70–80%) are strongly asymmetric. Thus, on most earthquake ruptures, slip ramps up roughly linearly from both tips to a peak value (more or less rounded apex). That peak may be in the fault center but is more often off to the side. In the latter case, the taper to the end nearest to the peak is much steeper than the taper on the other side. That gentle linear taper is long, roughly on the entire length (and width) of the event. These results are found at all scales analyzed (see also ES05 where slip profiles are distinguished on the basis of earthquake magnitudes) and for all focal mechanisms. The visual inspection of the additional slip models that we found in the literature (Table 3) reveals that most of them show a roughly regular slip decrease both along strike and dip from a maximum value close to one fault edge to zero (or almost) at the other fault edge. The corresponding maximum slip profiles are therefore also expected to be roughly triangular in shape and asymmetric both along strike and dip. This suggests that our results can be generalized to most earthquake ruptures.

[23] That all faults analyzed have triangular-shaped slip profiles is confirmed by Figure 10 that shows that, for each population of profiles, D_{max} is about twice D_{aver}, as expected for triangular functions. Therefore, on average, slip distributions on earthquakes are far from being elliptical as it is implicitly predicted from the simple crack model. Besides, the observed triangular shapes reveal linear tapers that are at the scale of the event itself and hence much longer than the "tip tapers" supposed to accommodate the stress singularities at the very rupture ends [e.g., *Barenblatt*, 1962; *Ida*, 1972; *Scholz*, 2002]. Thus the process responsible for this major discrepancy with the crack model cannot be solely controlled by the stress singularity at the fault tips.

3.2. Analyzing the Position of Hypocenter With Respect to Slip Distribution Patterns

[24] Having shown that slip distributions on earthquake faults have a well-defined overall shape, we now investigate if any particular relation exists between the "point" of earthquake initiation (i.e., the hypocenter) and these shapes. We are aware that hypocenters may not represent the exact points of rupture nucleation or start of moment release [e.g., *Campillo and Archuleta*, 1993; *Abercrombie and Mori*, 1994; *Mori*, 1996; *Perfettini et al.*, 1999]. We nevertheless assume that published hypocenters reasonably indicate the

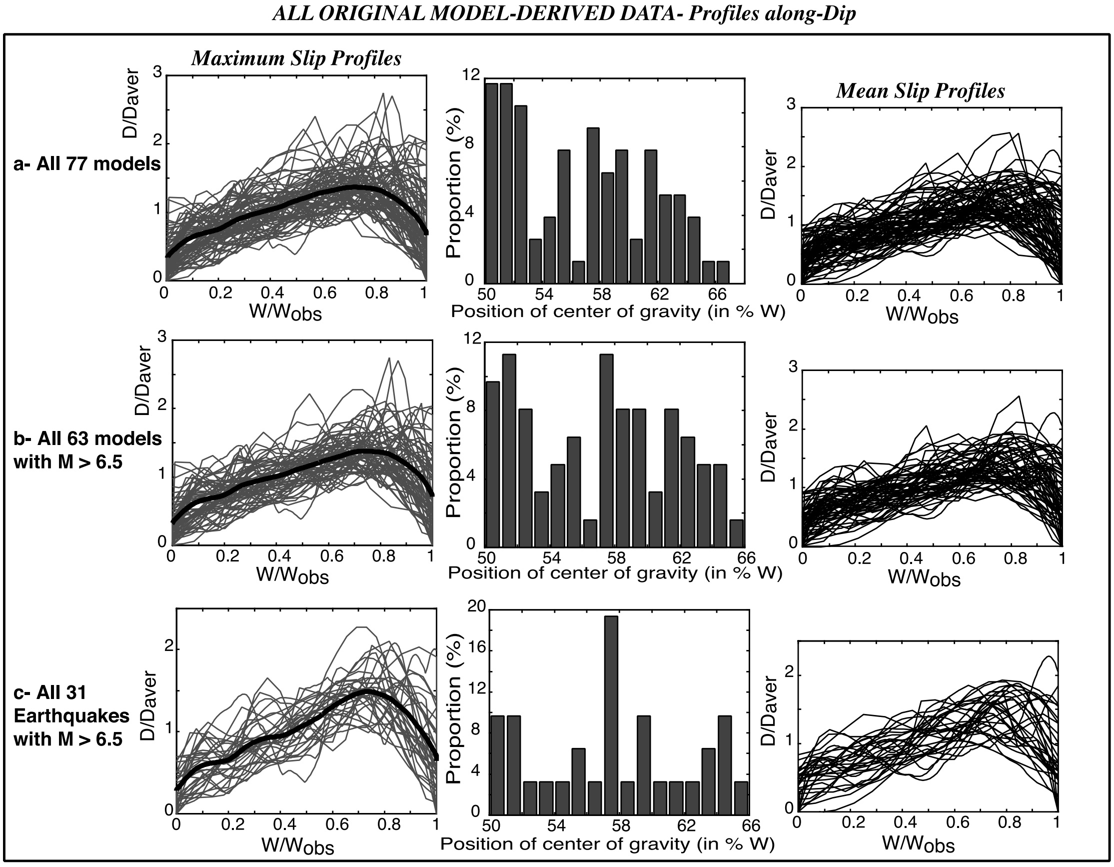

Figure 7. Overall shape of along-dip slip profiles extracted from inversion models (Table 2). (a) All 77 models. (b) All 63 models for earthquakes with M > 6.5. (c) All 31 earthquakes with M > 6.5 (i.e., one model only is kept per earthquake, chosen according to Table 2). Same as Figure 5, but with W replacing L. Profiles of maximum slip are obtained by extracting maximum slip value per line and plotting these values as a function of fault width. Profiles of mean slip are obtained by calculating the mean slip value per line and plotting these values as a function of fault width. Mean slip therefore depends on L, while maximum slip does not.

region where rupture initiated within the fault planes. Because of this difficulty, we have assigned to all hypocenter coordinates a large, 5 km uncertainty in both X and Z directions. Few studies (except *Somerville et al.* [1999] and *Mai et al.* [2005]) have been carried out to analyze the position of hypocenters within fault zones in a systematic way. As our goal is to analyze the positions of hypocenters with respect to the overall slip distributions, we use the (L_{obs}, W_{obs}) rupture plane dimensions.

3.2.1. Position of Hypocenters With Respect to Fault Plane Edges

[25] Figure 11a shows the position of hypocenters (from Table 2; averaged per earthquake) with respect to the edges of the rupture planes. The symbol surface is proportional to magnitude. Dip-slip and strike-slip (plus oblique) ruptures are in blue and red, respectively. Position along rupture length is analyzed with respect to closest lateral fault edge and hence along the fault half length. By contrast, position along rupture width is considered with respect to fault base and hence along the entire fault width. Figure 11a shows that hypocenters are quite evenly distributed along the width of the faults. A larger number is found, however, at 20 ± 10% of the fault width from its base, while only few hypocenters locate close to the fault top. Most large magnitude strike-slip earthquakes nucleate close to either the fault base or the half width, while most dip-slip earthquakes nucleate close to either the fault base or the top. These observations are similar to those made by *Somerville et al.* [1999] on a smaller data set. Together these show that while many earthquakes nucleate close to the base of the brittle crust [e.g., *Das and Scholz*, 1983; *Sibson*, 1984; *Choy and Dewey*, 1988; *Mendoza et al.*, 1994; *Boatwright and Cocco*, 1996; *Huc et al.*, 1998; *Chambon and Rudnicki*, 2001], many others do not and initiate at shallow depth. Most ruptures nucleating in the top half of the fault planes have their slip tapering downward (yellow circled symbols). Most ruptures nucleating in the bottom half of the planes have their slip tapering upward (green circled symbols).

[26] Figure 11b is similar to Figure 11a, but with symbol surfaces now proportional to D_{max}/L_{model} ratios (Figure 11b includes additional data from Table 3). These ratios give a first-order view of the amount of slip accumulated over the fault planes and an idea of the stress drop for the corresponding earthquakes (for a given range of W and in the hypothesis of elastic cracks). Figure 11b shows that the larger ratios (i.e., higher stress drops) are found for the ruptures nucleating close to the fault base. These are not necessarily the largest magnitude earthquakes. Largest events

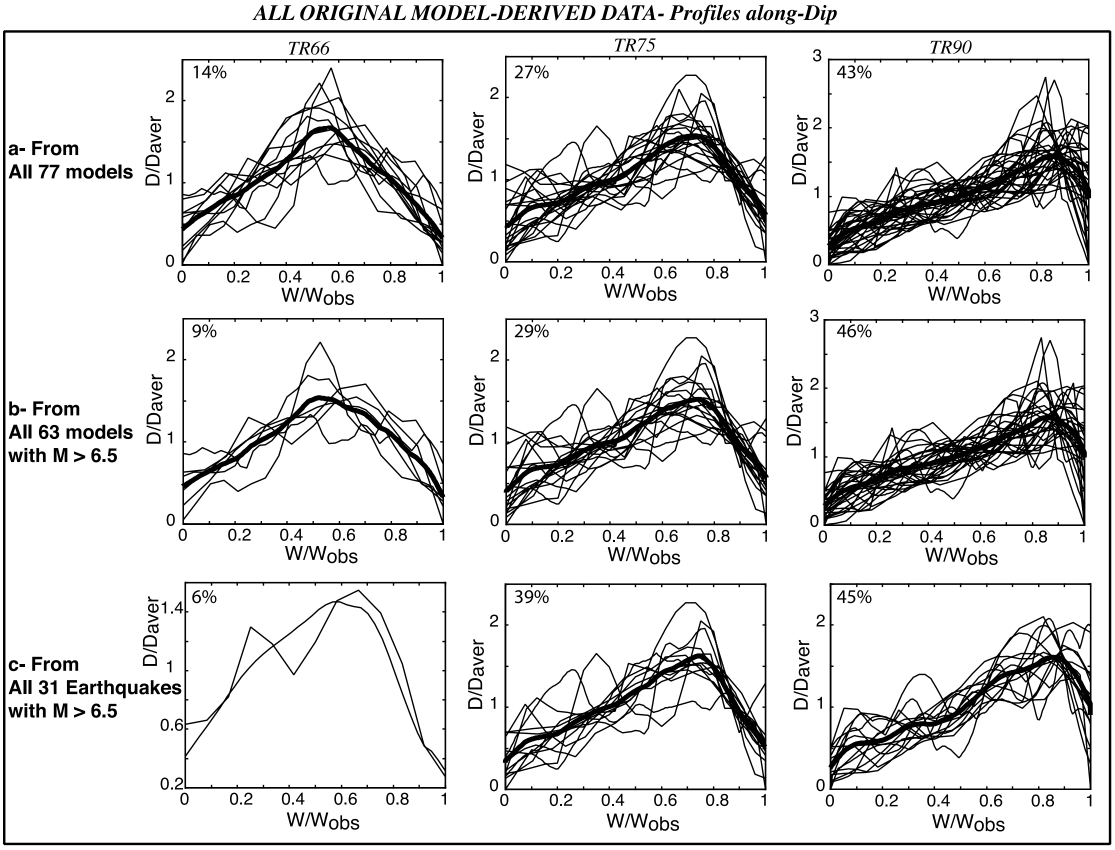

Figure 8. Dominant slip profile shapes identified from Figure 7 (maximum slip profiles only). (a, b, c) Same populations of profiles as in Figure 7. Each plot gathers profiles (percentages indicated) with same best correlating function (average curve in black). TRX as in Figure 3 (with L replaced by W).

actually seem to have the smallest ratios; that is, large earthquakes have smaller average stress drops than others.

3.2.2. Position of Hypocenters With Respect to Zone of Maximum Slip

[27] Zones of large slip (relative to the rest of the slip on the fault) on earthquake fault surfaces are usually defined as "asperities" [e.g., *Madariaga*, 1979; *Lay and Kanamori*, 1981; *Das and Kostrov*, 1983; *Mendoza*, 1993; *Ruff and Miller*, 1994; *Somerville et al.*, 1999; *Papageorgiou*, 2003; *Das*, 2003]. In section 5, we will discuss how these asperities relate to geological structures. The observation of overall triangular slip profiles on earthquake faults (both along strike and dip) make these profiles shaped by one single zone of maximum slip. Hence, while many events have slip profiles with several peaks [*Thatcher*, 1990; *Somerville et al.*, 1999], one is dominant (in terms of slip and moment) over the others. Here we analyze the position of hypocenters with respect to these major asperities (identified as the zones of maximum slip in the profiles) for the population of earthquakes that we found to have a triangular slip profile both along strike and dip. Figure 12a shows the hypocenter positions for data from Table 2 (averaged per earthquake, solid symbols) and Table 3 (open symbols). The X axis is the along-strike distance (HA_x) between an hypocenter and the apex (i.e., zone of maximum slip) of the reference triangle that best fits the along-strike maximum slip profile of its corresponding earthquake (for Table 2 data; otherwise, handmade measurements for Table 3

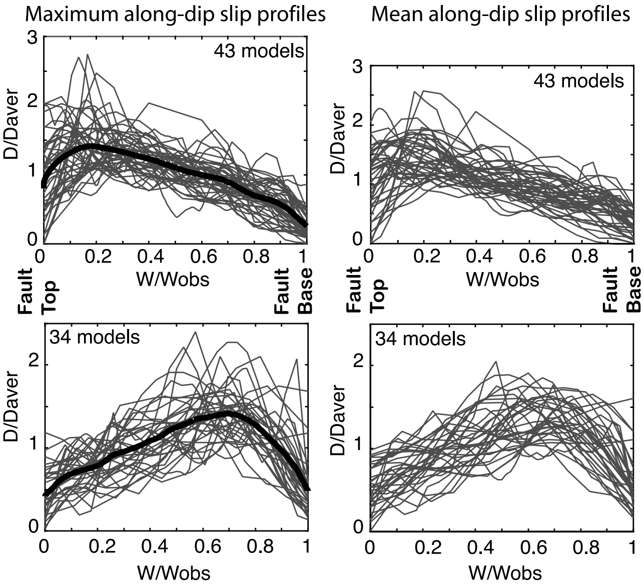

Figure 9. Influence of depth on overall shape of along-dip slip profiles. (left) Maximum and (right) mean slip profiles. (top) Profiles having their peak slip close to surface. (bottom) Profiles having their peak slip at depth. Otherwise as previous figures.

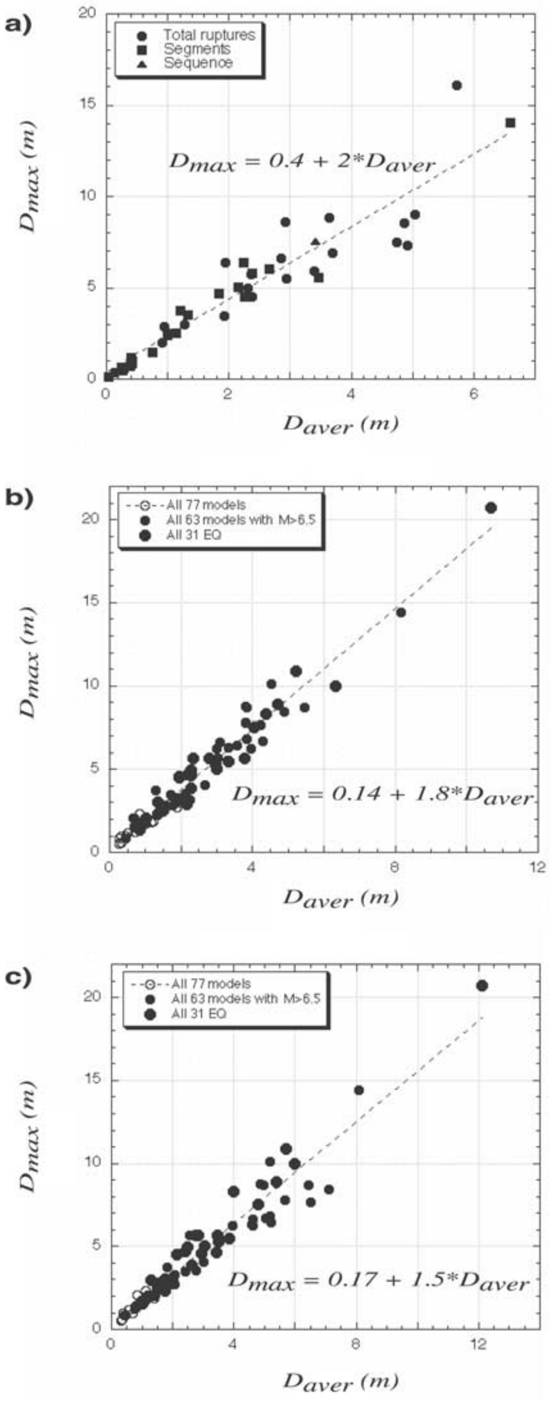

Figure 10. Plot of maximum (D_{max}) versus average (D_{aver}) displacement for the slip profiles analyzed. (a) Surface slip profiles from Table 1. (b) Along-strike maximum slip profiles from models in Table 2. (c) Along-dip maximum slip profiles from models in Table 2. Models with D_{max} > 21 m (i.e., unrealistic) are excluded from calculations. Ratio for along-dip profiles is slightly <2 because distribution of slip along fault width is quite poorly constrained.

data). Similarly, the Y axis is the along-dip distance (HA_z) between an hypocenter and the apex of the reference triangle that best fits the along-dip maximum slip profile of its corresponding earthquake (same remark). Distances are given in percent of L_{obs} and W_{obs}. Symbols are as before, with their surface proportional to magnitude. Symbol shapes indicate the degree of asymmetry of the slip profiles (see Figure 12 caption). Note that most hypocenters that fall on the X or Y axes come from teleseismic models (Table 3). Those are generally unable to properly constrain the relative positions of hypocenter and centroid. Most of these points may therefore be incorrect.

[28] Figure 12a shows that hypocenters are not evenly distributed within the whole plot. There is one domain where all hypocenters are, and one domain totally free of hypocenters. This suggests that there is a critical distance from a major "asperity" (here taken to be the zone of maximum slip, coinciding with the graph origin)

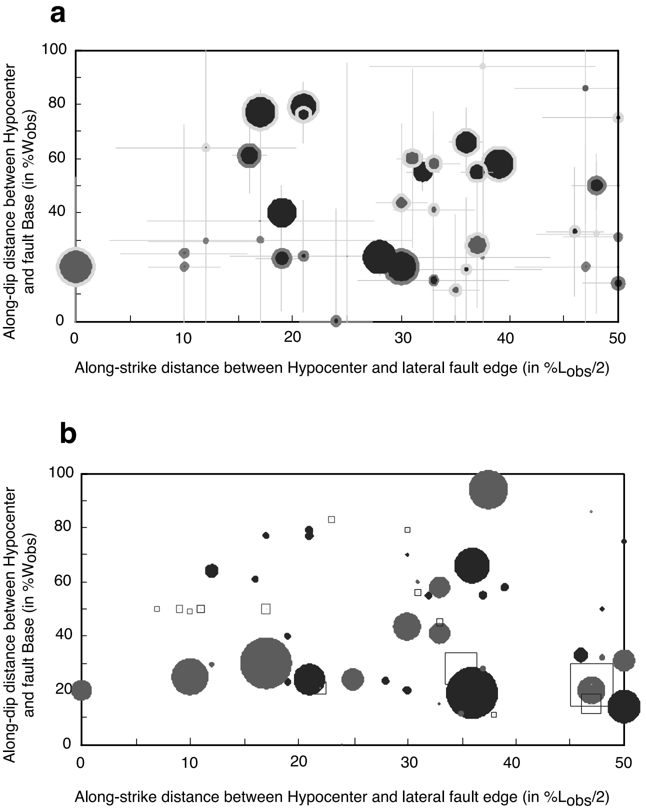

Figure 11. Distribution of hypocenters with respect to fault plane edges. X axis is along-strike position (in percent of L_{obs}) of hypocenters with respect to lateral fault plane edges (irrespective of which side). Y axis is along-dip position (in percent W_{obs}) of hypocenters with respect to fault plane base. Dip-slip and strike-slip faults are in blue and red, respectively. (a) Symbol size proportional to magnitude. Data are from Table 2 (averaged per earthquake; in few cases, best model is preferred). Uncertainties on hypocenter positions are assigned to 5 km in both x and y. Yellow and green circled symbols are for slip profiles tapering downward and upward, respectively. (b) Symbol size proportional to D_{max}/L_{model}. Data are from Tables 2 (solid symbols) and 3 (open symbols). See color version of this figure at back of this issue.

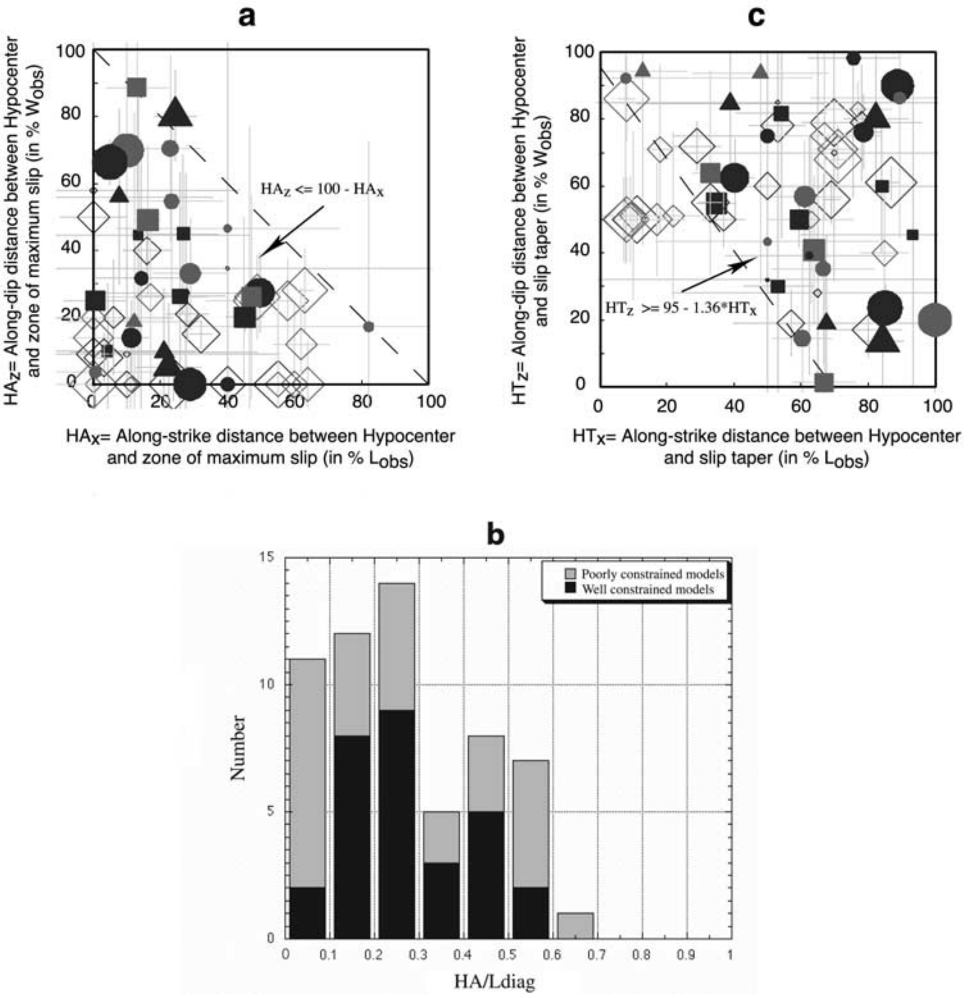

Figure 12. Position of hypocenters (H) with respect to zone of maximum slip (major asperity, A) and to slip taper (T) for earthquake faults with triangular slip profiles (both along strike and dip). Colors and uncertainties are as in Figure 11. Solid symbols are for best constrained models (from Table 2, as in Figure 11); open symbols are for poorly constrained models (from Table 3). Symbol shape indicates degree of asymmetry of along-strike slip profiles. For ruptures wider than 40 km, however, asymmetry is that of along-dip slip profiles. For models with tabular data, distances HA are those between hypocenter and apex of best fitting triangle. For models with no tabular data, distances HA and HT are estimated from visual inspection of the models (when hypocenters lie close to their zone of maximum slip, HA is fixed to zero; open symbols falling on any of the axes are therefore not well constrained). In all plots, symbol size is proportional to magnitude. (a) Position of hypocenter with respect to zone of maximum slip, with distances in percent of L_{obs} and W_{obs}. (b) Histogram of HA ($HA = (Ha_x{}^2 + Ha_z{}^2)^{0.5}$, all in km) normalized by diagonal length ($L_{diag} = (L^2 + W^2)^{0.5}$, all in km) of events. (c) Position of hypocenter with respect to slip taper, with distances in percent of L_{obs} and W_{obs}. See color version of this figure at back of this issue.

beyond which an earthquake does not nucleate. The limit separating the two domains is not clear, but we note that all hypocenters lie below a straight line. Any rupture nucleating quite far (in percent of L_{obs} or W_{obs}) in one direction from a major asperity apparently needs to be much closer from it in the perpendicular direction. The maximum distance (in percent of L_{obs} and W_{obs}) at which an earthquake can nucleate from the major asperity that it eventually breaks is ∼50% of its total length and width. Most earthquakes, however, seem to nucleate closer, with a hypocenter asperity distance (HA) on the order of 20–30% of their total length or width. This average value is similar to the mean normalized size of major asperities within earthquake fault planes as determined from smaller data sets by *Somerville et al.* [1999] and *Beresnev and Atkinson* [2002]. This suggests that earthquakes may actually nucleate at the edges of the major asperities that they eventually break. We note that rare are those nucleating in their final zone of peak slip (graph origin; see remark above on teleseismic models). These results are in agreement with those of *Mai et al* [2005], who statistically investigated the hypocenter position in inversion models and found that most ruptures nucleate in or close to regions of large slip.

[29] The size of the ‘‘major asperities’’ (taken to be the distance HA) broken by the earthquakes can be examined in

Figure 12b. Figure 12b is a histogram of these HA normalized by the diagonal length of the rupture planes. It confirms that in most cases HA averages 20–30% of the rupture size, whatever that size (i.e., earthquake magnitude) is. This makes HA scaling with the earthquake moment roughly as L does. Note that a similar result has been suggested by *Aki* [1992], *Somerville et al.* [1999], *Beresnev and Atkinson* [2002], and *Mai and Beroza* [2002]. Finally, we observe that HA never is greater than 60–70% of the rupture length. This suggests that earthquakes break larger surfaces than those of their major asperities.

3.2.3. Position of Hypocenters With Respect to Slip Tapers

[30] We here look for a possible relationship between the place where earthquakes initiate (hypocenters) and the place where they gently die out (gentle slip tapers). Figures 12c is similar to 12a, except that it shows the position of hypocenters with respect to the tapers of the triangular slip profiles (distances HT_x and HT_z; note that those are not necessarily complementary to HA_x and HA_z). If one omits the few poorly constrained models with a hypocenter arbitrarily located at half fault width, two different domains again appear, one where all hypocenters are, the other free of any. This suggests that an earthquake that would nucleate close to its slip taper in one direction (as Landers, Denali etc…), would nucleate far from its slip taper in the other direction (hence close to its zone of peak slip; note that "distances" are expressed in percent of L_{obs} and W_{obs}). All in all, earthquakes nucleate at distances from their tapers that are greater than their half length and width together. This shows that significant portions of the fault surfaces, i.e., those with low slip roughly linearly tapering to zero, cannot be the site of rupture initiation. This suggests that these portions are far from their rupture threshold when the earthquake nucleates. We will come back to this point in the discussion.

3.3. Analyzing the Scaling Relations for the Available Earthquakes

[31] The observation of slip profiles being similar in shape for the whole range of scales and focal mechanisms analyzed, suggests that slip distributions on earthquake faults are self-similar, i.e., scale invariant in the range of scales considered in this study. If this is true, the profiles of maximum slip should have their maximum displacement value (D_{max}) scaling roughly linearly with their length (either L or W). We address this question here. So far, a lot of studies have been carried out to determine whether or not mean slip would scale with rupture width or length, that is, stress drop would be independent of earthquake size or not [*Scholz*, 1982; *Romanowicz*, 1992; *Scholz*, 1994a, 1994b; *Bodin and Brune*, 1996; *Mai and Beroza*, 2000; *Shaw and Scholz*, 2001] (see *Scholz* [2002] for a review). After 20 years of debate (and of accumulating data), it now seems that all earthquakes but the largest ones are self-similar, i.e., have stress drops roughly constant overall (in the hypothesis of elastic cracks [e.g., *Scholz*, 2002]). In other words, for small and moderate earthquakes, D_{mean} scales roughly linearly with W, while increasing asymptotically with L. For the largest earthquakes, mean slip is suggested to saturate to an about constant value.

[32] Here, we use our data sets to further document this behavior. However, we only focus on the relations between D_{max} and L and W (for D_{mean} is poorly documented in our data sets, as in most data sets used before). For triangular profiles, however, $D_{max} = 2D_{mean}$ (see Figure 10) so that any conclusion drawn on D_{max}/L (or W) scaling applies to mean displacement length (or width) scaling as well. While surface measurements are well constrained, they generally only represent a fraction of the total slip (and length) on the rupture planes. By contrast, while slip maps inferred from inversions do not include all the details of the ruptures, they contain their main features at depth, both in terms of slip amplitude and spatial extension. We therefore combine these two data types to shed light on possible differences of scaling laws from depth to surface. For the inversion models, we use the original values of slip (D_{max} and D_{mean}) and dimensions (L_{model} and W_{model}) (to preserve seismic moment; Table 2). Where several models exist for an earthquake, we consider the averaged slip, length and width values (unrealistic values are excluded; see Table 2 and ES01). For surface data, we use L_{obs}. Hence, as length notations are different for the various data sets, lengths are simply referred to as L in the following.

[33] Figures 13a–13b plot D_{max} as a function of L for dip-slip and strike-slip earthquakes, respectively (see Figure 13 caption for details). Although the distribution of dip-slip data is not completely clear, it shows the same tendencies as described before [e.g., *Scholz*, 2002]; that is, maximum slip roughly linearly scales with length for earthquakes with $L \leq$ 100–150 km. For longer ruptures, there is no evidence of a systematic increase of D_{max} with L, the maximum slip saturating at 4 ± 2 m in most cases. The distribution of strike-slip data is different. The population of measurements defines three major trends, with very few data in between. The steepest trend coincides with that defined for short dip-slip ruptures. Along each trend, D_{max}/L is roughly constant (or slightly decreasing with length). In a following paper, we will show that earthquakes falling on one trend or another pertain to different tectonic regions, with different lithospheric thicknesses.

[34] Figure 13c shows D_{max} as a function of W for all available data (less numerous than before as W is rarely known). It suggests that for most ruptures (dip slip and strike slip) with $W \leq$ 30–40 km, D_{max} roughly scales with W. Note that these "constant stress drop ruptures" include most major strike-slip earthquakes. For wider ruptures ($W \geq$ 30–40 km; here they are the largest dip-slip earthquakes), there is no clear trend of linear scaling, suggesting that stress drop deduced from the simple crack model is no longer constant for these ruptures.

[35] The analysis above therefore confirms that all dip-slip and strike-slip earthquakes worldwide but the largest ones (= with L > 150 km and/or W > 40 km) obey self-similar scaling. Their ratios D_{max}/L and D_{max}/W are about constant (so their stress drops if they behave as elastic cracks), so that their along-strike and along-dip triangular slip profiles are self-similar. For largest strike-slip earthquakes, D_{max}/L is roughly constant along each of the three major trends observed. This makes the along-strike triangular slip profiles self-similar in shape along each given trend. D_{max} instead saturates for increasing W (largest dip-slip earthquakes), suggesting that along-dip

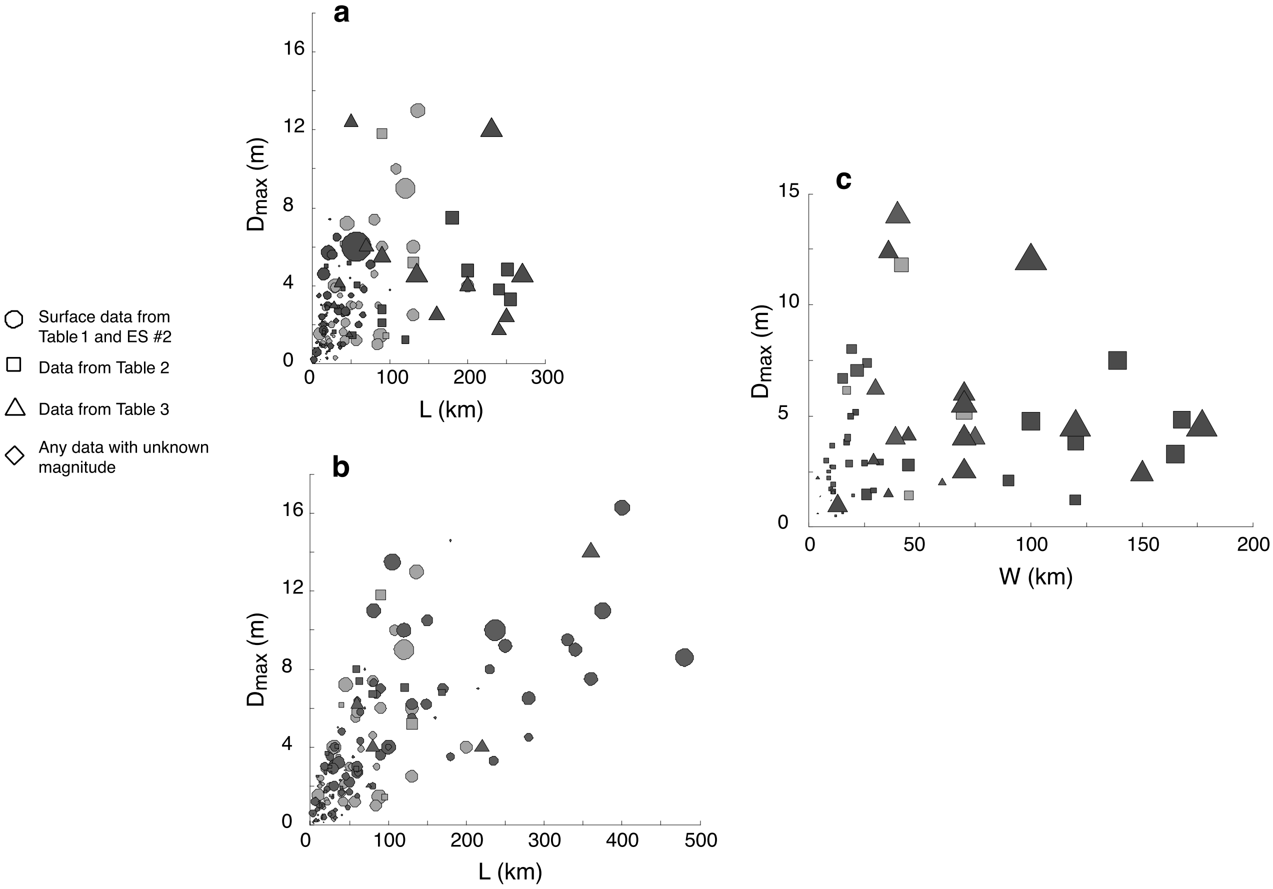

Figure 13. Scaling relations for the earthquakes analyzed. (a) Maximum displacement (D_{max}) versus length (L) for dip-slip (blue) and oblique (gray) faults (from Tables 1, 2, and 3 and ES02). (b) Maximum displacement (D_{max}) versus length (L) for strike-slip (red) and oblique (gray) faults (from Tables 1, 2, and 3 and ES02). (c) Maximum displacement (D_{max}) versus width (W) for dip-slip (blue), strike-slip (red), and oblique (gray) faults (from Tables 2 and 3). Symbol size is proportional to magnitude. Where that is unknown (as for earthquake sequences), symbol size is set to an arbitrary value (corresponding to M = 6). L is L_{obs} for data from Table 1, L_{meas} for data from ES022, and L_{model} for data from Tables 2 and 3 (same for W). See color version of this figure at back of this issue.

slip profiles on major dip-slip faults are not self-similar in shape.

4. Comparison Between Seismic and Cumulative ($\sim10^{-2}$ to 1 Ma) Slip Profiles

[36] So far we have examined a large number of earthquakes together and showed that this reveals common general properties of the coseismic slip on individual earthquake ruptures. With time, earthquakes repeat on a given fault and make it grow. Their individual slip profiles add to produce a total "cumulative" slip distribution on the fault. Provided that a large number of earthquakes is involved, the cumulative slip distributions therefore give an over time-averaged image of earthquakes. Hence, if earthquakes have general properties, those should appear in these cumulative slip distributions as well. We investigate this point below.

[37] It has long been shown that maximum displacement on long-term faults roughly linearly scales with their length, so that cumulative faults grow self-similar (whether they are strike slip or dip slip [e.g., *Manighetti et al.*, 2001; *Peacock*, 2002; *Scholz*, 2002, and references therein]). In the framework of elastic mechanics, such self-similarity is in agreement with faults growing by developing elliptical (or bell-shaped, that is with local tapers at their tips) cumulative slip profiles. This is why slip distributions on long-term faults have long been predicted and taken to be elliptical in shape [e.g., *Scholz*, 1990; *Cowie and Scholz*, 1992a, 1992b]. Yet, real measurements of cumulative slip profiles show that this is rarely the case [e.g., *Manighetti et al.*, 2001, and references therein; *Scholz*, 2002]. *Manighetti et al.* [2001] measured ~250 cumulative slip profiles on active normal faults and systems (Afar, East Africa) spanning a broad range of scales (L = $1-10^2$ km; D_{max} = $1-10^3$m) and ages (10^{-1} to 1 Ma; note that these ages imply that each fault has accumulated hundreds to thousands of earthquakes). Eighty-five percent of these profiles were found to be triangular in overall shape, and most of them were found to be asymmetric (64% over the 85%; see discussion by *Manighetti et al.* [2001]). The overall pattern most commonly found is shown in Figure 14 (stacking of ~80 profiles; see Figure 14 caption for details). It is similar to that that we found for seismic slip profiles (compare

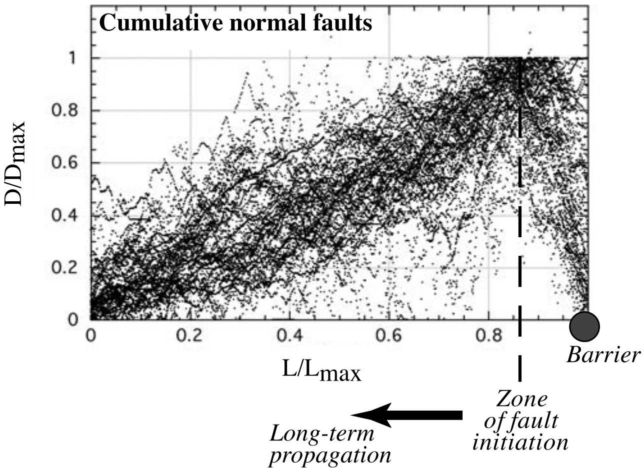

Figure 14. Overall slip distribution pattern on long-term normal faults. Plot shows ~80 cumulative slip profiles measured on normal faults of various ages (10^{-1}–1 Ma), lengths ($L = 1-10^2$ km), and displacements ($D = 1-10^3$ m). Profiles have been normalized by both L and D_{max} with some of them being flipped so that maximum slip is at right [from *Manighetti et al.*, 2001].

Figure 14 to Figures 2, 5, and 7). Although much more rare, the few slip (or slip rate) profiles that have been measured on strike-slip and reverse cumulative faults exhibit the same overall pattern. For instance, the long-term slip rates (10^{-2}–10^{-1} Ma) measured on the ~2000-km-long Altyn Tagh fault show an approximately regular decrease from a maximum value at about the fault center to zero (or almost) at the eastern fault end [*Tapponnier et al.*, 2001]. The cumulative (10^{-2}–10^{-1} Ma) slip distribution on that major strike-slip fault is therefore expected to be triangular (possibly symmetric). Similarly, the slip measurements that were performed on the ~40-km-long Quaternary Puente Hills reverse fault system [*Shaw et al.*, 2002] reveal triangular profiles, both on individual fault segments and on total fault system. Together these observations suggest that cumulative slip profiles on long-term faults are triangular in overall shape (with most of them asymmetric), regardless of fault scale, age, kinematics, location. They therefore resemble those on individual earthquakes. This confirms that considering a long time-averaged accumulation of earthquakes leads to smooth individual earthquake slip complexities and point out a common, general property that is the same than the one that emerged from the combination of a large number of events. That features created in tens of seconds and in tens of thousands to millions years resemble each other suggests that these features share common mechanical explanations.

5. Summary and Discussion

5.1. Summary of Major Observations

[38] We summarize our major observations before discussing them at greater length. We basically found the following:

[39] 1. While earthquakes are complex features with highly heterogeneous mechanical conditions on their planes (due to prestresses, static and dynamic stress loading/unloading by neighboring ruptures, host rock properties, etc.), they share some common, generic properties that appear when a large number of events are examined together: Most produce roughly triangular slip profiles (~70% are asymmetric) with well-defined, long linear tapers of the size of that of the event.

[40] 2. Cumulative faults, which result from the long-term addition of earthquakes (hence provide an over time-averaged image of seismic events), reveal the same property: Most grow by developing triangular and asymmetric slip profiles, with long linear tapers of the size of the fault.

[41] 3. Triangular slip distributions on earthquake faults (but the largest dip-slip ones) seem to be self-similar (in the range of scales analyzed), suggesting that they attest to a scale-invariant mechanical behavior.

[42] 4. That earthquake slip profiles are triangular along both strike and dip implies that seismic ruptures have one single zone of maximum slip and hence break one "major asperity" that is much larger than any others.

[43] 5. Most earthquakes do not nucleate in their zone of maximum slip but commonly nucleate at a distance from it that averages 20–30% of their total length. That distance likely measures the size of the major asperity; most earthquakes would therefore nucleate at the edge of the major asperity that they eventually break.

[44] 6. Most slip profiles are asymmetric, suggesting different behaviors at the two edges of the major asperity. The zone where slip abruptly drops to zero may be where the earthquake was stopped when encountering a rapid change of conditions, while the zone where slip gently tapers to zero may be where the rupture "passively" died out (damping zone). This vision is somehow similar to that of *King* [1986] and *Ward* [1997].

[45] 7. Earthquakes never nucleate in their "taper portions" (if they do so along strike, they do not along dip; or the opposite). This shows that significant fractions of the rupture planes would not have broken if not dynamically loaded.

5.2. Discussion of Major Observations

[46] We found that earthquakes break one major asperity only whose size is ≈a third of the total event size. What are the parameters that determine such asperity size, i.e., the size of the earthquake? In other words, does the distribution of slip entirely result from the dynamic process and the stress conditions (widely unknown at depth), or is the process controlled by some preexisting geological structures? In the latter case, earthquake hazard evaluation would strongly benefit from the identification of the tectonic (or any other) structures defining the potential major asperities. In the former case, earthquakes would remain deterministically unpredictable.

[47] Geological observations may help answering this question. ES06 describes the main features that were observed about where the 56 listed earthquakes initiated (column 5), had their maximum slip abruptly dropping to zero (column 6), and had their slip gently tapering to zero (column 7). Note that while aspects of these observations have been touched on by a number of authors [e.g., *Segall and Pollard*, 1980; *King*, 1986; *Sibson*, 1985, 1986; *Scholz*, 1990; *Harris et al.*, 1991; *Harris and Day*, 1993; *Kame and Yamashita*, 1999; *Oglesby and Day*, 2001; *Harris et al.*,

2002; *Das*, 2003], we have here compiled them for many more earthquakes than has been done before. That compilation reveals that most earthquakes initiated at or close to an intersection between two strongly oblique faults (in strike and in some cases also in dip), one eventually broke during the earthquake. It also shows that most earthquakes have their slip abruptly dropping to zero also at or close to where their plane intersects a strongly oblique fault (in strike or dip). Hence most earthquakes both initiate and abruptly stop at specific spots that bound, and hence define the major asperity, and are controlled by the preexisting fault geometries. The size of the major asperity (i.e., distance HA for the approximately two thirds of earthquakes that have asymmetric profiles) is thus controlled by factors preexisting the event, as the geometry of the fault itself or the presence of surrounding fault systems. The structural/mechanical discontinuities on and around faults exist at a broad range of scales, resulting in a similarly large range of earthquake sizes.

[48] As zones where oblique faults intersect may sustain higher stress concentrations than the surrounding medium [e.g., *King*, 1983, 1986; *Archuleta*, 1984], they may be close to their rupture threshold and capable to favor rupture nucleation. If the medium around is stressed at a "sufficiently" high level (or with sufficient connectivity between high-stress patches [e.g., *Nielsen and Olsen*, 2000; *Miller*, 2002]), the rupture may start propagating and growing. If the stress environment is favorable, the rupture is not supposed to stop [e.g., *Scholz*, 2002]. The arrest of the rupture can be produced, however, either by a strong region that is capable of sustaining high stresses without breaking (e.g., crosscutting fault unfavorably oriented for rupture, regions of tough rocks, zones where stresses have been relaxed by previous earthquakes or creep [e.g., *Aki*, 1979; *Rice*, 1980; *Sibson*, 1989]), or by a region weak enough to have accommodated the tectonic load (e.g., regions of soft material such as active volcanoes, densely fissured and faulted areas [e.g., *Husseini et al.*, 1975; *Boatwright and Cocco*, 1996]). These arresting features have long been observed and indifferently referred to as "barriers" [e.g., *Aki et al.*, 1978; *King*, 1983; *King and Yielding*, 1984; *King and Nabelek*, 1985; *King*, 1986; *Sibson*, 1989; *Wesnousky*, 1988, 1994; *Susong et al.*, 1990; *Poliakov et al.*, 2002; *Das*, 2003]. ES06 suggests that zones where oblique faults intersect can act as barriers. Other features are observed, however, which act similarly (step over areas, zones in which stresses have been relaxed by a previous earthquake, etc). Hence barriers exist at many scales. Yet, *Zhang et al.* [1999] [see also *King*, 1983; *Sibson*, 1989; *Lettis et al.*, 2002] have shown that the size of those capable of arresting earthquakes is related to these earthquake magnitudes.

[49] By contrast with the abrupt stop discussed above, in general, no particular features are observed where slip gently tapers to zero (ES06). Hence earthquakes can fade away anywhere along the faults. We also showed that earthquakes never nucleate within their "low slip areas" (corresponding to slip tapers both in strike and dip). This shows that these low slip areas of the rupture planes were not in the appropriate stress and/or energetic conditions to break when the earthquake initiated. Hence these portions likely started to break when their stress level was raised by dynamic overshoot [e.g., *Das and Aki*, 1977; *Mikumo and Miyatake*, 1978; *Day*, 1982]. We suggest that some and perhaps most portions of the fault plane extending outside of the major asperity (as defined above) broke when rupture of that asperity had released energy and increased stress enough to make them breakable despite of their unfavorable local energy balance. This scenario has been suggested by the dynamic modeling of *Favreau and Archuleta* [2003].

[50] The triangular slip profiles may therefore result from an "energetic scenario": An earthquake would initiate at some high-stress spot (commonly, an intersection zone between two oblique faults) and then grows in length, slip, and magnitude until a mechanical/structural barrier (commonly another fault intersection, but other features are possible; see ES06) stops its lateral propagation. The area broken during this "first stage" appears as the major asperity that shapes the total triangular slip distribution. Most of the moment is released by rupture of this area [see also *McGarr and Fletcher*, 2002]. This rupture produces dynamic stress overshoot in the surrounding fault plane. This overshoot makes some unfavorably stressed (or in inappropriate energetic conditions) portions of the fault plane in conditions to slip. The linear trends in the final slip profile are taken to be associated with the progressive dissipation of the energy provided by the dynamic rupture of the main asperity.

[51] In systems of parallel faults, linear slip tapers may result from elastic interaction (e.g., *Scholz* [2002] and S. Wolf et al. (Mechanics of normal fault networks subject to slip weakening friction, submitted to *Geophysical Journal International*, 2004) for a dynamic model). Stress shadowing effects cannot be put forward, however, when considering that major faults at large scale are isolated. It is difficult to reproduce triangular slip profiles on large earthquakes with present-day models without having ad hoc hypotheses on the distributions of friction properties or of stress. Since the triangular shape appears from averaging a large number of events, it must result from robust physical properties, not from peculiarities of initial conditions. We suggested above that the linear trends may be associated with the progressive dissipation of the energy provided by the dynamic rupture of the main asperity in regions that were not prone to slip. The self-similarity of the slip distributions implies that such dissipation is a scale-dependent process. This conclusion goes against the classical use of constant friction laws on faults embedded in elastic bodies.

[52] ES06 describes the features that are observed or evidenced around the low slip portions (tapers, i.e., damping zones) of the listed earthquakes (column 8). It shows that for most events, coseismic (or immediately postseismic) off-fault deformation is observed around the zones of low slip, mainly as secondary oblique faults slipping together with the main rupture (and generally continuing slipping during the few years following the earthquake), crack opening, distributed off-fault earthquakes (some are possibly coseismic) with high-stress drops and mechanisms differing from that of the main rupture. In most cases, these zones of off-fault deformation are large (several kilometers). It is therefore possible that a significant fraction of the dynamic energy dissipates in the surrounding medium (as suggested by *Poliakov et al.* [2002] and *McGarr and Fletcher* [2002]) through off-fault slip or "damage." Here we use the term damage in a much broader sense than

commonly done, as we consider that any off-fault deformation of the volume, pervasive or localized, plastic or elastic, of microscopic to macroscopic scale, can act as damage. Permanent (static) damage (used in the same broad sense) has been recently evoked to explain the development of self-similar triangular slip profiles on cumulative faults [*Manighetti et al.*, 2004]. Such permanent damage would accommodate the excess stresses that a triangular slip distribution would otherwise produce on the main fault plane. This would allow faults to grow in a self-similar way (i.e., homogeneous stress distribution on their plane) while maintaining triangular slip profiles. Introducing off-fault damage in the dynamic rupture models has rarely been done [*Dalguer et al.*, 2003; *Andrews*, 2005], but we suggest that it may be part of the key to understand why earthquake slip profiles are triangular. Dissipation in the volume around the earthquake faults could also help understanding better the friction and heat flow paradox [e.g., *Brune et al.*, 1969; *Scholz*, 2000; *Ben-Zion*, 2001; *Das*, 2003]. Also, if damage occurs preferentially on one side of the ruptures, as ES06 suggests, it may contribute to generate material contrasts on either sides of the fault. This could in turn partly explain why most earthquakes propagate unilaterally [*McGuire et al.*, 2002].

6. Conclusions

[53] We have investigated what slip distributions look like on earthquake faults. We addressed this issue by considering slip distributions on earthquakes large enough for the local perturbations at their tips to be neglected. We analyzed two types of data. On one hand, we compiled 44 slip profiles measured by geologists at the surface after major earthquakes of various focal mechanisms and magnitudes. On the other hand, we derived along-strike and along-dip slip profiles from 76 slip inversion models obtained by inversion of seismological and/or geodetic data for various earthquakes. We investigated the overall shape of these slip profiles, and found that these are basically triangular (for ~90% of the profiles), and most of them (70–80%) strongly asymmetric. We then compared these earthquake slip profiles to cumulative slip profiles measured on long-term faults of various ages (10^4–10^6 years), sizes (1–10^3 km), and kinematics and found that they are similar, i.e., overall triangular and asymmetric. This makes slip, whether it is seismic or cumulative, roughly linearly decreasing from a maximum at one fault tip to zero at the other fault tip. High slip gradients and long linear slopes (of the size of the seismic events or of the faults) therefore are the key ingredients to describe slip distributions on earthquake and long-term faults.

[54] The observation of triangular slip distributions therefore attests to a common, general property of faults, regardless of their scale (in space and time, as it applies from "instantaneous" earthquakes to long-term faults) and kinematics. Combining a dense population of earthquakes, or considering a long time-averaged accumulation of earthquakes (cumulative profiles), helps smoothing the individual slip complexities and points out a common, generic property. It appears that although earthquakes are irregular and heterogeneous in detail, they share homogeneous average properties that are similar on a wide range of length scales. Also, although individual earthquakes differ from one another in detail, they combine to produce homogeneous features at a longer timescale (and space scale) (cumulative profiles).

[55] That slip distributions on individual earthquakes are triangular confirms that triangular cumulative slip profiles do not result from the addition of elliptical seismic slip profiles, as it had been proposed [e.g., *Walsh and Watterson*, 1987, 1988; *Peacock and Sanderson*, 1996; *Chang and Smith*, 2002]. Instead, faults grow through the addition of triangular slip functions, and produce similar functions as they grow (we, however, ignore how the entire process works). The triangular slip profiles are furthermore shown to be self-similar, whether they are seismic or cumulative.

[56] Together these demonstrate that the earthquake process involves and produces heterogeneous stress conditions. This prevents the use of oversimplified linear homogeneous models to reproduce the observed generic properties of slip distributions. We suggest that introducing in the volume holding the earthquake ruptures, either plastic deformation or elastic distributed cracking and faulting, both involving nonlinear strain behavior, may be a way to reconcile the earthquake models with the observations.

[57] On average, slip distributions are dominated by one zone of large slip only, whose rupture accounts for most of the moment release. We found that earthquakes nucleate at a finite distance from this zone of maximum slip. That distance averages 20–30% of their total length, and likely measures the size of the major asperity broken by the earthquake. Compiling observations made where past earthquakes initiated and abruptly stopped, suggests that most of these asperities are fault segments or systems extending between two major structural discontinuities, mainly zones of oblique cross cutting faults. Most earthquakes are observed to nucleate where two strongly oblique (commonly roughly perpendicular) faults intersect. Then they propagate and grow unilaterally until they abut another structural discontinuity (a "barrier") after which they progressively die out in the form of long linear slip tapers. If this scenario is correct, it implies that knowing the long-term fault geometry may significantly help earthquake hazard quantitative evaluation.

[58] **Acknowledgments.** This work has been done during the 2 year visit of the first author in the SCEC Department, USC, Los Angeles. The first author particularly thanks Y. Delaby for his help with data processing. We are grateful to R. Dmowska, J. Rice and R. Archuleta for fruitful discussions. We thank J. Gomberg, C. Scholz, and an anonymous reviewer for their constructive comments. This is contribution 894 of SCEC; contribution 1344 of the Institute of Geophysics, ETH Zurich; and contribution 2036 of Institut de Physique du Globe de Paris, France.

References

Abercrombie, R., and J. Mori (1994), Local observations of the onset of a large earthquake: 28 June 1992 Landers, California, *Bull. Seismol. Soc. Am.*, *84*, 725–734.

Abercrombie, R. E., M. Antolik, K. Felzer, and G. Ekstrom (2001), The 1994 Java tsunami earthquake: Slip over a subducting seamount, *J. Geophys. Res.*, *106*, 6595–6607.

Aki, K. (1979), Characterization of barriers on an earthquake fault, *J. Geophys. Res.*, *84*, 6140–6148.

Aki, K. (1992), Higher-order interrelations between seismogenic structures and earthquake process, *Tectonophysics*, *211*, 1–12.

Aki, K., M. Bouchon, B. Chouet, and S. Das (1978), Quantitative prediction of strong motion for a potential earthquake fault, *Ann. Geofis.*, *30*, 341–368.

Akyuz, H. S., R. Hartleb, A. Barka, E. Altunel, G. Sunal, B. Meyer, and R. Armijo (2002), Surface rupture and slip distribution of the 12 November 1999 Duzce earthquake (*M* 7.1), North Anatolian fault, Bolu, Turkey, *Bull. Seismol. Soc. Am.*, *92*, 61–66.

Andrews, D. J. (2005), Rupture dynamics with energy loss outside the slip zone, *J. Geophys. Res.*, *110*, B01307, doi:10.1029/2004JB003191.

Antolik, M., and D. S. Dreger (2003), Rupture process of the 26 January 2001 M_w 7.6 Bhuj India earthquake from teleseismic broadband data, *Bull. Seismol. Soc. Am.*, *93*, 1235–1248.

Antolik, M., A. Kaverina, and D. Dreger (2000), Compound rupture of the great 1998 Antarctic plate earthquake, *J. Geophys. Res.*, *105*, 23,825–23,838.

Archuleta, R. J. (1984), A faulting model for the 1979 Imperial Valley earthquake, *J. Geophys. Res.*, *89*, 4559–4585.

Barenblatt, G. I. (1962), The mathematical theory of equilibrium cracks in brittle fracture, *Adv. Appl. Mech.*, *7*, 55–80.

Barka, A. (1996), Slip distribution along the north Anatolian fault associated with the large earthquakes of the period 1939 to 1967, *Bull. Seismol. Soc. Am.*, *86*, 1238–1254.

Barka, A., et al. (2002), The surface rupture and slip distribution of the 17 August 1999 Izmit earthquake (*M* 7.4), North Anatolian fault, *Bull. Seismol. Soc. Am.*, *92*, 43–60.

Bennett, R. A., R. E. Reilinger, W. Rodi, Y. Li, M. N. Toksöz, and K. Hudnut (1995), Coseismic fault slip associated with the 1992 M_w 6.1 Joshua Tree, California, earthquake: Implications for the Joshua Tree-Landers earthquake sequence, *J. Geophys. Res.*, *100*, 6443–6462.

Ben-Zion, Y. (2001), Dynamic ruptures in recent models of earthquake faults, *J. Mech. Phys. Solids*, *49*, 2209–2244.

Berberian, M., et al. (2001), The 1998 March 14 Fandoqa earthquake (M_w 6.6) in Kerman province, southeast Iran: Re-rupture of the 1981 Sirch earthquake fault, triggering of slip on adjacent thrusts and the active tectonics of the Gowk fault zone, *Geophys. J. Int.*, *146*, 371–398.

Beresnev, I. A., and G. M. Atkinson (2002), Source parameters of earthquakes in eastern and western North America based on finite-fault modeling, *Bull. Seismol. Soc. Am.*, *92*, 695–710.

Beroza, G. C. (1991), Near source modeling of the Loma Prieta earthquake: Evidence for heterogeneous slip and implications for earthquake hazard, *Bull. Seismol. Soc. Am.*, *81*, 1603–1621.

Beroza, G. C., and P. Spudich (1988), Linearized inversion for fault rupture behavior; application to the 1984 Morgan Hill California earthquake, *J. Geophys. Res.*, *93*, 6275–6296.

Boatwright, J., and M. Cocco (1996), Frictional constraints on crustal faulting, *J. Geophys. Res.*, *101*, 13,895–13,909.

Bodin, P., and J. N. Brune (1996), On the scaling of slip with rupture length for shallow strike-slip earthquakes: Quasi-static models and dynamic rupture propagation, *Bull. Seismol. Soc. Am.*, *86*, 1292–1299.

Bouchon, M., N. Toksöz, H. Karabulut, M. Bouin, M. Dietrich, M. Aktar, and M. Edie (2000), Seismic imaging of the 1999 Izmit (Turkey) rupture inferred from the near-fault recordings, *Geophys. Res. Lett.*, *27*, 3013–3016.

Bouchon, M., M. N. Toksoz, H. Karabulut, M. P. Bouin, M. Dietrich, M. Aktar, and M. Edie (2002), Space and time evolution of rupture and faulting during the 1999 Izmit (Turkey) earthquake, *Bull. Seismol. Soc. Am.*, *92*, 256–266.

Brune, J., T. Henyey, and R. Roy (1969), Heat flow, stress, and rate of slip along the San Andreas fault, California, *J. Geophys. Res.*, *74*, 3821–3827.

Campillo, M., and R. J. Archuleta (1993), A rupture model for the 28 June 1992 *M*7.4 Landers, California, earthquake, *Geophys. Res. Lett.*, *20*, 647–650.

Caskey, S. J., and S. G. Wesnousky (1997), Static stress changes and earthquake triggering during the 1954 Fairview Peak and Dixie Valley earthquakes, central Nevada, *Bull. Seismol. Soc. Am.*, *87*, 521–527.

Caskey, S. J., S. G. Wesnousky, P. Zhang, and D. B. Slemmons (1996), Surface faulting of the 1954 Fairview Peak (M_s 7.2) and Dixie Valley (M_s 6.8) earthquakes, central Nevada, *Bull. Seismol. Soc. Am.*, *86*, 761–787.

Chambon, G., and J. W. Rudnicki (2001), Effects of normal stress variations on frictional stability of a fluid-infiltrated fault, *J. Geophys. Res.*, *106*, 11,353–11,372.

Chang, W. L., and R. B. Smith (2002), Integrated seismic-hazard analysis of the Wasatch front, Utah, *Bull. Seismol. Soc. Am.*, *92*, 1904–1922.

Chi, W. C., D. Dreger, and A. Kaverina (2001), Finite-source modeling of the 1999 Taiwan (Chi-Chi) earthquake derived from a dense strong-motion network, *Bull. Seismol. Soc. Am.*, *91*, 1144–1157.

Choy, G. L., and J. W. Dewey (1988), Rupture process of an extended earthquake sequence: Teleseismic analysis of the Chilean earthquake of March 3, 1985, *J. Geophys. Res.*, *93*, 1103–1118.

Cohee, B. P., and G. C. Beroza (1994), Slip distribution of the 1992 Landers earthquake and its implications for earthquake source mechanics, *Bull. Seismol. Soc. Am.*, *84*, 692–712.

Cotton, F., and M. Campillo (1995), Frequency domain inversion of strong motions: Application to the 1992 Landers earthquake, *J. Geophys. Res.*, *100*, 3961–3975.

Cowie, P. A., and C. H. Scholz (1992a), Physical explanation for the displacement-length relationship of faults using a post-yield fracture mechanics models, *J. Struct. Geol.*, *14*, 1133–1148.

Cowie, P. A., and C. H. Scholz (1992b), Growth of faults by accumulation of seismic slip, *J. Geophys. Res.*, *97*, 11,085–11,095.

Crone, A. J., and M. N. Machette (1984), Surface faulting accompanying the Borah Peak earthquake, central Idaho, *Geology*, *12*, 664–667.

Dalguer, L. A., K. Irikura, and J. D. Riera (2003), Simulation of tensile crack generation by three-dimensional dynamic shear rupture propagation during an earthquake, *J. Geophys. Res.*, *108*(B3), 2144, doi:10.1029/2001JB001738.

Das, S. (2003), Spontaneous complex earthquake rupture propagation, *Pure Appl. Geophys.*, *160*, 579–602.

Das, S., and K. Aki (1977), A numerical study of two dimensional spontaneous rupture propagation, *Geophys. J. R. Astron. Soc.*, *50*, 643–668.

Das, S., and B. V. Kostrov (1983), Breaking a single asperity: Rupture process and seismic radiation, *J. Geophys. Res.*, *88*, 4277–4288.

Das, S., and B. V. Kostrov (1990), Inversion for seismic slip rate history and distribution with stabilizing constraints: Application to the 1986 Andreanof islands earthquake, *J. Geophys. Res.*, *95*, 6899–6913.

Das, S., and C. H. Scholz (1983), Why large earthquakes do not nucleate at shallow depths, *Nature*, *305*, 621–623.

Day, S. M. (1982), Three dimensional simulation of spontaneous rupture: The effect of non-uniform prestress, *Bull. Seismol. Soc. Am.*, *72*, 1881–1902.

Delouis, B., D. Giardini, P. Lundgren, and J. Salichon (2001), Details of the 1999 Izmit-Düzce (Turkey) mainshock sequence from geodetic and seismological data, paper presented at 26th General Assembly of the European Geophysical Society (EGS), Nice, France.

Delouis, B., D. Giardini, and P. Lundgren (2002), Joint inversion of Insar, GPS, teleseismic and strong-motion data for the spatial and temporal distribution of earthquake slip: Application to the 1999 Izmit mainshock, *Bull. Seismol. Soc. Am.*, *92*, 278–299.

Deng, Q., and P. Zhang (1984), Research on the geometry of shear fracture zones, *J. Geophys. Res.*, *89*, 5699–5710.

Dominguez, S., J. Avouac, and R. Michel (2003), Horizontal coseismic deformation of the 1999 Chi-Chi earthquake measured from SPOT satellite images: Implications for the seismic cycle along the western foothills of central Taiwan, *J. Geophys. Res.*, *108*(B2), 2083, doi:10.1029/2001JB000951.

Dreger, D. S. (1994), Empirical Green's function study of the January 17 1994 Northridge California earthquake, *Geophys. Res. Lett.*, *21*, 2633–2636.

Eberhart-Philipps, D., et al. (2003), The 2002 Denali fault earthquake, Alaska: A large magnitude, slip-partitioned event, *Science*, *300*, 1113–1118.

Favreau, P., and R. J. Archuleta (2003), Direct seismic energy modeling and application to the 1979 Imperial Valley earthquake, *Geophys. Res. Lett.*, *30*(5), 1198, doi:10.1029/2002GL015968.

Feigl, K. L., F. Sarti, H. Vadon, and R. Burgmann (2002), Estimating slip distribution for the Izmit mainshock from coseismic GPS, ERS-1, Radarsat, and SPOT measurements, *Bull. Seismol. Soc. Am.*, *92*, 138–160.

Harris, R. A., and S. M. Day (1993), Dynamics of fault interaction: Parallel strike-slip faults, *J. Geophys. Res.*, *98*, 4461–4472.

Harris, R. A., R. J. Archuleta, and S. M. Day (1991), Fault steps and the dynamic rupture process: 2D numerical simulations of a spontaneously propagating shear fracture, *Geophys. Res. Lett.*, *18*, 893–896.

Harris, R. A., J. Dolan, R. Hartleb, and S. M. Day (2002), The 1999 Izmit Turkey earthquake: A 3D dynamic stress transfer model of intraearthquake triggering, *Bull. Seismol. Soc. Am.*, *92*, 245–255.

Hartleb, R. D., et al. (2002), Surface rupture and slip distribution along the Karadere segment of the 17 August 1999 Izmit and the western section of the 12 November 1999 Duzce, Turkey, earthquakes, *Bull. Seismol. Soc. Am.*, *92*, 67–78.

Hartzell, S., and C. Langer (1993), Importance of model parameterization in finite fault inversions: Application to the 1974 M_W 8.0 Peru earthquake, *J. Geophys. Res.*, *98*, 22,123–22,134.

Hartzell, S., C. Lenger, and C. Mendoza (1994), Rupture histories of eastern North American earthquakes, *Bull. Seismol. Soc. Am.*, *84*, 1703–1724.

Hartzell, S., P. Liu, and C. Mendoza (1996), The 1994 Northridge, California, earthquake: Investigation of rupture velocity, risetime, and high-frequency radiation, *J. Geophys. Res.*, *101*, 20,091–20,108.

Hartzell, S. H. (1989), Comparison of seismic waveform inversion results for the rupture history of a finite fault: Application to the 1986 North Palm Springs, California, earthquake, *J. Geophys. Res.*, *94*, 7515–7534.

Hartzell, S. H., and T. H. Heaton (1983), Inversion of strong ground motion and teleseismic waveform data for the fault rupture history of the 1979 Imperial Valley California earthquake, *Bull. Seismol. Soc. Am.*, *73*, 1553–1583.

Hartzell, S. H., and T. H. Heaton (1986), Rupture history of the 1984 Morgan Hill California earthquake from the inversion of strong motion records, *Bull. Seismol. Soc. Am.*, *76*, 649–674.

Hartzell, S. H., and C. Mendoza (1991), Application of an iterative least-squares waveform inversion of strong-motion and teleseismic records to the 1978 Tabas Iran earthquake, *Bull. Seismol. Soc. Am.*, *81*, 305–331.

Heaton, T. H. (1982), The 1971 San Fernando earthquake: A double event?, *Bull. Seismol. Soc. Am.*, *72*, 2037–2062.

Hemphill-Haley, M. A., and R. J. Weldon II (1999), Estimating prehistoric earthquake magnitude from point measurements of surface rupture, *Bull. Seismol. Soc. Am.*, *89*, 1264–1279.

Henry, C., and S. Das (2002), The M_w 8.2, 17 February 1996 Biak, Indonesia, earthquake: Rupture history, aftershocks, and fault plane properties, *J. Geophys. Res.*, *107*(B11), 2312, doi:10.1029/2001JB000796.

Hernandez, B., F. Cotton, and M. Campillo (1999), Contribution of radar interferometry to a two-step inversion of the kinematic process of the 1992 Landers earthquake, *J. Geophys. Res.*, *104*, 13,083–13,099.

Hernandez, B., N. M. Shapiro, S. K. Singh, J. F. Pacheco, F. Cotton, M. Campillo, A. Iglesias, V. Cruz, J. M. Gómez, and L. Alcántara (2001), Rupture history of September 30, 1999 intraplate earthquake of Oaxaca, Mexico ($M_W = 7.5$) from inversion of strong-motion data, *Geophys. Res. Lett.*, *28*, 363–366.

Hough, S. E., and D. S. Dreger (1995), Source parameters of the 23 April 1992 M 6.1 Joshua Tree California earthquake and its aftershocks: Empirical Green's function analysis of GEOS and TERRAscope data, *Bull. Seismol. Soc. Am.*, *85*, 1576–1590.

Huc, M., R. Hassani, and J. Chéry (1998), Large earthquake nucleation associated with stress exchange between middle and upper crust, *Geophys. Res. Lett.*, *25*, 551–554.

Hudnut, K., L. Seeber, T. Rockwell, J. Goodmacher, R. Klinger, S. Lindvall, and R. McElwain (1989), Surface ruptures on cross-faults in the 24 November 1987 Superstition Hills California earthquake sequence, *Bull. Seismol. Soc. Am.*, *79*, 282–296.

Hudnut, K. W., Z. Shen, M. Murray, S. McClusly, R. King, T. Herring, B. Hager, Z. Feng, P. Fang, A. Donnellan, and Y. Block (1996), Coseismic displacements of the 1994 Northridge California earthquake, *Bull. Seismol. Soc. Am.*, *86*, 19–36.

Husseini, M. I., D. B. Jovanovich, M. J. Randall, and L. B. Freund (1975), The fracture energy of earthquakes, *Geophys. J. R. Astron. Soc.*, *43*, 367–385.

Ida, Y. (1972), Cohesive force across tip of a longitudinal shear crack and Griffith's specific energy balance, *J. Geophys. Res.*, *77*, 3796–3805.

Ide, S. (1999), Source process of the 1997 Yamaguchi, Japan, earthquake analyzed in different frequency bands, *Geophys. Res. Lett.*, *26*, 1973–1976.

Ide, S., M. Takeo, and Y. Yoshida (1996), Source process of the 1995 Kobe earthquake: Determination of spatio-temporal slip distribution by Bayesian modeling, *Bull. Seismol. Soc. Am.*, *86*, 547–566.

Ihmlé, P. F. (1998), On the interpretation of subevents in teleseismic waveforms: The 1994 Bolivia deep earthquake revisited, *J. Geophys. Res.*, *103*, 17,919–17,932.

Iwata, T., H. Sekiguchi, Y. Matsumoto, H. Miyake, and K. Irikura (2000), Source process of the 2000 western Tottori Prefecture earthquake and near-source strong ground motions, paper presented at 2000 Fall Meeting, Seismol. Soc. of Jpn., Tokyo.

Ji, C., D. J. Wald, and D. V. Helmberger (2002), Source description of the 1999 Hector Mine California earthquake, part II: Complexity of slip history, *Bull. Seismol. Soc. Am.*, *92*, 1208–1226.

Johnson, K. M., Y. J. Hsu, P. Segall, and S. B. Yu (2001), Fault geometry and slip distribution of the 1999 Chi-Chi, Taiwan earthquake images from inversion of GPS data, *Geophys. Res. Lett.*, *28*, 2285–2288.

Jonsson, S., H. Zebker, P. Segall, and F. Amelung (2002), Fault slip distribution of the 1999 M_w 7.1 Hector Mine California earthquake estimated from satellite radar and GPS measurements, *Bull. Seismol. Soc. Am.*, *92*, 1377–1389.

Kame, N., and T. Yamashita (1999), A new light on arresting mechanism of dynamic earthquake faulting, *Geophys. Res. Lett.*, *26*, 1997–2000.

Kaverina, A., D. Dreger, and E. Price (2002), The combined inversion of seismic and geodetic data for the source process of the 16 October 1999 M_w 7.1 Hector Mine California earthquake, *Bull. Seismol. Soc. Am.*, *92*, 1266–1280.

Kikuchi, M., and Y. Fukao (1985), Iterative deconvolution of complex body waves from great earthquakes: The Tokachi-Oki earthquake of 1968, *Phys. Earth Planet. Inter.*, *37*, 235–248.

King, G. C. P. (1983), The accommodation of strain in the upper lithosphere of the Earth by self-similar fault systems; the geometrical origin of *b*-value, *Pure Appl. Geophys.*, *121*, 761–815.

King, G. C. P. (1986), Speculations on the geometry of the initiation and termination processes of earthquake rupture and its relation to morphology and geological structure, *Pure Appl. Geophys.*, *124*, 567–583.

King, G. C. P., and J. Nabelek (1985), The role of bends in faults in the initiation and termination of earthquake rupture, *Science*, *228*, 984–987.

King, G., and G. Yielding (1984), The evolution of a thrust fault system: Processes of rupture initiation, propagation and termination in the 1980 El Asnam (Algeria) earthquake, *Geophys. J. R. Astron. Soc.*, *77*, 915–933.

Larsen, S., R. Reilinger, H. Neugebauer, and W. Strange (1992), Global positioning system measurements of deformations associated with the 1987 Superstition Hills earthquake: Evidence for conjugate faulting, *J. Geophys. Res.*, *97*, 4885–4902.

Lay, T., and H. Kanamori (1981), An asperity model of great earthquake sequences, in *Earthquake Prediction: An International Review*, *Maurice Ewing Ser.*, vol. 4, edited by D. Simpson and P. Richards, pp. 579–592, AGU, Washington, D. C.

Lettis, W., J. Bachhuber, R. Witter, C. Brankman, C. E. Randolph, A. Barka, W. D. Page, and A. Kaya (2002), Influence of releasing step-overs on surface fault rupture and fault segmentation: Examples from the 17 August 1999 Izmit earthquake on the north Anatolian fault, Turkey, *Bull. Seismol. Soc. Am.*, *92*, 19–42.

Lin, A. M., et al. (2002), Co-seismic strike-slip and rupture length produced by the 2001 M_s 8.1 Central Kunlun earthquake, *Science*, *296*, 015–017.

Liu, H., and D. V. Helmberger (1983), The near-source ground motion of the 6 August 1979 Coyote Lake California earthquake, *Bull. Seismol. Soc. Am.*, *73*, 201–218.

Ma, K. F., J. Mori, S. J. Lee, and S. B. Yu (2001), Spatial and temporal distribution of slip for the 1999 Chi-Chi Taiwan earthquake, *Bull. Seismol. Soc. Am.*, *91*, 1069–1087.

Machette, M. N., S. F. Personius, A. R. Nelson, D. P. Schwartz, and W. R. Lund (1991), The Wasatch fault zone, Utah: Segmentation and history of Holocene earthquakes, *J. Struct. Geol.*, *13*, 137–149.

Madariaga, R. (1979), On the relation between seismic moment and stress drop in the presence of stress and strength heterogeneity, *J. Geophys. Res.*, *84*, 2243–2250.

Mai, P. M., and G. C. Beroza (2000), Source scaling properties from Finite-fault rupture models, *Bull. Seismol. Soc. Am.*, *90*, 604–615.

Mai, P. M., and G. C. Beroza (2002), A spatial random field model to characterize complexity in earthquake slip, *J. Geophys. Res.*, *107*(B11), 2308, doi:10.1029/2001JB000588.

Mai, P. M., P. Spudich, and Boatwright (2005), Hypocenter locations in finite-source rupture models, *Bull. Seismol. Soc. Am.*, in press.

Manighetti, I., G. C. P. King, Y. Gaudemer, C. Scholz, and C. Doubre (2001), Slip accumulation and lateral propagation of active normal faults in Afar, *J. Geophys. Res.*, *106*, 13,667–13,696.

Manighetti, I., G. King, and C. Sammis (2004), The role of off-fault damage in the evolution of normal faults, *Earth Planet. Sci. Lett.*, *217*, 399–408.

McGarr, A., and J. B. Fletcher (2002), Mapping apparent stress and energy radiation over fault zones of major earthquakes, *Bull. Seismol. Soc. Am.*, *92*, 1633–1646.

McGill, S. F., and C. M. Rubin (1999), Surficial slip distribution on the central Emerson fault during the June 28 1992 Landers earthquake, California, *J. Geophys. Res.*, *104*, 4811–4833.

McGuire, J. J., D. A. Wiens, P. J. Shore, and M. G. Bevis (1997), The March 9, 1994 (M_w 7.6) deep Tonga earthquake: Rupture outside the seismically active slab, *J. Geophys. Res.*, *102*, 15,163–15,182.

McGuire, J. J., L. Zhao, and T. H. Jordan (2002), Predominance of unilateral rupture for a global catalog of large earthquakes, *Bull. Seismol. Soc. Am.*, *92*, 3309–3317.

Mendoza, C. (1993), Coseismic slip of two large Mexican earthquakes from teleseismic body waveforms: Implications for asperity interaction in the Michoacan plate boundary segment, *J. Geophys. Res.*, *98*, 8197–8210.

Mendoza, C. (1995), Finite-fault analysis of the 1979 March 14 Petatlan, Mexico, earthquake using teleseismic P waveforms, *Geophys. J. Int.*, *121*, 675–683.

Mendoza, C., and E. Fukuyama (1996), The July 12, 1993, Hokkaido-Nansei-Oki, Japan earthquake: Coseismic slip pattern from strong-motion and teleseismic recordings, *J. Geophys. Res.*, *101*, 791–801.

Mendoza, C., and S. H. Hartzell (1988), Inversion for slip distribution using teleseismic P waveforms: North Palm Springs, Borah Peak, and Michoacan earthquakes, *Bull. Seismol. Soc. Am.*, *78*, 1092–1111.

Mendoza, C., and S. Hartzell (1999), Fault slip distribution of the 1995 Colima-Jalisco, Mexico earthquake, *Bull. Seismol. Soc. Am.*, *89*, 1338–1344.

Mendoza, C., S. Hartzell, and T. Monfret (1994), Wide-band analysis of the 3 March 1985 central Chile earthquake: Overall source process and rupture history, *Bull. Seismol. Soc. Am.*, *84*, 269–283.

Michel, R., and J. Avouac (2002), Deformation due to the 17 August 1999 Izmit, Turkey, earthquake measured from SPOT images, *J. Geophys. Res.*, *107*(B4), 2062, doi:10.1029/2000JB000102.

Mikumo, T., and T. Miyatake (1978), Dynamic rupture process on a three dimensional fault with non-uniform friction and near-field waves, *Geophys. J. R. Astron. Soc.*, *54*, 417–438.

Miller, S. A. (2002), Properties of large ruptures and the dynamical influence of fluids on earthquakes and faulting, *J. Geophys. Res.*, *107*(B9), 2182, doi:10.1029/2000JB000032.

Mori, J. (1996), Rupture directivity and slip distribution of the *M* 4.3 foreshock to the 1992 Joshua Tree earthquake, southern California, *Bull. Seismol. Soc. Am.*, *86*, 805–810.

Nielsen, S. B., and K. Olsen (2000), Constraints on stress and friction from dynamic rupture models of the 1994 Northridge California earthquake, *Pure Appl. Geophys.*, *157*, 2029–2046.

Oglesby, D. D., and R. J. Archuleta (1997), A faulting model for the 1992 Petrolia earthquake: Can extreme ground acceleration be a source effect?, *J. Geophys. Res.*, *102*, 1877–1897.

Oglesby, D. D., and S. M. Day (2001), Fault geometry and the dynamics of the 1999 Chi-Chi (Taiwan) earthquake, *Bull. Seismol. Soc. Am.*, *91*, 1099–1111.

Papageorgiou, A. S. (2003), The barrier model and strong ground motion, *Pure Appl. Geophys.*, *160*, 603–634.

Peacock, D. C. P. (2002), Propagation, interaction and linkage in normal fault systems, *Earth Sci. Rev.*, *58*, 121–142.

Peacock, D. C. P., and D. J. Sanderson (1996), Effects of propagation rate on displacement variations along faults, *J. Struct. Geol.*, *18*, 311–320.

Pegler, G., and S. Das (1996), Analysis of the relationship between seismic moment and fault length for large crustal strike-slip earthquakes between 1977–92, *Geophys. Res. Lett.*, *23*, 905–908.

Peltzer, G., K. W. Hudnut, and K. L. Feigl (1994), Analysis of coseismic surface displacement gradients using radar interferometry: New insights into the Landers earthquake, *J. Geophys. Res.*, *99*, 21,971–21,981.

Peltzer, G., F. Crampé, and G. King (1999), Evidence of nonlinear elasticity of the crust from the M_w 7.6 Manyi (Tibet) earthquake, *Science*, *286*, 272–275.

Perfettini, H., R. S. Stein, R. Simpson, and M. Cocco (1999), Stress transfer by the 1988–1989 $M = 5.3$ and 5.4 Lake Elsman foreshocks to the Loma Prieta fault: Unclamping at the site of peak mainshock slip, *J. Geophys. Res.*, *104*, 20,169–20,182.

Poliakov, A. N. B., R. Dmowska, and J. R. Rice (2002), Dynamic shear rupture interactions with fault bends and off-axis secondary faulting, *J. Geophys. Res.*, *107*(B11), 2295, doi:10.1029/2001JB000572.

Rice, J. R. (1980), The mechanics of earthquake rupture, in *Physics of the Earth's Interior*, edited by A. Dziewonski and E. Boschi, pp. 555–649, Elsevier, New York.

Romanowicz, B. (1992), Strike-slip earthquakes on quasi-vertical transcurrent faults: Inferences for general scaling relations, *Geophys. Res. Lett.*, *19*, 481–484.

Roumelioti, Z., D. Dreger, A. Kiratzi, and N. Theodoulidis (2003), Slip distribution of the 7 September 1999 Athens earthquake inferred from an empirical Green's function study, *Bull. Seismol. Soc. Am.*, *93*, 775–782.

Ruff, L. J., and A. D. Miller (1994), Rupture process of large earthquakes in the northern Mexico subduction zone, *Pure Appl. Geophys.*, *142*, 101–149.

Salichon, J., B. Delouis, P. Lundgren, D. Giardini, M. Costantini, and P. Rosen (2003), Joint inversion of broadband teleseismic and interferometric synthetic aperture radar (InSAR) data for the slip history of the $M_w = 7.7$, Nazca ridge (Peru) earthquake of 12 November 1996, *J. Geophys. Res.*, *108*(B2), 2085, doi:10.1029/2001JB000913.

Scholz, C. H. (1982), Scaling laws for large earthquakes: Consequences for physical models, *Bull. Seismol. Soc. Am.*, *72*, 1–14.

Scholz, C. H. (1990), *The Mechanics of Earthquakes and Faulting*, 1st ed., Cambridge Univ. Press, New York.

Scholz, C. H. (1994a), A reappraisal of large earthquake scaling, *Bull. Seismol. Soc. Am.*, *84*, 215–218.

Scholz, C. H. (1994b), Reply to comments on "A reappraisal of large earthquake scaling," *Bull. Seismol. Soc. Am.*, *84*, 1677–1678.

Scholz, C. H. (2000), Evidence for a strong San Andreas fault, *Geology*, *28*, 163–166.

Scholz, C. H. (2002), *The Mechanics of Earthquakes and Faulting*, 2nd ed., 471 pp., Cambridge Univ. Press, New York.

Schwartz, D. P., and K. J. Coppersmith (1984), Fault behavior and characteristic earthquakes: Examples from the Wasatch and San Andreas faults, *J. Geophys. Res.*, *89*, 5681–5698.

Segall, P., and D. D. Pollard (1980), Mechanics of discontinuous faults, *J. Geophys. Res.*, *85*, 4337–4350.

Sekiguchi, H., and T. Iwata (2002), Rupture process of the 1999 Kocaeli Turkey earthquake estimated from strong-motion waveforms, *Bull. Seismol. Soc. Am.*, *92*, 300–311.

Sekiguchi, H., K. Irikura, T. Iwata, Y. Kakehi, and M. Hoshiba (1996), Determination of the location of faulting beneath Kobe during the 1995 Hyogo-ken Nanbu Japan earthquake from near-source particle motion, *Geophys. Res. Lett.*, *23*, 387–390.

Sharp, R. V. (1982), Comparison of 1979 surface faulting with earlier displacements in the Imperial Valley, in *The Imperial Valley, California, Earthquake of October 15, 1979*, *U.S. Geol. Surv. Prof. Pap.*, *1254*, 213–221.

Sharp, R. V., et al. (1989), Surface faulting along the Superstition Hills fault zone and nearby faults associated with the earthquakes of 24 November 1987, *Bull. Seismol Soc. Am.*, *79*, 252–281.

Shaw, B. E., and C. H. Scholz (2001), Slip-length scaling in large earthquakes: Observations and theory and implications for earthquake physics, *Geophys. Res. Lett.*, *28*, 2991–2994.

Shaw, J. H., A. Plesch, J. F. Dolan, T. L. Pratt, and P. Fiore (2002), Puente Hills blind-thrust system, Los Angeles, California, *Bull. Seism. Soc. Am.*, *92*, 2946–2960.

Sibson, R. H. (1984), Roughness at the base of the seismogenic zone: Contributing factors, *J. Geophys. Res.*, *89*, 5791–5799.

Sibson, R. H. (1985), Stopping of earthquake ruptures at dilatational fault jogs, *Nature*, *316*, 248–251.

Sibson, R. H. (1986), Earthquakes and rock deformation in crustal fault zones, *Annu. Rev. Earth Planet. Sci.*, *14*, 149–175.

Sibson, R. H. (1989), Earthquake faulting as a structural process, *J. Struct. Geol.*, *11*, 1–14.

Sieh, K. (1996), The repetition of large earthquake ruptures, *Proc. Natl. Acad. Sci. U.S.A.*, *93*, 3764–3771.

Sieh, K., et al. (1993), Near-field investigations of the Landers earthquake sequence, April to July 1992, *Science*, *260*, 171–176.

Somerville, P., K. Irikura, R. Graves, S. Sawada, D. Wald, N. Abrahamson, Y. Iwasaki, T. Kagawa, N. Smith, and A. Kowada (1999), Characterizing crustal earthquake slip models for the prediction of strong ground motion, *Seismol. Res. Lett.*, *70*(1), 59–80.

Spence, W., C. Mendoza, E. R. Engdahl, G. L. Choy, and E. Norabuena (1999), Seismic subduction of the Nazca ridge as shown by the 1996–97 Peru earthquakes, *Pure Appl. Geophys.*, *154*, 753–776.

Steidl, J. H., R. J. Archuleta, and S. H. Hartzell (1991), Rupture history of the 1989 Loma Prieta California earthquake, *Bull. Seismol. Soc. Am.*, *81*, 1573–1602.

Stein, R. S., and W. Thatcher (1981), Seismic and aseismic deformation associated with the 1952 Kern County, California, earthquake and relationship to the Quaternary history of the White Wolf fault, *J. Geophys. Res.*, *86*, 4913–4928.

Susong, D. D., S. U. Janecke, and R. L. Bruhn (1990), Structure of a fault segment boundary in the Lost River fault zone, Idaho, and possible effect on the 1983 Borah Peak earthquake rupture, *Bull. Seismol. Soc. Am.*, *80*, 57–68.

Takeo, M. (1988), Rupture process of the 1980 Izu-Hanto-Toho-Oki earthquake deduced from strong motion seismograms, *Bull. Seismol. Soc. Am.*, *78*, 1074–1091.

Takeo, M. (1990), Fault heterogeneity of inland earthquakes in Japan, *Bull. Earthquake Res. Inst. Univ. Tokyo*, *65*(2), 541–569.

Takeo, M., and N. Mikami (1987), Inversion of strong motion seismograms for the source process of the Naganoken-Seibu earthquake of 1984, *Tectonophysics*, *144*, 271–285.

Tanioka, Y., L. Ruff, and K. Satake (1996), The Sanriku-Oki Japan earthquake of December 28 1994 (M_w 7.7), Rupture of a different asperity from a previous earthquake, *Geophys. Res. Lett.*, *23*, 1465–1468.

Tapponnier, P., F. J. Ryerson, J. Van der Woerd, A.-S. Mériaux, and C. Lasserre (2001), Long-term slip rates and characteristic slip: Keys to active fault behaviour and earthquake hazard, *C. R. Acad. Sci., Ser. IIa Sci. Terre Planetes*, *333*, 483–494.

Tchalenko, J. S., and M. Berberian (1975), Dasht-e Bayaz fault, Iran: Earthquake and earlier related structures in bed rock, *Geol. Soc. Am. Bull.*, *86*, 703–709.

Thatcher, W. (1990), Order and diversity in the modes of circum-Pacific earthquake recurrence, *J. Geophys. Res.*, *95*, 2609–2623.

Thatcher, W., G. Marshall, and M. Lisowski (1997), Resolution of fault slip along the 470-km-long rupture of the great 1906 San Francisco earthquake and its implications, *J. Geophys. Res.*, *102*, 5353–5367.

Velasco, A. A., C. J. Ammon, T. Lay, and M. Hagerty (1996), Rupture process of the 1990 Luzon, Philippines (M_w 7.7) earthquake, *J. Geophys. Res.*, *101*, 2419–2434.

Wald, D. (1992), Strong motion and broadband teleseismic analysis of the 1991 Sierra Madre, California, earthquake, *J. Geophys. Res.*, *97*, 11,033–11,046.

Wald, D. J. (1996), A dislocation model of the 1995 Kobe Japan earthquake determined from strong motion, teleseismic and geodetic data, *J. Phys. Earth*, *44*, 489–503.

Wald, D. J., and T. H. Heaton (1994), Spatial and temporal distribution of slip for the 1992 Landers California earthquake, *Bull. Seismol. Soc. Am.*, *84*, 668–691.

Wald, D. J., and P. G. Somerville (1995), Variable slip rupture model of the great 1923 Kanto Japan earthquake: Geodetic and body-waveform analysis, *Bull. Seismol. Soc. Am.*, *85*, 159–177.

Wald, D. J., D. V. Helmberger, and S. H. Hartzell (1990), Rupture process of the 1987 Superstition Hills earthquake from the inversion of strong-motion data, *Bull. Seismol. Soc. Am.*, *80*, 1079–1098.

Wald, D. J., H. Kanamori, D. V. Helmberger, and T. H. Heaton (1991), Rupture model of the 1989 Loma Prieta earthquake from the inversion of strong-motion and broadband teleseismic data, *Bull. Seismol. Soc. Am.*, *81*, 1540–1572.

Wald, D. J., T. H. Heaton, and K. W. Hudnut (1996), The slip history of the 1994 Northridge California earthquake determined from strong motion, teleseismic, GPS and leveling data, *Bull. Seismol. Soc. Am.*, *86*, 49–70.

Walker, G. (1999), Volcanic rift zones and their intrusion swarms, *J. Volcanol. Geotherm. Res.*, *94*, 21–34.

Walsh, J. J., and J. Watterson (1987), Distribution of cumulative displacement and of seismic slip on a single normal fault surface, *J. Struct. Geol.*, *9*, 1039–1046.

Walsh, J. J., and J. Watterson (1988), Analysis of the relationship between displacements and dimensions of faults, *J. Struct. Geol.*, *10*, 238–347.

Ward, S. N. (1997), Dogtails versus rainbows: Synthetic earthquake rupture models as an aid in interpreting geological data, *Bull. Seismol. Soc. Am.*, *87*, 1422–1441.

Wells, D. L., and K. J. Coppersmith (1994), New empirical relationships among magnitude, rupture length, rupture width, rupture area, and surface displacement, *Bull. Seismol. Soc. Am.*, *84*, 974–1002.

Wesnousky, S. G. (1988), Seismological and structural evolution of strike-slip faults, *Nature*, *335*, 340–342.

Wesnousky, S. G. (1994), The Gutenberg-Richter or characteristic earthquake distribution, which is it?, *Bull. Seismol. Soc. Am.*, *84*, 1940–1959.

Willemse, E. J. M. (1997), Segmented normal faults: Correspondence between three dimensional mechanical models and field data, *J. Geophys. Res.*, *102*, 675–692.

Wu, C., M. Takeo, and S. Ide (2001), Source process of the Chi-Chi earthquake: A joint inversion of strong motion data and global positioning system data with a multifault model, *Bull. Seismol. Soc. Am.*, *91*, 1128–1143.

Yagi, Y., and M. Kikuchi (2000), Source rupture process of the Kocaeli Turkey earthquake of August 17 1999, obtained by joint inversion of near-field data and teleseismic data, *Geophys. Res. Lett.*, *27*, 1969–1972.

Yagi, Y., M. Kikuchi, and S. Yoshida (1999), Comparison of the coseismic rupture with the aftershock distribution in the Hyuga-Nada earthquakes of 1996, *Geophys. Res. Lett.*, *26*, 3161–3164.

Yoshida, S., K. Koketsu, B. Shibazaki, T. Sagiya, T. Kato, and Y. Yoshida (1996), Joint inversion of near- and far-field waveforms and geodetic data for the rupture process of the 1995 Kobe earthquake, *J. Phys. Earth*, *44*(5), 437–454.

Zachariasen, J., and K. Sieh (1995), The transfer of slip between two en echelon strike-slip faults: A case study from the 1992 Landers earthquake, southern California, *J. Geophys. Res.*, *100*, 15,281–15,301.

Zeng, Y. H., and J. G. Anderson (1996), A composite source model of the 1994 Northridge earthquake using genetic algorithms, *Bull. Seismol. Soc. Am.*, *86*, S71–S83.

Zeng, Y. H., and J. G. Anderson (2000), Evaluation of numerical procedures for simulating near-fault long-period ground motions using Zeng's method, *Rep. 2000/01*, Pac. Earthquake Eng. Res. Cent., Berkeley, Calif.

Zhang, P., F. Mao, and D. B. Slemmons (1999), Rupture terminations and size of segment boundaries from historical earthquake ruptures in the Basin and Range Province, *Tectonophysics*, *308*, 37–52.

Zhang, W., T. Iwata, K. Irikura, H. Sekiguchi, and M. Bouchon (2003), Heterogeneous distribution of the dynamic source parameters of the 1999 Chi-Chi, Taiwan, earthquake, *J. Geophys. Res.*, *108*(B5), 2232, doi:10.1029/2002JB001889.

Zobin, V. M., and V. I. Levina (1998), Rupture history of the January 1 1996 M_s 6.6 volcanic earthquake preceding the simultaneous eruption of Karymsky and Akademia Nauk volcanoes in Kamchatka, Russia, *J. Geophys. Res.*, *103*, 18,315–18,324.

Zobin, V. M., and V. I. Levina (2001), The rupture process of the M_w 7.8 Cape Kronotsky, Kamchatka, earthquake of 5 December 1997 and its relationship to foreshocks and aftershocks, *Bull. Seismol. Soc. Am.*, *91*, 1619–1628.

M. Campillo and I. Manighetti, Laboratoire de Géophysique Interne et Tectonophysique de Grenoble, BP 53, F-38041 Grenoble, France. (imanighe@obs.ujf-grenoble.fr)

G. King, Laboratoire de Tectonique, Institut de Physique du Globe de Paris, 4 Place Jussieu, F-75252 Paris, France.

P. M. Mai, Institute of Geophysics, ETH-Zurich, CH-8093 Zurich, Switzerland.

C. Sammis, Department of Earth Sciences, University of Southern California, Los Angeles, CA 90089-0740, USA.

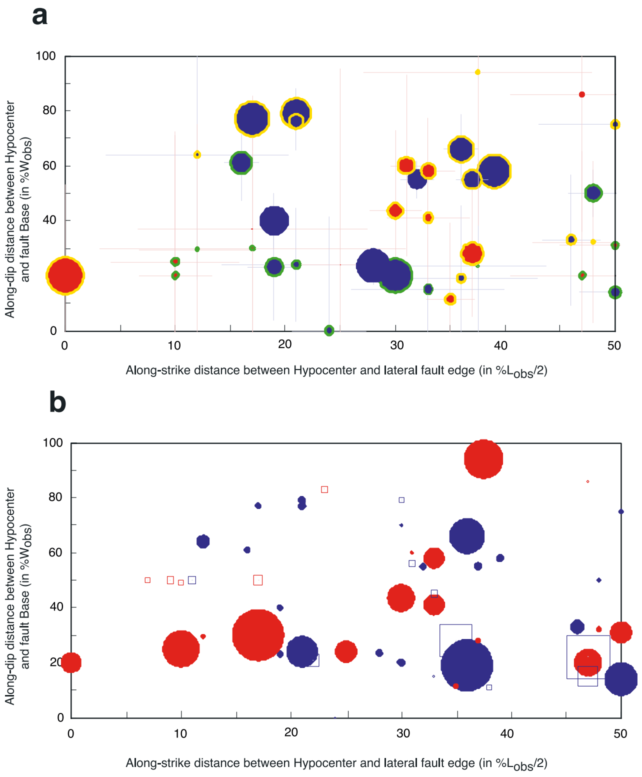

Figure 11. Distribution of hypocenters with respect to fault plane edges. X axis is along-strike position (in percent of L_{obs}) of hypocenters with respect to lateral fault plane edges (irrespective of which side). Y axis is along-dip position (in percent W_{obs}) of hypocenters with respect to fault plane base. Dip-slip and strike-slip faults are in blue and red, respectively. (a) Symbol size proportional to magnitude. Data are from Table 2 (averaged per earthquake; in few cases, best model is preferred). Uncertainties on hypocenter positions are assigned to 5 km in both x and y. Yellow and green circled symbols are for slip profiles tapering downward and upward, respectively. (b) Symbol size proportional to D_{max}/L_{model}. Data are from Tables 2 (solid symbols) and 3 (open symbols).

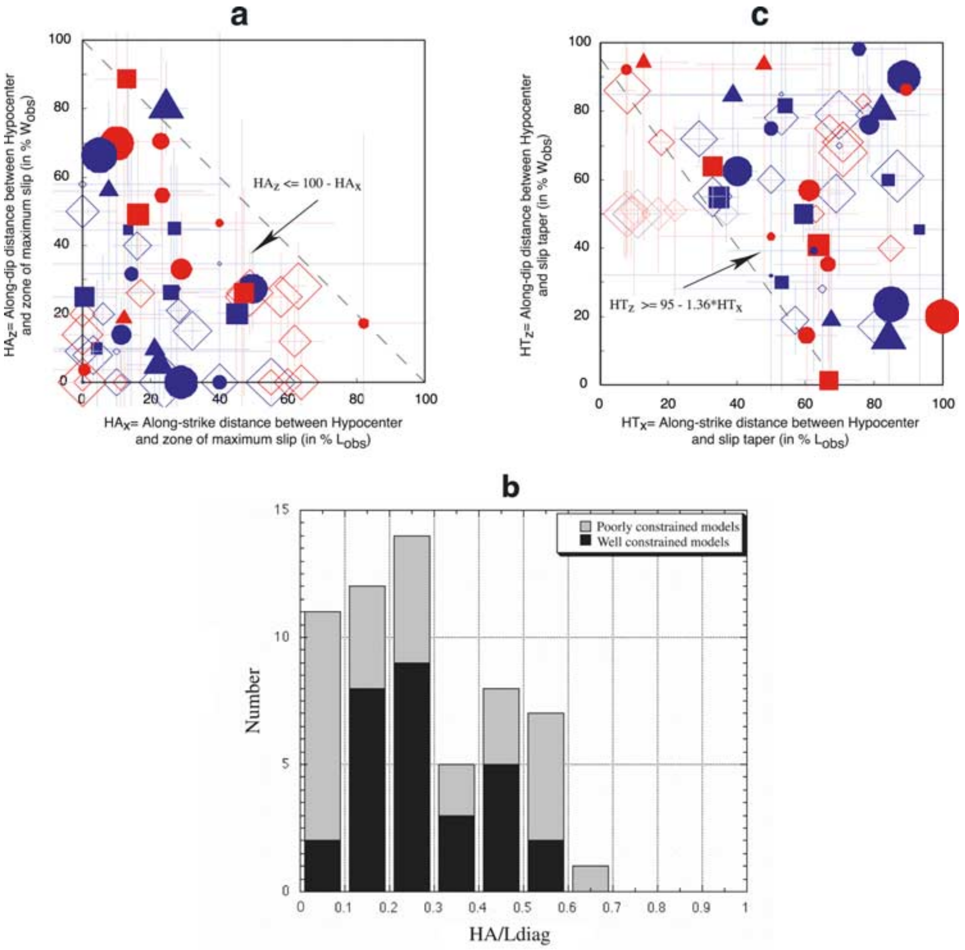

Figure 12. Position of hypocenters (H) with respect to zone of maximum slip (major asperity, A) and to slip taper (T) for earthquake faults with triangular slip profiles (both along strike and dip). Colors and uncertainties are as in Figure 11. Solid symbols are for best constrained models (from Table 2, as in Figure 11); open symbols are for poorly constrained models (from Table 3). Symbol shape indicates degree of asymmetry of along-strike slip profiles. For ruptures wider than 40 km, however, asymmetry is that of along-dip slip profiles. For models with tabular data, distances HA are those between hypocenter and apex of best fitting triangle. For models with no tabular data, distances HA and HT are estimated from visual inspection of the models (when hypocenters lie close to their zone of maximum slip, HA is fixed to zero; open symbols falling on any of the axes are therefore not well constrained). In all plots, symbol size is proportional to magnitude. (a) Position of hypocenter with respect to zone of maximum slip, with distances in percent of L_{obs} and W_{obs}. (b) Histogram of HA (HA = $(Ha_x^2 + Ha_z^2)^{0.5}$, all in km) normalized by diagonal length ($L_{diag} = (L^2 + W^2)^{0.5}$, all in km) of events. (c) Position of hypocenter with respect to slip taper, with distances in percent of L_{obs} and W_{obs}.

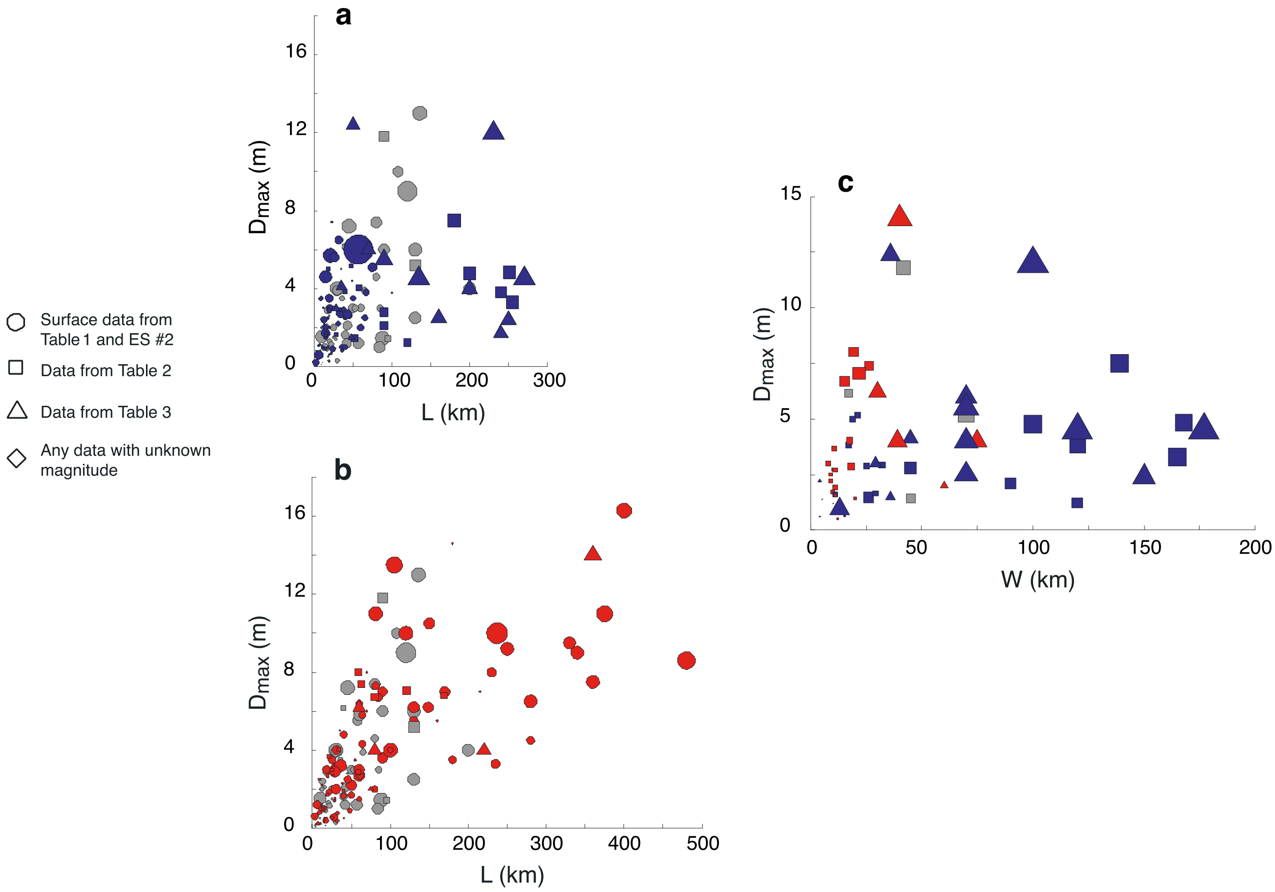

Figure 13. Scaling relations for the earthquakes analyzed. (a) Maximum displacement (D_{max}) versus length (L) for dip-slip (blue) and oblique (gray) faults (from Tables 1, 2, and 3 and ES02). (b) Maximum displacement (D_{max}) versus length (L) for strike-slip (red) and oblique (gray) faults (from Tables 1, 2, and 3 and ES02). (c) Maximum displacement (D_{max}) versus width (W) for dip-slip (blue), strike-slip (red), and oblique (gray) faults (from Tables 2 and 3). Symbol size is proportional to magnitude. Where that is unknown (as for earthquake sequences), symbol size is set to an arbitrary value (corresponding to M = 6). L is L_{obs} for data from Table 1, L_{meas} is for data from ES022, and L_{model} id for data from Tables 2 and 3 (same for W).

References and Notes

1. W. J. Bartz, Ed., *Engines and Automotive Lubrication* (Marcel Dekker, New York, 1993).
2. I. M. Hutchings, Ed., *Friction, Lubrication and Wear of Artificial Joints* (Professional Engineering Publishing, Bury St. Edmunds, UK, 2003).
3. B. Bhushan, *Tribology and Mechanics of Magnetic Storage Devices* (Springer-Verlag, New York, ed. 2, 1996).
4. H. P. Jost, *Wear* **136**, 1 (1990).
5. M. Urbakh, J. Klafter, D. Gourdon, J. Israelachvili, *Nature* **430**, 525 (2004).
6. U. Raviv, J. Klein, *Science* **297**, 1540 (2002).
7. B. Bhushan, J. B. Israelachvili, U. Landman, *Nature* **374**, 607 (1995).
8. S. Granick, *Phys. Today* **52**, 26 (1999).
9. M. Cieplak, E. D. Smith, M. O. Robbins, *Science* **265**, 1209 (1994).
10. M. Abdelmaksoud, J. W. Bender, J. Krim, *Phys. Rev. Lett.* **92**, 176101 (2004).
11. Z. Pawlak, *Tribochemistry of Lubricating Oils* (Elsevier, Amsterdam, 2003).
12. This has led to stricter controls on the concentrations of these elements in engine oils, which has limited the amount of ZDDP that can be incorporated into motor oil formulations.
13. The replacement of steel by aluminum is motivated by efforts to reduce vehicle weight as a means of improving fuel efficiency. For example, it has been estimated that a 10% reduction in vehicle weight can result in a 7% improvement in fuel economy. However, because of the inability of ZDDPs to adequately protect aluminum surfaces, automobile manufacturers have had to resort to engines composed of aluminum-based composite materials or to engine blocks that contain steel sleeves. These measures are costly and complicate engine fabrication.
14. M. L. Suominen Fuller, M. Kasrai, G. M. Bancroft, K. Fyfe, K. H. Tan, *Tribol. Int.* **31**, 627 (1999).
15. J. M. Martin, C. Grossiord, T. Le Mogne, S. Bec, A. Tonck, *Tribol. Int.* **34**, 523 (2001).
16. P. A. Willermet, D. P. Dailey, R. O. Carter III, P. J. Schmitz, W. Zhu, *Tribol. Int.* **28**, 177 (1995).
17. Y. Wan *et al.*, *Tribol. Ser.* **40**, 155 (2002).
18. Experiments show that zinc phosphate films almost 100 nm high can be formed after a few minutes of rubbing (*44*). The real contact time at the molecular level is significantly less than the rubbing time, because only a small fraction of the asperities are in contact with the opposing surface at a given time.
19. M. A. Nicholls *et al.*, *Tribol. Lett.* **17**, 205 (2004).
20. H. Spikes, *Tribol. Lett.* **17**, 469 (2004).
21. M. A. Nicholls, T. Do, P. R. Norton, M. Kasrai, G. M. Bancroft, *Tribol. Int.* **38**, 15 (2005).
22. A. B. Tutein, S. J. Stuart, J. A. Harrison, *Langmuir* **16**, 291 (2000).
23. G. He, M. H. Müser, M. O. Robbins, *Science* **284**, 1650 (1999).
24. J. A. Harrison, D. W. Brenner, *J. Am. Chem. Soc.* **116**, 10399 (1994).
25. S. Bair, C. McCabe, P. T. Cummings, *Phys. Rev. Lett.* **88**, 058302 (2002).
26. S. Jiang *et al.*, *J. Phys. Chem.* **100**, 15760 (1996).
27. N. J. Mosey, T. K. Woo, *J. Phys. Chem. A* **107**, 5058 (2003).
28. M. A. Wimmer, C. Sprecher, R. Hauert, G. Täger, A. Fischer, *Wear* **255**, 1007 (2003).
29. U. Landman, W. D. Luedtke, J. P. Gao, *Langmuir* **12**, 4514 (1996).
30. R. Car, M. Parinello, *Phys. Rev. Lett.* **55**, 2471 (1985).
31. M. Parrinello, *Solid State Commun.* **38**, 115 (1997).
32. C. Cavazzoni *et al.*, *Science* **283**, 44 (1999).
33. D. Alfè, M. J. Gillan, G. D. Price, *Nature* **401**, 462 (1999).
34. All AIMD simulations were performed with the CPMD software package (*45*). The potential energy was calculated using Kohn-Sham density functional theory with the gradient-corrected exchange-correlation functional of Perdew, Burke, and Ernzerhof (*46*); Troullier-Martins–type pseudopotentials; and a Γ-point plane wave expansion of the valence orbitals up to 120 Ry. A time step of 2.0 atomic units, equivalent to 0.0483 fs, was used in all simulations. Pressure was applied isotropically using the Parrinello-Rahman variable cell method (*47*, *48*), and preliminary calculations showed that well-converged values for the pressure were achieved using the theoretical approach outlined above. Temperatures of 100 and 1000 K were considered, with most simulations being performed at 100 K to isolate the effect of pressure. To give the reader an idea of the computational effort associated with these simulations, it is noted that one complete c/d cycle over a range of 0.25 to 32.5 GPa at 2.5 GPa/ps required nearly 5 weeks of CPU time on a Beowulf cluster of 24 Compaq Alpha ES40 computers running at 833 MHz.
35. A four-coordinate see-saw geometry can be derived by removing any two adjacent bond sites from a central atom with an originally six-coordinate octahedral geometry.
36. M. H. Müser, *Phys. Rev. Lett.* **89**, 224301 (2002).
37. The logarithmic-type dependence of the underlying chemical reactions on the compression rate can be rationalized within Eyring theory.
38. B. N. J. Persson, *J. Chem. Phys.* **115**, 3840 (2001).
39. S. Bec *et al.*, *Proc. R. Soc. London Ser. A* **455**, 4181 (1999).
40. J. F. Graham, C. McCague, P. R. Norton, *Tribol. Lett.* **6**, 149 (1999).
41. J. S. Sheasby, T. A. Caughlin, W. A. Mackwood, *Wear* **201**, 209 (1996).
42. M. Fuller *et al.*, *Tribol. Lett.* **1**, 367 (1995).
43. Z. Wisniewski, R. Wisniewski, J. L. Nowinski, *Solid State Ionics* **157**, 275 (2003).
44. M. Aktary, M. T. McDermott, G. A. McApline, *Tribol. Lett.* **12**, 155 (2002).
45. J. Hütter *et al.*, *CPMD* (MPI für Festkörperforschung Stuttgart and IBM Zurich Research Laboratory, Rueschlikon, Switzerland, 1995-2001).
46. J. P. Perdew, K. Burke, M. Ernzerhof, *Phys. Rev. Lett.* **77**, 3865 (1996).
47. M. Parrinello, A. Rahman, *Phys. Rev. Lett.* **45**, 1196 (1980).
48. P. Focher, G. L. Chiarotti, M. Bernasconi, E. Tosatti, M. Parrinello, *Europhys. Lett.* **36**, 345 (1994).

49. We thank P. R. Norton for inspiring us to work on this topic and P. R. Norton, M. Kasrai, Y.-T. Cheng, and W. Capehart for many useful discussions. The Natural Science and Engineering Research Council of Canada and General Motors R&D are acknowledged for providing financial support. Computational resources were made available by the Canadian Foundation for Innovation and SHARCNet of Canada.

24 November 2004; accepted 25 January 2005
10.1126/science.1107895

High-Resolution Surface-Wave Tomography from Ambient Seismic Noise

Nikolai M. Shapiro,[1]* Michel Campillo,[2] Laurent Stehly,[2] Michael H. Ritzwoller[1]

Cross-correlation of 1 month of ambient seismic noise recorded at USArray stations in California yields hundreds of short-period surface-wave group-speed measurements on interstation paths. We used these measurements to construct tomographic images of the principal geological units of California, with low-speed anomalies corresponding to the main sedimentary basins and high-speed anomalies corresponding to the igneous cores of the major mountain ranges. This method can improve the resolution and fidelity of crustal images obtained from surface-wave analyses.

The aim of ambitious new deployments of seismic arrays, such as the Program for the Array Seismic Studies of the Continental Lithosphere (PASSCAL) and USArray programs (*1*), is to improve the resolution of images of Earth's interior by adding more instruments to regional- and continental-scale seismic networks. Traditional observational methods cannot fully exploit emerging array data because they are based on seismic waves emitted from earthquakes, which emanate from select source regions predominantly near plate boundaries and are observed at stations far from the source regions, such as most locations within the United States. With such teleseismic observations, high-frequency information is lost because of intrinsic attenuation and scattering, and resolution is degraded by the spatial extent of the surface wave's sensitivity, which expands with path length (*2*–*4*). We have moved beyond the limitations of methods based on earthquakes and recovered surface-wave dispersion data from ambient seismic noise (*5*).

The basic idea of the new method is that cross-correlation of a random isotropic wavefield computed between a pair of receivers will result in a waveform that differs only by an amplitude factor from the Green function between the receivers (*6*, *7*). This property is reminiscent of the fluctuation-dissipation theorem (*8*), which posits a relation between the random fluctuations of a linear system and the system's response to an external force. The relation is widely used in a variety of physical applications and has its roots in early works on Brownian noise (*9*, *10*). Recent results in helioseismology (*11*), acoustics (*12*–*16*), and seismology (*5*, *17*)

---

[1] Center for Imaging the Earth's Interior, Department of Physics, University of Colorado at Boulder, Boulder, CO, USA. [2] Laboratoire de Géophysique Interne et de Tectonophysique, Université Joseph Fourier, Grenoble, France.

*To whom correspondence should be addressed. E-mail: nshapiro@ciei.colorado.edu

suggest that such a statistical treatment can be applied to nonthermal random wavefields, in particular to long series of ambient seismic noise, because the distribution of the ambient sources randomizes when averaged over long times. Ambient seismic noise is additionally randomized by scattering from heterogeneities within Earth (*18*). Surface waves are most easily extracted from the ambient noise (*5*), because they dominate the Green function between receivers located at the surface and also because ambient seismic noise is excited preferentially by superficial sources, such as oceanic microseisms and atmospheric disturbances (*19–22*). The seismic noise field is often not perfectly isotropic and may be dominated by waves arriving from a few principal directions. To reduce the contribution of the most energetic arrivals, we disregard the amplitude by correlating only one-bit signals (*15*, *17*) before the computation of the cross-correlation.

Examples of cross-correlations between pairs of seismic stations in California appear in Fig. 1 (*23*). Cross-correlations between two station pairs (MLAC-PHL and SVD-MLAC) in two short-period bands (5 to 10 s and 10 to 20 s) are presented using four different 1-month time series (January, April, July, and October 2002). For each station pair, results from different months are similar to one another and to the results produced by analyzing a whole year of data, but differ between the station pairs. Thus, the emerging waveforms are stable over time and characterize the structure of the earth between the stations. In addition, the cross-correlations of noise sequences are very similar to surface waves emitted by earthquakes near one receiver observed at the other receiver. This confirms that the cross-correlations approximate Green functions of Rayleigh waves propagating between each pair of stations and that 1 month of data suffices to extract Rayleigh-wave Green functions robustly in the period band of interest here (7 to 20 s).

We selected 30 relatively quiescent days (during which no earthquakes stronger than magnitude 5.8 occurred) of continuous data taken at a rate of one sample per second from 62 USArray stations within California (*24*) during August and September 2004. Short-period surface-wave dispersion curves are estimated from the Green functions using frequency-time analysis (*25–27*) from the 1891 paths connecting these stations. We rejected waveforms with signal-to-noise ratios smaller than 4 and for paths shorter than two wavelengths, resulting in 678 and 891 group-speed measurements at periods of 7.5 and 15 s, respectively (fig. S2). We then applied a tomographic inversion (*28*) to these two data sets to obtain group-speed maps on a 28 × 28 km grid across California (Fig. 2).

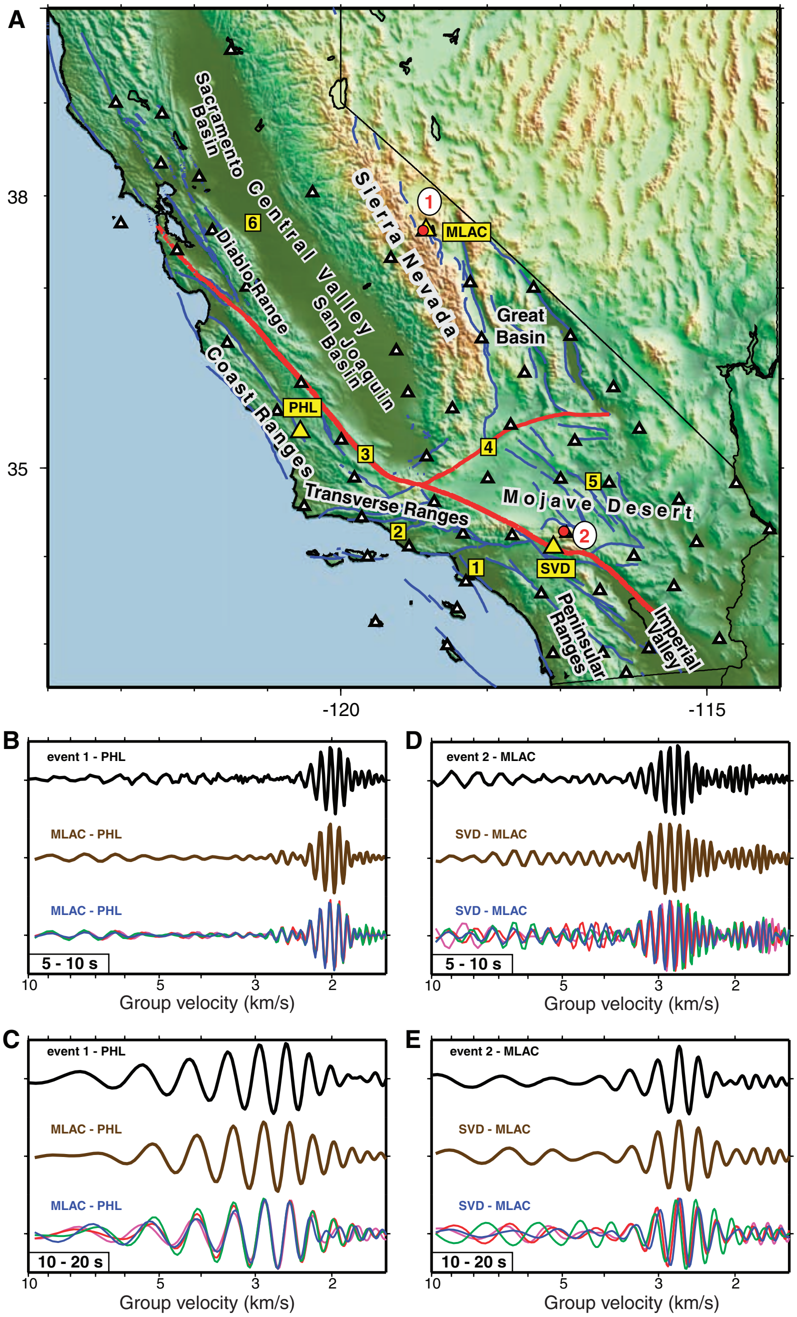

Fig. 1. Waveforms emerging from cross-correlations of ambient seismic noise compared with Rayleigh waves excited by earthquakes. (**A**) Reference map showing the locations of the principal geographical and geological features discussed in the text. White triangles show the locations of the USArray stations used in this study (5 of the 62 stations are located north of 40°N). Blue and red solid lines are the locations of known active faults. Yellow rectangles with digits indicate the following features: (1) Los Angeles Basin, (2) Ventura Basin, (3) San Andreas Fault, (4) Garlock Fault, (5) Mojave shear zone, and (6) Stockton Arch. (**B**) Comparison of waves propagating between stations MLAC and PHL [yellow triangles in (A)], bandpassed over periods between 5 and 10 s. The upper trace (black) is the signal emitted by earthquake 1 [white circle with red number in (A)] near MLAC observed at PHL; the middle trace (gold) is the cross-correlation from 1 year of ambient seismic noise observed at stations MLAC and PHL; and the lower traces are cross-correlations from 4 separate months of noise observed at the two stations in 2002 (magenta, January; red, April; green, July; blue, October). The earthquake-emitted signal was normalized to the spectrum of the cross-correlated ambient noise. (**C**) Similar to (B), but with the bandpass filter at periods between 10 and 20 s. (**D**) Similar to (B), but between stations SVD and MLAC [yellow triangles in (A)]. Earthquake 2 is near station SVD, observed at station MLAC. (**E**) Similar to (D), but with the bandpass filter at periods between 10 and 20 s.

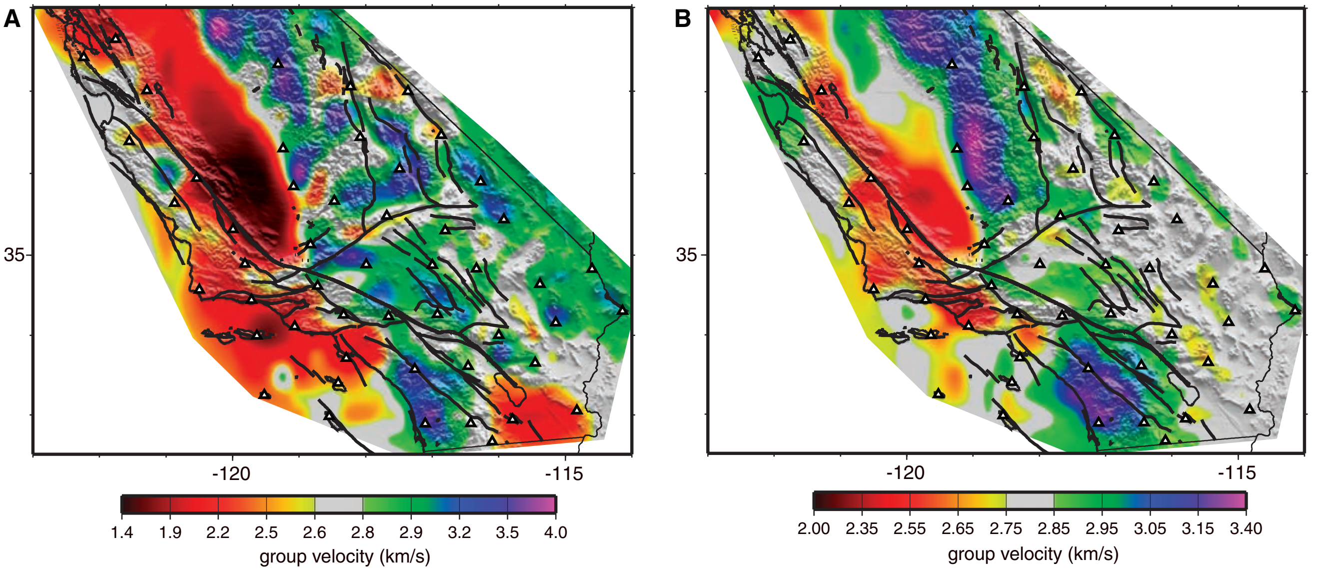

Fig. 2. Group-speed maps constructed by cross-correlating 30 days of ambient noise between USArray stations. **(A)** 7.5-s-period Rayleigh waves. **(B)** 15-s-period Rayleigh waves. Black solid lines show known active faults. White triangles show locations of USArray stations used in this study. Similar maps from a different single month of data are shown in the supporting online material.

The maps produced variance reductions of 93 and 76% at 7.5 and 15 s, respectively, relative to the regional average speed at each period. To test the robustness of the inversion, we applied the same procedure to a second month of data and produced similar tomographic maps (fig. S3). The resolution of the resulting images is about the average interstation distance, between 60 and 100 km across most of each map (fig. S4).

A variety of geological features (*29*) are recognizable in the estimated group-speed dispersion maps (Fig. 2). For the 7.5-s Rayleigh wave, which is most sensitive to shallow crustal structures no deeper than about 10 km, the dispersion map displays low group speeds for the principal sedimentary basins in California, including the basins in the Central Valley, the Salton Trough in the Imperial Valley, the Los Angeles Basin, and the Ventura Basin. Regions consisting mainly of plutonic rocks (the Sierra Nevada, the Peninsular Ranges, the Great Basin, and the Mojave Desert region) are characterized predominantly by fast group speeds. Somewhat lower speeds are observed in the Mojave Shear Zone and along the Garlock Fault. The Coast Ranges, the Transverse Ranges, and the Diablo Range, which are mainly composed of sedimentary rocks, are characterized by low group speeds, with the exception of the Salinian block located south of Monterey Bay.

For the 15-s Rayleigh wave, which is sensitive mainly to the middle crust down to depths of about 20 km, very fast group speeds correspond to the remnants of the Mesozoic volcanic arc: the Sierra Nevada and the Peninsular Ranges, composed principally of Cretaceous granitic batholiths. The map also reveals the contrast between the western and eastern parts of the Sierra Nevada (*30*). The group speeds are lower in the Great Basin and in the Mojave Desert, indicating that the middle crust in these areas is probably hotter and weaker than in the Sierra Nevada. In the Central Valley, slow group speeds are associated with two deep sedimentary basins: the San Joaquin Basin in the south and the Sacramento Basin in the north, separated in the middle by the igneous-dominated Stockton Arch (*31*). Group speeds are low in the sedimentary mountain ranges (the Transverse Ranges, the southern part of the Coast Ranges, and the Diablo Range). Neutral to fast wave speeds are observed for the Salinian block. In this area, the 15-s map shows a contrast between the high-speed western wall of the San Andreas Fault, composed of plutonic rocks of the Salinian block, and its low-speed eastern wall, composed of sedimentary rocks of the Franciscan formation.

These results establish that Rayleigh-wave Green functions extracted by cross-correlating long sequences of ambient seismic noise, which are discarded as part of traditional seismic data processing, contain information about the structure of the shallow and middle crust. The use of ambient seismic noise as the source of seismic observations addresses several shortcomings of traditional surface-wave methods. The method is particularly advantageous in the context of temporary seismic arrays such as the Transportable Array component of USArray or PASSCAL experiments, because it can return useful information even if earthquakes do not occur. The short-period dispersion maps produced by the method can provide homogeneously distributed information about shear wave speeds in the crust, which are hard to acquire with traditional methods. The new method enhances resolution because measurements are made between regularly spaced receivers, which may lie much closer to one another than to earthquakes.

It may seem initially surprising that deterministic information about Earth's crust can result from correlations of ambient seismic noise. This result reminds us that random fluctuations can, in fact, yield the same information as that provided by probing a system with an external force (*9*) and that not all noise is bad. In seismology, external probing through active seismic sources (such as explosions) may be prohibitively expensive, and earthquakes are both infrequent and inhomogeneously distributed. In many instances, merely "listening" to ambient noise may be a more reliable and economical alternative.

References and Notes

1. USArray (www.iris.iris.edu/USArray) is one of the components of the new EarthScope (www.earthscope.org) initiative in the United States. PASSCAL (www.iris.edu/about/PASSCAL) is a program of the Incorporated Research Institutions for Seismology (IRIS) (www.iris.edu).
2. G. Nolet, F. A. Dahlen, *J. Geophys. Res.* **105**, 19043 (2000).
3. J. Spetzler, J. Trampert, R. Snieder, *Geophys. J. Int.* **149**, 755 (2002).
4. M. H. Ritzwoller, N. M. Shapiro, M. P. Barmin, A. L. Levshin, *J. Geophys. Res.* **107**, 2235 (2002).
5. N. M. Shapiro, M. Campillo, *Geophys. Res. Lett.* **31**, L07614, 10.1029/2004GL019491 (2004).
6. R. L. Weaver, O. I. Lobkis, *Phys. Rev. Lett.* **87**, paper 134301 (2001).
7. R. Snieder, *Phys. Rev. E* **69**, 046610 (2004).
8. R. Kubo, *Rep. Prog. Phys.* **29**, 255 (1966).
9. S. Kos, P. Littlewood, *Nature* **431**, 29 (2004).
10. A. Einstein, *Ann. Phys.* **17**, 549 (1905).

11. T. L. Duvall, S. M. Jefferies, J. W. Harvey, M. A. Pomerantz, *Nature* **362**, 430 (1993).
12. R. L. Weaver, O. I. Lobkis, *J. Acoust. Soc. Am.* **110**, 3011 (2001).
13. A. Derode *et al.*, *J. Acoust. Soc. Am.* **113**, 2973 (2003).
14. P. Roux, W. A. Kuperman, *J. Acoust. Soc. Am.* **116**, 1995 (2004).
15. E. Larose, A. Derode, M. Campillo, M. Fink, *J. Appl. Phys.* **95**, 8393 (2004).
16. A. E. Malcolm, J. A. Scales, B. A. van Tiggelen, *Phys. Rev. E* **70**, 10.1103/PhysRevE.70.015601 (2004).
17. M. Campillo, A. Paul, *Science* **299**, 547 (2003).
18. R. Hennino *et al.*, *Phys. Rev. Lett.* **86**, 3447 (2001).
19. A. Friedrich, F. Kruger, K. Klinge, *J. Seismol.* **2**, 47 (1998).
20. T. Tanimoto, *Geophys. J. Int.* **136**, 395 (1999).
21. G. Ekström, *J. Geophys. Res.* **106**, 26483 (2001).
22. J. Rhie, B. Romanowicz, *Nature* **431**, 552 (2004).
23. Data processing was performed with the Seismic Analysis Code (SAC) (*32*).
24. We used 62 stations of the Transportable Array component of USArray in California (Fig. 1A). This includes 40 permanent stations of the Southern California TriNet system (www.trinet.org), 17 permanent stations of the Berkeley Digital Seismic Network (quake.geo.berkeley.edu/bdsn), 2 permanent stations of the Anza Seismic Network (eqinfo.ucsd.edu/deployments/anza.html), and 3 new USArray stations.
25. A. L. Levshin *et al.*, *Seismic Surface Waves in a Laterally Inhomogeneous Earth*, V. I. Keilis-Borok, Ed. (Kluwer Academic, Norwell, MA, 1989).
26. M. H. Ritzwoller, A. L. Levshin, *J. Geophys. Res.* **103**, 4839 (1998).
27. N. M. Shapiro, S. K. Singh, *Bull. Seism. Soc. Am.* **89**, 1138 (1999).
28. M. P. Barmin, M. H. Ritzwoller, A. L. Levshin, *Pure Appl. Geophys.* **158**, 1351 (2001).
29. C. W. Jennings, geologic map of California (California Division of Mines and Geology, Map No. 2, 1977).
30. C. H. Jones, H. Kanamori, S. W. Roecker, *J. Geophys. Res.* **99**, 4567 (1994).
31. A. M. Wilson, G. Garven, J. R. Boles, *GSA Bull.* **111**, 432 (1999).
32. P. Goldstein, L. Minner, *Seism. Res. Lett.* **67**, 39 (1996) (www.llnl.gov/sac).
33. The data used in this work were obtained from the IRIS Data Management Center. We are also particularly grateful to M. Barmin for help with the tomographic code and P. Goldstein for clarifications about the SAC program. We thank C. Jones for a tutorial on the geology of California and E. Larose, O. Lobkis, L. Margerin, R. Maynard, A. Paul, B. van Tiggelen, and R. Weaver for helpful discussions. We acknowledge the support from CNRS/Institut National des Sciences de l'Univers (program DyETI) and the Commissariat à l'Energie Atomique (France).

Supporting Online Material
www.sciencemag.org/cgi/content/full/307/5715/1615/DC1
Figs. S1 to S4

6 December 2004; accepted 19 January 2005
10.1126/science.1108339

Worldwide Phylogeography of Wild Boar Reveals Multiple Centers of Pig Domestication

**Greger Larson,[1]* Keith Dobney,[2] Umberto Albarella,[3]
Meiying Fang,[4] Elizabeth Matisoo-Smith,[5] Judith Robins,[5]
Stewart Lowden,[6] Heather Finlayson,[7] Tina Brand,[8]
Eske Willerslev,[1] Peter Rowley-Conwy,[2]
Leif Andersson,[4] Alan Cooper[1]*†**

Mitochondrial DNA (mtDNA) sequences from 686 wild and domestic pig specimens place the origin of wild boar in island Southeast Asia (ISEA), where they dispersed across Eurasia. Previous morphological and genetic evidence suggested pig domestication took place in a limited number of locations (principally the Near East and Far East). In contrast, new genetic data reveal multiple centers of domestication across Eurasia and that European, rather than Near Eastern, wild boar are the principal source of modern European domestic pigs.

The domestication of plants and animals led to one of the most important socioeconomic transitions in human history, yet little is known about whether the process took place in a limited number of geographic regions or was a more widespread innovation involving multiple, independent "events." Wild boar were important prey animals for early hunter-gatherers across wide areas of Eurasia (*1*) until the early Holocene, when this predator-prey relation radically shifted as they, and several other large mammals, were domesticated. An extensive zooarcheological record suggests that pigs were first domesticated ~9000 years ago in the Near East (*2*), whereas more recent molecular and archaeological evidence suggests a second, independent domestication in the Far East (*3*, *4*). In eastern Anatolia, several sites record gradual changes in pig morphology and demographic profile (principally a reduction in certain tooth dimensions and the increased predominance of younger animals in archaeological assemblages) (*5*, *6*) over several millennia, and these have been taken to represent the domestication process in situ. Although the independent domestication of wild boar in Europe has been suggested (*7*), others have concluded that, like cattle (*8*) and sheep, pigs derived from Near Eastern genetic stock were imported by Neolithic farmers into Europe (*9*).

The wild progenitors of many Eurasian domesticates are either extinct [e.g., the aurochs (*8*) and the wild horse (*10*)] or have little or no phylogeographic structure [e.g., the wolf (*11*)]. Consequently, the broad distribution of surviving wild boar populations across the Old World provides a unique opportunity to analyze the origins of modern domestic lineages. Previous studies (*3*, *12*) have identified three divergent clusters of *Sus scrofa* mitochondrial sequences, one Asian clade and two European groups, of which one consists solely of Italian wild boar. Both the Asian and European groups contain domestic breeds, yet molecular clock estimates indicate the split between the two groups significantly predates evidence for pig domestication, which suggests independent domestication events in each area from divergent wild boar lineages (*3*, *12*).

To investigate the relationships between domestic pigs and indigenous wild boar across their range, we sequenced 663 base pairs (bp) of the mitochondrial control region from 165 wild and feral pigs primarily from museum specimens, using appropriate ancient-DNA methods (*13*), and from 58 domestic pigs. An additional 463 individual pig sequences were obtained from GenBank, and phylogenetic analyses were performed using Bayesian Monte Carlo–Markov chain (MCMC) (*14*) and median-joining networks (*15*). The consensus tree (Fig. 1) shows that the basal lineages of *S. scrofa* occur in western island Southeast Asia (ISEA). An initial dispersal from this area into the Indian subcontinent was followed by subsequent radiations into East Asia and a final, progressive spread across Eurasia into Western Europe. The marked East-West split among wild boar is consistent with morpho-

---

[1]Henry Wellcome Ancient Biomolecules Centre, University of Oxford, Department of Zoology, South Parks Road OX1 3PS, UK. [2]Department of Archaeology, University of Durham, South Road, Durham DH1 3L, UK. [3]Department of Archaeology, University of Sheffield, West Street, Sheffield S1 4ET, UK. [4]Department of Animal Breeding and Genetics, Swedish University of Agricultural Sciences and Department of Medical Biochemistry and Microbiology, Uppsala University, Uppsala Biomedical Center, Box 597, SE-75124 Uppsala, Sweden. [5]Department of Anthropology and Allan Wilson Centre for Molecular Ecology and Evolution, University of Auckland, P.B. 92019, Auckland, New Zealand. [6]Jurox Pty Limited, 85 Gardiners Road, Rutherford, NSW, 2320, Australia. [7]Department of Genomics and Bioinformatics, Roslin Institute, Roslin, Midlothian, EH25 9PS, UK. [8]Department of Evolutionary Biology, Zoological Institute, University of Copenhagen, Universitetsparken 15, DK-2100, Copenhagen O, Denmark.

*To whom correspondence should be addressed. E-mail: greger.larson@zoo.ox.ac.uk (G.L.) and alan.cooper@adelaide.edu.au (A.C.)

†Present address: School of Environmental Sciences, University of Adelaide, Adelaide, SA 5005, Australia.

Long-Range Correlations in the Diffuse Seismic Coda

Michel Campillo* and Anne Paul

The late seismic coda may contain coherent information about the elastic response of Earth. We computed the correlations of the seismic codas of 101 distant earthquakes recorded at stations that were tens of kilometers apart. By stacking cross-correlation functions of codas, we found a low-frequency coherent part in the diffuse field. The extracted pulses have the polarization characteristics and group velocities expected for Rayleigh and Love waves. The set of cross-correlations has the symmetries of the surface-wave part of the Green tensor. This seismological example shows that diffuse waves produced by distant sources are sufficient to retrieve direct waves between two perfectly located points of observation. Because it relies on general properties of diffuse waves, this result has potential applications in other fields.

Seismologists have used coherent seismic waves to image the structure of Earth's interior. Velocity variations of seismic waves with depth can be derived from arrival times (with the use of ray theory) or from the dispersion properties of coherent surface waves. One difficulty with these imaging techniques is that they require energetic sources such as large explosions or earthquakes that can be located with a specified accuracy. Any approach that would help to evaluate the response of Earth to a perfectly known point source—that is, the Green function—would be most welcome.

This problem of imaging in strongly diffractive media is also a challenge for acoustics or optics. It was recently demonstrated in laboratory experiments with ultrasonic and thermal noise that the Green function can be measured from the correlation properties of diffuse fields (*1*, *2*). Here, we show that the use of field-to-field correlation to retrieve the Green function is a valid approach not only in the extremely controlled and favorable conditions of the laboratory but also with natural signals such as seismograms produced by earthquakes. In seismology, it has been recognized that coda waves, which make up the late part of seismic signals (Fig. 1), are the result of scattering from small-scale heterogeneities in the lithosphere (*3*–*5*). The physics of coda waves cannot be fully understood with classical ray theory. Multiple scattering plays a prominent part in the seismic coda, and seismologists have made use of the radiative transfer theory to model the coda intensity (*6*–*9*). Recently, the diffusive character of the coda was revealed (*10*) by investigating the property of mode equipartition (*11*). This phenomenon is a property of diffuse elastic waves and shows up as a stabilization of the ratio of *S*- and *P*-wave energies in time, independent of the source. Radiative transfer and diffusion are concepts that apply only to the evolution of the average energy of waves in random elastic media (*12*–*14*). They disregard the phase of the diffuse field despite experimental evidence of the importance of phase information in optics (*15*) and acoustics (*16*).

Here, we use the coherence of diffuse waves to retrieve direct waves between two points at Earth's surface. In this approach, the cross-correlation function between the wave fields produced by a single source at two points is averaged over the source location. Assuming a modal representation of the wave field, this spatially averaged correlation is an approximation of the Green function between the two points of observation (*1*, *2*, *17*, *18*). However, because we cannot expect a homogeneous distribution of earthquakes, we have to rely on the distribution of scatterers responsible for the diffusion to perform a sufficient averaging. An alternative argument can be found in the property of modal equipartition of the diffuse field. Equipartition occurs because multiple scattering tends to homogenize the phase space. For direct arrivals, the energy is distributed in the phase space in a manner that depends on the nature and position of the source. In contrast, energy becomes uniform in phase space when entering the diffusive regime. This property is independent of the details of the heterogeneities that produce the scattering. Considering a time window delayed enough from the first arrival for the waves to have become diffuse as a result of multiple scattering, we can write the displacement $\boldsymbol{u}$ at location $\boldsymbol{R}$ and time t in the form of its expansion in the eigenfunctions $\boldsymbol{\Phi}^n$ of the elastic medium:

$$\boldsymbol{u}(\boldsymbol{R},t) = \sum_n \varepsilon_n \boldsymbol{\Phi}^n(\boldsymbol{R}) \exp(-i\Omega_n t)$$

where Ω_n are the eigenfrequencies and ε_n are statistically identical independent random variables. The expression of the cross-correlation of the displacements at two different locations is, on average, close to the Green function between these two locations.

We applied this approach to a seismic data set from central Mexico that fits several basic criteria: (i) The region is seismically active, with numerous earthquakes of magnitude large enough to excite late coda ($M > 4.5$), (ii) good-quality broadband records of these events are available, (iii) the Green function is already known and displays features striking enough to be recognized easily in a noisy time series, and (iv) high-frequency coda waves exhibit a diffuse behavior in this region (*10*), a property that we expect to be verified in a broad frequency range.

The stations PLIG and YAIG were selected because of the availability of good-quality records of 101 regional events (Fig. 1). The horizontal components of the seismograms were rotated assuming the interstation great circle path to be the radial direction. No filter was applied to the broadband seismograms. For most records, the signal-to-noise ratio was good enough to process the seismograms over coda windows of a few hundred seconds (Fig. 1, inset). As a result of the exponential decrease of coda amplitude with time, a simple cross-correlation between the coda sig-

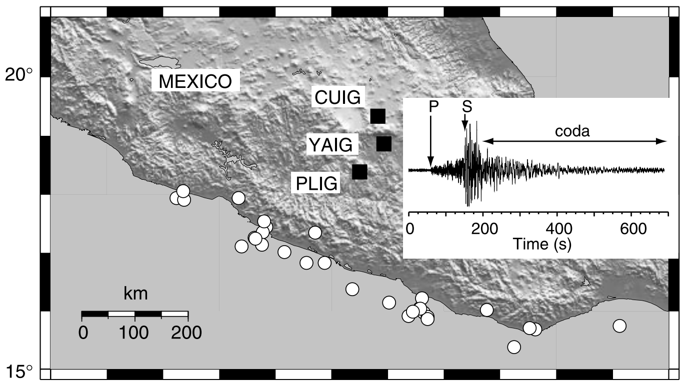

Fig. 1. Location map of the broadband stations CUIG, YAIG, and PLIG of the Mexican National Seismological Network (black squares) and epicenters of 30 earthquakes of the data set (white circles). Inset: An example of a record of one of these events at station PLIG (vertical component).

Laboratoire de Géophysique Interne et Tectonophysique, Observatoire de Grenoble, Université Joseph Fourier & CNRS, BP 53, 38041 Grenoble, France.

*To whom correspondence should be addressed. E-mail: Michel.Campillo@obs.ujf-grenoble.fr

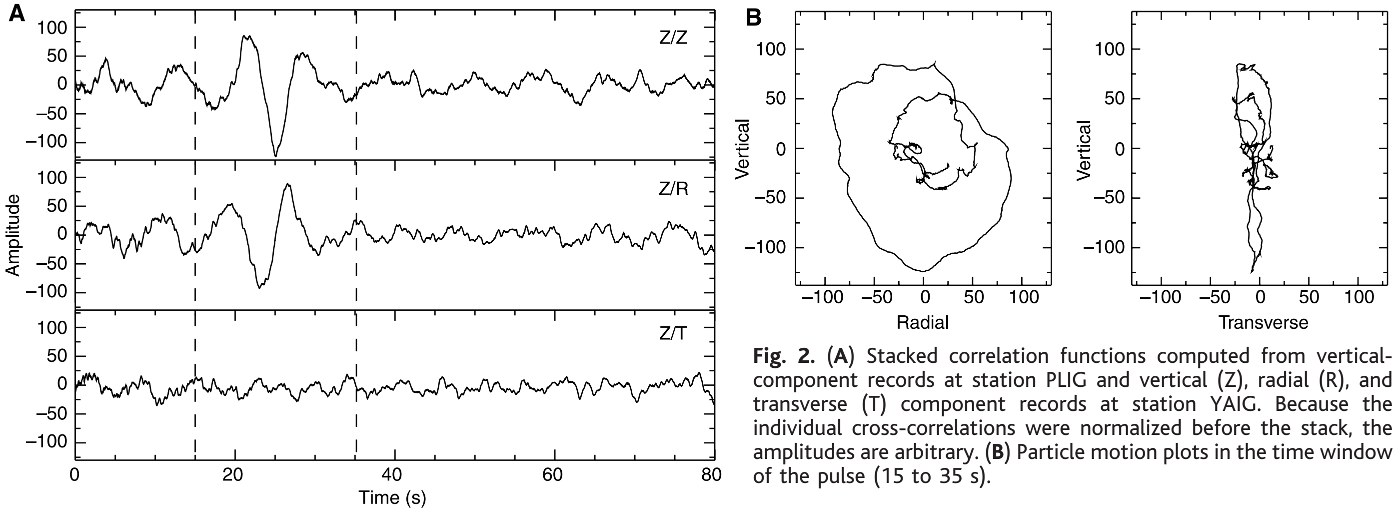

Fig. 2. (**A**) Stacked correlation functions computed from vertical-component records at station PLIG and vertical (Z), radial (R), and transverse (T) component records at station YAIG. Because the individual cross-correlations were normalized before the stack, the amplitudes are arbitrary. (**B**) Particle motion plots in the time window of the pulse (15 to 35 s).

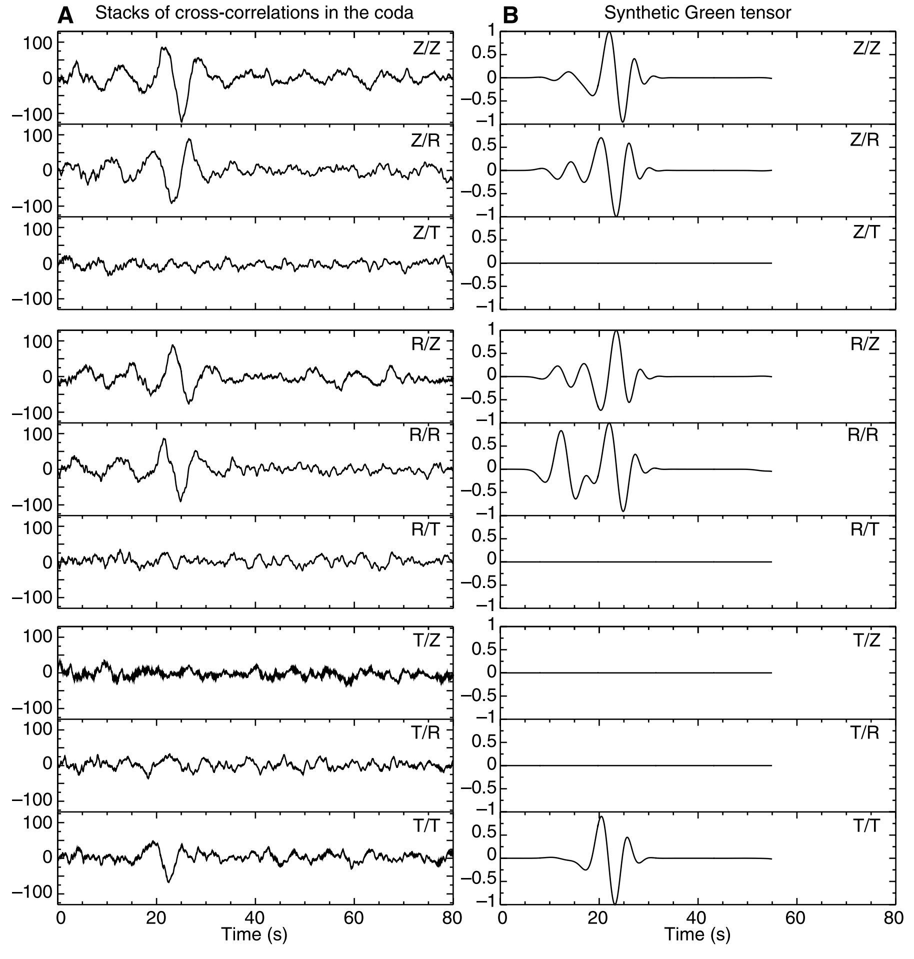

Fig. 3. Comparison between the nine stacks of correlation traces at stations PLIG and YAIG (**A**) and the nine components of the theoretical Green tensor (**B**) computed for a 69-km source-station distance. The 1-D average shear wave velocity model used here was measured for the crust of Central Mexico from inversion of group velocity dispersion curves estimated for paths between the Guerrero-Michoacàn subduction zone and Mexico City (*20*).

nals recorded at the two stations would strongly overweight the earliest part of the coda. To compensate for amplitude attenuation with time, we divided the coda windows into 100-s-long segments with an overlap of 25 s. Then we computed the cross-correlations between these truncated signals and normalized the amplitudes of each correlation to unit maximum. The resulting 595 normalized correlations were then stacked to give the signals (Fig. 2A). Similar results are obtained by disregarding the amplitude completely and considering one-bit signals (*19*, *20*).

The resulting average cross-correlations computed from vertical-component records (Z) at station PLIG and vertical, radial, and transverse component records (respectively Z, R, and T) at station YAIG (Fig. 2A) show a clear 8-s-period pulse between 20 and 30 s in both the vertical and radial traces, whereas no coherent signal is visible on the transverse component. During the stacking process, the amplitude of the pulse increases linearly with the summation order, showing that the pulse results from the stack of coherent signals present in most of the individual correlation traces. In contrast, the average amplitude of the noise varies as the square root of the number of individual windows, as expected for a summation of incoherent signals. The coherent signal is not visible in individual cross-correlations because the signal-to-noise ratio is only ~0.2 for the case of a 100-s window. The particle motion (Fig. 2B) is restricted to the propagation plane with elliptic polarization typical of a Rayleigh wave pulse, a disturbance propagating at the free surface of an elastic body.

We computed the average correlations between all components of the ground motion at the two stations (Fig. 3A). The theoretical Green tensor has been computed in a three-layer crustal model (*21*) and convolved with an 8-s-wide Ricker wavelet. It displays only a few distinct features. It is dominated by a strong Rayleigh pulse at 25 s for both the vertical and radial point-force sources, and a Love pulse—a horizontally polarized guided shear wave—for the transverse point-force source. For the radial force, the Rayleigh pulse on the radial component (R/R) is preceded by a strong-amplitude body wave. The tensor obtained by stacking correlations between coda records of regional earthquakes at stations PLIG and YAIG displays the same symmetries as the theoretical Green tensor (Fig. 3). Moreover, the arrival times of the pulses in the Z/Z, Z/R, R/Z, R/R, and T/T components of the stacked correlations coincide with those of the Rayleigh and Love signals in the Green tensor. This coincidence in arrival time, as well as the clear Rayleigh and Love polarization of the correlation pulses (Fig. 2B), proves that the observed signals are identified as the Rayleigh and Love pulses of the Green tensor and, most important, that the coda correlation technique does indeed retrieve the surface-wave part of the actual Green tensor between the two stations.

To make sure that the pulse is not simply a surface wave that is generated repeatedly at the coast by the conversion of oceanic waves and that propagates in the direction defined by the two stations, we performed the same test with another pair of stations, YAIG and CUIG, oriented in a different azimuth (Fig. 1). The stacked correlation signals also display pulses with arrival times and polarizations close to the Rayleigh and Love modes of the theoretical Green function (fig. S1), excluding the alternative interpretation of induced surface waves.

So far we have not been able to extract either the high-frequency part of the Green function or the body waves. The lack of high frequencies is most probably a result of the absence of high-frequency waves in the late coda because of anelastic absorption, which acts as a low-pass filter. Another explanation could be that the fundamental modes of Rayleigh and Love waves at low frequency are the part of the field with the simplest modal representation. Retrieving the Green function relies on the orthogonality of the set of eigenfunctions that constitutes the total random field. All cross-products vanish in the averaging, assuming a distribution of sources, or scatterers, that spans the whole space. However, the volume where the spatial source averaging is performed is in practice limited by the number of earthquakes and the locations of scatterers. We speculate that only eigenfunctions with amplitudes concentrated in a zone where inhomogeneities are densely distributed can be adequately extracted. This is the case with the Rayleigh and Love waves, the eigenfunctions of which have a limited penetration in the upper part of the crust where the distribution of scatterers is likely to be dense.

We expect to retrieve both the Green function and its time reciprocal if the diffuse field is perfectly random. This could be the case with an isotropic distribution of sources around the stations or in a finite body. Because all earthquakes are located south of both station PLIG and station YAIG, there is a preferential direction of transport of diffuse energy. This results in a better reconstruction of the Green function in one of the time directions. We also considered a couple of stations along the coast (fig. S2A) for which the distribution of epicenters is more symmetric. The wave propagation is much more complex there (*22*) than in central Mexico, but some features of the Green function emerge from the noisy correlation stacks, such as a clear dispersed Love wave that can be seen in the two directions of time (fig. S2B).

Digital seismic networks provide a large number of coda records, which can be used to compute impulse response between perfectly located positions. This new kind of seismogram could help to produce images of the inner Earth structures without the uncertainties of origin time and source location encountered with traditional earthquake data. A similar approach is applicable in other domains where time series of diffuse waves are available.

References and Notes

1. R. L. Weaver, O. I. Lobkis, *Phys. Rev. Lett.* **87**, 134301 (2001).
2. ———, *J. Acoust. Soc. Am.* **110**, 3011 (2001).
3. K. Aki, B. Chouet, *J. Geophys. Res.* **80**, 3322 (1975).
4. K. Aki, *Phys. Earth Planet. Inter.* **21**, 50 (1980).
5. H. Sato, M. Fehler, *Seismic Wave Propagation and Scattering in the Heterogeneous Earth* (Springer-Verlag and American Institute of Physics Press, 1998).
6. R. S. Wu, K. Aki, *Pure Appl. Geophys.* **128**, 49 (1988).
7. I. R. Abubakirov, A. A. Gusev, *Phys. Earth Planet. Inter.* **64**, 52 (1990).
8. M. Hoshiba, *Phys. Earth Planet. Inter.* **67**, 123 (1991).
9. M. Margerin, M. Campillo, N. M. Shapiro, B. van Tiggelen, *Geophys. J. Int.* **138**, 343 (1999).
10. R. Hennino *et al.*, *Phys. Rev. Lett.* **86**, 3447 (2001).
11. R. L. Weaver, *J. Acoust. Soc. Am.* **71**, 1608 (1982).
12. L. A. Apresyan, Y. A. Kravtsov, *Radiation Transfer: Statistical and Wave Aspects* (Gordon and Breach, Amsterdam, 1996).
13. R. L. Weaver, *J. Mech. Phys. Solids* **38**, 55 (1990).
14. L. V. Ryzhik, G. C. Papanicolaou, J. B. Keller, *Wave Motion* **24**, 327 (1996).
15. E. Akkermans, P. E. Wolf, R. Maynard, G. Maret, *J. Phys. France* **49**, 77 (1988).
16. A. Derode, P. Roux, M. Fink, *Phys. Rev. Lett.* **75**, 4206 (1995).
17. C. Dreager, M. Fink, *J. Acoust. Soc. Am.* **105**, 611 (1999).
18. P. Roux, M. Fink, *J. Acoust. Soc. Am.*, in press.
19. Time-reversal experiments of ultrasonic waves in multiple scattering media give similar results with one-bit signals as with complete wave forms. We computed the correlation functions on the entire length of one-bit coda records. The results are very close to correlations of windowed true-amplitude coda records.
20. A. Derode, A. Tourin, M. Fink, *J. Appl. Phys.* **85**, 6343 (1999).
21. M. Campillo *et al.*, *Geofis. Int.* **35**, 361 (1996).
22. N. M. Shapiro, M. Campillo, S. K. Singh, J. Pacheco, *Geophys. Res. Lett.* **25**, 101 (1998).
23. We thank N. Shapiro, J. Pacheco, and S. K. Singh (Instituto de Geofisica, Universidad Nacional Autónoma de México for making the data available and B. van Tiggelen, L. Margerin, A. Derode, E. Larose, R. Weaver, and G. Abers for enlightening discussions.

Supporting Online Material

www.sciencemag.org/cgi/content/full/299/5606/547/DC1

Figs. S1 and S2

18 September 2002; accepted 5 December 2002

A Nebular Origin for Chondritic Fine-Grained Phyllosilicates

Fred J. Ciesla,[1]* Dante S. Lauretta,[1] Barbara A. Cohen,[2] Lon L. Hood[1]

Hydrated minerals occur in accretionary rims around chondrules in CM chondrites. Previous models suggested that these phyllosilicates did not form by gas-solid reactions in the canonical solar nebula. We propose that chondrule-forming shock waves in icy regions of the nebula produced conditions that allowed rapid mineral hydration. The time scales for phyllosilicate formation are similar to the time it takes for a shocked system to cool from the temperature of phyllosilicate stability to that of water ice condensation. This scenario allows for simultaneous formation of chondrules and their fine-grained accretionary rims.

The CM carbonaceous chondrites are of particular interest to planetary science because they are rich in both water and organic molecules, making them prime candidates for the source of Earth's prebiotic material. The majority of their water is contained within phyllosilicates, which typically occur as small (10 to 100 nm) grains within the fine-grained rims (FGRs) around coarse-grained meteoritic components such as chondrules and calcium-aluminum–rich inclusions. FGR textures, specifically the direct contact of hydrous and anhydrous grains, suggest that these rims accreted on their host objects before being incorporated into their final parent bodies (*1*, *2*) (Fig. 1). If the formation of these phyllosilicates took place on the final parent body, more homogeneous hydration would be expected among the grains. In addition to these FGRs, the CM chondrites also contain evi-

---

[1]Department of Planetary Sciences, Lunar and Planetary Laboratory, University of Arizona, 1629 East University Boulevard, Tucson, AZ 85721, USA. [2]Hawaii Institute of Geophysics and Planetology, University of Hawaii, Honolulu, HI 96822, USA.

*To whom correspondence should be addressed. E-mail: fciesla@lpl.arizona.edu

Geophys. J. Int. (2002) **150,** 639–650

Testing group velocity maps for Eurasia

Nathalie Cotte and Gabi Laske

Cecil and Ida Green Institute of Geophysics and Planetary Physics, Scripps Institution of Oceanography, University of California San Diego, La Jolla, CA 92097-0225, *USA. E-mails: ncotte@mahi.ucsd.edu; glaske@ucsd.edu*

Accepted 2002 February 28. Received 2001 October 26; in original form 2001 April 15

SUMMARY

Group velocity maps for seismic surface waves play an important role in monitoring the Comprehensive Test Ban Treaty so their accuracy is crucial. Group velocity anomalies can be modelled in terms of lateral variations in crustal and shallow mantle structure, the knowledge of which is important for understanding wave propagation and the blockage of regional phases. Accurate group velocity maps are also indispensable tools in attempts to lower the detection threshold for seismic events and to distinguish between explosions and earthquakes. This paper investigates the feasibility of validating existing maps using a relatively small data set of path-averaged group traveltime data. We find that group velocity correction surfaces calculated for two sets of global maps and a set of regional maps in Eurasia exhibit significant differences. We compare our measurements with predictions from these maps and test whether any of these maps is consistent with our data. Large differences between measurements and predictions can occur for selected individual paths across Eurasia and we find that maps resulting from global inversions fit our data best. There are visually only subtle differences between global and regional maps but we speculate that the long-wavelength structure is relatively poorly constrained in the regional maps.

Key words: Eurasia, group velocity, surface waves, surface wave correction surface, validation of seismic models.

1 INTRODUCTION

Observations of seismic surface waves provide very useful constraints on the structure of the Earth's crust and upper mantle. Various methods exist to analyse such data. While one type of method models the waveforms in terms of variations in depth-dependent structure directly (e.g. in the partitioned waveform inversion of Nolet 1990), others involve the measurement of dispersion which is then interpreted in terms of structure (e.g. Knopoff 1972). The dispersion of surface waves can be described by both frequency-dependent phase and group velocities where, in principle, measuring only one of the two parameters is necessary in order to determine the depth-dependent structure that is causing the dispersion. A great majority of the published papers describe the processing of phase measurements, while relatively few workers have chosen to measure group traveltimes. The latter group can be found especially within the Comprehensive Test Ban Treaty (CTBT) community. Measuring group traveltimes has certain advantages over measuring phase anomalies, the greatest being that one does not need to calculate synthetic seismograms that are necessary for accurate phase measurements. Group traveltimes are also typically less affected by source effects than phase anomalies. In fact, source effects can be ignored for most group traveltime measurements, though some exceptions exist (Levshin *et al.* 1999).

The group velocity of surface waves is typically more sensitive to shallow structure than phase velocity at the same period and group velocity data between 100 and 20 s provide excellent constraints on crustal structure. Having accurate information on variations in crustal structure at hand is essential for successfully monitoring a CTBT because such variations largely affect the propagation of regional phases and ultimately the event location process. Group velocity maps can also be used to calculate so-called group velocity correction surfaces (e.g. Levshin & Ritzwoller 2001). Such surfaces are widely used in phase-matched filtering routines to extract low signal-to-noise wave packets from a seismogram. Hence accurate group velocity maps can tremendously lower the detection threshold for small events. And yet, while global maps of surface wave phase velocity anomalies have been published on a regular basis (e.g. Trampert & Woodhouse 1995; Laske & Masters 1996; Ekström *et al.* 1997), and are widely used in global mantle tomographic studies (e.g. Gu & Dziewonski 1999; Masters *et al.* 2000), maps of group velocity anomalies are surprisingly rare in the literature. In fact, such maps have mostly been of regional scale (e.g. Ritzwoller & Levshin 1998 for Eurasia; Pasyanos 2000 for Northern Africa/Middle East) and global maps have not been available until very recently (e.g. Barmin *et al.* 2001; Larson & Ekström 2001).

In this study we compare group traveltime predictions from the newly available maps with our own measurements. We are particularly interested in the question of whether the predictions are distinct enough, or our data precise enough, to help us decide which of the existing models is most consistent with our data. We should point out that our data set is far from being complete and is not comprehensive enough to make our own models. However, initial comparisons give us a valuable insight into obvious systematic differences between predictions and data. We regard our exercise as a validation of existing maps because our data are indeed independent: (1) our data were not used to make the maps; (2) the measurement techniques we apply use our own computer codes. It may be worthwhile to compare data sets of different workers (e.g. to identify systematic trends caused by one measurement technique or the other), but this is beyond the scope of this paper. We conclude this study by stressing the importance of embedding small-scale variations of regional structure in the appropriate global 'long-wavelength' context.

2 GROUP VELOCITY MAPS

Our study focuses on Eurasia, where nuclear tests are likely to occur and successfully monitoring the Comprehensive Test Ban Treaty is of particular interest. Accurate information on the 3-D seismic structure in this area is therefore essential. Starting with global group velocity maps, two sets of maps currently exist that can provide information concerning regional-scale variations in the area: one was derived by a group at Harvard University (Larson & Ekström 2001, LE maps hereafter) and the other by the group at the University of Colorado, Boulder (Levshin, Ritzwoller and Shapiro, personal communication; CUB hereafter). The LE maps were obtained by converting the phase measurements of Ekström *et al.* (1997) to group traveltimes and then inverting these for group velocity maps. The CUB maps were derived from measured group traveltimes, using the method of Barmin *et al.* (2001). A comparison of both sets of maps is particularly interesting because they are obviously obtained from different types of data. We also examine the regional group velocity maps of Ritzwoller & Levshin (1998) (RL hereafter). These cover the Eurasian continent between 10 and 170°E and between 10 and 80°N and are defined on a 1×1 deg^2 grid, the finest parametrization used among the three sets of maps.

Fig. 1(a) shows Rayleigh wave maps at 90 s and Fig. 1(b) Love wave maps at 40 s. For each wave type, the global maps are very similar, displaying structure of similar wavelengths and roughly the same amplitude, while the regional map obviously contains higher-amplitude short-wavelength structure. Large differences between global and regional maps occur close to the edges of the regional maps, e.g. most of the Pacific Ocean and the Arctic Ocean north of Siberia. These differences are probably a result of the considerably poorer resolution in the regional maps at their edges that are constrained by only a few data (see also Ritzwoller & Levshin 1998). Despite the obvious similarity of the global maps, there are some disagreements, one being the slightly larger amplitudes in the CUB map. In the Rayleigh wave maps, there are also obvious difference in the Near-East. In the LE map, anomalies are smoothly varying (between 0 and -5 per cent), while they are rapidly varying in the CUB and RL maps (between -6 per cent in the Red Sea and 3 per cent east of the Persian Gulf). The gradients of structure from northern India toward the northeast across the Tibetan Plateau is also markedly different among the maps. It is somewhat surprising that the global Love wave maps appear to be more similar than the Rayleigh wave maps. Love wave measurements are typically more difficult to obtain, which should be reflected in differences between the maps of different workers. One hardly noticeable difference is located in the Mediterranean Sea, where the CUB map is slightly more negative. As for Rayleigh waves, the regional Love wave map is quite different, the most obvious differences occurring in the Pacific Ocean and the Artic Ocean north of Siberia. All three maps are remarkably similar in the Near-East, the only difference being a small-scale positive velocity anomaly immediately west of the Red Sea (<2 per cent for the LE map, <4 per cent for the CUB map but up to 8 per cent for the RL map).

3 DATA AND GROUP VELOCITY MEASUREMENTS

In this and the following sections, we try to evaluate how significant the differences between the group velocity maps really are and what impact these discrepancies have for a typical data set. For a comparison between predictions and data we assemble three data sets. One comprises the records of the temporary Saudi Arabian Seismic Network (SAUDI array hereafter) (Vernon *et al.* 1996), the second are selected records from the permanent Kyrgyz Network (KNET) (Mellors *et al.* 1997) and the third included records from seven broad-band stations of permanent global networks: PET, TATO and YAK (IRIS/USGS), ABKT, ERM and NRIL (IRIS/IDA) and HYB (Geoscope) (Fig. 2). The SAUDI array was operational between 1995 November and 1997 March and consisted of nine broad-band stations. As its data set we select 158 shallow events (depth <200 km) with scalar seismic moments between 0.5×10^{18} and 4×10^{20} N m. KNET is composed of 10 broad-band stations, with an aperture of approximately 200 km and interstation distances between 30 and 90 km. For this array we select the same events as for the SAUDI array.

We use a standard frequency–time analysis technique (FTAN) to measure the group velocity, a comprehensive treatment of which can be found in Levshin *et al.* (1989). A slight modification is based on the work of Shapiro & Singh (1999). For a particular measurement the chosen frequency is corrected for effects caused by the frequency dependence of the spectral amplitude. Group traveltimes are measured between earthquakes and stations assuming propagation along the source–receiver great-circle. As suggested by Levshin *et al.* (1999), we ignore the source group time, which is negligible compared with uncertainties in source location and origin time. In the frequency–time domain, we determine the envelope of the signal for each frequency. The amplitude maximum of the envelope is picked as the group traveltime and the time window corresponding to 98 per cent of the amplitude peak is defined as an error bar. The traveltime is then converted to the path-averaged group velocity between the source and the receiver. The choice for the error bars sometimes results in a large scatter that may not reflect the actual precision of the measurement. For example, we obtain much larger error bars for long periods than for short periods, because the width of the time window is proportional to the period. Furthermore, for small epicentral distances the same traveltime error gives a larger group velocity error than for long epicentral distances. We therefore 'equalize' the errors by applying an empirical correction (new error [km s^{-1}] $= 0.1 \times$ original error $+ 0.02$), which effectively sets the maximum error at 0.1 km s^{-1}.

We use data only in a certain epicentral distance range to avoid systematic outliers in our measurements. Only events with epicentral distances greater than 20° are considered. This reduces the bias in the measurements caused by neglecting source effects. Events with epicentral distances larger than 150° are also discarded because the bias introduced by multipathing effects may be significant

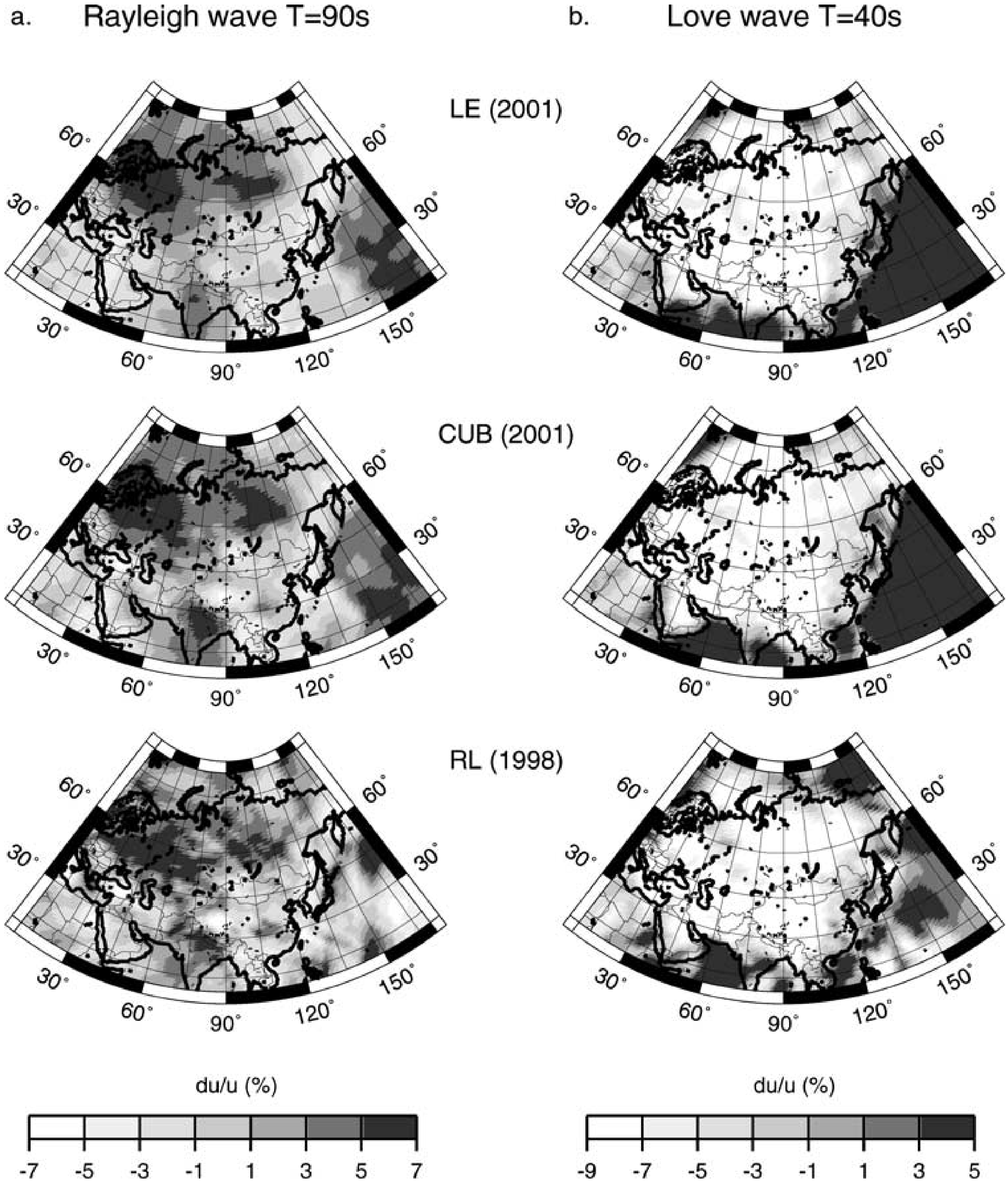

Figure 1. Group velocity maps used in this study: global map of Larson & Ekström (2001) on top, global map of Barmin *et al.* (2001) on middle and regional map of Ritzwoller & Levshin (1998) on bottom. Part (a) is for Rayleigh waves at 90 s and (b) is for Love waves at 40 s. The group velocities are expressed in perturbation with respect to the reference model anisotropic PREM anisotropic.

(Pavlis & Mahdi 1996). The source information is taken from the monthly preliminary determination of epicentres (PDE) provided by the NEIC. We note that this information can be quite different from the parameters published in the CMT catalogue (Dziewonski *et al.* 1981). We correct the group traveltimes adopting the 'assumed source duration' in the CMT catalogue, which results from the moment$^{1/3}$ rule, but discard events for which the assumed duration is 25 s or longer.

4 COMPARING AVERAGE DISPERSION CURVES

We validate the existing group velocity maps by comparing their predictions with our measurements. Each of the predictions are determined by integrating the group traveltime along the source–receiver great-circle using the published maps. The resulting time is then converted to an apparent (or path-averaged) group velocity.

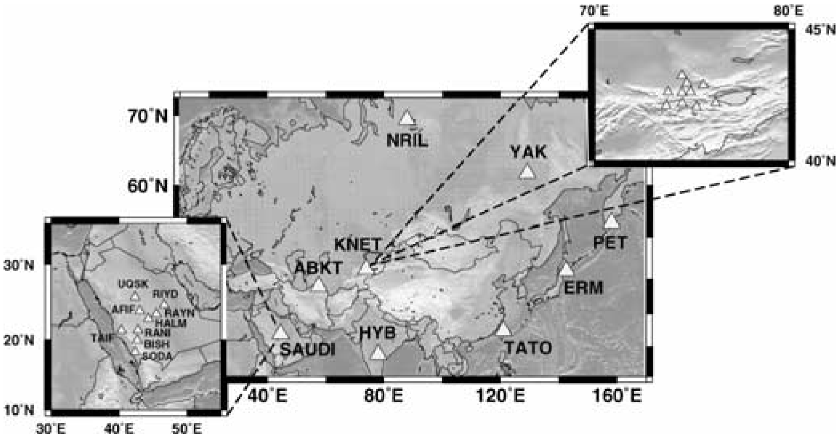

Figure 2. Broad-band stations used in this study: Saudi Arabian Seismic Network (bottom left-hand graph), installed from 1995 November to 1997 March, the permanent Kyrgyz array (top right-hand graph), and some permanent stations from global networks (Iris/Usgs, Iris/Ida and Geoscope).

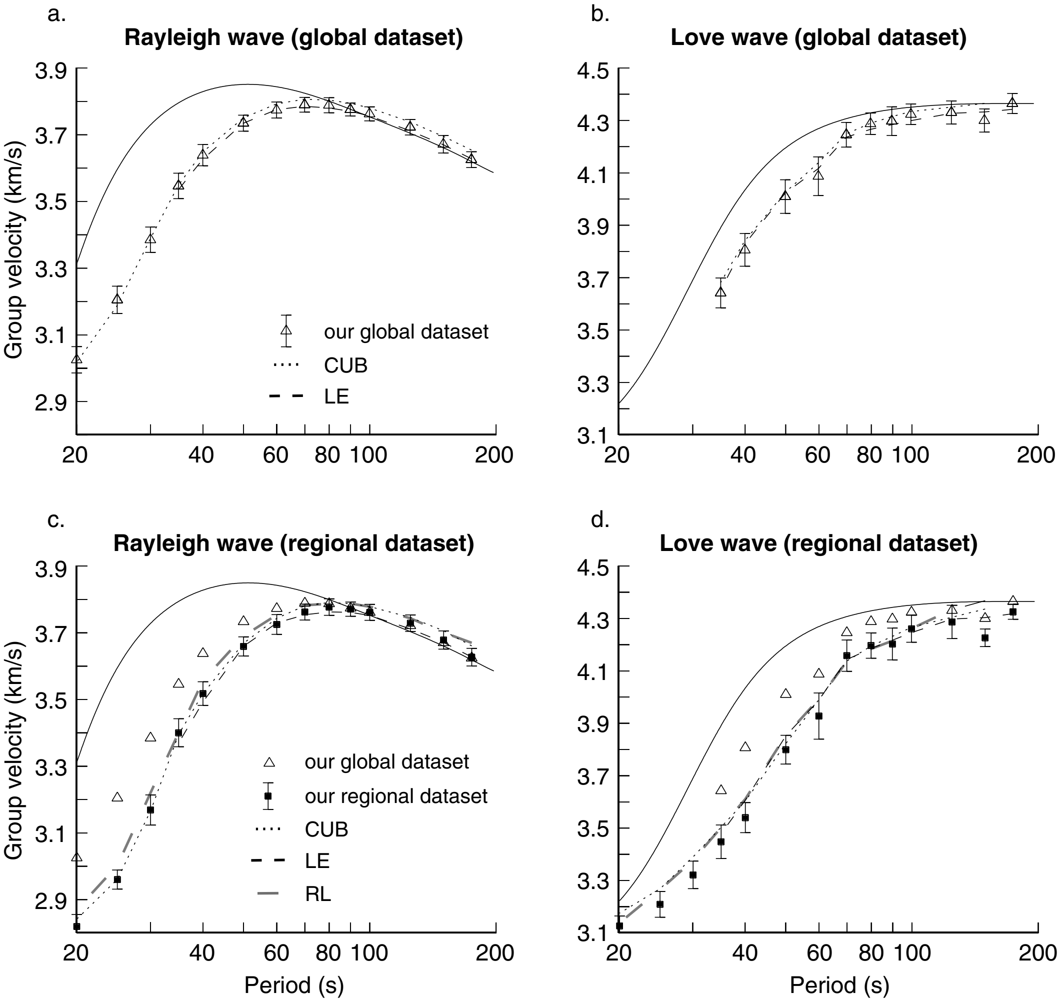

Figure 3. Comparison between measured and predicted path-averaged group velocities for data collected at the Saudi array, both for Rayleigh (a and c) and Love (b and d) waves. Results are obtained for our 'global data set' and for our 'regional data set'. Triangles represent our measurements (see text for the details on error bars) and the solid line is the anisotropic PREM model. Calculations were performed using the RL map (long dashed line), the LE one (intermediate dashed line) and the CUB one (short dashed line).

Fig. 3 shows the mean dispersion curves that are obtained by averaging all dispersion curves in our SAUDI data set. Also shown are their 'statistical error bars'. We prefer to work with the statistical errors instead of the original measurement errors because we regard them as being more representative of the actual scatter of data within the SAUDI array. As mentioned above, the measurement technique yields errors that are proportional to the period. We notice, however, that at long periods the variation in group velocity between stations is much less than the measurement errors would suggest. We infer from this that the group velocity can be measured more accurately than what is given by the measurement technique. We therefore derive a ‘statistical error’ which is the frequency-dependent average over the standard deviations of all events. The latter is simply the formal standard deviation of the measurements of a specific event and can be determined if more than one station recorded this event. In some cases this error is actually smaller at long periods than at short periods. The most likely explanation for this is that strongly heterogeneous shallow local structure causes a larger variance in the measurements at short periods than at long periods.

We perform a comparison for two cases. In the first one, we average over all available measurements (global data set), while in the second case, we only consider paths corresponding to sources that lie within the regional map (regional data set). We first notice a significant difference between the average dispersion curves of the ‘global data set’ and the ‘regional data set’. This is especially the case for periods shorter than 70 s for which the ‘global’ group velocities are higher than the ‘regional’ ones. The reason for this is that the ‘regional data set’ does not contain any measurements that include the oceanic paths that are typically faster for periods between 60 and 17 s. Also shown in Fig. 3 are the means of the predicted group velocities. There is a marginal but probably significant difference between the predicted curves using the global maps on one hand and the regional maps on the other hand. A possible discrepancy at long periods may be caused by the fact that the regional maps were made using a flat-Earth approximation (Levshin, personal communication) which we ignored when calculating the predictions. This becomes increasingly relevant for velocities of deeper structure, for which the velocities in the flat Earth are larger than in the spherical Earth, changing the surface wave dispersion at long periods accordingly. Ignoring the flat-Earth transformation would not explain, however, the good agreement between the regional RL curve and the global BRL curve (that presumably has no flat-Earth approximation) at long periods and the disagreement at short periods.

When comparing the observed dispersion curves for Rayleigh waves with the predicted ones, we find differences that are all smaller than 0.025 km s^{-1} (0.7 per cent). This is within the error bars, except for the RL maps for periods shorter than 35 s. The predictions of the two global maps are closer than 0.7 per cent for the ‘global data set’ and closer than 1.0 per cent for the ‘regional data set’. The predictions of the CUB maps fit our measurements extremely well at periods shorter than 60 s, but at longer periods our measurements tend towards the lower velocities predicted by the LE maps. At periods longer than 125 s, our data become increasingly inconsistent with the CUB maps (and with the RL maps). The reason for this is not entirely understood, especially since there is no noticeable difference between the observed ‘regional’ and ‘global’ dispersion curves at these periods. This suggests that the CUB and the RL maps contain a large-scale ‘fast’ component that is absent in the LE maps and also not required by our data. We notice that at long periods, the slow regions around the Tibetan Plateau are typically somewhat larger and slower in the LE maps than in the other maps, possibly causing the baseline shift in the mean dispersion curves seen in Fig. 3.

The observed average Love wave dispersion curves are not as smooth as those for Rayleigh waves. There are typically only half as many data for this wave type (Tables 1 and 2) and the individual data are noisier. The number of available ray paths also changes significantly with period. A certain ‘roughness’ of the curves for the predictions reflects the uneven averaging occurring over different seismic structure. This is especially the case for periods shorter than 40 s where all ray paths lie within the regional map and a ‘global data set’ does not really exist. There is an excellent agreement, however, between predictions of different maps, for periods shorter than roughly 70 s. This agreement may also be inferred from the great similarity of the maps shown in Fig. 1(b). Note, however, that the differences between measurements and predictions are greater than for Rayleigh waves and can reach 3.1 per cent, which is probably a result of the higher noise level in the Love wave data set.

Table 1. Percentage variance reduction relative to PREM for Rayleigh waves calculated with the SAUDI data set. Results both for sources at global (gl) scale and at regional (reg) scale are reported for periods between 20 and 200 s. The right-hand column gives the number of measurements for a regional and global comparison.

	Variance reduction for Rayleigh wave					
Period (s)	CUB (gl)	LE (gl)	CUB (reg)	LE (reg)	RL (reg)	Number
175	−17.10	17.77	−29.91	11.15	−70.32	96/232
150	14.06	29.95	7.41	28.75	9.12	113/291
125	31.26	42.14	37.35	34.68	37.51	131/336
100	28.93	44.50	37.78	43.89	34.89	168/388
90	23.04	36.86	46.70	48.52	45.47	173/397
80	39.21	45.52	46.59	51.98	51.07	185/421
70	57.35	60.90	72.61	**78.63**	73.65	182/419
60	**78.26**	**78.16**	**88.39**	**86.09**	**84.66**	187/442
50	**89.71**	**87.13**	**94.84**	**91.13**	**92.33**	170/422
40	**94.69**	**92.93**	**97.52**	**95.20**	**95.80**	169/437
35	**96.65**	**95.35**	**98.17**	**96.71**	—	144/376
30	**97.43**	—	**98.63**	—	**97.57**	80/223
25	**97.57**	—	**98.94**	—	**98.76**	57/147
20	**95.80**	—	**98.15**	—	**97.79**	36/78

Table 2. Percentage variance reduction for Love waves calculated with the SAUDI data set. Results both for sources at the global (gl) scale and at the regional (reg) scale are reported for periods between 20 and 175 s. The right-hand column gives the number of measurements for regional and global comparison.

	Variance reduction relative to PREM for Love wave					
Period (s)	CUB (gl)	LE (gl)	CUB (reg)	LE (reg)	RL (reg)	Number
175	—	−18.08	—	−0.11	—	8/36
150	11.33	35.63	27.68	47.76	−5.45	13/47
125	11.06	26.00	54.56	60.49	50.54	23/76
100	36.45	24.94	67.78	67.05	64.48	41/136
90	28.81	30.56	72.15	**77.95**	**77.01**	48/165
80	57.37	45.98	**83.57**	**85.64**	**84.02**	60/206
70	67.79	62.43	**84.61**	**86.65**	**83.84**	56/204
60	61.41	63.17	**81.71**	**82.73**	**80.35**	108/261
50	**79.92**	**77.28**	**92.97**	**91.04**	**92.22**	103/263
40	**82.74**	**82.47**	**92.97**	**92.96**	**91.66**	106/235
35	**86.82**	**86.86**	**93.05**	**93.17**	—	113/207
30	**88.53**	—	**88.56**	—	**87.71**	77/87
25	74.91	—	74.18	—	73.02	55/58
20	22.46	—	13.00	—	14.29	33/34

In order to quantify the discrepancies found in Fig. 3, we compare the variance reductions obtained for our measurements using the published maps (Tables 1 and 2). The variance reduction generally increases with decreasing period but is very similar for different models, at fixed period. Exception are at long periods (90 s and beyond) for which the LE maps give a significantly better fit to the data than the other maps. Variance reductions for all maps are especially high for periods shorter than 60 s for Rayleigh waves, for both global and regional data sets. For Love waves, variance reductions are highest for periods between 50 and 30 s for the ‘global

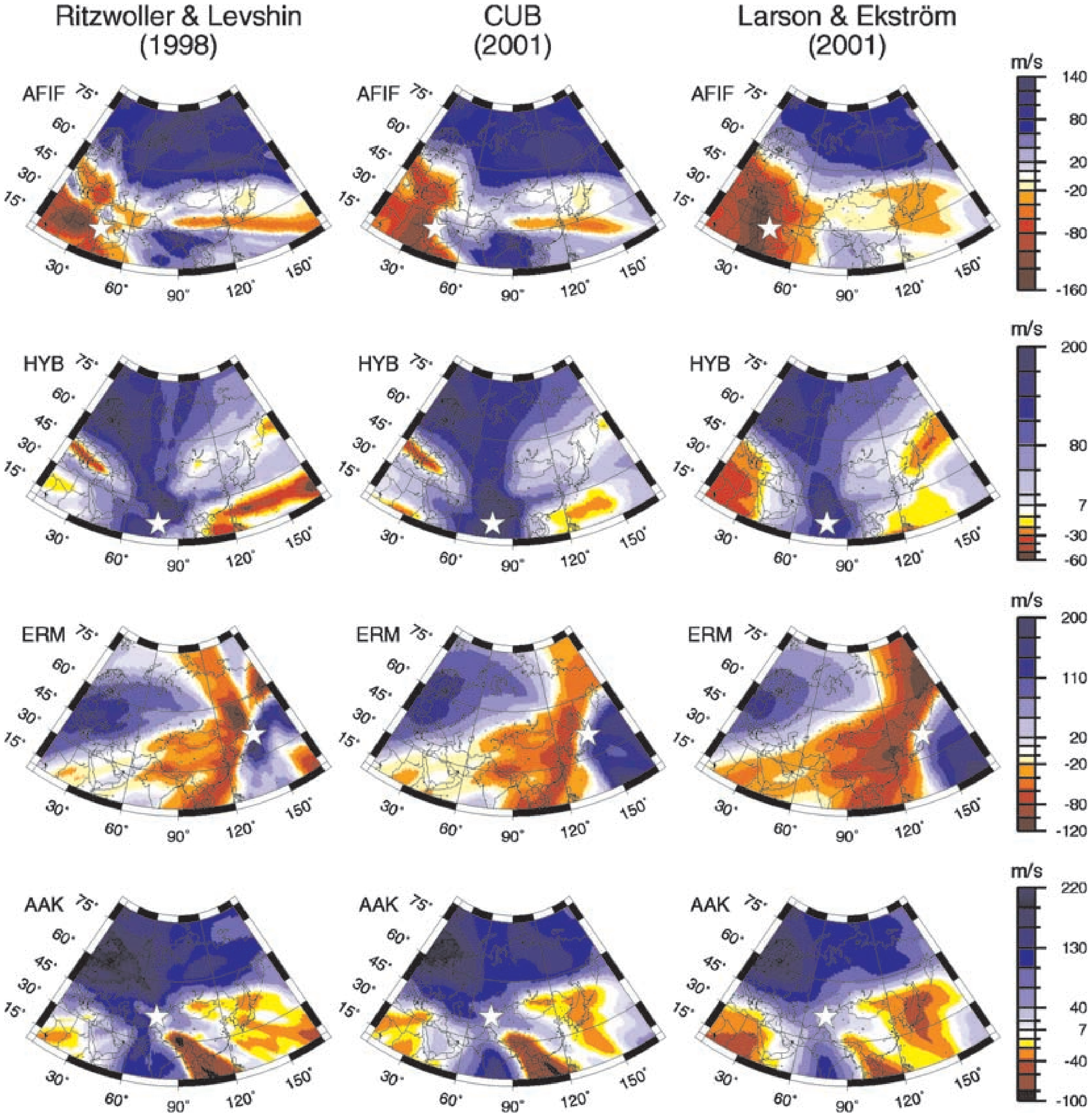

Figure 4. Group velocity correction surfaces for Rayleigh wave at 40 s. For all fictitious sources located on a grid we calculate path-averaged group velocities for each source-station path. These values are computed for 'reference station' AFIF, HYB, ERM and AAK from top to bottom. The grey-scale in m s^{-1}gives the results relative to reference model anisotropic PREM. The left-hand column is for the RL map, the middle column for the CUB map and the right-hand column for the LE map.

data set', and between 80 and 30 s for the 'regional data set'. Again, our observations seem to be best fitted by the LE maps at the longest periods beyond 100 s.

5 GROUP VELOCITY CORRECTION SURFACES

A useful tool to identify source regions for which the largest discrepancies in the predictions of different models are to be expected are so-called group velocity correction surfaces (GVCS). For a given group velocity map, such correction surfaces are calculated for each individual seismic station. For a given station, we compute the path-averaged group velocities for all fictitious sources on a grid within Eurasia. The calculated values are then plotted at the fictitious source locations. Fig. 4 shows the resulting GVCSs for Rayleigh waves at 90 s for stations AFIF (SAUDI), HYB (Geoscope), ERM and AAK (IRIS/IDA). For each of these stations, the largest differences between GVCSs for different group velocity maps are found close to the edges of the diagrams (e.g. for AFIF in the northeast or ERM in the Pacific Ocean). These differences are most pronounced when significant fractions of the ray paths are along the poorly resolved edges of the RL maps. For station AFIF, differences between the three GVCSs also occur in the Near- and Middle-East, where anomalies are more negative for the LE surface, and East of China and Japan, where the LE surface is smooth while the RL and CUB surfaces reveal significant changes from south to north. For station HYB, the LE surface has negative anomalies in Africa while the two other GVCSs have positive anomalies. For events in the Kuril Islands, the LE surface also reveals stronger negative anomalies than the other ones. The correction surfaces for station ERM are dominated by large-scale strongly negative anomalies, which are again strongest for the LE surface. The negative anomalies for events in Siberia are shifted toward the west in the RL surface compared with the GVCSs for the two global maps. Perhaps the group velocities between sources in this region and station ERM are less well resolved in the regional map. Note that values in this area are associated with rather short travel paths that have not yet undergone significant path-averaging effects. Hence, relatively small differences in the group velocity maps would manifest themselves as relatively large differences in the correction surfaces. The correction surfaces for station AAK are very similar with only small differences in the magnitude of the anomalies ($<$10–20 m s^{-1}). It may therefore be difficult to validate group velocity maps for Rayleigh waves at 40 s for Eurasia, especially the western and northern areas, using data from station AAK alone.

We would expect that discrepancies in published models should occur on small scales, because different data sets (and modelling techniques) used by different workers should differ in detail but not on average (or large scales). Consequently, the group velocity correction surfaces should differ on small scales and the predictions for individual paths should probably scatter but exhibit no obvious systematic behaviour. We expect a particularly large scatter at short periods for which Rayleigh waves are most sensitive to crustal structure, which is particularly complex around the Tibetan Plateau. Yet, for Rayleigh waves at 40 s, the main differences between group velocity maps (as well as between the corresponding areas in the correction surfaces) do not occur in this area (not shown). We note a long-wavelength component in the LE map that makes the group velocity correction surfaces more negative than those for the RL and CUB maps over a large area. This discrepancy supports the systematic shifts we found in Fig. 3, where the curves for the LE maps were systematically lower than those for the RL and CUB maps.

6 ANALYSING INDIVIDUAL TRAVEL PATHS

The comparison of group velocity correction surfaces for different group velocity maps has shown that significant discrepancies exist in the path-averaged group velocities for some source–receiver pairs. We now select individual paths within Eurasia and compare our measurements with the predictions from the three different sets of maps. Fig. 5 summarizes the selection of paths and Figs 6 and 7 compare our observed dispersion curves with predicted ones. We plot the dispersion curves as well as the percentage differences between the curves. For the two network data sets, SAUDI and KNET, we average the dispersion data for a given event over all stations. The resulting curve should give the average dispersion between an event and the networks. A slight scatter at fixed frequency is caused by the slightly different structure sensed along slightly different ray paths and differently sampled near-receiver structure. Figs 6(a) and 7(a) show observations and predictions for the SAUDI array. For the source located to the southeast of Tibet (no 1), the predictions for the regional maps fit our measurements very well over the whole period range (20–175 s). The global CUB maps fit our measurements only for periods longer than 60 s but underpredict them for shorter periods, while the global LE maps underpredict our measurements for periods shorter than 150 s, and differences can reach 6.0 per cent (e.g. for 35 s). For both sources in the Philippines (events nos 2 and 4), the RL maps slightly overpredict our measurements for periods shorter than 70 s. For both events, the LE maps underpredict the data over almost the whole period range, though the discrepancy is more obvious for event no 4. The CUB maps give the best fit to our data for both events, though there is some discrepancy at longer periods for event no 4. The events were relatively close so the measurements should agree. We speculate that possible overtone contamination at longer periods for event no 4 causes the relatively small difference. This example stresses, however, that a detailed validation process of models is only meaningful when using a comprehensive data set (i.e. different paths, repeat measurements for similar paths). For the two sources in Japan and northwest of Tibet (events nos 3 and 5), for which parts of the travel paths to the SAUDI array overlap, the measurements scatter significantly and are more difficult to interpret. In particular, reliable estimates for event no 5 are only possible for periods shorter than 70 s. In general, the two sets of global maps fit our data better, while again the regional maps slightly overpredict our data. The data from KNET (Figs 6b and 7b) exhibit a significant scatter, the cause of which is not entirely clear. We notice that the waveforms are generally much more coherent across the SAUDI array than across KNET despite the significantly wider station spacing. The frequency-dependent oscillations in individual dispersion curves (such as for event no 4 in Fig. 6b) are unphysical and reflect uncertainties for individual estimates. Such sections of the dispersion curve are not considered in the validation of a model. We suspect that strong lateral heterogeneity in the area around the Tibetan Plateau causes severe propagation effects (see e.g. Pavlis & Mahdi 1996) and hence affects our measurements. Note, however, that existing maps clearly seem to overpredict measurements for which paths cross the Tibetan Plateau (i.e. event no 1).

We conclude this comparison by presenting results for a few permanent global seismic network (GSN) stations. For stations PET and YAK, we choose an event located in the Adriatic Sea (events no 1 in Fig. 5c). Both sets of global maps fit our measurements very well, while the regional RL maps overpredict our data for PET (at periods shorter than 90 s) and to some extent for YAK. In some cases the discrepancy can reach 4 per cent, which is much larger than our most pessimistic error bars, and hence significant. For station ABKT, we choose three events located along the Pacific Rim, one in Northern Japan (no 2), one in the Philippines (no 3) and one in the Kuril Islands region (no 4). The three paths are very different (see Fig. 5c) so not surprisingly, the measured path-averaged group velocities are also rather different. For the two northern paths (events nos 2 and 4), differences between predictions as well as between predictions and measurements are exceptionally small, the only discrepancy being that the RL maps sometimes slightly overpredict the measurements. The LE maps slightly underpredict our long-period data for event no 4. For the source in the Philippines (event no 3), the differences are greater, and although the measurements are somewhat oscillatory, we can identify the CUB maps as the set of maps being most consistent with our data. Both sets of global maps are consistent with our measurements at station ERM (Figs 6d and 7d) and the regional RL maps overpredict them. For stations TATO and HYB, our measurements are clearly inconsistent with the RL maps.

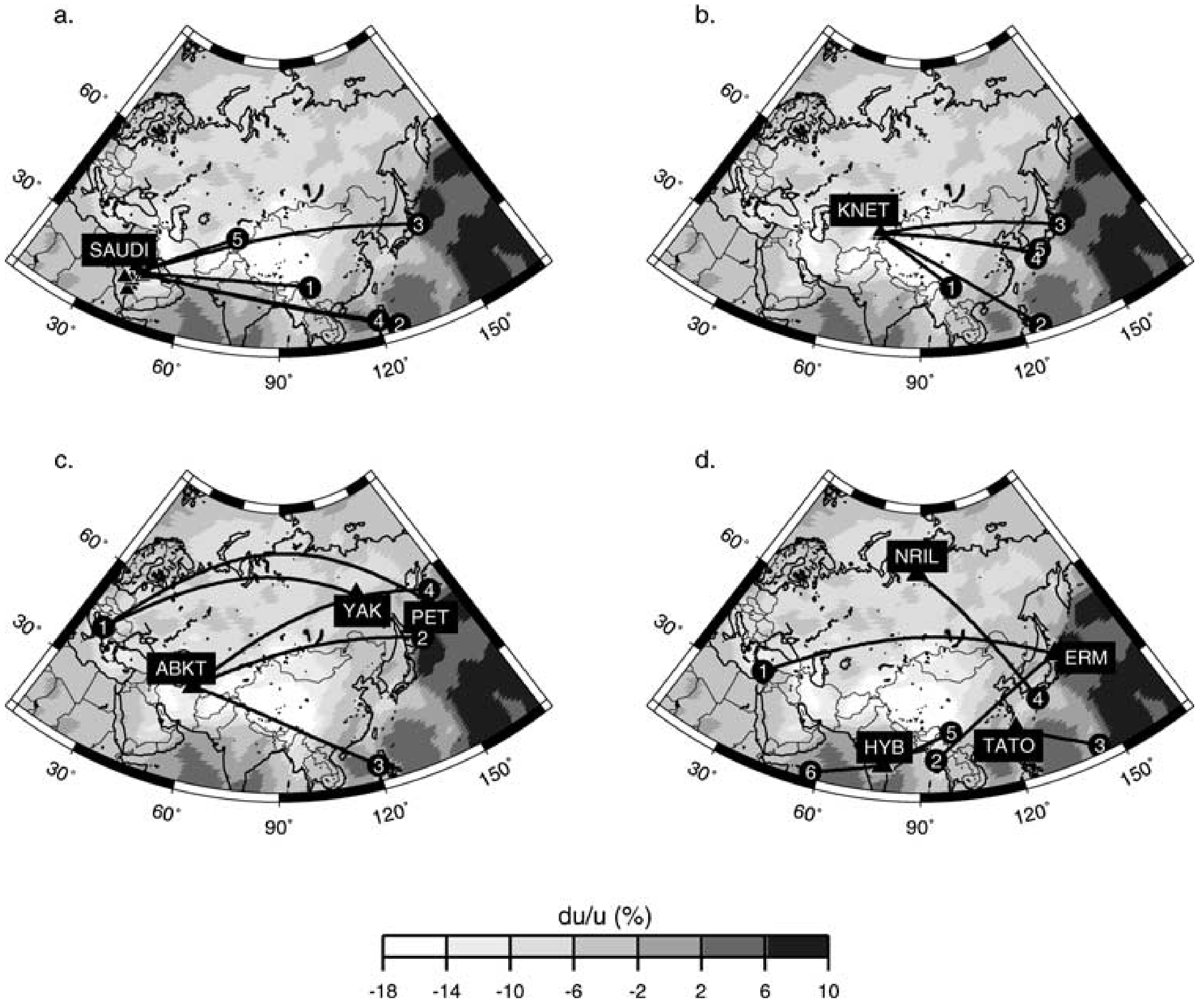

Figure 5. Travel paths corresponding to the path-averaged group velocity measurements selected for individual analyses. The solid line between source (black dot) and station (black triangle) is the great-circle between these two points. The background grey-scale is for the CUB map for Rayleigh waves at 40 s.

Both paths TATO-event no 3 and HYB-event no 6 lie along the edge of the regional map so this discrepancy is not too surprising. The case HYB-event no 5 is less obvious, however, and the LE global maps give the best fit to our data. Finally, the large scatter in the dispersion curves for NRIL does not allow a conclusive comparison. In summary, we find that the set of global maps fits our data best and may be the most appropriate to represent effects on the Rayleigh wave group velocity caused by variations in crustal and upper mantle structure in Eurasia.

7 SUMMARY AND DISCUSSION

The success of the seismic monitoring of a Comprehensive Test Ban Treaty depends largely on the quality of the structural models seismologists use to predict their data. In this study we present an attempt at validating some existing models for Eurasia using surface waves. We measure path-averaged group velocities using data from the Saudi Arabian Seismic Network, the Kyrgyz Network and from selected stations of the permanent global seismic networks. In our validation tests we compare these data with predictions using three sets of available group velocity maps. These maps are intrinsically rather different so a comparison is particularly interesting. On one hand, we have the opportunity to test predictions that ultimately came from very different data sets: one set of group velocity maps were constructed from group traveltime data and another one from phase data. We are also able to test how well global maps fare relative to more regional-scale maps, using regional-scale data sets. The regional maps provide the finest parametrization and display the largest amount of small-scale features. We therefore anticipated that the most obvious discrepancies between data and predictions as well as between predictions of different maps would occur for relatively short travel paths when path-averaging effects have not yet diminished the effects of small-scale structure below a detectable limit. Yet the group velocity correction surfaces for the regional Ritzwoller & Levshin (1998) maps and their global maps (CUB), which were made from group traveltimes and include the same regional data set, are generally astonishingly similar. Some exceptions exist and the regional maps indeed exhibit much larger anomalies for certain source locations. The group velocity correction surfaces for the global maps of Larson & Ekström (2001) (LE), that came from phase data, are rather smooth. It is intriguing that these correction surfaces also appear shifted systematically towards lower path-averaged group velocities.

We find large systematic discrepancies between our data and the regional maps, which often overpredict our measurements, especially at short periods, sometimes by as much as 3 per cent. We take

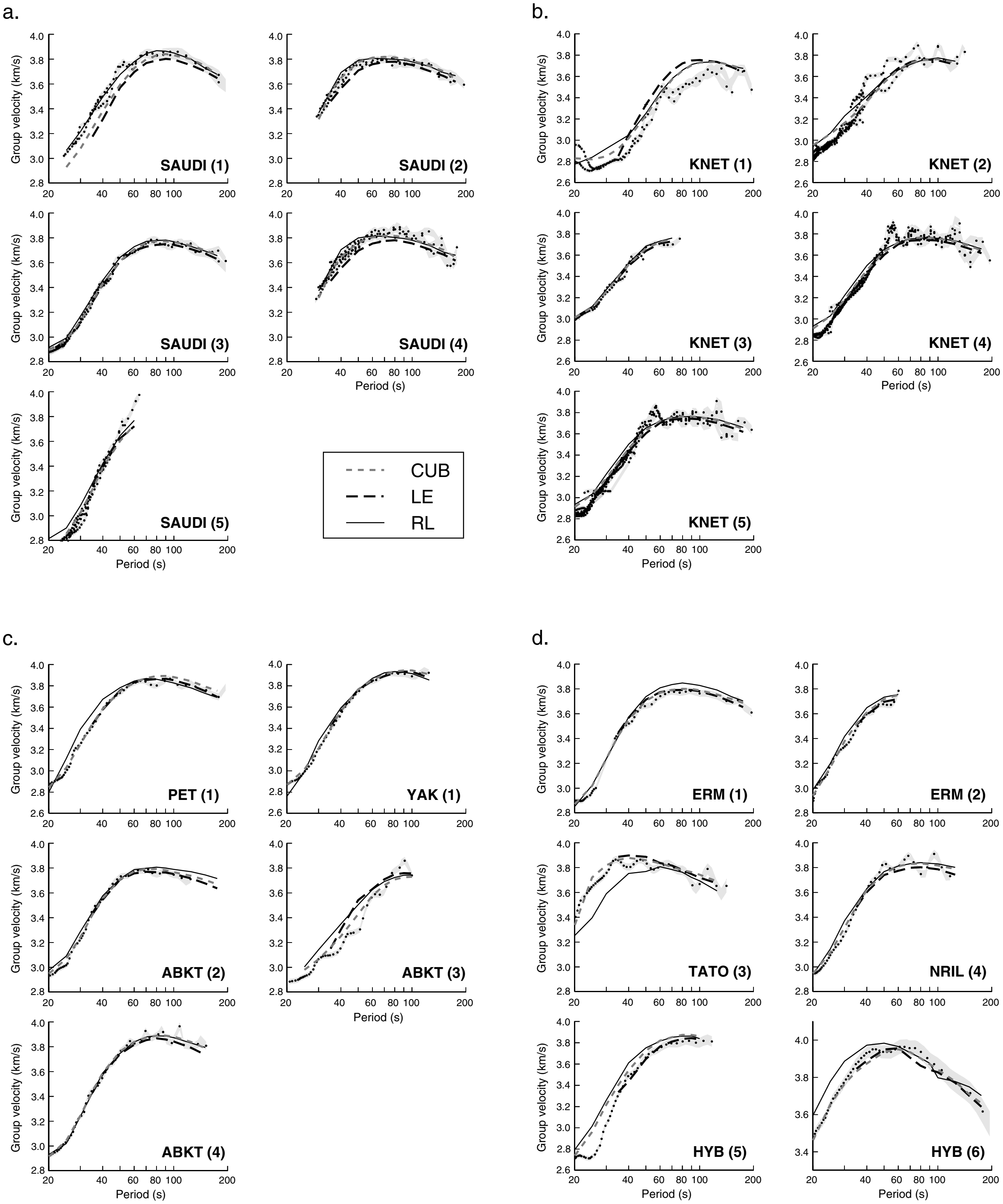

Figure 6. Comparison between measured (black dots and grey area for error bars as described in the text) and predicted path-averaged group velocities for source–receiver pairs shown in Fig. 5. The short dashed line is for the BRL, the long dashed line for the LE and the solid line for the RL maps.

this as being indicative of a significant lack of large-scale structure in these maps. The differences between predictions from the two global maps are usually small, rarely exceeding 3.0 per cent, but differences between regional and global maps are usually larger and can reach 3.8 per cent. The global maps usually provide a good fit to our data where the CUB maps appear most consistent with measurements of selected travel paths. This is particularly the case for periods shorter than 70 s for which our measurement errors are small. On average, however, these maps seem to have a systematic offset toward high velocities with respect to our data, especially at long periods (Fig. 3) though discrepancies lie just within our error bars. The global LE maps are in excellent agreement with our average dispersion curves at periods above 45 s. These results are somewhat puzzling as we expect these maps to be least consistent with our data. We are left to conclude that the CUB maps are the best models to describe short-period Rayleigh wave group

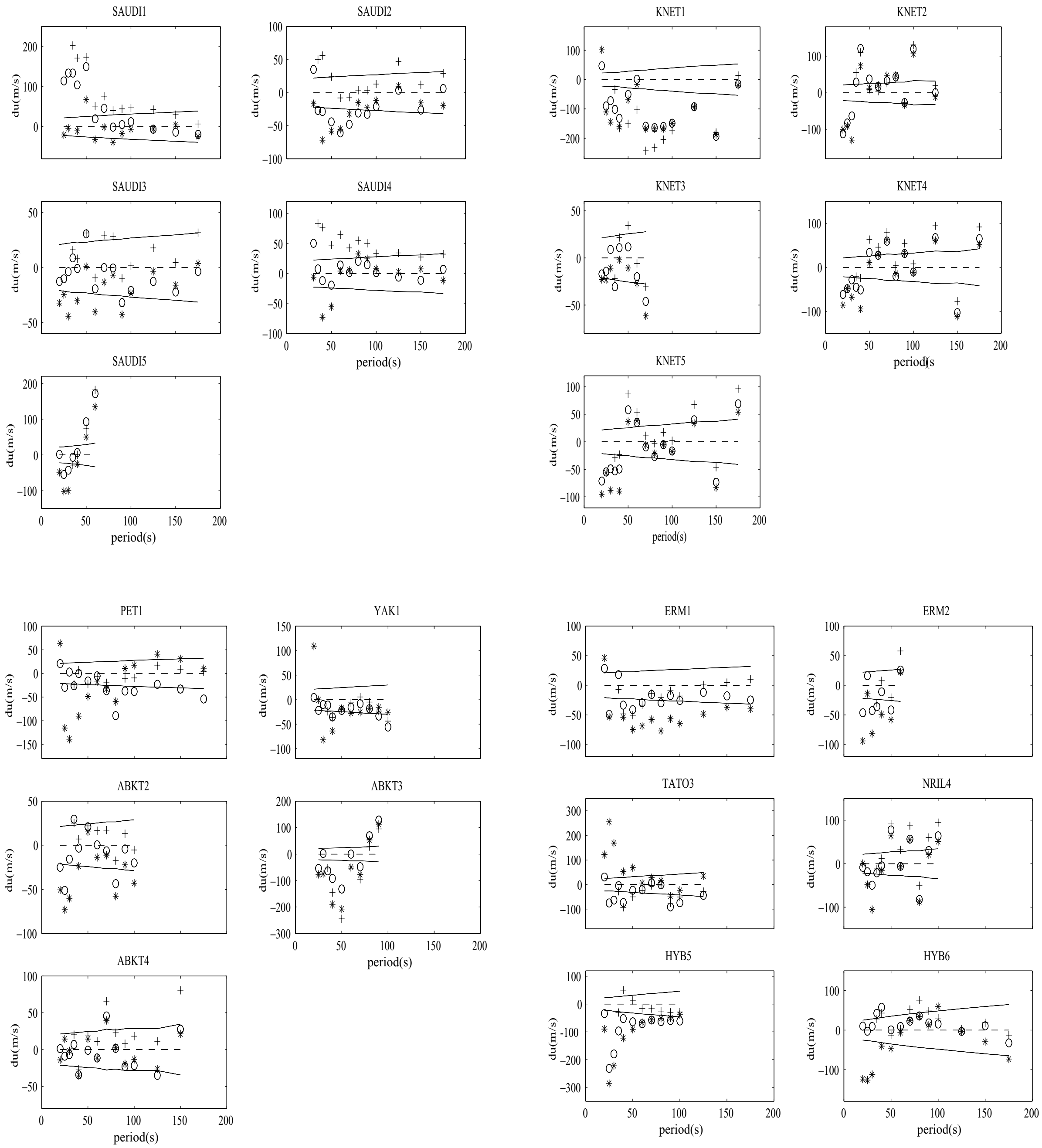

Figure 7. Difference between measurements and predictions (du) of group velocities for the curves shown in Fig. 6. The plus signs mark the differences between the data and the LE maps, the circles between the data and the CUB maps and the stars between the data and the RL maps. The solid lines trace the measurement errors and mark the range of predictions that are still consistent with our data.

velocities within Eurasia. For the purpose of using the CUB maps in the monitoring of a CTBT, however, we recommend an adjustment to the long-wavelength component at longer periods.

Our observations stimulate us to participate in the discussion on the compatibility of regional and global models. Chevrot *et al.* (1998a,b) find no obvious gap between the power spectral density of global and regional Love wave phase velocity maps in a region covering the Tibetan Plateau. On the other hand, there appears to be considerable disagreement between the spectra of certain global shear velocity models (Zhang & Tanimoto 1993; Ekström & Dziewonski 1998) and the regional model of the Australian continent by Zielhuis & van der Hilst (1996), at wavelengths where the models overlap. Although we do not further quantify our comparison, we find that in our study the regional group velocity maps also have long-wavelength spectral amplitudes that are different from those of the global maps. We speculate that these gaps between global and regional models can occur because the bulk of the data used for regional modelling have significantly shorter travel paths than those for global models. Such data are intrinsically less sensitive to long-wavelength structure so the resulting model errors are larger. To estimate possible trade-offs in global and regional models, we perform a test using synthetic data. We take a map similar to the phase velocity map of Laske & Masters (1996) at 10 mHz that is the result of a grossly underdamped Occam inversion and hence has

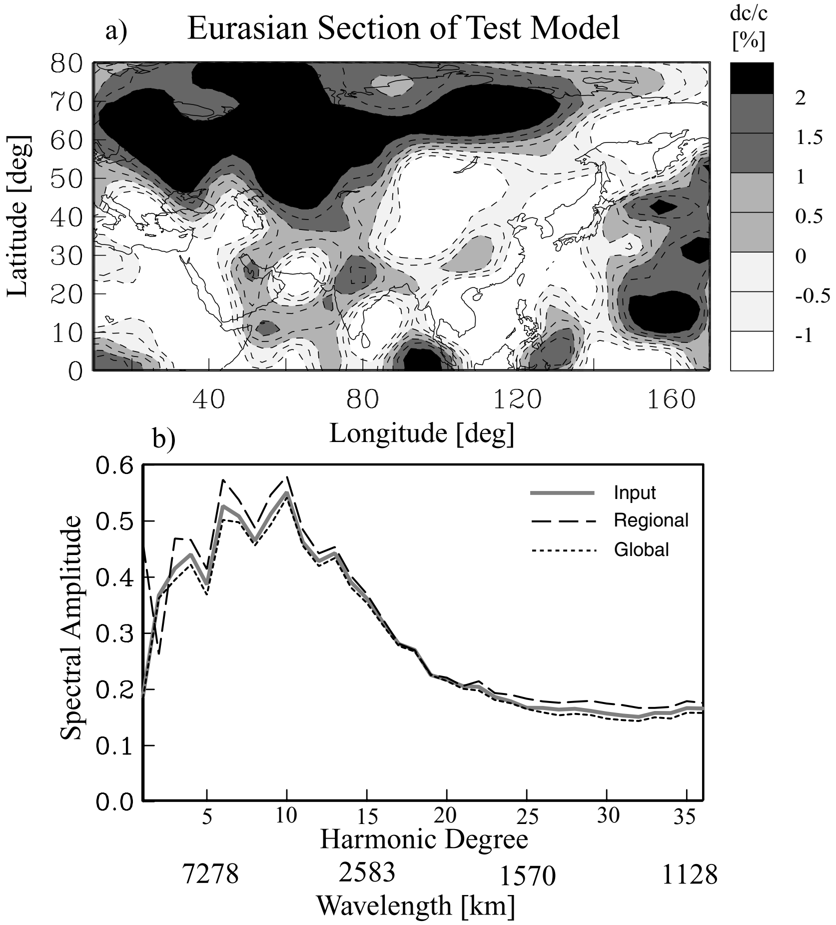

Figure 8. (a) Eurasian section of the global input map of the synthetic experiment. The map is a rough version of the Rayleigh wave phase velocity map of Laske & Masters (1996) at 10 mHz. Anomalies are given as percentage velocity perturbations with respect to a spherical average. (b) Amplitude spectra of the Eurasian section of the input and output maps. The spectra are obtained by expanding the maps in surface spherical harmonics considering only values within the regional section show in Fig. 8(a). The amplitudes are normalized so that the spectrum of a spike would be flat.

significant amounts of short-wavelength structure, up to spherical harmonic degree 36 (Fig. 8a). We calculate 6000 synthetic R1, R2 and great-circle data for this map (global data set). A second data set of 1500 data (regional data set) is constructed that includes only paths with sources and receivers that lie within a box with boundaries 10°–170° in longitude and 0°–80° in latitude. The median of the length of travel paths is 46° in the regional data set and 85° for the global R1 data so the regional data set is expected to be less sensitive to long-wavelength structure. We perform two inversions for equal area block maps (the block size at the equator is 5°), one for a global map using the global data set and one for a regional map using the regional data set. The maps are obtained with the iterative LSQR technique of Masters *et al.* (2000). The input and output maps are virtually identical (not shown) and both output maps fit their respective data sets. The amplitude spectra of the spherical harmonic expansions of the input and output maps, considering only values within the regional box, are shown in Fig. 8(b). The spectra of the input map and the 'global map' agree well at wavelengths longer than 2500 km but there is considerable disagreement between the input and the 'regional' map. The average values of phase velocity perturbation in the regional box are −0.27 per cent (input), −0.32 per cent (global) and 0.52 per cent (regional). The regional map is therefore obviously composed of long-wavelength structure that is significantly different from both the input and 'global' output maps. Such a map can potentially mispredict the averages of data sets with long travel paths, similar to the cases we have shown in this study. Of course, when combing the data sets in a third inversion the resulting output map is much closer to the input map (not shown). We speculate that a combination of global and regional data can greatly diminish the problems we have described, especially when using a variable parametrization to accommodate the strongly varying resolution capabilities of the data (e.g. Boschi & Ekström 2000).

ACKNOWLEDGMENTS

We are grateful to the operators of the Saudi and Kyrgyz Networks, Robert Mellors and Frank Vernon and the GSN operators for installing, maintaining and making available the data sets from which this study has greatly benefited. The IRIS Data Management Center provides easy standardized access to these data. We would like to thank Anatoli Levshin, Mike Ritzwoller and Nicolai Shapiro for providing their global dispersion maps prior to publication. Thanks also go to Erik Larson and Göran Ekström for giving us their group velocity maps. We are also indebted to Levshin, Ritzwoller and Jeannot Trampert for thoughtful reviews. This research was funded by National Science Foundation grant EAR-98-09706, SAIC subcontract 44000025260 and the Cecil H. and Ida M. Green Foundation.

REFERENCES

Barmin, M.P., Ritzwoller, M.H. & Levshin, A.L., 2001. A fast and reliable method for surface wave tomography, *Pure Appl. Geophys.,* **158,** 1351–1375.

Boschi, L. & Ekström, G., 2000. The tranversely isotropic shear velocity structure of the upper mantle: tomographic images of variable resolution, *EOS Trans, Am. geophys. Un.,* **81,** F860.

Chevrot, S., Montagner, J.-P. & Snieder, R., 1998a. The spectrum of tomographic earth models, *Geophys. J. Int.,* **133,** 783–788.

Chevrot, S., Montagner, J.-P. & Snieder, R., 1998b. The spectrum of tomographic earth models; Corrigendum, *Geophys. J. Int.,* **135,** 311.

Dziewonski, A., Chou, T. & Woodhouse, J., 1981. Determination of earthquake source parameters from waveform data for studies of global and regional seismicity, *Geophys. J. R. astr. Soc.,* **86,** 2825–2852.

Ekström, G. & Dziewonski, A.M., 1998. The unique anisotropy of the Pacific upper mantle, *Nature,* **394,** 168–172.

Ekström, G., Tromp, J. & Larson, E., 1997. Measurements and global models of surface wave propagation, *J. geophys. Res.,* **102,** 8137–8157.

Gu, Y. & Dziewonski, A.M., 1999. Mantle discontinuities and 3-D tomographic models, *EOS Trans, Am. geophys. Un.,* **80,** F717.

Knopoff, L., 1972. Observation and inversion of surface-wave dispersion, *Tectonophysics,* **13,** 497–519.

Larson, E. & Ekström, G., 2001. Global models of surface-wave group velocity, *Pure Appl. Geophys.,* **158,** 1377–1399.

Laske, G. & Masters, G., 1996. Constraints on global phase velocity maps from long-period polarization data, *J. geophys. Res.,* **101,** 16 059–16 075.

Levshin, A.L. & Ritzwoller, M.H., 2001. Automated detection, extraction, and measurement of regional surface waves, *Pure Appl. Geophys.,* **158,** 1531–1545.

Levshin, A.L., Yanovskaya, T.B., Lander, A.V., Bukchin, B.G., Barmin, M.P., Ratnikova, L.I. & Its, E.N., 1989. *Seismic Surface Waves in a Laterally Inhomogeneous Earth,* ed. Keilis-Borok, V.I., Kluwer, Dordrecht.

Levshin, A.L., Ritzwoller, M.H. & Resovsky, J.S., 1999. Source effects on surface wave group travel times and group velocity maps, *Phys. Earth planet. Inter.,* **115,** 293–312.

Levshin, A.L., Ritzwoller, M.H., Barmin, M.P. & Villaseñor, A., 2001. New constrains on the Arctic crust and uppermost mantle: surface wave group velocities, P_n,and S_n, *Phys. Earth planet. Inter.,* in press.

Masters, G., Laske, G., Bolton, H. & Dziewonski, A.M., 2000. The relative behaviour of shear velocity, bulk sound speed, and compressional velocity in the mantle: implications for chemical and thermal structure, in *Earth's Deep Interior, Mineral Physics and Tomography From the Atomic to the Global Scale,* pp. 63–87, eds Karato, S., Forte, A.M., Liebermann, R.C., Masters, G. & Stixrude, L., AGU Monograph Vol. 117, AGU, Washington, DC.

Mellors, R.J., Vernon, F.L., Pavlis, G.L., Abers, G.A., Hamburger, M.W., Ghose, S. & Iliasov, B., 1997. The $M(s) = 7.3$ 1992 Suusamyr, Kyrgystan, earthquake. 1. Contraints on fault geometry and source parameters based on aftershocks and body-wave modeling, *Bull. seism. Soc. Am.,* **87,** 11–22.

Nolet, G., 1990. Partitioned waveform inversion and two-dimensional structure under the network of autonomously recording seismographs, *J. geophys. Res.,* **95,** 8499–8512.

Pasyanos, M.E., 2000. Predicting geophysical measurements: testing a combined empirical and model-based approach using surface waves, *Bull. seism. Soc. Am.,* **90,** 790–796.

Pavlis, G.L. & Mahdi, H., 1996. Surface wave propagation in central Asia: observations of scattering and multipathing with the Kyrgyzstan broadband array, *J. geophys. Res.,* **101,** 8437–8455.

Ritzwoller, M.H. & Levshin, A.L., 1998. Eurasian surface wave tomography: Group velocities, *J. geophys. Res.,* **103,** 4839–4878.

Shapiro, N.M. & Singh, S.K., 1999. A systematic error in estimating surface-wave group-velocity dispersion curves and a procedure for its correction, *Bull. seism. Soc. Am.,* **89,** 1138–1142.

Trampert, J. & Woodhouse, J.H., 1995. Global phase velocity maps of Love and Rayleigh waves between 40 and 150 seconds, *Geophys. J. Int.,* **122,** 675–690.

Vernon, F.L., Mellors, R.J., Berger, J., Al-Amri, A.M. & Zollweg, J., 1996. Initial results from the deployment of broad-band seismometers in the Saudi Arabian shield, in *Proc. 18th Annual Seismic Research Symposium on Monitoring a Comprehensive Test Ban Treaty,* pp. 108–117.

Zhang, Y.-S. & Tanimoto, T., 1993. High-resolution global upper mantle structure and plate tectonics, *J. geophys. Res.,* **98,** 9793–9823.

Zielhuis, A. & van der Hilst, R.D., 1996. Upper-mantle shear velocity beneath eastern Australia from inversion of waveforms from SKIPPY portable arrays, *Geophys. J. Int.,* **127,** 1–16.

ELSEVIER

Tectonophysics 360 (2002) 75–88

TECTONOPHYSICS

www.elsevier.com/locate/tecto

Sharp contrast in lithospheric structure across the Sorgenfrei–Tornquist Zone as inferred by Rayleigh wave analysis of TOR1 project data

N. Cotte, H.A. Pedersen*, TOR Working Group[1]

Laboratoire de Géophysique Interne et Tectonophysique, Université Joseph Fourier, BP 53X, 38041, Grenoble Cedex 9, France

Received 18 August 2000; accepted 21 November 2001

Abstract

This work is a part of the TOR1 project (1996–1997) and is devoted to determining the lithospheric structure across the Sorgenfrei–Tornquist Zone in Northern Europe. For the first time in Europe, a very dense seismic broadband array has offered the possibility of determining very sharp lateral variations in the structure of the lithosphere at small scales using surface wave analysis. We measure phase velocities for Rayleigh waves with periods ranging between 10 and 100 s, both within arrays with apertures of 40–50 km (small compared to the wavelength), and along long profiles of at least 100 km. Dispersion curves are then inverted and shear-wave velocity models down to the depth of 200 km are proposed. We show that the Sorgenfrei–Tornquist Zone is a major tectonic feature within the whole lithosphere. North–east of this feature, in Sweden beneath the Baltic Shield, no lithosphere–asthenosphere boundary is observed to exist to depths of 200 km. South–west of the Sorgenfrei–Tornquist Zone, beneath Denmark, we find a lithospheric thickness of 120 ± 20 km. The transition across the Sorgenfrei–Tornquist Zone is sharp and determined to be very steeply dipping to the south–west. We also demonstrate the existence of a sharp discontinuity between the lithospheres beneath Denmark (120 ± 20 km thick) and beneath Germany (characterized by thicknesses of 50 ± 10 km in the northernmost part and 100 ± 20 km in the southwest). This discontinuity is most likely related to the Trans-European Fault at the surface.

Keywords: Lithospheric structure; Sorgenfrei–Tornquist Zone; Rayleigh wave analysis; TOR1 project data

---

* Corresponding author.

E-mail address: helle.pedersen@obs.ujf-grenoble.fr (H.A. Pedersen).

[1] TOR Working Group: S. Gregersen (coordinator), A. Berthelsen, H. Thybo, K. Mosegaard, T. Pedersen and P. Voss (Denmark); L.B. Pedersen, R.G. Roberts and H. Shomali (Sweden); R. Kind, G. Bock, J. Gossler, K. Wylegalla, W. Rabbel, I. Woelbern, M. Budweg, H. Busche, M. Korn and S. Hock (Germany); A. Guterch, M. Grad, M. Wilde-Piórko and M. Zuchniak (Poland); J. Plomerová (Czech Rep.); J. Ansorge, E. Kissling, R. Arlitt, F. Waldhauser and P. Ziegler (Switzerland); U. Achauer, H.A. Pedersen and N. Cotte (France); H. Paulssen (The Netherlands); E.R. Engdahl (USA).

PII: S0040-1951(02)00348-7

1. Introduction

All previous studies (see below) agree in proposing significant lateral variations in the structure of the lithosphere across the Tornquist Zone. The Sorgenfrei–Tornquist Zone (STZ) divides Central Europe (Phanerozoic) from Fennoscandia (Proterozoic), whereas Central Europe and Eastern Europe are separated by the Teysseire–Tornquist Zone (TTZ). These two branches of the Tornquist Zone join between Germany and Sweden (e.g., Berthelsen, 1992; Guterch et al., 1986, 1994).

The STZ is the north-eastern border of the Tornquist Fan. This region is delimited to the south–west by the Trans-European Fault (TEF) (e.g., Berthelsen, 1992) and includes Denmark. The Tornquist Fan has an ambiguous origin: on the one hand, the STZ marks a sharp transition in the tectonic properties of the crust from the Baltic Shield (35–45 km thick) to the Tornquist Fan (≃ 32 km) (e.g., Tryggvason et al., 1998); on the other hand, however, the basement of the Tornquist Fan is similar to that of the Baltic Shield (e.g., Berthelsen, 1992). Compounding the ambiguity is the fact that lateral variations in the structure of the lithosphere are not as well constrained as crustal ones, as no dense, passive seismic experiment have been carried out in the area. Crustal models have been determined by reflection and refraction seismic studies such as FENNOLORA (Guggisberg and Berthelsen, 1987), European GeoTraverse (1992), EUGENO-S Working Group (1988) and BABEL, and are well reported in the literature (Guggisberg et al., 1991; Thybo, 1990; Berthelsen, 1992; BABEL Working Group, 1993; Tryggvason et al., 1998; Thybo et al., 1998).

It is now well known that strong lateral variations exist in the lithosphere between the “old” Eastern Europe and the “young” Central Europe. Several surface wave studies have focused on this structure. Snieder (1988) determined a very sharp transition in lithospheric structure from one side of the TTZ to the other, between the depths of 100 and 200 km. Zielhuis and Nolet (1994) determined the seismic structure of the TTZ to a depth of at least 140 km, below which the contrast in velocity from a side to the other of the TTZ is smaller. Subsequently, Marquering and Snieder (1996) showed the existence of large lateral variations in lithospheric structure in the vicinity of the TTZ between the depths of 80 and 140 km, representing a sharp transition. Alsina and Snieder (1996) determined the direction of incident surface waves on the TTZ and showed that large lateral refractions occur on this zone. Using body waves, Schweitzer (1995) showed how the TTZ presents a blockage for P_n and P_g rays perpendicular to it. His observation of shadow areas leads to the proposal of a LVZ extending to a depth of 200 km. There is therefore no doubt that the TTZ is a major discontinuity down to depths of at least 200 km.

North of the TTZ, several studies have provided information about the thickness of the Baltic Shield and showed how it varies from one side of the STZ to the other. Using P-wave residuals, Husebye and Ringdal (1978) and Husebye and Hovland (1982) demonstrated that the Baltic Shield was characterized by high velocities down to depths of 250–300 km. From P- and S-wave refraction, Sacks et al. (1979) determined a Baltic Shield thickness of 250 ± 15 km at 2–3° from the NORSAR array. In 1990, Dost showed that the lithosphere–asthenosphere boundary does not appear beneath the Baltic Shield. Using the fundamental and first two higher modes of Rayleigh waves, Calcagnile (1991) determined a LVZ extending between 140 and 350 km depth beneath Sweden, and between 220 and 290 km depth under the Baltic Sea. In 1994, Pedersen et al. employed an analysis of Rayleigh waves to determine that such a LVZ does not appear beneath Norway but exists beneath Denmark, between the depths of 120 and 220 km. Finally, by correlating lithospheric thicknesses with heat flux, Pollack and Chapman (1997) argued for the existence of a 200-km thick shield.

All these studies, except the one of Calcagnile (1991), agree in proposing a thick lithosphere for the Baltic Shield although disagreements remain with respect to the inferred value of the thickness and shear-wave velocities. In the south, the transition is expected to be sharp across the TTZ, while the sharpness is more disputed in the north across the STZ, especially because rocks of Proterozoic age have been found south–west of the STZ, and no seismic data on the area have had sufficient resolution to study the STZ on a lithospheric scale. This present study is thus devoted to the determination of the lithospheric structures across the STZ and the TEF.

2. The TOR1 seismic experiment and broad-band data

The TOR1 experiment ("Teleseismic TOmography Experiment across the TORnquist Zone") took place in 1996–1997 with the goal of inferring the structure of the lithosphere across the Tornquist Zone by using tomography, receiver-function, anisotropy and surface wave studies (Gregersen at al., 1999). It represented a multinational effort (the participating countries and workers are listed at the beginning of the paper) and was part of EUROPROBE program.

One hundred twenty seismometers were installed from Göttingen (Germany) to Stockholm (Sweden) during the period covering September 1996 to May 1997. The location of the seismic stations is shown in Fig. 1 (modified after Gregersen et al., 1999). Among the seismic stations, 38 were broadband stations either from permanent networks or from the temporary experiment, which records are used for studying surface waves.

Six mini-arrays composed of three broadband stations are defined, some on each side of the STZ: two in Sweden (named S1 and S2), two in Denmark

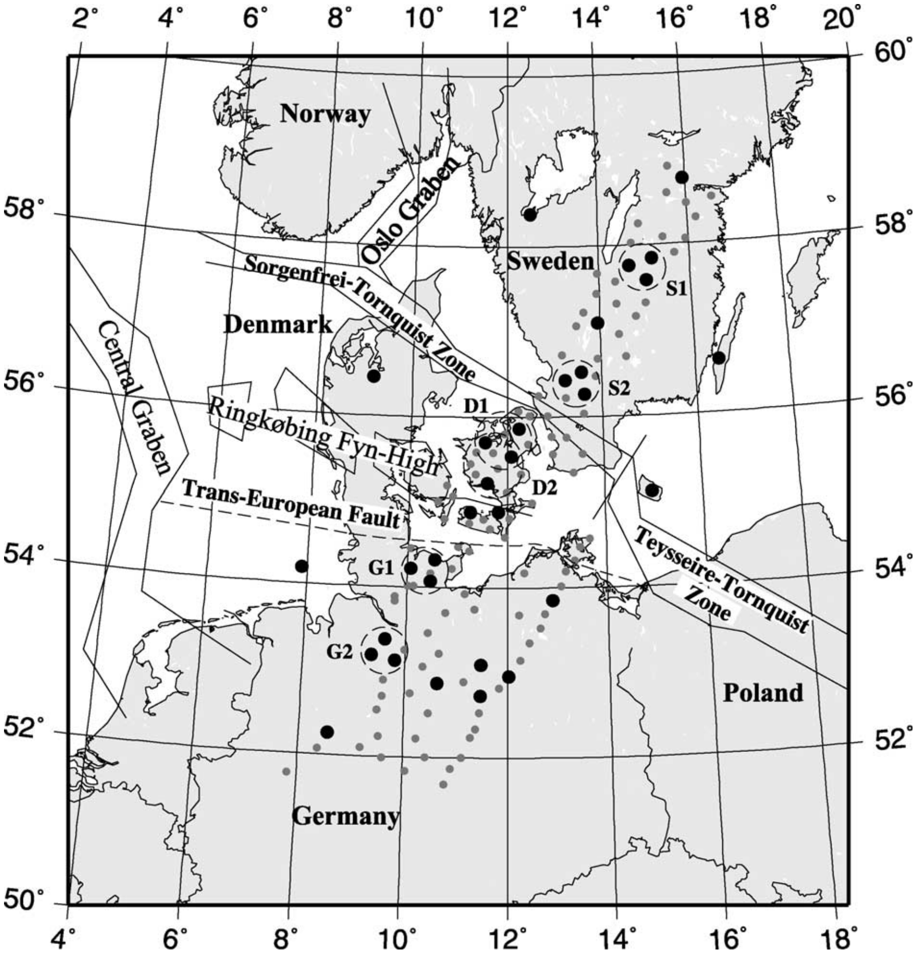

Fig. 1. Location of the short period stations (small grey points) and broadband stations (large black points) operating during the TOR1 experiment, from September 1996 to May 1997 (modified after Gregersen et al., 1999). Dashed circles represent the mini-arrays we used in this study.

(D1 and D2) and two in Germany (G1 and G2) (see Fig. 1). The stations are installed in triangles of 40–50 km width. The positioning of the mini-arrays permits the study of variations of lithospheric structure on the small scale of a few dozens of kilometers. Note that D2 and D1 arrays have two stations in common, but do not overlap in space. Phase velocities measured within these two arrays therefore correspond to different structures. One more array was available in Denmark, but could not be used due to GPS timing errors.

We selected 99 events for this study, with a magnitude greater than 5.1. The epicentral distance ranges from 15° to 155° and the azimuth coverage is very good, as shown in Fig. 2, as there is only a small gap between 310° and 345°. We discarded events for which the epicentral distance was larger than 155° to avoid problems due to multipathing and focusing/defocusing effects which can occur when the source is close to the antipodes. Data were filtered between 5 and 200 s and corrected from the instrument response.

Fig. 3 shows 26 seismograms recorded on the vertical component by temporary and permanent broadband stations for a source located in the Atlantic ocean. The incident surface waves thus arrive from the south–west. The seismograms are all sorted by epicentral distance and the amplitude scale is the same for all of them. The first phase, recorded approximately at 1100 s by the nearest station to the source and at 1200 s by the further one, is the direct shear-wave. The main phase in amplitude is the Rayleigh wave, between 1700 and 2200 s. We note the good signal-to-noise ratio and the good coherence between records. Unfortunately, the signal-to-noise ratio of the horizontal components does not allow us to consider Love waves in the analysis. This is due to the thickness of the

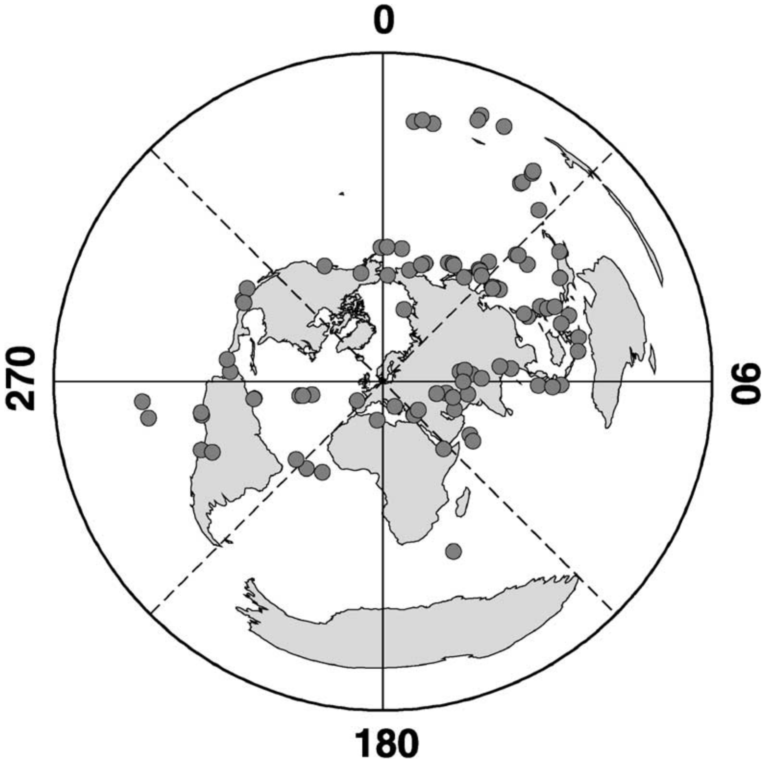

Fig. 2. Geographical distribution of the 99 events (grey dots) used in this study. The polar representation is centered in Denmark (55°N–12°E).

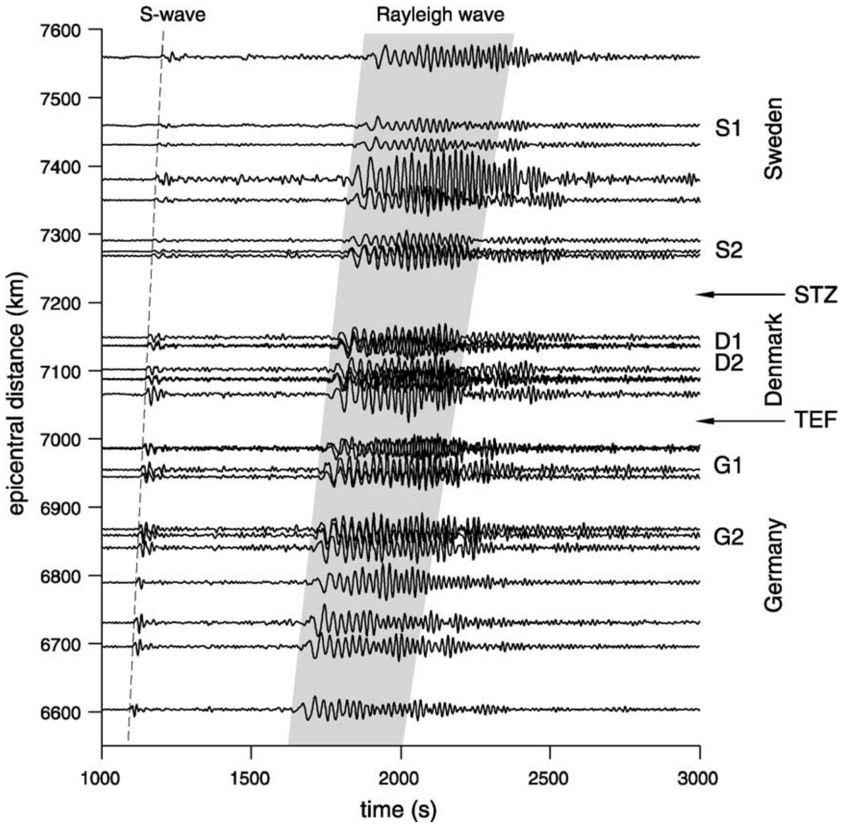

Fig. 3. Example of seismograms recorded on the vertical component by temporary and permanent broadband stations for the TOR1 experiment for an event located in the mid-Atlantic ridge (December 12, 1996). The seismograms are filtered between 5 and 200 s and corrected for instrument response. They are all sorted by epicentral distance and we use the same amplitude scale in all cases. The coherency between signals is high, so phase velocity measurements based on coherency can be performed.

sediments as well as noise from the sea affecting most of the stations.

3. Phase velocity measurements for Rayleigh waves

This section is devoted to phase velocity measurements of Rayleigh waves, both within mini-arrays and along long profiles of more than hundred kilometers. Within the mini-arrays, we used the method described by Cotte et al. (2000). In this paper, we presented the way to measure the phase velocity within arrays whose size is small compared to the wavelength of the surface waves. This analysis is possible thanks to the high coherence between stations. Firstly, we measure the arrival direction of the incident wave. For each frequency, we measure the time delay for all the pairs of stations using the phase of the cross-spectrum. Knowing the distances between stations, the time delays are inverted to obtain the slowness vector. We directly get the arrival direction of the incident wave. Secondly, we report on a diagram the time delays as a function of the interstation distance corrected from the off-great circle deviation as determined by the slowness vector. Then, a linear regression through the points, and passing by the origin gives the phase velocity as the inverse of the slope of the line.

Large distances between stations are not necessary as long as the coherency between records is very high, so the phase velocity measurement within a small array is better adapted for studying laterally heterogeneous media than a measurement along a long profile, more than 100 km long, which neglects the lateral heterogeneities. Measuring the phase velocity within a mini-array presents the advantage to take the observed off-great circle deviations into account. Cotte et al. (2000) showed that these deviations can reach up to 30° at 30 s period in the French Alps. It is however necessary to apply severe selection criteria to the data, and eliminate all records with an unstable phase. Nonetheless, for covering a large area of study we also measure the phase velocity along long profiles (several hundreds of kilometers). For this regional approach, we present phase velocities obtained along profiles averaged within each major tectonic unit.

Fig. 4a and b shows the dispersion curves measured for the Rayleigh wave in Denmark (D1 and D2 arrays) and Germany (G1 and G2 arrays), with respectively three, eight, four and five events. We did not succeed in measuring the phase velocities using the arrays located in Sweden because large amounts of data were missing, the data were very noisy, and the frequency band was too narrow for studying the lithospheric structure. The grey area is the confidence interval that we used in the inversion, determined by all our measurements. The black dots show the average value of the measured phase velocity.

In Fig. 4a, we can see that the phase velocity increases rapidly when the period varies from 20 to 35 s, and more slowly when the period varies from 35

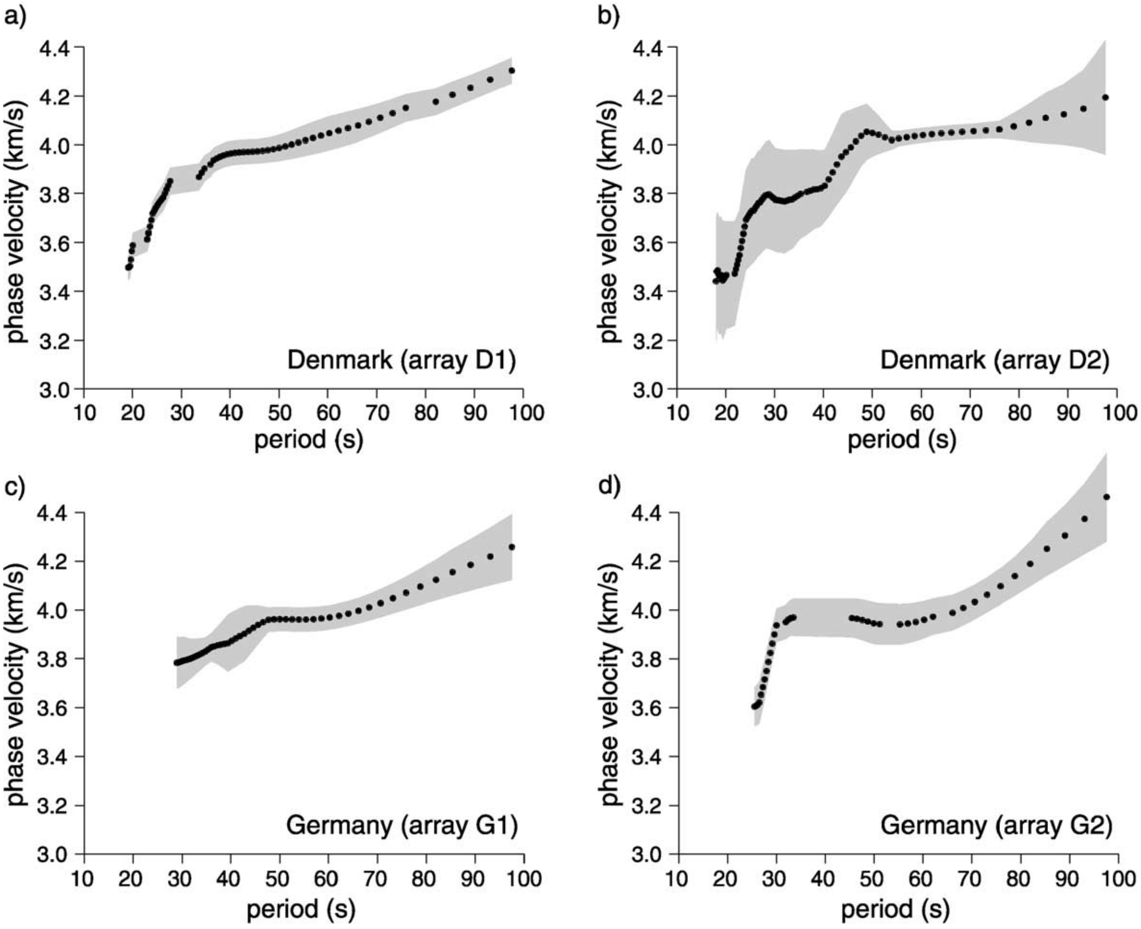

Fig. 4. Dispersion curves measured for the Rayleigh wave using the D1 and D2 arrays in Denmark (a and b) and the G1 and G2 arrays in Germany (c and d). The grey area is the confidence interval that we used in the inversion for determining lithospheric models. The black dots show the average value of the measured phase velocity.

to 100 s for the D1 array measurements. For the D2 array, a large scatter is observed in the measurements for periods shorter than 50 s and longer than 90 s. We thus decided to discard measurements lying outside 50–90 s. Within this frequency range, the phase velocity increases slightly with period and the confidence interval in velocity is small. For the G1 array (Fig. 4c), the phase velocity steadily increases when the period varies from 30 to 100 s. At 80–85 s period, the confidence interval is large, up to ± 1.5 km/s. Finally, the G2 array presents an important increase of the velocity when the period varies from 25 to 30 s, a constant velocity when the period varies from 30 to 70 s, and an increasing velocity for greater periods, reaching 4.4 km/s at 100 s period.

We also measured the phase velocity along profiles for which the interstation distance was greater than the wavelength at 30 s period, i.e. 100–120 km, using the Wiener filtering method (Wiener, 1949; see also Nakanishi, 1979; Taylor and Toksöz, 1982; Hwang and Mitchell, 1986). Fig. 5 shows all the profiles we used. We divided the area into three different zones which correspond to three tectonic units: Sweden (Baltic Shield, dark grey profiles), Denmark (between STZ and TEF, black profiles), and Germany (Phanerozoic Europe, light grey profiles). We respectively

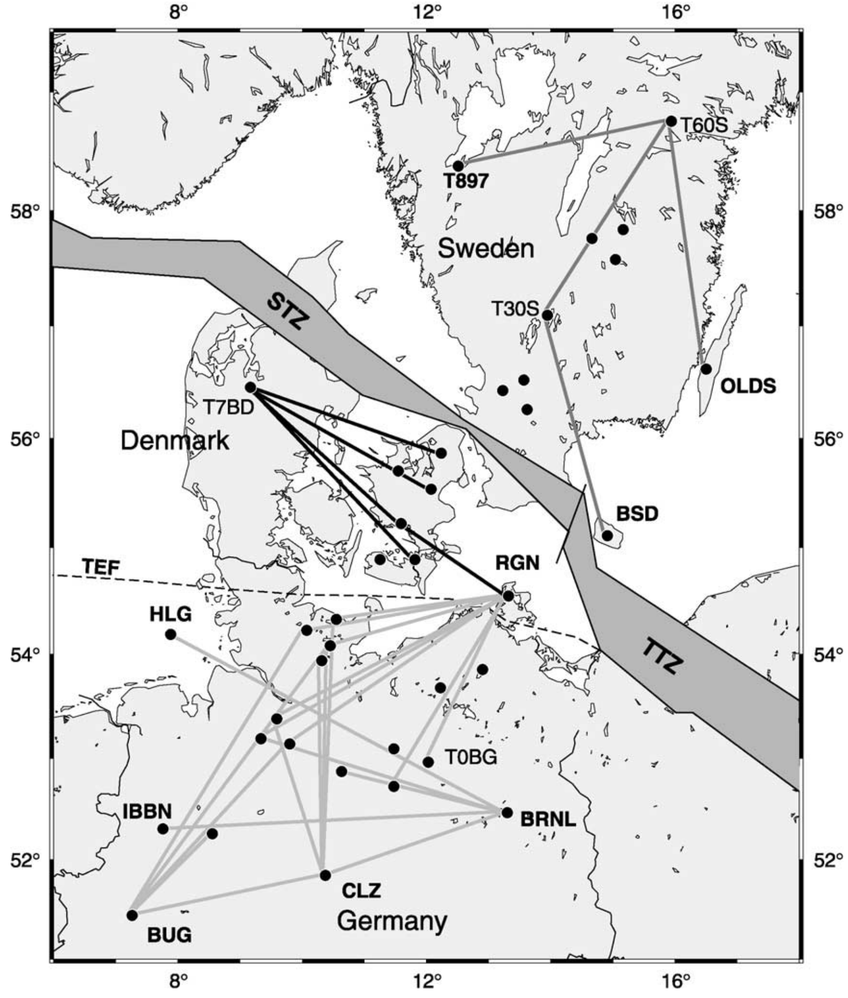

Fig. 5. Profiles of broadband stations used for measuring the phase velocity in Sweden (dark grey profiles), Denmark (black profiles), and Germany (light grey profiles) which correspond to three different tectonic areas.

made 9, 11 and 47 measurements along profiles, using 7, 6 and 28 different events, some of the measurements corresponding to a same event, but events are always selected so that the theoretical path and the station pairs present a misalignment lower than 5°. This precaution is for minimizing the effect due to off-great circle propagation as we can not correct the phase velocity of the great-circle deviation. We also verified that events from different directions yield approximately the same dispersion curves.

Results of phase velocity measurement along profiles are shown in Fig. 6. We can see in the shape of the dispersion curves that lithospheric models for the three areas must be different. For short periods, the phase velocity is low in Germany (3.45 km/s at 20 s) as compared to Denmark and Sweden (3.65 and 3.60 km/s at 20 s). For intermediate periods (30–50 s), Denmark and Germany have same phase velocities, while they are up to 0.2 km/s larger for Sweden. Finally, for periods greater than 70 s, Sweden is characterized by larger phase velocity values (up to 4.5 km/s at 90 s) than Germany or Denmark (4.15 and 4.05 km/s). The dispersion curves within the arrays are different to the ones along the long profiles. The reason is that long profiles average the structure between the stations, while within a small array it is more obvious to work on a 1D model, assuming that the lateral heterogeneities of wavelength of 50–300

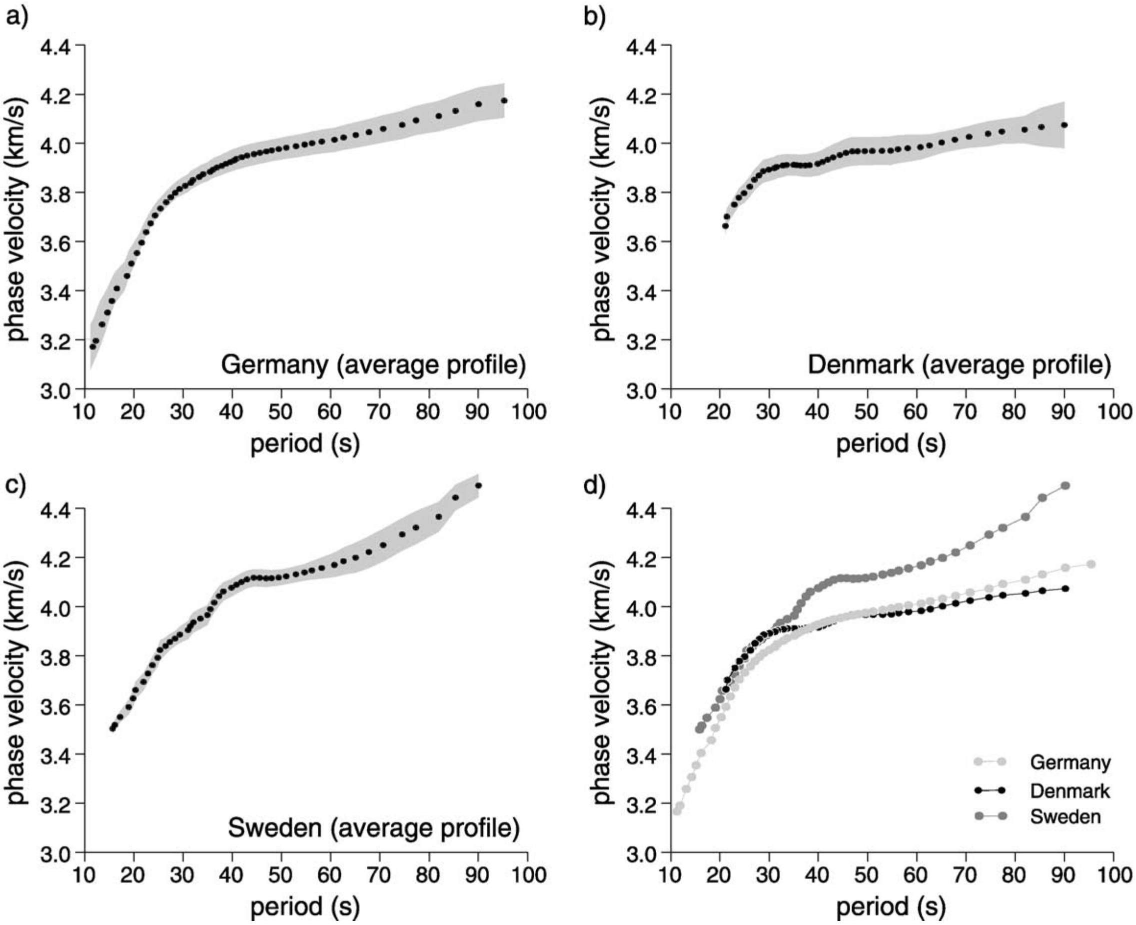

Fig. 6. Dispersion curves measured for Rayleigh waves along long profiles in Germany (a), Denmark (b) and Sweden (c). These three dispersion curves are superimposed on graph (d). The grey area is the confidence interval that we used in the inversion for determining lithospheric models. The black dots show the average values of the measured phase velocity.

km are large compared to the array aperture (40–50 km). Therefore, measurements along long profiles and within arrays must be inverted separately and will give complementary information on the lithospheric structures.

4. Inversion of dispersion curves: construction of lithospheric models

Using the seven dispersion curves of Figs. 4 and 6, we performed inversions to determine the corresponding lithospheric models in shear-wave velocity. We used the two-step method suggested by Shapiro et al. (1997). The first step consists in using a linearized inversion scheme as the one of Herrmann (1987). We get a simple lithospheric model, which is obtained by a root mean square fitting of the phase velocity dispersion curve. From this model, the second step consists in applying a random change either in velocity or in thickness for all the different layers. If the new model has a theoretical dispersion curve, which falls within our confidence interval, then the model is kept as a new solution and a new change is applied to it. Otherwise, we reconsider the last solution and apply a new change. This Monte-Carlo method allows us to explore the solutions for describing the set of possible models for which the dispersion curve fits within our confidence interval. By testing thousands of different models, we finally get a large set of solutions. The advantage is that we can explore all possible solutions and therefore avoid selecting a model corresponding to a secondary minimum in the inversion. We allow changes in the model to be up to 0.2 km/s in velocity for each layer, and of a few kilometers for the interface depth (the deeper is the interface, the bigger can be the change). We only accepted models for which crustal thicknesses and uppermost mantle velocities were coherent with results from refraction and/or reflection seismic profiling (e.g. Gregersen et al., 1993; Tryggvason et al., 1998; Thybo et al., 1998; Pedersen et al., 1999). The limits imposed were for crustal thicknesses 38 ± 2 km (Sweden), 32 ± 2 km (Denmark) and 30 ± 2 km (Germany). The imposed upper mantle velocities were 4.50–4.80 km/s (Sweden), 4.50–4.70 km/s (Denmark) and 4.40–4.70 km/s (Sweden). Below this layer, no conditions are imposed on the S-wave velocities.

Fig. 7 shows in grey lines all the set of models found by inversion for the arrays. They are shear-wave velocity models expressed as a function of the depth and are reliable to depths of 200 km. For greater depths, we do not have the necessary resolution that would allow us to constrain the models. For all depths, we determine both the mean velocity as the average for all the possible models (solid line) and the mean using the minimal and maximal velocities (dashed line) to show the values given by ‘extreme’ models. The mean model is not one particular solution of the inversion. We determine the velocity in the uppermost mantle as the mean value found within the first kilometers beneath the Moho. The velocity at the minimum in the asthenosphere is the smallest value found by averaging all the models. Determining the lithospheric thickness is less obvious as there is a great variability in the models. We defined the minimum lithospheric thickness as the depth below which two-thirds of the models have an inverse gradient and the maximum lithospheric thickness as the depth where the velocity equals the minimum velocity of the asthenosphere + 10% of its standard deviation. The average lithospheric thickness is determined as the average of these two values. We emphasize that having a rather smooth mean model makes the determination of the lithospheric thickness somewhat difficult, but this is a problem of real earth structure and not of the inversion procedure.

In Fig. 7, we can see that beneath the G1 and G2 arrays, the lithosphere–asthenosphere boundary is inferred to be at depths of 50 ± 10 and 75 ± 25 km, respectively. Shear-wave velocities in the upper mantle are respectively 4.43 ± 0.06 and 4.57 ± 0.08 km/s, and are 4.39 ± 0.05 and 4.36 ± 0.09 km/s at the minimum in the asthenosphere. For the G1 array, the large difference between the mean velocity (4.43 ± 0.06 km/s) in the uppermost mantle and the value given by the two extreme models (4.54 ± 0.16 km/s) shows that this velocity is not well determined. Beneath the D1 array, no lithosphere–asthenosphere boundary appears as the shear-wave velocity steadily increases with depth, to depths of at least 200 km. As the incident Rayleigh waves all arrive from north–east, we cannot exclude the possibility of a signature of the propagation in Sweden strongly affecting what

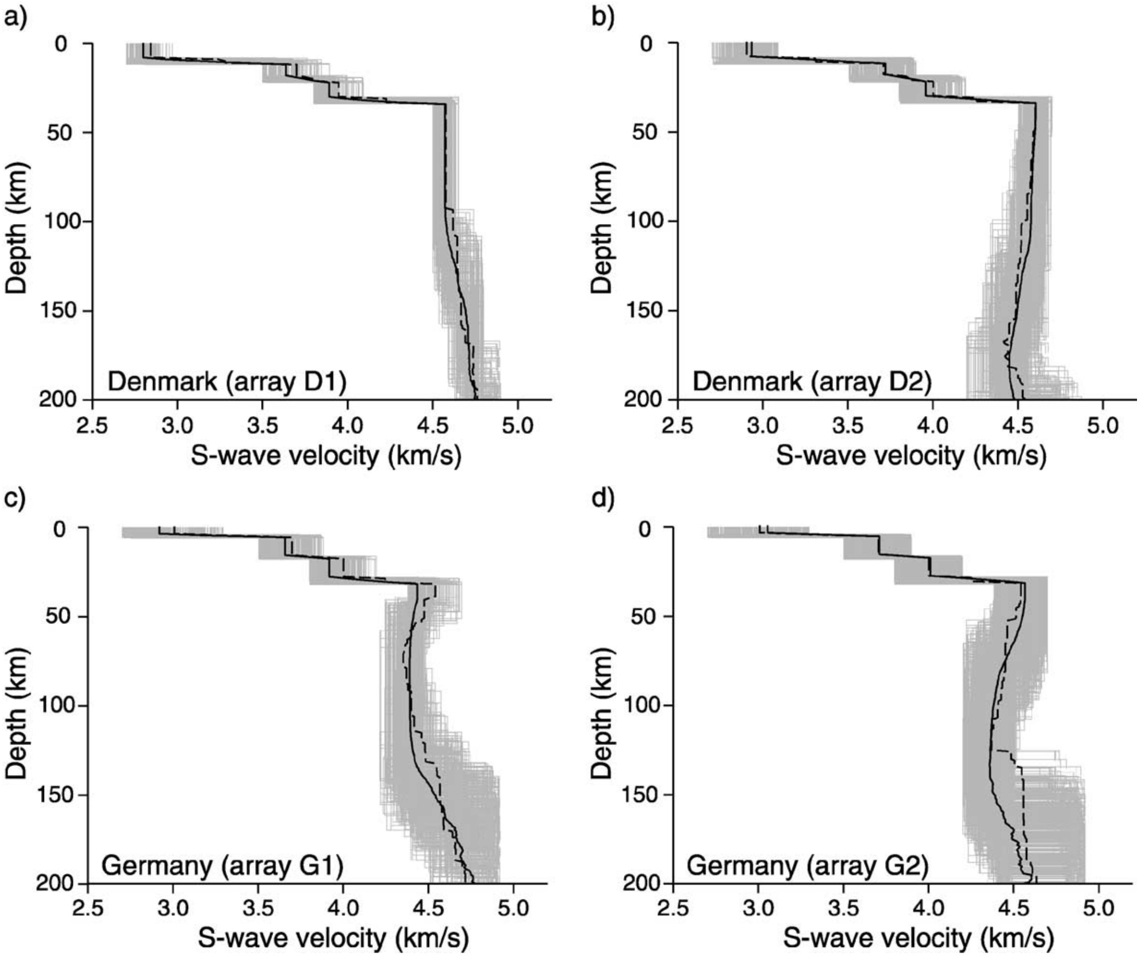

Fig. 7. Lithospheric models determined by inversion of the Rayleigh wave dispersion curves for the D1 and D2 arrays in Denmark (a and b) and the G1 and G2 arrays in Germany (c and d). Grey lines show all the models solution of the inversion, while solid black line gives the mean velocity over all models and the dashed black line is the average between the minimal and maximal velocities.

we determine within the D1 array. Fifty kilometers to the south–west of this array, beneath the D2 array, we determine a lithosphereasthe–asthenosphere boundary located at the depth of 120 ± 20 km, with shear-wave velocity of 4.60 ± 0.04 km/s in the upper mantle and 4.45 ± 0.09 km/s at the minimum in the asthenosphere.

The same inversion procedure was used for the dispersion curves measured along profiles in Germany, Denmark, and Sweden (see Fig. 6). Results for these three areas are presented in Fig. 8. Beneath Germany (Fig. 8a), the lithosphere is rather thin with an average thickness of 100 ± 20 km, and shear-wave velocities of 4.54 ± 0.03 and 4.46 ± 0.08 km/s in the upper mantle and at the minimum in the asthenosphere, respectively. The lithospheric structure determined along long profiles is thicker than the one determined beneath the G1 and G2 arrays, but profiles cover a much greater area than the two arrays. Surprisingly, the velocity at the minimum in the asthenosphere is larger using all profiles than the ones found beneath the two arrays. We speculate that this is due to the fact that the velocity is determined as a greater depth as compared to the arrays, which might be correlated to the thicker lithosphere. Beneath Denmark (Fig. 8b), the lithosphere is 120 ± 20 km thick and the shear-wave velocities are almost the same as in Germany: 4.57 ± 0.06 km/s in the upper mantle and 4.43 ± 0.08 km/s at the minimum in the asthenosphere. In that case, the lithosphere thickness and velocities are the same as the ones determined beneath the D2 array. This may indicate that no large lateral heterogeneities are likely to exist beneath Denmark, apart from the variation between D1 and D2. Finally, we show the inversion for measurements along profiles in Sweden (Fig. 8c). This model does not present any lithosphere–asthenosphere boundary to depth of at least 200 km. No array analysis was available for this area. The shear-wave velocity determined in the upper mantle, of 4.66 ± 0.03 km/s, is higher than the ones determined for Denmark or Germany.

5. Discussion and conclusion

In Table 1, we have summarized our results for the thicknesses of the lithosphere and the shear-wave velocities in the upper mantle that we determined under Sweden, Denmark and Germany by the inversion of Rayleigh wave dispersion curves. We propose in Fig. 9 a lithospheric model along the TOR1 profile. This model is constructed using the results from the four arrays, and outside them using the available information from the three average models from Sweden, Denmark and Germany.

North of the Sorgenfrei–Tornquist Zone, beneath the Baltic Shield in Sweden, no lithosphere–asthenosphere boundary is inferred to depths of at least 200 km. Our results are consistent with the ones of Husebye and Ringdal (1978), Stuart (1978), Husebye and Hovland (1982), Sacks et al. (1979), Dost (1990), Pedersen et al. (1994) and Pollack and Chapman (1997). They are consistent with the result of Calcagnile (1982, 1991) for the Danish area, but in disagreement on the structure beneath southern Sweden. However, due too a poor station coverage of the area prior the TOR experiment, direct comparison between their studies and ours is somewhat difficult. We also have no lithosphere–asthenosphere boundary appearing under the D1 array located just south–west of the

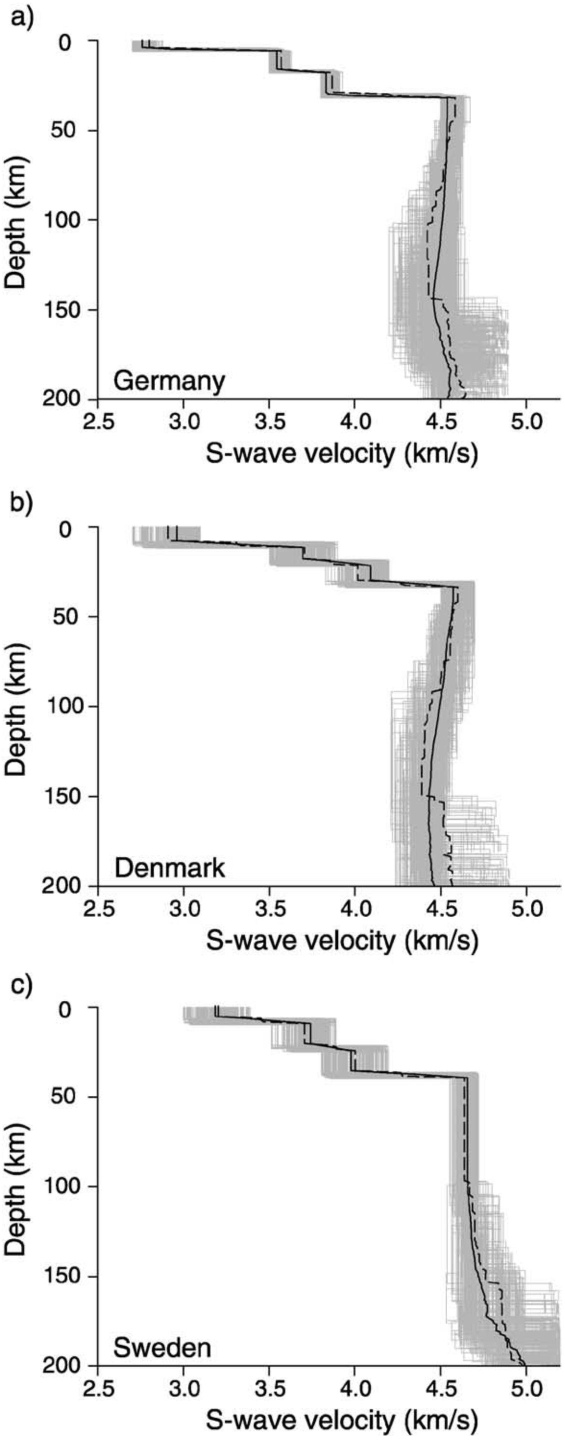

Fig. 8. Lithospheric models determined by inversion of the Rayleigh wave dispersion curves under Germany (a), Denmark (b) and Sweden (c).

Table 1
Lithospheric thickness (Z) in km and shear-wave velocities in the upper mantle (V_{S0}) and at the minimum in the asthenosphere (V_{S1}), in km/s, as determined by the inversion of Rayleigh wave dispersion curve

Area	Z	V_{S0}	V_{S1}
S	>200	4.66 ± 0.03	
D1	>200	4.57 ± 0.04	
D2	120 ± 20	4.60 ± 0.04	4.45 ± 0.09
D	120 ± 20	4.57 ± 0.06	4.43 ± 0.08
G1	50 ± 10	4.43 ± 0.06	4.39 ± 0.05
G2	75 ± 25	4.57 ± 0.08	4.36 ± 0.09
G	100 ± 20	4.54 ± 0.03	4.46 ± 0.08

See text for details. Bold letters are for long aperture profiles located in the three different countries (Sweden, Denmark and Germany) and the others are the arrays (D1, D2, G1 and G2).

Sorgenfrei–Tornquist Zone. Beneath Denmark, with the exception of the structure determined under the D1 array, the lithospheric thickness is 120 ± 20 km. We observed no lateral variations in the depth of the lithosphere–asthenosphere boundary and only small variations for the shear–wave velocities in the upper mantle and at the minimum in the asthenosphere. Finally, beneath Germany we determined a very thin lithosphere of thickness smaller or equal to 100 ± 20 km, in particular close to Denmark where the G1 and G2 arrays are located.

We thus conclude that the major discontinuity in the lithospheric structure across the Tornquist Fan is located between Denmark and Sweden, where the Sorgenfrei–Tornquist Zone lies at the surface. Indeed, within a few dozens of kilometers the lithospheric structure changes laterally very rapidly and the Sorgenfrei–Tornquist Zone is confirmed to be a major tectonic feature to depths of at least 200 km. As we have the same lithospheric structure beneath Sweden and beneath the D1 array located in Denmark, just south–west to the Sorgenfrei–Tornquist Zone, we conclude that the tectonic transition is sharp, dipping steeply to the south–west. The Baltic Shield extends under the D1 array, but does not appear under the D2 array, which is 50 km further from the STZ.

A second and smaller discontinuity is also determined across the Trans-European Fault located between Denmark and Germany, south of the Ringkbing Fyn High (Fig. 1). North of it, in Denmark, the lithosphere is 120 ± 20 km thick and the shear-wave velocity at the minimum in the asthenosphere is approximately 4.43–4.45 km/s. South of it, in Germany, the thickness of the lithosphere is smaller, of 50 ± 10 km under the G1 array, and the shear-wave velocity inferred to be 4.39 km/s at the minimum in the asthenosphere beneath the G1 array is rather low. Even if the Trans-European fault is a postulated one (Berthelsen, 1984), our results show significant contrasts in the lithospheric structure across its assumed location.

The only other previous surface wave study that specifically adresses the STZ (Pedersen et al., 1994) showed a significant difference between Western Denmark and Eastern Norway. They determined a 120-km thick lithosphere beneath the former, and no lithosphere–asthenosphere boundary beneath the latter,

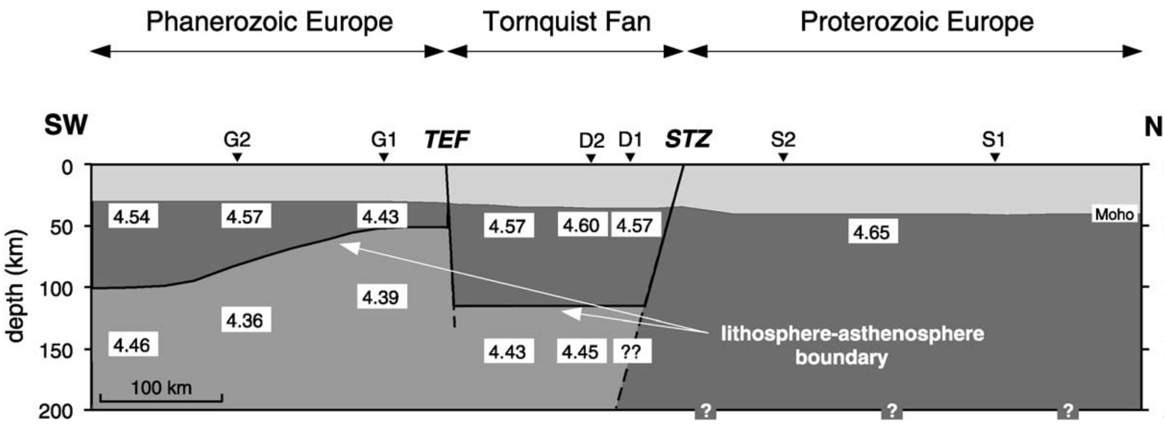

Fig. 9. Model of the lithosphere beneath the TOR1 profile, from Germany to Sweden through Denmark, based on the analysis of Rayleigh waves presented in the text. STZ = Sorgenfrei–Tornquist Zone. TEF = Trans-European Fault.

which is consistent with our results. We improved the constraint of lateral variation by having much more stations and by performing array analysis on a small scale as compared to the wavelength of the studied Rayleigh waves, thereby limiting the contrast in lithospheric structure to the STZ.

More recently, by performing P-wave tomography within the context of the TOR1 experiment, Arlitt et al. (2000) showed that no lithosphere–asthenosphere boundary exists beneath the Baltic Shield to a depth of 200 km and that the lithosphere is 120 km beneath Denmark but otherwise relatively thin (50 km) beneath Germany. Note that they did not have a good resolution at this depth due to the limit of the "crustal" model (50 km thick) used for the travel time inversion (Arlitt et al., 1999). Their results for the thickness of the lithosphere and the geometry of the tectonic feature beneath the Sorgenfrei–Tornquist Zone, dipping steeply to the south–west, are in good agreement with ours. On the other hand, Pedersen et al. (1999) found that this Zone presented a dipping steeply to the north–east, as a conclusion of their P-wave travel time residuals. Their results are then in contradiction with ours and the ones of Arlitt et al. (2000). However, we clearly find the same structure as this latter by using very different and independent methods applied to different phases of the signals recorded by the TOR1 experiment. As expected, the relative variations in velocities at the minimum in the asthenosphere are higher as we analyze shear-wave velocities, which are more sensitive to the partial melt. Accepting that the thickness and velocity models are now well constrained across the Sorgenfrei–Tornquist Zone, it becomes important to better understand the mechanisms that led to the juxtaposition of such different lithospheric structures.

Acknowledgements

NC thanks S. Gregersen for giving her the opportunuity to go to Copenhagen and to participate in the fieldwork, and also for fruitful discussions and comments of this work. The authors are indebted to A. Paul for careful commenting a preliminary version of the manuscript, and to M. Grad and an anonymous reviewer for constructive reviews. NC was supported by a contract between the Centre National de la Recherche Scientifique and the Laboratoire de Détection et de Géophysique, No. 72B 087/00.

This is a EUROPROBE publication.

References

Alsina, D., Snieder, R., 1996. Constraints on the velocity structure beneath the Tornquist–Teisseyre Zone from beam-forming analysis. Geophys. J. Int. 126, 205–218.

Arlitt, R., Kissling, E., Ansorge, J., TOR Working Group, 1999. 3-D crustal structure beneath the TOR array and effects on teleseismic wavefronts. Tectonophysics 314, 309–319.

Arlitt, R., et al., TOR Working Group, 2000. P-wave velocity structure of the lithosphere–asthenosphere system across the TESZ in Denmark. Presented to the European Geophysical Society Meeting, Nice, France, April 2000. EGS Newsletter, vol. 74, p. 77.

BABEL Working Group, 1993. Deep seismic reflection/refraction interpretation of crustal structure along BABEL profiles A and B in the southern Baltic Sea. Geophys. J. Int. 112, 325–343.

Berthelsen, A., 1984. The early (800–300 Ma) crustal evolution of the off-shield region in Europe. In: Galson, D.A., Mueller, St. (Eds.), First EGT Workshop, The Northern Segment. European Science Foundation, Strasbourg, pp. 125–142.

Berthelsen, A., 1992. Mobile Europe. In: Blundell, D., Freeman, R., Mueller, S. (Eds.), The European Geotraverse: A Continent Revealed. Cambridge Univ. Press, Cambridge, pp. 153–164.

Calcagnile, G., 1982. The lithosphere–asthenosphere system in Fennoscandia. Tectonophysics 90, 19–35.

Calcagnile, G., 1991. Deep structure of Fennoscandia from fundamental and higher mode dispersion of Rayleigh waves. Tectonophysics 195, 139–149.

Cotte, N., Pedersen, H.A., Campillo, M., Farra, V., Cansi, Y., 2000. Off-great circle propagation of intermediate period surface waves as observed on a dense array in the French Alps. Geophys. J. Int. 142, 825–840.

Dost, B., 1990. Upper mantle structure under western Europe from fundamental and higher mode surface waves using the NARS array. Geophys. J. Int. 100, 131–151.

EUGENO-S Working Group, 1988. Crustale structure and tectonic evolution of the transition between the Baltic Shield and the North German Caledonides (the EUGENO-S Project). Tectonophysics 150, 253–348.

European Geotraverse, 1992. In: Blundell, D., Freeman, R., Mueller, S. (Eds.), 1992. The European Geotraverse: A Continent Revealed. Cambridge Univ. Press, Cambridge.

Gregersen, S., Thybo, H., Perchuć, E., 1993. Interpretation from explosion seismograms of crustal inhomogeneities in Statu Nascendi. Pol. Acad. Sci. 255, 87–89.

Gregersen, S., Tor Working Group, 1999. Important findings expected from Europe's largest seismic array. EOS Trans. 80, 1–2.

Guggisberg, B., Berthelsen, A., 1987. A two-dimensional velocity model for the lithosphere beneath the Baltic Shield and its possible tectonic significance. Terra Cognita 7, 631–637.

Guggisberg, B., Kaminski, W., Prodehl, C., 1991. Crustal structure of the Fennoscandian Shield: a traveltime interpretation of the long-range FENNOLORA seismic refraction profile. Tectonophysics 195, 105–137.

Guterch, A., Grad, M., Materzok, R., Perchuć, E., 1986. Deep structure of the earth's crust in the contact zone of the Paleozoic and Precambrian platforms in Poland (Tornquist–Teisseyre zone). Tectonophysics 128, 251–279.

Guterch, A., Grad, M., Janik, T., Materzok, R., Luosto, U., Yliniemi, J., Lück, E., Schulze, A., Förste, K., 1994. Crustal structure of the transition zone between Precambrian and Variscan Europe from new seismic data along LT-7 profile (NW Poland and eastern Germany). C. R. Acad. Sci. Paris 319 II, 1489–1496.

Herrmann, R.B., 1987. Computer programs in seismology. Saint Louis University.

Husebye, E.S., Hovland, J., 1982. The upper mantle seismic heterogeneities beneath Fennoscandia. Tectonophysics 90, 1–17.

Husebye, E.S., Ringdal, F., 1978. Seismic mapping of the Fennoscandian lithosphere and asthenosphere with special reference to the Oslo graben. In: Ramberg, I.B., Neumann, E.-R. (Eds.), Tectonics and Geophysics of Continental Rifts. Dordrecht, Holland, pp. 297–311.

Hwang, H.J., Mitchell, B.J., 1986. Interstation surface wave analysis by frequency-domain Wiener deconvolution and modal isolation. Bull. Seism. Soc. Am. 76, 847–864.

Marquering, H., Snieder, R., 1996. Shear-wave velocity structure beneath Europe, the northeastern Atlantic and western Asia from waveform inversion including surface-wave mode coupling. Geophys. J. Int. 127, 283–304.

Nakanishi, I., 1979. Phase velocity and Q of mantle Rayleigh waves. Geophys. J. R. Astron. Soc. 58, 35–59.

Pedersen, H.A., Campillo, M., Balling, N., 1994. Changes in the lithospheric structure across the Sorgenfrei–Tornquist Zone inferred from dispersion of Rayleigh waves. Earth Planet. Sci. Lett. 128, 37–46.

Pedersen, T., Gregersen, S., Tor Working Group, 1999. Project TOR: deep lithospheric variation across the Sorgenfrei–Tornquist Zone, Southern Scandinavia. Bull. Geol. Soc. Den. 46, 13–24.

Pollack, H.N., Chapman, D.S., 1997. On the regional variation of heat flow, geotherms and lithospheric thickness. Tectonophysics 38, 279–296.

Sacks, I.S., Snoke, J.A., Husebye, E.S., 1979. Lithosphere thickness beneath the Baltic Shield. Tectonophysics 56, 101–110.

Shapiro, N.M., Campillo, M., Paul, A., Singh, S.K., Jongmans, D., Sanchez-Sesma, F.J., 1997. Surface-wave propagation across the Mexican Volcanic Belt and the origin of the long-period seismic-wave amplification in the valley of Mexico. Geophys. J. Int. 128, 151–166.

Schweitzer, J., 1995. Blockage of regional seismic waves by the Teisseyre–Tornquist zone. Geophys. J. Int. 123, 260–276.

Snieder, R., 1988. Large-scale waveform inversions of surface waves for lateral heterogeneity: 2. Application to surface waves in Europe and the Mediterranean. J. Geophys. Res. 93, 12067–12080.

Stuart, G.W., 1978. The upper mantle structure of the North Sea region from Rayleigh wave dispersion. Geophys. J. R. Astron. Soc. 52, 367–382.

Taylor, S.R., Toksöz, M.N., 1982. Measurement of interstation phase and group velocities and Q using Wiener filtering. Bull. Seism. Soc. Am. 72, 73–91.

Thybo, H., 1990. A seismic velocity model along the EGT profile from the North German Basin into the Baltic Shield. In: Freeman, R., Giese, P., Mueller, S. (Eds.), The European Geotraverse: Integrative Studies. European Science Foundation, Strasbourg, pp. 99–108.

Thybo, H., Perchuć, E., Gregersen, S., 1998. Interpretation in statu nascendi of seismic wide-angle reflections based on EUGENO-S data. Tectonophysics 289, 281–294.

Tryggvason, A., Lund, C.-E., Friberg, M., 1998. A two-dimensional seismic velocity model across the transition zone between the Baltic Shield and the North German Basin—the EUGENO-S profile 1 revisited. Tectonophysics 290, 47–58.

Wiener, N., 1949. Time Series. MIT Press, Cambridge, MA, 163 pp.

Zielhuis, A., Nolet, G., 1994. The deep seismic expression of an ancient plate boundary in Europe. Science 265, 79–81.

Journal of Seismology (2006)
DOI: 10.1007/s10950-005-9006-7

Criteria for selecting and adjusting ground-motion models for specific target regions: Application to Central Europe and rock sites

Fabrice Cotton[1,*], Frank Scherbaum[2], Julian J. Bommer[3] & Hilmar Bungum[4]
[1]*LGIT, Université Joseph Fourier, BP 53, F-38041, Grenoble, France;* [2]*Inst. Geowissenschaften, Universität Potsdam, P.O. Box 601553, D-14415, Potsdam, Germany;* [3]*Dept. Civil & Environmental Engineering, Imperial College London, SW7 2AZ, UK;* [4]*NORSAR/ICG, P.O. Box 53, 2027 Kjeller, Norway*
[*]*Author for correspondence: e-mail: fabrice.cotton@obs.ujf-grenoble.fr*

Received 28 December 2004; accepted in revised form 11 November 2005

Key words: epistemic uncertainty, ground-motion models, logic trees, seismic hazard analysis

Abstract

A vital component of any seismic hazard analysis is a model for predicting the expected distribution of ground motions at a site due to possible earthquake scenarios. The limited nature of the datasets from which such models are derived gives rise to epistemic uncertainty in both the median estimates and the associated aleatory variability of these predictive equations. In order to capture this epistemic uncertainty in a seismic hazard analysis, more than one ground-motion prediction equation must be used, and the tool that is currently employed to combine multiple models is the logic tree. Candidate ground-motion models for a logic tree should be selected in order to obtain the smallest possible suite of equations that can capture the expected range of possible ground motions in the target region. This is achieved by starting from a comprehensive list of available equations and then applying criteria for rejecting those considered inappropriate in terms of quality, derivation or applicability. Once the final list of candidate models is established, adjustments must be applied to achieve parameter compatibility. Additional adjustments can also be applied to remove the effect of systematic differences between host and target regions. These procedures are applied to select and adjust ground-motion models for the analysis of seismic hazard at rock sites in West Central Europe. This region is chosen for illustrative purposes particularly because it highlights the issue of using ground-motion models derived from small magnitude earthquakes in the analysis of hazard due to much larger events. Some of the pitfalls of extrapolating ground-motion models from small to large magnitude earthquakes in low seismicity regions are discussed for the selected target region.

1. Introduction

The prediction of the expected ground motion and its intrinsic variability at a particular site for earthquake sources with given characteristics is the factor to which seismic hazard is most sensitive. This has been demonstrated, for low exceedance frequencies, by recent seismic hazard analyses for critical facilities, particularly Yucca Mountain (Stepp et al., 2001) and PEGASOS (Abrahamson et al., 2002). Such predictions, usually of acceleration spectral ordinates, are generally performed using ground-motion models that describe the distribution of expected ground motions as a function of a few independent parameters, such as magnitude, source-to-site distance and site classification. The distribution of expected ground motions described by any one ground-motion model is given in terms of median spectral amplitudes and intrinsic variability, the latter usually referred to as aleatory variability and represented by the standard deviation (sigma) of the logarithmic residuals.

The hazard analyst will never be able to identify a single model that can be taken as consistently predicting correctly the ground motions from the hypothetical future events considered in probabilistic seismic hazard analysis (PSHA), simply because the characteristics of these events are, by definition, subject to considerable uncertainty. This is the case even for those few regions with large databases of strong-motion recordings, since the number of source-path-site combinations covered is small compared with the range of scenarios considered in a probabilistic seismic hazard analysis. Therefore, in addition to the aleatory variability in each model there is uncertainty, usually referred to as epistemic (knowledge related), on the median and the sigma value of the model itself. For most regions of the world there is not a large database of indigenous earthquake recordings and therefore the epistemic uncertainty in any model is even greater. In several regions, including many where seismic hazard may be an issue, the lack of native recordings is such that there are no region-specific ground-motion models at all, and consequently larger still epistemic uncertainty.

Given the above, a robust seismic hazard analysis must take into account the multitude of potentially applicable ground-motion models for the region under study. This is currently achieved by using more than one ground-motion model within the framework of a logic-tree approach in which the ground-motion models occupy different branches (Kulkarni et al., 1984). The analyst assigns weights to these branches reflecting the relative confidence in each model (Bommer et al., 2005). The importance of these weights on the hazard results decreases as the number of ground-motion models included in the logic tree increases; recent studies have shown that the definition of these weights can become considerably less important than the actual selection of ground-motion models (Sabetta et al., 2005; Scherbaum et al., 2005). This paper specifically addresses the critical issue of selection of ground-motion models to populate a logic tree for seismic hazard analysis.

Due to the improvement and expansion of strong-motion networks, the number of empirical ground-motion models has increased considerably in the last decade. Douglas (2003) summarizes over 120 studies that have derived equations for the estimation of peak ground acceleration and 80 studies that derived equations for the estimation of response spectral ordinates. Although this large number of published ground-motion models seemingly makes the selection of appropriate models for a particular target area easier for the analyst, in practice this is often not the case, in particular for low-to-moderate seismicity regions. In such areas the logic tree will inevitably include ground-motion models imported from other parts of the world. Then the selection process becomes even more complicated since ground-motion models, even if they have been generated from data sets with good coverage of the predictor variables, may poorly predict ground motion in the particular study area, which is referred to as the target region. This arises if there are systematic differences in terms of seismic sources, wave propagation or site response between the target region and the host region from where the data used to derive the model was obtained. If such differences between host and target regions are identified, as will be the case for at least some of the models in a logic tree, the analyst has two options, either simply to accommodate these differences through the weighting strategy or to follow the proposition of Campbell (2003) for host-to-target conversions.

The goal of this paper is to discuss the criteria and procedures for selecting and adjusting suites of ground-motion models for seismic hazard analysis. These issues are illustrated by application to rock sites in a moderate seismicity region comprising eastern France, southwest Germany and northern Switzerland, which is referred to here as West Central Europe (WCE). The choice of this region is for demonstration purposes, since it is an area with few indigenous ground-motion models, but was motivated by the participation of the authors in the PEGASOS project (Abrahamson et al., 2002) in Switzerland, a SSHAC Level 4 PSHA (Budnitz et al., 1997).

2. Selection of candidate ground-motion models

Ideally, the ground-motion model selection process should result in the smallest set of independent models that capture, potentially after host-to-target conversion, the analyst's estimate of the range of possible ground motions in the target region. An overview of the complete process by which such a selection may be made is presented in Figure 1.

2.1 Pre-selection of candidate equations

For simple practical reasons, e.g. considering the large number of potential candidate models, the selection process will naturally start with the identification of those models which are judged to potentially provide relevant independent information which the analyst wants to include in the logic tree. This is referred to herein as the pre-selection stage, in which all available models are tested against some very general criteria which would justify a rejection from further

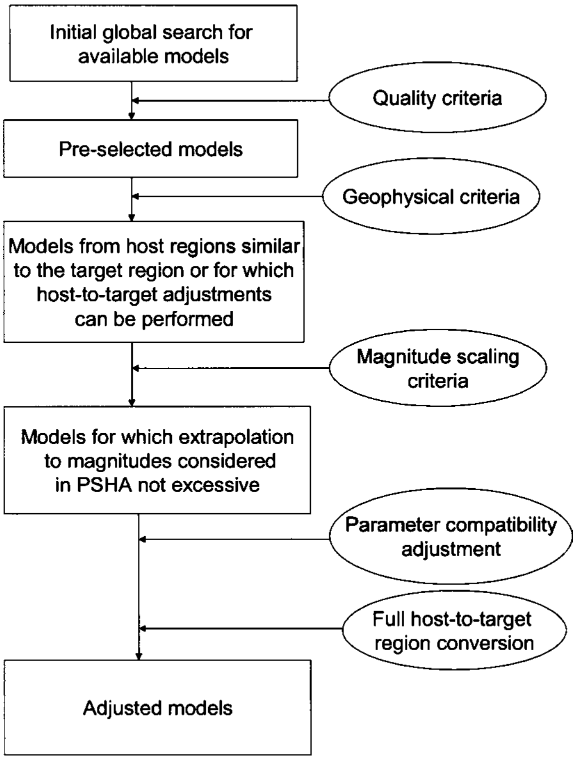

Figure 1. Overview of procedure for the selection of ground-motion models for PSHA.

considerations. The opinion of the authors of this paper is that it is preferable to adopt a procedure whereby reasons must be found for exclusion (i.e., models are innocent until proven guilty) rather than for inclusion because it safeguards against judgments being made on the basis of familiarity with particular regions or particular strong-motion modelers. A case in point is that it might be proposed that seismic hazard analyses for California should include equations derived from Turkish strong-motion records such as Gulkan and Kalkan (2002) and Özbey et al. (2004), which are strongly influenced by the 1999 Kocaeli earthquake. These equations therefore reflect the observed motions from a large magnitude earthquake on the North Anatolian fault which shares many similarities with the San Andreas fault; since there are as yet very few recordings from events of similar size in California, the possibility that the relatively low ground-motion amplitudes observed in Turkey could also occur in the USA should be considered. Following this rejection rather than adoption procedure, however, the analyst must exercise discipline in order to not lose sight of the final goal of the selection to identify the smallest set of independent models that capture the range of possible ground motions in the region under study.

Assuring the independence of a set of ground motion models, however, is easier said than done in practice. At present, no agreed-upon method exists to judge the degree of dependence resulting from a partial overlap in data sets from which ground-motion models were generated or from similarities of model parameterizations or functional forms. Assuring the exhaustiveness of the model set is an even more open problem. Although it is beyond the scope of this paper to discuss this in detail, it should be noted that this is not purely a philosophical issue. It is directly linked to the problem of whether weights on logic tree branches can be interpreted as probabilities, which down the road affects the whole interpretation of hazard curves. This whole issue has recently been started to be discussed in a number of opinion papers to which we refer the interested reader (Abrahamson and Bommer, 2005; McGuire et al., 2005; Musson, 2005).

The following are criteria that could be considered for rejecting equations from the complete list of available candidate models, arranged in order of descending hierarchy:

1. The model is from a clearly irrelevant tectonic regime.
2. The model is not published in an international peer-reviewed journal.
3. The documentation of model and its underlying dataset is insufficient.
4. The model has been superseded by more recent publications.
5. The frequency range of the model is not appropriate for engineering application.
6. The model has an inappropriate functional form.
7. The regression method or regression coefficients are judged to be inappropriate.

The rationale behind these criteria merits some discussion. With regards to criterion [1] it would clearly not be appropriate to use an equation derived for a subduction zone for hazard analysis in a region of crustal seismicity, and vice versa.

Peer review of the candidate equations, specified in criterion [2], is necessary since the peer review process usually ensures that the models are clearly described. The peer review also ensures that basic tests (analysis of residuals, comparison with previous studies) have been performed. Dissemination of a model also favors the detection of mistakes. There have been several examples in the last decade where published ground motion models have been corrected by their authors during the review process or after the first candid use of the model. For this reason, models which have been extensively used and tested should be favored. Examples given in the original publication should be reproduced by the users to avoid any mistake in the empirical model implementation. The original dataset used in the study, specified as criterion [3], must be presented in the publication (or another accessible reference) since the seismic hazard process has to be transparent in order to convince decision makers. Moreover, the user needs to have the possibility to check the data quality, so the data processing must be described and the parameters used in the regressions tabulated. This last point is particularly true when corrected analog data are used, and is vital not only for the decision regarding inclusion or exclusion but also for the subsequent weighting strategy. Criterion [4] is also related to publication: if the authors of a particular model have updated their equations, this places an onus on the analyst to use the most recent available model.

Criterion [5] refers to the fact that the usable frequency range of strong-motion accelerograms, particularly those from analog instruments, is limited (e.g. Boore and Bommer, 2005). For engineering applications where high frequencies (>10 Hz) or low frequencies (<0.3 Hz) are relevant, ground-motion models derived from analog accelerograms may not provide reliable estimates, even if the authors of the model have presented regression coefficients for such frequencies. However, this may not necessarily be a criterion for rejection since it can be accounted for within the weighting strategy if this is performed considering the relative merits of models in different bins of magnitude, distance and response frequency.

The final criteria, [6] and [7], are somewhat vague but an analyst may consider that a particular model is over- or under-parameterized (the former is more likely), or that for some other reason the functional form is inappropriate. A potentially important point in this respect is the way in which the (possibly non-linear) magnitude scaling is handled (e.g. Anderson, 1999). Similarly, the analyst may reject the equation if the regression technique is not considered appropriate, such as if the dataset shows a high correlation between magnitude and distance, whence use of a one-stage direct regression will be susceptible to trade-off effects (e.g. Joyner and Boore, 1981; Fukushima and Tanaka, 1990). Other issues that may need to be taken into consideration include the effect of soil non-linearity, which is often not included in the derivation of ground-motion prediction equations. In such cases, if the shape of the attenuation curves is determined from the entire data set then the effect of neglecting nonlinearity in soil response may be to distort the shape of the attenuation function for rock sites.

The resulting set of pre-selected models might be quite different if pre-selection were done based on admittance criteria, by which, loosely speaking, all models are initially assumed to be inappropriate unless proven otherwise. Therefore, the pre-selection should not be treated lightly and its results should be, before proceeding to the next stages of the selection process, critically judged against the selection goal, namely the smallest number of models needed to capture the range of possible future ground motions.

Beyond the pre-selection phase, as indicated in Figure 1, the next stage is to consider geophysical criteria regarding the degree of similarity, or otherwise, between the host regions from where the candidate models have been derived and the target region where the hazard analysis is being calculated. This involves identifying the key parameters that characterize the host and target regions, and then determining reliable values for these parameters, as described in the two following sub-sections.

2.2. *Source properties in host and target regions*

Several aspects are considered relevant regarding the source properties of the target region. In the present context, the so-called stress drop is merely a parameter controlling the high-frequency content of the ground motion. Although the stress drop of individual earthquakes of a given magnitude is believed to be an aleatory variable, mean stress drops are often assumed to be indicative of the tectonic environment: Scholz et al. (1986) suggested that average earthquake stress drops are correlated with deformation rates, related in turn to corresponding differences between fault slip and length (Scholz, 1994). Later studies support this hypothesis, indicating that, for example, ENA (Eastern North America) earthquakes have higher stress drops on average than Western North America earthquakes (e.g. Atkinson, 1996). It should be kept in mind here, however, that the scatter among stress drop estimates for different earthquakes of similar magnitude is also considerable when compared to the regional averages.

The question has been raised as to whether, and if so in which way, the shape of Fourier source spectra seems may be dependent on tectonic environments. For example, it has been suggested that the Fourier spectra observed in ENA feature two corner frequencies

(Atkinson, 1993; Atkinson and Silva, 1997) as compared to a single corner frequency (Brune, 1970, 1971) in WNA. The suggested two corner-frequency model has, however, been disputed (Haddon, 1996; 1997; 2000; Atkinson, 1996; Atkinson and Boore, 1988; 2000), and this question should not yet be considered resolved. This uncertainty in source spectral shape, affecting in particular larger magnitude and higher frequency ground motions, has clear implications for the host-to-target conversions discussed in this paper.

2.3. *Path and site properties*

2.3.1 *Geometrical spreading*

For simplicity, or because of the shortage of data, geometrical spreading is often approximated as spherical geometrical spreading in attenuation relations (e.g., Atkinson and Boore, 1997) or estimated as a single free parameter of regression, the same for all distances (e.g., Boore et al., 1997). However, the layered structure of the Earth's crust means that the dependence of ground-motion amplitudes on distance may not display a smooth decrease with distance due to the dominance of individual seismic phases over specific distance ranges. Herrmann and Kijko (1983) introduced to this end an 'intuitional' model for Fourier spectral estimates in which the geometrical spreading is spherical out to a distance which often is set at 100 km (depending on crustal structure and focal depth), and cylindrical beyond.

At close distances (say within 50 km) the largest ground motions are caused by waves that travel upwards from the source to the site. As distance from the source increases, the direct wave becomes weaker and the reflection of downgoing waves from interfaces below the source increase in amplitude. Eventually they reach the critical angle and undergo total reflection (Somerville et al., 1990). The large contrast between the crust and the mantle represented by the Moho discontinuity causes these reflections to have large amplitudes. The arrival of these critical reflections beginning at about 50 km causes the flattening of the attenuation relation out to distances of 100 kilometres or more.

When discussing the geometrical spreading it is worth keeping in mind that strong-motion studies in general are based on a theoretically-based assumption regarding geometrical spreading, leaving whatever remains of the amplitude decay to the anelastic term. This may lead to physically unacceptable results, for example, regressions performed with an assumed 1/R decay may give a negative Q as found by Berge-Thierry et al. (2003), Ambraseys et al. (1996) and Boore et al. (1997). For this reason alone it makes little sense to extract equivalent Q values from the anelastic term in a strong-motion equation, since such Q values would depend more on the spreading model than on the real crustal anelasticity. Weak-motion studies are in principle subjected to the same problems with respect to the geometrical spreading assumptions. In practice they are different in that they usually employ Fourier spectra and moreover cover larger distance ranges, mostly beyond the distance where a cylindrical spreading can be safely assumed for L_g waves. This provides a more reliable basis for Q studies from weak motion data, albeit without a simple application to the strong-motion situation. An exception here is the work by Rietbrock et al. (2005), who actually invert independently for both geometrical spreading and Q, based on the Swiss data used by Bay et al. (2003).

2.3.2. *Anelastic attenuation*

Anelastic properties are not considered to be magnitude dependent. The direct use of weak motion results to compare host and target region anelastic properties is, however, difficult. It still remains a challenge to extract this information from direct S waves in a fully satisfactory way and numerous approaches have been suggested for this purpose, all of which have different advantages and drawbacks (e.g. Scherbaum, 1990; Rietbrock, 2001; Bay et al., 2003). Depending on the underlying assumptions, the results are subject to different trade-offs and ambiguities. Hence caution should be exercised in comparing, separately, values of a given stochastic parameter model such as the stress drop or the quality factor obtained from analysis of direct S waves. In contrast, such problems are less apparent when anelastic attenuation properties are provided through L_g analysis. The L_g wave train, interpreted as a superposition of multiply reflected S waves within the crust, is particularly well adapted for attenuation measurements since the L_g decay does not depend on magnitude but only on crustal attenuation and a particular station response which can be removed.

2.3.3. *Site properties comparison*

Local site conditions at an accelerograph station can dramatically affect the strong ground-motion recorded (e.g Bard and Riepl-Thomas, 1999). The definition of "rock" used in each of the equations is different and hence there is another additional source of incompatibility that needs to be considered within the selection process. The publications in which the equations are presented generally include relatively little of the source information on which the site classifications are based, which hampers the interpretation of the defined rock category in each equation. For most of the equations in Table 1, only a range of shear-wave velocities is known for the rock class, a range that moreover often will be a nominal one rather than the actual values encompassed by the data. To overcome the subjectivity of site classifications some studies have used directly measured properties of the ground beneath the accelerograph station. The most commonly used measurement is the near-surface shear-wave velocity (V_S). Shear-wave velocity is usually only measured down to shallow depths so 30m is often used as the reference depth to which to compute the average shear-wave velocity (V_{S30}). Mean values and uncertainty bounds for the V_{S30} of each attenuation model presented in Table 1 have been estimated and are reported in Table 2.

2.3.4. *Host and target region "kappa" properties comparison*

Observations have shown that acceleration spectral density falls off rapidly beyond some maximum frequency. This fall-off at high frequencies has been attributed to near-surface attenuation (Hanks, 1982; Anderson and Hough, 1984) or to source processes (Papageorgiou and Aki, 1983). This distance independent filter, which the authors of this paper interpret to be a site parameter, is taken as $e^{(-\pi kf)}$ where f is the frequency. Recent results of Silva et al. (2000) show that there is an approximate correlation between rock quality and near-surface attenuation. This could indicate that the 'shallow site effects' taken into account through the V_{S30} correction may not really be decoupled from 'deeper site effects' which are partially captured by the kappa value. The overall effect of the upper crustal attenuation can be very significant, particularly in regions associated with relatively young rocks. A downhole array in California has identified that over 50% of the anelastic attenuation occurred in the top 300 m of the Earth and 90% in the upper 3 km (Abercrombie, 1995). In old stable shield regions of Central and Eastern North America, little upper crustal attenuation appears. Microearthquake signals carry important information about attenuation site effects, kappa and stress release in the source region. However, as already discussed, it still remains a challenge to extract this information in a fully satisfactory way and parameters of stochastic models found from weak motions studies may trade off considerably as shown by Scherbaum (1990) for stress drop against kappa and/or Q. Moreover, a large scatter of the kappa values for a given region has been demonstrated by the analysis of Rietbrock et al. (2006) in Switzerland. In conclusion, it is still difficult to determine and compare kappa values of host and target regions.

2.4. *Selection or rejection of weak motion data models (magnitude scaling criteria)*

Several studies have recently used background seismicity weak-motion recordings for the purpose of producing predictive relationships for the ground motion (e.g. Malagnini et al., 2000 and Bay et al., 2003, both for Europe). These methods are a promising way of estimating ground motion in areas where past recordings from large earthquakes are unavailable since the excitation and the attenuation of these models are calibrated at the regional scale. The general question of to what degree models derived from weak-motion data models could be used for strong-motion prediction is however currently poorly understood and still discussed in the seismological and earthquake engineering communities:

- First, it is still not clear if small and large earthquakes have similar properties with respect to rupture physics.
- Second, there is some evidence that the decay rate of ground motions could be dependent on the magnitude of the causative earthquake.

2.4.1. *Radiated energy vs. magnitude: A scaling issue*

The relation between seismic moment, M_0, and a length scale, (e.g., square root of the rupture area, rupture length, corner frequency), of earthquakes has been widely used in seismology as a useful gross scaling relation between static parameters. The ratio of the slip to the fault size defines the static stress drop (difference between the final and starting stress levels on the fault). This scaling relation between the moment and the fault area has been shown to be earthquake independent (e.g. Kanamori and Anderson, 1975). For many reasons, however, including assumptions regarding the geometry of the fault plane, the estimate of this static stress drop is in general quite uncertain. Even so, the approximate range 0.1–10 MPa is considered to be robust.

The relation between the radiated energy, E_R, and the seismic moment, M_0, of an earthquake can also

Table 1. Data coverage and parameters definitions of the selected empirical models

	Magnitude definition	Horizontal component definition	Distance definition	Dataset magnitude-range	Dataset distance range	f-range	Area and dataset time coverage	Distance coverage rated as good by the authors of the present paper	Magnitude coverage rated as good by the authors of the present paper
Abrahamson and Silva (1997)	M_w	Geom. mean	R_{rup}	4.4–7.4	3–150	0.2–100	Worldwide (90% WNA) 1940–1994	3–150	5.0–7.0
Ambraseys et al (1996)	M_s	Larger envelope	R_{jb} R_{epi} ($M_s < 6$)	4.0–7.0	0–260	0.5–10	Europe Middle East 1969–1994	0–100	4.0–7.3
Ambraseys and Douglass (2003)	M_s	Larger envelope	R_{jb}	5.8–7.8	<15	0.5–10	Worldwide (mainly WUS)	0–15	4.8–7.8
Berge-Thierry et al (2003)	M_s	Both	R_{hypo}	4.0–7.3		0.1–33	Europe California (17%) 1952–1997	10–100	4.5–7.3
Boore et al (1997)	M_w	Random	R_{jb}	5.3–7.7	1–80	0.5–10	WNA 1940–1992	1–80	6–7.5
Campbell and Bozorgnia (2003)	M_w	Geom. mean	R_{seis}	4.7–7.7	3–60	0.25–20	Worldwide 1957–1997	3–60	5–7.7
Lussou et al (2001)	M_{jma}	Both	R_{hypo}	3.7–6.3	10–200	0.1–50	Japan 1996–1998	10–200	3.7–6.3
Sabetta and Pugliese (1996)	M_s and M_l	Larger PGA	R_{jb}	4.6–6.8	0–100	0.25–25	Italy 1976–1984	10–100	4.6–6.8
Spudich et al (1999)	M_w	Geom. mean	R_{jb}	5.1–6.9	10–100	0.5–10	Worldwide extensional (62% WNA) 1972–1995	10–100	5–6.5

Table 2. Site conditions of the selected empirical models

Equations	$V_{s,30}$ lower estimate	$V_{s,30}$ best estimate	$V_{s,30}$ upper estimate
Abrahamson and Silva (1997)	450	600	900
Ambraseys et al. (1996)	550	800	1200
Ambraseys and Douglas (2003)	450	800	1200
Berge-Thierry et al. (2000)	550	800	1200
Boore et al. (1997)	550	620	750
Campbell and Bozorgnia (2003)	450	600	900
Lussou et al. (2001)	350	500	900
Sabetta and Pugliese (1996)	700	1000	1300
Spudich et al. (1999)	550	800	1100

be considered a dynamic scaling relation because the radiated energy reflects the dynamics of faulting. In practice, the ratio $\tilde{e} = E_R/M_0$ has long been used in seismology as a useful parameter that characterizes the dynamic properties of an earthquake (Aki, 1966; Wyss and Brune, 1968). When multiplied by rigidity this ratio becomes apparent stress. The ratio can be interpreted as being proportional to the energy radiated per unit area and per unit slip. In many studies, $\tilde{e}$ is found to decrease as the magnitude, M_w decreases. However, because of the large uncertainties in the measurements, whether $\tilde{e}$ is scale independent or not has been vigorously debated (e.g., Ide and Beroza, 2001), and the problem remains unresolved.

Recent improvements in data quality and methodology have, however, significantly improved the accuracy of E_R estimates (e.g. Abercrombie, 1995; Mayeda and Walter, 1996; Izutani and Kanamori, 2001; McGarr and Fletcher, 2002; Boatwright et al., 2002; Venkataraman et al., 2002). The recent results of Kanamori and Rivera (2004) and Oye et al. (2005), despite the large scatter, confirms that the ratio $\tilde{e}$ decreases as the magnitude, M_w, decreases. For large earthquakes ($M_w = 7$), $\tilde{e}$ is approximately 5^*10^{-5}; but it is approximately a factor of 10 smaller at $M_w = 3$ and a factor of 100 smaller at -1. Recently, Kanamori and Rivera (2004) have investigated the relation between the static scaling relation, M_0 (seismic moment) versus f_0 (spectral corner frequency), and the dynamic scaling relation between M_0 and E_R (radiated energy), suggesting that small and large earthquakes could have significantly different rupture physics properties. Kanamori and Heaton (2000) and Brodsky and Kanamori (2001) explained this scale dependence of energy to moment ratio in terms of friction change. In conclusion, the authors feel that the use of weak-motion data for strong-motion prediction is still an open issue.

2.4.2. *Decay rate vs. magnitude: Another scaling issue*

From recent ground-motion studies there are also some indications that the decay rate of ground-motions could be dependent on the magnitude of the causative earthquake (e.g. Anderson, 2000; Bragato and Slejko, 2005). Recently, Ambraseys et al. (2005) have shown that their data support a decay rate that varies with magnitude, where ground motions from small earthquakes decay more rapidly than ground motions from large earthquakes. Atkinson and Boore (2003) have also adopted magnitude-dependent far-field decay rate for empirical models in subduction zones. Frankel et al. (1990) shows that a steep amplitude decay can be explained by the reflection of the up-going direct wave at the underside of the layers. The geometrical decay should therefore be dependent also on the depth of the earthquake. The fact that geometrical decays could be magnitude dependent is therefore another reason for rejecting ground-motion models if magnitude scenarios are significantly outside the range of the data used to derive the models, the primary reason being the magnitude extrapolation itself.

2.4.3. *Magnitude scaling criteria*

Both the scaling of stress drops and geometrical spreading with magnitude suggest that weak motion models could easily lead to erroneous estimation the ground motions of large earthquakes. These two points are still discussed in the seismological community and no definitive conclusions can be drawn about the use of such weak motion models to predict strong motions. The fact that radiated energy and geometrical decays could be magnitude dependent favors the rejection of ground-motion models if magnitude scenarios are significantly outside the range of the data used to derive the models (magnitude scaling criteria). As a result of these two potential scaling effects, the weak motion models will be difficult to accept within our selection procedure (Figure 1). These weak motion models are, however, essential for host-to-target adjustments.

2.5. *Requirements for the ground-motion section of a logic tree*

Logic trees have become a popular tool that facilitates taking into account the multitude of models considered applicable for seismic hazard analysis in a particular region. In this context, the weight on each branch-tip reflects the analyst's degree-of-belief in the corresponding model. At first glance, the selection of ground-motion models does not seem to be linked to the interpretation of branch weights in terms of their statistical properties, but it is worth pointing out that this is not completely correct. Whilst it is not a view taken by the authors, it is worth mentioning that in case branch tip weights are interpreted as probabilities of the corresponding models to be true, sometimes referred to as veridical probabilities, the Kolmogoroff axioms require that the corresponding models must span the total model space (exhaustiveness) and are mutually exclusive. Even though it is difficult to achieve in practice, within such a line of thought the selection process has to assure that these conditions are met. If weighting factors are not assumed to be veridical probabilities, the analyst may still want to reduce the effect of inter-dependent models, for example created by overlapping datasets used for the model generation (e.g. Berge-Thierry et al., 2003; Ambraseys et al., 1996) which pragmatically can also be achieved through the weighting strategy. For further discussion of the effects of model dependence on the overall degree-of-belief on ground motion in a composite model framework the reader is referred to Scherbaum et al. (2005).

3. Adjustments of ground-motion models

Whenever two or more ground-motion models are combined in a logic tree, there will almost always be incompatibilities amongst the equations; in order for the logic tree to correctly capture the epistemic uncertainty in the ground-motion model, appropriate adjustments need to be made to compensate for the incompatibilities. The first group of adjustments is related to the definitions of ground-motion parameters and independent variables, and these must always be applied. The second group of adjustments corresponds to systematic differences between the host and target regions. These host-to-target adjustments do not necessarily need to be applied, since the analyst may choose instead to accommodate the differences through the weighting strategy applied to the logic-tree branches; herein, however, it is assumed that the analyst will opt for the application of host-to-target adjustments, if possible.

3.1. *Adjustments for parameter compatibility*

There are several options available to strong-motion modelers for the definition of each of the parameters used in ground-motion models. The different definitions will lead to systematic differences between the predicted median values that distort the estimate of the epistemic uncertainty which the models are selected to capture. Adjustments for different parameter definitions therefore must be made in order to achieve compatibility amongst the equations as well as between the equations and the model of seismic sources used in the hazard calculations.

Although regression based on vertical components have been carried out, most studies deal only with the more important (from an engineering point of view) horizontal components. Since there are usually two perpendicular components of recorded horizontal motion, there are different options for combining the motion from the two traces, these including the larger of the two, their geometric mean and the random component. None of these options can be described as being superior to the others; the only important issue is that the selected component definition is consistent with the specification of the seismic loading used in the engineering analysis for which the hazard analysis is being performed. Once the convention for the horizontal motion is chosen for a project, simple scalar adjustments, which vary with response period, can be applied to the median motions from those models based on different definitions (Beyer and Bommer, 2005).

Although ground-motion models increasingly use moment magnitude, M_w, as the measure of earthquake size, several equations are based on other measures, most commonly surface-wave magnitude, M_s, and M_{JMA}. For this parameter, the choice will be dictated by the magnitude scale in which the earthquake catalogue, and hence the recurrence relationships, are defined, so that there is compatibility between the seismicity and ground-motion models. For those predictive equations in the logic tree that use magnitude scales other than that used for the recurrence relationships, adjustments can be easily made using empirical correlations (Bommer et al., 2005).

Several distance metrics have been used in the derivation of ground-motion models (e.g. Abrahamson and Shedlock, 1997; Reiter, 1990). The distance definition to be used in the hazard calculations will depend on the way in which individual earthquake sources are modeled in the hazard software. Incompatibilities will often exist because in many widely used hazard codes the distance definition is implicitly based on point sources (i.e. epicentral or hypocentral distance) whereas most ground-motion models use distance definitions based on extended source models. Moreover, combinations of three or more equations will almost always result in at least two different distance metrics appearing in the logic tree. Scherbaum et al. (2004a) present distance conversion coefficients developed specifically for any given target region based on the distributions of focal depth, rupture mechanism and dip angle. The application of the distance conversions is considerably more complex than the horizontal component and magnitude conversions described above, because they are both magnitude and distance dependent. The distance conversions will often have a greater impact on the resulting median ground motions than the other two conversions together.

The empirical equations used to apply the adjustments for the three parameters discussed above each have an associated aleatory variability. The effect of this variability on the overall aleatory variability in the ground-motion model must be accounted for through the laws of error propagation (Bommer et al., 2005). The variability increase caused by the distance conversion is again much greater than that due to the magnitude conversion, although the latter is generally too large to be neglected.

3.2. *Host-to-target adjustments*

3.2.1. *Style-of-faulting adjustments*

The influence of style-of-faulting (or focal mechanism) on the amplitude of earthquake ground motion is a subject of ongoing research. Whilst there is broad agreement that the motions produced by reverse faulting events are higher, on average, than those from strike-slip earthquakes, the nature and degree of the differences is partially osbcured by the lack of consensus on the classification of different focal mechanisms into generic groups. Bommer et al. (2003) have developed a scheme for introducing style-of-faulting into ground-motion predictions that do not include this parameter.

3.2.2. *Site effects adjustments*

In order to make adjustments to a common site profile or V_{S30}, as introduced previously, several methods can be applied. One solution here is that simple site conditions adjustments can be made using factors derived from attenuation equations such as Boore et al. (1997). Their adjustments are based on a using the V_{S30} velocities directly and not on soil classes, thereby being particularly well suited to adjust for differences defined in terms of site velocity. Generic rock models with V_{S30} as a single free parameter can also be used. These generic profiles are characterized by a base rock velocity equal to the target rock velocity and a surface velocity V_{S30} equal to the host region velocity. Such models are used to correct for the differences between the sites which are assumed to be representative for the ground-motion models under consideration, and the reference rock site for the target region. We suggest to generate the model set such that for a V_{S30} of 620 m/s the model matches the Californian rock model (Boore and Joyner, 1997, Table 1) while for V_{S30} of 2800 m/s it matches the hard rock model for ENA (Boore and Joyner, 1997, Table 2). For each chosen V_{S30} rock velocity an interpolation fraction $\mathrm{Ifrac}_{V_{S30}}$ is defined (in log scale) with respect to V_{S30} of the two Boore and Joyner (1997) rock models ($V_{S30} = 620$ and 2800 m/s):

$$\mathrm{Ifrac}_{V_{S30}} = \frac{\log(\mathrm{V_{S30}}) - \log(620)}{\log(2800) - \log(620)} \tag{1}$$

where V_{S30} is given in m/s

The generic models of Boore and Joyner (1997) are anchored at $\mathrm{z_a} = 1, 30, 190, 4000$ and 8000 meters (Table 3). Our generic shear-wave velocities for a given interpolation fraction are then defined at these anchoring depths using the following formula:

$$\beta_{\mathrm{V_{S30}}}(\mathrm{z_a}) = 10^{(\mathrm{Ifrac_{V_{S30}}}\cdot(\mathrm{Log}(\beta_{\mathrm{za2}})-\mathrm{Log}(\beta_{\mathrm{za1}}))+\mathrm{Log}(\beta_{\mathrm{za1}}))} \tag{2}$$

where β_{za2} and β_{za1} are the values of Boore and Joyner (1997) rock models at the anchoring depths (Table 3).

Finally, in each depth segment (between two anchoring depths) the generic model shear wave velocities are represented by a power law model which goes through the velocities at the anchoring depths defined in Equation (2). For each segment, the velocity is de-

Table 3. Rock models of Boore and Joyner (1997)

za	1 m	30 m	190	4000	8000
β_{za1}	336	850	1800	3300	3500
β_{za2}	2768	2791	2914	3570	3600

Table 4. β_0 and p_0 values for several V_{s30} and depth ranges

z	0–1 m	1–30 m	30–190	190–4000	4000–8000	>8000
β_0(600 m/s)	232.48	322.12	830.03	1782.74	3294.81	3498.03
p_0(600 m/s)	0.	0.278	0.414	0.202	0.086	0.
β_0(900 m/s)	444.54	560.72	1134.52	2023.40	3363.63	3524.02
p_0(900 m/s)	0.	0.207	0.313	0.167	0.067	0
β_0(1200 m/s)	705.59	835.99	1421.03	2216.69	3414.11	3542.88
p_0(1200 m/s)	0.	0.156	0.241	0.142	0.05	0.
β_0(1500 m/s)	1011.13	1143.56	1695.57	2381.15	3454.23	3557.74
p_0(1500 m/s)	0.	0.116	0.184	0.122	0.043	0.
β_0(1800 m/s)	1358	1480.52	1961.31	2525.86	2487.66	2815.80
p_0(1800 m/s)	0.	0.082	0.137	0.106	0.034	0.
β_0(2100 m/s)	1744.22	1844.71	2220.23	2656.00	3516.38	3580.54
p_0(2100 m/s)	0.	0.054	0.0970	0.009	0.026	0.
β_0(2400 m/s)	2627.11	2648.54	2722.44	2884.78	3564.13	3597.88
p_0(2400 m/s)	0.	0.008	0.003	0.069	0.014	0.
β_0(2700 m/s)	2627.11	2648.54	2722.44	2884.78	3564.13	3597.88
p_0(2700 m/s)	0.	0.008	0.003	0.069	0.014	0.

scribed by the following equation:

$$\beta_{V_{S30}}(z) = \beta_0(V_{S30}, z) \cdot z^{p_0(V_{S30}, z)} \tag{3}$$

Table 4 gives the values of β_0 and p_0 for several V_{S30} and depth ranges. Figures 2 and 3 show velocity-depth models and corresponding site amplification functions, respectively, captured by this model for V_{S30} values of 600, 900, 1200, 1500, 1800, 2100, 2400, 2700 m/s

Since these generic rock profiles are rather smooth (V_S increasing slowly with depth), it is also possible to consider some more realistic rough profiles based on site investigations. However, the availability of site velocity profiles near strong-motion stations is still poor and the total number of such profiles available for the European region is limited (Rey et al., 2002). The correction factors for adjustments to a reference site velocity of 650 m/s on the predicted spectra are illustrated in Figure 4 (top).

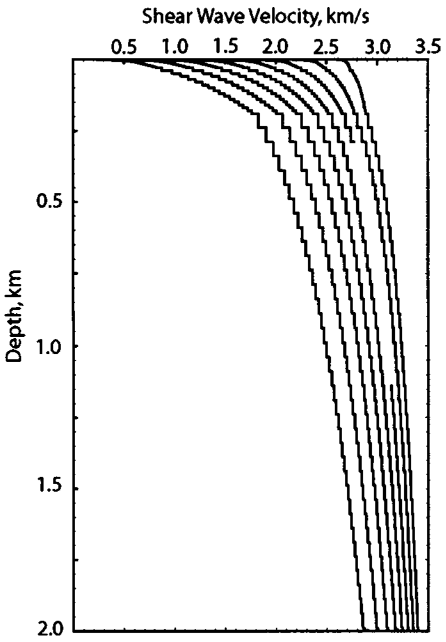

Figure 2. Generic single parameters rock site models to be used for site conversions (V_{S30} values of 600, 900, 1200, 1500, 1800, 2100, 2400, 2700 m/s).

3.2.3. *Full host-to-target geophysical adjustments*

Empirical ground-motion models, even if they are based on good data sets in terms of magnitude, distance and frequency coverage, may still perform poorly for a particular region if strong systematic differences exist between the target region and the host region of the ground-motion model (GMM) regarding the properties of wave propagation and source properties. These differences can, however, be corrected for, and one way to do this is based on the idea of the hybrid empirical approach of

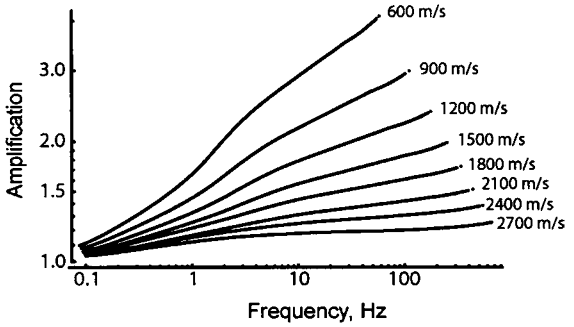

Figure 3. Site amplification functions (surface over half-space motion) for the generic rock models shown in Figure 2 calculated by the quarter-wavelength approach as described by Boore (2003a, Equations (11) to (18)).

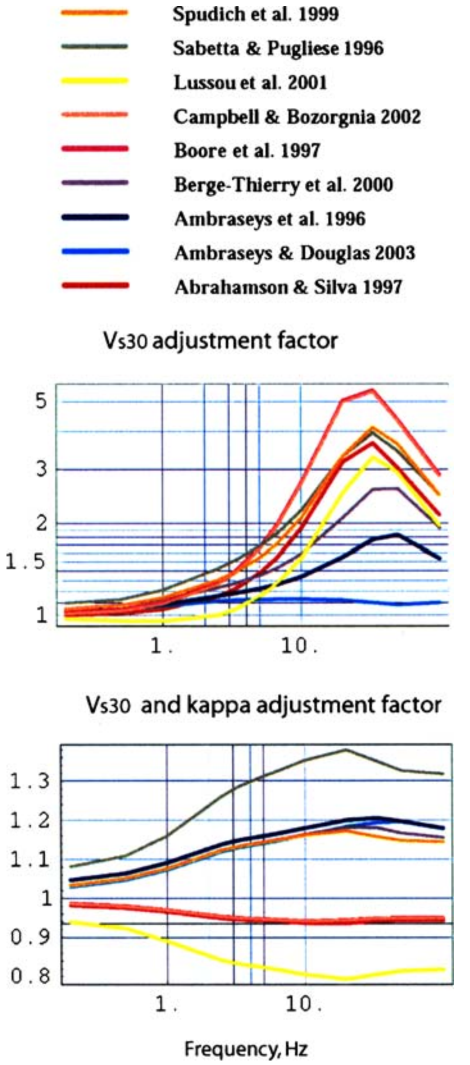

Figure 4. Adjustment factors. (top) V_{S30} adjustment factors using generic rock models. Host region V_{S30} velocities are described in Table 2 (best estimate values). The target velocity is equal to 650 m/s. (bottom) V_{S30} and kappa adjustment factors; host region parameters are described in Table 5. The target kappa value is equal to 0.0125 s.

Campbell (2003), connecting host and target regions through stochastic predictions based on Random Vibration Theory, RVT (Boore and Joyner, 1984; Boore, 2003a).

Both for the host and the target region, several authors (e.g. Boore, 1983; Raoof et al., 1999; Malagnini et al., 2000; Bay et al., 2003; Rietbrock et al., 2006) have used seismograms of background seismicity and RVT (Boore, 1983; Boore and Joyner, 1984) to derive stochastic models of ground motion. As suggested by Campbell (2003), these stochastic models can be used to generate response spectral correction filters for each ground-motion model to account for differences in source, path and site parameters between host and target regions (see also Scherbaum et al., 2005). The host-to-target conversion factors are equal to the ratio between the response spectral ground motions estimated using the stochastic method (Boore, 1983) for the target region and the host region. In order to apply the stochastic method for the calculation of these conversion factors a number of parameters need to be defined for the target region. These parameters include (e.g. Boore, 2003a,b) type of source spectrum, stress drop ($\Delta\sigma$), geometric attenuation, source duration, path duration, path attenuation, shear-wave velocity at the source, density at the source, local site diminution, and a local shear-wave velocity and density profile at the site. Reference models in terms of these parameters have to be specified for each GMM as well as for the target region.

Response spectra in the host and target can be obtained via time domain simulation or directly using RVT theory. In essence, RVT provides an estimate of the ratio between peak motion and *rms* motion, and Parseval's theorem is then used to obtain the *rms* motion in terms of an integral of the squared amplitude spectrum. The ratio between peak motion and *rms* motion is then calculated using the number of cycles of quasi-stationary motion of the oscillator. This number depends on ground-motion duration and oscillator damping. The response spectral transfer functions are hence dependent on attenuation and time-history duration difference between the host and the target region, and they are different from Fourier transfer function used, for example, in site response analysis.

4. Application to the West Central Europe (WCE) region

West Central Europe (WCE) comprises eastern France, southwest Germany and northern Switzerland, and is introduced here for illustration purposes.

4.1. *Selection of ground-motion models*

4.1.1. *Target region source properties*

Slip and deformation rates in the Alpine area are less than 1 mm/year (e.g. Vigny et al., 2002). North of the Western Mediterranean, Western Europe is a continental domain, part of the Eurasian plate, where significant active deformation is restricted to a few structures such as the Rhine graben. Recent results of Nocquet et al. (2003) show that intraplate deformation and fault slip rates in active tectonic structures such as the Rhine Graben and the western Alps are still below the accuracy (1mm/year) of current space geodetic techniques. Recent paleoseismic studies (e.g. Ferry et al., 2005) suggest active extensions of 1–1.5 mm/year within the lower and the upper Rhine Graben structures.

According to the Scholz et al. (1986) classification, the Alps, the Jura and the Rhine Graben constitute a plate boundary related area, while the Alpine Foreland is an intraplate related area. Since regional average stress drop may increase with average recurrence time, large stress drops – and large variations in stress drops– cannot be excluded for WCE. This in turn calls for the use of spectral attenuation relations available for the various types of source properties in order to cover the epistemic uncertainty.

4.1.2. *Target region path properties*

In the target region, Moho depth increases with distance from the Alpine chain, from 25 to 30 km in northern Switzerland to about 60 km beneath the Alps in southern Switzerland (Waldhauser et al., 1998). According to Mooney et al. (1998) the northern part of our target region belongs to the 'extended crust' type which is also typical of a large part of western US and western Europe. The southern part (Swiss and French Alps) belongs to the 'orogen' type with a larger crustal thickness.

Anelastic attenuation as inferred from Lg wave studies in western Europe (e.g. Campillo and Plantet, 1991) shows that the attenuation in the target region lies between the values typical of active and stable regions (e.g. Singh and Herrmann, 1983; Nuttli, 1982). More recently, the Xie and Nuttli (1988) method has been applied around the world (Western US, Eastern US, Africa and Eurasia) which facilitates more stable regional comparisons (Mitchell, 1995). In Eurasia, Lg coda Q at 1Hz exhibits large regional variations (Mitchell et al., 1997). Large Q values (low attenuation) are confined to portions of the East European shield, the Indian shield and western Siberia. These values are close to those found in eastern US. Low Q values (high attenuation), close to those obtained in western US, are found in the Tethyside region that extends from the southern part of western Europe, through the Middle East and Central Asia. Most of the strong-motion records used to derive European ground-motion models (Ambraseys et al., 1996; Sabetta et al., 1996; Berge-Thierry et al., 2003) have been collected in this region. The Mitchell et al. (1997) results also confirm the Campillo and Plantet (1991) results in that the French and Swiss Alpine Forelands display intermediate Q values.

4.1.3. *Target region site properties*

Bay et al. (2003) have found that the average site amplification in the Alpine Foreland is twice as high as in the Alps. The stations in the Alpine Foreland generally show a strong amplification and the Alpine stations show de-amplification. Alpine region rock sites are very hard rock outcrops created during glaciation in the last ice age. The reference rock velocity is chosen as 650 m/s. A large scatter of the kappa values in the target region has been demonstrated by the analysis of Rietbrock et al. (2006) in Switzerland. A reference kappa of 0.0125s has been finally been chosen, for illustration purposes; the authors acknowledge that there is considerable uncertainty in this value.

4.1.4. *Host region models*

For the purpose of illustrating the parameter and host-to-target adjustments, a suite of 9 ground-motion models have been selected (Table 1). This suite was not compiled by strict application of the previously stated selection criteria, but rather to provide an illustrative set of models covering various host regions and the use of many parameter definitions. Nonetheless, the defined procedures outlined in this paper could be expected to produce a similar suite of models for the logic tree. The rigorous testing of the applicability of these 9 equations to the WCE region is outside the scope of this paper.

A first set of models is provided by European 'plate boundary related' empirical models (Sabetta and Pugliese, 1996; Ambraseys et al., 1996; Berge-Thierry et al., 2003). Globally based or western US relations provide better data quality, near source, larger magnitude coverage or better site categorization (Abrahamson and Silva, 1997; Campbell and Bozorgnia, 2003; Lussou et al., 2001; Spudich et al., 2003; Ambraseys and Douglas, 2003). Relations developed for eastern North America cannot be excluded because of low deformation rates of Central Europe. However the application of the hybrid empirical model to stochastic models such as Atkinson and Boore (1997) and Toro et al. (1997) is ill advised since in those cases one should simply generate new spectral estimates with the appropriate stochastic parameter set for the target region. To apply the hybrid empirical method to stochastically-derived equations would lead to the propagation of unnecessarily large uncertainties. Therefore, in this paper, we only discuss the treatment of empirical ground motion models. The nine candidate models are described in Table 1.

Engineering goals usually imply ground motion evaluation due to earthquakes of magnitude greater than 5. As discussed above, magnitude-distance sampling effects cannot be adjusted and therefore are one of the major selection criteria. Central Europe models based on weak motions (e.g. Malagnini et al., 2000; Bay et al., 2003; Rietbrock et al., 2006) have therefore not been selected for strong ground-motion evaluation in the present study. Such weak motion models are, however, essential for host-to-target adjustments.

The magnitude and distance applicability range of the selected models is different from the range of magnitude and distance sampled by the dataset used in the regression analysis: for example, the dataset used by Ambraseys et al. (1996) includes data from distances up to 260 km and magnitudes up to $M_S 7.9$; however, both of these values correspond to a single recording, with no other data at distances beyond 210 km and no other earthquakes of magnitude greater than $M_S 7.3$. Analysis of the candidate models presented in Table 2 shows that some of them poorly sample large magnitude or short distances, which in a logic-tree context can be taken care of through a weighting scheme based on a binning in magnitude-distance-frequency space. The magnitude and distance validity range has been evaluated for the candidate models and is presented in Table 1.

4.2. *Selected ground-motion models adjustments*

4.2.1. *Parameter compatibility adjustments*

The candidate models (Table 1) use four different magnitude definitions, four different distance metric definitions and six different ways of combining the horizontal components. Median grounds motion values for frequencies of 1 Hz, 5 Hz and 10 Hz have been calculated for an earthquake of magnitude equal to 6.5 (Figure 5). For the left column in Figure 5, distances from 0 to 200 km are simply entered to each equation without any correction and all magnitude scales are assumed equal; for the equations that include style-of-faulting as a predictor variable, the coefficients are set to reverse rupture. Without any adjustments the differences between ground motion predictions reflects mainly the intrinsic parametric distance definitions. For example, the higher motions at short distances are predicted by models which are based on the hypocentral distance.

Parameter compatibility adjustments have then been applied to the selected ground motion models. The resulting spectral ordinates are given for an earthquake of moment magnitude $M_w = 6.5$ in a Joyner-Boore distance range of 0-200 km (central column in Figure 5). The figure shows in particular the impact of distance conversions for hypocentral distances models (Lussou et al., 2001 and Berge-Thierry et al., 2003) now predict similar values as the one of models derived in the same area (e.g. Ambraseys et al., 1996). This result confirms that of all adjustments, the distance conversion has the largest impact (this point is also discussed by Scherbaum et al., 2005). After these parametric adjustments the spread of the predictions has been strongly reduced.

4.2.2. *Full host-to-target adjustments*

In the present paper, the target region stochastic model of Bay et al. (2003) has been chosen as a reference for host-to-target adjustments. The site conversion factors have been calculated with respect to $V_{S30} = 650\,\mathrm{m/s}$. For most of the equations in Table 1, only a range of shear-wave velocities is known for the rock class and a furthermore this range will often be a nominal range rather than the actual values encompassed by the data. Mean values and uncertainty bounds for the V_{S30} of each attenuation model presented Table 1 have been analyzed and are reported in Table 2.

Equivalent stochastic models for all empirical ground-motion models have been derived by Scherbaum et al. (2006). The inversion scheme used gives the opportunity to obtain stochastic model parameters for the host region even if the host empirical models have been derived with a global dataset. The description of the 9 ground-motion models stochastic parameters are given in Table 5. Figure 5 provides a fairly complete picture of the relative impact of all

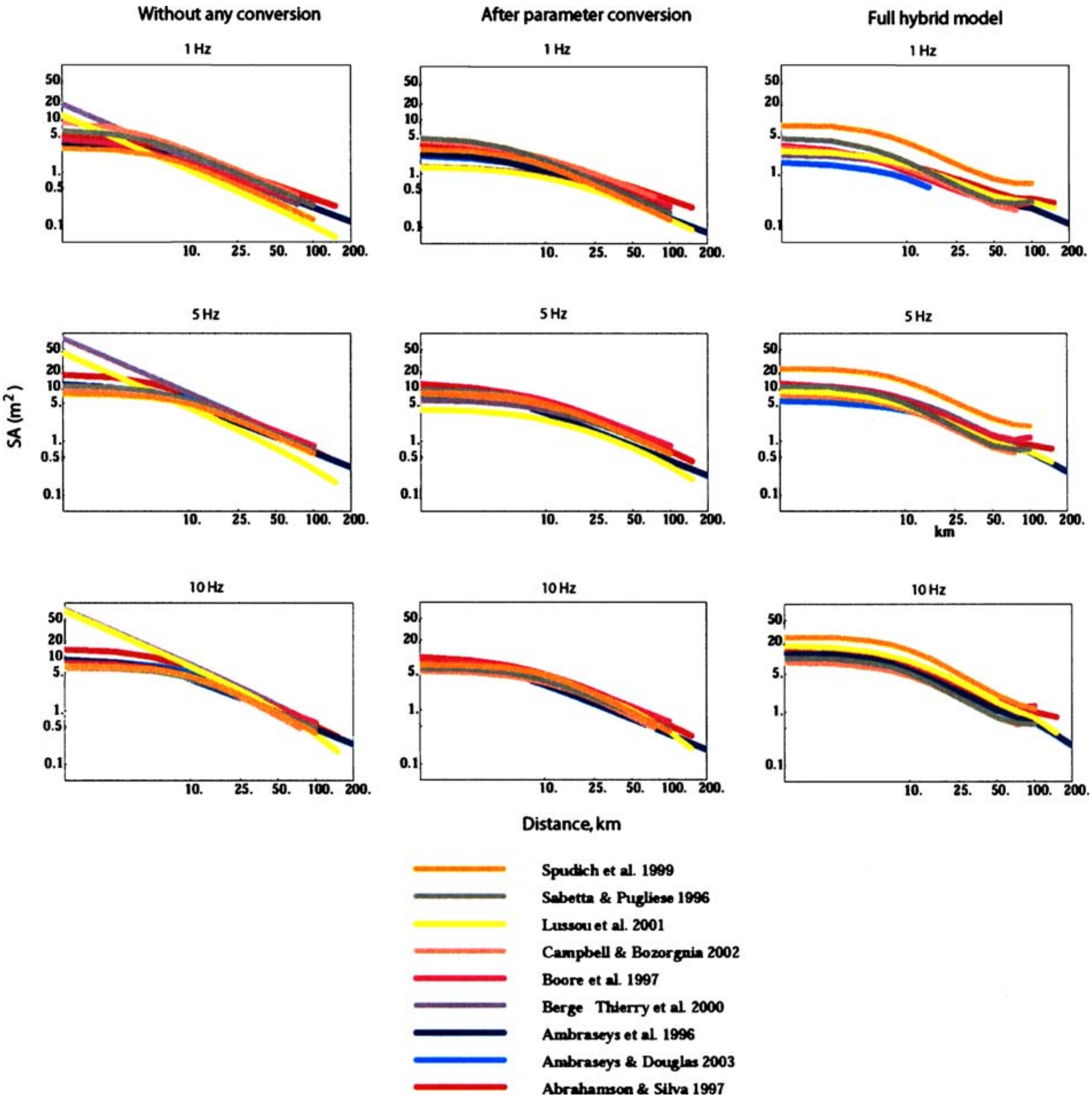

Figure 5. Median acceleration spectra (1Hz, 5Hz and 10Hz) from the candidate equations for a magnitude M_w 6.5 earthquake (left) without adjustments, (middle) after complete parameter conversions for style-of-faulting, component, magnitude and distance conversions, and (right) after full host-to-target adjustments.

host-to-target adjustments. After these host-to-target adjustments the predicted values at 10 Hz are higher mainly because of the V_{S30} and kappa adjustments factors (Figure 4). One can notice that the Spudich et al. (1999) model now gives the higher values, which can be explained by the fact that Scherbaum et al. (2006) found that this model could not be reproduced well by a stochastic point source model.

5. Discussion

The seismotectonic conditions of the target region of WCE is complex, including the Alps and the Alpine Foreland, with the former being more plate boundary related and the latter more intraplate related. The selection process applied shows that the crustal conditions of this target region cannot be considered directly

Table 5. Stochastic model parameters for the host region ground-motion models. The geometrical spreading exponent a_3 up to infinity was set to 0.5, $R_{\Theta\phi} = 0.55$, $V = {}^{1}/_{\sqrt{2}}$, $F = 2$. The density and velocity were set to $\rho_s = 2700$ kg/m^3 and $\beta_s = 3500$ m/s

Model name	$\Delta\sigma$, bar	κ_0(sec)	Q_0	α	R_1(km)	a_1	R_2(km)	a_2	r	V_{S30}	Dist
Abrahamson and Silva, 1997	79	0.039	196	0.46	44.6	−1.0	73.8	−0.25	0.04	484	ATSCA
Ambraseys and Douglas, 2003	132	0.039	52	0.79	45.6	−0.85	81.1	0.0	0.02	646	HYP
Ambraseys et al., 1996	18	0.046	550	0.49	10.0	−0.8	68.9	−0.95	0.03	450	SEIS
Berge-Thierry et al., 2003	46	0.047	256	0.96	31.9	−1.0	69.8	−0.9	0.04	451	HYP
Boore et al., 1997	77	0.061	83	0.06	49.9	−0.8	83.1	−0.3	0.06	453	HYP
Campbell and Bozorgnia, 2003	89	0.051	166	0.52	47.3	−0.8	97.8	−0.65	0.03	532	RRMS
Lussou et al., 2001	44	0.031	167	0.77	14.5	−1.0	74.3	−0.9	0.03	562	HYP
Sabetta and Pugliese, 1996	56	0.044	89	0.99	44.7	−0.8	102.9	−0.7	0.03	504	SEIS
Spudich et al., 1999	12	0.029	103	1.00	18.7	−0.6	65.8	−1.0	0.06	456	RMS

equivalent to the host region properties of any of the existing strong-motion models. This in turn calls for the use of ground-motion models available for the various types of seismotectonic regimes in order to capture the epistemic uncertainty. Although applied herein specifically to the region of western Central Europe, the situation is representative of many, if not most, seismic hazard studies. The magnitude-distance sampling effects or instrumentation effects cannot be adjusted and therefore are important selection criteria, although these aspects can equally be accounted for in the weighting strategy for the logic-tree branches.

An important question that arises in such regions of low or moderate seismicity is the degree to which models derived from weak-motion data can be used for strong-motion prediction. Both the scaling of stress drops and the variation of the decay with magnitude suggest that these models could erroneously estimate the ground motions of larger earthquakes, which favors the rejection of models whose range of applicability is outside the magnitude range used for the hazard evaluation. Host region empirical model studies provide a firm basis for ground-motion estimates in areas like central Europe that are lacking the necessary strong-motion data for a purely empirical approach, provided that host-to-target conversions are applied. The sensitivity analyses performed herein show particularly the importance of distance and kappa filter corrections, if these can be applied. Host region models derived in regions with associated weak motion studies or host empirical models for which the associated stochastic models parameters have been derived have therefore to be favored in the selection.

Once the adjustments have been performed, it is important to evaluate the performance of the host-to-target region conversions. This is particularly needed since the physical basis for some of the adjustments (i.e. the kappa filter) is still a matter of debate and investigation. A rather small data set collected in the target region can help to assess the adjusted ground-motion models. The visual comparison between the observed spectral values and the model predictions provide only a qualitative visual evaluation of the fit between data and model predictions. Scherbaum et al. (2004b) show to this end how observed ground-motion records can help to guide this process in a more systematic way. A key element in this context is a new, likelihood-based, goodness-of-fit measure which has the property not only to quantify the model fit but also to measure to some degree how well the underlying statistical model assumptions are met. By design it naturally scales between 0 and 1 with a value of 0.5 for a situation in which the model perfectly matches the sample distribution both in terms of mean and standard deviation. This data driven evaluation allows to quantify the performance the ground-motion model selection and particular host-to-target region conversions.

The results of such evaluations may sometimes indicate that the host-to-target conversions have not been successful. This may occur for a number of reasons, not necessarily connected to the characterization of the target region. In Figure 5, it can be appreciated that the application of the host-to-target conversion to the equations of Spudich et al. (1999) seems to be problematic, which would partially be the result of the 'virtual' host region – encompassing a number of tectonic regimes around the world, albeit nominally united by being 'extensional' – being difficult to characterize by a single suite of representative parameters. For this reason, the authors of this paper do not recommend the universal and blind application of the hybrid empirical approach: the results must always be inspected and assessed.

On the same issue of the host-to-target adjustments, it is also important to acknowledge that the procedures presented in this paper have not included consideration of the uncertainty on the ground-motion variability due to the host-to-target conversions. The effect could be to reduce the sigma values of some models in some situations and to increase the scatter in others; this is an area requiring investigation.

Another aspect that has not been considered in this study, and which could well prove very useful for the selection of appropriate ground-motion models, is the possibility of using intensity attenuation characteristics as an analogy in the selection of ground-motion models. Correlations between macroseismic intensities and instrumental ground-motion parameters exist but mostly concern active regions like western United States (e.g. Wald et al., 1999; Atkinson and Sonley, 2000; Kaka and Atkinson, 2004) and generally have very large associated scatters. Such information is, however, a significant source of information to be used in order to validate (at least qualitatively) the characteristization of regional attenuation. Analysis of intensity attenuation versus distance in central Europe (e.g. Rüttener, 1995), for example, leads to the definition of distinct regions with different attenuation properties. The highest attenuation is observed in the sub-Alpine chains (Helvetic and Ultrahelvetic nappes) and the lowest in the crystalline basement and Pennic nappes of the Alps. Macroseismic data therefore confirms that the crustal properties of the WCE target region are complex and that ground-motion models available for various types of seismotectonic regimes are needed to capture the epistemic uncertainty.

6. Conclusions

Most seismic hazard analyses, especially if one considers the number of people exposed to the associated seismic risk, are performed for locations outside the few regions of the world (essentially California and Japan) with abundant strong-motion data and indigenous ground-motion prediction equations. Since there will rarely be a clearly analogous region to the one under study from which ground-motion models can simply be borrowed, most hazard analysts are faced with the difficult question of selecting appropriate equations to be used in the calculations. The analyst will generally select two or more equations in order to take account of the epistemic uncertainty in both the median estimates and the aleatory variability (sigma values) of the models in terms of their applicability to the target region.

Hazard analyses employing multiple ground-motion models generally make use of logic trees. Reports and papers on hazard studies often focus on the weighting strategy applied to the logic-tree branches, conveying the impression that the selection of the candidate models to populate the logic tree in the first place is relatively unimportant. It has been shown recently that the selection of ground-motion models is vitally important and generally exerts a much greater influence on the hazard results than the details of the weighting scheme (Sabetta et al., 2005). To this end this paper attempts to provide some clear guidelines that analysts may follow for the selection of ground-motion models to be used in a logic tree, instead of the rather vague procedures often employed in current practice, whereby an analyst's choice is governed by familiarity with certain models, regions and ground-motion modelers.

The guidelines proposed herein for model selection effectively oblige the analyst to begin by becoming familiar with the full suite of models available globally and then to reduce this list by a process of objective evaluation. The authors feel that the use of regional weak-motion data for strong-motion prediction is still an open issue. We rather suggest to select empirical strong ground-motion models and to correct these models for systematic differences between host and target regions using the hybrid empirical method (Campbell, 2003; Scherbaum et al., 2005).

Acknowledgements

This paper is contribution EG2/DT-05 from a series of studies inspired by participation in the PEGASOS project (Abrahamson et al., 2002). We thank the following people for providing a stimulating environment and continuous support for the development of ideas presented herein: Norm Abrahamson, Philip Birkhauser, Jim Farrington, Andreas Hölker, Philippe Roth, Patrick Smit and Christian Sprecher. We also acknowledge the benefit derived from our many discussions with Fabio Sabetta on these issues throughout the course of the project. We also would like to give a special mention to Ms Anna Hikel for taking care of us and supplying us with excellent coffee during long working sessions at Imperial College London. F.C. benefited from the

support of the INSU Program "ACI Risques Naturels et Changements Climatiques.

References

Abercrombie, R.E., 1995, Earthquake source scaling relationships from -1 to 5 M_L using seismograms recorded at 2.5 km depth, *J. Geophys. Res.* **100**, 24015–24036.

Abrahamson, N.A. and Bommer, J.J., 2005, Probability and uncertainty in seismic hazard analysis, *Earthquake Spectra* **21**(2), 603–607.

Abrahamson, N.A., Birkhauser, P., Koller, M., Mayer-Rosa, D., Smit, P.M., Sprecher, C., Tinic, S. and Graf, R., 2002, PEGASOS- A comprehensive probabilistic seismic hazard assessment for nuclear power plants in Switzerland, *Proceedings of the Twelfth European Conference on Earthquake Engineering*, Paper no 633, London.

Abrahamson, N.A. and Shedlock, K.M., 1997, *Overview. Seism. Res. Lett.* **68**(1), 9–23.

Abrahamson, N.A. and Silva, W.J., 1997, Empirical response spectral attenuation relations for shallow crustal earthquakes, *Seism. Res. Lett.* **68**, 94–127.

Aki, K., 1966, Generation and propagation of G waves from the Niigata earthquake of June, 1964, Part 2: Estimation of earthquake moment, from the G wave spectrum, *Bull. Earthquake Res. Inst. Tokyo Univ.* **44**, 73–88.

Ambraseys, N.N. and Douglas, J., 2003, Near-field horizontal and vertical ground motion relations, *Soil Dyn. Earthquake Eng.* **23**, 1–18.

Ambraseys, N.N., Douglas, J., Smit, P. and Sarma, S.K., 2005, Equations for the estimation of strong ground motions from shallow crustal earthquakes using data from Europe and the Middle East: Horizontal peak ground acceleration and spectral acceleration, *Bull. Earthquake Eng.* **3**(1), 1–53.

Ambraseys, N.N., Simpson, K.A. and Bommer, J.J., 1996, Prediction of horizontal response spectra in Europe, *Earth. Eng. Struct. Dyn.* **25**, 371–400.

Anderson, J.G., 2000, Expected shape of regressions for ground-motion parameter on rock, *Bull. Seim. Soc. Am.* **90**(6B), S42–S52.

Anderson, J.G. and Hough, S.E., 1984, A model for the shape of the Fourier amplitude spectrum of acceleration at high frequencies, *Bull. Seism. Soc. Am.* **74**(5), 1969–1993.

Atkinson, G.M., 1993, Earthquake source spectra in eastern North America, *Bull. Seism. Soc. Am.* **83**, 1778–1798.

Atkinson, G.M., 1996, The high frequency shape of the source spectrum for earthquakes in eastern and western Canada, *Bull. Seism. Soc. Am.* **86**, 106–112.

Atkinson, G.M. and Boore, D.M., 1988, Evaluation of models for earthquake source spectra in Eastern North America, *Bull. Seism. Soc. Am.* **88**, 917–934.

Atkinson, G.M. and Boore, D.M., 1997, Some comparisons between recent ground-motion relations, *Seism. Res. Lett.* **68**, 24–40.

Atkinson, G.M. and Boore, D.M., 2000, Reply to Comment on "Evaluation of models for earthquake source spectra in eastern North America by Gail M. Atkinson and David M. Boore, *Bull. Seism. Soc. Am.* **90**, 1339–1341.

Atkinson, G.M. and Boore, D., 2003, Empirical ground-motion relations for subduction zone earthquakes and their application to Cascadia and other regions, *Bull. Seism. Soc. Am.* **93**(4), 1703–1729.

Atkinson, G.M. and Sonley, E., 2000, Empirical relationships between modfied Mercalli intensity and response spectra, *Bull Seism. Soc. Am.* **90**, 537–544.

Bard, P.Y. and Riepl-Thomas, J., 1999, Wave propagation in complex geological structures and local effects on strong motion, In: E. Kausel and G.D. Manolis (eds.), *Wave motion in earthquake engineering, Advances in Earthquake Engineering*, WIT Press, pp. 38–95.

Bay, F., Fäh, D., Malagnini, L. and Giardini, D., 2003, Spectral shear-wave ground motion scaling in Switzerland, *Bull. Seism. Soc. Am.* **93**, 414–429.

Berge-Thierry, C., Cotton, F., Scotti, O., Griot-Pommera, D.A. and Fukushima, Y., 2003, New empirical response spectral attenuation laws for moderate European earthquakes, *J. Earthquake Eng.* **7**, 193–222.

Beyer, K. and Bommer, J.J., 2005, Relationships between median values and aleatory variabilities for different definitions of the horizontal component of motion, submitted to *Bull. Seism. Soc. Am.*

Boatwright, J., Choy, G.L. and Seekins, L.C., 2002, Regional estimates of radiated seismic energy, *Bull. Seism. Soc. Am.* **92**, 1241–1255.

Bommer, J.J., Douglas, J. and Strasser, F.O., 2003, Style-of-faulting in ground-motion prediction equations, *Bull. Earthquake Eng.* **1**(2), 171–203.

Bommer, J.J., Scherbaum, F., Bungum, H., Cotton, F. and Sabetta, F., 2005, On the use of logic trees for ground-motion prediction equations in seismic hazard analysis, *Bull. Seism. Soc. Am.* **95**(2), 377–389.

Boore, D.M., 1983, Stochastic simulation of high frequency ground motion based on seismological models of the radiated spectra, *Bull. Seism. Soc. Am.* **73**, 1865–1894.

Boore, D.M., 2003, SMSIM-Fortran programs for simulating ground motions from earthquakes: Version 2.0-A revision of OFR 96–80–A, USGS.

Boore, D.M., 2003a, Simulation of ground motion using the stochastic method, *Pure Appl. Geophys.* **160**, 635–676.

Boore, D.M., 2003b, SMSIM-Fortran programs for simulating ground motions from earthquakes: version 2.0-A revision of OFR 96–80–A, USGS.

Boore, D.M. and Bommer, J.J., 2005, Processing strong-motion accelerograms: Needs, options and consequences, *Soil Dyn. Earthquake Eng.* **25**, 93–115.

Boore, D.M. and Joyner, W.B., 1984, A note on the use of random vibration theory to predict peak amplitudes of transient signals, *Bull. Seism. Soc. Am.* **74**(5), 2035–2039.

Boore, D.M. and Joyner, W.B., 1997, Site amplifications for generic rock sites, *Bull. Seism. Soc. Am.* **87**(2), 327–341.

Boore, D.M., Joyner, W.B and Fumal, T.E., 1997, Equations for estimating horizontal response spectra and peak acceleration from Western North American earthquakes: A summary of recents work, *Seism. Res. Lett.* **68**(1), 128–153.

Bragato, L. and Slejko, D., 2005, Empirical ground-motion attenuation relations for the eastern Alps in the magnitude range 2.5–6.3, *Bull. Seism. Soc. Am.* **95**(1), 252–276.

Brodsky, E.E. and Kanamori, H., 2001, The elastohydrodynamic lubrication of faults, *J. Geophys. Res.* **106**, 16357–16374.

Brune, J.N., 1970, Tectonic stress and seismic shear waves from earthquakes, *J. Geophys. Res.* **75**, 4997–5009.

Brune, J.N., 1971, Correction, *J. Geophys. Res.* **76**, 5002.

Budnitz, R.J., Apostolakis, G., Boore, D.M., Cluff, L.S., Coppersmith, K.J., Cornell, C.A. and Morris, P.A., 1997, Recommendations for probabilistic seismic hazard analysis: guidance on uncertainty and use of experts. NUREG/CR–6372.

Campbell, K.W., 2003, Prediction of strong ground motion using the hybrid empirical method and its use in the development of ground motion (attenuation) relations in eastern North America, *Bull. Seism. Soc. Am.* **93**, 1012–1033. Erratum: vol 94, p2418.

Campbell, W. and Bozorgnia, Y., 2003, Updated near source ground motion relations for horizontal and vertical components of peak ground acceleration, peak ground velocity and pseudo-absolute acceleration response spectra, *Bull Seism. Soc. Am.* **93**, 314–331, Errata: vol93 p 1413, vol 94 p 2417.

Campillo, M. and Plantet, J.L., 1991, Frequency dependence and spatial distribution of seismic attenuation in France: experimental results and possible interpretations, *Phys. Earth and Planet. Int.* **67**, 48–64.

Douglas, J., 2003, Earthquake ground motion estimation using strong-motion records: a review of equations for the estimation of peak ground acceleration and response spectra ordinates, *Earth Science Review* **61**, 43–104.

Ferry, M., Meghraoui, M., Delouis, B. and Giardini, D., 2005, Evidence of Holocene palaeoseismicity along the Basel-Reinach active normal fault (Switzerland): a seismic source for the 1356 earthquake in the Upper Rhine graben, *Geophys J. Int.* **160**, 554–572.

Frankel, A., McGarr, A., Bicknell, J., Mori, J., Seeber, L. and Cranswick, E., 1990, Attenuation of high-frequency shear waves in the crust: Measurements from New York state, South Africa and southern California, *J. Geophys. Res.* **95**(B11), 17441–17457.

Fukushima, Y. and Tanaka, T., 1990, A new attenuation relation for peak horizontal acceleration of strong earthquake ground motion in Japan, *Bull. Seism. Soc. Am.* **80**, 757–783.

Gulkan, P. and Kalkan, E., 2002, Attenuation modelling of recent earthquakes in Turkey, *J. Seism.* **6**(3), 397–409.

Haddon, R.A.W., 1996, Earthquake source spectra in Eastern North America, *Bull. Seism. Soc. Am.* **86**, 1300–1313.

Haddon, R.A.W., 1997, Reply to Comments by G.M. Atkinson, et al. on 'Earthquake source spectra in eastern North America,' *Bull. Seism. Soc. Am.* **87**, 1703–1708.

Haddon, R.A.W., 2000, Comment on "Evaluation of models for earthquake source spectra in eastern North America" by Gail M. Atkinson and David M. Boore, *Bull. Seism. Soc. Am.* **90**, 1332–1338.

Hanks, T., 1982, fmax, *Bull. Seism. Soc. Am.* **72**, 1867–1879.

Herrmann, R.B. and Kijko, A., 1983, Modeling some empirical component Lg relations, *Bull. Seism. Soc. Am.* **73**, 157–171.

Ide, S. and Beroza, G.C., 2001, Does apparent stress vary with earthquake size? Geophys, *Res. Lett.* **28**(17), 3349–3352.

Izutani, Y. and Kanamori, H., 2001, Scale dependence of seismic energy-to-moment ratio for strike-slip earthquakes in Japan, *Geophys. Res. Lett.* **28**, 4007–4010.

Joyner, W.B. and Boore, D.M., 1981, Peak horizontal acceleration and velocity from strongmotion records including records from the 1979 Imperial Valley, California, earthquake, *Bull. Seism. Soc. Am.* **71**(6), 2011–2038.

Kaka, S.I. and Atkinson, G.M., 2004, Relationships between instrumental ground-motion parameters and modified Mercalli intensity in Eastern North-America, *Bull. Seism. Soc. Am.* **94**(5), 1728–1736.

Kanamori, H. and Anderson, D.L., 1975, Theoretical basis of some empirical relations in seismology, *Bull. Seism. Soc. Am.* **65**(5), 1073–1095.

Kanamori, H. and Heaton, T., 2000, Microscopic and macroscopic mechanism of earthquakes, In: D.L.T.a.W.K. J. Rundle (Editor), Geocomplexity and Physics of Earthquakes, American Geophysical Monograph, pp. 147–163.

Kanamori, H. and Rivera, L., 2004, Static and dynamic scaling relations for earthquakes and their implication for rupture speed and stress drop, *Bull. Seism. Soc. Am.* **94**, 314–319.

Kulkarni, R.B., Youngs, R.R. and Coppersmith, K.J., 1984, Assessment of confidence intervals for results of seismic hazard analysis, Proceedings of the Eighth World Conference on Earthquake Engineering, San Francisco, pp. 263–270.

Lussou, P., Fukushima, Y., Bard, P.Y. and Cotton, F., 2001, Seismic design regulation codes: contribution of Knet data to site effect evaluation, *J. Earthquake Eng.* **5**(1), 13–33.

Malagnini, L., Herrmann, R.B. and Koch, K., 2000, Regional ground-motion scaling in central Europe, *Bull. Seism. Soc. Am.* **90**(4), 1052–1061.

Mayeda, K. and Walter, W.R., 1996, Moment, energy, stress drop and source spectra of western United State earthquakes from regional code envelopes, *J. Geophys. Res.* **101**, 11195–11208.

McGarr, A. and Fletcher, J.B., 2002, Mapping apparent stress and energy radiation over fault zones of major earthquakes, *Bull. Seism. Soc. Am.* **92**, 1633–1646.

McGuire, R.K., Cornell, C.A. and Toro, G.R., 2005, The case of using mean seismic hazard, *Earthquake Spectra*, **21**(3), 879–886.

Mitchell, B.J., 1995, Anelastic structure and evolution of the continental crust and upper mantle from seismic surface wave attenuation, *Rev. Geophys.* **33**, 441–462.

Mitchell, B.J., Pan, Y.P., Xie, J. and Cong, L., 1997, Lg coda Q variation across Eurasia and its relation to crustal evolution, *J. Geophys. Res* **102**, 22767–22779.

Musson, R.M.W., 2005, Against fractiles, *Earthquake Spectra* **21**(3), 887–891.

Mooney, W.D., Laske, G. and Masters, T.G., 1998, CRUST 5.1: A global crustal model at $5^\circ \times 5^\circ$, *J. Geophys. Res* **103**(B1), 727–747.

Nocquet, J.M. and Calais, E., 2003, Crustal velocity field of western Europe from permanent GPS array solutions, 1996-2001, *Geophys. J. Int.* **154**, 72–88.

Nuttli, O., 1982, The earthquake problem in the eastern United States, *J. Struct. Div. Soc. Eng.* **108**, 1302–1312.

Oye, V., Bungum, H. and Roth, M., 2005, Source parameters and scaling relations for mining related seismicity with the Pyhäsalmi ore mine, Finland, *Bull. Seism. Soc. Am.* **95**(3), 1011–1026.

Özbey, C., Sari, A., Manuel, L., Erdik, M. and Fahjan, Y., 2004, An empirical attenuation relationship for northwestern Turkey ground motion using a random effects approach, *Soil Dyn. Earthquake Eng.* **24**, 115–125.

Papageorgiou, A.S. and Aki, K., 1983, A specific barrier model for the quantitative description of inhomogeneous faulting and the prediction of strong ground motion, *Bull. Seism. Soc. Am.* **73**(4), 693–722.

Raoof, M., Herrmann, R.B. and Malagnini, L., 1999, Attenuation and excitation of three-component ground motion in Southern California, *Bull. Seism. Soc. Am.* **89**(4), 888–902.

Reiter, L., 1990, Earthquake Hazard Analysis: Issues and Insights, Columbia University Press, New York, Oxford.

Rey, J., Faccioli, E. and Bommer, J.J., 2002, Derivation of design soil coefficients (S) and response spectral shapes for Eurocode 8 using the European Strong-Motion Database, *J. Seismol.* **6**, 547–555.

Rietbrock, A., 2001, P wave attenuation structure in the fault area of the 1995 Kobe earthquake, *J. Geophys. Res.* **106**(B3), 4141–4154.

Rietbrock, A., Scherbaum, F., Cotton, F. and Fäh, D., 2006, On the determination of source, path, and site effects from microearthquake recordings for strong ground motion prediction, in revision to Bull. Seism. Soc. Am.

Rüttener, 1995, Earthquake hazard evaluation for Switzerland, Géol. Suisse, Nr29, Schweizerische Geophysikalische Kommission, ETH-Zürich, 106.

Sabetta, F., Lucantoni, A., Bommer, J.J. and Bungum, H., 2005, Sensitivity of PSHA results to ground-motion prediction relations and logic-tree weights, *Soil Dyn. Earthquake Eng.* **25**(4), 317–329.

Sabetta, F. and Pugliese, A., 1996, Estimation of ground motion and simulation of Nonstationary earthquake ground motions, *Bull. Seism. Soc. Am.* **86**, 337–352.

Scherbaum, F., 1990, Combined inversion for the three-dimensional Q structure and source parameters using microearthquake spectra, *J. Geophys. Res* **95**(B8), 12423–12438.

Scherbaum, F., Schmedes, J. and Cotton, F., 2004a, On the conversion of source-to-site distance measures for extended earthquake source model, *Bull. Seism. Soc. Am.* **94**, 1053–1059.

Scherbaum, F., Cotton, F. and Smit, P., 2004b, On the use of response spectral reference data for the selection of ground-motion models for seismic hazard analysis: the case of rock motion, *Bull. Seism. Soc. Am.* **94**(6), 1–22.

Scherbaum, F., Bommer, J.J., Bungum, H., Cotton, F. and Abrahamson, N.A., 2005, Composite ground-motion models and logic trees: methodology, sensitivities and uncertainties, *Bull. Seism. Soc. Am.* **95**(5), 1575–1593.

Scherbaum, F., Cotton, F. and Staedtke, H., 2006, The estimation of minimum-misfit stochastic models from empirical ground-motion equations, *Bull. Seim. Soc. Am.*, in press.

Scholz, C.H., 1994, Reply to comments on ‘A reappraisal of large earthquake scaling’, *Bull. Seism. Soc. Am.* **84**, 1677–1678.

Scholz, C.H., Aviles, C.A. and Wesnousky, S.G., 1986, Scaling differences between large interplate and intraplate earthquakes, *Bull. Seism. Soc. Am.* **76**(1), 384–397.

Silva, W., Darragh, D., Gregor, N., Martin, G., Abrahamson, N. and Kircher, C., 2000, Reassessment of site coefficients and near fault factors for building code provisions, Program Element: II, 98-HQ-GR-1010. Report to USGS.

Singh, S.K. and Herrmann, R.B., 1983, Regionalization of crustal coda Q in the continental United States, *J. Geophys. Res.* **88**, 527–538.

Somerville, P.G., McLaren, J.P., Saikia, C.K. and Helmberger, D.V., 1990, The 25 November 1988 Saguenay, Quebec, earthquake: source parameters and the attenuation of strong ground motion, *Bull. Seism. Soc. Am.* **80**(5), 1118–1143.

Spudich, P., Joyner, W.B., Lindh, A.G., Boore, D.M., Margaris, M. and Fletcher, J.B., 1999, SEA99: A revised ground motion prediction relation for use in extensional tectonic regimes, *Bull. Seism. Soc. Am.* **89**, 1156–1170.

Stepp, J.C., Wong, I., Whitney, J., Quittemeyer, R., Abrahamson, N., Toro, G., Youngs, R., Coppersmith, K., Savy, J. and Sullivan, T., 2001, Probabilistic seismic hazard analyses for ground motions and fault displacements at Yucca Mountain, Nevada, *Earthquake Spectra* **17**(1), 113–151.

Toro, G.R., Abrahamson, N.A. and Schneider, J.F., 1997, Model of strong ground motions for earthquakes in central and eastern north-america, *Seism. Res. Lett.* **68**, 41–57.

Venkataraman, A., Rivera, L. and Kanamori, H., 2002, Radiated energy from the October 16, 1999 Hector Mine earthquake: regional and teleseismic estimates, *Bull. Seism. Soc. Am.* **92**, 1256–1265.

Vigny, C., Chery, J., Duquesnoy, T., Jouanne, F., Amman, J., Andizei, M., Avouac, J.P., Barlier, F., Bayer, R., Briole, P., Calais, E., Cotton, F., Duquenne, F., Feigl, K., Ferhat, G., Flouzat, M., Gamont, J.F., Geiger, A., Harmel, A., Kasser, M., Laplanche, M., LePape, M., Martinet, J., Menard, G., Meyer, B., Ruegg, J.C., Scheubel, J.M., Scotti, O. and Vidal, G., 2002, GPS network monitor the western Alps deformation over a five year period, 93–98, *Journal of Geodesy* **76**, 63–76.

Wald, D.J., Quitoriano, V., Heaton, T.H. and Kanamori, H., 1999, Relationships between peak ground acceleration, peak ground velocity, and modified Mercalli intensity in California, *Earthquake Spectra* **15**(3), 557–564.

Waldhauser, F., Kissling, J., Ansorge, J. and Mueller, S., 1998, Three-dimensional interface modelling with two-dimensional seismic data: The Alpine crust-mantle boundary, *Geophys. J. Int.* **135**, 264–278.

Wyss, M. and Brune, J.N., 1968, Seismic moment, stress and source dimensions for earthquakes in the California-Nevada region, *J. Geophys. Res.* **73**, 4781–4694.

Xie, J. and Nuttli, O.W., 1998, Interpretation of high frequency coda at large distances: Stochastic modeling and method of inversion, *Geophys. J. Int.* **95**, 579–595.

JOURNAL OF GEOPHYSICAL RESEARCH, VOL. 110, B03306, doi:10.1029/2004JB003194, 2005

The 2000 Tottori earthquake: A shallow earthquake with no surface rupture and slip properties controlled by depth

Fethi Semmane, Fabrice Cotton, and Michel Campillo
Laboratoire de Géophysique Interne et Tectonophysique, Université Joseph Fourier, Grenoble, France

Received 27 May 2004; revised 16 December 2004; accepted 3 January 2005; published 26 March 2005.

[1] The M_w6.8 Tottori earthquake, Japan, does not exhibit any surface trace but was particularly well instrumented. Strong motion displacement records and GPS coseismic data are used to constrain the evolution of the slip on the fault plane in time and space. We adopt in this study a two-plane fault geometry based on aftershock distributions and analysis of close station records. In a first step, our inversion allowed surface slip. The model obtained has a significant surface slip, which contradicts the absence of clear surface slip reported by geologists. In a second step, models with no slip at the surface (buried faults), compatible with geological observations, have been tested. The tests with different fault depths show that when slip is allowed to occur close to the surface, the fit to seismological and geodetic data is increased. These tests confirm that slip actually occurred at shallow depth. Despite the nonuniqueness of the solution, all the inverted source models show (1) a large slip amplitude patch at a depth of about 4–5 km and (2) relatively small slip in the hypocentral area. The rupture velocity is about 2750 m/s in the asperity region. The total rupture duration is about 8 s. The slip distribution seems to be controlled by the variation of fault properties with depth. Another feature that could control the rupture of this earthquake is a fault plane almost perpendicular to the main fault NW of the epicenter, which apparently inhibits further rupture propagation.

Citation: Semmane, F., F. Cotton, and M. Campillo (2005), The 2000 Tottori earthquake: A shallow earthquake with no surface rupture and slip properties controlled by depth, *J. Geophys. Res.*, *110*, B03306, doi:10.1029/2004JB003194.

1. Introduction

[2] The Tottori, Japan, earthquake (M_w = 6.6 ∼ 6.8) occurred on 6 October 2000 at 0430:18.07 UT. The epicenter is located at 35.269°N and 133.357°E [*Iwata and Sekiguchi*, 2002]. The 2000 Tottori earthquake was the first important earthquake recorded by the KIK-net network (National Research Institute for Earth Science and Disaster Prevention) and thus provides a unique set of near field data (http://www.kik.bosai.go.jp/kik). This accelerometer network, installed after the 1995 Kobe earthquake, consists of sensors located both at the surface and at depth (100 m and greater). These data provide the opportunity to compare inversions performed with ground motions recorded at the surface and at depth. The borehole records allow the evaluation of possible site effects that can contaminate surface records and introduce a bias in the source inversion process. In this study, we evaluate the site-effect bias by comparing the kinematic models of the 2000 Tottori earthquake derived from borehole records and from surface records, respectively.

[3] The 2000 Tottori earthquake is an almost pure left-lateral strike-slip event for which different focal depths have been proposed. The different published centroid moment tensor (CMT) solutions also give significantly different moments and origin times (Table 1). Furthermore, since there is no clear surface expression of this earthquake, it is almost impossible to derive fault geometry from geological observations. The first goal of this paper is to better constrain the fault geometry and origin time of this earthquake using data from close strong motion stations.

[4] So far, few studies of the rupture of the 2000 Tottori earthquake have been carried out [e.g., *Iwata and Sekiguchi*, 2002; *Peyrat and Olsen*, 2004]. The second goal of this paper is to retrieve the source kinematics using a frequency domain inversion procedure [*Cotton and Campillo*, 1995; *Hernandez et al.*, 1999]. We use both geodetic and strong motion data to better constrain the source properties.

[5] Many moderate earthquakes (M_w = 6–7) have produced little or no surface trace such as the 1984 Morgan Hill [*Hartzell and Heaton*, 1986], the 1989 Loma Prieta [*Uhrhammer and Bolt*, 1991], the 1992 Joshua Tree, and the northern part of the 1995 Kobe earthquakes [*Sekiguchi et al.*, 2000]. However, even if several recent earthquakes show that large shallow rupture can take place not only on faults that cut the Earth's surface but also on hidden faults, there is a lack of information on how shallow the large slip asperities are. In the present study, we will discuss the minimum depth of the Tottori earthquake's slip area, searching for a rupture model that satisfies near field records and complies with the absence of clear surface slip observations.

0148-0227/05/2004JB003194$09.00

Table 1. CMT Solutions and Inversions[a]

CMT Inversion	Moment, × 10^{18} N m	Magnitude M_w	Origin Time, UT	Hypocentral Depth, km	Data Type Used
ERI	2.93	6.2	0430	31.3	Ts
USGS	7.4	6.5	0430:23.37	12	Ts
Harvard	11	6.66	0430:25.8	19.9	Ts
Y. Yagi and M. Kikuchi (unpublished manuscript, 2000)	11	6.6	?	11	Ts + SM
Iwata and Sekiguchi [2002]	19	6.8	0430:18.07	7.8	SM
This study	14.7	6.74	0430:18.07	14.5	SM

[a] CMT, centroid moment tensor; ERI, Earthquake Research Institute; USGS, U.S. Geological Survey; Ts, teleseismic; SM, strong motions.

[6] The 2000 Tottori earthquake caused relatively moderate damage: 182 people were injured and about 400 buildings destroyed. This low impact is largely due to the fact that the epicenter was located in a mountainous area. Nevertheless earthquakes of this magnitude can be very destructive, like the Kobe earthquake. According to *Kagawa et al.* [2004], ground motions generated by buried fault are larger than ground motions generated by earthquakes that rupture the surface. It is therefore essential to better constrain the source properties (rupture velocity, subevent size), as knowledge of them is required for strong ground motion simulations for earthquakes scenarios. For this reason, our results will be compared and discussed with the predictions of recent empirical relations between moment magnitude and source properties [*Somerville et al.*, 1999].

2. Data

[7] Both seismic waveforms and GPS data are used to constrain the fault model. Strong motion waveforms are inverted alone at first and, in a second step, with the a priori slip distribution deduced from GPS data inversion, as proposed by *Hernandez et al.* [1999].

2.1. Strong Motion Data

2.1.1. Data Selection and Site Effect Analysis

[8] To study the general characteristics of the slip history of the 2000 Tottori earthquake, strong motion data from 10 KIK-net stations and 13 K-net stations (http://www.kik.bosai.go.jp) are considered. The station locations are plotted in Figure 1 and are listed in Table 2. A particularity of the KIK-net data is that they provide the opportunity to compare, in the frequency range of kinematics inversions [0.1–1.0] Hz, seismograms recorded at depth (100–400 m) and at the surface. This comparison shows that surface motions are in general very similar to motions recorded at depth in this frequency range (Figure 2). However, some stations show great discrepancies on one, two or three components. We have observed the following:

[9] 1. The two stations located in the north of the seismogenic area, SMNH11 and SMNH10, have late arrivals that could be explained by surface waves generated in the sediments close to the sea shore. These two stations are not included in the inversion.

[10] 2. The two horizontal surface records from station TTRH02 show evidence of a site effect in the frequency range considered. This site effect has been confirmed by other studies and involves nonlinear soil response [e.g., *Bonilla et al.*, 2003]. The same effect (nonlinear site effect) is observed at station OKYH007 on the two horizontal components and on the E-W component of station SMNH02.

[11] Therefore two data sets were chosen containing recordings showing no obvious complex propagation or site effect contamination. One data set of surface recordings (Table 2) consists of records collected on 11 K-net and 7 surface KIK-net stations, and the "borehole" records data set (Table 2) consists of records collected on 8 borehole KIK-net stations.

2.1.2. Data Processing and Weighting

[12] Original acceleration waveforms are band-pass filtered in the frequency range of 0.1–1.0 Hz using a two-pole Butterworth filter applied forward and backward, resampled to a sampling interval of 0.47 s and then doubly integrated to obtain the particle displacement. Following the first inversion runs some vertical components were given less weight compared to the horizontal ones, because the vertical component of S waves is very sensitive to the angle of incidence for small angles. They are not well modeled by our simple one-dimensional (1-D) average velocity structure.

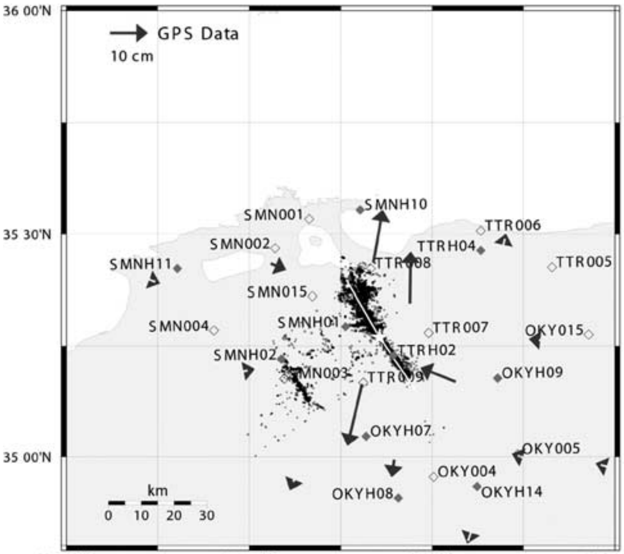

Figure 1. GPS station locations and estimated horizontal vector displacement (arrows), location of the 2000 Tottori earthquake (star), and near-field accelerometric station locations (KIK-net (solid diamonds) and K-net (open diamonds)). Solid line shows the fault trace of the plane adopted in this study. Aftershock locations are from *Fukuyama et al.* [2003].

Table 2. Stations and Records Used in This Study[a]

Station	Distance From Epicenter, km	Components N-S	E-W	U-D	Affiliation	Surface Record Set	Downhole Record Set
SMNH01	8	+	+	+	KIK-net	+	+
SMNH02	24	+	+	+	KIK-net	+	+
SMNH10	31	–	–	–	KIK-net	–	–
SMNH11	52	–	–	–	KIK-net	–	–
TTRH02	7	+	+	–	KIK-net	–	+
TTRH04	33	+	+	–	KIK-net	+	+
OKYH07	26	+	+	+	KIK-net	+	+
OKYH08	41	+	+	+	KIK-net	+	+
OKYH09	32	+	+	+	KIK-net	+	+
OKYH14	45	+	+	–	KIK-net	+	+
SMN001	33	–	–	–	K-net	–	
SMN002	33	–	–	–	K-net	–	
SMN003	25	+	+	–	K-net	+	
SMN004	40	+	+	–	K-net	+	
SMN015	19	+	+	+	K-net	+	
TTR005	47	+	+	–	K-net	+	
TTR006	37	+	+	–	K-net	+	
TTR007	13	+	+	+	K-net	+	
TTR008	16	+	+	+	K-net	+	
TTR009	13	+	+	+	K-net	+	
OKY004	38	+	+	+	K-net	+	
OKY005	46	+	+	+	K-net	+	
OKY015	53	+	+	+	K-net	+	

[a] A plus indicates the record has been used in this study and a minus indicates that it was not used.

The time window used in the inversion is 60 s for all records. Both data and synthetics were normalized by the peak amplitude of the data to avoid giving too much weight in the inversion to the records with the largest amplitudes [e.g., *Hartzell and Heaton*, 1983; *Cotton and Campillo*, 1995].

2.2. Geodetic Data

[13] The geodetic data available for the 2000 Tottori earthquake consist of coseismic GPS measurements in the form of displacement vectors for GPS sites and leveling surveys around the focal region [*Sagiya et al.*, 2002]. These data were collected by the Japanese nationwide continuous GPS observation network. Only the coseismic displacement vectors are used for the inversion. The measurements were made by differencing locations measured several weeks prior to the earthquake and about 2 months after the earthquake. The maximum displacement (~17 cm) was observed south of the epicenter. The 14 closest stations associated with significant displacement have been selected in the inversion process. Figure 1 shows the selected GPS stations and the observed horizontal displacement vectors.

3. Waveform Inversion Methodology

3.1. Inversion Method

[14] A nonexhaustive list of inversion methods to study the rupture history developed during the last two decades includes those by *Olson and Apsel* [1982], *Hartzell and Heaton* [1983], *Takeo* [1987], *Beroza and Spudich* [1988], *Olson and Anderson* [1988], *Mendoza and Hartzell* [1988a, 1988b, 1989], *Das and Kostrov* [1990, 1994], *Hartzell et al.* [1991], *Hartzell and Liu* [1995, 1996], *Cotton and Campillo* [1995], *Sekiguchi et al.* [2000], *Ji et al.* [2002], and *Liu and Archuleta* [2004]. As discussed by *Olson and Apsel* [1982], *Beroza and Spudich* [1988], and *Das and Kostrov* [1990], in some cases, more than one slip model distribution can fit the

Figure 2. Displacement seismograms recorded at the surface (dashed), in boreholes (solid), and band passed in the frequency range 0.1–1.0 Hz. Note that, in particular, horizontal components of TTRH02 are not usable after a double integration.

data, which leads to different stress accumulation patterns and histories on the fault. The linearized frequency domain inversion method was described in detail by *Cotton and Campillo* [1995] and *Hernandez et al.* [1999]. We recall briefly the essential points of the method. The fault plane is divided into small subfaults. Each subfault is itself composed of several point sources equally distributed over the subfault. The Green functions for a layered velocity model are calculated numerically between each point source and each station and then linearly combined into the displacement due to a subfault where rupture propagates at a prescribed velocity. For each subfault, we allocate a source time function, which corresponds to a ramp function in slip (Figure 3). The local slip is characterized through three parameters: the start time of the rupture, the risetime, and the slip amplitude. With this parameterization, the ground displacement V at ith station and a given frequency, ω, can be represented as a linear sum of n subfault contributions, with given slip amplitude and duration, each one appropriately delayed in time to account for rupture propagation:

$$V_i(\omega) = \sum_{k=1}^{n} \mathrm{slip}_k \exp[-i\omega\, t_k] u_{ki}(\omega) S_k[\tau_k, \omega], \tag{1}$$

$$S(t) = 0.5\{1 + \tanh[(t + \tau/2)/(\tau/2)]\} \tag{2}$$

where u_{ki} represents the ground motion for a unit constant slip on the subfault k with a given source mechanism, ω is the angular frequency, slip_k, t_k and S_k are the slip, the rupture time, and the source function of the kth subfault, respectively. The latter depends on a single variable: the risetime τ_k (Figure 3). The analytical form of the source function S is given by expression (2). This simple parameterization limits the number of model parameters with respect to the technique proposed by *Olson and Anderson* [1988]. For each subfault, the rupture time, the risetime and the slip amplitude are evaluated simultaneously using the spectral components of the records.

[15] We invert equation (1) by iterative minimization in the least squares sense [*Tarantola and Valette*, 1982]. *Olson and Apsel* [1982], *Hartzell and Heaton* [1983], *Das and Kostrov* [1990, 1994], and *Hartzell and Liu* [1995, 1996], among others, have identified physical and nonphysical constraints to limit oscillations in the solution. In this study we introduce three types of constraints: a positivity constraint (positive slip for all points on the fault for all times), allowing each subfault to slip only once and a smoothing constraint. Since our inversion is only able to reconstruct smooth models of the rupture process, we introduce a smoothing constraint to stabilize the solution. The smoothing constraint is introduced through the covariance matrix C_M that describes the a priori information on the model parameters following *Tarantola* [1987]. The elements of the covariance matrix between a pair of ith and jth subfaults are given by

$$C_{M,ij} = \sigma_i \sigma_j \exp\left(-\frac{1}{2}\frac{d_{ij}^2}{\Delta l^2}\right) \tag{3}$$

σ is the a priori model parameter variance (the variance is the same for all subfaults, ($\sigma_i = \sigma_j$), d is the distance between the two subfaults and Δl is the correlation length. Note that no smoothing is introduced on the rupture time.

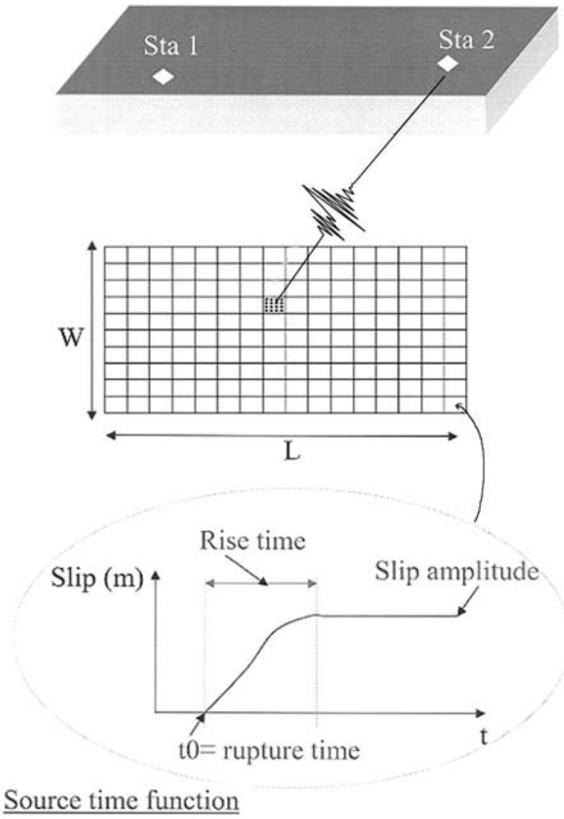

Figure 3. Source parameterization. We divide the fault plane into small subfaults. Each subfault is represented by an array of point sources. The point source Green functions are calculated for a layered velocity model for each station. A smoothed ramp function in displacement is used for each subfault.

3.2. Crustal Structure Model and Green's Functions

[16] An elastic half-space is often used to model static deformation [e.g., *Okada*, 1985; *Freymueller et al.*, 1994; *Peltzer et al.*, 2001]. *Cattin et al.* [1999] studied the difference between inverted coseismic displacements for a vertical dip-slip fault using a layered half- space and a homogeneous half-space. In agreement with *Savage* [1998], they concluded that the resulting displacement could differ by 10–20%. The horizontal displacements are more affected than the vertical ones. To avoid this overestimation, we used the same layered crustal model to calculate both static deformations and seismograms as already done by *Hernandez et al.* [1999]. The crustal velocity model is shown in Table 3. This model is used for the hypocenter determination by Research Center for Earthquake Prediction–Disaster Prevention Research Institute (RCEP-DPRI), Kyoto University. An attenuation coefficient for both P and S waves is added. All borehole stations used in this study are at about 100 m depth. Because the wavelength of the waves used in the inversion is greater than 500 m, we calculate at each station only one Green's function for both sensors. The Green's functions used to calculate the strong motion

Table 3. Velocity Structure

h, km	V_p, km/s	V_s, km/s	d, kg/m^3	Q_p	Q_s
0	5.50	3.179	2600	500	200
2	6.05	3.497	2700	500	200
16	6.60	3.815	2800	500	200
38	8.03	4.624	3100	500	200

synthetics are computed numerically for the layered velocity model described in Table 3, using AXITRA computer package [*Coutant*, 1989].

3.3. Origin time

[17] In several recent cases it has been observed that the beginning of major slip is preceded a few seconds by a foreshock. This observation has been interpreted to be related to the initiation phase of sliding before the propagation phase of rupture [*Iio*, 1992; *Ellsworth and Beroza*, 1995; *Campillo and Ionescu*, 1997]. For example, such phenomena were reported for the following events: Landers, 1992 [*Campillo and Archuleta*, 1993], Hector Mine, 1999 [*Ji et al.*, 2002]; and Sanriku-Haruka-Oki, 1994 [*Nakayama and Takeo*, 1997]. In the case of the 2000 Tottori earthquake, the beginning of major slip began several seconds after a first break. In our study we adopt the origin time given by *Iwata and Sekiguchi* [2002] (Table 1).

4. Results

4.1. Fault Plane Geometry Selection

[18] For our starting models we first adopted the fault geometry used by *Iwata and Sekiguchi* [2002], i.e., a fault plane with strike N150°E and dip 90°. The dimensions are set to a length of 32 km and a depth of 20 km. We consider two discretizations, one with large subfaults of size 4 km × 4 km (the hypocenter is located at a depth of 14 km) and the other with small subfaults of size 2 km × 2 km (the hypocenter is located at a depth of 15 km for convenience).

[19] We observed that the synthetics do not fit the record at the nearest station (TTRH02, located east of the N150° fault plane) with the geometry defined by *Iwata and Sekiguchi* [2002]. On the opposite side at station SMNH01, which is almost at the same distance, we obtained a good agreement. This observation suggests a mislocation of the fault plane with respect to TTRH02. We therefore consider a possible change of strike in the southern part of the fault. Figure 4 presents the comparison between the 150° and 146° strikes for the southern part of the fault. The N-S component is discriminant and shows that the 146° strike for which station TTRH02 is located west of the fault plane is in agreement with the observed ground motion. The aftershocks plotted in Figure 1 are relocated by *Fukuyama et al.* [2003] using the high-resolution technique developed by *Waldhauser and Ellsworth* [2000]. We observe a good agreement between our two fault plane segments directions and the relocated seismicity. This geometry is finally used in our study.

4.2. GPS Inversion

[20] The geodetic displacements are calculated in the same layered velocity structure used in computing the strong motion waveforms (Table 3). The observed coseismic displacement vectors are displayed with arrows in Figure 1. On Figure 1, the coseismic deformation pattern clearly shows left lateral strike slip motion. For the GPS data inversion, we used an initial model which consists of two vertical fault plane segments (Figure 4). The length along strike is 32 km and 20 km along dip. We discretized the fault plane into a total of 40 large subfaults (4 km × 4 km) or 160 small subfaults (2 km × 2 km). A constant initial slip of 35 cm is used for each subfault. Knowing that surface static displacement is mostly sensitive to the shallow part of the fault [*Hernandez et al.*, 1999], the details of the slip distribution at depth cannot be resolved.

[21] The spatial distribution of slip obtained from inversion of geodetic data is given in Figure 5a. In Figure 5b, synthetic horizontal displacement field (gray) are compared with the observed GPS data (black). The maximum strike slip at 2–3 km depth is about 170 cm and extends over about 6 km. The total seismic moment deduced from the slip distribution is 13.8×10^{18} N m ($M_w = 6.73$). This result is discussed later.

4.3. Strong Motion Inversion

[22] We tested a range of initial models with constant rupture velocity, risetime, and slip. Table 4 shows the misfits obtained for different initial models. We tried a range of values of velocity from 2500 to 3000 m/s and risetimes between 0.9 and 2.7 s. For these inversions we used large subfaults (4 km × 4 km) and the set of strong motion borehole records. We found the best variance reduction when taking an initial model with a rupture velocity of 2800 m/s and a risetime of 1.2 s.

4.3.1. Data and Subfaults Size Choices

4.3.1.1. Borehole Records and Subfault Parameterization

[23] *Hartzell and Langer* [1993] and *Das and Suhadolc* [1996] have pointed out some examples of the significant effects on a finite fault inversion that are produced by changes in model parameters such as subfault size. The slip distribution obtained using borehole records and large subfaults is displayed in Figure 6a. The maximum slip equals 230 cm. The total moment estimate is 15.5×10^{18} N m, equivalent to a moment magnitude of 6.76.

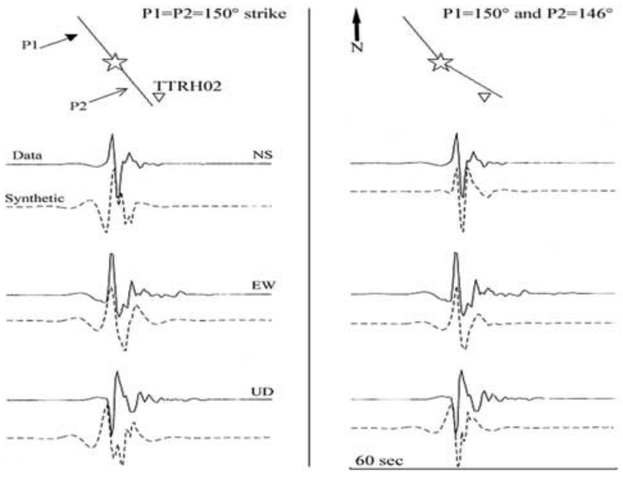

Figure 4. Fit between data (solid) and synthetics (dashed) at station TTRH02. These tests show that the fault plane is located east of station TTRH02.

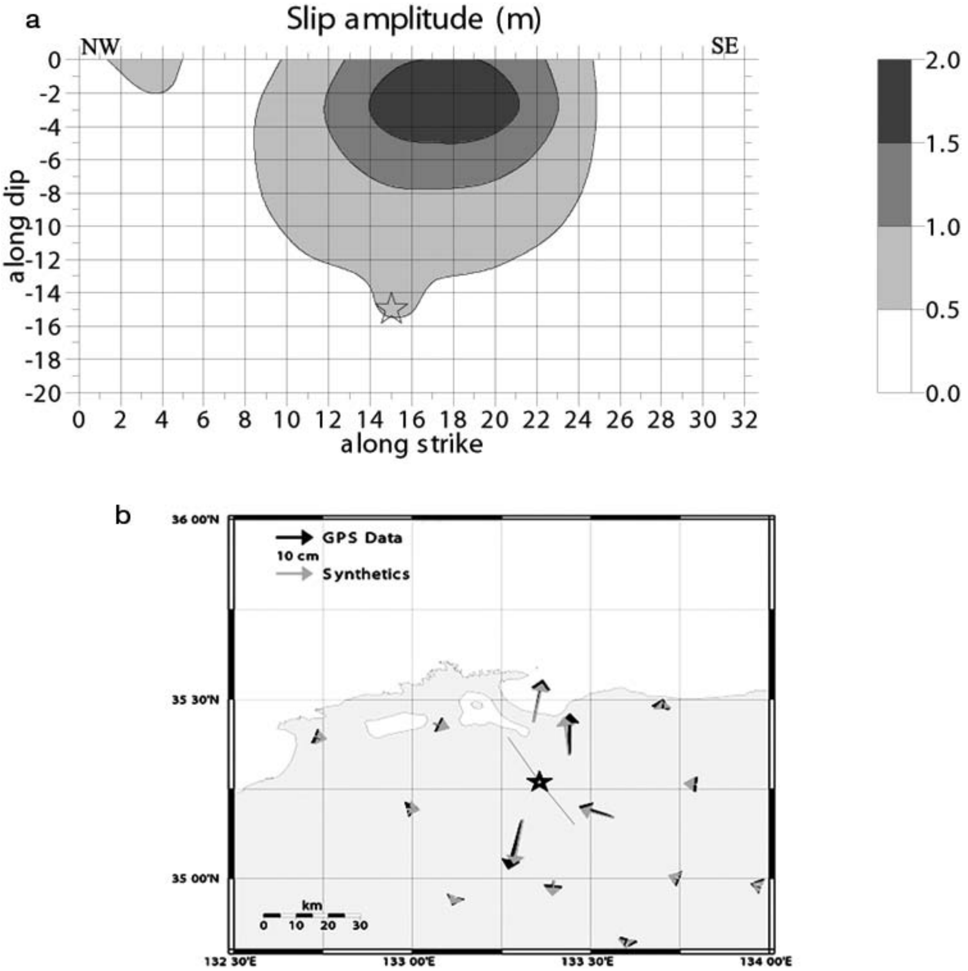

Figure 5. (a) Slip distribution model using the least squares inversion scheme for GPS data. The best fault model geometry described in Figure 4 (right) is used with an initial 35 cm slip on each subfault. The final seismic moment is 13.8 × 10^{18} N m (M_w = 6.73). (b) Comparison between data (black vector) and synthetic (gray vector) after a direct modeling.

The variance reduction is about 68%. While the slip distribution (Figure 6a) is rougher than the one obtained from GPS data (Figure 5a), we observe in both cases a large asperity in the same region of the fault plane. Note that in order to compare this model with the model obtained using surface data, station TTRH02 is ignored since it is not in the surface record data set, due to instrumental problem (see Figure 2).

[24] Figure 6b presents the model obtained with small 2 × 2 km^2 subfaults, and borehole records. It shows that the single asperity found in the large subfault model between 0 and 8 km depth and 6 and 24 km in the strike direction is in fact a fusion of several asperities of smaller size. The seismic moment associated with the small subfaults solution is 14.4 × 10^{18} N m (M_w = 6.74), very close to the one obtained for larger subfaults. The variance reduction is about 70%. The maximum slip is 280 cm. The slip distribution at the top of the fault is not the same for the large subfault or small subfault models.

4.3.1.2. Surface Data Records and Subfault Parameterization

[25] Until now only borehole records have been used. Figure 6c shows the slip model obtained using surface records in the case of the large subfault model. We notice that compared with the solution derived from borehole records (Figure 6a), the maximum slip amplitude occupies a slightly smaller area, but in general the form of the asperity is the same. The maximum slip amplitude is 207 cm and the moment magnitude does not change. On the other hand, the variance reduction is about 62% (less than the variance reduction obtained with borehole records) the difference is probably due to site effects that are not considered in our direct problem but are important at some KIK-net stations.

[26] A similar test performed with the small subfault parameterization is presented on Figure 6d. It must be

Table 4. Summary of Inversion Set

Rupture Velocity, m/s	Risetime, s	Variance Reduction, %
2500	1.2	63.16
2700	1.2	65.10
2800	1.2	65.34
2900	1.2	64.72
3000	1.2	62.72
2800	2.7	62.96
2800	2.2	64.59
2800	1.7	61.95
2800	1.2	65.34
2800	0.9	64.90

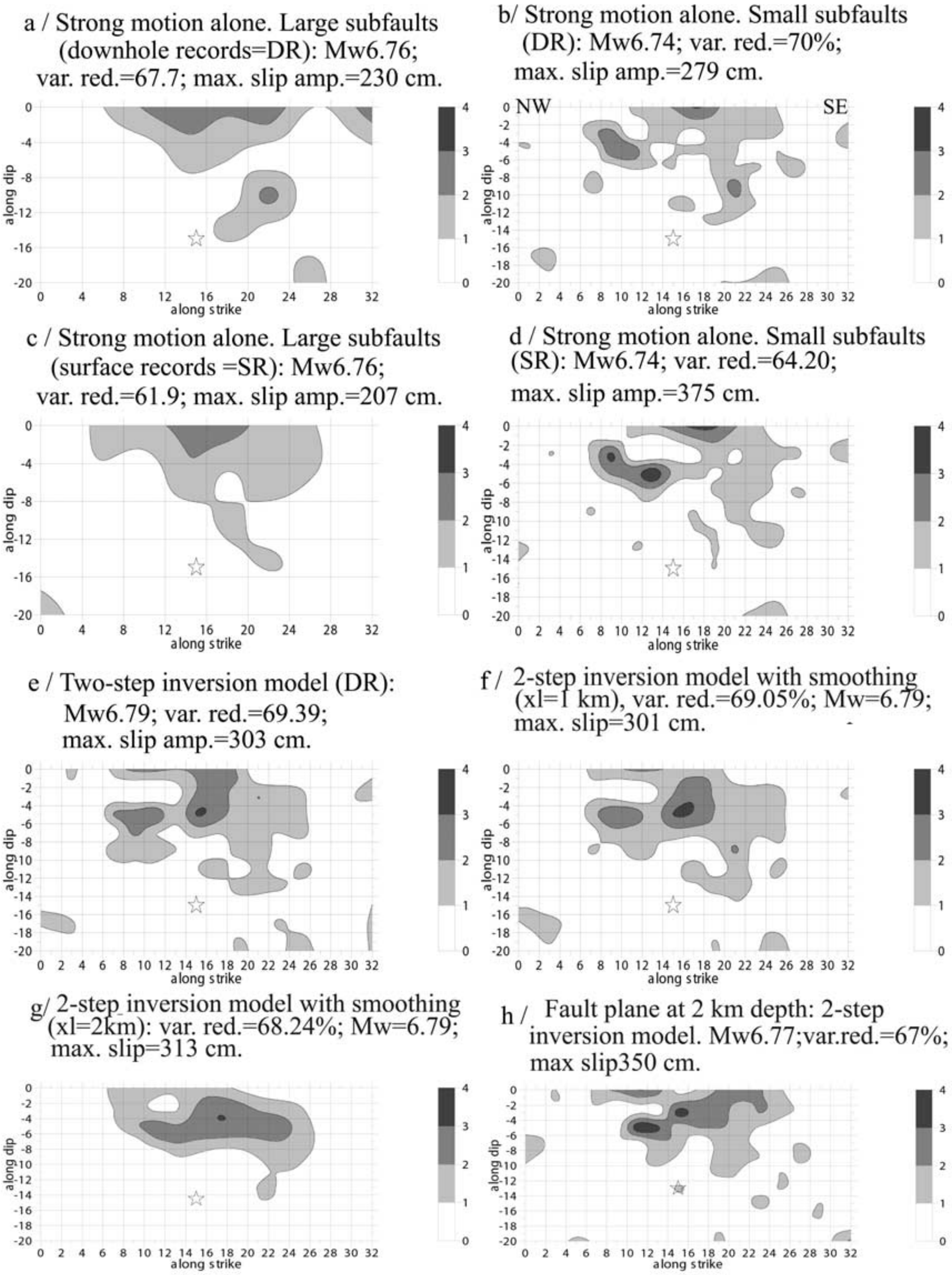

a / Strong motion alone. Large subfaults (downhole records=DR): Mw6.76; var. red.=67.7; max. slip amp.=230 cm.

b/ Strong motion alone. Small subfaults (DR): Mw6.74; var. red.=70%; max. slip amp.=279 cm.

c / Strong motion alone. Large subfaults (surface records =SR): Mw6.76; var. red.=61.9; max. slip amp.=207 cm.

d / Strong motion alone. Small subfaults (SR): Mw6.74; var. red.=64.20; max. slip amp.=375 cm.

e / Two-step inversion model (DR): Mw6.79; var. red.=69.39; max. slip amp.=303 cm.

f / 2-step inversion model with smoothing (xl=1 km), var. red.=69.05%; Mw=6.79; max. slip=301 cm.

g/ 2-step inversion model with smoothing (xl=2km): var. red.=68.24%; Mw=6.79; max. slip=313 cm.

h / Fault plane at 2 km depth: 2-step inversion model. Mw6.77;var.red.=67%; max slip350 cm.

Figure 6. Different slip distribution models derived in this study. Contour interval is 1 m. Top left corner is the NW direction, and top right corner is the SE direction. Star is the hypocenter.

compared with the results obtained with borehole records on Figure 6b. The global shape of the asperity is the same but again the maximum slip amplitude is greater (375 cm). The seismic moment is very similar to the one inferred from borehole records (M_w = 6.74). Note that the use of contaminated surface data in this study slightly decreases the variance reduction (about 2–6%). Consequently, for the following final inversion runs we will use only borehole records and small subfault parameterization.

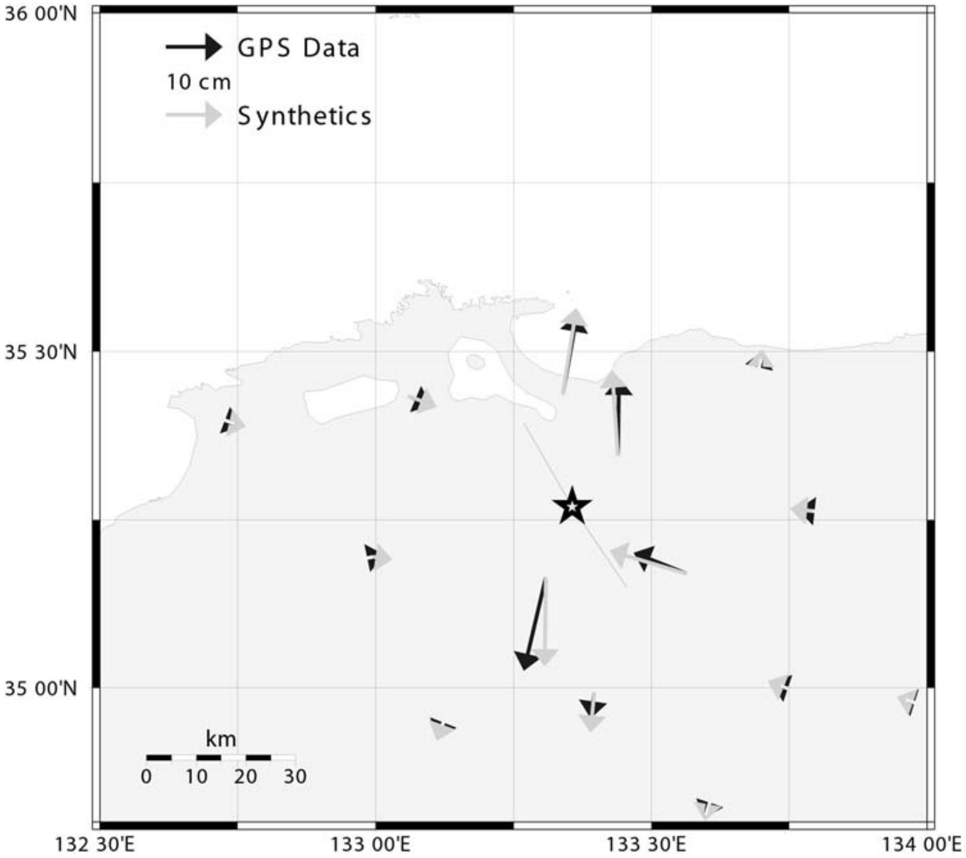

Figure 7. Observed (black) GPS data. Synthetics (gray) GPS horizontal vector displacement calculated using as input for the direct modeling the two-step inverted model with fault plane at 0.5 km depth.

4.4. Two-Step Inversion With Slip Allowed at the Surface

[27] To improve the quality of the inversion, *Hernandez et al.* [1999] proposed to use a two-step inversion. It uses the information obtained from the inversion of geodetic data (slip distribution and uncertainties) to build an a priori model for the strong motion inversion. We applied the two step inversion without a priori smoothing constraint to borehole records.

[28] The slip distribution is presented in Figure 6e. The variance reduction is 69.4%. The solution obtained has a large asperity with a maximum amplitude of slip equal to 303 cm located above the hypocenter at about 5 km depth. This model yields a seismic moment of 1.7×10^{19} N m corresponding to a moment magnitude of 6.79. Note that applying a 1000 m correlation length smoothing reduces the slip at the top of the fault from about 3 m to about 2 m (Figure 6f) and the shape of the asperity does not change. Applying a 2 km correlation length smoothing (Figure 6g), the maximum slip lies on a larger area and the variance reduction slightly decreases. The moment magnitude does not change.

4.5. Two-Step Inversion Model With No Slip at the Surface

[29] The two-step inversion with a fault reaching the surface results in large slip (larger than 2 m) for the shallow subfaults. This shallow slip is not in agreement with geological observations, which indicate that slip did not reach the surface. In order to constrain the depth of the rupture top, we performed a two-step inversion where the fault model is shifted downward by 2 km, keeping constant the number of parameters. The result of the GPS data inversion (first step) shows one large asperity located above the hypocenter, in agreement with the result in Figure 5a. This slip model is then used to invert strong motion records (second step). The results are shown in Figure 6h. The peak slip is 350 cm. The variance reduction is about 67%, which is slightly less than the one associated to the previous model (with a shallower slip). The seismic moment is 15.9×10^{18} N m corresponding to $M_w = 6.77$. We performed two other inversions giving different depths to the fault top (1 km, 0.5 km). Shallow faults show the highest variance reduction. These tests confirm that slip actually occurred at very shallow depths. We therefore consider the fault with top at 0.5 km our preferred model since it is in agreement simultaneously with geodetic and seismological data and also geological observations. The fit between the synthetics generated by this model (a two-step inverted model) and the GPS observed data is shown in Figure 7.

[30] Figure 8 is a comparison of the observed and the calculated strong motions using the model with fault plane top at 0.5 km depth. In general the waveforms are well matched (68.2% variance reduction). In Figure 9 we

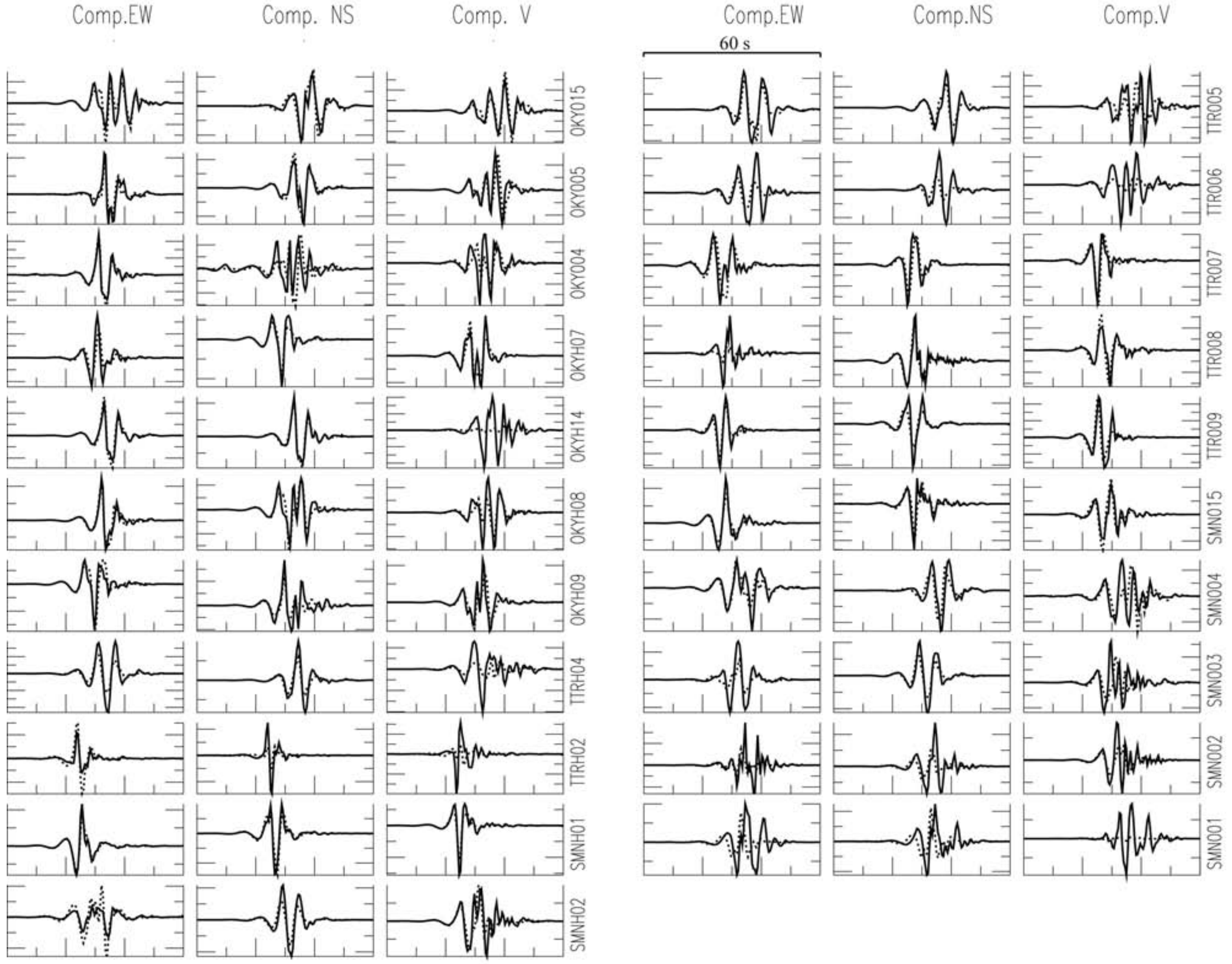

Figure 8. Observed (solid line) and synthetic (dashed line) strong motion records. Original acceleration waveforms are band passed in the frequency range 0.1–1.0 Hz using a two-pole Butterworth filter applied forward and backward then doubly integrated to obtain the particle displacement. The vertical components of some strong ground motion are not used in the inversion (see Table 1) because of incomplete knowledge of the seismic velocity structure. All components (synthetics and observed) at each station are normalized with the data peak amplitude. Each pair of observed and calculated seismograms is plotted at the same amplitude scale.

plotted for each frequency the variance reduction between data and synthetics for all the stations. The fit in the frequency range [0.1–0.3] Hz exceeds 40%, and over the range 0.3–0.5 Hz it is greater than 30%. Figure 9 indicates the limited frequency band in which the rupture model is actually resolved. We interpret the upper frequency limit as the limit of applicability of the simplified layered crustal model employed to calculate the Green's functions.

[31] The result of the three inverted parameters (slip amplitude, rupture time, and risetime) of our preferred model (at 0.5 km depth) is shown in Figure 10, and the evolution of rupture is displayed in Figure 11. The main asperity breaks 1 s after the first break in the north direction then grows first upward and then parallel to the Earth's surface. The total rupture duration is about 8 s. Figure 11 shows that the significant slip (>1 m) occurs away from the hypocenter and propagates laterally. The maximum of the

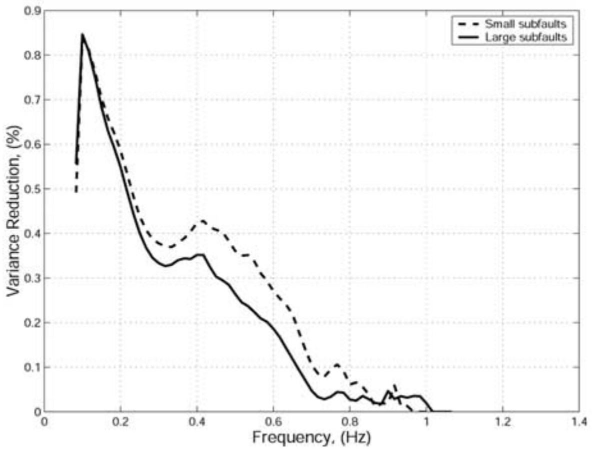

Figure 9. Variance reduction between data and synthetic computed for all the stations for each frequency. It is shown that the data are fitted on the frequency range 0.1–0.3 Hz.

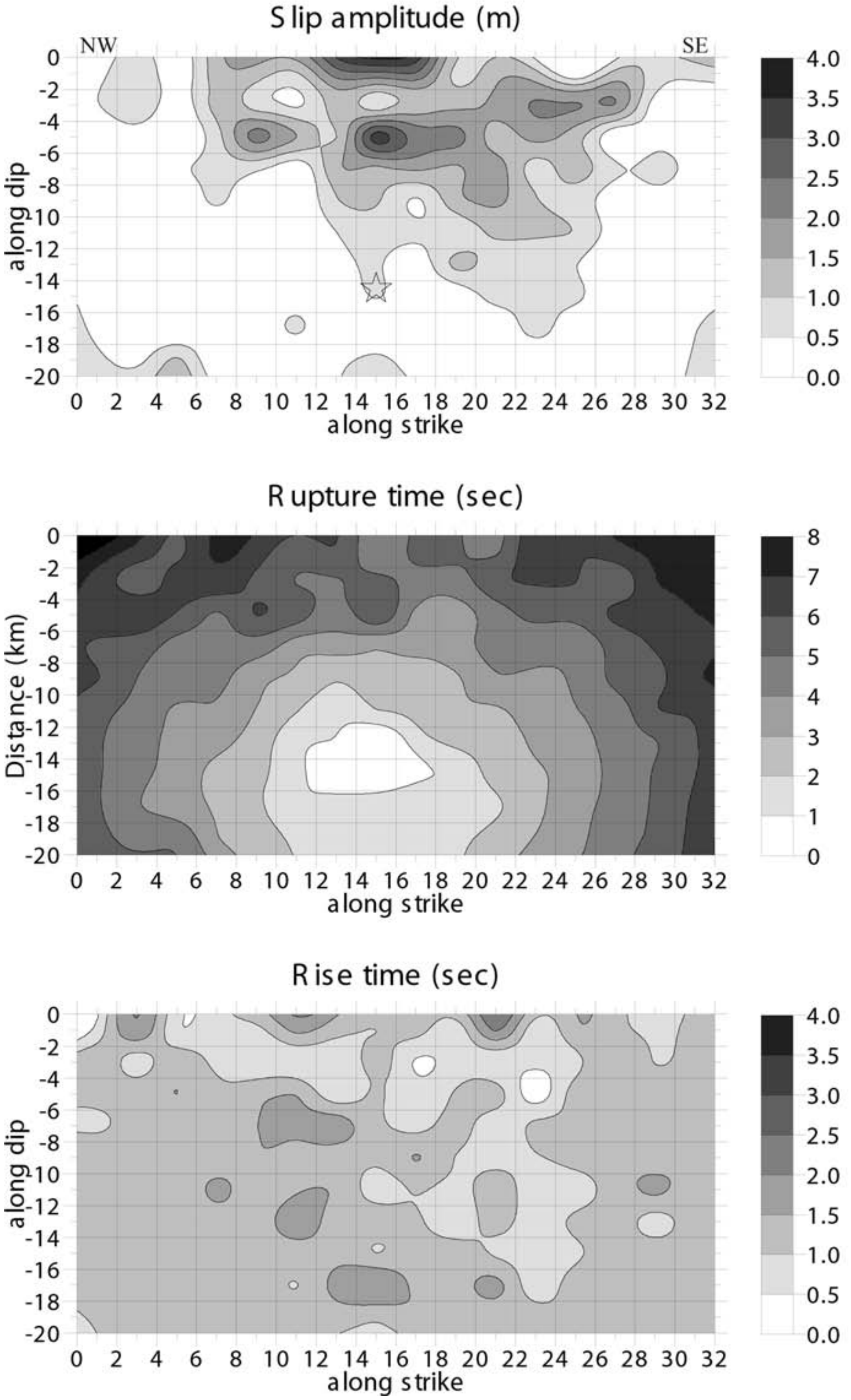

Figure 10. Three parameters inversion results using the geometry fault shown in Figure 4 (right) and borehole records. (top) Recovered slip distribution on the fault plane, (middle) rupture front evolution, and (bottom) slip duration.

slip takes place at about 5 km depth. During the earthquake, the region at depth, west of the hypocenter does not slip.

5. Discussion and Conclusions

[32] Uncertainties exist in kinematic source models deduced from inversions but these are difficult to quantify since they have a variety of origins (e.g., model parameterization, data weighting, and inversion procedure). The knowledge of the nonuniqueness in kinematic parameters is important because these kinematic solutions are often used to determine the dynamic source parameters of earthquakes (i.e., stress drop and strength distribution) and for prediction of strong ground motion. In our study we have

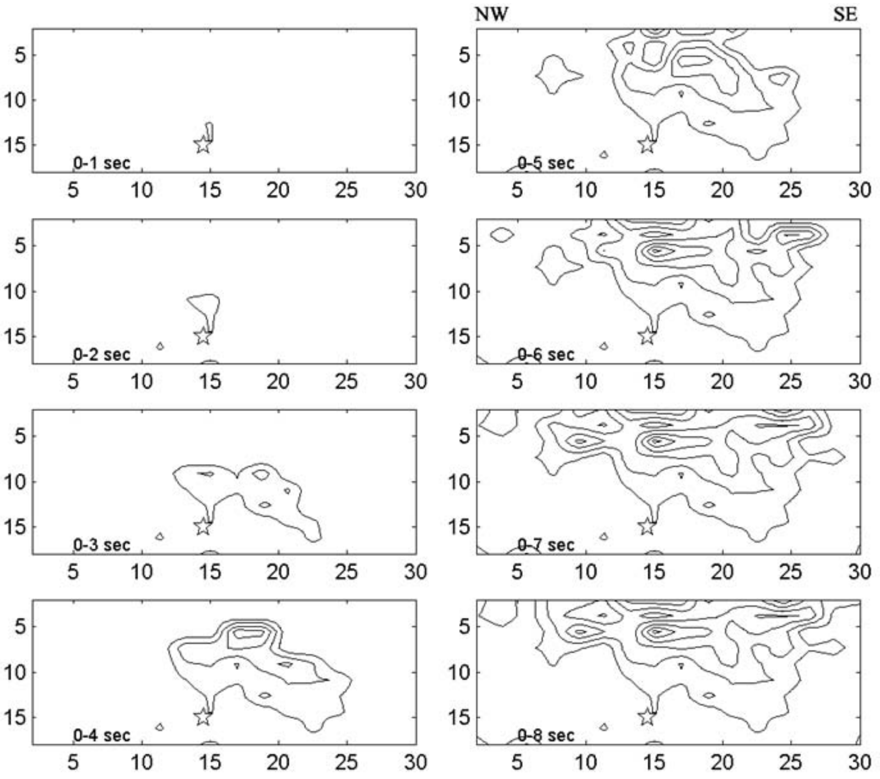

Figure 11. Spatiotemporal slip evolution of the preferred rupture model. Contour intervals are equal to 0.5 m.

used borehole and surface records of KIK-net network to compare borehole with surface ground motions. At some stations there is a significant difference between the two records. We noticed that, systematically the variance reduction decreases using surface data, the general shape of the mean asperity remains unchanged, and the seismic moment also does not change significantly.

[33] The maximum slip amplitude and its position change whether using small or large subfaults. The one-block asperity at the vertical of the hypocenter, found with large subfault model, consists of a merger of several small asperities of comparable slip amplitude revealed when using small size subfault parameterization.

[34] For earthquakes occurring on hidden faults, it is possible to determine the location and orientation of the fault plane using the 3-D aftershock distribution. Seismological stations close to the rupture area also help to better constrain the fault plane orientation. We have seen in this study how change in the strike direction of the southern part of the fault plane strongly affects the fit at station TTRH02.

[35] The slip distributions we obtain agree with those of *Iwata and Sekiguchi* [2002] and Y. Yagi and M. Kikuchi

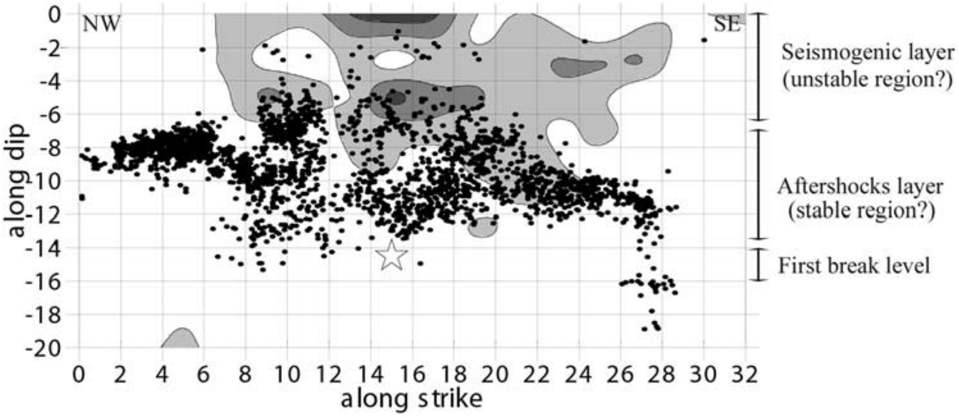

Figure 12. Relocated aftershocks (1 km on both sides of our fault plane) plotted over our slip map. The contour interval for the slip distribution is 1.0 m. The star indicates the main shock hypocenter. The perpendicular plan (NW of epicenter) highlighted by the aftershocks distribution (see Figure 1) could play a role in stopping the rupture propagation.

Table 5. Slip Model Properties Comparison

Parameters	*Somerville et al.* [1999][a]	This Study
Risetime, s	1.4	1.2
Average slip, cm	75	62
Largest asperity, km^2	102	108

[a] With a moment of about 1.5 × 10^{19} N m.

(Source rupture process of the Tottori-ken Seibu earthquake of Oct. 6, 2000, unpublished manuscript, 2000) even though the fault parameterization and inversion schemes are very different. All three models show that slip propagated in the SE direction from the epicenter. We selected the relocated aftershocks of *Fukuyama et al.* [2003] (in a 1 km band width on both sides of the fault plane) and plotted them on our slip map (Figure 12). The majority of aftershocks occurred in the middle of the fault at about 6–12 km depth. This suggests that the region between the hypocenter and the large asperity sustained a high stress level without large coseismic slip. Numerical experiments done by *Das and Aki* [1977] and *Mikumo and Miyatake* [1978] showed that a rupture can propagate leaving behind it unbroken barriers [*Aki*, 1984]. A striking feature of Figure 12 is that the crust exhibits a depth-varying behavior. Failure begins at about 15 km depth. Then we find above the aftershocks (perhaps a barrier or a "stable" slip area), the asperity layer (seismogenic or unstable layer) and finally the superficial layer where neither slip (according to geological observations) nor aftershocks are observed. We report here two analogies between the 2000 Tottori and the 1979 Imperial Valley earthquakes: (1) Negative values of the dynamic stress drop near the free surface (*Dalguer et al.* [2002] for Tottori and *Quin* [1990] for Imperial Valley) and (2) the lack at shallow depth of microseismicity (*Fukuyama et al.* [2003] for Tottori and *Doser and Kanamori* [1986] and *Mendoza and Hartzell* [1988b] for Imperial Valley). Borehole data available in the epicentral region (e.g., TTRH02, SMNH01, TTR008, and SMN015) show that superficial sedimentary layers are thin (about 15 m). These boreholes show rock materials (either granite or basalt) at depths between 15 and 100 m. We have no information for depths greater than 100 m. This relatively thin layer (15 m) of sediments in Tottori cannot be put forward to explain these two phenomena as it has been suggested for the Imperial Valley earthquake.

[36] According to the results of *Fukuyama et al.* [2003] the earliest aftershocks are concentrated in the SE part of the seismogenic region. The NW part was activated later with a large number of events concentrated in the region that did not slip during the main shock. The details of the horizontal distribution of the aftershocks indicates the existence of at least one plane NW of the epicenter almost perpendicular to the fault plane activated during the main shock. This plane is located where the dynamic rupture propagation in the NW direction stops. In this region, strongly loaded by the main shock, aftershocks are more abundant. This area is what *Boatwright and Cocco* [1996] called a slightly velocity-weakening frictional behavior.

[37] The tests with different fault depths performed above (section 4.5) show that when slip is allowed to occur close to the surface, the variance reduction is increased. These tests confirm that slip actually occurred at shallow depth. Such shallow rupture with no surface rupture has been observed previously (e.g., Morgan Hill, in 1984; northern part of the Kobe earthquake, in 1995). This study of the 2000 Tottori earthquake benefits from a larger number of observations and definitely shows that large shallow asperities can occur without any surface break. This suggests that large strike slip earthquakes may have occurred in the past without cutting the surface. This phenomenon could complicate the interpretation of paleoseismological data. Return periods of damaging earthquakes could be overestimated if such shallow earthquakes with no surface rupture (blind fault) occurred. A more comprehensive study, beyond the scope of this investigation, should be performed in order to understand the geological and mechanical parameters that control the absence of surface slip of such shallow earthquakes.

[38] Finite sources simulations are used in seismic hazard studies to evaluate potential strong ground motion near faults. Empirical relationships have been proposed recently to evaluate the representative rupture properties of such simulations. *Somerville et al.* [1999] have proposed an empirical study where they quantify the asperities of 15 earthquakes and examined their average characteristics. Table 5 shows that the empirical relationships of *Somerville et al.* [1999] also predict the main features of the 2000 Tottori earthquake for a moment release rate of about 1.5 × 10^{19} N m. However, the studies of systematic features of asperities (e.g., rupture area, average slip) and their scaling with seismic moment for strong ground motion prediction do not commonly consider the relative asperity position on the fault plane. Our study shows that shallow and elongated asperities have to be taken into account in such simulations. Indeed, large asperities at shallow depth should have a significant contribution to ground motion. Such models, which could have been considered as extreme or unrealistic before the 2000 Tottori earthquake, are useful to capture the epistemic uncertainty of ground prediction or to evaluate maximum ground motion [*Bommer et al.*, 2004].

[39] **Acknowledgments.** We thank Tomotaka Iwata for his precious advice regarding the strong motion records and Takeshi Sagiya for providing GPS data. We are grateful to Eichi Fukuyama and William Ellsworth, who kindly provided the catalog of aftershocks. Joan Gomberg, Honn Kao, and an anonymous reviewer made a many helpful suggestions on the paper. Comments by Michel Bouchon and Christophe Voisin helped to improve the first version of the manuscript. Thanks to KIK-net and K-net for providing strong motion data. Some figures are made using Generic Mapping Tools (GMT).

References

Aki, K. (1984), Asperities, barriers, characteristic earthquakes and strong motion prediction, *J. Geophys. Res.*, *89*, 5867–5872.

Beroza, G. C., and P. Spudich (1988), Linearized inversion for fault rupture behavior: Application for the 1984 Morgan Hill, California, earthquake, *J. Geophys. Res.*, *93*, 6275–6296.

Boatwright, J., and M. Cocco (1996), Frictional constraints on crustal faulting, *J. Geophys. Res.*, *101*, 13,895–13,910.

Bommer, J. J., et al. (2004), The challenge of defining upper bounds on earthquake ground motions, *Seismol. Res. Lett.*, *75*(1), 31.

Bonilla, L. F., F. Cotton, and R. J. Archuleta (2003), Quelques renseignements sur les effets de site non-linéaires en utilisant des données de forage: La base de mouvements forts KIK-Net au Japon (title in French, paper in English), paper presented at VIe Colloque National AFPS, Ecole Polytech., Palaiseau, France.

Campillo, M., and R. J. Archuleta (1993), A rupture model for the 28 June 1992 M7.4 Landers, California, earthquake, *Geophys. Res. Lett.*, *20*, 647–650.

Campillo, M., and I. R. Ionescu (1997), Initiation of antiplane shear instability under slip-dependent friction, *J. Geophys. Res.*, *102*, 20,363–20,371.

Cattin, R., P. Briole, H. Lyon-Caen, P. Bernard, and P. Pinettes (1999), Effects of superficial layers on coseismic displacements for a dip-slip fault and geophysical implications, *Geophys. J. Int.*, *137*, 149–158.

Cotton, F., and M. Campillo (1995), Inversion of strong ground motion in the frequency domain: Application to the 1992 Landers, California, earthquake, *J. Geophys. Res.*, *100*, 3961–3975.

Coutant, O. (1989), Program of numerical simulation AXITRA (in French), research report, Lab. de Geophys. Interne et Tectonophys., Grenoble, France.

Dalguer, L. A., K. Irikura, W. Zhang, and J. D. Riera (2002), Distribution of dynamic and static stress changes during 2000 Tottori (Japan) earthquake: Brief interpretation of the earthquake sequences; foreshocks, mainshock and aftershocks, *Geophys. Res. Lett.*, *29*(16), 1758, doi:10.1029/2001GL014333.

Das, S., and K. Aki (1977), Fault planes with barriers: A versatile earthquake model, *J. Geophys. Res.*, *82*, 5648–5670.

Das, S., and B. V. Kostrov (1990), Inversion of seismic slip rate history and distribution with stabilizing constraints: Application to the 1986 Andreanof Islands earthquake, *J. Geophys. Res.*, *95*, 6899–6913.

Das, S., and B. V. Kostrov (1994), Diversity of solutions of the problem of earthquake faulting inversion; application to *SH* waves for the great 1989 Macquarie Ridge earthquake, *Phys. Earth Planet. Inter.*, *85*, 293–318.

Das, S., and P. Suhadolc (1996), On the inverse problem for earthquake rupture: The Haskell-type source model, *J. Geophys. Res.*, *101*, 5725–5738.

Doser, D. I., and H. Kanamori (1986), Depth of seismicity in the Imperial Valley region (1977–1983) and its relationship to heat flow, crustal structure, and the October 15, 1979, earthquake, *J. Geophys. Res.*, *91*, 675–688.

Ellsworth, W. L., and C. G. Beroza (1995), Seismic evidence for an earthquake nucleation phase, *Science*, *268*, 851–855.

Freymueller, J. T., N. E. King, and P. Segall (1994), The co-seismic slip distribution of the Landers earthquake, *Bull. Seismol. Soc. Am.*, *84*, 646–659.

Fukuyama, E., W. L. Ellsworth, F. Waldhauser, and A. Kubo (2003), Detailed fault structure of the 2000 western Tottori, Japan, earthquake sequence, *Bull. Seismol. Soc. Am.*, *93*, 1468–1478.

Hartzell, S. H., and T. H. Heaton (1983), Inversion of strong ground motion and teleseismic waveform data for the fault rupture history of the 1979 Imperial Valley, California earthquake, *Bull. Seismol. Soc. Am.*, *73*, 1553–1583.

Hartzell, S. H., and T. H. Heaton (1986), Rupture history of the 1984 Morgan Hill, California, earthquake from the inversion of strong motion records, *Bull. Seismol. Soc. Am.*, *76*, 649–674.

Hartzell, S. H., and C. Langer (1993), Importance of model parameterization in finite fault inversions; application to the 1974 M_w8.0 Peru earthquake, *J. Geophys. Res.*, *98*, 22,123–22,134.

Hartzell, S. H., and P. C. Liu (1995), Determination of earthquake source parameters using a hybrid global search algorithm, *Bull. Seismol. Soc. Am.*, *85*, 516–524.

Hartzell, S. H., and P. C. Liu (1996), Calculation of earthquake rupture histories using a hybrid global search algorithm: Application to the 1992 Landers, California, earthquake, *Phys. Earth Planet. Inter.*, *95*, 79–99.

Hartzell, S. H., S. S. Gordon, and C. Mendoza (1991), Comparison of L1 and L2 norms in a teleseismic waveform inversion for the slip history of the Loma Prieta, California, earthquake, *Bull. Seismol. Soc. Am.*, *81*, 1518–1539.

Hernandez, B., F. Cotton, and M. Campillo (1999), Contribution of radar interferometry to a two-step inversion of the kinematic process of the 1992 Landers earthquake, *J. Geophys. Res.*, *104*, 13,083–13,100.

Iio, Y. (1992), Slow initial phase of the *p*-wave velocity pulse generated by microearthquakes, *Geophys. Res. Lett.*, *19*, 477–480.

Iwata, T., and H. Sekiguchi (2002), Source process and near-source ground motion during the 2000 Tottori-ken Seibu earthquake, paper presented at 11th Japan Earthquake Engineering Symposium, Earthquake Eng. Res. Liaison Comm., Sci. Counc. of Jpn., Tokyo.

Ji, C., D. J. Wald, and D. V. Helmberger (2002), Source description of the 1999 Hector Mine, California, earthquake, Part II: Complexity of slip history, *Bull. Seismol. Soc. Am.*, *92*, 1208–1226.

Kagawa, T., K. Irikura, and P. G. Somerville (2004), Differences in ground motion and fault rupture process between the surface and buried rupture earthquakes, *Earth Planets Space*, *56*(1), 3–14.

Liu, P., and R. J. Archuleta (2004), A new nonlinear finite fault inversion with three-dimensional Green's functions: Application to the 1989 Loma Prieta, California, earthquake, *J. Geophys. Res.*, *109*, B02318, doi:10.1029/2003JB002625.

Mendoza, C., and S. H. Hartzell (1988a), Inversion for slip distribution using teleseismic P waveforms: North Palm Springs, Borah Peak, and Michoacan earthquakes, *Bull. Seismol. Soc. Am.*, *78*, 1092–1111.

Mendoza, C., and S. H. Hartzell (1988b), Aftershock patterns and main shock faulting, *Bull. Seismol. Soc. Am.*, *78*, 1438–1449.

Mendoza, C., and S. H. Hartzell (1989), Slip distribution of the 19 September 1985 Michoacan, Mexico, earthquake: Near-source and teleseismic constraints, *Bull. Seismol. Soc. Am.*, *79*, 655–669.

Mikumo, T., and T. Miyatake (1978), Dynamical rupture process on a three-dimensional fault with non-uniform frictions, and near-field seismic waves, *Geophys. J. R. Astron. Soc.*, *54*, 417–438.

Nakayama, W., and M. Takeo (1997), Slip history of the 1994 Sanriku-Haruka-Oki, Japan, earthquake deduced from strong motion data, *Bull. Seismol. Soc. Am.*, *87*, 918–931.

Okada, Y. (1985), Surface deformation due to shear and tensile faults in a half-space, *Bull. Seismol. Soc. Am.*, *75*, 1135–1154.

Olson, A. H., and J. G. Anderson (1988), Implications of frequency-domain inversion of earthquake ground motions for resolving the space-time dependence of slip on an extended fault, *Geophys. J.*, *94*, 443–455.

Olson, A. H., and R. J. Apsel (1982), Finite fault and inverse theory with applications to the 1979 Imperial Valley earthquake, *Bull. Seismol. Soc. Am.*, *72*, 1969–2001.

Peltzer, G., F. Crampe, and P. Rosen (2001), The M_w 7.1, Hector Mine, California earthquake: Surface rupture, surface displacement field, and fault slip solution from ERS SAR data, *C. R. Acad. Sci.*, *333*, 545–555.

Peyrat, S., and K. B. Olsen (2004), Nonlinear dynamic rupture inversion of the 2000 Western Tottori, Japan, earthquake, *Geophys. Res. Lett.*, *31*, L05604, doi:10.1029/2003GL019058.

Quin, H. (1990), Dynamic stress drop and rupture dynamics of the October 15, 1979 Imperial Valley, California earthquake, *Tectonophysics*, *175*, 93–117.

Sagiya, T., T. Nishimura, Y. Hatanaka, E. Fukuyama, and W. L. Ellsworth (2002), Crustal movements associated with the 2000 western Tottori earthquake and its fault models (in Japanese with English abstract), *J. Seismol. Soc. Am.*, *54*, 523–534.

Savage, J. C. (1998), Displacement field for an edge dislocation in a layered half-space, *J. Geophys. Res.*, *103*, 2439–2446.

Sekiguchi, H., K. Irikura, and T. Iwata (2000), Fault geometry at the rupture termination of the 1995 Hyogo-ken Nanbu earthquake, *Bull. Seismol. Soc. Am.*, *90*, 117–133.

Somerville, P., K. Irikura, R. Graves, S. Sawada, D. J. Wald, N. Abrahamson, Y. Iwasaki, T. Kagawa, N. Smith, and A. Kowada (1999), Characterizing crustal earthquake slip models for the prediction of strong ground motion, *Seismol. Res. Lett.*, *70*, 59–80.

Takeo, M. (1987), An inversion method to analyze the rupture process of earthquakes using near-field seismograms, *Bull. Seismol. Soc. Am.*, *77*, 490–513.

Tarantola, A. (1987), *Inverse Problem Theory*, Elsevier, New York.

Tarantola, A., and B. Valette (1982), Generalized nonlinear inverse problems solved using the least squares criterion, *Rev. Geophys.*, *20*, 219–232.

Uhrhammer, R., and B. A. Bolt (1991), The seismic magnitude of the 1989 Loma Prieta mainshock determined from strong motion records, *Bull. Seismol. Soc. Am.*, *81*, 1511–1517.

Waldhauser, F., and W. L. Ellsworth (2000), A double-difference earthquake location algorithm: Method and application to the northern Hayward fault, *Bull. Seismol. Soc. Am.*, *90*, 1353–1368.

M. Campillo, F. Cotton, and F. Semmane, Laboratoire de Géophysique Interne et Tectonophysique, Université Joseph Fourier, BP53, F-38041 Grenoble, France. (campillo@obs.ujf-grenoble.fr; fcotton@obs.ujf-grenoble.fr; fsemmane@obs.ujf-grenoble.fr)

GEOPHYSICAL RESEARCH LETTERS, VOL. 33, L20310, doi:10.1029/2006GL027193, 2006

Displacement field and slip distribution of the 2005 Kashmir earthquake from SAR imagery

E. Pathier,[1] E. J. Fielding,[2] T. J. Wright,[1] R. Walker,[1] B. E. Parsons,[1] and S. Hensley[2]

Received 10 June 2006; revised 9 August 2006; accepted 14 September 2006; published 24 October 2006.

[1] The 8th October 2005 Kashmir Earthquake M_w 7.6 involved primarily thrust motion on a NE-dipping fault. Sub-pixel correlation of ENVISAT SAR images gives the location of the 80 km-long fault trace (within 300–800 m) and a 3D surface displacement field with a sub-metric accuracy covering the whole epicentral area. The slip distribution inverted using elastic dislocation models indicates that slip occurs mainly in the upper 10 km, between the cities of Muzaffarabad and Balakot. The rupture reached the surface in several places. In the hanging wall, horizontal motions show rotation from pure thrust to oblique right-lateral motion that are not observed in the footwall. A segmentation of the fault near Muzaffarabad is also suggested. North of the city of Balakot, slip decreases dramatically, but a diffuse zone of mainly vertical surface displacements, which could be post-seismic, exists further north, where most of the aftershocks occur, aligned along the NW-SE Indus-Kohistan Seismic Zone. **Citation:** Pathier, E., E. J. Fielding, T. J. Wright, R. Walker, B. E. Parsons, and S. Hensley (2006), Displacement field and slip distribution of the 2005 Kashmir earthquake from SAR imagery, *Geophys. Res. Lett.*, *33*, L20310, doi:10.1029/2006GL027193.

1. Introduction

[2] On 8th October 2005, a M_w 7.6 earthquake occurred in northern Pakistan in the mountainous Kashmir region (Figure 1) causing more than 80,000 deaths. The Kashmir earthquake (also called the Pakistan Earthquake) is the latest in a series of large historical earthquakes located along the southern front of the Himalaya [*Bilham*, 2004]. The moment tensor solutions from Harvard and the USGS National Earthquake Information Center (NEIC) were available on the web a few hours after the earthquake, rapidly followed by the first slip models from seismological data (e.g., Martin Vallée, http://www-geoazur.unice.fr/SEISME/PAKISTAN081005/note1.html; Yuji Yagi, http://www.geo.tsukuba.ac.jp/press_HP/yagi/EQ/2005Pakistan), indicating a NE-dipping fault with primarily thrust motion. On 2 November, we made available a more precise fault location established from sub-pixel correlation of Synthetic Aperture Radar (SAR) images (http://comet.nerc.ac.uk/news_kashmir.html). This preliminary analysis was done within a few days after the first suitable post-event ENVISAT SAR acquisition, thanks to efforts of the European Space Agency (ESA) who made these data available as soon as possible. Using a similar approach, *Fujiwara et al.* [2006] showed that location of the highest displacement gradient match pre-existing fault traces previously mapped by *Nakata et al.* [1991].

[3] First analyses from seismology and remote-sensing suggested a large amount of shallow slip, locally in excess of 6 m, explaining the intensity of damage and number of casualties, and revealed heterogeneity in the slip distribution and possibly segmentation of the fault. The fault is located at the western end of the Himalaya, at the Hazara Syntaxis, where an old major geologic boundary of the range, the Main Boundary Thrust (MBT), bends around by 180°. The fault trace runs from Bagh to Balakot via the Jhelum river valley and the city of Muzaffarabad (Figure 1). In its northern part, it follows the MBT trace along the south-western boundary of the Hazara syntaxis. The fault is also aligned with a zone of seismicity recorded by the Tarbela Seismic Network in 1973–1976, called the Indus-Kohistan Seismic Zone (IKSZ) that extends some 100 km to the NW of Balakot and has been proposed to be a NE-dipping ramp [*Armbruster et al.*, 1978]. *Parsons et al.* [2006] point out that, due to static stress changes, there is an increased stress on the IKSZ portion close to the fault, where most of the aftershocks occur. Possible structural controls over the slip distribution remain to be investigated. In this paper, we present a more extensive analysis of the surface deformation including new SAR data acquired with different geometries. These data allow us to construct a three-dimensional surface displacement field caused by the earthquake and to invert for the slip distribution on the fault plane using a homogeneous linear elastic model.

2. SAR Offset Data

[4] Near global coverage and all-weather, day-night capability make SAR data suitable for remote-sensing analysis of natural hazards. In this study, we used ENVISAT ASAR data (Table 1) because they have extensive coverage, high spatial resolution and the existing archive of previous acquisitions allows selection of pairs of pre- and post-event images with suitable baselines (distance separating the two orbits of a pair of images) and time interval. These last two parameters should be as small as possible when measuring coseismic displacements caused by earthquakes with SAR imagery. As shown in Figure 2, the epicentral area is well covered by three selected tracks in ascending and descending modes (i.e., satellite flying from south to north or from north to south, respectively).

[5] To measure surface deformation using SAR imagery, two main techniques are available: interferometric SAR

---

[1] Centre for the Observation and Modelling of Earthquakes and Tectonics, Department of Earth Sciences, University of Oxford, Oxford, UK.

[2] Jet Propulsion Laboratory, California Institute of Technology, Pasadena, California, USA.

0094-8276/06/2006GL027193$05.00

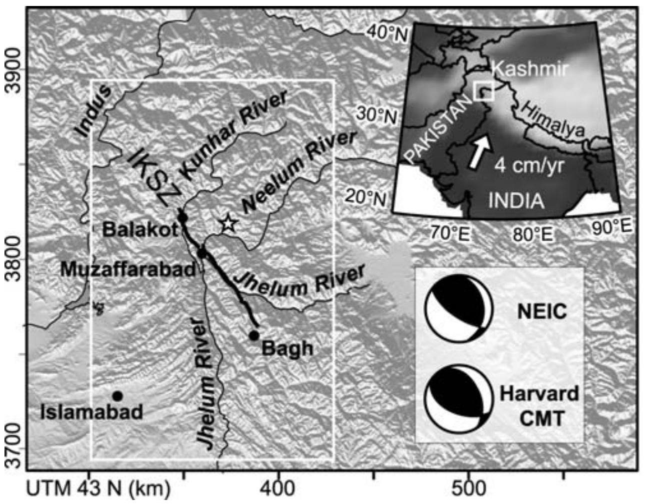

Figure 1. Inset: DEM showing the study area located in Kashmir at the Western Syntaxis of the Himalayan range. Main figure: shaded DEM of the Kashmir region. The star is the epicenter of the 8 October 2005 earthquake from NEIC. At about 100 km from Islamabad, the fault rupture (thick black line) runs from Balakot to Bagh via Muzaffarabad, and is aligned with the Indus-Kohistan Seismic Zone (IKSZ). Thin black lines are rivers and the white frame shows the extent of Figure 2.

(InSAR) [e.g., *Rosen et al.*, 2000] and sub-pixel image correlation [e.g., *Michel et al.*, 1999]. For the Kashmir earthquake, conventional InSAR, the most accurate technique (centimetric), can only give reliable measurement on a narrow band of the footwall in the Jhelum valley and in some far field areas where temporal and geometrical signal decorrelation (due to high topography and steep slopes) and decorrelation due to the large earthquake deformation itself are less severe. Although less accurate (∼0.2–1.0 m), sub-pixel SAR image correlation is more robust for mountainous environments such as in Kashmir. This technique is based on measurement of line and column offset between two amplitude images. At the end of the process, two maps can be constructed for each track (Figure 2), giving two components of the displacements that occurs between the two acquisitions: one parallel to the satellite track (azimuth offset) and the other along its line of sight (range offset). Offsets have been computed using the Jet Propulsion Laboratory/California Institute of Technology ROI_pac software [*Rosen et al.*, 2004], using overlapping matching windows of 64 by 64 pixels (i.e., ∼300 m by ∼500 m in azimuth and range direction respectively) applied to full resolution images (4 m in azimuth, 8 m in slant range) with steps of 8 pixels in range and 16 in azimuth. Formal errors of the offset measurements are estimated from the width of the peak in the cross-correlation surface for each match. It is only a lower bound on the total error, but provides a criterion for discarding poor matches. Offsets with a formal error (1 σ) larger than 0.7 m and with a magnitude larger than 8 m are removed. These thresholds are based on a qualitative analysis, trying to reduce noise in the data while keeping a good data coverage. A weighted averaging procedure that uses the inverse of the variance of each match as a weighting is applied with a window of 5 samples in range by 11 samples in azimuth. We correct estimated offsets for image distortions due to the fact that images are not acquired exactly from the same point of view. For range offsets, distortions have been modeled using a DEM and precise orbital data, and we correct for a constant shift using far field data where we assumed no coseismic displacement. For azimuth offsets, we only apply long-wavelength flattening using a quadratic surface fit. Results are geocoded at 120 m resolution in UTM zone 43 using ROI_pac and a SRTM DEM.

[6] A clear deformation signal appears in the epicentral area (see Figure 2). The fault line oriented NW-SE is very straight in its southern portion. The largest displacements occur to the east of the fault on the hanging wall around the slightly curved north portion where the azimuth displacement shows a larger lobe than the range one. In the range offset data of ascending track 270 (data set with highest SNR), north of UTM northing 3830 km, a more diffuse zone of deformation is visible. Associated formal errors are about 0.35 m in average but vary with the geometry of acquisition, and with the topography and slopes (see auxiliary material Figure S1[1]). On average, due to its lower and smoother topography, footwall measurement are more accurate (∼0.30 m) than the hanging wall ones (∼0.39 m).

3. 3D Surface Displacements Map

[7] Each offset map is the projection of the full 3D displacement field in the range or azimuth direction. Where three or more such scalar components are available, it is possible to solve for the full 3D displacements field (i.e., the East, North and Up components). The resulting map (see Figure 3a) is easier to interpret than the offset maps. To construct the 3D displacement and associated formal error maps, we followed the method described by *Wright et al.* [2004]. We computed displacements only for points where azimuth and range offset data for both ascending and descending tracks are available (i.e., four to six scalar components of displacement are used for each point). Errors are propagated from formal errors in the measured offsets. The north-south component is the best constrained ($\sigma = 0.07$ m on average in the footwall and $\sigma = 0.13$ m in the hanging wall), while the east-west component is the least well constrained ($\sigma = 0.19$ m on average in the footwall and $\sigma = 0.46$ m in the hanging wall). For the vertical component, σ is about 0.09 m on average in the footwall and 0.20 m in the hanging wall; see auxiliary material Figure S2 for more details.

[8] Results show high gradient or discontinuity of displacement across an almost continuous 80 km-long NE-SW line that we interpret as the fault trace, the location of which can be mapped with an accuracy of ∼600 m. There is a left-step of about 1.5 km in the fault trace located just west of the area in Figure 3b, suggesting fault segmentation. This left step is located at the transition zone between the Muzaffarabad-Bagh 55 km-long straight southern portion of the fault, where the displacement across the fault is lower (with a maximum in the middle), and the curved

---

[1] Auxiliary materials are available in the HTML. doi:10.1029/2006GL027193.

Table 1. Details of the Six Offset Data Sets Used in This Study[a]

Direction	Track	Beam	Pre-Event	Start Date	End Date	⊥ Baseline, m	Azimuth (East North)	Range (East North Up)
Ascending	270	I6	5	25-06-2005	12-11-2005	60	[−0.18 −0.98]	[−0.67 −0.12 0.73]
Ascending	499	I6	4	19-09-2005	24-10-2005	270	[−0.18 −0.98]	[−0.63 −0.11 0.77]
Descending	463	I2	20	17-09-2005	26-11-2005	90	[0.21 −0.98]	[0.38 −0.08 0.92]

[a] Offsets are measured on pairs of ENVISAT ASAR images (in image mode) acquired before and after 8 October 2005. Each line corresponds to a pair. The number of images acquired during the two years preceding the event is given in column 4. For each pair, azimuth (component along track) and range (component along line of sight) offsets are measured. Exact orientation of these components depends on the geometry of acquisition and on the position of the measured point within the images. The last two columns give the unit vector of the measured components for a point near Muzaffarabad.

Muzaffarabad-Balakot 25 km-long portion where greater displacements occur. The largest displacements are concentrated on this part of the hanging wall and probably explains why Balakot and Muzaffarabad were the cities most affected by the earthquake. North of Balakot, displacements decrease abruptly, but there is still a diffuse zone of displacement (dominated by uplift) suggesting slip on a deeper fault. This zone coincides with the IKSZ and is also the area where most of the aftershocks occur.

[9] It is noteworthy that from north to south, there are changes in the direction of horizontal motion in the hanging wall. Approximately north of a line joining the epicenter to Muzaffarabad, displacements involve nearly pure thrust motion toward the SW. To the south, there is a progressive rotation of displacements toward the south implying a significant increase of the right-lateral slip and consequently some along-strike extension in the hanging wall. However, close to the fault trace, the right-lateral component tends to decrease. This observation is consistent with the Harvard and NEIC moment tensor solutions that indicate a right lateral component of the slip. In contrast, displacement in the footwall are more uniformly toward the north-east.

[10] Existence of surface rupture suggested by the presence of high gradients of displacement in Figures 2 and 3 is supported by high resolution Quick-Bird optical imagery analysis. Comparing pre- and post-event 60 cm resolution images, evidence of surface rupture can be found at several locations on the inferred fault trace. Figures 3b and 3c–3d illustrate two examples of surface ruptures. One is north of Muzzafarabad near the Neelum river and corresponds to a scarp, which is one of those recognized in the field and reported to be coseismic [see *Yeats et al.*, 2006, Figure 1].

4. Slip Distribution Model

[11] To model static deformation on the fault, we used a homogeneous linear elastic halfspace model assuming that the fault dislocation is a rectangular plane reaching the surface [*Okada*, 1985]. Slip distribution is estimated in two steps. First, the geometry of the fault plane is optimized assuming uniform slip and looking for a global minimum misfit with the offset data (that are downsampled using a quad-tree algorithm to about 2000 points per data set). The minimum misfit is found for the following parameters: strike 321.5°, dip 31.5°, depth 0–10 km, length 74 km. Second, this fault plane is then extended along strike and down dip to give a length of 100 km and a width of 30 km (corresponding bottom depth is 15.7 km, see Figure 3 and auxiliary material Figure S3 for location) and subdivided into 2 by 2 km patches. We then invert for the slip distribution with the same data, solving for the dip-slip and strike-slip motion of each patch and applying a Laplacian smoothing constraint to prevent unrealistic oscillations. This approach using a non-negative least-squares algorithm is described in more detail by *Funning et al.* [2005]. Note that due to the curved geometry of the real fault trace, some data points are on the wrong side of our simplified fault plane model. Such points are masked out in this second step. Among the solutions found for different smoothing factors we select the one shown in Figure 4,

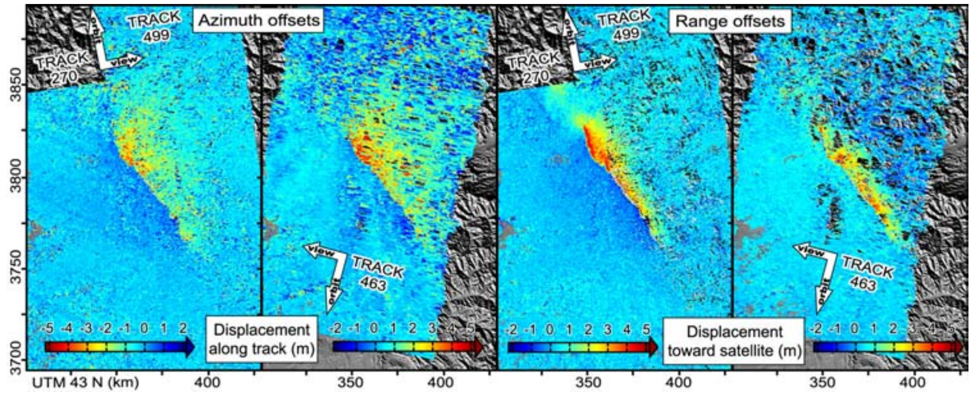

Figure 2. Azimuth and range offset measurements from ASAR ENVISAT images geocoded at 120 m resolution (range offsets are positive for a displacement toward the satellite). One descending and two ascending tracks are used to cover the epicentral area. Coseismic displacements of several meters, consistent with a NE-dipping thrust fault, are clearly visible at the center of the figure where the sharp color discontinuity delineates a highly deformed hanging wall to the east from a slightly deformed footwall to the west.

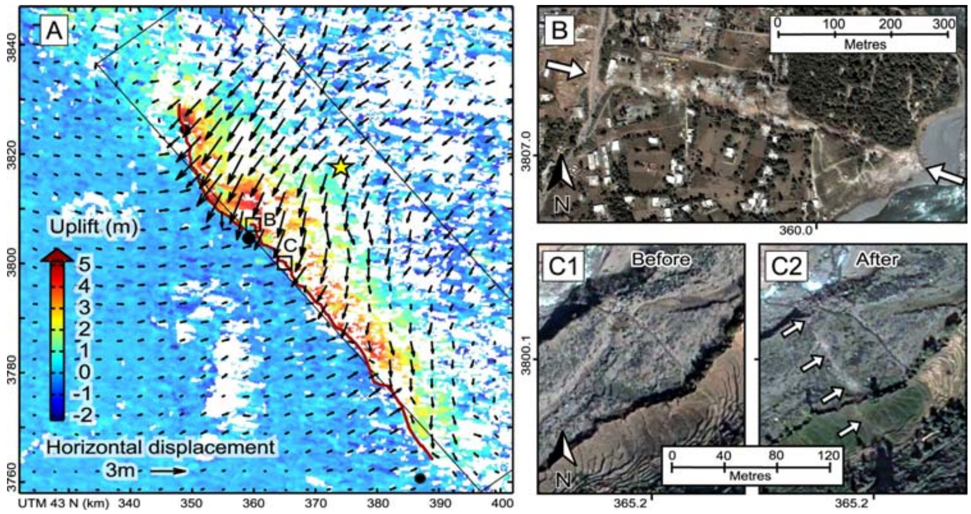

Figure 3. (A) 3D surface displacement field constructed from azimuth and range offset data sets. Arrows indicate horizontal displacements, and colors vertical displacements. Arrows are every 3.5 km and corresponds to the average displacements over a 4 km window (masking footwall data for hanging wall arrows and conversely for footwall arrows). From north to south, the black circles are the cities of Balakot, Muzaffarabad and Bagh. The squares indicate the location of the Quickbird imagery extracts (on the right side) showing evidences of surface rupture. The red line shows surface rupture trace inferred from satellite imagery (SAR, Quickbird and Landsat). The star is the NEIC epicenter and the thin black lines show the map projection of the plane used to model the fault. (B) Surface rupture located north of Muzaffarabad on the eastern bank of the Neelum river. Images (C1) before and (C2) after the earthquake showing the coseismic formation of a new fault scarp in the river bed of a tributary of the Jhelum river on the eastern flank of the valley.

based on a trade-off between high RMS misfit/low smoothness and low RMS misfit/high smoothness and on the minimization of the seismic moment (auxiliary material Figures S4a and S4b). The corresponding moment is 3.36×10^{20} N.m, which is larger than the moment of the Harvard CMT solution (2.94×10^{20} N.m). The global RMS misfit to the whole data set is ∼58 cm and the 3D surface displacements constructed from the model show similar pattern to the one described in Figure 3 (see auxiliary material Figures S5, S6 and S7 for details). In order to estimate error on the model, the same inversion is applied to 100 data sets perturbated by introducing noise with characteristics similar to the noise found in the data. For each patch of the fault plane, the standard deviation of the 100 solutions gives an error estimation, which increase with depth up to 1.5 m (for details, see *Funning et al.* [2005] and auxiliary material Figure S8).

[12] The slip distribution pattern shows a main zone of slip larger than 6 m with a peak slip of 9.6 m (±1.1 m) at 4 km depth, located beneath the Muzaffarabad-Balakot segment. Beneath the southern segment, smaller slip occurs distributed on a second zone elongated along strike with a peak slip up to 7 m at 4 km depth. Slip larger than 3 m occurs down to depth of about 13 km (±1 km). The zone of maximum slip in our model is located further north than in the slip distribution derived by *Avouac et al.* [2006] from seismic waveforms and slip measurements at the fault trace (from correlation of optical satellite images). The difference is more pronounced when comparing with their slip distribution derived from the modeling of seismic waveforms alone. This suggests that geodetic measurements consistently indicate a zone of maximum slip within the Muzaffarabad-Balakot segment. In this part of the fault, our slip distribution shows more slip at depth than in their model, which could be explained by the different spatial coverage of the geodetic data used in the two studies, the surface measurements of *Avouac et al.* [2006] being limited to the fault trace. Alternatively, the geometry of the modeled fault plane could also account for the difference: *Avouac et al.* [2006] use a two segments geometry that follows more closely the fault trace in its northern part than in our study that used a single plane and consequently could require more slip at depth.

5. Discussion and Conclusion

[13] Using SAR offsets we have extracted a synoptic view of the surface displacements covering the whole epicentral area of the Kashmir earthquake. From simple

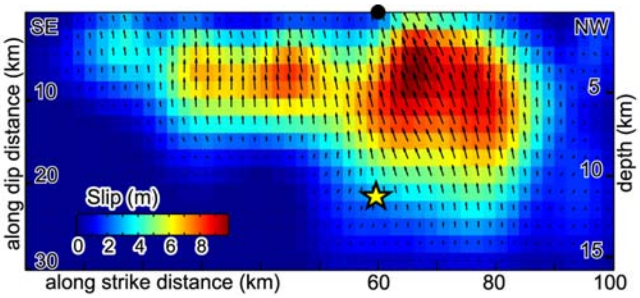

Figure 4. Slip distribution for a fault plane 100 km long, 30 km wide and dipping 31.5°NE (see location on Figure 3), inverted from the azimuth and range offset data sets. Magnitude of displacement is represented by color and slip vectors by the arrows. The star is the projection on the fault plane of the NEIC epicenter. The black dot represents the city of Muzaffarabad.

elastic modeling, we have estimated the slip distribution on the fault plane, which is able to reproduce the main features of the observed displacements. This spatially detailed analysis allows comparison with geological features that could have influenced the rupture process.

[14] The slip distribution shows that most of the slip corresponds to the rupture of the Balakot-Muzaffarabad northern segment. The left-step between the northern and southern fault segments is aligned with the North-South Jhelum valley southward of Muzaffarabad. *Tapponnier et al.* [2006], from geomorphic analysis, suggested that this left step could result from current left-lateral motion of the Jhelum fault, which runs along this valley. Another coincidence between slip distribution and geological features is that the fault trace follows more or less the MBT trace in its northern part and that displacements decrease abruptly north of Balakot where there is a dramatic bend of the MBT.

[15] All these observations are consistent with previous observations suggesting that the location of the rupture initiation or arrest tends to be at the location of intersecting faults or other features, implying a structural control on the slip distribution [e.g., *Manighetti et al.*, 2005]. In the case of the Kashmir earthquake, the hypocenter located at the down-dip edge of the zone of maximum slip is also at the transition zone between the two segments. However, such interpretation should be taken with caution as large errors can affect the hypocenter location (its depth $\sim$12 km is estimated from projection of the NEIC epicenter on the model fault plane).

[16] Regarding the zone of diffuse displacement observed north of Balakot that also coincide with the main concentration of aftershocks, triggered slip on a deeper part of the IKSZ ramp can be invoked. The data set used in this study does not allow us to discriminate between early post-seismic or coseismic deformation, as our first post-event image of that area was acquired on the 12th of November. This question deserves further investigations into the possible continuation of post-seismic displacements.

[17] Finally, we emphasize that for large ($M > 6$) shallow continental earthquakes, the robust, all-weather SAR correlation technique can be applied to produce precise fault locations and preliminary displacement maps, just days after post-event image acquisition using ESA crisis procedure for data distribution. The potential of remote sensing analysis, such as that described here, for operational use in the relief effort or rapid scientific investigation (such as postseimic study) should not be overlooked.

[18] **Acknowledgments.** This research has been supported by the UK Natural Environment Research Council through COMET. TJW is supported by a Royal Society University Research Fellowship. Part of this research was performed at the Jet Propulsion Laboratory, Caltech, under contract with NASA. We are grateful to the European Space Agency for providing the ENVISAT data used in this study (project AOE-621 and AOE-668). We thank Gareth Funning, who wrote parts of the code used for the slip inversion, and Nicola Capes of Nigel Press Associates for her help in obtaining the Quickbird imagery. We thank J. P. Avouac and two anonymous reviewers for helpful comments.

References

Armbruster, J., L. Seeber, and K. H. Jacob (1978), The northwestern termination of the Himalayan mountain front: Active tectonics from microearthquakes, *J. Geophys. Res.*, *83*(B1), 269–282.

Avouac, J.-P., F. Ayoub, S. Leprince, O. Konca, and D. V. Helmberger (2006), The 2005, Mw 7.6 Kashmir earthquake: Sub-pixel correlation of ASTER images and seismic waveforms analysis, *Earth Planet. Sci. Lett.*, *249*(3–4), 514–528, doi:10.1016/j.epsl.2006.06.025.

Bilham, R. (2004), Earthquakes in India and the Himalaya: Tectonics, geodesy and history, *Ann. Geophys.*, *47*, 839–858.

Fujiwara, S., et al. (2006), Satellite data give snapshot of the 2005 Pakistan earthquake, *Eos Trans. AGU*, *87*(7), 73–84.

Funning, G. J., B. E. Parsons, T. J. Wright, J. A. Jackson, and E. J. Fielding (2005), Surface displacements and source parameters of the 2003 Bam (Iran) earthquake from Envisat advanced synthetic aperture radar imagery, *J. Geophys. Res.*, *110*, B09406, doi:10.1029/2004JB003338.

Manighetti, I., M. Campillo, C. Sammis, P. M. Mai, and G. C. P. King (2005), Evidence for self-similar, triangular slip distributions on earthquakes: Implications for earthquake and fault mechanics, *J. Geophys. Res.*, *110*, B05302, doi:10.1029/2004JB003174.

Michel, R., J.-P. Avouac, and J. Taboury (1999), Measuring ground displacements from SAR amplitude images: Application to the Landers earthquake, *Geophys. Res. Lett.*, *26*(7), 875–878.

Nakata, T., H. Tsutsumi, S. H. Khan, and R. D. Lawrence (1991), *Active Faults of Pakistan*, 141 pp., Res. Cent. for Reg. Geogr., Hiroshima Univ., Hiroshima, Japan.

Okada, Y. (1985), Surface deformation due to shear and tensile faults in a half-space, *Bull. Seismol. Soc. Am.*, *75*(4), 1135–1154.

Parsons, T., R. S. Yeats, Y. Yagi, and A. Hussain (2006), Static stress change from the 8 October, 2005 $M = 7.6$ Kashmir earthquake, *Geophys. Res. Lett.*, *33*, L06304, doi:10.1029/2005GL025429.

Rosen, P. A., S. Hensley, I. R. Joughin, F. K. Li, S. N. Madsen, E. Rodriguez, and R. M. Goldstein (2000), Synthetic aperture radar interferometry, *Proc. IEEE*, *88*(3), 333–382, doi:10.1109/5.838084.

Rosen, P. A., S. Hensley, G. Peltzer, and M. Simons (2004), Updated repeat orbit interferometry package released, *Eos Trans. AGU*, *85*(5), 47.

Tapponnier, P., G. C. P. King, and L. Bollinger (2006), Active faulting and seismic hazard in the western Himalayan syntaxis, Pakistan, in *International Conference on 8 October 2005 Earthquake in Pakistan*, edited by A. B. Kausar, T. Karim, and T. Khan, pp. 2–3, Geol. Surv. of Pakistan, Quetta, Pakistan.

Wright, T. J., B. E. Parsons, and Z. Lu (2004), Toward mapping surface deformation in three dimensions using InSAR, *Geophys. Res. Lett.*, *31*, L01607, doi:10.1029/2003GL018827.

Yeats, R. S., A. B. Kausar, and T. Nakata (2006), Conferees examine deadly 2005 Kashmir earthquake, *Eos Trans. AGU*, *87*(11), 115.

B. E. Parsons, E. Pathier, R. Walker, and T. J. Wright, Centre for the Observation and Modelling of Earthquakes and Tectonics (COMET), Department of Earth Sciences, University of Oxford, Parks Road, Oxford OX1 3PR, UK. (erwan.pathier@earth.ox.ac.uk)

E. J. Fielding and S. Hensley, Jet Propulsion Laboratory, M.S. 300-233, California Institute of Technology, 4800 Oak Grove Drive, Pasadena, CA 91109, USA.

Available online at www.sciencedirect.com

SCIENCE @ DIRECT®

Earth and Planetary Science Letters 212 (2003) 73–88

EPSL

www.elsevier.com/locate/epsl

Coseismic displacements of the footwall of the Chelungpu fault caused by the 1999, Taiwan, Chi-Chi earthquake from InSAR and GPS data

Erwan Pathier[a,*], Bénédicte Fruneau[b], Benoît Deffontaines[c], Jacques Angelier[a], Chung-Pai Chang[d], Shui-Beih Yu[e], Chyi-Tyi Lee[f]

[a] *Laboratoire de Tectonique, University of Paris 6, E1, T26, Case 129, 4 Place Jussieu, 75252 Paris Cedex, France*
[b] *Institut Francilien des Géosciences, University of Marne-la-Vallée, 5 Boulevard Descartes, 75454 Marne-la-Vallée Cedex, France*
[c] *Laboratoire de Géomorphologie et Environnement Littoral, EPHE, 15 Boulevard de la Mer, 35800 Dinard, France*
[d] *Center for Space and Remote Sensing Research, National Central University, Chungli 320, Taiwan*
[e] *Institute of Earth Sciences, Academia Sinica, P.O. Box 1-55, Nankang, Taipei, Taiwan*
[f] *Institute of Applied Geology, Central University, Chungli, Taiwan*

Received 5 November 2002; received in revised form 16 April 2003; accepted 6 May 2003

Abstract

The differential SAR interferometry technique (interferometric synthetic aperture radar, InSAR) is applied on the Chelungpu fault surface rupture zone of the September 20, 1999, Taiwan, Chi-Chi earthquake using six ERS-2 images covering the period from February 1999 to January 2000. As compared with available geodetic data, InSAR measurements result in more extensive analysis because of high spatial sampling and centimetric accuracy. However, coseismic displacements can be evaluated only on the footwall of the fault. The analysis of interferograms shows the existence of a linear trend in phase difference mainly caused by orbital errors, which we removed from interferograms using GPS data. The corrected interferograms provide a precise map of the InSAR component of the coseismic displacement, showing a continuous decrease over the footwall from a maximum of 36.7 cm at the fault east of Taichung city to a value of about 5 cm at the coastline 30 km further west. The map analysis reveals that the Changhua fault (whose surface trace is located about 20 km west of the Chelungpu one) and the Tuntzuchio fault influence the displacement field. We interpret this in terms of minor reactivation of these faults triggered by the earthquake. A 1.7 cm uncertainty, estimated from the GPS data, is proposed to quantify the precision of the map. Beyond this single value, we highlight the interest of having several coseismic interferograms to evaluate the reliability of the map in a more comprehensive way. Comparisons with displacements inferred from models of slip distribution inverted without InSAR data highlight the advantage of carrying out a joint inversion including our results as new constraints.

Keywords: earthquakes; SAR; interferometry; GPS; coseismic processes; Taiwan

---

* Corresponding author. Tel.: +33-1-44-27-71-81; Fax: +33-1-44-27-50-85.
E-mail address: erwan.pathier@lgs.jussieu.fr (E. Pathier).

0012-821X/03/$ – see front matter © 2003 Elsevier Science B.V. All rights reserved.
doi:10.1016/S0012-821X(03)00244-9

1. Introduction

On 21 September 1999, the $M_w = 7.6$ Chi-Chi earthquake occurred in central western Taiwan. This earthquake was related to an out-of-sequence reactivation of a major north–south-trending thrust of the Taiwanese Foothills, the Chelungpu fault [1,2] (Fig. 1). The deformation front of the fold-and-thrust belt of the Foothills is located 15–20 km west of the Chelungpu fault at the Changhua fault [3]. Rupture that developed over the Chelungpu fault plane reached the Earth's surface, causing a spectacular 90-km-long scarp between the hangingwall to the east and the footwall to the west [4]. Because of both the density and the quality of Taiwanese strong motion and Global Positioning System (GPS) networks, the Chi-Chi earthquake was among the best instrumentally recorded earthquakes. Several analyses have been presented to quantify the earthquake surface displacements from GPS measurements [5,6], strong motion records [7], SPOT satellite optical images [8] and field measurements along the fault trace [9,10]. These results have been used to model the distribution of slip on the fault surface [11–14]. However, between the different resulting models, discrepancies remain in terms of geometry, slip distribution and predicted coseismic displacements.

Aiming to better constrain the coseismic displacement field of the Chi-Chi earthquake and consequently the models, this study uses data provided by interferometric synthetic aperture radar (InSAR). The InSAR technique is a complement to other geodetic methods because of its dense spatial sampling over a large surface, its precision and its high sensitivity to vertical displacement. In this paper, we first describe how we implement the

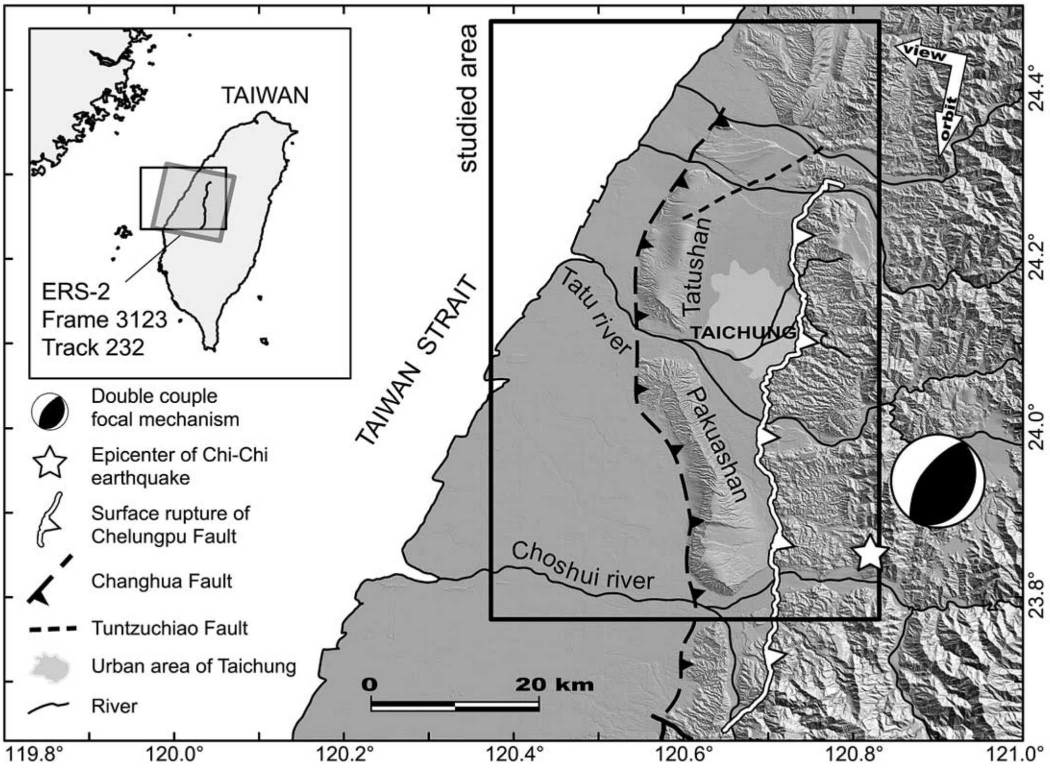

Fig. 1. Location of the footwall of the Chelungpu fault. Inset: The grey rectangle indicates the ERS SAR image frame used in this study; the black rectangle shows the location of the main figure. Main figure: in the background, shaded DEM of the epicentre area; the black rectangle shows the location of Figs. 3 and 4. The white arrows correspond to orbit track and viewing directions of the ERS satellite.

InSAR technique. Then, analysis of the resulting interferograms focuses on retrieving quantitative information about the permanent surface coseismic displacements. Corrections and processing are applied to the interferograms in order to obtain a map of InSAR coseismic displacements that permits geophysical analysis and interpretation, particularly on the behaviour of the Changhua and Tuntzuchio faults at the time of the Chi-Chi earthquake. Finally, we discuss the validity of the resulting map and we compare the results with two existing slip models of the Chelungpu fault.

2. InSAR: method and data

2.1. Method

For this study, we apply the InSAR technique in the two-pass approach using the DIAPASON software [15]. The method, also called differential InSAR, requires at least two SAR images of the same area acquired at two different times in similar conditions, topographic information on the studied area and satellite orbit information for both acquisitions. See Massonnet et al. [16] and Massonnet and Feigl [17] for details on requirements and limits of the method. As the main result, an image called an interferogram is produced, as a map of the phase difference $\Delta\Phi$ of both SAR images, so that for each pixel:

$$\Delta\Phi = \Delta\Phi_{\mathrm{d}} + \Delta\Phi_{\mathrm{a}} + \Delta\Phi_{\mathrm{te}} + \Delta\Phi_{\mathrm{oe}} + \Delta\Phi_{\mathrm{dc}} + \Delta\Phi_{\mathrm{n}} \tag{1}$$

where $\Delta\Phi_{\mathrm{d}}$ is related to the displacement of the surface between the two acquisitions, $\Delta\Phi_{\mathrm{a}}$ is related to the difference of atmospheric states, $\Delta\Phi_{\mathrm{te}}$ is related to errors in the topographic model, $\Delta\Phi_{\mathrm{oe}}$ depends on errors in orbital information, $\Delta\Phi_{\mathrm{dc}}$ represents phase changes caused by geometric and temporal decorrelation, and $\Delta\Phi_{\mathrm{n}}$ gathers phase changes due to thermal noise, SAR image processing errors and misregistration errors of both SAR images [18–20]. For a comprehensive review of these different terms see Hanssen [21]. For each pixel of an interferogram, $\Delta\Phi$ can record the displacement of the corresponding cell of resolution: $\Delta\Phi_{\mathrm{d}}$ is proportional to the component of the full displacement vector along the radar line of sight. Hereafter, this component is called SRD (slant range displacement). We adopt the following convention: a positive SRD is from ground to satellite. An SRD that is $\lambda/2$ (λ being the radar wavelength) corresponds to a $\Delta\Phi_{\mathrm{d}}$ equalling 2π radians.

Due to phase ambiguity, values of $\Delta\Phi$ are given modulo 2π. Phase ambiguity prevents access to absolute value, so that a $\Delta\Phi$ value from only one pixel is useless. However, such a value makes sense while measuring changes in $\Delta\Phi$ by comparison with other pixels. Measuring changes in $\Delta\Phi$ requires several conditions that limit interferogram analysis, especially low $\Delta\Phi_{\mathrm{dc}}$ and $\Delta\Phi_{\mathrm{n}}$ contributions and a not too high gradient of $\Delta\Phi$ [17]. $\Delta\Phi_{\mathrm{dc}}$ and $\Delta\Phi_{\mathrm{n}}$ terms induce changes in $\Delta\Phi$ that are not coherent from one pixel to another. Once coherent changes in $\Delta\Phi$ on the interferogram have been identified, the analysis of interferograms consists in estimating the part of the different contributions of $\Delta\Phi$. For our purpose, which is to extract SRD information from interferograms, the main goal is to estimate $\Delta\Phi_{\mathrm{d}}$ values.

2.2. The data

We selected six SAR images in order to obtain several coseismic interferograms that we can compare. The SAR image selections have been based on two major criteria: making their baselines (distance between two orbit trajectories) as short as possible, which results in smaller $\Delta\Phi_{\mathrm{te}}$ and $\Delta\Phi_{\mathrm{dc}}$ contributions, and having the shortest time interval between acquisitions in order to reduce the temporal decorrelation effects.

Regarding the choice of the SAR sensor, no JERS images being available since 1998, we retained ERS (European remote sensing satellite) data because they offered more possibilities than Radarsat to obtain several coseismic couples meeting the requirements. In addition, a previous study [22] had demonstrated the feasibility of InSAR measurements with ERS data in the Foothills of southwestern Taiwan. Finally, we used

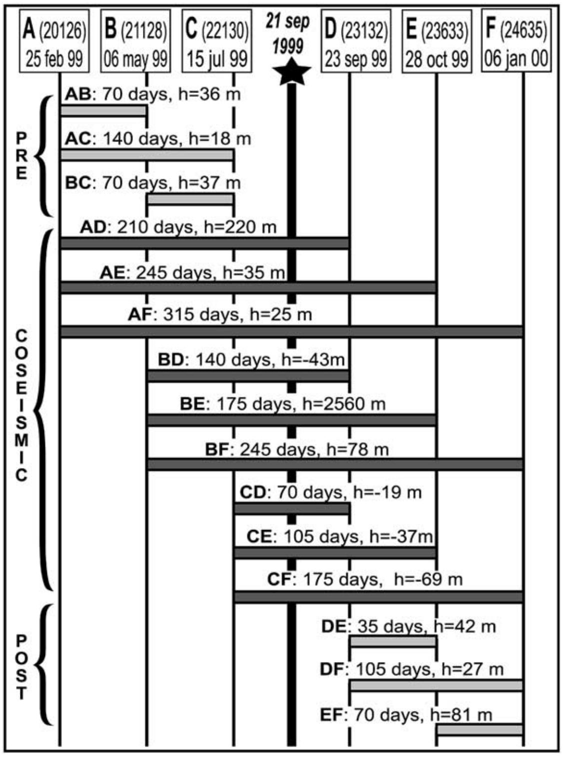

Fig. 2. ERS data list. List of the 15 interferograms processed from the six ERS2 SAR images. Orbit number and date of acquisition of each image (A,B,C,...) are given. Each grey bar corresponds to an interferogram with its name used in this paper, its time span and its height of ambiguity (*h*, in metres).

only images from the SAR sensor of ERS-2 operating at 5.3 GHz ($\lambda = 5.6$ cm), as no ERS-1 images covered the earthquake period. We chose images in descending orbit, because the shortest time interval (about 3 years) available in ascending mode was too long.

In order to capture the coseismic SRD, we selected three images acquired before and three images after the earthquake (Fig. 2). All of these images cover the same zone (Track 232, frame 3129, see location in Fig. 1) corresponding to the fault zone. The other data we used are a 40 m × 40 m grid spacing DEM (digital elevation model) with a vertical accuracy of about 5 m, and precise orbits of ERS-2 determined by the Delft Institute for Earth-Oriented Space Research [23].

3. Interferogram analysis

3.1. Detection of coseismic displacements and perturbations

Among the 15 resulting interferograms, three span a preseismic period, nine a coseismic one,

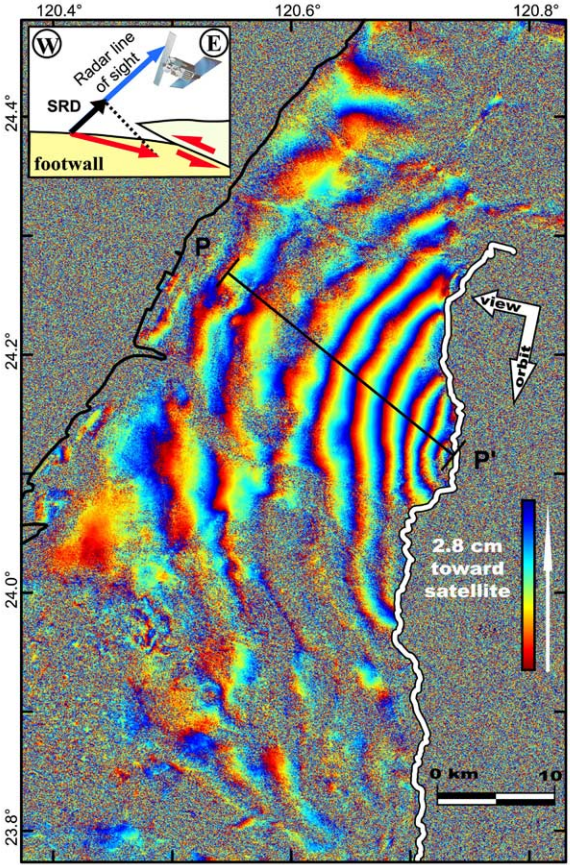

Fig. 3. Coseismic interferogram of the Chi-Chi earthquake. Filtered interferogram AD (25 Feb. 99–23 Sept. 99) showing coseismic displacement. To first order, each cycle of colour (a fringe) from blue to red corresponds to 2.8 cm of relative displacement toward the satellite. White thick line, Chelungpu fault trace; black line, coastline; black segment, location of profile PP′ (see Fig. 4). Inset: Geometry of acquisition. The red vector represents the coseismic displacement; the black vector corresponds to the SRD measured by InSAR (projection of the red vector on the radar line of sight). The three components of the unit vector from ground to satellite, at the centre of the studied area, expressed in local terrestrial reference are: up = 0.924, east = 0.375, north = −0.079. These components vary gently over the interferogram, the incidence angle ranging from 20.5 to 24.9° on the studied area.

and three a postseismic one (Fig. 2). The coherence of these different interferograms is principally a function of the baseline and of the time interval: the smaller these parameters are, the better the coherence is. In all coseismic interferograms, there is coherent information only in the footwall area (Fig. 3). Even in pre- or postseismic interferograms, most of the hangingwall domain lacks coherence (Fig. 4b). The footwall is largely urbanised, which favours numerous stable scatterers having a low temporal decorrelation, whereas the hangingwall is essentially covered by dense vegetation, causing rapid temporal phase decorrelation. Two other factors accentuate this contrast: (1) as shown by GPS [6], the displacement gradients close to the fault are much larger in the hangingwall than in the footwall and could exceed the upper limit of the phase gradient discernible by ERS InSAR (about 10^{-3} [21]); (2) the deformation and earthquake destruction in the hangingwall contribute to phase decorrelation in the affected cells of resolution.

In the footwall, coseismic interferograms show a similar pattern formed by a dozen fringes as illustrated in Fig. 3. As these fringes are present in all coseismic interferograms and because they

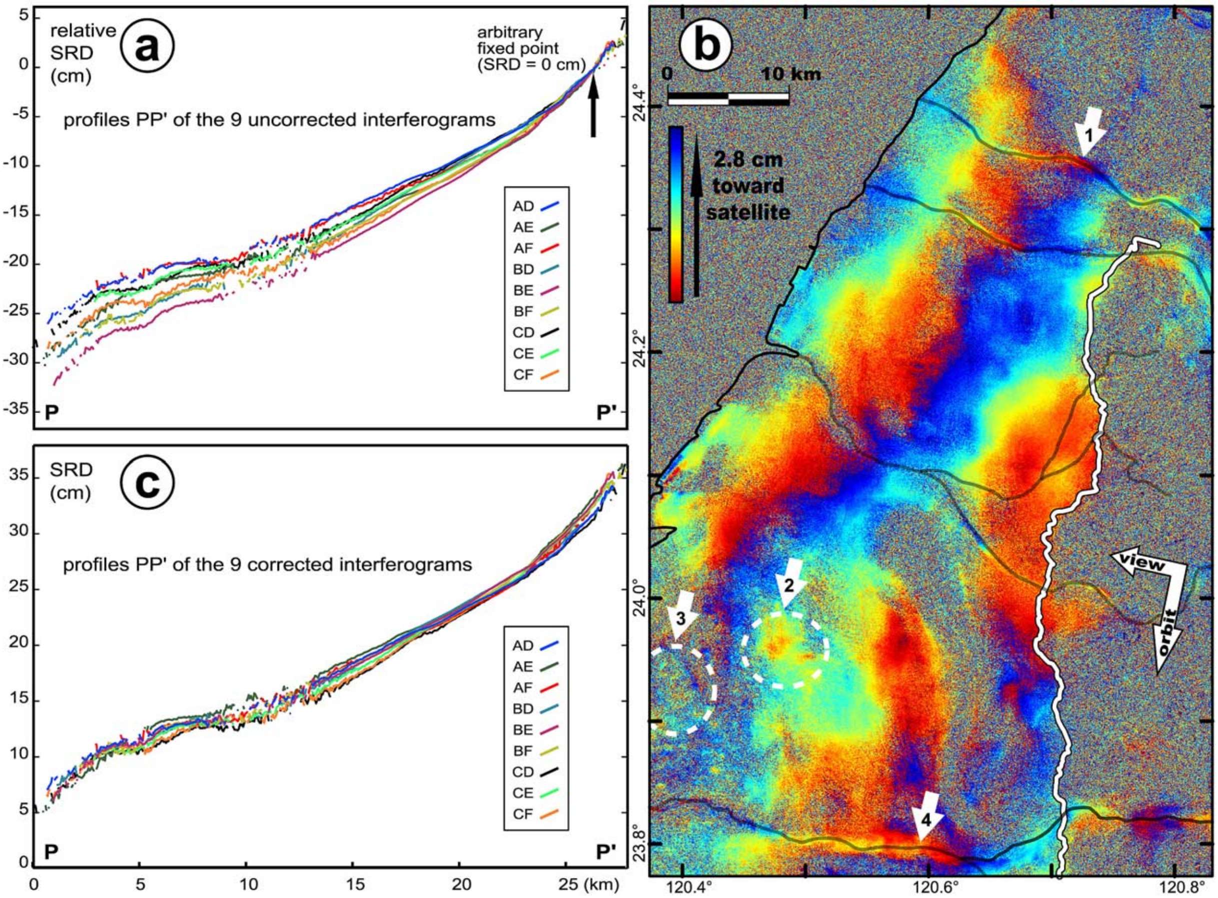

Fig. 4. Perturbations affecting the InSAR measure of the coseismic displacements. (a) Profile PP′ (location in Fig. 3) of unwrapped and uncorrected coseismic interferograms, showing large-scale perturbation. (b) Pre-seismic filtered interferogram AB showing large fringes mainly related to orbital errors and locally disturbed by medium-scale perturbations. White arrows show location of non-coseismic displacement: 1 and 4, perturbations at river beds; 2 and 3, subsiding areas located west of Pakuashan (see Section 3.2). (c) Profile PP′ of unwrapped coseismic interferograms after linear trend correction by GPS.

are consistently correlated with the fault trace, we interpret the major part of these changes in $\Delta\Phi$ as being $\Delta\Phi_d$ changes related to coseismic displacement of the ground surface. Thus, in first approximation, the fringes can be read as contour lines (with a spacing of $\lambda/2$, that is 2.8 cm) of a contour map of coseismic SRD. Under this hypothesis, there is an increase in SRD towards the fault trace relative to a point at the coastline chosen as reference. The highest SRD values are close to the fault, in the fault trace concavity east of the city of Taichung. Taking into account the radar line of sight direction (Fig. 3), interferograms give constraints on three-dimensional coseismic displacements. Additional sources of information on the coseismic displacements, such as GPS data, locally help to remove ambiguity on full vector displacement and improve the interpretation. Note that in the particular case of our InSAR observation of the Chi-Chi earthquake the coseismic interferograms indicate positive SRD although the GPS indicates a downward displacement of the footwall. As illustrated in Fig. 3, this situation results from a greater horizontal displacement moving the ground closer to the satellite than the vertical displacement moving the ground away from the satellite.

Fig. 4a, which illustrates the different SRDs inferred from the nine coseismic interferograms assuming $\Delta\Phi = \Delta\Phi_d$ on coherent pixels, shows that this hypothesis needs to be refined. The discrepancies in SRD indicate that, although the main part of the changes in $\Delta\Phi$ in coseismic interferograms can be interpreted as coseismic displacements, the resulting fringes are also more or less influenced by other factors, as mentioned in Eq. 1, as well as by non-coseismic displacements (coseismic interferograms cover a time period larger than the coseismic event period). Hereafter we call perturbations the changes in $\Delta\Phi$ that are not caused by coseismic displacements.

In the absence of perturbation, coseismic interferograms should be identical and pre- and postseismic ones should not show any coherent change in $\Delta\Phi$. In fact, we observed perturbations in interferograms that can be decomposed into three main types. The first kind of perturbations affects the whole interferogram (hereafter large-scale perturbation) and consists of a relatively constant gradient of $\Delta\Phi$ for a given interferogram. In pre- and postseismic interferograms (AB, BC, DE and EF), where they are best expressed, such large-scale perturbations are represented by large and roughly parallel fringes (Fig. 4b). In coseismic interferograms, they are superimposed on the coseismic signal, inducing large trend variations (Fig. 4a). The second kind of perturbation consists of kilometre- to hectometre-scale smooth variations of $\Delta\Phi$ (hereafter medium-scale perturbations) that give an irregular aspect to the interferogram and disturb the large-scale fringe in pre- and postseismic interferograms (Fig. 4a,b). The third kind of perturbation (hereafter small-scale perturbation) corresponds to rapid change from one pixel to the nearest pixel, well expressed in lower-coherence area and resulting in a ‘noisy’ aspect in the interferograms.

3.2. *Origin of perturbations*

The small-scale perturbations are mainly related to $\Delta\Phi_{dc}$ and $\Delta\Phi_n$ terms. Considering large-scale perturbations, their fringe pattern (Fig. 4b) is typical of residual orbital fringes related to errors in positioning of orbit trajectories. We cannot exclude, however, a large-scale atmospheric effect, or a combination of both of these origins. The variability with time in direction and magnitude of these perturbations indicates that large-scale displacements (tectonic or not) cannot contribute much to these gradients. This observation also discards a perturbation due to large-scale DEM errors ($\Delta\Phi_{te}$), because it is expected always to have the same direction whatever the interferogram considered and to have a magnitude proportional to the baseline.

If we interpret these phase gradients as only caused by errors on the baseline values, the highest gradient will correspond to an error of about 1 m. Note that such errors are larger than those expected with a 95% likelihood for DEOS precise orbit that we used [21]. We also compute preseismic interferograms with other orbital data: the DLR precise orbits [24]. The resulting interferograms present a slightly higher $\Delta\Phi$ gradient and it is noteworthy that the orientation of fringes resembles those obtained with DEOS orbits. This observation argues for an orbital error origin, because if these fringes were mainly caused by large-scale atmospheric perturbation in interferograms processed with DEOS orbits, parallelism between such fringes and those introduced by the DLR orbit error would be unlikely. On the other hand, such parallelism can result from similar calculation methods for the two kinds of orbits. This leads us to assume that the major part of the large-scale phase gradient is due to orbital errors (these errors also cause perturbations correlated with the relief; however, in our case, their low values make these effects negligible).

Regarding the medium-scale perturbations in pre- and postseismic interferograms, we exclude a significant influence of $\Delta\Phi_{te}$ because medium-scale perturbations are not correlated with the baseline. Direct observations of interferograms show that most of the perturbations are changing in space from one interferogram to another. Thus, we suppose an atmospheric main origin for most of them. These perturbations are not visibly correlated with the relief on the footwall. The topography of the footwall ranges from 0 m near the coast to 450 m at Pakuashan, and 60% of coherent points have elevation less than 100 m, which is moderate compared to relief where correlation between atmospheric effect and topography have been found in other studies [25]. Note that we do not propose to evaluate the correlation between $\Delta\Phi$ and the topography using the GPS data as control because of the number of GPS points available and their altitude distribution: 18 of the 28 stations that we used are below 100 m elevation and the highest station (TECS) has an elevation of only 245 m. We finally consider in first approximation that most of the medium-scale perturbations are randomly variable in magnitude and location from one interferogram to another. We extrapolate this assumption, made on pre- and postseismic interferograms, to coseismic interferograms, where perturbations and coseismic effects are mixed, which makes such an analysis difficult.

However, to a lesser extent, other kinds of medium-scale perturbations are constant in location (Fig. 4b). Slight changes in $\Delta\Phi$ that are exactly located at river beds could be linked to the local variation of the water vapour content in the atmosphere due to the presence of the rivers. These changes in $\Delta\Phi$ could also be interpreted as non-coseismic subsiding displacements. We also incriminate non-coseismic displacement (subsidence) to explain systematic changes in all of the pre- and postseismic interferograms at two locations west of the Pakuashan hills (Fig. 4b). Other non-coseismic displacements can affect the interferograms. Such displacements involve preseismic secular motion (recorded by the GPS), displacements caused by postseismic slip on the fault or by aftershocks. Postseismic subsidence or rebound phenomena could be notably caused by the widespread coseismic change in pore water pressure recorded by the network of hydrologic monitoring wells [26]. However, as they cannot be detected by direct observation of the interferograms, the magnitudes of such displacements are small compared to the perturbations caused by the atmospheric effects.

4. Interferogram correction from GPS data

4.1. The GPS data

As we have no sufficient information about orbital error or atmospheric effect, we cannot determine how far the coseismic interferograms are affected by the perturbations in the absence of an a priori knowledge of the coseismic displacements. External information is needed in order to achieve the coseismic displacement estimation.

GPS data can give such information about the coseismic displacements. This information is punctual and gives an absolute displacement, whereas InSAR covers large areas and indicates relative displacement. The comparison with GPS data requires unambiguous phase information, which we obtain by unwrapping all the interferograms using a semi-automatic method based on 'residu-branch-cut' algorithm [27] with possible manual intervention to connect isolated unwrapped areas when the automatic process fails. The number of pixels unwrapped in an interferogram (see Table 2) depends of its quality. To fa-

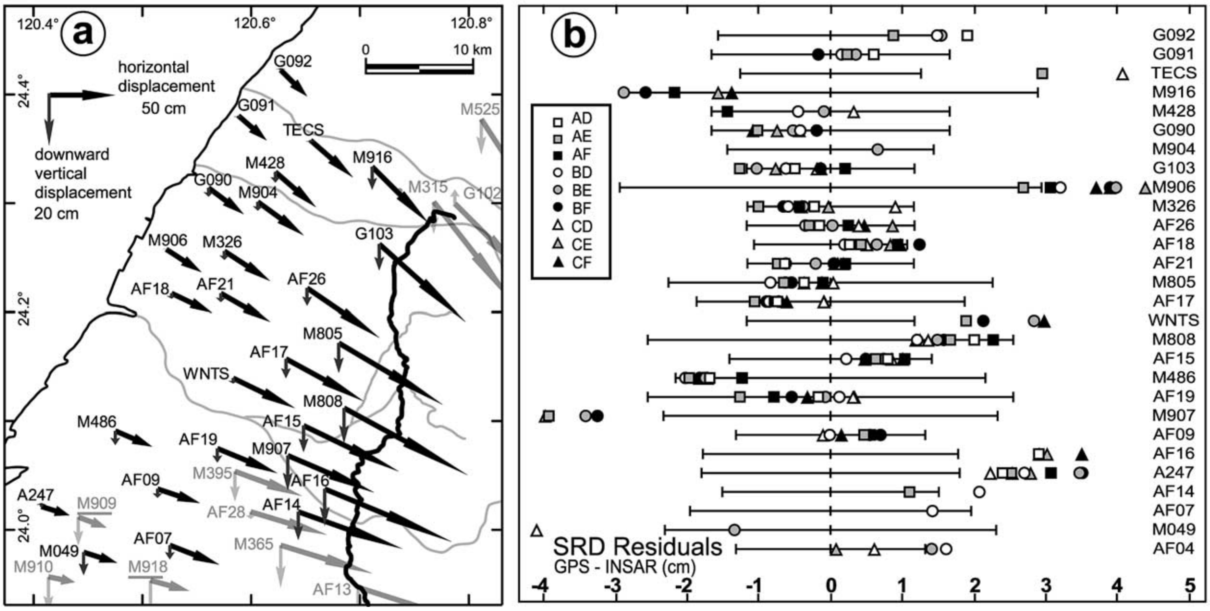

Fig. 5. GPS data and comparison with corrected InSAR data. (a) Map of the coseismic displacements at GPS stations from Yu et al. [6]; stations in faint grey are not used in this study, the two underlined stations (southwest corner) have been discarded from the selection (see text). (b) Residuals of the interferogram corrections: the black lines are the GPS error bars at each station sorted by latitude. The squares, circles and triangles indicate the difference (in cm) between the coseismic displacements along the radar line of sight (SRD) inferred from GPS data at each station and the SRD from each corrected interferogram.

cilitate unwrapping, we apply a filter that smooths the small-scale perturbations [28]. The spatial distribution of the available GPS stations in the footwall from Yu et al. [6] (Fig. 5a) allows us to constrain the large-scale perturbations, but is too sparse to constrain the medium-scale perturbations. Among the 59 stations in the footwall, 54 are in the InSAR-studied area. We used only 28 of these 54 stations because the other 26 are located outside all unwrapped areas of our coseismic interferograms. In addition, two GPS stations (M918 and M909, see location in Fig. 5a) are discarded because they reveal large differences with respect to the corrected interferograms (about −12 and −18 cm, respectively) and seem poorly representative of the regional displacement with respect to the neighbouring stations. The uncertainties given for these two stations resemble those of other stations, so that local site effects that would have affected these two stations may account for the discrepancy. Amongst the 28 selected stations, 12 stations always have their corresponding pixel unwrapped in all of the interferograms (Table 1).

Yu et al. [6] corrected the data for preseismic secular motions by fitting the velocity of 24 stations (surveyed from 1992 to 1999), by a first-order trend surface. They also made postseismic corrections, but at the stations that we selected they indicate that there are no postseismic displacements. As our interferograms are not exactly coseismic, we adapt the preseismic corrections made on GPS data for each interferogram according to the date of its preseismic image, assuming a preseismic secular motion constant with time (Table 1). According to this method, the amount of preseismic SRD is maximal in the interferograms using image A. In this case, taking into account the 28 selected stations, the standard deviation of preseismic SRD is 0.18 cm and the average value is 0.1 cm. The extreme values are at stations TECS (−0.5 cm) and M049 (0.5 cm). The perturbations caused by preseismic displacement are minor relative to those observed that are mainly due

Table 1
GPS data used for interferogram corrections

Station	Latitude (°)	Longitude (°)	East[a]	North[a]	Up[a]	East[b]	North[b]	Up[b]	Cos.[c]	AX[d]	BX[d]	CX[d]	#[e]
A247	120.408	24.020	21.3	−6.2	1.7	0.397	−0.083	0.914	10.5	10.4	10.4	10.5	9
AF04	120.534	23.871	32.3	−6.7	−5.2	0.379	−0.080	0.922	8.0	7.7	7.8	7.9	4
AF07	120.525	23.985	37.9	−14.8	−5.3	0.383	−0.081	0.920	10.8	10.5	10.6	10.7	1
AF09	120.514	24.037	33.2	−10.7	−3.3	0.385	−0.081	0.919	10.6	10.3	10.4	10.5	7
AF14	120.643	24.015	79.2	−28.4	−10.4	0.370	−0.078	0.926	21.9	21.8	21.8	21.9	2
AF15	120.648	24.094	72.6	−35.3	−10.1	0.372	−0.079	0.925	20.4	20.3	20.3	20.4	9
AF16	120.668	24.036	96.2	−39.9	−14.3	0.368	−0.078	0.927	25.3	25.2	25.2	25.2	4
AF17	120.632	24.156	59.1	−32.1	−7.4	0.375	−0.079	0.924	17.9	17.8	17.8	17.8	9
AF18	120.527	24.216	31	−15.8	−2.4	0.388	−0.082	0.918	11.1	11	11	11.1	9
AF19	120.569	24.073	45.7	−18.8	−4.9	0.380	−0.080	0.921	14.4	14.2	14.2	14.3	9
AF21	120.572	24.216	37.9	−22.2	−3.6	0.383	−0.081	0.920	13.0	12.9	13	13	9
AF26	120.651	24.221	55.8	−38.3	−6.7	0.375	−0.079	0.924	17.7	17.7	17.7	17.7	9
G090	120.562	24.312	26	−20.2	−3.3	0.387	−0.081	0.919	8.7	8.6	8.6	8.6	7
G091	120.589	24.379	21.2	−19.1	−0.8	0.386	−0.081	0.919	9.0	8.9	8.9	9	5
G092	120.628	24.421	19.4	−19.8	0.8	0.382	−0.081	0.921	9.7	9.7	9.7	9.7	4
G103	120.718	24.260	66.3	−59.2	−10	0.368	−0.078	0.927	19.8	19.8	19.8	19.8	9
M049	120.446	23.979	26	−8.1	−8.6	0.391	−0.082	0.917	3.0	2.5	2.7	2.8	2
M326	120.575	24.254	35.3	−22.6	−3.4	0.384	−0.081	0.920	12.3	12.2	12.2	12.2	9
M428	120.622	24.327	30.9	−27.1	−4.2	0.381	−0.080	0.921	10.1	10.2	10.2	10.1	4
M486	120.475	24.090	29	−12.3	−5.5	0.391	−0.082	0.917	7.3	6.9	7.1	7.2	9
M805	120.681	24.171	79.8	−47.4	−11.5	0.370	−0.078	0.926	22.6	22.5	22.6	22.6	9
M808	120.686	24.111	93.7	−51.7	−13.3	0.368	−0.078	0.927	26.2	26.1	26.1	26.2	9
M904	120.607	24.299	33.8	−25.5	−2.9	0.382	−0.080	0.921	12.3	12.4	12.4	12.3	1
M906	120.522	24.256	27.9	−18.1	0.1	0.390	−0.082	0.917	12.5	12.2	12.3	12.4	8
M907	120.633	24.068	67	−29.5	−13.9	0.373	−0.079	0.925	14.4	14.3	14.4	14.4	4
M916	120.712	24.332	42.9	−43	−8.6	0.371	−0.078	0.925	11.3	11.3	11.3	11.3	5
TECS	120.655	24.356	31.7	−28.2	−0.4	0.378	−0.080	0.922	13.9	14.4	14.2	14	2
WNTS	120.584	24.138	46.8	−22.3	−2.3	0.380	−0.080	0.921	17.5	17.6	17.6	17.5	4

[a] Components (cm) of the coseismic displacement from [6] corrected for preseismic secular motion.

[b] Unit vector from ground to satellite at the station.

[c] Coseismic displacement along the SRD (cm) at the station.

[d] SRD (cm) integrating the coseismic displacement and the preseismic secular motion for an interferogram XX (with X = A, B or C).

[e] Number of coseismic interferograms where a given station corresponds to a coherent pixel.

to atmospheric effect. We do not correct the interferograms from the preseismic SRD, because of the difficulty to estimate a velocity trend surface that is controlled only by four GPS stations in our interferograms and because of high uncertainties of the preseismic SRD reconstructed from GPS data relative to their magnitudes.

4.2. Model and method

For each interferogram, we model the large-scale perturbation by a phase ramp characterised by two constant gradients along east–west and north–south direction, which implies that these large-scale perturbations for an interferogram correspond to equally spaced parallel fringes. Our approach is similar to that of Murakami et al. [29]: we compute the difference between each unwrapped interferogram and the GPS measurements to perform a least-squares adjustment. In this least-squares adjustment the model is expressed by:

$$V_i = G_{\mathrm{E-W}}\, X_i + G_{\mathrm{N-S}}\, Y_i + C \qquad (2)$$

where V_i is the difference between the interferogram and GPS at the ith GPS station, X_i and Y_i are the coordinates of the corresponding pixel of

Table 2
Coseismic interferogram information

Name	Unwrapped[a] (%)	E–W[b] (10^{-5})	N–S[b] (10^{-5})	GPS stations[c]	GPS rms diff.[d] (cm)	SRD map rms diff.[e] (cm)
AD	0.73	−0.02	−0.08	15	1.35	0.31
AE	0.72	−0.10	−0.06	21	1.67	0.62
AF	0.56	0.00	−0.02	16	1.5	0.59
BD	0.95	−0.19	−0.35	21	1.34	0.35
BE	1	−0.32	−0.33	24	1.72	0.31
BF	0.78	−0.21	−0.27	19	1.76	0.33
CD	0.69	−0.11	−0.09	21	2.02	0.58
CE	0.63	−0.21	−0.05	17	1.67	0.57
CF	0.7	−0.10	−0.02	18	1.69	0.41

[a] Proportion of unwrapped pixels with respect to interferogram BE (626 817 unwrapped pixels).

[b] E–W and N–S gradients of large-scale perturbation (10^{-5} or cm/km).

[c] Number of GPS stations used to calculate the gradients.

[d] Rms difference between the displacements along the radar line of sight (SRD) at GPS stations and the SRD given by a corrected coseismic interferogram.

[e] Rms differences between the SRD map (average of interferograms AD, BE et CF) and the SRD of a given coseismic interferogram.

the ith GPS station, $G_{\mathrm{E-W}}$ and $G_{\mathrm{N-S}}$ represent the two gradients of phase ramp and C is the constant between the interferogram and GPS data. To compute the V_i value, we transform the three components of the GPS displacement vector into an SRD value, taking into account the local unit vector from ground to satellite given in Table 1. The adjusted phase ramp is then subtracted from the interferogram, resulting in a corrected interferogram. Relative changes in $\Delta\Phi$ in interferogram are measured only to within an additive constant, which is estimated by the parameter C in Eq. 2. Then, a constant correction is also applied changing from relative to absolute unwrapped interferograms. This method assumes that errors on GPS data do not introduce a systematic bias.

Theoretically, the GPS data could be used for more complex modelling of the $\Delta\Phi$ perturbation (e.g. by polynomial or spline methods). We justify our model for two main reasons. First, we assume that large-scale perturbations are mainly caused by orbital errors. In such a case, this model, which has already been used successfully [30], is acceptable if there are few residual orbital fringes and if the study area is only a portion of an ERS scene. In this study, these conditions are fulfilled, as illustrated by the pre- and postseismic interferograms (Fig. 4b). Second, considering the number of available GPS data, this simple model limits the possible influences of GPS data errors on interferogram corrections. The results of the adjustment are listed in Table 2.

5. InSAR coseismic displacement map

Comparison between Fig. 4a,c illustrates the results of the corrections that remove the large-scale perturbations. The differences between coseismic SRD calculated from GPS measurements and SRD obtained from corrected interferograms at each GPS station are given in Fig. 5b. It shows that differences are less than ±4.5 cm and mainly lie within the error bars of the GPS data. The root mean square (rms) differences for each interferogram range from 1.35 to 2.02 cm (Table 2). Taking into account the nine coseismic interferograms the rms difference is 1.66 cm. The absence of significant large-scale residual perturbations in the corrected interferogram supports the phase ramp model that we adopted. In the corrected interferograms, medium- and small-scale perturbations remain, which are principally related to the atmospheric effect and cannot be modelled with GPS data. The dispersion of the corrected $\Delta\Phi$ values is expressed in Fig. 6a: it shows for each pixel the standard deviation of the nine $\Delta\Phi$

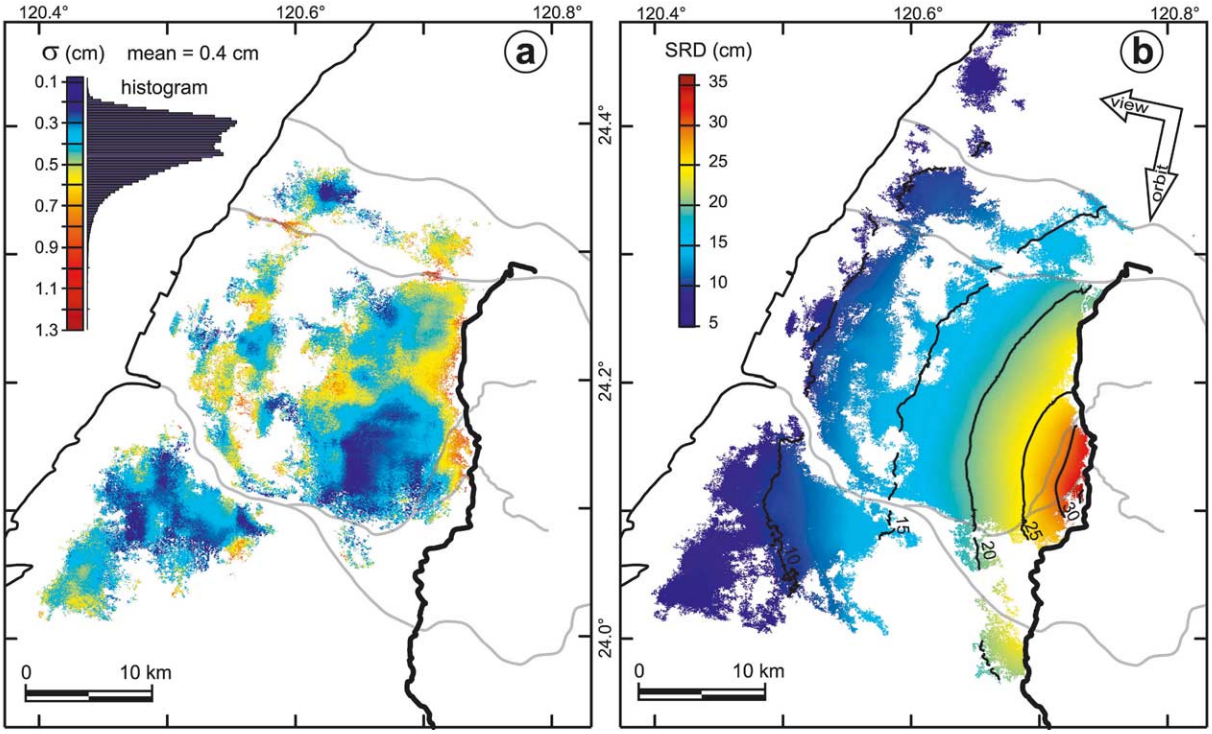

Fig. 6. Standard deviation of corrected coseismic interferograms and map of coseismic SRD. (a) Standard deviation σ (cm) of the corrected coseismic interferograms. Black thick line, Chelungpu fault; light grey line, rivers. σ is calculated only where the nine coseismic interferograms have been unwrapped. (b) Map of coseismic SRD that is the mean of the corrected interferograms AD, BE and CF. Thin black lines are iso-contours of SRD in cm. The white arrows correspond to orbit track and viewing directions of the satellite. The map shows a continuous seaward decrease in SRD, with a maximum at the concavity of the Chelungpu fault trace near the city of Taichung. The global trend is a seaward decrease in SRD gradient (spaces between iso-contours are wider).

values available for this pixel (only the pixels that have been unwrapped in all of the nine coseismic interferograms are thus considered). These values are quite constant over the available pixels, except for river anomalies where standard deviations reach 1.38 cm. The mean standard deviation is 0.4 cm.

To reconstruct the coseismic SRD map (Fig. 6b), we average the coseismic interferograms, expecting that this averaging should reduce the main unmodelled perturbations. This assumes a random distribution of the perturbations, as one can reasonably expect considering the observed atmospheric perturbations. Rather than using the nine available coseismic interferograms, we consider a combination of independent interferograms. The six SAR images allow us to choose amongst three possible combinations of three independent interferograms. The most coherent combination is obtained with AD, BE and CF interferograms. This method yields more reliable points than that using the nine interferograms. The rms differences between each coseismic interferograms and the coseismic SRD map range between 0.3 and 0.6 cm (Table 2), showing good consistency between the coseismic interferograms. We propose to use the rms difference between GPS and all the coseismic interferograms, which is 1.7 cm, as an uncertainty for the map (see discussion in Section 6.1).

The map of the coseismic SRD shows displacements ranging from 36.7 cm (in the westwardconcave bend of the Chelungpu fault near Taichung) to 4.9 cm near the coast of the Taiwan Strait. There is a seaward continuous decrease in SRD (Figs. 4c and 6b). Considering the gradient of SRD, the global trend is a decrease of the gradient from the fault trace to the coastline (Fig. 7). Looking in detail at the displacement gradient, we locally observe a quasi-systematic re-increase of the gradient from east to west, which contrasts with the global decrease towards the west. This anomaly (arrows 1 in Fig. 7) follows a line that exactly corresponds to the Changhua fault trace. This observation is significant with respect to the uncertainties of the map. One may question the origin of this anomaly, as the profiles P_1P', P_2P' and P_4P' in Fig. 7 show that the gradient anomaly is (as the fault) correlated with a topographic feature. However, we observed a similar change in gradient in profile P_3P', which crosses the Changhua fault in a flat plain area: an artefact that would be correlated with the relief is thus ruled out. We consequently interpret this anomaly as related to the Changhua fault, whose surface trace is located 10–20 km further west of the Chelungpu fault. To explain this anomaly, we propose that a minor reactivation of the Changhua fault zone may have occurred in response to the Chi-Chi earthquake, a phenomenon similar to that reported by Genrich et al. [31] in California (see also [32,44], who make reference to other triggered slip). This triggered reactivation does not necessarily reveal fault slip reaching the surface; it may reflect surface flexuring in a relatively narrow zone, related to deeper reactivation of the Changhua thrust ramp. In any case, such a displacement along the Changhua fault would account for the change in coseismic displacement field that induced the SRD gradient

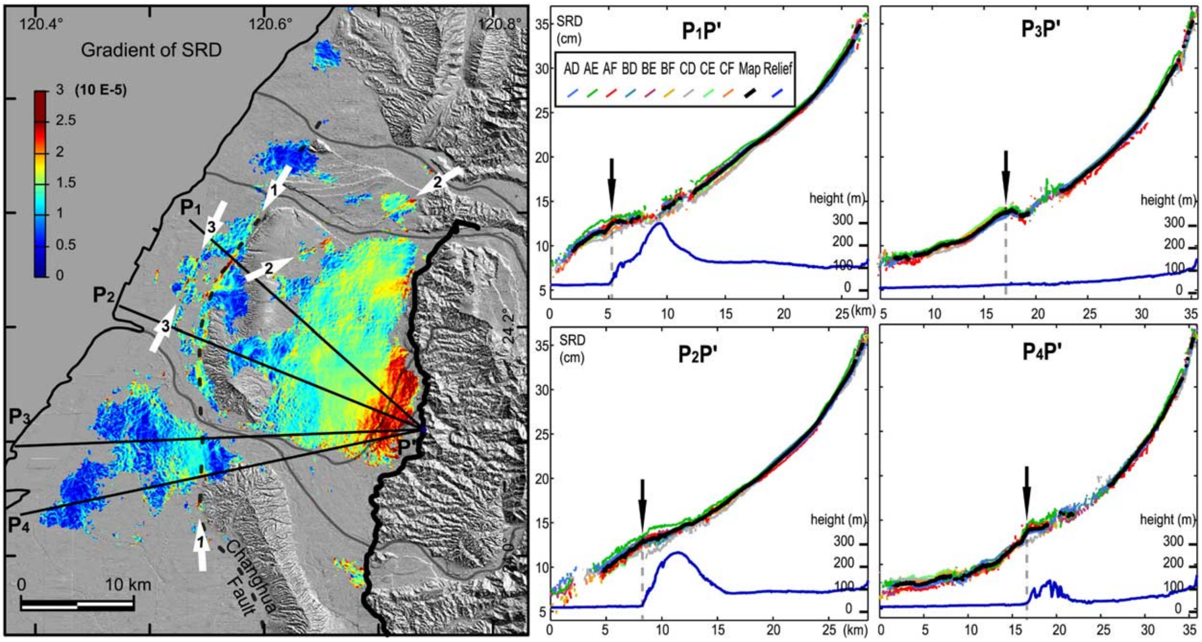

Fig. 7. Effect of the Changhua fault on the coseismic displacement field. (a) Map of gradient of coseismic SRD (with low-pass filter). It shows a global trend: a decrease (from red to dark blue) from east to west. The Changhua fault (dark grey dashed line) exactly fits an anomaly in this trend indicated by the white arrows 1. This anomaly, characterised by a re-increase in SRD from east to west, separates a blue-green area to the east from a red-yellow-green area to the west, contrasting with the global trend. White arrows 2 indicate an anomaly that corresponds to the Tuntzuchio fault (compare with Fig. 1). White arrows 3 indicate another, similar anomaly that could correspond to an unknown fault. (b–e) Four profiles (location in panel a) of the corrected coseismic interferograms, of the SRD map (black line) and of the relief (thin blue line) illustrating the anomaly 1. The black arrows show the location of the re-increase in SRD gradient. The profile P_3P', which crosses a flat area, also shows the anomaly excluding an artefact linked to the relief.

anomaly that we observed. Similar observations and analyses can be made regarding two other anomalies indicated by arrows 2 and 3 in Fig. 7. Anomaly 2 exactly fits the surface rupture of the Tuntzuchio fault caused by the major 1935 earthquake [33] (see location in Fig. 1). Anomaly 3, west of the Changhua fault, does not correspond to an identified fault; however, following the two other correlations it is possible that this anomaly also corresponds to a fault.

6. Discussion and conclusion

6.1. *Reliability of results*

To quantify the reliability of our coseismic SRD map, we have proposed to attribute an uncertainty value of 1.7 cm to the map, using the rms difference between the SRD calculated from GPS data and the SRD of the nine coseismic interferograms. This value is greater than the usual estimation of the uncertainty corresponding to the rms difference between GPS data and the SRD map, which is 1.2 cm in our study. These two estimates are affected by the GPS errors, which can be more than 3 cm in SRD, causing an overestimate of the map uncertainty. The mean standard deviation of the coseismic interferograms (Fig. 6a), which is also an indicator of the uncertainty of the SRD map, is 0.4 cm. Then, the uncertainty evaluated from GPS data may be overestimated; however, the standard deviation of coseismic interferograms depends on nine measures that are not completely independent and does not take into account possible systematic errors in coseismic interferograms. Moreover, GPS data are not really independent of the SRD map, because they are used to evaluate the phase ramp gradients and the constants of the interferograms (parameters $G_{\mathrm{E-W}}$, $G_{\mathrm{N-S}}$ and C, respectively, in Eq. 2). Thus, GPS data could introduce systematic errors in the SRD map that are not taken into account by the previous methods. Finally, as a precaution, we retained the 1.7 cm uncertainty given by the first method that is likely an upper bound throughout the map.

If such a single value is statistically representative of the uncertainty of the coseismic SRD map, it does not express the spatial variation of the uncertainty across the map. The map of standard deviation (Fig. 6a) is more informative to assess these variations than to consider the changes, from one GPS station to another, of the difference between GPS data and the SRD map. Fig. 6a shows that the highest values of the standard deviation map are distributed over areas of several kilometres, for example at a river bed north of Taichung or close to the fault. Regarding the different sources of errors of the coseismic SRD map, atmospheric effects and non-coseismic displacements are the main errors that can explain this spatial distribution. Changes in atmospheric state are not evenly distributed and can result in areas where variability between interferograms is high. Non-coseismic displacements can also produce a similar pattern in the spatial distribution. To distinguish between atmospheric effects and non-coseismic displacements, we need to analyse the temporal evolution between interferograms: atmospheric perturbations are expected to have no continuous evolution with time. For instance, regarding the variability close to the fault trace, both origins can be suspected. The area is located along a height change in the topography that can favour atmospheric variation. Regarding non-coseismic displacements, significant postseismic displacements are observed in the hangingwall by GPS [34,35], and also by InSAR (small hangingwall areas in postseismic interferograms show fringes that are consistent with deformation revealed by the GPS analysis). These displacements are related to a postseismic slip on the fault [34]. Thus, postseimic displacements on the footwall are possible near the fault trace. Yu et al. [6] did not apply any postseismic correction in the footwall. However, the GPS network coverage is low close to fault. The analysis of the temporal evolution between interferograms shows that the SRDs do not follow the logic of postseismic displacements and that their variations have rather an atmospheric origin. If the postseismic displacements suspected in this part of the footwall exist, they are too small relative to the atmospheric effects to be detected by our InSAR analysis. The SRD temporal analyses made at the gradient anomalies (see Fig. 7) lead to similar conclusions.

This discussion illustrates the limit of an estimate of the uncertainty only based on GPS data and shows the importance of having several coseismic interferograms to better determine the spatial distribution of the uncertainties on the coseismic SRD map. Moreover, several coseismic interferograms allow analysis of the temporal evolution of the perturbations and, for instance, the revealing of non-coseismic displacements that are disregarded by the GPS network. This is particularly important as the shortest coseismic interferogram is not necessarily the best in quality.

6.2. *Comparison with modelling of the distribution of slip on the fault plane*

Complementing information obtained from seismicity, geodetic data have notably been used to constrain the distribution of slip on the fault surface of the Chi-Chi earthquake. Discrepancies exist between the different published slip distribution models of the fault owing to different geometries of the fault, different inversion methods and data sets. Regarding the data, most of the models are determined by the inversion of both GPS and strong motion data [7,13,14,36]. Ma et al. [11] also include teleseismic data, whereas Johnson et al. [12] use only GPS data and Chi et al. [37] only strong motion data. Dominguez et al. [8] combine GPS data with horizontal coseismic displacement inferred from correlation of SPOT satellite images.

InSAR results can be integrated as new geodetic constraints on the fault geometry and slip distribution [30,38–40]. Although the coseismic SRD map simply gives one-dimensional constraints on the coseismic displacement, it provides a much larger spatial coverage than the GPS network. To check the interest of such InSAR integration, we compare our results with two models of slip distribution, from Dominguez et al. [8] and Wang et al. [13]. These models are inverted with Okada's method in homogeneous elastic half-space [41,42]; we use the Range–Change programme [43] to reconstruct the predicted coseismic SRD. Although both these models are globally consistent in trend with our results, they tend to overestimate the displacements. For instance, regarding the model from Dominguez et al. [8], the rms difference between the model and the coseismic SRD map is 29 cm. Even excluding a 5 km wide strip along the fault trace, where the largest discrepancies may be expected (notably because of the approximate geometry of the fault used in the model), the rms difference remains as large as 15 cm. Moreover, it is noteworthy that the deformation pattern observed is smoother than those in the models. Model comparison with InSAR results is particularly interesting as it gives more precise information than comparison with GPS data on the spatial distribution of the model errors. In this way, we determined that the model of Dominguez et al. [8] significantly overestimates the coseismic SRD in the area between Pakuashan and the fault trace, which may result from approximations in modelling the local fault geometry. Concerning the regional overestimate of the coseismic displacement by the models, Ji et al. [14] noted that a layered-Earth model is better than the half-space model for generating static response. They indicated that for a thrust, the fault response generated by the half-space Earth model is, by 30% or more, larger than that obtained with the layered model in the footwall. Furthermore, because the largest coseismic displacements occur on the hangingwall, the inversions are certainly more influenced by the hangingwall data than by the footwall ones.

Considering a joint inversion including our results, the asymmetrical spatial distribution of InSAR measurement in the footwall only deserves consideration because it can introduce a bias on modelling [38]. Another problem, related to data uncertainty, is the weighting of the data from different sources, which may also introduce bias in the modelling [30].

Taking into account these precautions, our results provide new constraints to improve the present-day knowledge on the Chi-Chi earthquake through modelling, especially in terms of coseismic slip distribution or fault geometry. Our valuable records of coseismic displacement caused by the Chi-Chi earthquake are available in most of the footwall domain of the reactivated

Chelungpu fault. The use of InSAR combined with the GPS information enables us to produce a map of the coseismic displacement on the footwall with centimetre accuracy, and with high resolution especially in the Taichung area. This result allows us to detect the influence of the Changhua and Tuntzuchio faults on the coseismic displacement of the Chi-Chi earthquake, that we suppose to be caused by slight slip along these faults triggered by the Chi-Chi earthquake. Based on these observations, we also suppose the presence of another fault west of the Changhua fault where a similar anomaly of the coseismic displacement occurs. Thus, not only does the InSAR technique provide a powerful tool to extrapolate the results of geodetic analyses, but it also has high potential to reveal features that other methods fail to reveal because of their punctual character (GPS network or strong motion network) or limitation in accuracy (correlation of SPOT satellite images).

Acknowledgements

We thank J.-P. Avouac and S. Dominguez, who provided results in advance of publication, and also the GDR-INSAR group and the CSRSR Centre of the National Central University of Chungli (Taiwan) for their help. This work was supported by the European Space Agency (ESA EO project C1P-1046 and ESA AO project), by the Taiwan–France cooperation programme (French Institut in Taipei and National Science Council of Taiwan) and by the French CNRS-INSU in the framework of the PNRN. We are grateful to Hu Jyr-Ching and to the reviewers for their comments that improved the manuscript. ***[AC]***

References

[1] H. Kao, W.P. Chen, The Chi-Chi earthquake sequence: Active, out-of-sequence thrust faulting in Taiwan, Science 288 (2000) 2346–2349.

[2] T.C. Shin, T.l. Teng, An overview of the 1999 Chi-Chi, Taiwan earthquake, Bull. Seismol. Soc. Am. 91 (2001) 895–913.

[3] T.L. Hsu, H.C. Chang, Quaternary faulting in Taiwan, Mem. Geol. Soc. China 3 (1979) 155–165.

[4] A. Lin, T. Ouchi, A. Chen, T. Maruyama, Co-seismic displacements, folding and shortening structures along the Chelungpu surface rupture zone occurred during the 1999 Chi-Chi (Taiwan) earthquake, Tectonophysics 330 (2001) 225–244.

[5] M. Yang, R.J. Rau, J.Y. Yu, T.T. Yu, Geodetically observed surface displacements of the 1999 Chi-Chi, Taiwan, earthquake, Earth Planet. Space 52 (2000) 403–413.

[6] S.B. Yu, L.C. Kuo, Y.J. Hsu, H.H. Su, C.C. Liu, C.S. Hou, J.F. Lee, T.C. Lai, C.C. Liu, C.L. Liu, T.F. Tseng, C.S. Tsai, T.C. Shin, Preseismic deformation and coseismic displacements associated with the 1999 Chi-Chi, Taiwan, earthquake, Bull. Seismol. Soc. Am. 91 (2001) 995–1012.

[7] C. Wu, M. Takeo, S. Ide, Source process of the Chi-Chi earthquake; a joint inversion of strong motion data and Global Positioning System data with a multifault model, Bull. Seismol. Soc. Am. 91 (2001) 1128–1143.

[8] S. Dominguez, J.P. Avouac, R. Michel, Horizontal coseismic deformation of the 1999 Chi-Chi earthquake measured from SPOT satellite images: implications for the seismic cycle along the western foothills of Central Taiwan, J. Geophys. Res. 108,

[9] Central Geological Survey, Map of the surface ruptures along Chelungpu fault during the Chi-Chi earthquake, Taiwan, scale 1:25,0000, Central Geological Survey, Ministry of Economical Affairs, Taiwan, 1999.

[10] Central Geological Survey, Report of the geological survey of the 1999 Chi-Chi earthquake (in Chinese), Central Geological Survey, Ministry of Economical Affairs, Taiwan, 1999, 315 pp.

[11] K.F. Ma, J. Mori, S.J. Lee, S.B. Yu, Spatial and temporal distribution of slip for the 1999 Chi-Chi, Taiwan, earthquake, Bull. Seismol. Soc. Am. 91 (2001) 1069–1087.

[12] K.M. Johnson, Y.J. Hsu, P. Segall, S.B. Yu, Fault geometry and slip distribution of the 1999 Chi-Chi, Taiwan earthquake imaged from inversion of GPS data, Geophys. Res. Lett. 28 (2001) 2285–2288.

[13] W.H. Wang, S.H. Chang, C.H. Chen, Fault slip inverted from surface displacements during the 1999 Chi-Chi, Taiwan earthquake, Bull. Seismol. Soc. Am. 91 (2001) 1167–1181.

[14] C. Ji, D.V. Helmberger, T.R.A. Song, K.F. Ma, D.J. Wald, Slip distribution and tectonic implication of the 1999 Chi-Chi, Taiwan, earthquake, Geophys. Res. Lett. 28 (2001) 4379–4382.

[15] Centre National d'Etudes Spatiales (C.N.E.S), PRISME/DIAPASON Software package, version 1.0, CNES, Toulouse, 1997.

[16] D. Massonnet, F. Adragna, M. Rossi, CNES general-purpose SAR correlator, IEEE Trans. Geosci. Remote Sens. 32 (1994) 636–643.

[17] D. Massonnet, K.L. Feigl, Radar interferometry and its application to changes in the Earth's surface, Rev. Geophys. 36 (1998) 441–500.

Geophys. J. Int. (2006) **167,** 421–444 doi: 10.1111/j.1365-246X.2006.03019.x

Mechanical deformation model of the western United States instantaneous strain-rate field

Fred F. Pollitz and Mathilde Vergnolle*

USGS, Menlo Park, CA, 94025, *USA. E-mail: fpollitz@usgs.gov*

Accepted 2006 March 20. Received 2006 March 17; in original form 2005 September 8

SUMMARY

We present a relationship between the long-term fault slip rates and instantaneous velocities as measured by Global Positioning System (GPS) or other geodetic measurements over a short time span. The main elements are the secularly increasing forces imposed by the bounding Pacific and Juan de Fuca (JdF) plates on the North American plate, viscoelastic relaxation following selected large earthquakes occurring on faults that are locked during their respective interseismic periods, and steady slip along creeping portions of faults in the context of a thin-plate system. In detail, the physical model allows separate treatments of faults with known geometry and slip history, faults with incomplete characterization (i.e. fault geometry but not necessarily slip history is available), creeping faults, and dislocation sources distributed between the faults. We model the western United States strain-rate field, derived from 746 GPS velocity vectors, in order to test the importance of the relaxation from historic events and characterize the tectonic forces imposed by the bounding Pacific and JdF plates. Relaxation following major earthquakes ($M \gtrsim 8.0$) strongly shapes the present strain-rate field over most of the plate boundary zone. Equally important are lateral shear transmitted across the Pacific–North America plate boundary along ∼1000 km of the continental shelf, downdip forces distributed along the Cascadia subduction interface, and distributed slip in the lower lithosphere. Post-earthquake relaxation and tectonic forcing, combined with distributed deep slip, constructively interfere near the western margin of the plate boundary zone, producing locally large strain accumulation along the San Andreas fault (SAF) system. However, they destructively interfere further into the plate interior, resulting in smaller and more variable strain accumulation patterns in the eastern part of the plate boundary zone. Much of the right-lateral strain accumulation along the SAF system is systematically underpredicted by models which account only for relaxation from known large earthquakes. This strongly suggests that in addition to viscoelastic-cycle effects, steady deep slip in the lower lithosphere is needed to explain the observed strain-rate field.

Key words: crustal deformation, GPS, viscoelasticity.

1 INTRODUCTION

Deformation in continental regions is commonly interpreted in terms of two end-member models (King *et al.* 1994; Thatcher 2003). The first ('block model') views the lithosphere as composed of a number of microplates/blocks that behave rigidly over sufficiently long time intervals, the different blocks being separated by faults. The rigid behaviour of individual blocks is realized over a timescale that is much longer than the earthquake cycle associated with a typical fault. This view, originally conceived to explain geologic and palaeomagnetic data in many regions, has the flexibility to accommodate elastic strain accumulation effects over the interseismic period (e.g. Matsu'ura *et al.* 1986). The second end-member model, known as the 'thin sheet model' (England & McKenzie 1982) accommodates the view that lithospheric deformation over length scales longer than the lithospheric thickness is essentially continuous and that over long time periods the lithosphere behaves as a viscous fluid. This model is generally applied to the thermally defined lithosphere, to which an effective viscosity can be derived that depends on the variation of temperature with depth and an assumed rheology of the lithosphere.

Although the relative merits of each end-member model are ardently debated (e.g. Tapponnier *et al.* 2001), we believe that the complexity of crustal deformation phenomena over the totality of spatial and temporal scales of relevance demands a compromise

---

*Now at: Université du Luxembourg, Faculté des Sciences, de la Technologie et de la Communication, L-1511 Luxembourg.

between the two. The need for a more unified approach is highlighted by the inherent difference between short- and long-term deformation rates. Constraints on long-term deformation rates through fault slip rates and palaeomagnetic measurements of block rotations are often found incompatible with constraints on short-term deformation rates through GPS measurements and principal stress directions as inferred from seismic focal mechanisms. The existence of a 'GPS–geologic' discrepancy is documented in many cases in which the GPS velocity field around a major fault is not in accord with the corresponding geologic slip rate. Examples include the Altyn Tagh fault (Mériaux *et al.* 2004; Wallace *et al.* 2004) (GPS inferred rate of ∼9 mm yr^{-1}, geologic slip rate of ∼25 mm yr^{-1}), the Owens Valley fault (Dixon *et al.* 2000) (GPS rate ∼7 mm yr^{-1}, geologic rate ∼2 mm yr^{-1}), the Garlock fault (Peltzer *et al.*, 2001 and references therein) (GPS rate <∼2 mm yr^{-1}, geologic rate ∼7 mm yr^{-1}), the Agua Blanca and San Miguel-Vallecitos faults (Hirabayashi *et al.* 1996; Dixon *et al.* 2002) (GPS rate ∼2–3 mm yr^{-1}, geologic rate ∼6 mm yr^{-1} for Agua Blanca fault; GPS rate ∼3–4 mm yr^{-1}, geologic rate ∼1 mm yr^{-1} for San Miguel-Vallecitos fault), and the Wasatch fault (Friedrich *et al.* 2003) (GPS rate ∼2.7 mm yr^{-1}, geologic rate 0.2–0.3 mm yr^{-1}).

It has been proposed in several of the above studies that apart from uncertainties in GPS measurements and fault slip rates, these discrepancies are to a large extent explained by the behaviour of a fault system during a viscoelastic deformation cycle. In several parts of the western United States (US) the characterization of active continental crust and mantle in terms of a relatively thin (∼15–30 km) mechanical lithosphere underlain by a ductile, relaxing 'asthenosphere' is supported by numerous studies of post-seismic relaxation (e.g. Pollitz *et al.* 2000, 2001; Nishimura & Thatcher 2003) and crustal response to removal of lacustrine loads (Bills *et al.* 1994) or lake filling (Kaufmann & Amelung 2000). In the case of a 2-D strike-slip regime, if the fault occupies an elastic upper layer underlain by a viscoelastic substrate, then analytic solutions are available to describe the evolution, accounting for the effects of periodic fault slip and subsequent viscoelastic relaxation compounded over many cycles (Savage & Prescott 1978; Pollitz 2001; Smith & Sandwell 2004). These solutions indicate that during the early part of a (periodic) cycle, crustal velocity around the fault is elevated above the average slip rate, while late in the cycle, crustal velocity is less than the average slip rate (Fig. 1). Many of the above-quoted discrepancies have been rationalized in terms of viscoelastic cycle behaviour, for example, Owens Valley fault: last earthquake in 1872, early in cycle (Dixon *et al.* 2000, 2003); Wasatch fault: last earthquake ∼1200–1300 yr BP, late in cycle (Malservesi *et al.* 2003). To these examples could be added many others for which viscoelastic relaxation effects early in the cycle are likely dominant, for example, elevated GPS velocities around the 1992 Landers and 1999 Hector Mine ruptures (Deng *et al.* 1998; Pollitz *et al.* 2000; Pollitz 2003a) or rapid uplift around the 1959 Hebgen Lake rupture (Nishimura & Thatcher 2003).

Pollitz (2003b) constructed a viscoelastic deformation cycle model and obtained a simple relationship between short-term deformation rates and average long-term fault slip rates. It was obtained by considering the average (or expected) behaviour of the lithosphere over the viscoelastic coupling cycle of a single deformation component and summing over all dislocation sources. The purpose of this paper is twofold:

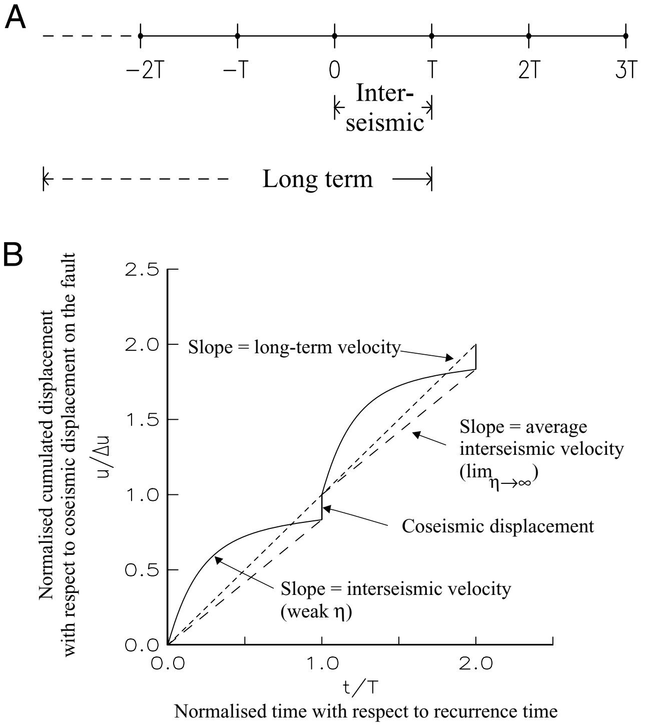

Figure 1. (a) A repeating earthquake occurs at a given location with periodicity T. The expected interseismic velocity field is the average velocity during an interseismic period (i.e. time 0^+ to T^-). The long-term velocity is the average over a long time interval, which includes several earthquakes. (b) Viscoelastic deformation cycle for a point located outside of the fault. Accumulated displacements over the interseismic period result from the superposition of the secular displacements and transient post-seismic displacements due to viscoelastic relaxation following periodic faulting events. The slope of the short dashed line represents the long-term velocity, the slope of the long dashed line the average interseismic velocity for high viscosity and the slope of the continuous line the interseismic velocity for low viscosity.

(1) To generalize the Pollitz (2003b) treatment further to account explicitly for additional types of sources, including viscoelastic relaxation effects on faults for which the slip history is sufficiently known and, in the thin-plate framework, steady slip along creeping portions of faults and

(2) To apply the new treatment to a GPS data set in the western US.

The proposed model is a departure from the well-known block model, in which GPS strain gradients are primarily driven by slip beneath numerous defined fault zones and viscoelastic effects from past earthquakes produce little time-dependent behaviour (e.g. McCaffrey 2005; Meade & Hager 2005; d'Alessio *et al.* 2005) (see also Supplementary Appendix B). Our model is essentially an extension of numerical models in which active continental deformation is produced by secularly increasing, horizontally transmitted tectonic forces either in isolation (e.g. Williams & McCaffrey 2001) or in superposition with transient viscoelastic effects (e.g. Roy & Royden 2000; Lynch & Richards 2001). Smith & Sandwell (2006) also apply a superposition of interseismic, post-seismic (viscoelastic), and steady-creep effects to describe the instantaneous velocity field along the San Andreas fault (SAF). Their model is more comprehensive than ours in accounting for relaxation of numerous moderate $M \sim 7$ events that may affect the present velocity field. However, their methodology differs in detail, particularly in how the plate boundary zone is loaded over time.

2 QUANTIFICATION OF CONTINENTAL DEFORMATION RATES FROM DISLOCATION SOURCES AND FORCES

2.1 Instantaneous velocity field

We assume that the continental lithosphere and underlying substrate may be divided into elastic and viscoelastic portions. The lithosphere deforms through the combined effect of elastic dislocations and forces applied to the elastic portions. The model constructed by Pollitz (2003b) describes dislocation sources in terms of the moment tensor density rate $\dot{\mathbf{m}}$ and the force density rate $\dot{\mathbf{f}}$, which is considered to arise from an externally applied force acting on an isolated portion of lithosphere (it could be associated with convergence of two plates along a well-defined boundary). Let $\mathbf{r}'$ be a variable denoting the location of a dislocation source and t denote time. The moment density $\mathbf{m}(\mathbf{r}', t)$ and force density $\mathbf{f}(\mathbf{r}', t)$ are assumed to be associated with repeating source(s) with definite mean periodicities, that is,

$$\mathbf{m}(\mathbf{r}', t) = \sum_{j\geq 0} \mathbf{m}(\mathbf{r}') H[t - t_0(\mathbf{r}') + jT(\mathbf{r}')], \tag{1}$$

and a similar expression for $\mathbf{f}\,(\mathbf{r}', t)$ as a separable function of a space-dependent function $\mathbf{f}\,(\mathbf{r}')$ and a time-dependent function. In eq. (1), H is the Heaviside step function, $t_0(\mathbf{r}')$ is the time of the last dislocation event at point $\mathbf{r}'$, and $T(\mathbf{r}')$ is the corresponding interevent time. In general $T(\mathbf{r}')$ can be a distribution of interevent times that depends on the event index j, but we retain the form of eq. (1) for simplicity. Let V define a volume within which contributing dislocation sources and forces are acting. In the statistical sense, the expected interseismic velocity $\mathbf{v}(\mathbf{r})$ is given by (Pollitz 2003b, his eq. 7):

$$\mathbf{v}(\mathbf{r}) = \int_V d^3\mathbf{r}'\dot{\mathbf{m}}(\mathbf{r}') : \left[\mathbf{G}^{(d)}(\mathbf{r}, \mathbf{r}', \infty) - \mathbf{G}^{(d)}(\mathbf{r}, \mathbf{r}', 0^+)\right] + \int_V d^3\mathbf{r}'\dot{\mathbf{f}}(\mathbf{r}') : \left[\mathbf{G}^{(f)}(\mathbf{r}, \mathbf{r}', \infty) - \mathbf{G}^{(f)}(\mathbf{r}, \mathbf{r}', 0^+)\right]. \tag{2}$$

Here $\mathbf{G}^{(d)}(\mathbf{r}, \mathbf{r}', t)$ and $\mathbf{G}^{(f)}(\mathbf{r}, \mathbf{r}', t)$ represent the response of the viscoelastic system to the various components of dislocation sources and forces, respectively, applied at $\mathbf{r}'$ and evaluated at point $\mathbf{r}$ and time t. The expressions in brackets represent the difference between the completely relaxed response and the initial elastic response. In a single-fault system, eq. (2) represents the average interseismic velocity between two successive earthquakes on that fault. It is to be distinguished from the long-term velocity field which is the average interseismic velocity plus the average rate of coseismic displacements produced over many earthquake cycles (Fig. 1).

For the forces likely to arise in the context of continental deformation, it is more realistic to work not with periodically increasing but rather continuously increasing forces, that is,

$$\mathbf{f}(\mathbf{r}', t) = \mathbf{f}(\mathbf{r}') \times (t - t_{\text{initial}}), \tag{3}$$

where t_{initial} is a long-past initial time ($t - t_{\text{initial}} \gg 0$). This force term is the fictitious force that would accumulate if the relative plate motion were not relieved by faulting. The total stress at the interplate boundary where this force is applied (or any other point within the continental interior) is the superposition of that due to the force term in eq. (3) and that from the viscoelastic cycle effects. These two types of contributing stress sources balance each other and produce, in principle, an average stress level that is bounded. With $\mathbf{f}\,(\mathbf{r}', t)$ given by eq. (3), the bracketed term with $\mathbf{G}^{(f)}$ in eq. (2) is replaced with $\mathbf{G}^{(f)}(\mathbf{r}, \mathbf{r}', -t_{\text{initial}})$. In the limit $t_{\text{initial}} \rightarrow -\infty$ we have

$$\mathbf{v}(\mathbf{r}) = \int_V d^3\mathbf{r}'\dot{\mathbf{m}}(\mathbf{r}') : \left[\mathbf{G}^{(d)}(\mathbf{r}, \mathbf{r}', \infty) - \mathbf{G}^{(d)}(\mathbf{r}, \mathbf{r}', 0^+)\right] + \int_V d^3\mathbf{r}'\dot{\mathbf{f}}(\mathbf{r}').\mathbf{G}^{(f)}(\mathbf{r}, \mathbf{r}', \infty). \tag{4}$$

Eq. (4) provides a relationship between instantaneous velocity, observed during a relatively short time interval that does not include any dislocation events, and the rate of moment release and tectonic force accumulation applied to elastic portions of the lithosphere. Since it is valid in the statistical sense, it is most appropriate when estimates of past event activity ($t_0(\mathbf{r}')$ and $T(\mathbf{r}')$) are not available.

However, with knowledge of past event history one can obtain a more general relationship. The space- and time-dependent response to dislocation sources of the form of eq. (1) can be written ($\dot{\mathbf{f}}$—terms dropped for brevity)

$$\mathbf{v}(\mathbf{r}, t) = \int_V d^3\mathbf{r}'\mathbf{m}(\mathbf{r}') : \left[\sum_{j\geq 0} \dot{\mathbf{G}}^{(d)}(\mathbf{r}, \mathbf{r}', t - t_0(\mathbf{r}') + jT(\mathbf{r}'))\right]. \tag{5}$$

For a single past dislocation event at a single point (e.g. $j = 0$ and fixed $\mathbf{r}'$), eq. (5) represents the velocity field associated with relaxation of the viscoelastic earth (observed at point $\mathbf{r}$ and time $t - t_0(\mathbf{r}')$ after the dislocation event). As a check upon eq. (4), the expected interseismic velocity field can be derived from eq. (5) by averaging the response over the period $(t_0(\mathbf{r}') + 0^+, t_0(\mathbf{r}') + T(\mathbf{r}'))$ separately for each dislocation source $\mathbf{r}'$:

$$\int_V d^3\mathbf{r}' \frac{\mathbf{m}(\mathbf{r}')}{T(\mathbf{r}')} : \left[\int_{t_0(\mathbf{r}')+0^+}^{t_0(\mathbf{r}')+T(\mathbf{r}')} dt \sum_{j\geq 0} \dot{\mathbf{G}}^{(d)}(\mathbf{r}, \mathbf{r}', t - t_0(\mathbf{r}') + jT(\mathbf{r}'))\right]. \tag{6}$$

Carrying out the time integration and j—summation of the bracketed term and equating the quantity $\mathbf{m}(\mathbf{r}')/T(\mathbf{r}')$ with $\dot{\mathbf{m}}(\mathbf{r}')$, the expression in eq. (6) results in the dislocation component of $\mathbf{v}(\mathbf{r})$ in eq. (4).

Note that eq. (5) depends on the viscoelastic structure because of the time dependence of $\dot{\mathbf{G}}^{(d)}$, but eq. (4) does not depend on the entire viscoelastic structure but rather on the decomposition of the earth model into elastic and viscoelastic parts. If the viscoelastic structure is correctly specified, then eq. (5) is a more accurate representation of the velocity field. Depending on our knowledge of past slip history, one may choose to employ eq. (5) when such history is available and eq. (4) when it is unavailable. In general, eq. (4) is applicable to either continuous distributions of $\dot{\mathbf{m}}(\mathbf{r}')$ and $\dot{\mathbf{f}}(\mathbf{r}')$ or discontinuous distributions localized on a fault plane. By the nature of intended 'slip events', eq. (5) is applicable to discontinuous distributions of $\mathbf{m}(\mathbf{r}')$ that are associated with slip on one or more fault planes. It is thus useful to decompose V into a set of fault surfaces Γ_{fault} and the remaining volume $V - \Gamma_{\text{fault}}$ (Fig. 2). One may further decompose Γ_{fault} into those fault surfaces Γ_n for which slip history is known and those fault surfaces Γ_m for which slip history is unknown. Thus $\Gamma_{\text{fault}} = \{\Gamma_n\} \cup \{\Gamma_m\}$. In the first case we define the triplet (Γ_n, t_n, T_n) to be the nth fault surface and the associated time of the last event and the interevent time. In this framework we form an estimate of interseismic velocity v^{inst} that accounts for known slip history using eq. (5) and otherwise falls back on the statistical average eq. (4). We may further account for the effect of steady fault creep and/or distributed steady slip in the bulk material. In this case we define a set of discrete creeping surfaces Γ_{cr} on which moment release rate is temporally constant. The remaining volume $V - \Gamma_{\text{cr}}$ may accommodate steadily slipping dislocations at a rate that may be laterally variable. Putting together the contributions of all

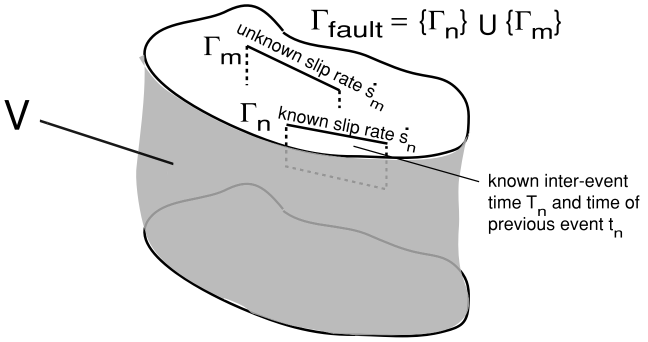

Figure 2. A volume V is assumed to contain both distributed and discrete dislocation sources that contribute to the instantaneous velocity field. Discrete dislocation sources are divided into two classes: (1) Γ_n on which the past slip rate $\dot{s}_n$, time of previous earthquake t_n, and interevent time t_n are considered known (or estimated) from geologic information, (2) Γ_m on which the long-term slip rate $\dot{s}_m$ is possibly known but slip history is poorly constrained.

deformation sources yields

$$\begin{aligned}
v^{\mathrm{inst}}(\mathbf{r}, t) = {} & \sum_n \int_{\Gamma_n} d^3\mathbf{r}'\, \mathbf{m}(\mathbf{r}') : \left[\sum_{j \geq 0} \dot{\mathbf{G}}^{(d)}(\mathbf{r}, \mathbf{r}', t - t_n + jT_n) \right] \\
& + \sum_m \int_{\Gamma_m} d^3\mathbf{r}'\, \dot{\mathbf{m}}(\mathbf{r}') : \left[\mathbf{G}^{(d)}(\mathbf{r}, \mathbf{r}', \infty) - \mathbf{G}^{(d)}(\mathbf{r}, \mathbf{r}', 0^+) \right] \\
& + \int_{V - \Gamma_{\mathrm{fault}}} d^3\mathbf{r}'\, \dot{\mathbf{m}}(\mathbf{r}') : \left[\mathbf{G}^{(d)}(\mathbf{r}, \mathbf{r}', \infty) - \mathbf{G}^{(d)}(\mathbf{r}, \mathbf{r}', 0^+) \right] \\
& + \int_V d^3\mathbf{r}'\, \dot{\mathbf{f}}(\mathbf{r}') . \mathbf{G}^{(f)}(\mathbf{r}, \mathbf{r}', \infty) \\
& + \int_{\Gamma_{\mathrm{cr}}} d^3\mathbf{r}'\, \dot{\mathbf{m}}(\mathbf{r}') : \mathbf{G}^{(d)}(\mathbf{r}, \mathbf{r}', \infty) \\
& + \int_{V - \Gamma_{\mathrm{cr}}} d^3\mathbf{r}'\, \dot{\mathbf{m}}(\mathbf{r}') : \mathbf{G}^{(d)}(\mathbf{r}, \mathbf{r}', \infty). \qquad (7)
\end{aligned}$$

The first, second, and fifth terms in eq. (7) are to be integrated over a volume surrounding the fault surface Γ_n, Γ_m, or Γ_{cr} of vanishingly small thickness.

Eq. (7) may be thought of as a combined deterministic and statistical estimate of instantaneous velocity due to dislocation sources and forces applied to the lithosphere. The first term accounts exactly for past fault movements using space- and time-dependent viscoelastic response functions; $\mathbf{m}(\mathbf{r}')$ for $\mathbf{r}' \in \Gamma_n$ may be considered associated with a uniform slip s_n, and the corresponding average slip rate is $\dot{s}_n = s_n / T_n$. In the second term, past fault movements are accounted for with a statistical average; $\dot{\mathbf{m}}(\mathbf{r}')$ for $\mathbf{r}' \in \Gamma_m$ may be considered associated with a uniform slip rate $\dot{s}_m$. The third term represents the contribution of relaxation from distributed faulting with a statistic average, and the fourth term the contribution of externally applied forces. Finally, the fifth and sixth terms account for the effects of steady fault creep on discrete creeping surfaces and steady slip distributed over the remaining volume, respectively.

2.2 Long-term velocity field

At a timescale that is much larger than the interevent time of a typical fault in the system, one may obtain the average long-term velocity as the time-averaged instantaneous velocity field plus the average velocity field produced by the compounded coseismic displacement fields of all dislocation sources. The latter is given by

$$\int_V d^3\mathbf{r}'\, \dot{\mathbf{m}}(\mathbf{r}') : \mathbf{G}^{(d)}(\mathbf{r}, \mathbf{r}', 0^+). \qquad (8)$$

The time-averaged instantaneous velocity field is given by eq. (7) but with the fault elements Γ_n and Γ_m grouped together into the second term [because of the time-averaging process as carried out in eq. (6)]. This results in a long-term velocity field:

$$\begin{aligned}
v^{\mathrm{long}}(\mathbf{r}) = {} & \sum_n \int_{\Gamma_n} d^3\mathbf{r}'\, \dot{\mathbf{m}}(\mathbf{r}') : \mathbf{G}^{(d)}(\mathbf{r}, \mathbf{r}', \infty) \\
& + \sum_m \int_{\Gamma_m} d^3\mathbf{r}'\, \dot{\mathbf{m}}(\mathbf{r}') : \mathbf{G}^{(d)}(\mathbf{r}, \mathbf{r}', \infty) \\
& + \int_{V - \Gamma_{\mathrm{fault}}} d^3\mathbf{r}'\, \dot{\mathbf{m}}(\mathbf{r}') : \mathbf{G}^{(d)}(\mathbf{r}, \mathbf{r}', \infty) \\
& + \int_V d^3\mathbf{r}'\, \dot{\mathbf{f}}(\mathbf{r}') . \mathbf{G}^{(f)}(\mathbf{r}, \mathbf{r}', \infty) \\
& + \int_{\Gamma_{\mathrm{cr}}} d^3\mathbf{r}'\, \dot{\mathbf{m}}(\mathbf{r}') : \mathbf{G}^{(d)}(\mathbf{r}, \mathbf{r}', \infty) \\
& + \int_{V - \Gamma_{\mathrm{cr}}} d^3\mathbf{r}'\, \dot{\mathbf{m}}(\mathbf{r}') : \mathbf{G}^{(d)}(\mathbf{r}, \mathbf{r}', \infty). \qquad (9)
\end{aligned}$$

In contrast with the instantaneous velocity field (eq. 7), the long-term velocity field in eq. (9) depends only on the response functions calculated in the completely relaxed state.

3 WESTERN US VELOCITY AND STRAIN-RATE FIELDS

The instantaneous surface velocity field of the western US with respect to fixed North America (NA) is shown in Supplementary Fig. A1. It is a composite of the GPS velocity fields determined in nine separate USGS GPS surveys plus the WUSC velocity field determined by Bennett *et al.* (1999) (version 002 of the WUSC velocity field, ftp://cfa-ftp.harvard.edu/pub/rbennett/WUSC) using continuous and campaign GPS data and VLBI data. The USGS campaign measurements are extracted from online sources (http://quake.wr.usgs.gov/research/deformation/gps/auto/CL.html and http://quake.wr.usgs.gov/research/deformation/gps/qoca/index.html) and are described in numerous prior publications (Savage *et al.* 1998, 1999a,b; Thatcher *et al.* 1999; Prescott *et al.* 2001; Savage *et al.* 2001a,b; Svarc *et al.* 2002a,b; Hammond & Thatcher 2004; Savage *et al.* 2004). The campaign measurements are generally conducted at intervals of 3 to 4 yr, and the associated velocity field is a composite of such measurements conducted between 1993 and 2003. The velocity field for the San Francisco Bay region is based upon not only USGS campaign measurements but also continuous GPS time-series from the CORS (Continuously Operating Reference Sites) and the BARD (Bay Area Regional Deformation) networks (Prescott *et al.* 2001).

The WUSC velocity field is a composite of continuous and campaign GPS measurements conducted collectively between 1986 and 2000. Additional VLBI data used in the solution span the period 1979 to 1998. Data from the WUSC velocity field have been corrected by its authors for coseismic offsets of significant earthquakes. No correction for short-term post-seismic deformation has been applied to these data.

Each of the nine USGS campaigns data sets were processed at the USGS using the GIPSY/OASIS II software (Zumberge *et al.* 1997). Velocities are provided in a fixed North American reference frame based on ITRF2000 (Altamimi *et al.* 2002). Similarly, the WUSC velocity field is referenced to fixed North America. There are a total of 486 GPS velocity vectors contributed by the USGS campaign data and 260 velocity vectors contributed by the WUSC velocity field. The two data sources (USGS campaign; WUSC) have 84 common sites, and we determined a rotation between the two associated velocity fields that aligns the two velocity fields to within the measurement errors (generally ~1 mm yr^{-1} standard deviation in both east and north components for the USGS campaign measurements; ~0.5 mm yr^{-1} for the WUSC continuous measurements). The RMS of the difference at the 84 common sites are 1.7 mm yr^{-1} and 1.1 mm yr^{-1} for the east and north component. The velocity shift between the two data sets is practically a uniform translation of (-0.6 mm yr^{-1} east, -1.4 mm yr^{-1} north).

After correction of the velocity for the estimated effects of steady creep on the SAF system (Supplementary Fig. A2), the associated strain-rate field is depicted in Supplementary Figs A3–A6. We choose to model strain rate rather than the original GPS velocity field for several reasons. First, modelling strain rate avoids the issue of absolute reference frame of the GPS measurements. Second, our quantitative framework is not a kinematic model but rather a dynamic model in which instantaneous deformation rates are related to a series of underlying physical processes. This involves serious challenges when attempting to fit the GPS velocity field in detail. For example, the viscoelastic process that is of first order importance is a diffusive process with long-range effects. The potential inadequacy of the assumption of laterally homogeneous viscoelastic structure can lead to substantial errors in predicted velocity at long wavelength (i.e. far from the earthquake source region). Other unmodelled effects may include basal drag and more spatially variable forcing rates. Omission of such key ingredients can compromise a direct fit of the velocity field, and we judge that neglected processes are associated with long-wavelength effects that carry less weight when working with strain rate.

Because the GPS measurements represent a discrete sample of the total velocity field, it is necessary to smooth the underlying strain field in some manner. The procedure for deriving a strain field from the surface velocity field at a given spatial scale is a slightly modified version of the method of Shen *et al.* (1996) and is described in Supplementary Appendix A. Supplementary Figs A3 and A4 show the velocity gradient field at spatial scales of 40 and 30 km, respectively, while Supplementary Fig. A5 shows a composite map derived from the previous two figures. Fig. 3 (also presented as Supplementary Fig. A6) represents the velocity gradient field of Supplementary Fig. A5 in terms of the magnitude and directions of the principal horizontal strain rate axes plus the rotational strain rate $\dot{\omega}(\mathbf{r})$, defined as

$$\dot{\omega}(\mathbf{r}) = \frac{1}{2}\left[\frac{\partial u(\mathbf{r})}{\partial \beta} - \frac{\partial v(\mathbf{r})}{\partial \gamma}\right], \qquad (10)$$

where u and v are east and north velocity and γ and β measure distance in the due east and north directions, respectively.

Fig. 3 reveals that, as one would expect, deformation rates are generally greatest near the North American plate boundary zones adjacent to the JdF and Pacific plates. The JdF–NA plate boundary zone deformation is characterized by primarily ENE–WSW shortening combined with strong clockwise rotation in the Pacific Northwest at ~50–100 nanostrain yr^{-1}. The Pacific–North American plate boundary zone deformation is characterized by right-lateral shear strain parallel to the strike of the SAF zone and the Eastern California Shear Zone (ECSZ) at rates of ~180 and ~50–100 nanostrain yr^{-1}, respectively, combined with strong clockwise rotation, resulting essentially in deformation under simple shear. These characteristics have been remarked in many earlier studies (e.g. Savage *et al.* 1999b; McCaffrey *et al.* 2000; Savage *et al.* 2001a,b; Svarc *et al.* 2002a). Further in the plate interior in the Basin and Range Province, strain rates are characterized by WNW–ESE extension at relatively small rates ~25–50 nanostrain yr^{-1} (Hammond & Thatcher 2004).

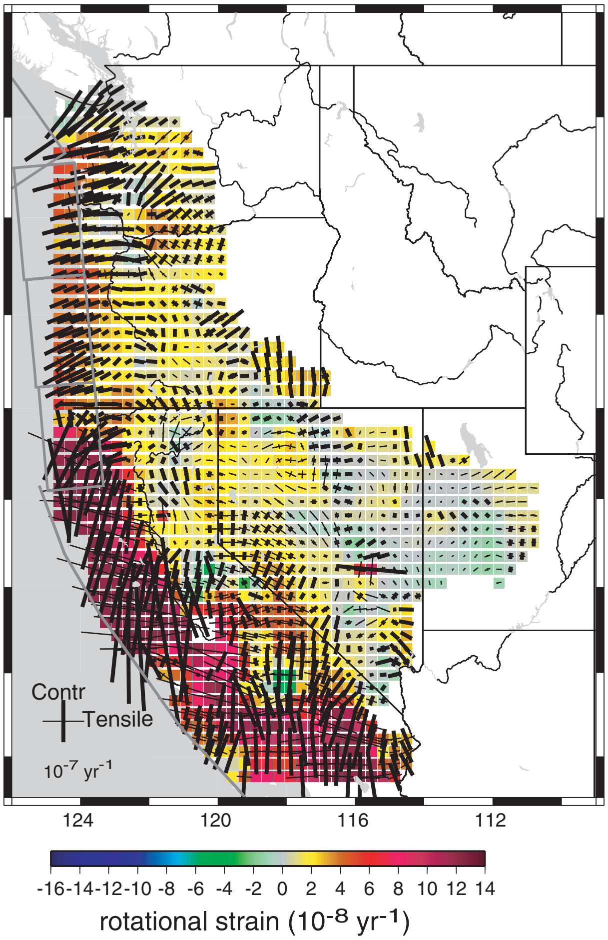

Figure 3. Representation of western US strain-rate field in terms of the amplitudes and directions of the principal strain-rate axes (thick and thin line segments denoting a principal contractile or tensile strain-rate axis, respectively) and rotational strain rate (indicated by colour shading). There is no restriction on the standard deviations of the velocity gradient values. Grey lines indicate outlines of planes upon which Juan de Fuca–North America and Pacific–North America forces are imposed.

4 MODEL CONSIDERATIONS

4.1 Rheology of the western US continental lithosphere

Most information about depth-dependent rheology in the western US is provided by studies of post-seismic relaxation (Pollitz *et al.* 2001; Nishimura & Thatcher 2003; Pollitz 2003a; Freed & Bürgmann 2004), removal of lacustrine loads (Bills *et al.* 1994) or glacial loads (James *et al.* 2001), or lake filling (Kaufmann & Amelung 2000). Among these studies, those of Bills *et al.* (1994), Nishimura & Thatcher (2003), and Kaufmann & Amelung (2000), all of which pertain to the Basin and Range province, prefer a rheology involving an elastic upper crust and relatively strong lower crust underlain by relatively weak mantle, implying that the uppermost portion of the crust (or the entire crust) is the strength-carrying portion of the lithosphere. Essentially the same conclusion is reached for the Mojave desert region (Pollitz *et al.* 2001; Pollitz 2003a; Freed & Bürgmann 2004) and northwestern Washington (James *et al.* 2001). In northwestern Nevada, the relative strength of the lower crust and upper mantle has not been conclusively resolved, and a broader range of rheologies may be consistent with available post-seismic

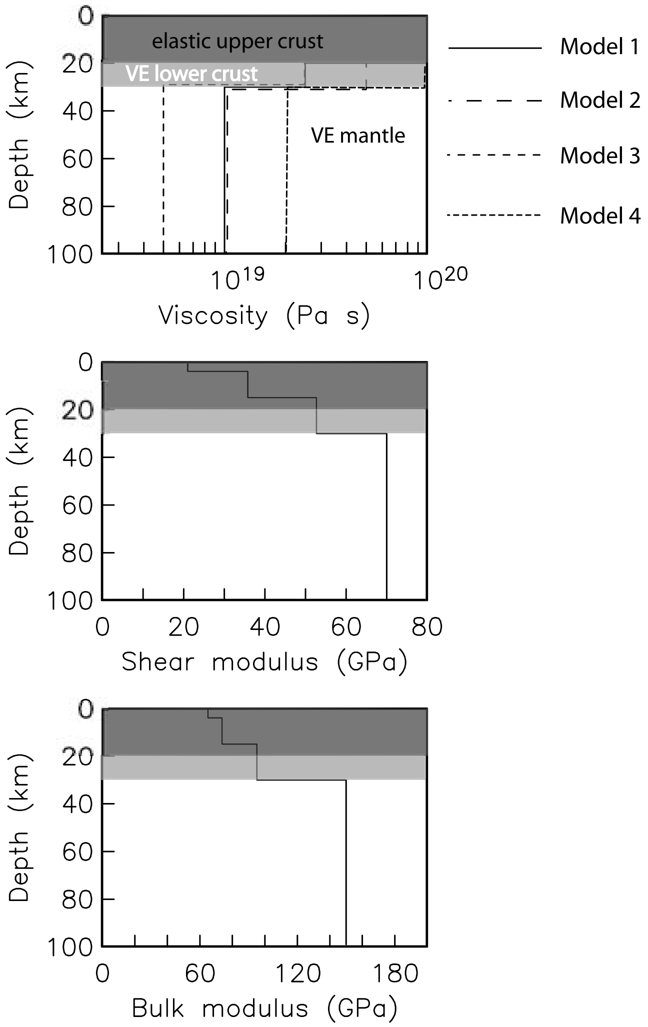

Figure 4. Rheological stratification of four candidate models considered in this study, each characterized by an elastic upper layer that includes the upper crust and part of the lower crust underlain by the remaining viscoelastic lower crust and viscoelastic mantle. A Maxwell rheology is assumed for the viscoelastic layers with indicated viscosity values.

deformation data (e.g. Hetland & Hager 2003), admitting the possibility of a relatively strong mantle lithosphere.

In Fig. 4 we present four candidate rheology models based on the results of the above studies. They are intended to be representative of the western US as a whole. All four models are characterized by an elastic plate thickness of 20 km, which could correspond to the upper crust plus a boundary layer occupying the upper portion of the lower crust. The remaining lower crust to a depth of 30 km and the underlying mantle are assumed Maxwell viscoelastic with viscosity η_c and η_m, respectively. In all cases, we assume a relatively weak mantle with low viscosity (5×10^{18} to 2×10^{19} Pa s) and a range of lower crust strength with low to moderate viscosity (2.5×10^{19} to 1×10^{20} Pa s). Although lateral variations in rheology are almost certainly present in this large area based on variations in mantle seismic velocity (Humphreys & Dueker 1994) and other physical properties (Lowry *et al.* 2000; Provost & Chéry 2006), we believe that these simple rheological models provide useful layered starting models that are representative of much of the western US. In addition, by considering how well the observed strain-rate field is matched in specific subregions of the western US, we may discriminate among these rheology models on a region-by-region basis.

4.2 Characterization of forces driving plate boundary zone deformation

The western US exhibits active deformation over a wide range of spatial scales and tectonic regimes (Smith 1978; Zoback & Zoback 1989; Hammond & Thatcher 2004) (Fig. 3). The strike-slip regime of northern California is dominated by the SAF to the west, quasi-rigid block motion of the Sierra Nevada block to its east, and a combination of right-lateral strike-slip strain, with maximal shear trending ~N35°W, and normal faulting with minimum principal stress axis ~N70°W, in the northern continuation of the ECSZ. The deformation style becomes increasingly dominated by normal faulting further east in the Basin and Range province, the transition between the strike-slip and normal faulting regimes occurring roughly between the Central Nevada Seismic Zone (CNSZ) in western Nevada and the northern Walker Lane in northeastern California. These patterns yield to ENE–WSW horizontal compression in the Pacific Northwest related to JdF–NA subduction. These tectonic patterns reflect the roles of several tectonic driving forces and their interaction in different regions of the western US crust.

In order to quantify the influence of the bounding Pacific and JdF plates on the deformation of the North American plate, we note that an oceanic plate is characterized by relatively strong lithosphere compared with the continental lithosphere with which it is in contact. The oceanic mechanical plate thickness, assuming that it is associated with the ~700°C isotherm, is only about 15–20 km for the relatively young oceanic lithosphere adjacent to the Pacific Northwest or California. This is based on the age-heat flow relationships provided by Stein & Stein (1992). This is even slightly less than the ~15–30 km thickness of the continental mechanical lithosphere estimated in numerous localities in the western US (Section 4.1). However, we note that the rigidity of olivine is about 2.5 times as great as that of crustal materials. This great strength contrast ensures that the oceanic lithosphere will be highly resistant to internal deformation compared with adjacent continental lithosphere, even if the mechanical plate thickness is comparable. We therefore assume that, as a first approximation, the western US continental lithosphere possesses a thin mechanical lithosphere and responds passively to forces exerted by the bounding oceanic plates. An implication of this assumption is that the process of oceanic plate to continental plate interaction along their common interplate boundary may be well described as the response (of the continental lithosphere) to secularly increasing forces exerted on that boundary (Section 2.1, eq. 3).

Fig. 5 shows the two main interplate boundaries that affect western North American plate deformation. The first interplate boundary forms the western boundary of the SAF system which divides the Pacific plate from the NA plate boundary zone. The Pacific moves laterally with respect to the NA plate at a rate of about 48 mm yr^{-1} (DeMets & Dixon 1999) parallel to the interplate boundary. The force of this interaction is opposed during the interseismic period by strain accumulation among the faults distributed throughout the broad western NA plate boundary zone. Although the role of deep dislocations in driving strain accumulation is often debated (e.g. Savage *et al.* 1999b), we shall assume that this interaction is described purely through a distribution of horizontal forces along the interplate boundary. This loading mechanism is also implicit

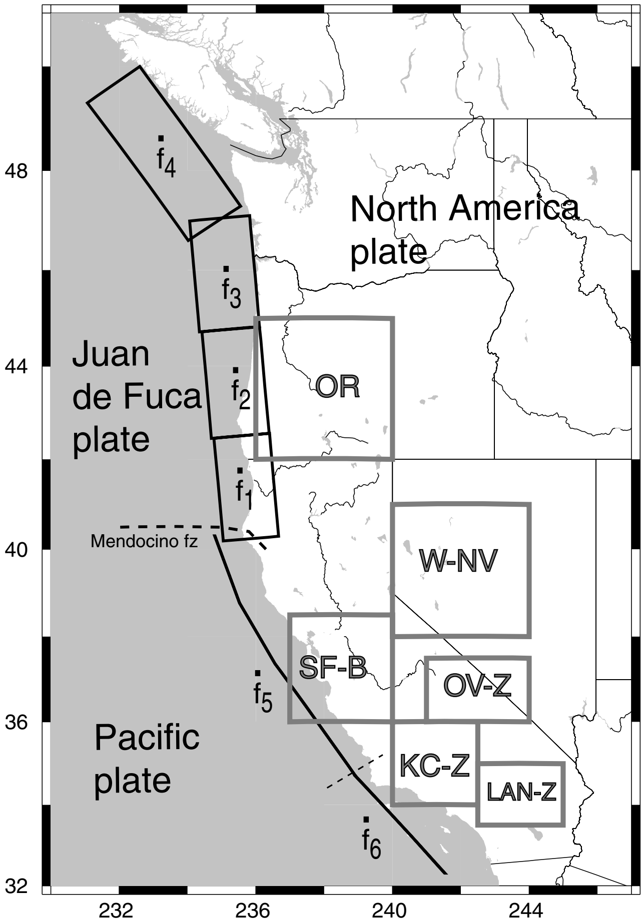

Figure 5. Distribution of surfaces on which major oceanic plates (Pacific, Juan de Fuca) exert a force on the North American plate. The exerted force per unit area is assumed uniform along the given surface for each of the interplate boundaries. The corresponding forcing rate parameter ($\dot{f}_1$, etc.) is indicated for each force plane. The rectangular outlines indicate the 6 subregions discussed in the text (Section 6) and in Fig. 16.

in those models, which describe the Pacific–NA interaction as the loading of a shear zone driven from the sides (e.g. Roy & Royden 2000; Lynch & Richards 2001).

The second interplate boundary is along the Cascadia subduction zone, which divides the JdF plate from the NA plate. In a similar manner to the SAF system, we assume that loading of the continental lithosphere along the subduction zone is described through a distribution of forces directed parallel to the JdF–NA relative motion resolved onto the slab interface, that is, directed down the slab. This defines a mechanism of interseismic strain accumulation at subduction zones that is similar to, but not identical with, the backslip model of Savage (1983). In the latter model, interseismic deformation within the continental lithosphere is driven by shear dislocations distributed along the interplate boundary, with magnitude equal to the negative of the coseismic slip divided by the recurrence interval (i.e. the negative of the long-term slip rate). Williams & McCaffrey (2001) implemented the framework of distributed forces (which they termed a 'finite plate model') to describe JdF to Cascadian forearc interactions. They found important differences between the finite plate model and the conventional backslip model when both are calibrated to fit geodetic data, such that stressing rates transmitted at the JdF–NA interplate boundary are smaller in the finite plate model.

The tectonic loading process is here assumed steady state. Cast in terms of eq. (7), it follows that we may approximate the steady-state loading process for both the Pacific and JdF interactions in terms of a distribution of forcing rates $\dot{\mathbf{f}}(\mathbf{r}')$ along the idealized continental shelf (SAF system) or the subduction interface (Cascadia system).

Note that the contribution of secularly increasing forces to the stress field is balanced in the long term by those contributions from coseismic and post-seismic stress changes associated with earthquakes. That is, the fourth term of eq. (7) and the remaining terms of eq. (7), each become arbitrarily large with increasing time, but the sum of all terms, in principle, remains finite. (In practice, however, imperfect specification of forcing rates and fault geometries or histories would lead to large stress fields at sufficiently large times.) In addition, horizontal forces arising from lateral gradients in gravitational potential energy likely play a role in driving western US active deformation (Flesch *et al.* 2000). However, such forces do not play an explicit role in shaping the active deformation in our framework because, according to eq. (7), a constant force (i.e. $\dot{\mathbf{f}} = 0$) does not contribute to the instantaneous velocity or strain-rate fields. Indirectly, these forces generate an absolute stress field, which promotes Basin and Range normal faulting and fault-perpendicular shortening around the SAF system. The moment release associated with these dislocation sources contribute to the instantaneous velocity field.

4.3 Model parametrization

Instantaneous deformation of the western US continental lithosphere is modelled as a superposition of the effects embodied in the various terms of eq. (7). Here we describe how these terms are parametrized.

Table 1 lists the parameters of force interaction between the oceanic Pacific and JdF plates and the continental NA plate. Note that the force interaction is meant to represent that between the oceanic plate and the portion of western US lithosphere with which it is in contact. In the case of the 'JdF–NA' boundary, the force vector is chosen appropriate for relative motion between the JdF plate and Cascadia forearc which is migrating northwards at about 10 mm yr^{-1} with respect to fixed North America (Wells & Simpson 2001; McCaffrey *et al.* 2000; Svarc *et al.* 2002b). As noted by McCaffrey *et al.* (2000) and Williams & McCaffrey (2001) and seen in Fig. 3 this leads to an horizontal strain rate in the Cascadia region dominated by ENE–WNW shortening. For that reason we have chosen a JdF–Cascadia forearc force interaction that is directed N65°E. In order to account for possible segmentation of the Cascadia margin (e.g. Trehu *et al.* 1994), we subdivide the JdF–NA plate interface into four subplanes. The corresponding forcing rates, which are assumed uniformly distributed on each respective subplane, are denoted $\dot{f}_1$, $\dot{f}_2$, $\dot{f}_3$, and $\dot{f}_4$, as labelled in Fig. 4. The P-NA boundary is taken to coincide with the North American continental shelf, which is generally the western limit of significant faulting. This boundary of total length 1200 km, upon which P-NA forcing rates are applied, is located $\sim$100 to 200 km west of the SAF system. It consists of a total of four vertical planes which are grouped into a northern set, which is approximately locally parallel to the Pacific–Sierra Nevada/Great Valley (SNGV) relative motion direction (Argus & Gordon 2001), and a southern set, which is approximately locally parallel to the P-NA relative plate motion direction. The corresponding forcing rates are denoted $\dot{f}_5$, and $\dot{f}_6$, as labelled in Fig. 4.

Table 2 lists the geometry and slip history associated with selected major and minor faults in the western US, including the

Table 1. Parametrization of Tectonic Forces.

Plate boundary	$L^{(a)}$ (km)	W $^{(b)}$ (km)	Endpoint$^{(c)}$	Strike (○)	Dip$^{(d)}$ (○)	Rake (○)	Parameter	Inverted$^{(e)}$ (10^{12} Nyr^{-1})
JdF–NA	253	135	42.56°N,123.60°W	355	8.5	110	$\dot{f}_1$	23.3
JdF–NA	253	135	44.83°N,123.89°W	355	8.5	110	$\dot{f}_2$	−0.4
JdF–NA	253	135	47.10°N,124.18°W	355	8.5	110	$\dot{f}_3$	7.5
JdF–NA	368	135	44.83°N,123.89°W	325	8.5	90	$\dot{f}_4$	44.8
Pacific–NA$^{(f)}$	180	20	40.30°N,125.20°W	340	90	180	$\dot{f}_5$	193.8
	180	20	38.78°N,124.48°W	330	90	180		
	360	20	37.38°N,123.44°W	325	90	180		
Pacific-NA	360	20	34.72°N,121.11°W	318	90	180	$\dot{f}_6$	35.6

$^{(a)}$ L = segment length; $^{(b)}$ W = segment width.

$^{(c)}$ Location of lower edge corner closest to strike direction. (Upper and lower segment edge depths are 0 and 20 km).

$^{(d)}$ Force is applied on footwall (oceanic side) to hanging wall (continental side).

parallel to slip vector (specified by strike, dip, rake).

$^{(e)}$ Inverted force rates on Model 4 with $\{s_j \mid j = 1, 2, 3\}$ inverted.

$^{(f)}$ Forcing is uniformly distributed over the three subsegments.

Table 2. Parametrization of Major (Class 1) and Minor (Class 2) Faults.

Name &Class	$t_0^{(a)}$	T$^{(b)}$ (yr)	Dip (○)	Rake (○)	Slip Value$^{(e)}$ (m)	Parameter (m)	M_w	Ref.
Cascadia (1)	1700	500	8.5	110	8 (6.4)	s_1	9.0	1,2
San Francisco (1)	1906	250	90	180	∼5 (∼5.5)	s_2	8.0	3$^{(c)}$
Fort Tejon (1)	1857	350	90	180	6$^{(d)}$ (7.5)	s_3	8.0	4
Pleasant Valley (2)	1915	7000	60	−90	5 (2.5)	s_4	7.7	5,6
Owens Valley (2)	1872	4150	80	170	6.1 (3.05)	s_5	7.6	7
Landers (2)	1992	1000	90	180	∼3.5 (∼3.5)	s_6	7.3	8$^{(c)}$
Kern County (2)	1952	420	75	24, 83	4.8, 1.3 (4.8, 1.3)	s_7	7.2	9$^{(c)}$
Fairview Peak (2)	1954	50 000	60	−127	4.8 (2.4)	s_8	7.2	10
Cedar Mountain (2)	1932	3600	90	180	1.6 (1.6)	s_9	7.1	11
Dixie Valley (2)	1954	6000	40	−90	1 (0.7)	s_{10}	7.1	10
Pyramid Lake (2)	1852	2100	90	180	4 (2)	s_{11}	7.1	12
Olinghouse (2)	1960s	8000	90	0	3.9 (1.95)	s_{12}	7.0	12

$^{(a)}$ t_0 = date of last rupture; $^{(b)}$ T = recurrence interval.

$^{(c)}$ Distributed fault slip; $^{(d)}$ Rupture approximated with uniform slip.

$^{(e)}$ *A priori* slip value followed in parentheses by the 'revised' slip value on Model 4 according to estimated slip value shown on Fig. 10.

^{1}Atwater & Hemphill-Haley (1997); ^{2}Hyndman & Wang (1995); ^{3}Thatcher *et al.* (1997)

^{4}Sieh (1978); ^{5}Wallace (1977); ^{6}Hetland & Hager (2003); ^{7}Beanland & Clark (1994)

^{8}Wald & Heaton (1994); ^{9}Bawden (2001); ^{10}Caskey *et al.* (1996); ^{11}Bell *et al.* (1999)

^{12}DePolo *et al.* (1997).

date of last major rupture. It includes only those faults whose combined magnitude and slip history as such as to be deemed capable of contributing substantial viscoelastic relaxation signals to the present-day strain-rate field. The contributions of countless other faults will be accommodated in other ways, as described below and in Section 5.4. (It would be inappropriate to use the information in Table 2 to construct any budget of long-term slip. It is commonly the case that faults, which are important contributors to the long-term velocity field are practically opaque with respect to the interseismic velocity field. We refer the reader to Supplementary Appendix B for further elaboration.) Note that the 1999 Hector Mine event is omitted because the southern California GPS observations originate from Release 2 of the SCEC velocity field (http://www.scecdc.scec.org/group_e/release.v2), which was released in 1998.

For purpose of classification we refer to the major ($M \geq \sim 8.0$) and minor ($M \geq 6.8$) ruptures as Class 1 and Class 2 faults, respectively. The three Class 1 and nine Class 2 faults considered here are indicated by red and purple line segments, respectively, in Fig. 6, and the corresponding slip parameters of the events are denoted $\{s_j \mid j = 1, \ldots, 12\}$ (Table 2). In most cases the recurrence time T is poorly constrained. However, for Class 1 faults such as the northern SAF (accommodating the 1906 earthquake) or the Cascadia subduction zone (accommodating the 1700 earthquake), T is well constrained. Although viscoelastic relaxation effects tend to be dominated by relaxation from the last event, the contributions from preceding events are generally important at great distance from the fault zone. The concept of cyclicity is dubious for many fault zones where earthquakes occur in clusters and that this may affect the expected viscoelastic response (Meade & Hager 2004). However, we believe that our framework accounts well to first order the viscoelastic effects generated by past sequences of earthquakes on at least the major fault zones.

There are important fault strands parallel to the SAF, indicated by green lines in Fig. 6. There is known large moment release in the past 100 yr on the San Jacinto, Salton trough, and Imperial faults, and in the past 150–300 yr on the Macama and Rodgers Creek–Hayward faults. Several M6.5–7.5 earthquakes are involved on each fault strand, and some of these faults (i.e. Hayward fault; Imperial fault) are thought to be low-friction faults that may accommodate episodic creep. Therefore, we choose to incorporate the contributions of these faults to interseismic deformation using

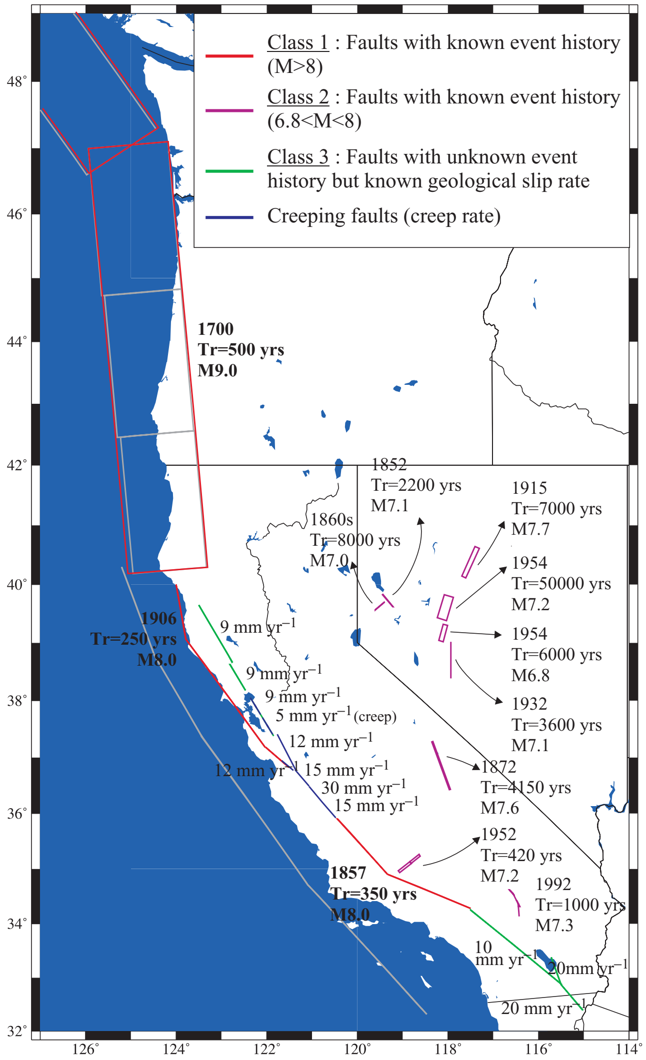

Figure 6. Red and purple lines indicate major faults (Class 1 faults) and minor faults (Class 2 faults) associated with historic earthquakes with known slip history (Table 2). For each fault we calculate the contributions of viscoelastic cycle effects on the instantaneous strain-rate field. Green lines indicate active faults with less certain slip history (Class 3 faults) (Table 3) and corresponding *a priori* slip rates, for which we calculate averaged interseismic effects on the instantaneous strain-rate field. Blue lines indicate creeping faults slipping at the indicated rates. Superimposed are the outlines of the force planes from Fig. 5.

the assumption of uniformly distributed moment release during the seismic cycle on each respective fault segment. For the averaged interseismic velocity to be accommodated along these faults, it is then appropriate to utilize the second term of eq. (7). The moment rate density distribution $\dot{\mathbf{m}}(\mathbf{r}')$ for one of these fault segments is prescribed by the fault geometry and long-term slip rate. We fix the fault geometry and respective long-term slip rates with parameters as assigned in Table 3, where they are termed 'Class 3 faults'. For the six listed faults these slip rates are denoted $\{\dot{s}_k \mid k = 13, \ldots, 18\}$.

Distributed faulting or steady slip within the western US lithosphere is evaluated here using a vertical average over a prescribed depth range and smooth functions to describe the horizontal dependence. Following Pollitz (2003b), one tensor component of moment release rate $\dot{m}$, which would be associated with a particular dislocation geometry over the volume $V - \Gamma_{\text{fault}}$ (for faulting) or $V - \Gamma_{\text{cr}}$ (for steady slip), is assumed laterally variable but uniform in depth from an upper depth d_1 to lower depth d_2. We define $\dot{m}'$ to be the vertically integrated moment release rate:

$$\dot{m}'(\hat{\mathbf{r}}; d_1, d_2) = \int_{d_1}^{d_2} \dot{m}(\mathbf{r})\, dr. \qquad (11)$$

It is parametrized in terms of Hermite–Gauss functions. Letting $\hat{\mathbf{r}} = (x, y)$:

$$\dot{m}'(\hat{\mathbf{r}}; d_1, d_2) = \sum_{l \geq 0} \sum_{m \geq 0} a_{ijlm} h_l\left(\frac{x}{L_1}\right) h_m\left(\frac{y}{L_1}\right) \times \exp\left[-\frac{1}{2}\left(\left(\frac{x}{L_1}\right)^2 + \left(\frac{y}{L_2}\right)^2\right)\right], \qquad (12)$$

where $l + m \leq l_{\max}$ for fixed $l_{\max} = 20$, the h_m are normalized Hermite polynomials such that

$$\int_{-\infty}^{\infty} \mathrm{d}x\, h_l(x) h_m(x) \exp(-x^2) = \delta_{lm}, \qquad (13)$$

and L_1 and L_2 are proportional to the dimensions of the rectangular grid which, in our application, covers a $1112 \times 1051\ \text{km}^2$ area. We choose values such that $1112\ \text{km}/L_1 = 1051\ \text{km}/L_2$ equals the last local maximum of the HG function of degree $l_{\max}$. Most of the HG functions so defined taper off smoothly at the edges of the rectangular area, and only the smaller-wavelength functions contain some signal near the edges. With $l_{\max} = 16$ the above expansion involves 152 parameters.

4.4 Other sources shaping the active deformation field

Predicted deformation fields are further shaped by fault creep and known lateral variations in viscoelastic structure (i.e. the relatively thick SNGV lithosphere), each of which produces a first order effect on the predicted lithospheric response.

The effect of fault creep is specified on portions of the central San Andreas, Hayward, and Calaveras faults at rates ranging from 12 to 30 mm yr^{-1}. It is based on measured surface creep on the respective fault traces (refer to Pollitz & Nyst 2004, for a more complete description). In the present study creep rates of the central SAF are fixed at rates based on known surface creep rates and assumed constant from the surface down to specified depths. One complication is that when steady fault creep penetrates to the surface, as for the central SAF, the true velocity field is discontinuous, and the method of estimating the continuous velocity gradient field presented in Supplementary Appendix A breaks down. This is an issue when many GPS measurements are present on both sides of a creeping fault, as is the case for much of the San Francisco Bay area. Since the *a priori* creep considered for the central San Andreas, Hayward, and Calaveras faults all penetrate to the surface, the most practical way to account for *a priori* creep is to correct the GPS velocity field for this effect prior to estimating the continuous velocity gradient. The velocity field associated with steady creep (Supplementary Fig. A2) has been subtracted from the observed velocity field (Supplementary Fig. A1) prior to estimating the velocity gradient field.

The mantle lithosphere beneath the SNGV is thicker than that of surrounding western US lithosphere based on seismic tomography (e.g. Benz *et al.* 1993; Humphreys & Dueker 1994). For simplicity, we assume that the mantle lithosphere beneath the SNGV block extends to 40 km depth, which constitutes a large contrast with respect

Table 3. Parametrization of Class 3 Faults.

Name	Type	$d_u^{(a)}$ (km)	$d^{(b)}{}_l$ (km)	*A priori* Slip Rate (mm yr^{-1})	Parameter (mm yr^{-1})	Ref. or Comment
Rodgers Creek	strike slip$^{(c)}$	0	20	9	$\dot{s}_{13}$	1
Hayward	strike slip$^{(c)}$	5	20	9	$\dot{s}_{14}$	1
Macama	strike slip$^{(c)}$	0	20	9	$\dot{s}_{15}$	$^{(e)}$
San Jacinto	strike slip$^{(c)}$	0	20	10	$\dot{s}_{16}$	2, 3
Salton Trough	oblique slip$^{(d)}$	0	20	20	$\dot{s}_{17}$	4
Imperial	strike slip$^{(c)}$	0	20	20	$\dot{s}_{18}$	5

$^{(a)}$ Upper fault edge depth.
$^{(b)}$ Lower fault edge depth.
$^{(c)}$ Pure right-lateral slip.
$^{(d)}$ Relative motion of west side with respect to east side is directed N310°E, which is resolved onto a N340°E-striking fault.
$^{(e)}$ Assume *a priori* rate equals that of Rodgers Creek fault.
^{1} Working Group on California Earthquake Probabilities (2003); ^{2}Sharp (1981); ^{3}Wesnousky *et al.* (1991); ^{4}Anderson *et al.* (2003); ^{5}Thomas & Rockwell (1996).

to the surrounding lithosphere of assumed thickness 20 km. The effect of this lateral heterogeneity on the response to applied forces and post-seismic relaxation of the system can be estimated from first order perturbation theory (Pollitz 2003c). The lateral heterogeneity is represented as a contrast in depth-dependent shear modulus in the Laplace transform domain. The perturbation in the deformation field is then prescribed in three steps:

(1) The response to tectonic forces and relaxation following earthquakes on the laterally homogeneous model is evaluated in the volume where the lateral heterogeneity is present,
(2) By converting these 'incident' deformation fields into virtual sources of deformation within the laterally heterogeneous volume and
(3) Evaluating the consequent effect on the deformation fields.

We find that this approach allows us to capture the relative rigidity of the SNGV block (e.g. Fig. 3) with a reasonably realistic model of the relatively thick SNGV lithosphere.

5 INTERPRETATION OF WESTERN US STRAIN-RATE FIELD

We aim to characterize the tectonic forces which act upon the North American lithosphere, the rheology of the western US lithosphere-asthenosphere system as a whole, and the distribution of moment release. A key question is: How well does a laterally homogeneous rheological model capture the principal deformation characteristics of the instantaneous velocity field? To a large extent, evaluation of candidate rheologies is bound to the assumed fault geometry and slip associated with the earthquakes through their corresponding post-seismic relaxation signals. In order to systematically model the velocity field (or, equivalently, the velocity gradient field) with this complexity, we perform a succession of parameter estimations based on least-squares inversion of the observed velocity gradient field. In subsequent sections we describe the inversion procedure, results, and implications for characterizing the sources of western US active deformation.

5.1 Inversion for model parameters

Let α_k denote the collection of model parameters, including: forcing rates $\dot{f}_1, \dot{f}_2 \cdots \dot{f}_6$, slip values $s_1, s_2, \ldots, s_{12}$, slip rates $(\dot{s}_{13}, \ldots, \dot{s}_{18})$, and distributed-moment HG expansion coefficients a_{ijlm}. Using the notation of Supplementary Appendix A, suppose that we have a velocity gradient field $\{\Psi_{11}(\mathbf{r}_i), \Psi_{12}(\mathbf{r}_i), \Psi_{21}(\mathbf{r}_i), \Psi_{22}(\mathbf{r}_i) - i = 1, \ldots I\}$. Let $\boldsymbol{\Psi}$ be a vector containing the collection of velocity gradient components at all I points, and let $\mathbf{C}$ be the *a priori* covariance matrix among these observables. In the inverse problem we minimize a functional of the form

$$\chi^2 = (\Delta\boldsymbol{\Psi}_1 \Delta\boldsymbol{\Psi}_2 \cdots \Delta\boldsymbol{\Psi}_I)^T \cdot \boldsymbol{C}^{-1} \cdot (\Delta\boldsymbol{\Psi}_1 \Delta\boldsymbol{\Psi}_2 \cdots \Delta\boldsymbol{\Psi}_I) + S \sum_{i,j} |\nabla \dot{m}'_{ij}(\mathbf{r};\, d_1,\, d_2)|^2 \, d^2\mathbf{r}, \tag{14}$$

where

$$\Delta\boldsymbol{\Psi}_i = \boldsymbol{\Psi}_i - \sum_k G_{ik}\alpha_k, \tag{15}$$

In eq. (15), G_{ik} represents the Greens function response of the system at observable i to model parameter α_k. In eq. (14) the first term represents the data misfit, and the second term represents the integrated roughness of the lateral gradients in vertically integrated moment release rate, weighted by S; the integration in the roughness term is over the regions of distributed faulting $V - \Gamma_{\text{fault}}$ and/or distributed steady slip $V - \Gamma_{\text{cr}}$.

Minimization of eq. (14) with respect to the model parameters leads to the normal equations

$$\sum_k \frac{1}{2} \left(\frac{\partial^2}{\partial\alpha_q \partial\alpha_k} \chi^2 \right) \bigg|_{(i)} \alpha_k = -\frac{1}{2} \frac{\partial \chi^2}{\partial \alpha_q} \bigg|_{(i)}, \tag{16}$$

where q and k span the set of model parameter indices, and the subscript (i) means that the derivatives are evaluated using initial values of α_k, which we assume to be zero. Inversion of eq. (16) yields estimates of the model parameters and associated marginal covariances among them.

5.2 Estimation of tectonic forces

Initial estimates of the tectonic forcing rates may be obtained by jointly inverting the strain-rate field for the force parameters $\{\dot{f}_i \mid i = 1, \ldots, 6\}$ and all three Class 1 $\{s_j\}$ (Tables 1 and 2). The resulting forcing rates are shown in Fig. 7 for each of the four rheological models. It is noteworthy that estimated forcing rates do not depend greatly on the assumed rheology. The value of $\dot{f}_2$ is very small for all rheology models. This suggests that the coupling of the JdF and NA plates is very small in central Oregon. The corresponding stressing rates $\dot{\tau}$ on the JdF–NA subduction interface or the Pacific-NA transcurrent interface are given by the forcing rate divided by

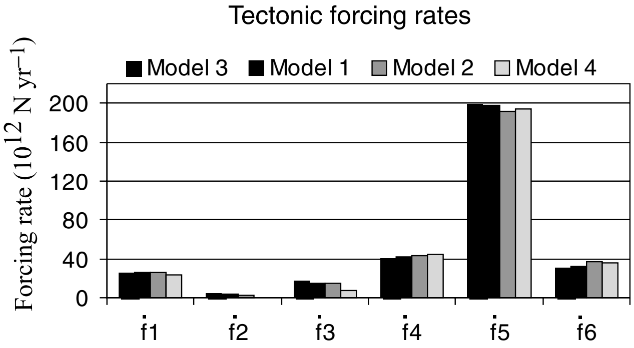

Figure 7. Tectonic forcing rates obtained through inversion of the strain-rate field for the forces parameters $\{\dot{f}_i \mid i = 1, \ldots, 6\}$ and all three Class 1 fault parameters $\{s_j\}$. Rheological models are given in Fig. 4.

the area of the segment, i.e,

$$\dot{\tau}_i = \frac{\dot{f}_i}{L_i W_i}, \tag{17}$$

where L_i and W_i for segment i are given in Table 1. On Model 4, for example, this yields $\dot{\tau}_1 = 0.7\,\mathrm{kPa\,yr^{-1}}$, $\dot{\tau}_2 = -0.01$ kPa yr^{-1}, $\dot{\tau}_3 = 0.2$ kPa yr^{-1}, $\dot{\tau}_4 = 0.9$ kPa yr^{-1}, $\dot{\tau}_5 = 13.4$ kPa yr^{-1}, and $\dot{\tau}_6 = 4.9$ kPa yr^{-1}. For the JdF–NA interaction $\{i = 1, \ldots, 4\}$, these values are only about 10 to 50 per cent of the stressing rates of ~2 kPa yr^{-1} estimated by Williams & McCaffrey (2001) for the Cascadia megathrust. The disparity between estimated stressing rates is compensated by the inclusion of post-1700 relaxation in our model. This is seen by considering all of the contributions to the model strain-rate field on Model 4 (Figs 8a and c). At the present stage of the Cascadia seismic cycle, the contractile strain rate perpendicular to the Cascadia coastline is contributed primarily by post-1700 relaxation, and similarly for the stressing rate. This tendency is obtained for all four rheological models considered.

5.3 Estimation of repeating slip and average slip rates

Unlike the forcing rates, repeating slip values s_j and average slip rate values $\dot{s}_k$ are highly dependent on the rheological model. The influence of post-earthquake relaxation is demonstrated by successively adding one or more major faults to the set of deformation sources. In a first test, we hold fixed $\{\dot{f}_i \,|i = 1, \ldots, 4\}$ according to the values found previously (Fig. 7, Section 5.2) and invert jointly for $\{\dot{f}_i \,|i = 5, 6\}$ and one Class 1 $\{s_j\}$, or for $\{\dot{f}_i \mid i = 5, 6\}$ and all three Class 1 $\{s_j\}$. The overall fits to the strain-rate field for these cases are shown in Fig. 9. By examining the improvement in fit by the addition of relaxation from a single earthquake sequence, the figure shows that relaxation from repeating 1906 events has the greatest impact among the major faults tested. Fig. 10(a) shows the corresponding slip values obtained in the case where $\{\dot{f}_i \,|i = 5, 6\}$ and all three Class 1 $\{s_j\}$ are inverted simultaneously with $\{\dot{f}_i \,|i = 1, \ldots, 4\}$ held fixed. For Models 1, 2, and 3, estimated slip amplitudes for the 1857 and 1906 sources are generally very large, about 300–600 and 150–350 per cent of *a priori* slip values, respectively (Fig. 10a, Table 1). For these models, the estimated slip value for the 1700 source is consistently less than the *a priori* value. For Model 4, however, estimated 1700, 1857 and 1906 slip amplitudes are much closer to *a priori* values. These tendencies of the inverted slip values lead us to construct a set of 'revised' slip amplitudes for the Class 1 faults. The *a priori* s_j are scaled up by +10 per cent for the 1906 source, +25 per cent for the 1857 source, and −20 per cent for the 1700 source. Inversion for forcing rates with all three Class 1 $\{s_j\}$ held at the revised values ['revised' case in Fig. 9 (left)] improves the fit relative to the case where the slip rates are held fixed at *a priori* values for all rheological models. Given the tenuous constraints on slip and magnitude of the last major rupture on the major source faults, the revised slip values are a plausible alternative.

The fit of the strain-rate field is further improved by inclusion of post-earthquake relaxation effects from Class 2 and Class 3 faults [Fig. 9 (right)]. For simplicity, the Class 3 slip rates are fixed at their respective *a priori* values (Table 3) in these tests. More precisely, in these tests $\{\dot{f}_i \,|i = 5, 6\}$ and all nine Class 2 $\{s_j\}$ are inverted simultaneously with $\{\dot{f}_i \,|i = 1, \ldots, 4\}$ fixed at the values determined in the previous section (Table 1), Class 1 slip values fixed at 'revised' values, and Class 3 slip rates fixed at *a priori* values. The resulting predicted strain-rate field is shown in Fig. 8(d). Most of the improvement is from the inclusion of Class 3 faults, with slight additional improvement when Class 2 slip magnitudes are estimated rather than fixed [Fig. 9 (right)]. Estimated Class 2 slip magnitudes (Fig. 10c) are not as well constrained as estimated Class 1 slip magnitude. The standard deviation in a Class 2 s_j estimate can be of the same order as s_j itself, in particular with Model 3 rheology and for Pyramid Lake and Olinghouse faults ($s_{11} + s_{12}$). It is difficult to discriminate the rheology with the faults located in the CNSZ $\{s_i \,|i = 4, 8, 9, 10\}$. However, regardless of the rheology, estimated slip amplitudes are close to (or exceed) *a priori* slip amplitudes for strike-slip fault in this area (Cedar Mountain fault, s_9) whereas they are reduced for oblique or normal faulting (Pleasant Valley, Dixie Valley and Fairview Peak faults; s_4, s_{10}, s_8, respectively) (Fig. 10b). These results are in good agreement with recent GPS results showing dextral shear motion with no dilatation in the westernmost Basin and Range (Hammond *et al.* 2004). The estimated slip amplitude for the three faults in the south ($\{s_i \,|i = 5, 6, 7\}$, Owens Valley, Landers and Kern County faults, respectively) depend more strongly on the rheology, and estimated slip amplitudes with Model 4 show somewhat better agreement with the *a priori* values (Fig. 10b).

According to these results, estimated slip amplitudes for Class 1 and Class 2 faults are generally closer to the *a priori* values with Model 4 rheology than with Model 1, 2 and 3 rheologies. In addition, for Model 4 the inverted Class 1 slip values are much greater than the associated standard deviations, and inverted Class 2 slip values are statistically greater than zero to within one or two standard deviations (Fig. 10c). Thus Model 4 is the most consistent with the geological and seismological slip estimates for the twelve events associated with these faults. The Model 4 rheology also yields better fits to the data set than Models 1 and 2, although the differences are not statistically significant. The variance reduction obtained for Model 4 with these slip values, relative to a model with forcing rates alone, is 39.5 per cent. The good overall agreement between estimated and *a priori* Class 1 and Class 2 slip values for Model 4 leads us to prefer this rheology over the other rheology models. It is convenient to define 'revised' slip values for Class 2 faults using the Model 4 inversion results given in Fig. 9 as a guide. The revised slip values $\{s_i \,|i = 4 - 12\}$ are assigned 50, 70 or 100 per cent of the *a priori* values, as indicated in Table 2.

5.4 Unaccounted deformation sources

When only background tectonic forces and relaxation from slip events on specified faults contribute to model strain rates, there are significant misfits to the strain rates. For all rheology models

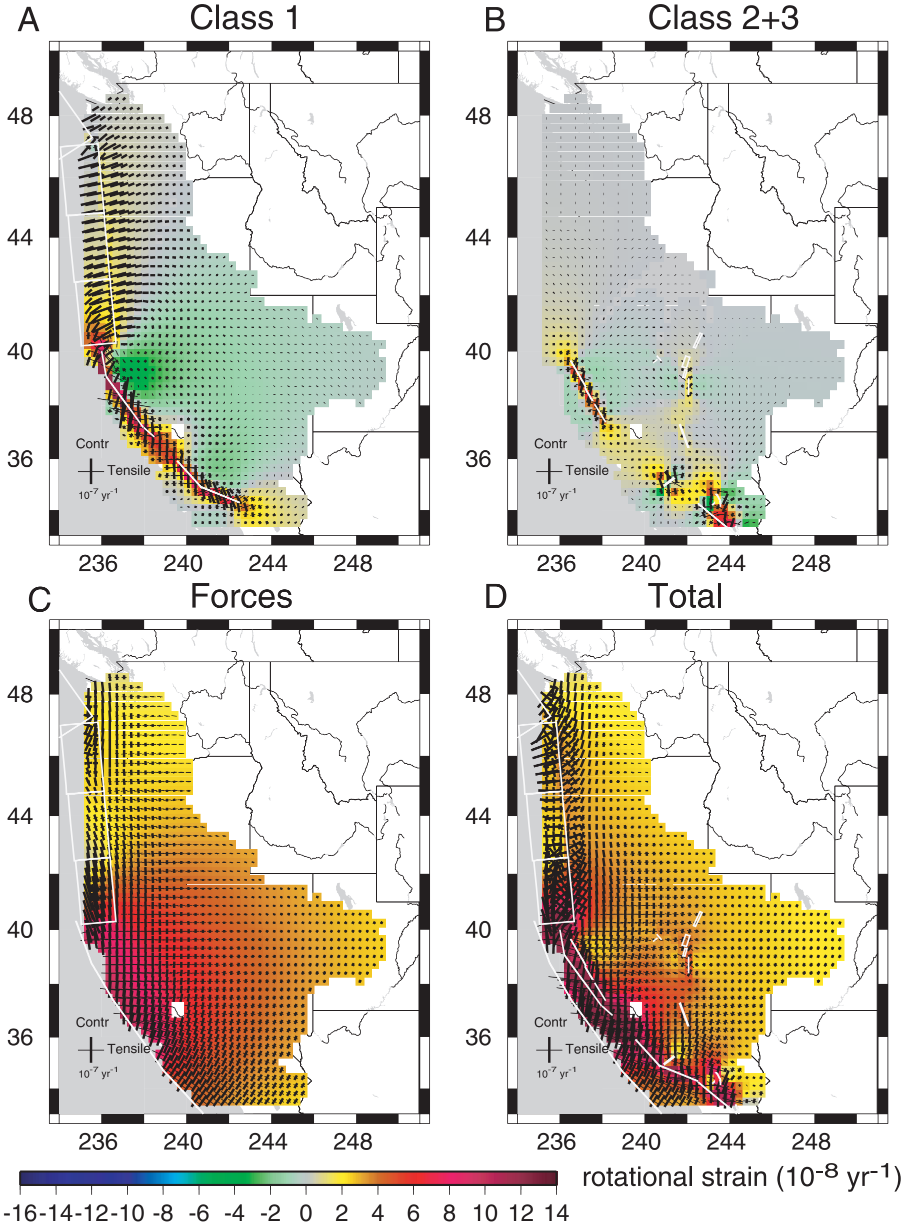

Figure 8. For the inversion described in Section 5.3, the components of the strain-rate field on Model 4 contributed by: (a) relaxation following earthquakes on Class 1 faults using the 'revised' slip amplitudes; (b) relaxation following earthquakes on Class 2+3 faults using estimated slip amplitudes and *a priori* amplitude, respectively; (c) tectonic forces and (d) sum of all contributions.

considered, predicted tensor strain rate around the SAF system is much lower than observed, and in the plate interior east of about 119°W it is too large. We admit two main possibilities for explaining the strain that is unaccounted for by the viscoelastic cycle model. The first is that steady deep slip in the lower part of the elastic upper lithosphere may be localized beneath some or all faults. The second is that (periodic) faulting events at locations distributed over the broad areas between the eighteen identified source faults may contribute additional viscoelastic relaxation signals.

The budget of moment accumulation and release along the Pacific–North American plate boundary system also demonstrates the need to complement the set of eighteen considered faults (Table 2) with additional deformation sources. Slip accumulation at a rate of 50 mm yr^{-1} along a 1000-km long, 20-km wide plate boundary with average shear modulus of 37 GPa yields a moment accumulation rate of 3.7×10^{19} N m yr^{-1}. This is about 2.5 times larger than the moment release rate of 1.47×10^{19} N m yr^{-1} arising from earthquake-cycle deformation based on slip values in Table 2, excluding the Cascadia megathrust. The remainder must be made up with distributed moment release on additional faults, steady deep slip, or a combination of the two. In Section 5.5 we consider the former, in Section 5.6 the latter, and in Section 5.7 a combination of the two. It is worth noting that there is theoretically no requirement in crustal dynamics that there be any deep slip beneath faults. For example, the viscoelastic coupling model of Savage & Prescott (1978) provides a comprehensive explanation of the seismic cycle of an idealized fault system without any deep dislocations. Our introduction of steady slip in the lower elastic lithosphere reflects the inadequacy

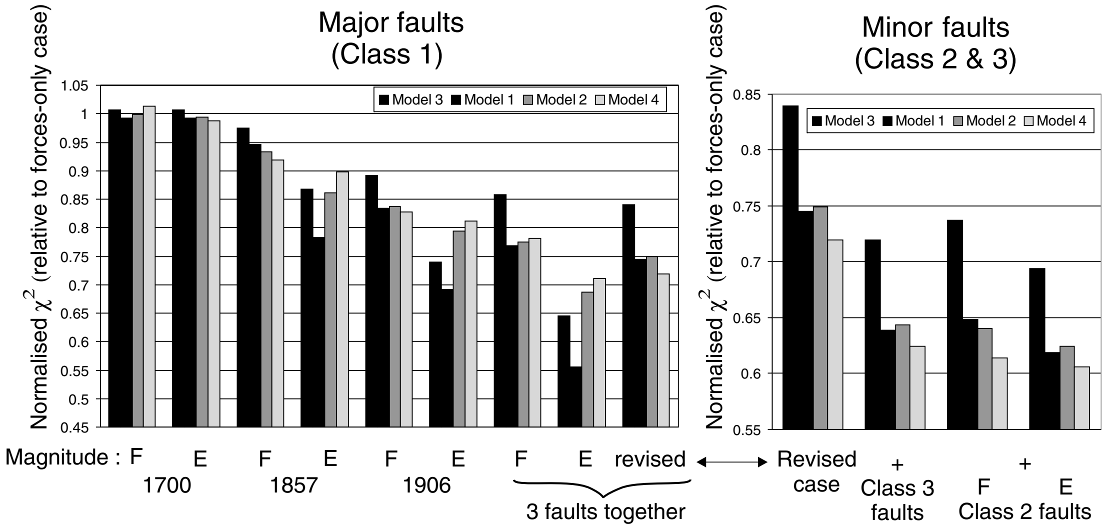

Figure 9. (left) Fits to the strain-rate field of models derived by joint inversion for $\{\dot{f}_i\ |i = 5, 6\}$ and one Class 1 s_j with $\{\dot{f}_i\ |i = 1, \ldots, 4\}$ held fixed. Two variations are considered: event magnitude is fixed ('F') to an *a priori* value (Table 2) or estimated ('E') with the inversion. Also shown is the result of joint inversion for $\{\dot{f}_i\ |i = 5, 6\}$ and all three Class 1 faults with $\{\dot{f}_i\ |i = 1, \ldots, 4\}$ held fixed, including a case in which the slip magnitudes $\{s_j\}$ are held fixed at 'revised' values (see text). (right) Fits derived by joint inversion for $\{\dot{f}_i\ |i = 5, 6\}$ and $\{s_j\}$ for Class 2 faults, with $\{\dot{f}_i\ |i = 1, \ldots, 4\}$ held fixed, $\{s_j\}$ of Class 1 faults held fixed at 'revised' values and $\{\dot{s}_k\}$ of Class 3 faults held fixed at *a priori* values (Table 3). Class 2 faults are included either by fixing ('F') the slip magnitude at *a priori* values (Table 2) or estimating the slip ('E'). All fits are plotted relative to that fit obtained by inversion of the data set for $\{\dot{f}_i\ |i = 1, \ldots, 6\}$ alone.

of viscoelastic-cycle deformation to account for all observed strain localization.

5.5 Relaxation from distributed faulting

The space of possible moment release includes right-lateral strike slip on NW–SE-trending faults and normal slip on NNE–SSW-trending faults in the California-Nevada area. The geometry of $\dot{m}'^{\text{Normal}}$ involves pure normal slip on a 45°-dipping, N20°E-striking plane; the geometry of $\dot{m}'^{\text{Strike-slip}}$ involves right-lateral strike-slip motion on a vertical N40°W-striking plane. We use the parametrizations for $\dot{m}'^{\text{Strike-slip}}(\hat{\mathbf{r}}; d_1, d_2)$ and $\dot{m}'^{\text{Normal}}(\hat{\mathbf{r}}; d_1, d_2)$ given by eqs (11) and (12) in Section 4.3. We assume uniformity of moment release rate from the surface to the base of the elastic lithosphere (20 km) and hence $d_1 = 0$ km and $d_2 = 20$ km. These moment release rates are related to the velocity field, and hence strain rate, field via the third term in eq. (7). We invert the instantaneous strain-rate field for the distributions of $\dot{m}'^{\text{Strike-slip}}$ and $\dot{m}'^{\text{Normal}}$ jointly with $\{\dot{f}_i\ |i = 1, 6\}$ assuming the Model 4 rheology. Because of the tradeoffs with Class 1 slip magnitudes and Class 3 slip rates, these parameters are held fixed at the 'revised' slip values (Table 2) and *a priori* slip rates (Table 3), respectively. The Class 2 slip amplitudes are held fixed at the revised values specified in Table 2. The roughness weight S in eq. (15) is chosen at a value that results in a modest contribution of distributed faulting to the overall moment release budget. The obtained vertically integrated moment rate distributions are shown in Fig. 11(a). The estimated $\dot{m}'^{\text{Normal}}$ pattern is not consistent with the tectonic environment around the SAF, but the signal associated with it is small. The much larger $\dot{m}'^{\text{Strike-slip}}$ is positive over most of the western US and reaches a maximum of $\sim 0.6 \times 10^{14}$ N m (km^2 yr)$^{-1}$ around the SAF. The standard error in a point estimate of $\dot{m}'^{\text{Strike-slip}}$ or $\dot{m}'^{\text{Normal}}$ is about 0.1×10^{14} Nm (km^2 yr)$^{-1}$. Distributed strike-slip faulting is thus formally well resolved above the noise level, while distributed normal faulting is not well resolved. Figs 11(b) and (c) show the contributions of relaxation from distributed faulting and the Sierra Nevada perturbation, respectively. The latter acts to account for the quasi-rigidity of the Sierra Nevada block lithosphere (Section 4.4).

The variance reduction of this model is 66.5 per cent, an improvement of 48 per cent over the model obtained with forcing rate alone, an improvement of 28 per cent over the modelled obtained with the forcing rate and the revised Class 1 parameters (Section 5.2), and an improvement of 14 per cent over the model obtained with revised deformation parameters without distributed moment release (Section 5.3). The total calculated strain-rate field (Fig. 12) is correspondingly an improvement over that obtained previously, for example, with *a priori*/revised deformation parameters and without distributed moment release (Fig. 8d). Strain rate magnitudes over the SAF system, the Pacific Northwest, and the Basin and Range Province, while still smaller than observed (Fig. 3), are of higher amplitude with distributed moment release than without it. Similarly, strain rate magnitudes east of 119°W are of smaller amplitude with distributed moment release than without it, in better accord with observation.

5.6 Distributed steady deep slip

In the case of steady deep slip we define moment release rates over the depth range 15–20 km (any depth range concentrated near the base of the elastic crust would suffice). For simplicity we focus on the single distribution $\dot{m}'^{\text{Strike-slip}}$ ($\hat{\mathbf{r}}$; 15 km, 20 km). This quantity is parametrized with eqs (11) and (12) and is related to the velocity field via the sixth term of eq. (7). We invert simultaneously for $\dot{m}'^{\text{Strike-slip}}$ and all forcing rates $\{\dot{f}_i\ |i = 1, 6\}$ assuming the Model 4 rheology. As in the previous section, Class 1 slip magnitudes and Class 3 slip rates are held fixed at the 'revised' slip values (Table 2) and *a priori* slip rates (Table 3), respectively, and the Class 2 slip amplitudes are held fixed at the revised values specified in Table 2.

The resulting pattern of deep slip in Fig. 13(a) is concentrated primarily around the SAF system. The contributions of distributed

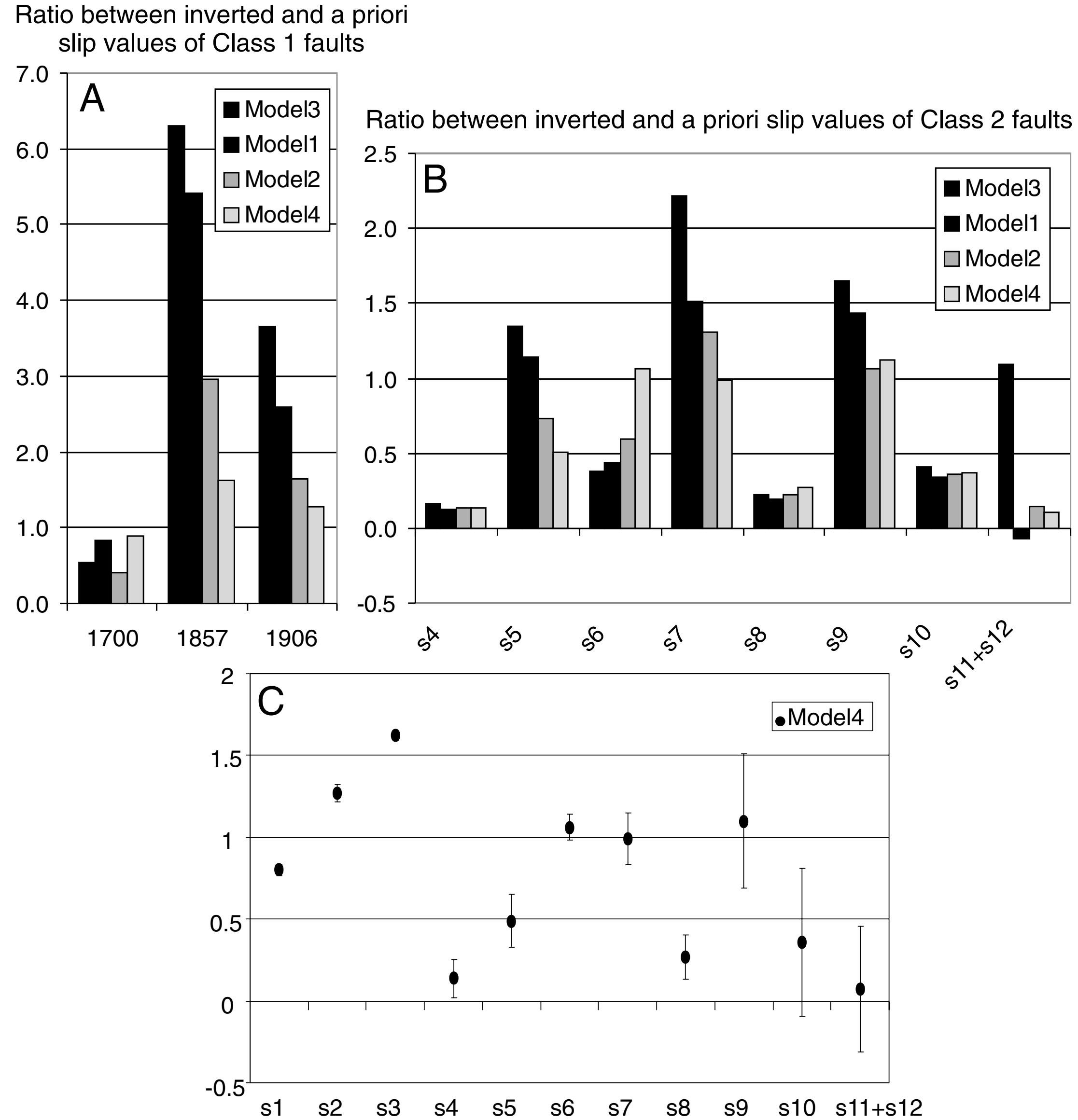

Figure 10. (a) Ratio between inverted and *a priori* slip value of Class 1 faults obtained through inversion of the strain-rate field for $\{\dot{f}_i \mid i = 5, 6\}$ and all three Class 1 s_j with $\{\dot{f}_i \mid i = 1, \ldots, 4\}$ held fixed. (b) Ratio between inverted and *a priori* slip values of Class 2 faults obtained through inversion of the strain-rate field for $\{\dot{f}_i \mid i = 5, 6\}$ and Class 2 $\{s_j \mid j = 4, \ldots, 12\}$ with slip values of Class 1 faults $\{s_j \mid j = 1, 2, 3\}$ held fixed at revised values and slip rate values of Class 3 faults $\{\dot{s}_k \mid k = 13, \ldots, 18\}$ held fixed at the *a priori* values given in Table 3. Rheological models are given in Fig. 4. (c) Estimated Class 1 & Class 2 slip ratio and standard deviation for inversion described above for Model 4.

deep slip and the Sierra Nevada perturbation are shown in Figs 13(b) and (c). The contribution to the strain-rate field in Fig. 13(b) not only helps localize strain beneath the SAF system but also removes excess strain from the Basin and Range province. In this model, the integrated moment release rate from aseismic slip in the deep lithosphere is $\sim 1.3 \times 10^{19}$ Nm yr^{-1}, roughly equal to the moment release rate from earthquakes (excluding the Cascadia event). This is equivalent to the moment release rate that would be generated by 50 mm yr^{-1} slip on a 1000-km-long, 5-km-wide vertical dislocation at the base of the elastic layer. This would imply either aseismic slip in the lower 5 km of the lithosphere at the Pacific–North American relative plate motion rate or, invoking perturbation theory (Pollitz 2003c), that the lower 5 km of the lithosphere along an equivalent 1000 km length is absent in the western part of the plate boundary zone. The total predicted strain field in Fig. 14 is similar to that generated with relaxation from distributed faulting (Fig. 12).

5.7 Combined distributed faulting and steady deep slip

We perform a joint inversion for distributed faulting $\dot{m}'^{\text{Strike-slip}}(\hat{\mathbf{r}}; 0, 20\,\text{km})$ (which contribute to the deformation through relaxation via the third term in eq. 7), distributed steady deep slip $\dot{m}'^{\text{Strike-slip}}(\hat{\mathbf{r}}; 15\,\text{km}, 20\,\text{km})$ (the sixth term of eq. 7), and all forcing rates $\{\dot{f}_i \mid i = 1, 6\}$ assuming the Model 4 rheology. As before, Class 1 slip magnitudes and Class 3 slip rates are held fixed at the 'revised' slip values (Table 2) and *a priori* slip rates (Table 3), respectively, and the Class 2 slip amplitudes are held fixed at the

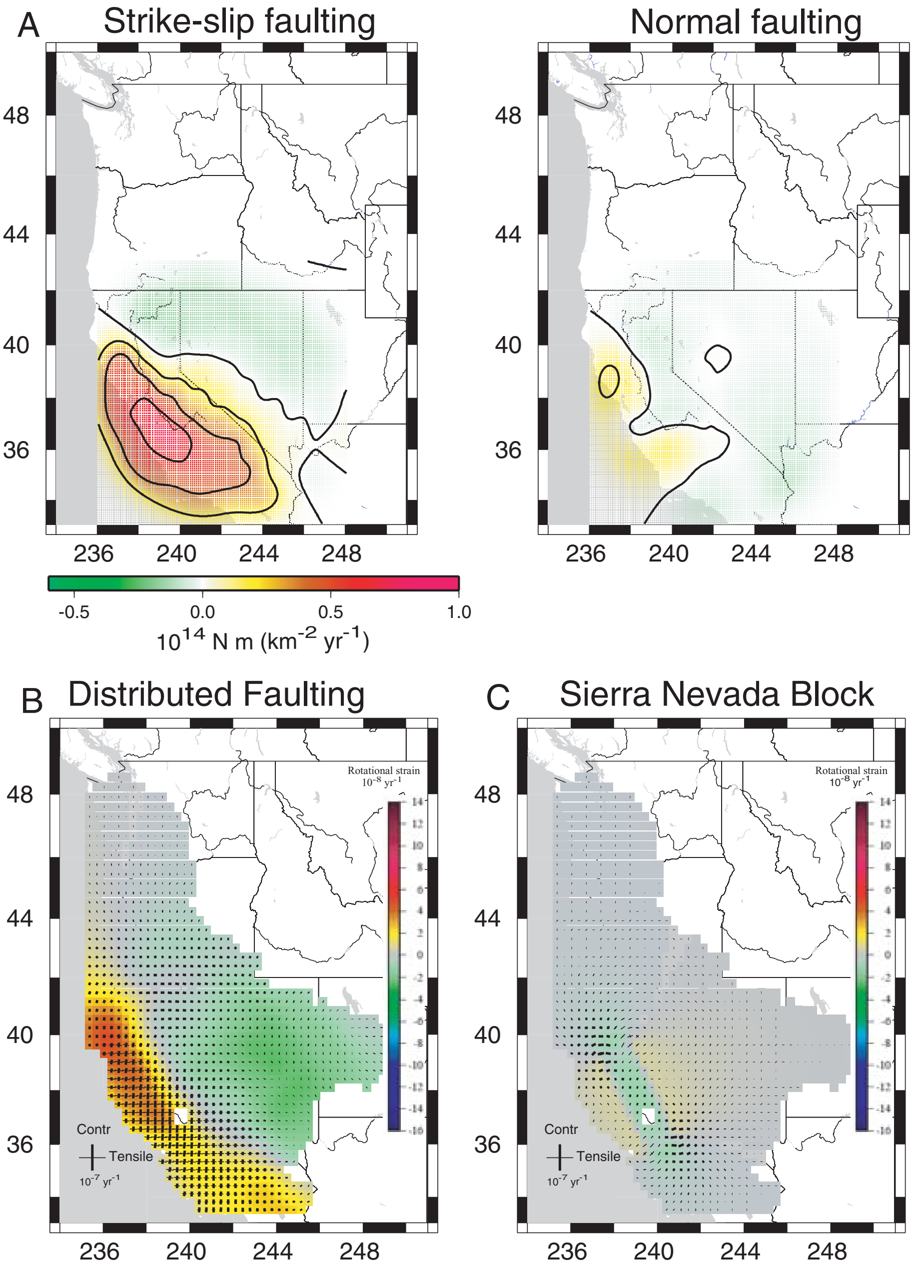

Figure 11. (a) Distributed moment release rates $\dot{m}'^{\text{Strike-slip}}(\hat{\mathbf{r}}; 0, 20\,\text{km})$ and $\dot{m}'^{\text{Normal}}(\hat{\mathbf{r}}; 0, 20\,\text{km})$ after inversion of the strain-rate field for distributed faulting and $\{\hat{f}_i\ |i = 1, 6\}$ with Class 1, 2 and 3 faults held fixed to 'revised' or *a priori* values (see text, Sections 5.3 and 5.5). Isolines are each 0.2×10^{14} N m (km^2 yr)$^{-1}$. $\dot{m}'^{\text{Strike-slip}}$ and $\dot{m}'^{\text{Normal}}$ are related to the strain-rate field via the third term of eq. (7) and are associated with relaxation following hypothetical slip events distributed throughout the 20 km-thick elastic lithosphere. The contributions of relaxation from distributed faulting (B) and the Sierra Nevada block perturbation (c) to strain-rate field are shown in terms of the amplitudes and directions of the principal strain-rates axes and rotational strain rate.

revised values specified in Table 2. The roughness weight S in eq. (15) is chosen such that the summed moment release rate of all fault and steady-slip sources equals the moment accumulation rate of 3.7×10^{19} Nm yr^{-1}.

The distributions of moment release from faulting-related $\dot{m}'^{\text{Strike-slip}}(\hat{\mathbf{r}}; 0, 20\,\text{km})$ and steady deep-slip $\dot{m}'^{\text{Strike-slip}}(\hat{\mathbf{r}}; 15\,\text{km}, 20\,\text{km})$ are shown in Fig. 15(a), and the corresponding contribution to the strain-rate field is shown in Fig. 15(b). Combined with the contributions of relaxation following discrete faulting events (Figs 15d and e) and tectonic forcing (Fig. 15f), the additional dislocations sum to a total predicted strain-rate field (Fig. 15g) that agrees well with the observed strain field (Fig. 3) in both high- and low-strain regions. The variance reduction achieved by this model is 70.9 per cent. We note that steady slip in the lower elastic layer beneath the SAF in southern California was also inferred by Pollitz (2001) from a GPS profile using a viscoelastic coupling model with repeating 1857 Fort Tejon-type events. Although marginally resolved here as a localized feature, the pattern of deep slip between the Mojave Desert and Owens Valley is consistent with observed strain localization in the southern ECSZ (Peltzer *et al.* 2001).

The existence of additional faulting sources as depicted in Fig. 15(a) is supported by the occurrence of other historical earthquakes. In southern California additional sources could include

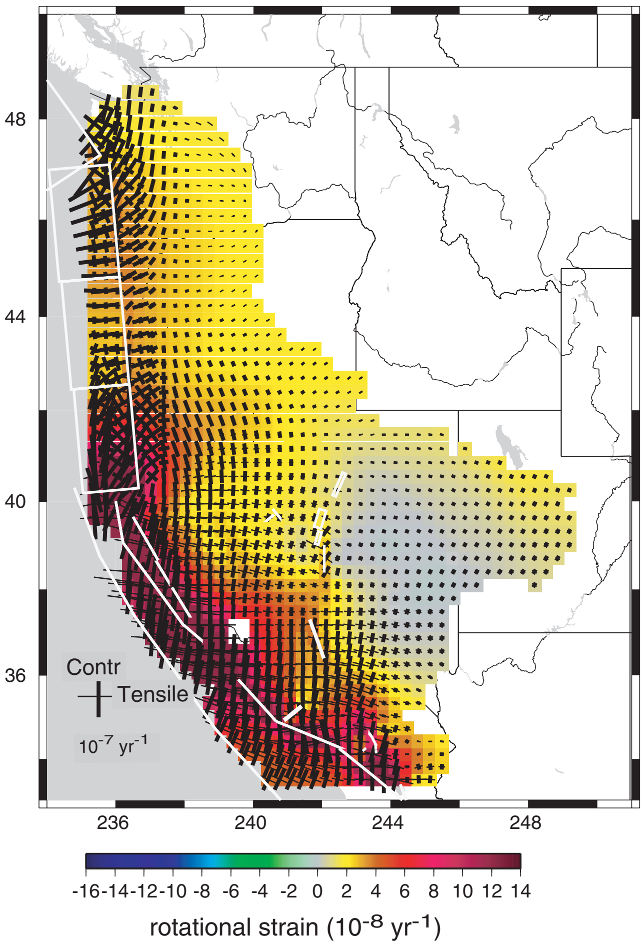

Figure 12. Total calculated strain-rate field on Model 4, described in Section 5.5. It takes account for the relaxation following earthquakes on Class 1, 2 and 3 faults, the tectonic forces, and the relaxation from the distributed faulting and Sierra Nevada block perturbation (Figs 11b and c).

repeating 1812-type sources, which ruptured at least the Pallett Creek and Wrightwood localities on the southern SAF (Fumal *et al.* 2002b). Similarly, the slip budget of southern California south of Wrightwood demands a total of about 50 mm yr^{-1} long-term slip across the fault system, but the San Jacinto and Landers source faults included here represent only a fraction of the expected total. One could append to these two faults others which accommodate a substantial fraction of the long-term slip rate (and which would complete the budget of expected long-term slip), but the potential viscoelastic relaxation signals from these faults (i.e. their contribution to the present interseismic velocity field) are judged to be very small. Notably, the SAF between Wrightwood and the Coachella Valley, which last ruptured in the late 17th century with modest slip (Sieh & Williams 1990; Fumal *et al.* 2002a; McGill *et al.* 2002), is expected to contribute only small viscoelastic relaxation signals to the present deformation field, and, therefore, much of the episodic slip contributed by the southern SAF may be difficult to detect (see Supplementary Appendix B). However, Fig. 15(a) suggests that steady deep slip beneath the southern SAF accounts for part of the slip budget, and it is manifested as a substantial localized strain rate (Fig. 15b).

The slip budget in the San Francisco Bay area also demands the additional sources. Long-term slip rates are (Table 2) 22 mm yr^{-1} for the SAF and 9 mm yr^{-1} for the Hayward-Rodgers Creek-Macama fault system; the sum of 31 mm yr^{-1} is only about 80 per cent of the Pacific-Sierra Nevada relative motion rate (Argus & Gordon 2001), demanding additional deformation sources on the north-central SAF.

Finally, thrust faulting accommodating northward convergence between the Pacific and North American plates in the Los Angeles region is not included in any of our models. Account for numerous $M \sim 7$ events such as the 1971 San Fernando and 1994 Northridge events would qualitatively increase the predicted north–south contractile strain and better match the observed strain rate in that region.

6 DISCUSSION

In the tests for which Class 1 slip values are variable (Fig. 10a, Section 5.2), the estimated slip amplitude on the 1857 rupture is ~500 per cent and ~300 per cent greater than the *a priori* slip with Model 1 and 2 rheologies, respectively. There is a possibility that 1857 slip was much larger than given by palaeoseismic estimates (Sieh 1978) as proposed by Runnerstrom *et al.* (2002) for the Cholame segment. Average slip near 14 m rather than 6 m would be consistent with the strain build-up expected between the previous event ~1480 and 1857, given a long-term geologic slip rate of ~3.4 cm yr^{-1} (Sieh 1984). If true, then Models 1 and 2 would be more plausible in southern California. However, there is no direct evidence for slip values near 14 m except possibly on the Cholame segment, and therefore, we prefer the results derived assuming an average 7.5 m slip, which is consistent with palaeoseismic evidence (Grant & Sieh 1993) and which favours Model 4 in southern California.

In addition to their impact on the various slip estimates and global data fits, the candidate rheology models may be evaluated by the fits to specific subregions. In the following we refer to the results of joint inversion for $\{\dot{f}_i \,|i = 5, 6\}$ and $\{s_j\}$ for Class 2 faults, with $\{s_j\}$ of Class 1 faults held fixed at 'revised' values (Table 2) and $\{\dot{s}_k\}$ of Class 3 faults held fixed at *a priori* values (Table 3). Fig. 16 shows the fits to the strain-rate field in each of six subregions and for the entire data set. The Model 4 rheology ($\eta_m = 2 \times 10^{19}$ Pa s and $\eta_c = 1 \times 10^{20}$ Pa s) fits the entire data set slightly better than the Models 1 and 2 rheologies, and it better fits most of the subregional data sets, particularly western Nevada and southern California around the Landers, Kern County, Owens Valley rupture zones. On the other hand, the Oregon subregion and the San Francisco Bay subregion strain-rate fields are better fit with the Model 1 rheology that has a weaker upper mantle and lower crust ($\eta_m = 1 \times 10^{19}$ Pa s and $\eta_c = 2.5 \times 10^{19}$ Pa s). This suggests, first, that different regions are governed by different viscosity structures, pointing to lateral heterogeneity in viscosity structure in the western US. Second, the average 1-D long-term viscosity structure in the western US found in this study shows higher upper mantle and lower crust viscosity than in smaller regions in this area over shorter timescale (e.g. Dixon *et al.* 2004). This suggests possibly multiple material timescales in the relaxing portions of the Earth. Pollitz (2003a) suggests two material time constants ~0.07 and ~2 yr for the mantle rheology beneath the Mojave Desert, based on modelling 2.5 yr of post-seismic time series after the 1999 Hector Mine earthquake with a Burghers body rheology. At longer times, however, it is conceivable that a broader spectrum of relaxation times, including times of order 20 yr as implied by Model 4, are needed to adequately describe the viscous component of the complete rheology.

Fig. 17 shows the predicted GPS displacement field based on the combination model described in Section 5.7. Qualitatively it

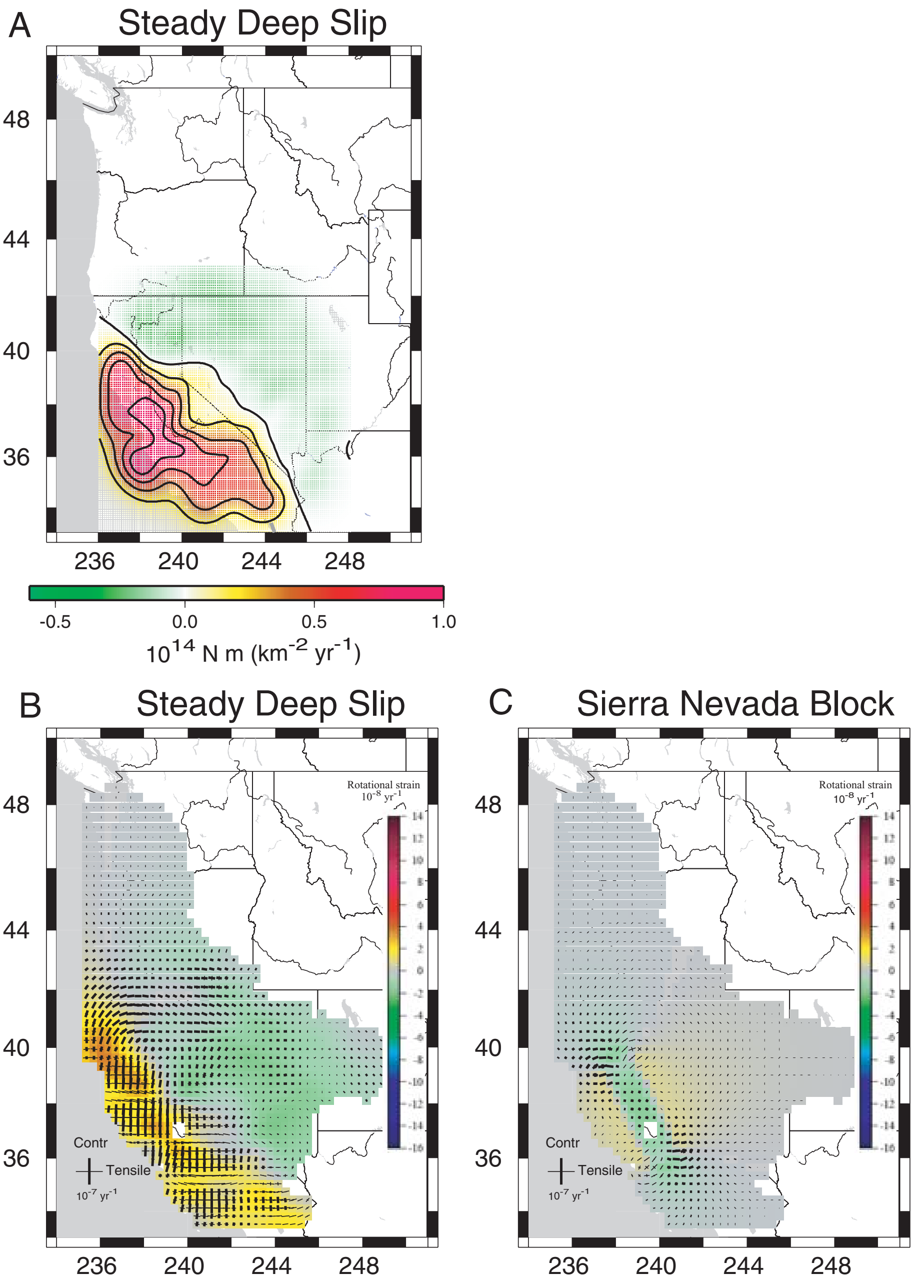

Figure 13. (a) Distributed moment release rates $\dot{m}'^{\text{Strike-slip}}(\hat{\mathbf{r}}; 15\,\text{km}, 20\,\text{km})$ after inversion of the strain-rate field for distributed steady deep slip and $\{\dot{f}_i \mid i = 1, 6\}$ with Class 1, 2 and 3 faults held fixed to 'revised' or *a priori* values (see text, Sections 5.3 and 5.6). Isolines are each 0.2×10^{14} N m (km^2 yr)$^{-1}$. $\dot{m}'^{\text{Strike-slip}}$ is related to the strain-rate field via the sixth term of eq. (7) and is associated with steady slip in the lower elastic lithosphere. The contributions of the distributed deep slip (b) and Sierra Nevada block perturbation (c) to strain-rate field are shown in terms of the amplitudes and directions of the principal strain-rates axes and rotational strain rate.

reproduces the gross features of the observed velocity field (Supplementary Fig. A1), particularly the large right-lateral shear strains along the SAF system and the east–west contraction and rotation of the Cascadia region. Many details of the predicted velocity pattern, however, do not conform to the observed velocity field. This includes the observed rapid decrease in velocity as one moves inland from the Pacific Northwest and the observed west–southwest azimuth of motion south of about 36°N. To produce these features in the model velocity field would require, in the absence of additional deformation sources, west-directed basal drag in the Pacific Northwest and southwest-directed basal drag in the southwest US. (An alternative remedy for southern California is that steady slip at depth follows the trend of the Big Bend rather than the local Pacific–American relative motion vector (Lisowski *et al.* 1991).) Mantle flow fields consistent with such basal drag have been proposed for these respective regions by Williams & McCaffrey (2001) and Liu & Bird (2002). This raises the question as to what extent imposed forces must be balanced in this type of model, how the compensating forces are distributed in the sublithosphere, and what mechanisms maintain them. To properly answer these questions will require consideration of not only the surface velocity field but also the sublithospheric flow field induced by tectonic interactions and mantle convection.

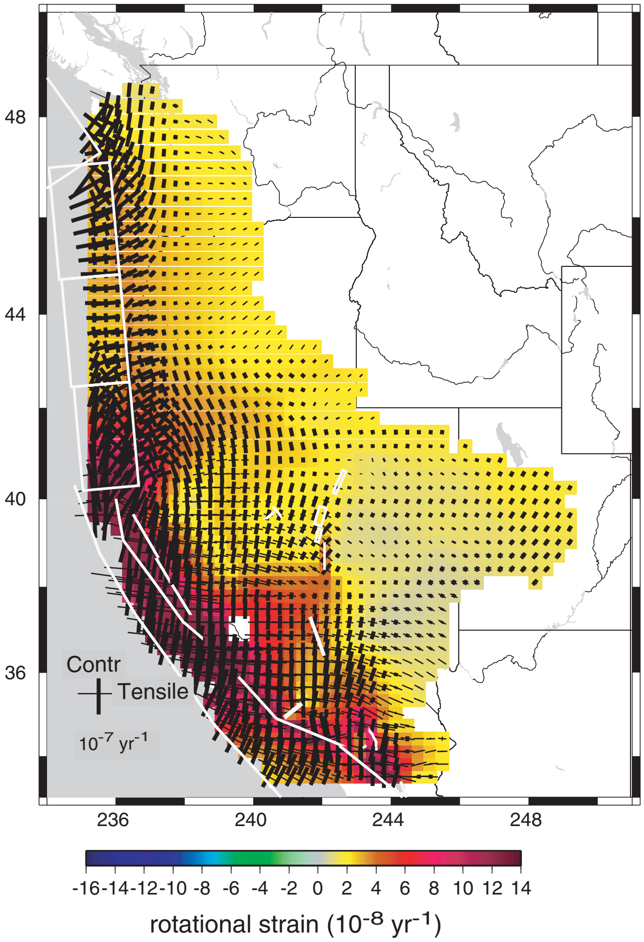

Figure 14. Total calculated strain-rate field on Model 4, described in Section 5.6. It takes account for the relaxation following earthquakes on Class 1 faults (Fig. 8a), the relaxation following earthquakes on Class 2+3 faults (Fig. 8b), the tectonic forces, and the steady slip in the lower elastic lithosphere and Sierra Nevada block perturbation(Figs 13b and c).

In the Pacific Northwest north of the Mendocino triple junction, the tectonic forcing pattern implies a substantial component N–S contractile strain (Fig. 8c). This is in good agreement with principal stress directions in east-central Washington and northern Oregon (Smith 1978; Zoback & Zoback 1989; Wang 2000), E–W-trending thrust faults and folds in Washington (Wells & Simpson 2001) and the expected long-term northward displacement of the Oregon-Washington forearc 'block' with respect with North America. Closer to the subduction front, the relaxation from the repeating 1700 events generate E–W compression, perpendicular to the Cascadia coastline (Fig. 8a). The superposition of these two processes shapes the net strain-rate field (Fig. 8d), which exhibits a N70E compression near coastal Washington and Oregon (Fig. 3). Moreover, the tectonic forcing rates obtained along the strike of the Cascadia subduction zone show variable coupling of the JdF and NA plates, with apparently no coupling in central Oregon. (The forcing rate is $\dot{f}_2 = -0.36 \pm 5.3 \times 10^{12}$ N yr^{-1}, which is statistically indistinguishable from zero.) This is qualitatively consistent with reduced E–W contractile strain perpendicular to the coast from 43.5°N to 46.0°N that is seen in the observed strain pattern (Fig. 3) as well as relatively small GPS velocity vectors between these latitudes after correction for the Cascadia forearc rotation (Fig. 3c of Wang *et al.* 2003). However, it conflicts with independent inferences of strain accumulation along the entire Cascadia subduction zone (McCaffrey *et al.* 2000; Wang 2000; Svarc *et al.* 2002b; Wang *et al.* 2003). The chosen $\dot{f}_2$ plane samples portions of the coast with both relatively high E–W contractile strain (south of about 43.5°N) and relatively small E–W strain north of 43.5°N, each with different magnitudes in the landward strain gradient. This suggests that a more detailed analysis is warranted for this region, for example, allowing for additional along-strike and downdip variations in forcing rates. The assumption of uniform slip of the 1700 earthquake also affects inferred forcing rates. Too much coast-perpendicular convergence may be generated with post-1700 relaxation that is artificially large around Oregon. Reduction of prescribed 1700-event slip in this area would be expected to translate into larger and likely positive $\dot{f}_2$ comparable in magnitude with the other $\dot{f}_i$. Nevertheless, low tectonic forcing rates in central Oregon are correlated both with the presence of the thickest part of the Siletz terrane (Trehu *et al.* 1994) and the presence of the lowest forearc seismicity (Trehu *et al.* 1994). Our results are qualitatively consistent with the recent results of Verdonck (2004), who suggests a strong coupling north and south of central Oregon and a low coupling in central Oregon on the basis of observed vertical deformation rates across the boundary zone.

In California and Nevada, tectonic forcing and post-seismic relaxation following repeating 1906 and 1857 events constructively interfere around the SAF system but destructively interfere further east in the plate boundary zone (Figs 8a and c). This helps explain the large strain accumulation localized around the SAF fault and much smaller and variable strain accumulation further inland. Contributions from the Class 2 and 3 faults are necessary to localize the deformation in secondary deformation zones such as the ECSZ. Relaxation effects from the modelled events in western Nevada (i.e. CNSZ) are small but tangible (Fig. 8b). Estimated slip amplitudes of the 1954 Fairview Peak and 1932 Cedar Mountain earthquakes are similar to *a priori* values and statistically well above zero (i.e. inverted s_8 and s_9 in Fig. 9). This agrees qualitatively with Hetland & Hager (2003), who isolated the post-seismic relaxation signal of the central Nevada earthquakes in the GPS velocity field directly. Nevertheless, our methodology may be limited in its ability to detect a strong relaxation signal in the CNSZ because the discretization of the strain-rate field with $\sim 30 \times 30$ km^2 cells may smooth out a very localized post-seismic relaxation signal from the CNSZ earthquakes.

The component of steady slip in the lower elastic plate reinforces the constructive interference of tectonic forcing and post-seismic relaxation along the SAF system. We believe that a revised approach to modelling the steady-deep-slip component would be more effective in localizing predicted strain gradients in areas where they are observed. The most obvious improvement would come from constraining hypothetical deep slip to occur only along the deeper extensions of discrete faults. The excellent fit of the interseismic velocity field to those obtained by block models (e.g. Meade & Hager 2005; McCaffrey 2005; d'Alessio *et al.* 2005) supports the idea that much of the steady slip that occurs in the lower elastic plate should occur on or near the deeper extension of locked portions of faults. In the context of our model, however, such additional steady deep slip is required only to the extent needed to produce local velocity gradients that cannot be explained by other means (e.g. viscoelastic-cycle effects).

7 CONCLUSIONS

The application of a viscoelastic cycle model to a comprehensive GPS data set in western US shows that the instantaneous velocity

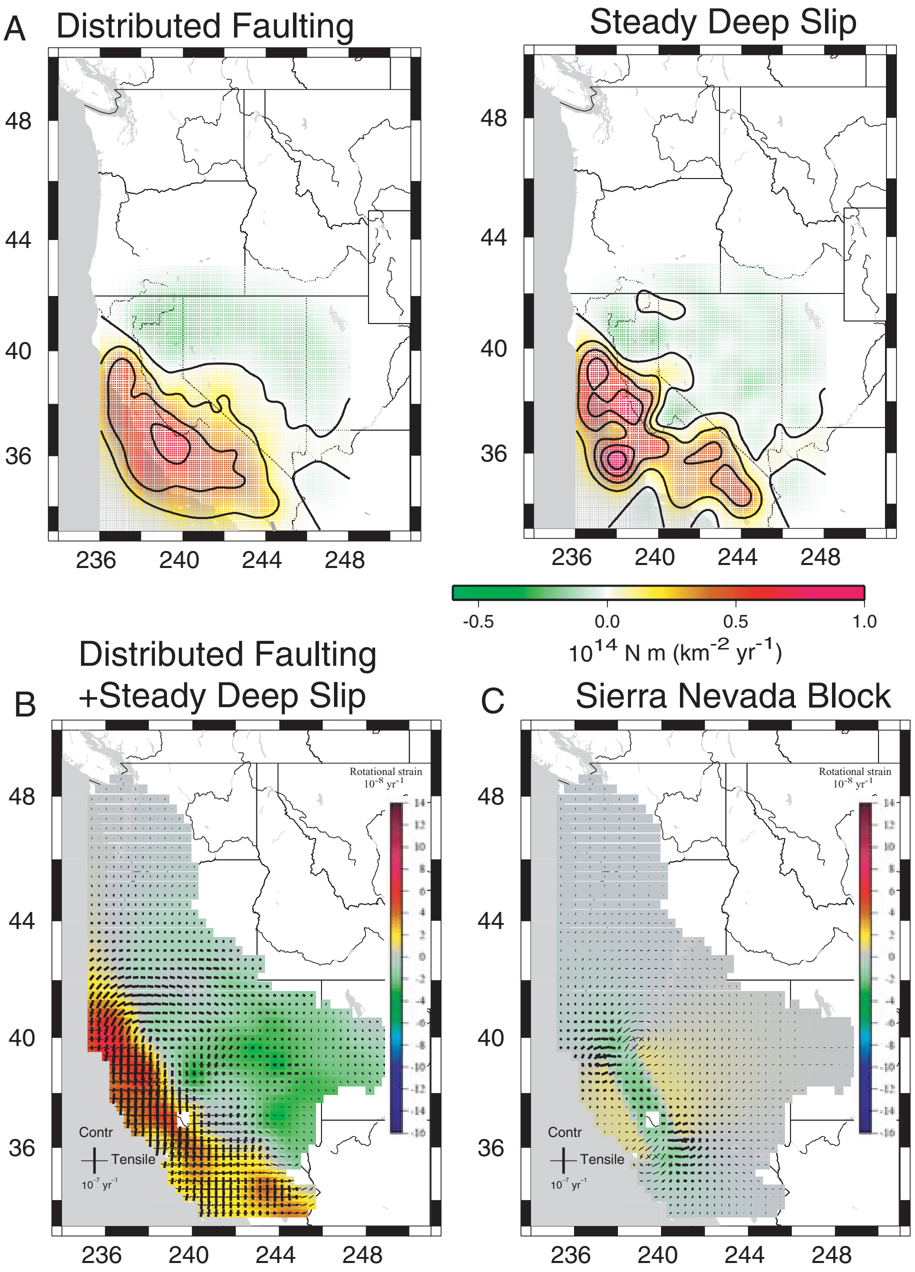

Figure 15. (a) Distributed moment release rates $\dot{m}'^{\text{Strike-slip}}(\hat{\mathbf{r}}; 0, 20\,\text{km})$ and $\dot{m}'^{\text{Strike-slip}}(\hat{\mathbf{r}}; 15\,\text{km}, 20\,\text{km})$ after inversion of the strain-rate field for distributed faulting, distributed steady deep slip, and $\{\dot{f}_i\ |i = 1, 6\}$ with Class 1, 2 and 3 faults held fixed to 'revised' or *a priori* values (see text, Sections 5.3 and 5.6). Isolines are each 0.2×10^{14} N m (km^2 yr)$^{-1}$. The combined contributions of distributed faulting and distributed deep slip (b) and Sierra Nevada block perturbation (c) to strain-rate field are shown in terms of the amplitudes and directions of the principal strain-rates axes and rotational strain rate. For the inversion described in Section 5.7, the components of the strain-rate field on Model 4 contributed by: (d) relaxation following earthquakes on Class 1 faults using the 'revised' slip amplitudes; (e) relaxation following earthquakes on Class 2+3 faults using estimated slip amplitudes and *a priori* amplitude, respectively and (f) tectonic forces. Parts D and E are identical to Figs 7(a) and (b), respectively. (g) sum of all contributions shown in parts (c) to (f). Thick and thin green line segments denote contractile and tensile principal strain axes, respectively, at selected points for visual clarity.

gradient field is well explained through the physical behaviour of an elastic-viscoelastic coupled system. The system is driven by the forces imparted on the NA lithosphere by the oceanic JdF and Pacific plates, viscoelastic relaxation from well-constrained past fault ruptures, cycle-averaged viscoelastic relaxation from less-constrained faults (including unrecognized faults), and steady creep/deep slip.

Post-earthquake relaxation (combined with steady deep slip) and tectonic forcing constructively interfere near the western margin of the plate boundary zone, producing, locally large strain accumulation along the SAF system. However, they destructively interfere further into the plate interior, resulting in smaller and more variable strain accumulation patterns in the eastern part of the plate boundary zone. The best rheological model that applies to western US as a whole (Model 4) exhibits a higher mantle viscosity than in smaller regions in this area over shorter timescale. This may hint at the influence of multiple material relaxation times in the

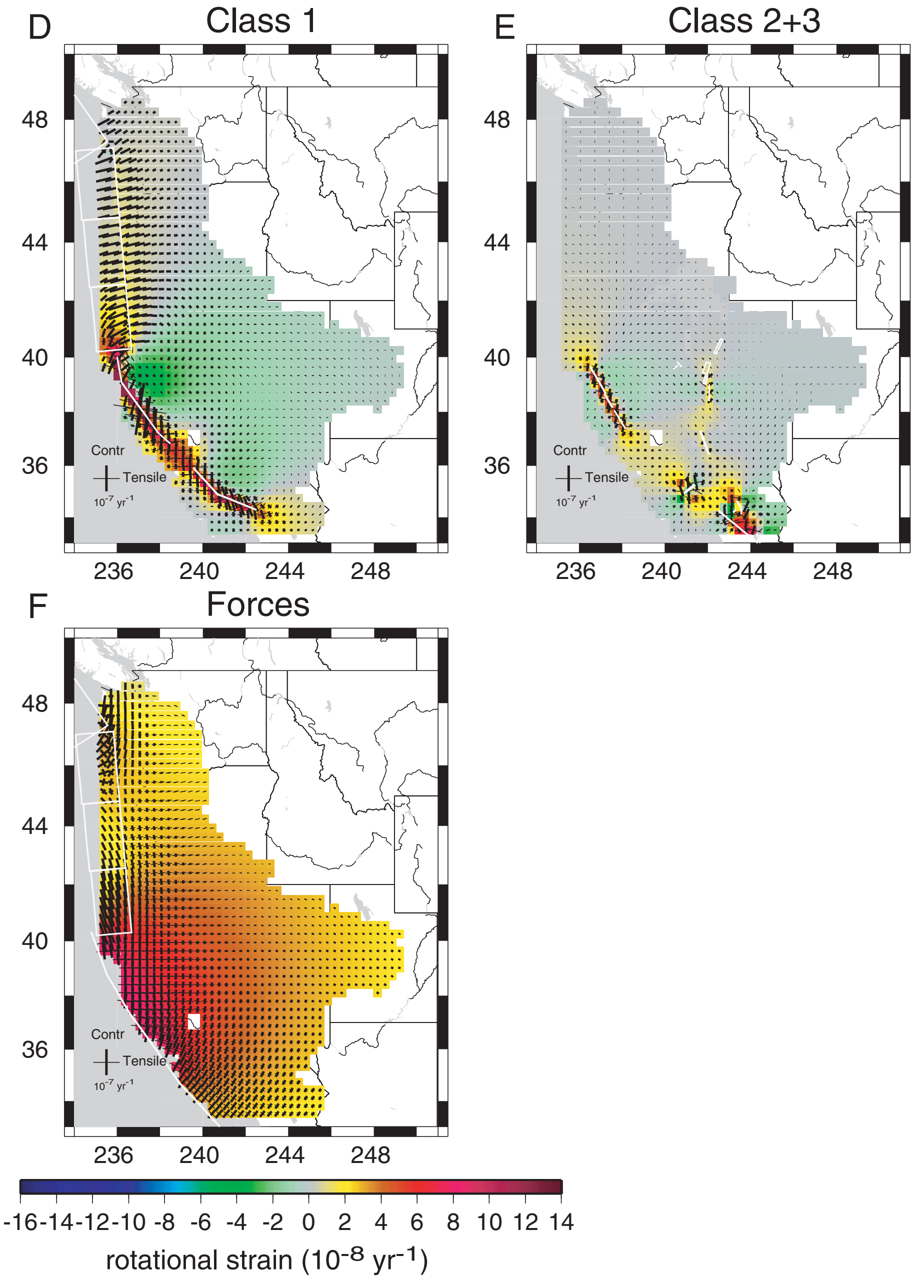

Figure 15. (*Continued.*)

complete mantle rheology, for example, a transient rheology (e.g. Yuen & Peltier 1982; Pollitz 2003a), as well as lateral variations in rheology as suggested by numerous indicators of lithospheric mechanical properties (Lowry *et al.* 2000).

A combination of several mechanical processes generates a strain-rate field that agrees in pattern with the observed strain-rate field in the western US: (1) Pacific to North America and JdF to North America tectonic forcing, (2) viscoelastic relaxation cycles over active faults and (3) steady deep slip. When restricted to processes (1) and (2) using 18 identified fault zones, the predicted amplitude around the SAF system is too small, while the predicted amplitude around the Basin and Range province and elsewhere east of about 119°W is too large. Consideration of the budget of moment accumulation and release along the ∼1000 km-long plate boundary system also shows that past events on recognized fault zones represent only a fraction of the needed moment release in the system. Matching of observed strain rates is improved by introducing additional sources of moment release distributed over the broad areas between the eighteen identified source faults. This includes viscoelastic cycle effects on otherwise unaccounted faults (likely repeating $M \sim 7$ sources) treated in a cycle-averaged sense and steady slip in the lower lithosphere (nominally from 15 km to the base of the elastic plate at 20 km depth). We view the requirement of some degree of steady deep slip in addition to viscoelastic cycle effects as the most important conclusion of this study.

We have assumed throughout that viscoelastic cycle effects dominate the non-steady state component of strain accumulation in the western US, with slip in repeating events generally constrained by

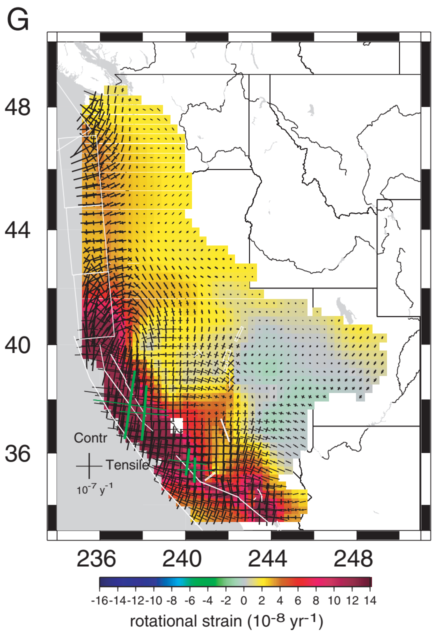

Figure 15. (*Continued.*)

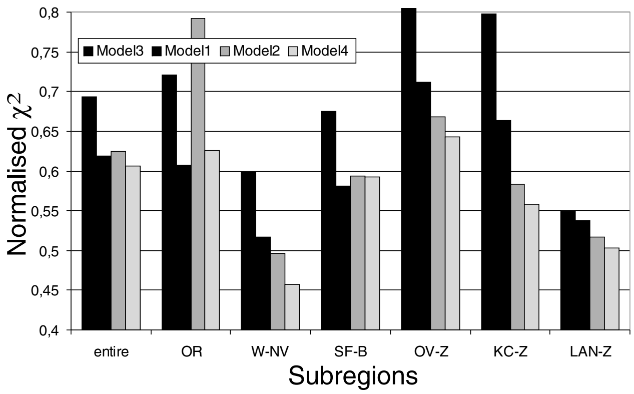

Figure 16. Fits to specific subregions (Fig. 5) derived by joint inversion for $\{\dot{f}_i \,|i = 5, 6\}$ and $\{s_j\}$ for Class 2 faults, with $\{\dot{f}_i|i = 1, ..., 4\}$ held fixed, $\{s_j\}$ of Class 1 faults held fixed at 'revised' values and $\{\dot{s}_j\}$ of Class 3 faults held fixed at *a priori* values (Table 3). The fit to the entire data set is shown on the extreme left.

palaeoseismology. While this may be a reasonable approach for well-understood large fault systems (e.g. northern and southern SAF), it is unclear how applicable it is to fault zones in the Basin and Range province (Wallace 1987). Dixon *et al.* (2003) find congruity between viscoelastic cycle effects and geologic slip rates for many faults in the ECSZ. However, Chang & Smith (2002), Hetland & Hager (2003) and Wernicke *et al.* (2004) point out that non-cyclic viscoelastic effects and/or steady deep slip at rates exceeding recent geologic slip rates appear necessary in other localities.

Numerous issues remain to be clarified in future studies. What are the relative importance of viscoelastic cycle effects and steady deep slip in the context of a thin plate model? To what extent do relaxation and steady slip related to SAF-perpendicular shortening shape the instantaneous strain-rate field? Is a laterally heterogeneous viscoelastic structure and/or a more complicated (i.e. non-Maxwellian) rheology required to explain the instantaneous crustal strain-rate field? Are deformation measurements spatially distributed enough to permit determination of spatially variable forcing rates along the western margin of North America? Do deeper creep rates vary significantly with time, presumably in step with the seismic cycles of the major fault zones? Is basal shear a key component of a dynamic model of instantaneous crustal deformation? The framework adopted here is flexible to permit further investigation of these issues in more detailed studies.

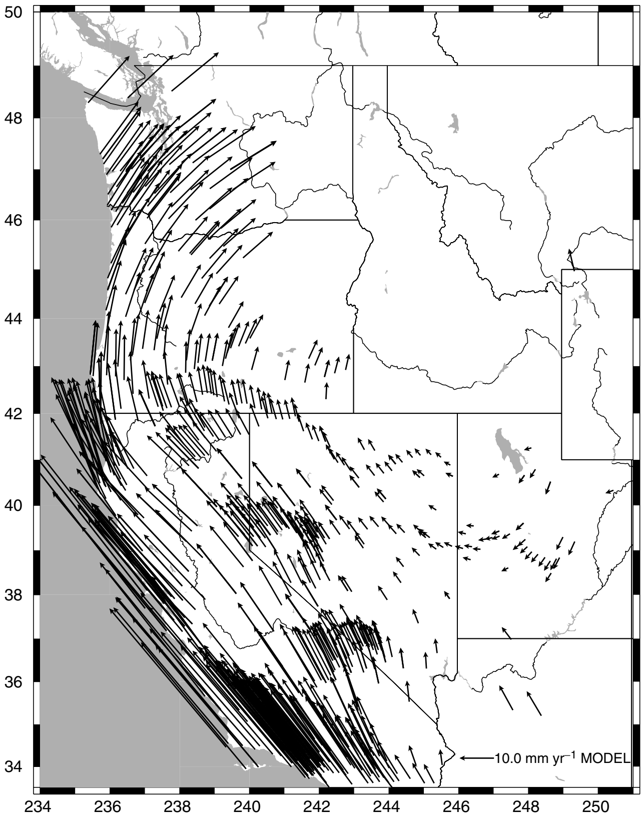

Figure 17. Predicted GPS velocity field based on the combination model of Section 5.7, shifted to produce a negligible velocity field around Great Salt Lake. The effect of background fault creep (e.g. Supplementary Fig. A2) has been added, rendering the resulting velocity field directly comparable with the observed velocity field of Supplementary Fig. A1.

ACKNOWLEDGMENTS

This research has made use of Smithsonian Astrophysical Observatory WUSC velocity solution version 002 obtained from ftp://cfa-ftp.harvard.edu/pub/rbennett/WUSC. The authors are grateful to Jerry Svarc for generating the USGS campaign GPS results presented here. MV is particularly grateful to the French Ministry of Foreign Affairs, whose support through the Lavoisier grant allowed her to carry out one year of postdoctoral research in the *Earthquake Hazard Team*, USGS, Menlo Park. This paper was improved by constructive criticisms from Brendan Meade, Bridget Smith and the associate editor. The authors thank Ruth Harris, Jim Savage, and Wayne Thatcher for their comments on a preliminary draft.

REFERENCES

Altamimi, Z., Sillard, P. & Boucher, C., 2002. ITRF2000: A new release of the International Terrestrial Reference Frame for earth science applications, *J. geophys. Res.,* **107,** ETG2–1–ETG2–19.

Anderson, G., Agnew, D.C. & O, J.H., 2003. Salton Trough regional deformation estimated from combined trilateration and survey-mode GPS data, *Bull. geol. Soc. Am.,* **93,** 2402–2414.

Argus, D.F. & Gordon, R.G., 2001. Present tectonic motion across the Coast Ranges and San Andreas fault system in central California, *Geol. Soc. Am. Bull.,* **113,** 1580–1592.

Atwater, B. & Hemphill-Haley, E., 1997. Recurrence intervals for great earthquakes of the past 3500 years at northern Willapa Bay, Washington, *USGS Prof. Pap.,* **1576**.

Bawden, G., 2001. Source parameters for the 1952 Kern County earthquake, California: a joint inversion of leveling and triangulation observations, *J. geophys. Res.,* **106,** 771–785.

Beanland, S. & Clark, M., 1994. The Owens Valley Fault Zone, eastern California, and surface faulting associated with the 1872 earthquake, *USGS Prof. Pap.,* **1982**.

Bell, J.W., dePolo, C.M., Ramelli, A.R., Sarna-Wojcicki, A.M. & Meyer, C., 1999. Surface faulting and paleoseismic history of the 1932 Cedar Mountain earthquake area, west-central Nevada, and implications for modern tectonics of the Walker Lane, *Geol. Soc. Am. Bull.,* **111,** 791–807.

Bennett, R.A., Davis, J.L. & Wernicke, B.P., 1999. Present-day pattern of Cordilleran deformation in the western United States, *Geology,* **27,** 371–373.

Benz, H.M., Zandt, G. & Oppenheimer, D., 1993. Lithospheric structure of northern (c)alifornia from teleseismic images of the upper mantle, *J. geophys. Res.,* **97,** 4791–4807.

Bills, B.G., Currey, D.R. & Marshall, G.A., 1994. Viscosity estimates for the crust and upper mantle from patterns of lacustrine shoreline deformation in the Eastern Great Basin, *J. geophys. Res.,* **99**(B11), 22 059–22 086.

Caskey, S., Wesnousky, S., Zhang, P. & Slemmons, D., 1996. Trace faulting of the 1954 Fairview Peak (m_S 7.2) and Dixie Valley (m_S 6.8) earthquakes, Central Nevada, *Bull. seism. Soc. Am.,* **86,** 761–787.

Chang, W.-L. & Smith, R., 2002. Integrated seismic-hazard snalysis of the Wasatch front, Utah, *Bull. seism. Soc. Am.,* **92,** 1904–1922.

d'Alessio, M., Johanson, I., Bürgmann, R., Schmidt, D. & Murray, M., 2005. Slicing up the San Francisco Bay Area: block kinematics and fault slip rates from GPS-derived surface velocities, *J. geophys. Res.,* **110,** B06403, doi:10.1029/2004JB003496.

DeMets, C. & Dixon, T.H., 1999. New kinematic models for Pacific-North America motion from 3 Ma to present, I: evidence for steady motion and biases in the NUVEL-1A model, *Geophys. Res. Lett.,* **26,** 1921–1924.

Deng, J., Gurnis, M., Kanamori, H. & Hauksson, E., 1998. Viscoelastic flow in the lower crust after the 1992 Landers, California, earthquake, *Science,* **282,** 1689–1692.

DePolo, C., Anderson, J., DePolo, D. & Price, J., 1997. Earthquake occurrence in the Reno-Carson City urban corridor, *Seismol. Res. Lett.,* **68,** 401–412.

Dixon, J., Dixon, T., Bell, D. & Malservisi, R., 2004. Lateral variation in upper mantle viscosity: role of water, *Earth planet. Sci. Lett.,* **222,** 451–467.

Dixon, T. *et al.*, 2002. Seismic cycle and rheological effects on estimation of present-day slip rates for the Agua Blanca and San Miguel-Vallecitos faults, northern Baja California, Mexico, *J. geophys. Res.,* **107,** doi:10.1029/2000JB000099.

Dixon, T., Norabuena, E. & Hotaling, L., 2003. Paleoseismology and Global Positioning System: earthquake-cycle effects and geodetic versus geologic fault slip rates in the eastern California shear zone, *Geology,* **31,** 55–58.

Dixon, T.H., Miller, M., Farina, F., Wang, H. & Johnson, D., 2000. Present-day motion of the Sierra Nevada block and some tectonic implications for the Basin and Range province, North American Cordillera, *Tectonics,* **19,** 1–24.

England, P. & McKenzie, D.P., 1982. A thin viscous sheet model for continental deformation, *Geophys. J. R. astr. Soc.,* **70,** 295–321.

Flesch, L.M., Holt, W.E., Haines, A.J. & Shen-Tu, B., 2000. Dynamics of the Pacific-North America plate boundary in the Western United States, *Science,* **287,** 834–836.

Freed, A. & Bürgmann, R., 2004. Evidence of powerlaw flow in the Mojave Desert mantle, *Nature,* **430,** 548–551.

Friedrich, A., Wernicke, B.P., Niemi, N.A., Bennett, R.A. & Davis, J.L., 2003. Comparison of geodetic and geologic data from the Wasatch region, Utah, and implications for the spectral character of Earth deformation at periods of ten to ten million years, *J. geophys. Res.,* **108,** doi:10.1029/2001JB000682.

Fumal, T., Rymer, M. & Seitz, G., 2002a. Timing of large earthquakes since A.D. 800 on the Mission Creek strand of the San Andreas fault zone at Thousand Palms Oasis, near Palm Springs, California, *Bull. seism. Soc. Am.,* **92,** 2841–2860.

Fumal, T., Weldon, R., II, Biasi, G., Dawson, T., Seitz, G., Frost, W. & Schwartz, D., 2002b. Evidence for large earthquakes on the San Andreas fault at the Wrightwood, California, paleoseismic site: A.D. 500 to Present, *Bull. seism. Soc. Am.,* **92,** 2726–2760.

Grant, L. & Sieh, K., 1993. Stratigraphic evidence for seven meters of dextral slip on the San Andreas fault during the 1857 earthquake in the Carrizo Plain, *Bull. seism. Soc. Am.,* **83,** 619–635.

Hammond, W.C. & Thatcher, 2004. Contemporary tectonic deformation of the Basin and Range province, western United States: 10 years of observation with the Global Positioning System, *J. geophys. Res.,* **109,** B08403, doi:10.1029/2003JB002746.

Hammond, W.C., Thatcher, W. & Blewitt, G., 2004. Crustal deformation across the Sierra Nevada-Northern Walker Lane, Basin and Range Transition, Western Unied States measured with GPS, 2000-2004, *EOS, Trans. Am. geophys. Un.,* **85**(47), Fall Meet. Suppl., abstract G31D–07.

Hetland, E.A. & Hager, B.H., 2003. Postseismic relaxation across the Central Nevada Seismic Zone, *J. geophys. Res.,* **108,** doi:10.1029/2002JB002257.

Hirabayashi, C.K., Rockwell, T., Wesnousky, S., Stirling, M. & Suarez-Vidal, F., 1996. A neotectonic study of the San Miguel-Vallecitos fault, Baja California, Mexico, *Bull. seism. Soc. Am.,* **86,** 1770–1783.

Humphreys, E.D. & Dueker, K.G., 1994. Western US upper mantle structure, *J. geophys. Res.,* **99,** 9615–9634.

Hyndman, R. & Wang, K., 1995. The rupture zone of Cascadia great earthquakes from current deformation and the thermal regime, *J. geophys. Res.,* **100,** 22 133–22 154.

James, T., Clague, J., Wang, K. & Hutchinson, I., 2001. Postglacial rebound at the northern cascadia subduction zone, *Quaternary Science Reviews,* **19,** 1527–1541.

Kaufmann, G. & Amelung, F., 2000. Reservoir-induced deformation and continental rheology in the vicinity of Lake Mead, Nevada, *J. geophys. Res.,* **105,** 16 341–16 358.

King, G., Oppenheimer, D. & Amelung, F., 1994. Block versus continuum deformation in the western United States, *Earth planet. Sci. Lett.,* **128,** 55–64.

Lisowski, M., Savage, J. & Prescott, W., 1991. The velocity field along the San Andreas fault in central and southern California, *J. geophys. Res.,* **96,** 8369–8389.

Liu, P. & Bird, P., 2002. North America plate is driven westward by lower mantle flow, *Geophys. Res. Lett.,* **29,** 2164, doi:10.1029/2002GL016002.

Lowry, A.R., Ribe, N.M. & Smith, R.B., 2000. Dynamic elevation of the Cordillera, western United States, *J. geophys. Res.,* **105,** 23 371–23 390.

Lynch, J. & Richards, M., 2001. Finite element models of stress orientations in well-developed strike-slip fault zones: implications for the distribution of lower crustal strains, *J. geophys. Res.,* **106,** 26 707–26 730.

Malservesi, R., Dixon, T., La Femina, P. & Furlong, K., 2003. Holocene slip rate of the Wasatch fault zone, Utah, from geodetic data: Earthquake cycle effects, *Geophys. Res. Lett.,* **30,** doi:10.1029/2003GL017408.

Matsu'ura, M., Jackson, D.D. & Cheng, A., 1986. Dislocation model for aseismic crustal deformation at Hollister, California, *J. geophys. Res.,* **91,** 12 661–12 674.

McCaffrey, R., 2005. Block kinematics of the Pacific - North America plate boundary in the southwestern US from inversion of GPS, seismological, and geologic data, *J. geophys. Res.,* **110,** B12406, doi:10.1029/2004JB003241.

McCaffrey, R., Long, M.D., Goldfinger, C., Zwick, P.C., Nabelek, J.L., Johnson, C.K. & Smith, C., 2000. Rotation and plate locking at the southern Cascadia subduction zone, *Geophys. Res. Lett.,* **27,** 3117–3120.

McGill, S. *et al.*, 2002. Paleoseismology of the San Andreas fault at Plunge Creek, near San Bernardino, California, *Bull. seism. Soc. Am.,* **92,** 2803–2840.

Meade, B. & Hager, B., 2004. Viscoelastic deformation for a clustered earthquake cycle, *Geophys. Res. Lett.,* **31,** doi:10.1029/2004GL019643.

Meade, B. & Hager, B., 2005. Block models of crustal motion in southern California constrained by GPS, measurements, *J. geophys. Res.,* **110,** doi:10.1029/2004JB003209.

Mériaux, A.S., Ryerson, F.J., Tapponnier, P., Van der Woerd, J., Finkel, R.C., Xu, X., Xu, Z. & Caffee, M.W., 2004. Rapid slip along the central Altyn Tagh Fault: morphochronologic evidence from Cherchen He and Sulamu Tagh, *J. geophys. Res.,* **109**(B06401), doi:10.1029/2003JB002558.

Nishimura, T. & Thatcher, W., 2003. Rheology of the lithosphere inferred from postseismic uplift following the 1959 hebgen lake earthquake, *J. geophys. Res.,* **108,** 10.1029/2002JB002191..

Peltzer, G., Crampe, F., Hensley, S. & Rosen, P., 2001. Transient strain accumulation and fault interaction in the Eastern California Shear Zone, *Geology,* **29,** 975–978.

Pollitz, F.F., 2001. Viscoelastic shear zone model of a strike-slip earthquake cycle, *J. geophys. Res.,* **106,** 26 541–26 560.

Pollitz, F.F., 2003a. Transient rheology of the uppermost mantle beneath the Mojave Desert, California, *Earth planet. Sci. Lett.,* **215,** 89–104.

Pollitz, F.F., 2003b. The relationship between the instantaneous velocity field and the rate of moment release in the lithosphere, *Geophys. J. Int.,* **153,** 595–208.

Pollitz, F.F., 2003c. Postseismic relaxation theory on a laterally heterogeneous viscoelastic model, *Geophys.J. Int.,* **155,** 57–78.

Pollitz, F.F. & Nyst, M.C.J., 2004. A physical model for strain accumulation in the San Francisco Bay Region, *Geophys. J. Int.,* **160,** 302–317.

Pollitz, F.F., Peltzer, G. & Bürgmann, R., 2000. Mobility of the continental mantle: evidence from postseismic geodetic observations following the 1992 Landers earthquake, *J. geophys. Res.,* **105,** 8035–8054.

Pollitz, F.F., Wicks, C. & Thatcher, W., 2001. Mantle flow beneath a continental strike-slip fault: postseismic deformation after the 1999 Hector Mine earthquake, *Science,* **293,** 1814–1818.

Prescott, W.H., Savage, J.C., Svarc, J.L. & Manaker, D., 2001. Deformation across the Pacific-North America plate boundary near San Francisco, California, *J. geophys. Res.,* **106,** 6673–6682.

Provost, A.-S. & Chéry, J., 2006. Relation between effective friction and fault slip rate across the Northern San Andreas fault system, in Analogue and Numerical Modelling of Crustal-Scale Processes, GSL Special Publications, Bath, UK.

Roy, M. & Royden, L., 2000. Crustal rheology and faulting at strike-slip plate boundaries (1): an analytic model, *J. geophys. Res.,* **105,** 5599–5613.

Runnerstrom, E.E., Grant, L.B., Arrowsmith, J.R., Rhodes, D.D. & Stone, E.M., 2002. Displacement across the Cholame Segment of the San Andreas Fault between 1855 and 1893 from cadastral surveys, *Bull. seism. Soc. Am.,* **92,** 2659–2669.

Savage, J., Simpson, R.W. & Murray, M.H., 1998. Strain accumulation rates in the San Francisco Bay area, 1972-1998, *J. geophys. Res.,* **103,** 18 039–18 051.

Savage, J.C., 1983. Strain accumulation in western United States, *Annu. Rev. Earth Planet. Sci.,* **368,** 11–43.

Savage, J.C. & Prescott, W.H., 1978. Asthenospheric readjustment and the earthquake cycle, *J. geophys. Res.,* **83,** 3369–3376.

Savage, J., Svarc, J. & Prescott, W., 1999a. Strain accumulation at Yucca Mountain, Nevada, 1983-1998, *J. geophys. Res.,* **104,** 17 627–17 631.

Savage, J.C., Svarc, J.L. & Prescott, W.H., 1999b. Geodetic estimates of fault slip rates in the San Francisco Bay area, *J. geophys. Res.,* **104,** 4995–5002.

Savage, J.C., Gan, W. & Svarc, J.L., 2001a. Strain accumulation and rotation in the Eastern California Shear Zone, *J. geophys. Res.,* **106,** 21 995–22 008.

Savage, J.C., Svarc, J.L. & Prescott, W.H., 2001b. Strain accumulation near Yucca Mountain, Nevada, *J. geophys. Res.,* **106,** 16 483–16 488.

Savage, J.C., Gan, W., Prescott, W.H. & Svarc, J.L., 2004. Strain accumulation across the Coast Ranges at the latitude of San Francisco, *J. geophys. Res.,* **109,** doi:10.1029/2003JB002612.

Sharp, R.V., 1981. Variable rates of Late Quaternary strike-slip on the San Jacinto fault zone, *J. geophys. Res.,* **86,** 1754–1762.

Shen, Z.-K., Jackson, D. & Ge, B., 1996. Crustal deformation across and beyond the Los Angeles Basin from geodetic measurements, *J. geophys. Res.,* **101,** 27 957–27 980.

Sieh, K., 1978. Slip along the San Andreas fault associated with the Great 1857 earthquake, *Bull. seism. Soc. Am.,* **68,** 1421–1428.

Sieh, K., 1984. Lateral offsets and revised dates of large prehistoric earthquakes at Pallett Creek, southern california, *J. geophys. Res.,* **89,** 7641–7670.

Sieh, K.E. & Williams, P., 1990. Behavior of the southernmost San Andreas fault during the past 300 years, *J. geophys. Res.,* **95,** 6629–6645.

Smith, B. & Sandwell, D., 2004. A 3-D semi-analytic viscoelastic model for time-dependent analysis of the earthquake cycle, *J. geophys. Res.,* **109,** doi:10.1029/2004JB003185.

Smith, B. & Sandwell, D., 2006. A model of the earthquake cycle along the San Andreas fault system for the past 1000 years, *J. geophys. Res.,* **111,** B01405, doi:10.1029/2005JB003703.

Smith, R., 1978. Seismicity, crustal structure, and intraplate tectonics of the interior of the western Cordillera, *Geol. Soc. Am. Mem.,* **152,** 111–144.

Stein, C. & Stein, S., 1992. A model for the global variation in oceanic depth and heat flow with lithospheric age, *Nature,* **359,** 123–128.

Svarc, J.L., Savage, J.C. & Prescott, W.H., 2002a. Strain accumulation and rotation in western Nevada, 1993-2000, *J. geophys. Res.,* **107,** doi:10.1029/2001JB000579.

Svarc, J.L., Savage, J.C., Prescott, W.H. & Murray, M.H., 2002b. Strain accumulation and rotation in western Oregon and southwestern Washington, *J. geophys. Res.,* **107,** doi:10.1029/2001JB000625.

Tapponnier, P., Ryerson, F.J., Van der Woerd, J., Mériaux, A.S. & Lasserre, C., 2001. Long-term slip rates and characteristic slip: keys to active fault behaviour and earthquake hazard, *C. R. Acad. Sci. Paris, Sciences de la Terre et des planètes,* **333,** 483–494.

Thatcher, W., 2003. GPS constraints on the kinematics of continental deformation, *Int. Geol. Rev.,* **45,** 191–212.

Thatcher, W., Marshall, G. & Lisowski, M., 1997. Resolution of fault slip along the 470-km-long rupture of the great 1906 San Francisco earthquake and its implications, *J. geophys. Res.,* **102,** 5353–5367.

Thatcher, W., Foulger, G.R., Julian, B.R., Svarc, J., Quilty, E. & Bawden, G.W., 1999. Present day deformation across the Basin and Range Province, western United States, *Science,* **282,** 1714–1718.

Thomas, A.P. & Rockwell, T.K., 1996. A 300-to 550-year history of slip on the Imperial fault near the US-Mexico border: missing slip at the imperial fault bottleneck, *J. geophys. Res.,* **101,** 5987–5997.

Trehu, A.M., Asudeh, I., Brocher, T.M., Luetgert, J., Mooney, W., Nabelek, J.L. & Nakamura, Y., 1994. Crustal architecture of the Cascadia forearc, *Science,* **266,** 237–243.

Verdonck, D., 2004. Uplift and subsidence along the Cascadia subduction zone determined from historical repeated leveling, *EOS, Trans. Am. geophys. Un.,* **85**(47), Fall Meet. Suppl., abstract S43D–06.

Wald, D. & Heaton, T., 1994. Spatial and temporal distribution of slip for the 1992 Landers, California, earthquake, *Bull. seism. Soc. Am.,* **84,** 668–691.

Wallace, K., Yin, G. & Bilham, R., 2004. Inescapable slow slip on the Altyn Tagh fault, *Geophys. Res. Lett.,* **31,** doi:10.1029/2004GL019724.

Wallace, R., 1977. Profiles and ages of young fault scarps, north-central Nevada, *Geol. Soc. Am. Bull.,* **88,** 1267–1281.

Wallace, R., 1987. Grouping and migration of surface faulting and variation in slip rates on faults in the Great Basin province, *Bull. seism. Soc. Am.,* **77,** 868–877.

Wang, K., 2000. Stress-strain 'paradox', plate coupling, and forearc seismicity at the Cascadia and Nankai subduction zones, *Tectonophysics,* **319,** 321–338.

Wang, K., Wells, R., Mazzotti, S., Hyndman, R. & Sagiya, T., 2003. A revised dislocation model of interseismic deformation of the cascadia subduction zone, *J. geophys. Res.,* **108,** doi:10.1029/2001JB001227.

Wells, R.E. & Simpson, R.W., 2001. Microplate motion of the Cascadia forearc and implications for subduction deformation, *Earth Planets Space,* **53,** 275–283.

Wernicke, B., Davis, J., Bennett, R., Normandeau, J., Friedrich, A. & Niemi, N., 2004. Tectonic implications of a dense continuous GPS velocity field at Yucca Mountain, Nevada, *J. geophys. Res.,* **109,** doi:10.1029/2003JB002832.

Wesnousky, S., Prentice, C. & Sieh, K., 1991. An offset Holocene stream channel and rate of slip along the northern reach of the San Jacinto fault zone, San Bernardino Valley, California, *Geol. Soc. Am. Bull.,* **103,** 700–709.

Williams, C.A. & McCaffrey, R., 2001. Stress rates in the central Cascadia subduction zone inferred from an elastic plate model, *Geophys. Res. Lett.,* **28,** 2125–2128.

Working Group on California Earthquake Probabilities, 2003. Earthquake probabilities in the San Francisco Bay region, *US Geological Survey Open-file Report,* **03-214**.

Yuen, D. & Peltier, W., 1982. Normal modes of the viscoelastic earth, *Geophys. J. R. astr. Soc.,* **69,** 495–526.

Zoback, M. & Zoback, M., 1989. Tectonic stress field of the continental united states, *Geol. Soc. Am. Mem.,* **172,** 523–539.

Zumberge, J., Heflin, M., Jefferson, D., Watkins, M. & Webb, F., 1997. Precise point positioning for the efficient and robust analysis of GPS data from large networks, *J. geophys. Res.,* **102,** 5005–5017.

SUPPLEMENTARY MATERIAL

The following supplementary material is available for this article online:

Appendixes A and B

This material is available as part of the online article from http://www.blackwell-synergy.com/doi/abs/10.1111/j.1365-246X.2006.03019.x

JOURNAL OF GEOPHYSICAL RESEARCH, VOL. 108, NO. B10, 2502, doi:10.1029/2002JB002374, 2003

Constraints on the viscosity of the continental crust and mantle from GPS measurements and postseismic deformation models in western Mongolia

Mathilde Vergnolle
UMR 6526 CNRS Géosciences Azur, University of Nice, Valbonne, France

Fred Pollitz
U.S. Geological Survey, Menlo Park, California, USA

Eric Calais
Department of Earth and Atmospheric Sciences, Purdue University, West Lafayette, Indiana, USA

Received 27 December 2002; revised 18 May 2003; accepted 23 June 2003; published 25 October 2003.

[1] We use GPS measurements and models of postseismic deformation caused by seven *M*6.8 to 8.4 earthquakes that occurred in the past 100 years in Mongolia to assess the viscosity of the lower crust and upper mantle. We find an upper mantle viscosity between 1×10^{18} and 4×10^{18} Pa s. The presence of such a weak mantle is consistent with results from independent seismological and petrological studies that show an abnormally hot upper mantle beneath Mongolia. The viscosity of the lower crust is less well constrained, but a weak lower crust (3×10^{16} to 2×10^{17} Pa s) is preferred by the data. Using our best fit upper mantle and lower crust viscosities, we find that the postseismic effects of viscoelastic relaxation on present-day horizontal GPS velocities are small (<2 mm yr^{-1}) but still persist 100 years after the 1905, *M*8.4, Bolnay earthquake. This study shows that the GPS velocity field in the Baikal-Mongolia area can be modeled as the sum of (1) a rigid translation and rotation of the whole network, (2) a 3–5 mm yr^{-1} simple shear velocity gradient between the Siberian platform to the north and northern China to the south, and (3) the contribution of postseismic deformation, mostly caused by the 1905 Bolnay-Tsetserleg sequence and by the smaller, but more recent, 1957 Bogd earthquake. *INDEX TERMS:* 1208 Geodesy and Gravity: Crustal movements—intraplate (8110); 8107 Tectonophysics: Continental neotectonics; 8123 Tectonophysics: Dynamics, seismotectonics; *KEYWORDS:* postseismic, viscoelastic, GPS, crust-lithosphere rheology, Mongolia

Citation: Vergnolle, M., F. Pollitz, and E. Calais, Constraints on the viscosity of the continental crust and mantle from GPS measurements and postseismic deformation models in western Mongolia, *J. Geophys. Res.*, *108*(B10), 2502, doi:10.1029/2002JB002374, 2003.

1. Introduction

[2] In the traditional view of lithospheric rheology, a weak (ductile) lower crust overlies a strong upper mantle [e.g., *Brace and Kohlstedt*, 1980; *Chen and Molnar*, 1983; *Strehlau and Meissner*, 1987; *Kirby and Kronenberg*, 1987; *Molnar*, 1992]. Although such a model has prevailed over the past 20 years, recent studies suggest that the upper mantle in many regions may actually be more ductile than the lower crust. For instance, *Pollitz et al.* [2000, 2001], using postseismic deformation data following the 1992 Landers and 1999 Hector Mine earthquakes in southern California, found an upper mantle viscosity ranging from 3×10^{17} to 8×10^{17} Pa s and a lower crust viscosity on the order of 10^{19} Pa s. Similarly, *Kaufmann and Amelung* [2000] and *Bills et al.* [1994], using transient surface deformation data following water level fluctuations in large lakes of the western United States, found an upper mantle viscosity on the order of 1×10^{18} Pa s and a lower crust viscosity greater than 4×10^{19} Pa s.

[3] The apparent conflict with the traditional view stems from the fact that earlier ideas were based almost entirely on laboratory data on the rheology of specific minerals considered to be representative of the crust and mantle. Generally, quartz and dry olivine have been used as proxies for the behavior of the crust and mantle, respectively. Since the strength of quartz greatly decreases at temperatures greater than about 350°C, a temperature reached at midcrustal depth, it was concluded that a brittle-ductile transition occurs in the midcrust, in apparent agreement with the general cessation of crustal seismicity at depths below that where this temperature is reached [*Sibson*, 1982]. Furthermore, at temperatures of about 600 to 700°C, that prevail at the crust-mantle boundary and at considerable depth beneath it, dry olivine has relatively high strength, completing

0148-0227/03/2002JB002374$09.00

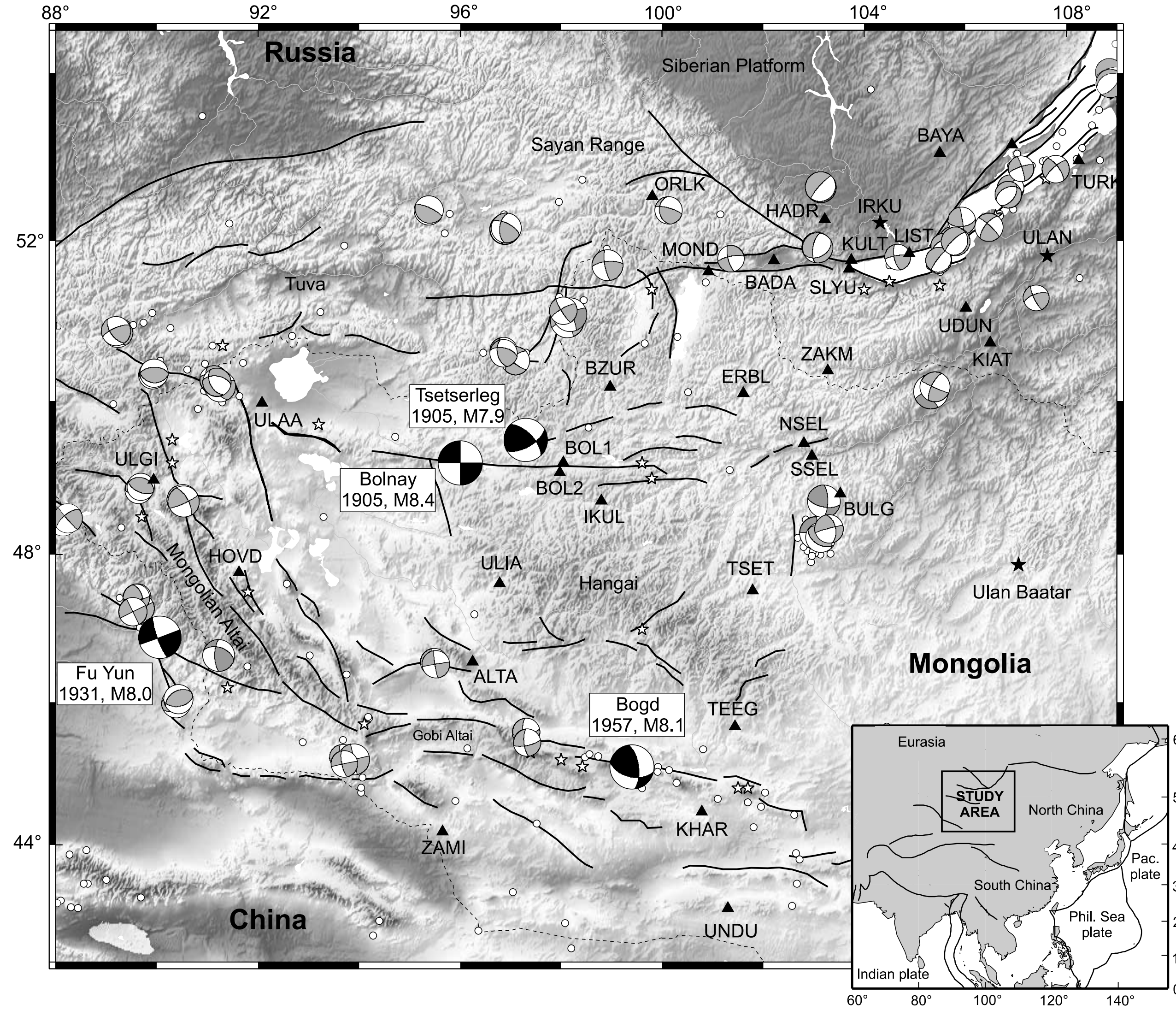

Figure 1. Seismotectonic setting and location of the GPS sites, main active faults, and major earthquakes of Mongolia and Baikal regions. White circles, recent earthquakes (ISC catalog); white stars, historical earthquakes [*Khilko et al.*, 1985; *Schlupp*, 1996]. Focal mechanisms, $6 < M < 8$ in grey, $M > 8$ in black [*Bayasgalan*, 1999]. Triangles, location of campaign GPS sites; black stars, continuous GPS sites. The topography shows strong elevation changes from the Siberian craton to the north (~450 m), to the Hangay dome and Mongolia-Altay belt (~4500 m) to the south.

the picture of a strong upper crust, weak lower crust, and strong uppermost mantle. However, the significance of the cutoff in seismicity has been questioned and reinterpreted as the transition from unstable to stable sliding [*Tse and Rice*, 1986]. In addition, it is generally recognized that quartz is likely only a minor constituent of the lower crust. Its more important constituents are feldspar and pyroxene in amphibolite and granulite facies rocks [*Rudnick and Fountain*, 1995], which maintain a higher strength than quartz at lower crustal conditions. The concept of a weak lower crust may only be valid in thickened crust, for which temperatures near or exceeding the homologous temperature of quartz may be reached. In western Mongolia, we shall advocate here a strong crust down to about 30 km depth, underlain by a weak lower crust. Furthermore, it has been increasingly recognized that the upper mantle in many regions may be hydrated, especially in continental areas affected by subduction in the recent geologic past [*Brandon et al.*, 1996] or by a mantle plume [*Wallace*, 1998]. Laboratory experiments on wet olivine indicate a much weaker behavior than dry olivine at similar temperatures [*Hirth and Kohlstedt*, 1996].

[4] Western Mongolia has been the most seismically active intracontinental region in the world in the past century. Four earthquakes of magnitude 8 and greater have occurred between 1905 and 1957 (Figure 1). They have ruptured three major fault systems along several hundred kilometers: the Bolnay fault system (Tsetserleg earthquake, M = 7.9, July 1905; Bolnay earthquake, M = 8.4, July 1905), the Altai fault system (Fu Yun earthquake, M = 8.0, 1931), and the Gobi-Altai fault system (Bogd earthquake, M = 8.1, 1957) [*Okal*, 1976, 1977; *Khilko et al.*, 1985; *Schlupp*, 1996; *Kurushin et al.*, 1997]. The Bolnay-Tsetser-

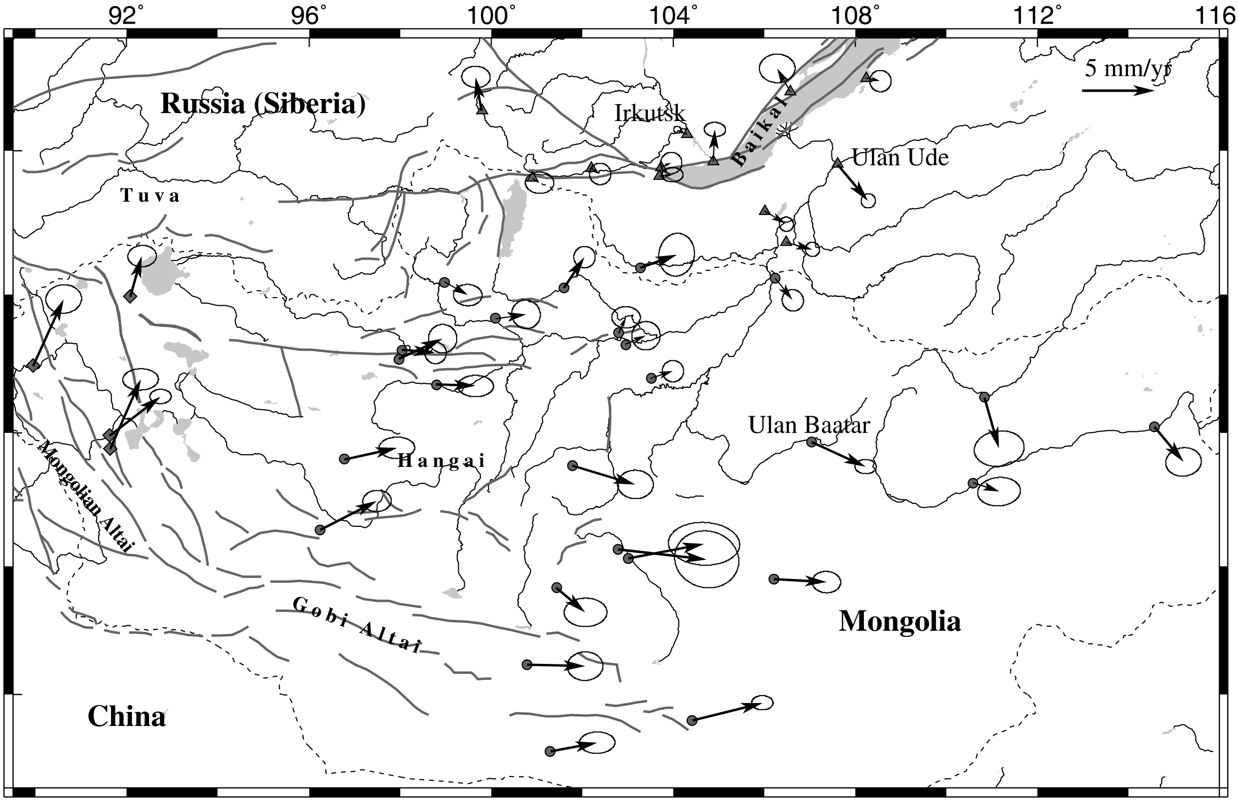

Figure 2. GPS-derived velocities with their 95% confidence error ellipse, shown with respect to Eurasia [*Calais et al.*, 2003]. Circles show the central Mongolia data set; circles and diamonds together show the Mongolia data set; circles, diamonds, and triangles show the Mongolia-Baikal data set.

leg earthquake sequence, in particular, has released the largest amount of seismic energy ever observed inside a continent.

[5] Postseismic strain following large earthquakes can persist over a large area and for several decades after the event. Such long-lasting postseismic effects have been observed after large earthquakes such as the 1906, M = 8.3, San Francisco earthquake [*Thatcher*, 1975; *Kenner and Segall*, 2000], the 1857, M = 8, Fort Tejon earthquake [*Pollitz and Sacks*, 1992], the 1964, M_w = 9.2, Great Alaskan earthquake [*Savage and Plafker*, 1991; *Freymueller et al.*, 2000], and the 1946, M = 8.2, Nankaido earthquake [*Thatcher*, 1984]. In western Mongolia, *Calais et al.* [2002] showed that postseismic strain following the M_w = 8.4, 1905, Bolnay earthquake may still continue through the present-day. They assumed that viscoelastic relaxation in the lower crust is the only mechanism driving postseismic strain following this earthquake, in which case it was concluded that postseismic deformation affects an area that extends up to 300 km away from the rupture zone. Although the largest postseismic effects in this model occur during the first 20–30 years after the earthquake, they showed that postseismic readjustment may still contribute up to 7 mm yr^{-1} to present surface velocities in western Mongolia, more than 95 years after the Bolnay earthquake. However, Calais et al.'s results are strongly dependent on the viscosity of the lower crust and the assumed high strength of the mantle. They assumed a lower crust viscosity of 3×10^{18} Pa s, similar to some other estimates for continental domains [*Ranalli and Murphy*, 1987; *Piersanti*, 1999], but with no regional data to support it. Also, *Calais et al.* [2002] assumed that relaxation occurs only in the lower crust, whereas other authors have proposed that in other regions it may also affect the upper mantle [*Freed and Lin*, 2001; *Pollitz et al.*, 2000, 2001].

[6] Several authors have used transient signals in GPS-derived velocities to infer the viscosity of the crust and/or mantle in various tectonic environments, e.g., rifting [*Pollitz and Sacks*, 1996; *Hofton and Foulger*, 1996], strike-slip [*Pollitz et al.*, 2000, 2001; *Rydelek and Sacks*, 2001], compression [*Pollitz and Dixon*, 1998; *Piersanti*, 1999], postglacial rebound [*Milne et al.*, 2001]. In this work, we use GPS-derived velocities in western Mongolia [*Calais et al.*, 2003], together with postseismic viscoelastic relaxation models for the main earthquakes in the area, in order to assess the viscosity of the lower crust and upper mantle. We compare our results with thermobarometric and petrologic analysis of lower crustal and mantle xenoliths in central Mongolia, with seismic tomography results and with gravity modeling applied to this region. In the companion paper, *Pollitz et al.* [2003] use the viscosities found here in order to investigate stress transfer trough viscoelastic relaxation in an attempt to explain the clustering of large earthquakes in Mongolia in this century.

2. Modeling GPS Velocities

2.1. Interseismic Velocities

[7] We model the GPS velocity field (Figure 2) as the combination of (1) a rigid translation of the whole GPS

Table 1. List of Earthquakes Used in the Viscoelastic Relaxation Models and Their Rupture Parameters

Earthquake	Date	Strike	Dip	Rake	Slip, cm	Depth, km	Length, km	M_o, N m	M	Reference[a]
Tsetserleg	9 July 1905	72.7	90	000	343	35	177	8.81×10^{20}	7.9	1
Bolnay	23 July 1905	85.9	90	000	877	35	90	4.95×10^{21}	8.4	1
		95.5					218			
		97.10					80			
Fu Yun	10 Aug. 1931	161.7	90	180	1114	20	171	1.26×10^{21}	8.0	2
Mondy	4 April 1950	100	75	000	188	15	30	3×10^{19}	7.0	3
Bogd	4 Dec. 1957	101.4	70	009	1005	20	264	1.76×10^{21}	8.1	4, 5
Baikal	29 Aug. 1959	248	53	−50	198	10	30	1.63×10^{19}	6.8	6
Mogod	5 Jan. 1967	002	90	180	241	10	15	1.2×10^{19}	7.1	7, 8
		020	90	165	362	10	20	2.4×10^{19}		
		310	24	90	503	6	12	1.19×10^{19}		

[a] References: 1, *Schlupp* [1996]; 2, *Khilko et al.* [1985]; 3, *Delouis et al.* [2002]; 4, *Okal* [1976]; 5, *Kurushin et al.* [1997]; 6, *Doser* [1991]; 7, *Huang and Chen* [1986]; 8, *Bayasgalan* [1999].

network, (2) a rigid rotation of the whole GPS network (3) a simple shear component modeled as a north-south linear velocity gradient between the Siberian platform to the north and northern China to the south, and (4) the episodic and transient deformation attributable to earthquake faulting. Note that in a spherical geometry, components 1 and 2 could, in principle, be represented together as a rigid rotation of the network about an Euler pole. The first three components describe the long-term velocity field, whereas the fourth one represents coseismic deformation caused by earthquake(s) that occurred during the GPS survey time span as well as postseismic deformation following recent large earthquakes. We shall give explicit forms for these components in section 3.

[8] Since no significant earthquake occurred in the study area during the period of the GPS observations, the GPS velocity field can be decomposed into a term representing the long-term background displacements (rigid rotation, translation, and simple shear), and a term representing postseismic deformation from the large 20th century earthquakes. The aim of our study is to find the viscosity structure that best fits the observed GPS velocities, given the model described above, and to determine the contribution of postseismic effects to current deformation in the Mongolia-Baikal area.

2.2. Postseismic Deformation Model

2.2.1. Viscoelastic Relaxation Approach

[9] Transient deformation is often attributed to postseismic processes following major earthquakes. Three different mechanisms are usually considered: afterslip on the rupture plane and its downdip extension [e.g., *Savage and Svarc*, 1997; *Bürgmann et al.*, 1997; *Kenner and Segall*, 2000], pore pressure reequilibration [e.g., *Peltzer et al.*, 1996], and postseismic relaxation of the lower crust and upper mantle [e.g., *Pollitz*, 1997; *Deng et al.*, 1998]. Viscoelastic relaxation is the only process susceptible to produce postseismic deformation over a long time periods (10 years and longer) and large spatial scales (over 100 km) [*Rydelek and Sacks*, 1990; *Pollitz*, 1992; *Pollitz and Sacks*, 1992; *Pollitz et al.*, 2000]. Moreover, *Pollitz* [1997] showed that after a sufficiently long time (typically a few Maxwell relaxation times of the viscoelastic medium), postseismic effects become larger than the coseismic effects at distances several times the elastic plate thickness and greater. The long time elapsed since the major twentieth century Mongolian earthquakes (e.g., 97 years since the 1905 Bolnay event) creates the conditions for potentially large and measurable long-wavelength postseismic transient signals.

[10] Viscoelastic relaxation results from the coupling between a brittle/elastic crustal layer and an underlying viscoelastic layer. Large deviatoric stress levels caused by stress redistribution following an earthquake cannot be sustained in ductile layers for long periods of time. Relaxation of the ductile regions, typically the continental lower crust and uppermost mantle, couples into persistent straining of the elastic layer with time. In this study, we use the VISCO1D program [*Pollitz*, 1997] to compute these postseismic viscoelastic relaxation effects. For a spherically stratified viscoelastic elastic earth, assuming a Maxwell rheology, VISCO1D computes the spatial distribution of stresses generated by a given point source (in the elastic portion of the crust) at given time intervals. The stresses are computed in terms of a spherical harmonic expansion of spheroidal and toroidal components and are evaluated using a modal summation. The finite faults considered in this study are modeled as the discrete sum of a large number of representative point sources.

[11] The most important factors controlling the viscoelastic relaxation are the rupture parameters (fault geometry and slip) and the Earth model characteristics (thicknesses of the elastic and viscoelastic layers and viscosity structure). The spatial pattern of the relaxation is mainly controlled by the relative thickness of the elastic and dominant viscoelastic regions whereas the temporal evolution is constrained primarily by the viscosity [*Pollitz*, 1992]. We discuss hereafter the rupture parameters of the earthquakes used in this study and the parameterization of the rheological structure of western Mongolia.

2.2.2. Rupture Parameters

[12] We model the viscoelastic relaxation due to the seven largest earthquakes that occurred in Mongolia and surroundings in the past 100 years. Their magnitude range from 6.8 to 8.4 (Table 1). For the sake of simplicity, we associate a given earthquake with one or several rectangular fault plane(s). Fault parameters are specified by the rupture length, maximum and minimum edge depths, and strike, dip, slip, and rake. We derived these parameters from published information [*Okal*, 1977; *Khilko et al.*, 1985; *Huang and Chen*, 1986; *Déverchère et al.*, 1991; *Baljinnyam et al.*, 1993; *Schlupp*, 1996; *Delouis et al.*, 2002]. We fix the rupture length (L) and width (W) at preferred values and

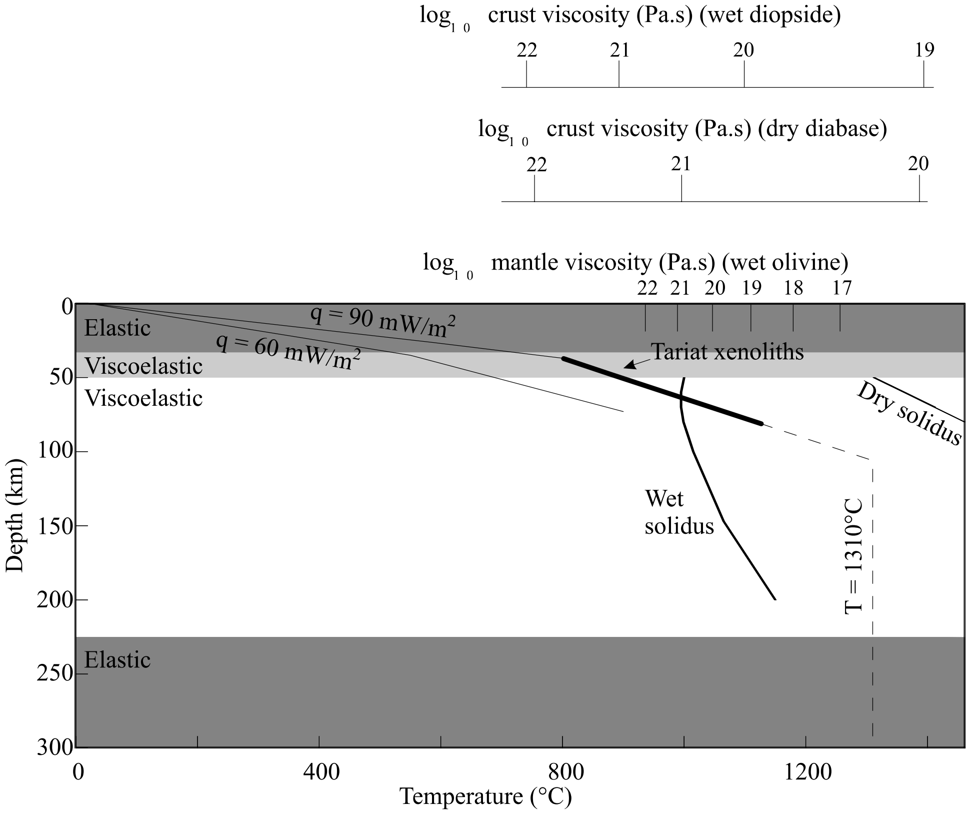

Figure 3. Viscoelastic stratification used to model postseismic deformation in western Mongolia. The thick black line represents the geotherm for the Tariat region [*Ionov et al.*, 1998], the thin black lines are theoretical conductive geotherms for continental domains for surface heat flows of 60 and 90 mW m^{-2} [*Pollack and Chapman*, 1977]. The experimentally derived viscosity laws are for wet olivine for dry diabase from *Hirth and Kohlstedt* [1996], and for wet diopside from *Mackwell et al.* [1998]. These laws are computed with $\dot{\varepsilon}$ constant ($\dot{\varepsilon} = 2, 2 \times 10^{-15} s^{-1}$) for the crust and σ constant ($\sigma = 0, 3$ MPa yr^{-1}) for the mantle.

determine the coseismic slip (U) in conformity with the known seismic moment (M_o) using the relation $M_o = \mu LWU$. Since we assume uniform slip, we use an effective rigidity μ which is a weighted average of rigidity values along the given fault plane according to the elastic stratification ($\mu = 3.3 \times 10^{10}$ Pa for a fault depth shallower than 20 km, $\mu = 4.15 \times 10^{10}$ Pa for deeper faults).

2.2.3. Rheological Structure

[13] We specify the rheological structure of the region in terms of its elastic structure, the location of the major rheological discontinuities, and the viscosities of the ductile portions of the model. Layering is assumed to be spherically symmetric, it therefore depends on depth only. The elastic structure is essentially provided by PREM (preliminary reference Earth model [*Dziewonski and Anderson*, 1981]). The first 20 km of the crust, however, are derived from *Nolet*'s [1977] surface wave study in order to better match the regional characteristics.

[14] Thermobarometric and petrologic analysis of mantle and lower crustal xenoliths in western Mongolia indicate that the crust-mantle boundary is located at a depth of 45 km on average [*Ionov et al.*, 1998], reaching 50 km beneath the northern Hangai area [*Stosch et al.*, 1995; *Kopylova et al.*, 1995]. These results are consistent with a seismic tomography study [*Villaseñor et al.*, 2001] that shows a crustal thickness of 50–60 km in western Mongolia, and with forward modeling of gravity data [*Petit et al.*, 2002], which indicates a 48 km thick crust. In addition, wide-angle seismic data show crustal thicknesses of 45 km south of lake Baikal, about 500 km to the northeast of the Bolnay rupture but in the same geological domain (Khamar–Daban range), and 48–49 km about 250 km north of the Bolnay fault [*Krylov et al.*, 1991]. We therefore use a crustal thickness of 50 km in the models (Figure 3).

[15] *Déverchère et al.* [2001] recently analyzed the earthquake depth distribution in the Baikal rift zone and northern central Mongolia using a subset of 632 relocated earthquakes extracted from an instrumental seismicity catalog covering the past 30 years (Institute of the Earth Crust, Irkutsk, Russia). Although most of the hypocenters are concentrated between 10 and 20 km, they show that a significant seismicity persists at greater depth, with 9–15% of the hypocenters located between 25 and 35 km and 7–13% located between 35 and 40 km. The occurrence of relatively deep earthquakes (30–40 km) had previously been evidenced in the northern part of the Baikal rift zone by *Déverchère et al.* [1993] and *Vertlib* [1981]. *Déverchère et al.* [2001] use the hypocenter depth distribution to infer a brittle-ductile transition at about 25 km and a seismogenic thickness of 35 ± 5 km (assuming a 100 Ma thermal

lithosphere), with a quartz rheology in the upper 10 km and a diabase one from 10 to 45 km. In Mongolia, *Bayasgalan* [1999] performed waveform modeling of several recent earthquakes and found that 5 out of 29 earthquakes with $m_b > 5.0$ occurred at depths between 20 and 30 km. These observations therefore indicate that the lower limit of the seismogenic upper crust in the western Mongolia-Baikal area may reach a depth of 30–40 km. In our models, we will use a 35 km thick upper elastic crust. We also tested a 25 km thick upper crust and found no significant impact on the results presented here (see section 4.2.4).

[16] The ductile behavior of the upper mantle can be represented by power law creep [*Weertman*, 1978]:

$$\dot{\varepsilon} = A_0 \exp\left(-\frac{E^* + PV^*}{RT}\right)\sigma^n, \tag{1}$$

where $\dot{\varepsilon}$ is the strain rate, A_0 is a preexponential factor, E^* is the activation energy, V^* is the activation volume, R is the gas constant, σ is the stress, n is the power law exponent (3.5 in the mantle), P is the pressure, and T is the absolute temperature. In the shallow mantle, the strain rate depends primarily on temperature rather than pressure. Hence, since T increases with depth, for a given stress, the viscosity is predicted to decrease with depth. At depths greater than 200–300 km, the effect of pressure dominates, resulting in a viscosity increase with depth [*Karato and Wu*, 1993]. We assign a sharp boundary to what is most likely a gradual transition from a lower to higher viscosity mantle and neglect possible viscosity variations within the uppermost mantle. As a compromise, we fix the bottom depth of the ductile portion of the upper mantle at 220 km and assign uniform viscosity to the mantle from 50 to 220 km depth. Below 220 km, we assume an elastic mantle (Figure 3).

3. Inversion

[17] At a given position r on the spherical Earth, let x and y measure distance in the local east and north directions, respectively, and let $\hat{x}$ and $\hat{y}$ be the corresponding local unit vectors. We model the observed horizontal velocities $V = v_x\hat{x} + v_y\hat{y}$ at point r between times t_1 and t_2 as

$$V(r; t_1, t_2) = V_{\mathrm{trans}}(r) + V_{\mathrm{rot}}(r) + V_{sz}(r) + V_{ps}(r; t_1, t_2; \eta_c, \eta_m). \tag{2}$$

In equation (2), V_{trans} and V_{rot} represent velocity vectors associated with a rigid translation and rotation, respectively:

$$V_{\mathrm{trans}}(r) = (A_1\hat{x} + A_2\hat{y}) \tag{3}$$

$$V_{\mathrm{rot}}(r) = \frac{A_3(\hat{r}_0 r)}{R}, \tag{4}$$

where without loss of generality, $\hat{r}_0$ represents an arbitrary reference position near the study area and R is Earth's radius. V_{sz} represents the velocity field associated with a simple shear zone. On the basis of the regional pattern of faulting [*Schlupp*, 1996; *Cunningham et al.*, 1996a, 1996b], we assume a constant north-south velocity gradient through the deformed area from China in the south to the Siberian platform in the north:

$$V_{sz}(r) = \left[\frac{A_4(y - y_0)}{W}\right]\hat{x}, \tag{5}$$

where without loss of generality, y_0 represents the position of an arbitrary constant latitude near the study region and W = 1110 km is the width of the shear zone bounded by latitudes 52°N and 42°N. Finally, V_{ps} represents the postseismic velocity, which depends on the viscosity structure through parameters η_c (lower crust viscosity) and η_m (mantle viscosity).

[18] It is useful to define the total rotation rate contributed by the rotational and shear zone velocity fields, i.e., $v' = V_{\mathrm{rot}} + V_{sz}$:

$$\dot{\omega}_{xy} = \frac{1}{2}\left[\frac{\partial v'_x}{\partial y} - \frac{\partial v'_y}{\partial x}\right]. \tag{6}$$

Substituting equations (4) and (5) into equation (6) gives

$$\dot{\omega}_{xy} = \frac{1}{2}\left[-\frac{A_3}{R} + \frac{A_4}{W}\right]. \tag{7}$$

We may write a similar formula for the horizontal shear strain:

$$\varepsilon_{xy} = \frac{1}{2}\left[\frac{\partial v'_x}{\partial y} + \frac{\partial v'_y}{\partial x}\right] = \frac{1}{2}A_4, \tag{8}$$

which is negative for left-lateral shear along vertical east-west trending planes.

[19] Let $\{V^n_{\mathrm{obs}}\ (r_n;\ t_1,\ t_2) | n = 1,..N\}$ with associated east and north components $v^n_{x\mathrm{obs}}$ and $v^n_{y\mathrm{obs}}$, respectively, represent the observed velocity field at N GPS sites located at r_n, and let C be their associated covariance matrix. Our modeling strategy is to minimize the fit of this data with the model of equation (2) by performing a grid search in the space $\{\eta_c, \eta_m\}$, correcting the observed velocity field for predicted postseismic velocities, and estimating the parameters A_1, A_2, A_3, A_4 by least squares inversion. Specifically, for each pair of trial viscosities η_c and η_m, we minimize the χ^2 statistic

$$\begin{aligned} \chi^2 &= [\Delta v_1 \Delta v_2 \ldots \Delta v_N] C [\Delta v_1 \Delta v_2 \ldots \Delta v_N]^T \\ \Delta \nu_n &= \left[\left(v_x(r_n; t_1, t_2) - v^n_{x\mathrm{obs}}\right)\left(v_y(r_n; t_1, t_2) - v^n_{y\mathrm{obs}}\right)\right] \end{aligned} \tag{9}$$

with respect to the four parameters A_1, A_2, A_3, and A_4 by least squares inversion. Thus the factors V_{trans}, V_{rot}, and V_{sz} are determined by inversion of the data, and the resulting minimum χ^2 is a function of η_c and η_m. We are at liberty to include or exclude any of V_{trans}, V_{rot}, or V_{sz} in this inversion (i.e., $A_1 = A_2 = 0$ or $A_3 = 0$ or $A_4 = 0$ a priori). Likewise, we can estimate one or more of these background velocity components without postseismic relaxation (i.e., $V_{ps} = 0$ a priori).

[20] In addition, we find that there are strong tradeoffs between the estimations of V_{rot} and V_{sz}, so that it is desirable to impose an external constraint on these parameters.

According to the geologic slip rates known on the two main E-W left-lateral ruptures in Mongolia (in the Gobi Altay and Bolnay), the shear velocity (= A_4) is at least 3 mm yr^{-1} [*Ritz et al.*, 1995, 2003]. Taking into account other possible left-lateral strike-slip faults (e.g., Sayan in the northern edge of the defined shear zone) and distributed deformation which is not localized near a major fault, we consider that the maximum amount of left-lateral shear is 10 mm yr^{-1}. Thus, in one class of inversions that we implement, we impose the constraint $3 < A_4 < 10$ mm yr^{-1}. We shall refer to inversions that have this constraint as "V_{sz} restricted", whereas inversions with A_4 unrestricted will be called "V_{sz} unrestricted".

[21] Postseismic velocities are computed a priori, using the method described above. For the standard Earth model, we computed a set of 375 viscoelastic relaxation models for the 1997–2002 period, varying the upper mantle viscosities from 3×10^{17} to 3×10^{22} Pa s and the ratio of the lower crust to upper mantle viscosity from 0.03 to 10 (i.e., lower crust viscosities ranging from 9×10^{15} to 3×10^{23} Pa s).

4. Models and Tests

[22] We perform a series of tests in order to understand the tradeoffs between the parameters estimated in the inversion, the impact of the uncertainties on the GPS velocities, and the subset of sites used in the inversion.

[23] One of the issues of the inversion process is the assignment of a proper weight to the GPS data. In principle, the a priori covariance matrix C should simply reflect the formal errors of the GPS-derived velocities. However, the fact that the number of GPS measurement epoch per site and the total measurement time span vary significantly across the network implies an uneven spatial distribution of the GPS uncertainties, with the best determined velocities in the Baikal rift zone. In order to investigate the influence of this uneven distribution of the GPS uncertainties, we ran three series of tests with the diagonal terms of the a priori covariance matrix C: (1) derived from the formal GPS errors ("true errors"); (2) derived from the formal GPS errors, except for stations with formal errors less than 1 mm yr^{-1}, for which they are set to 1 mm yr^{-1} ("mixed errors"); and (3) fixed to 1 mm yr^{-1} for all stations ("fixed errors").

[24] Also, since the study area shows three major areas of contrasting tectonic regime (right-lateral transpression in the Altay, left-lateral shear in western Mongolia, and left-lateral transpression to normal faulting in the Baikal rift zone), we tested three different subsets of the data: (1) the entire GPS data set (41 velocities, all GPS stations on Figure 2); (2) a data set without GPS sites from the Baikal area (Mongolia, 29 velocities, circles and diamonds on Figure 2); and (3) data set without GPS sites from both the Altay and Baikal areas (central Mongolia, 25 velocities, circles on Figure 2).

[25] For each of these tests, we further implemented the V_{sz}-restricted and the V_{sz}-unrestricted inversions (see above) and use the three covariance matrices C defined above. Finally, we tested the influence of a 25 km thickness for the elastic upper crust.

4.1. "Benchmark" Model

[26] Before the details of the parameter tests, we first present the results of a benchmark model based on the Mongolian GPS data set, using mixed errors (see above), and the V_{sz}-restricted inversion scheme. We first test whether allowing for postseismic strain significantly improves the model fit to the data by comparing inversions performed with and without postseismic effects. As shown on Figure 4a, we find a χ^2 improvement when postseismic effects are taken into account. An F test [e.g., *Stein and Gordon*, 1984] shows that this χ^2 improvement is significant at the 80% confidence level, given the degrees of freedom of the inversions (58 data, $n_2 = 6$ unknown parameters (A_1, A_2, A_3, A_4, η_c, and η_m) with postseismic effects, $n_1 = 4$ without postseismic effects).

[27] Figure 4b shows the χ^2 in the $[\eta_m/(\eta_c/\eta_m)]$ domain. We find that the minimum χ^2 is obtained for two domains of upper mantle viscosity, independently of the $[(\eta_m/\eta_c)]$ ratio: a low-viscosity domain ($<6 \times 10^{18}$ Pa s) and high-viscosity domain ($>6 \times 10^{20}$ Pa s). We used the F test statistics to delineate the 70% and 80% confidence level area (bold lines on Figure 4b). We find two domains in which postseismic effects significantly improve the inversion results, corresponding to either a weak viscoelastic structure (2×10^{18} Pa s $< \eta_m < 3 \times 10^{18}$ Pa s and 6×10^{16} Pa s $< \eta_c < 9 \times 10^{16}$ Pa s, 80% confidence), or a strong viscoelastic structure (5×10^{20} Pa s $< \eta_m < 1 \times 10^{21}$ Pa s and a 9×10^{20} Pa s $< \eta_c < 1 \times 10^{22}$ Pa s, 70% level confidence) (Tables 2 and 3). These results are not altered when we use a different subset of GPS sites in the inversion or by the assumption about formal errors of the data. In the first case (low upper mantle/lower crust viscosity), postseismic stresses will relax rapidly after each event. In the second case (high upper mantle/lower crust viscosity), postseismic stresses will relax slowly. In both cases, surface deformation due to postseismic relaxation for a 5 year period, 100 years after major earthquakes, are therefore expected to be small.

4.2. Tests

4.2.1. Influence of the GPS Data Subset

[28] We tested the influence of using 3 different GPS data subsets (see above) in the inversion and found that, regardless of the GPS data subset used, χ^2 minimum are located in the same $[\eta_m/(\eta_c/\eta_m)]$ domains (Tables 2 and 3). The F tests always favor a low-viscosity structure, but levels depend on the data used in the inversion (Table 2). The confidence level for the low-viscosity χ^2 minimum decreases from 90% when using the most restricted GPS data set (central Mongolia stations) to 70% when using the entire GPS data set. For the stronger viscosity χ^2 minimum, using the entire data set and the Mongolia data set both result in a 70% confidence level domain whereas the restricted data set results in a 62% confidence level only (Table 3).

[29] This dependency of the F test confidence level on the GPS data set used in the inversion may result from the different tectonic regimes in the study area (right-lateral shear in western Mongolia, left-lateral shear in central Mongolia, NW-SE extension in the Baikal area) or may reflect lateral variations of the viscosity structure (Tables 2 and 3).

4.2.2. Influence of the GPS Uncertainties

[30] We tested the influence of the uncertainties on the GPS data using the three cases described above ("true", "mixed", or "fixed" errors). We find that the χ^2 in the $[\eta_m/(\eta_c/\eta_m)]$ domain for the mixed errors and the fixed errors does not change, whereas it is 8 times higher for the χ^2

minimum using the true errors. This suggests that there are signals in the observed velocities that are not accounted for in our model. In particular, lateral variations in elastic and viscoelastic properties would modify the response to background tectonic forces or earthquakes. For example, large velocity gradients are observed locally in the eastern Hangai region (48°N, 103°W) which are not matched in the model (Figure 5). However, this region is underlain by very slow seismic velocity mantle [*Friederich*, 2003] and is characterized by a steep thermal gradient [*Ionov et al.*, 1998; *Ionov*, 2002; *Kopylova et al.*, 1995], suggesting more compliant crust and mantle. This region could thus accommodate a higher-than-normal background strain for given tectonic background forces, and it may also respond to postseismic stresses in a different manner than surrounding regions. Nevertheless, the χ^2 pattern and minima in the $[\eta_m/(\eta_c/\eta_m)]$ space remain the same in the three cases.

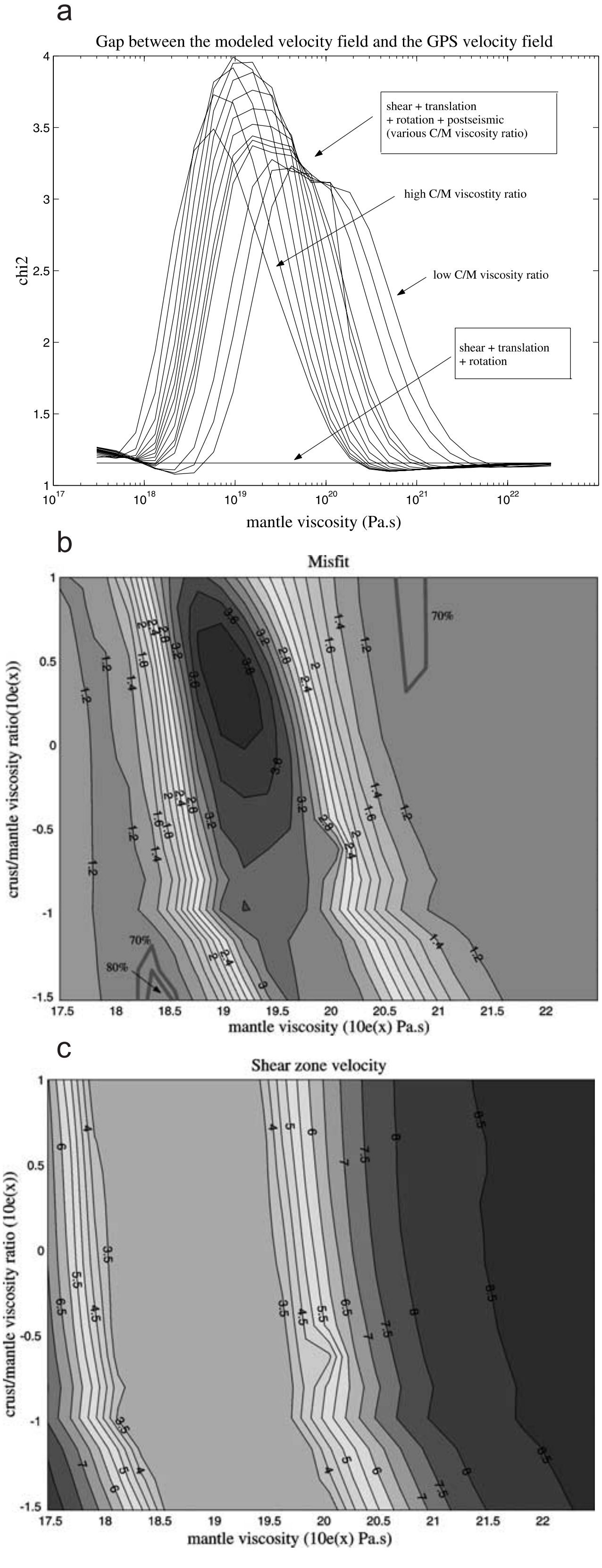

4.2.3. Influence of the Shear Velocity

[31] We find best fit models in the same $[\eta_m/(\eta_c/\eta_m)]$ domains when we invert the data using the V_{sz}-unrestricted scheme or V_{sz}-restricted scheme. The difference between the minimum χ^2 between the two strategies is less than 10^{-4}. For the weak viscosity structure, we find a best fit shear zone velocity that ranges from 3 to 5.5 mm yr^{-1} using the entire GPS data set and fixed or mixed velocity uncertainties. We find a slightly larger shear velocity (3 to 6.5 mm yr^{-1}) when using the true GPS uncertainties (Table 2). For the strong viscosity structure, we find a best fit shear zone velocity that ranges from 6.5 to 9 mm yr^{-1}. The higher velocity is obtained when inverting the entire GPS data set (Table 3). The results are similar to the former one if we assume no postseismic component (Table 2). These results are discussed in section 4.3.

4.2.4. Influence of the Elastic Upper Crust Thickness

[32] We tested the effect of a 25 km thick elastic upper crust instead of the 35 km used in our standard model (Table 4). The general χ^2 pattern in the $[\eta_m/(\eta_c/\eta_m)]$ domain shows little change compared to a 35 km thick upper crust. However, we find that a 25 km thick upper crust results in a best fit mantle viscosity twice smaller than in the 35 km thick upper crust case. The best fit viscosities for the 25 km thick upper crust range from 5×10^{17} Pa s to 2×10^{18} Pa s for the mantle and from 2×10^{16} Pa s to 1×10^{17} Pa s for the lower crust (Table 4).

4.3. Final Results

[33] The tests presented above show that the mantle and crust viscosities derived from the inversion of the GPS data are not strongly dependent on the GPS data set, the

Figure 4. (opposite) Result for the inversion of the Mongolia GPS data set (29 stations), with a covariance matrix derived from the formal GPS errors with the restriction that the standard deviation in any velocity component must be greater than 1 mm yr^{-1} and with V_{sz}-restricted scheme. (a) χ^2 as a function of upper mantle viscosity with postseismic effects (curves), without postseismic effects (horizontal line). (b) Logarithmic misfit of GPS data with respect to the viscoelastic relaxation model as a function of mantle viscosity and crust-to-mantle viscosity ratio. The contours show the 70% and 80% confidence area where the null hypothesis is verified by an *F* test (i.e., accounting for postseismic effects significantly improves the χ^2). (c) Shear velocities across Mongolia obtained from this inversion (in mm/yr).

Table 2. Viscosities, Shear Zone Velocity, and *F* Test Results for the Weak Mantle Viscosity Minimum[a]

GPS Data Set	Uncertainties	Weak Viscoelastic Structure: η_m, Pa s	η_c, Pa s	V_{sz}, mm/yr	*F* Test, %	V_{sz} (Without PS), mm/yr
Central Mongolia	fixed and mixed	2×10^{18} to 2.5×10^{18}	6×10^{16} to 7.6×10^{16}	3.5–4	90	7.3
		1×10^{18} to 4×10^{18}	3×10^{16} to 1.5×10^{17}	3–5	80	7.3
		1×10^{18} to 4×10^{18}	3×10^{16} to 2×10^{17}	3–5	70	7.3
	true	8×10^{17} to 3×10^{18}	2.5×10^{16} to 1×10^{17}	3–5.5	–	7.3
Mongolia	fixed and mixed	2×10^{18} to 3×10^{18}	6×10^{16} to 9×10^{16}	3.5–5.5	80	8.6
		1.5×10^{18} to 4×10^{18}	4.5×10^{16} to 2×10^{17}	3–5.5	70	8.6
	true	1×10^{18} to 4×10^{18}	3×10^{16} to 1×10^{17}	4.5–6.5	–	8.6
Mongolia and Baikal	fixed and mixed	2×10^{18} to 2.7×10^{18}	6×10^{16} to 8.1×10^{16}	5–5.5	70	8.9
	true	–	–	–	–	9.4
Summary		1×10^{18} to 4×10^{18}	3×10^{16} to 2×10^{17}	3–5.5	–	–

[a] The GPS data subset and covariance matrix used in the inversion (true, mixed, and fixed) are given. The depth of the interfaces is 35 km for the upper/lower crust boundary, 50 km for the Moho, and 220 km for the lower limit of the upper mantle.

background shear strain, the GPS data uncertainties, or the upper/lower crust limit. The results obtained with the GPS data errors and/or all of the GPS stations inverted yield somewhat worse fits because of the disproportionate weight given to some GPS sites and the possible effect of a laterally variable viscosity structure. However, regardless of the data set or inversion scheme, we find that the mantle viscosity beneath Mongolia ranges fits both a high viscosity model ($5 \times 10^{20} < \eta_m < 1 \times 10^{21}$ Pa s) and a low-viscosity model ($1 \times 10^{18} < \eta_m < 4 \times 10^{18}$ Pa s). As shown above, the statistical tests slightly favor a low-viscosity model. Also, the shear zone velocity associated with the low-viscosity model (3 to 5.5 mm yr^{-1}) is more consistent with the cumulative slip rate on active faults in Mongolia [*Ritz et al.*, 1995, 2003].

[34] The viscosity of the lower crust is not as well constrained as that of the upper mantle. The *F* test favors a lower crust viscosity ranging from 3×10^{16} to 2×10^{17} Pa s for the weak mantle models and ranging from 6×10^{20} to 1×10^{22} Pa s for the strong mantle models (Tables 2 and 3).

5. Discussion

5.1. A Weak Upper Mantle in Mongolia?

[35] The usually assumed ''jelly sandwich'' model of the continental lithosphere is consistent with the strong mantle models found above. However, our data tend to favor a weak mantle model. Recent results derived from modeling transient surface deformation signals sensitive to uppermost mantle rheology also support low viscosity values for the upper mantle [*Bills et al.*, 1994; *Pollitz et al.*, 2000; *Kaufmann and Amelung*, 2000; *Pollitz et al.*, 2001]. We review hereafter regional arguments that support the hypothesis of the existence of a weak mantle beneath western Mongolia.

[36] *Villaseñor et al.* [2001] and *Friederich* [2003], using surface wave tomography, found a low-velocity anomaly in the upper mantle (about −4% at 100 km depth), centered under western Mongolia, that may be interpreted as an anomalously hot mantle, qualitatively consistent with the low-viscosity found here.

[37] *Ionov et al.* [1998], *Ionov* [2002], and *Kopylova et al.* [1995], using thermobarometric and petrologic analysis of crustal and mantle xenoliths embedded in Miocene to Quaternary alkali basalts from central Mongolia (Tariat volcanic field, Hangai region), found a high upper mantle temperature and a much steeper geotherm in that area than in the adjacent cratonic Asia lithosphere (90 mW m^{-2} against 60 mW m^{-2}). This geotherm, together with an experimentally derived law for the rheology of wet olivine [*Hirth and Kholstedt*, 1996], indicates an average viscosity of 10^{17} to 10^{18} Pa s for the upper mantle (50 to 220 km, Figure 3), consistent with our results.

[38] *Kopylova et al.* [1995] suggest a thermal perturbation by advection under Mongolia, possibly caused by a recent magmatic underplating and the intrusion of basaltic magma at the crust-mantle boundary and in the uppermost mantle. *Kopylova et al.* [1995] and *Ionov* [2002] both find that the fertile composition of the uppermost mantle in Mongolia, as sampled by the xenoliths, and the moderately high geothermal gradient are consistent with low seismic velocities in the upper mantle.

[39] Finally, *Petit et al.* [2002] modeled the Bouguer gravity anomaly in western Mongolia and propose the existence of a thermal anomaly at 100 to 200 km depth beneath the Hangai-Hövsgöl area, caused by mantle upwelling. They also propose the existence of a mafic body underplated at the crust-mantle boundary in order to explain the high topography/low gravity anomaly centered on the Hangai-Hövsgöl area.

Table 3. Same as Table 2 for the Higher Mantle Viscosity Minimum

GPS Data Set	Uncertainties	Strong Viscoelastic Structure: η_m, Pa s	η_c, Pa s	V_{sz}, mm/yr	*F* Test, %
Central Mongolia	fixed and mixed	$>3 \times 10^{21}$	$>9 \times 10^{19}$	7–7.5	<70
	true	$\sim 6 \times 10^{20}$	9×10^{20} to 6×10^{21}	6.5–7	–
Mongolia	fixed and mixed	5×10^{20} to 1×10^{21}	9×10^{20} to 1×10^{22}	8–9	70
	true	3.8×10^{20} to 8.3×10^{20}	9.5×10^{20} to 8.3×10^{21}	7.5–8.5	–
Mongolia and Baikal	fixed and mixed	6×10^{20} to 1×10^{21}	6×10^{20} to 1×10^{22}	8–8.5	70
	true	3×10^{20} to 4.5×10^{21}	4.5×10^{20} to 4.5×10^{22}	8.5–9.5	–
Summary		5×10^{20} to 1×10^{21}	6×10^{20} to 1×10^{22}	6.5–9.5	–

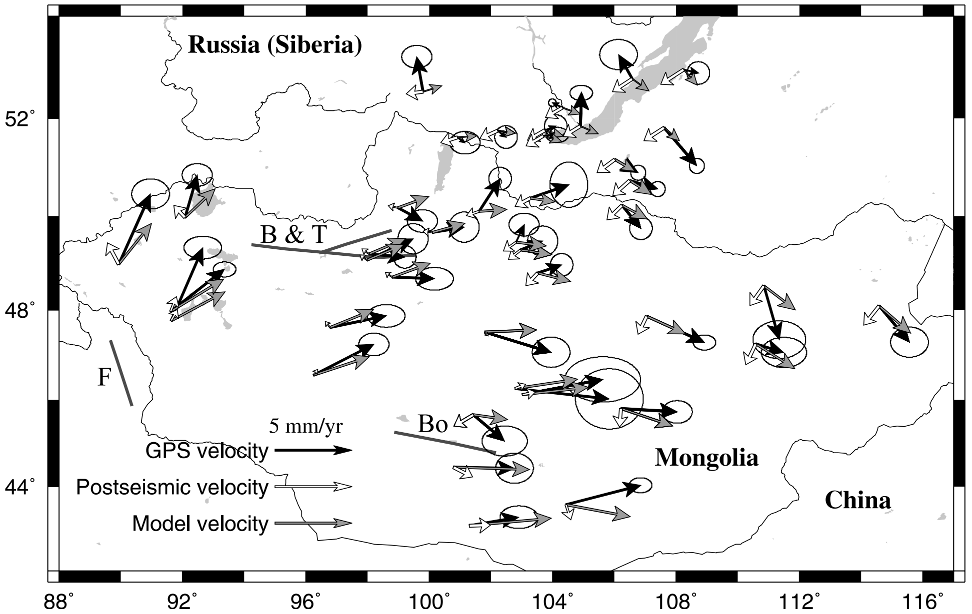

Figure 5. Comparison between observed (black arrows) and modeled (grey arrows) horizontal GPS velocities. Modeled velocities combine (1) a rigid translation and rotation of the whole network, (2) a 3–5 mm yr^{-1} simple shear velocity gradient between the Siberian platform and northern China to the south, and (3) postseismic deformation caused by the Bolnay-Tsetserleg sequence (1905), the Fu Yun earthquake (1931), and the Bogd earthquake (1957). $\eta_m = 2.2 \times 10^{18}$ Pa s, $\eta_c = 1 \times 10^{17}$ Pa s, $V_{sz} =$ 3 mm yr^{-1}. The white arrows show the contribution of postseismic velocities only. B & T, Bolnay and Tsetserleg modeled ruptures; F, Fu Yun modeled rupture; Bo, Bogd modeled rupture.

[40] All these results point to a high-temperature anomaly at the base of the crust and/or in the upper mantle below western Mongolia. A possible scenario may be that a large part of the basaltic magmas generated by the heating of the asthenosphere above the solidus are underplated at the crust-mantle boundary instead of reaching the surface. These underplated magma would then quickly heat up the upper mantle and the base of the crust, with a high-temperature front advancing upward by conduction and fluid percolation [*Ionov*, 2002]. This high-temperature anomaly at the base of the crust and/or in the upper mantle, combined with the olivine composition of the upper mantle, are consistent with the relatively low viscosity found here.

5.2. Lower Crust Viscosity

[41] As shown above, the viscosity of the lower crust is more difficult to constrain, with possible values ranging from 1×10^{16} to 1×10^{19} Pa s or more narrowly restricted values of $3 \times 10^{16} - 2 \times 10^{17}$ Pa s in the low mantle viscosity case. The lower crust composition is known from xenolith studies to be that of a mafic granulite derived from a basic protolith [*Kopylova et al.*, 1995; *Stosch et al.*, 1995]. The most important minerals in these granulites are plagioclase and pyroxene. *Stosch et al.* [1995] found that the Mongolia granulites are also quite rich in SiO_2 and that quartz is present as an accessory mineral. According to the temperature estimates for the Mongolia granulites (840 ± 30°C) and the temperature range obtained for mantle xenoliths (850–1050°C) [*Ionov*, 1986; *Ionov et al.*, 1998], they inferred no abrupt temperature change across the crust-mantle boundary and that the geotherm in the lower crust is similar to that in upper mantle. In addition, *Ionov et al.* [1998] found evidence for hydrated minerals at the base of the lower crust. The experimentally derived law for the

Table 4. Same as Table 2 for a 25 km Upper Elastic Crust Thickness Instead of 35 km

		25 km Upper Crust Thickness			
GPS Data Set	Uncertainties	η_m, Pa s	η_c, Pa s	V_{sz}, mm/yr	*F* Test, %
Central Mongolia	fixed and mixed	8×10^{17} to 2×10^{18}	2.4×10^{16} to 8×10^{16}	3–5	90
		5.3×10^{17} to 2.2×10^{18}	1.6×10^{16} to 1.6×10^{17}	3–5.5	80
		4.5×10^{17} to 2.2×10^{18}	1.35×10^{16} to 9.5×10^{17}	3–5.5	70
	true	6×10^{17} to 1.7×10^{18}	1.8×10^{16} to 4×10^{16}	3–5.5	–
Mongolia	fixed and mixed	1×10^{18} to 2×10^{18}	3×10^{16} to 2×10^{16}	3.5–5.5	90
		8×10^{17} to 2.3×10^{18}	2.4×10^{16} to 8×10^{16}	3–6	80
		5×10^{17} to 2.4×10^{18}	1.5×10^{16} to 9×10^{16}	3–6.5	70
	true	7.7×10^{17} to 2×10^{18}	2.3×10^{16} to 7×10^{16}	3.5–6.5	–
Mongolia and Baikal	fixed and mixed	1×10^{18} to 2×10^{18}	3×10^{16} to 6.5×10^{16}	3.5–6	80
		8×10^{17} to 2×10^{18}	2.4×10^{16} to 6×10^{16}	3.5–6.5	70
	true	–	–	–	–
Summary		5×10^{17} to 2×10^{18}	2×10^{16} to 8×10^{16}	3–6	–

rheology of wet diopside or dry diabase [*Mackwell et al.*, 1998] (Figure 3), assuming a dislocation creep deformation mechanism, together with the geotherm proposed by *Ionov et al.* [1998], indicates that the viscosity of the lower crust in Mongolia should be greater than 10^{21} Pa s (Figure 3). Dry clinopyroxene is predicted to be even stronger than these materials [*Bystricky and Mackwell*, 2001], and our estimated viscosity thus does not agree with available laboratory measurements. There is no available robust flow law for wet diabase or similar mixtures of plagioclase and clinopyroxene. Hence we can not compare our results with experimentally derived law based on these materials that may occupy the lower crust under Mongolia.

[42] An alternate explanation is to invoke a non-Newtonian rheology. Indeed, laboratory experiments show that lithospheric minerals deform in a non-Newtonian manner with a power law viscosity (strain rate proportional to stress raised to a power, usually 2–4 [*Kirby and Kronenberg*, 1987; *Karato and Wu*, 1993; *Kohlstedt et al.*, 1995]). A power law rheology will result in a smaller short term strength than a Newtonian rheology, but in a stronger long term strength. *Pollitz et al.* [2001] suggest nonlinear rheology as a possible source of apparent differences in inferred viscosities for different time intervals following the Landers and Hector Mine earthquakes. Alternatively, *Ivins and Sammis* [1996] investigated the rheology of polymineralic materials and found that they may exhibit a transient rheology with two distinct relaxation times. This behavior can be modeled as a Burgher's body, which may be represented as a Maxwell element in series with a Kelvin-Voigt element. The resulting time-dependent response involves a rapid short-term relaxation associated with a low transient viscosity caused by weak inclusions in a harder dominant matrix, and a slow long-term relaxation associated with a higher viscosity of the matrix. *Ivins* [1996] proposes that a 5% concentration level of weak material in the lower crust is sufficient to induce a substantial weakening effect. Thus either a non-Newtonian rheology or a transient rheology will produce a viscoelastic material characterized by a spectrum of relaxation times. In general, a short decay constant will be associated with the initial part of the relaxation close to the source fault or with the onset of significant postseismic deformation at great distance from the fault. The latter case corresponds to the arrival of a postseismic stress pulse, which can be sharp when the layering is characterized as a thin low-viscosity channel embedded between stronger materials [e.g., *Rydelek and Sacks*, 1990; *Calais et al.*, 2002]. The largest postseismic velocities in our preferred model are achieved at large distance from the 1905 (and 1957) source ruptures (i.e., easternmost and westernmost Mongolia in Figure 5). According to this interpretation, these regions are located within a broad "front" of postseismic stress diffusion after decades of diffusion away from the source faults.

[43] Substantial weakening of the lower crust could also result from the presence of partial melt through either melt-enhanced diffusional creep at low melt fractions [*Dell'Angelo and Tullis*, 1988] or melt-enhanced embrittlement at larger melt fractions [*Davisdon et al.*, 1994]. Temperatures sufficient to melt quartz and feldspar in the deeper crust are suggested by the geotherm of *Ionov et al.* [1998]. That is, from temperatures above about 820°C, a condition which is reached in the thick crust beneath Mongolia [*Ionov et al.*, 1986; *Stosch et al.*, 1995], quartz and feldspar may be partially molten [*Presnall*, 1995; *Ivins*, 1996]. Such a biviscous rheology would imply rapid strain rates during the early postseismic phase while the lower crust behavior is dominated by its weak components, followed by a slow long-term relaxation associated with the higher viscosity of the matrix. *Pollitz* [2003] finds that such a rheology can also match the observed time-dependent GPS site motions following the 1999 Hector Mine earthquake.

[44] There are geological arguments for the presence of weak material in the lower crust in Mongolia. *Kopylova et al.* [1995] found evidence for fusion at grain boundaries in many of the granulite samples they studied. Moreover, H_2O-saturated plagioclase is partially molten at temperatures above about 800°C [*Presnall*, 1995], a temperature which is likely reached in the Mongolian lower crust (Figure 3).

5.3. Current Contribution of Postseismic Deformation

[45] We used the best fit lower crust and upper mantle viscosities found here (10^{17} Pa s and 2×10^{18} Pa s, respectively) to compute the contribution of postseismic deformation to horizontal surface velocities for the 1997–2002 period in Mongolia (Figure 5). The model velocities include 3 mm yr^{-1} of simple shear between north China and the Siberian platform, a -0.569×10^{-9} yr^{-1} rigid rotation rate, and a 3.8 mm yr^{-1} eastward and 0.2 mm yr^{-1} northward rigid translation. We find a fair agreement between the model and the observations, with a weighted RMS of 0.8 mm yr^{-1} for the east velocity component and 1.2 mm yr^{-1} for the north component, consistent with the uncertainties of the GPS velocities. We find that the current contribution of postseismic deformation on horizontal surface velocities does not exceed 2 mm yr^{-1} over the entire study area and is less than 1 mm yr^{-1} in the Hangai region (Figure 5). This small contribution of postseismic deformation on present-day horizontal surface velocities is due to the weak lower crust and upper mantle of our best fit model, which imply that most of the postseismic strain was released in the first 20 years after each event. Figure 6 shows the accumulated strain within 5 year periods during the following ten years after each major events (Bolnay-Tsetserleg sequence earthquake in 1905, Fu Yun earthquake in 1931, and Bogd earthquake in 1957) and at present (1995–2000). The evolution of the relaxation of strain (and strain rate) since 1905 supports the hypothesis of a nonlinear rheology to explain the viscosity results, knowing that it will result in an effective viscosity that is small at large strain rate, which is the case after each event.

[46] Our models show that the postseismic signal currently observable in Mongolia is due to the long-lasting effect of the Bolnay-Tsetserleg earthquake sequence, that diffuse away from the source at distances up to several hundreds of kilometers, and to the smaller but more recent contribution of the Bogd earthquake. In the models, the postseismic signal around the Bolnay-Tsetserleg rupture is only due to the postseismic effect of Bogd earthquake, as all the postseismic strain generated by the Bolnay-Tsetserleg sequence has now been relaxed in that area. We find that the postseismic effects of the Fu Yun earthquake do not exceed a few tenths of millimeters per year for the whole studied domain.

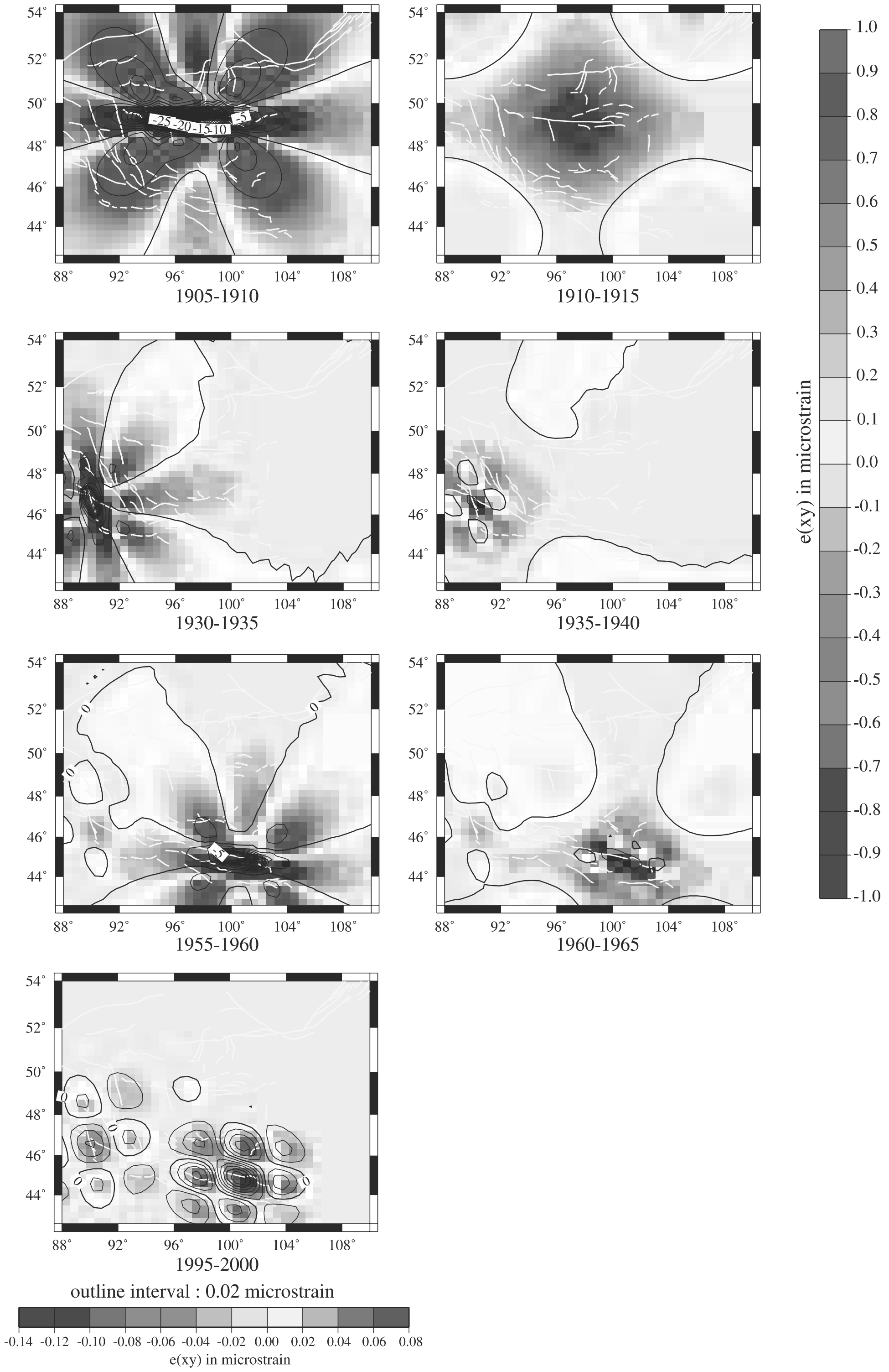

Figure 6. Map of the accumulated postseismic strain within selected 5 year periods during the following 10 years after each major events: Bolnay-Tsetserleg sequence earthquake in 1905, Fu Yun earthquake in 1931, and Bogd earthquake in 1957 and at present (1995–2000). Scale on the right corresponds to the maps on its left side, and isolines on these maps are every microstrain. Scale on the bottom correspond to present period (1995–2000), and isolines on this map are every 0.02 μstrain. The postseismic strain is obtained using the best fit lower crust and upper mantle viscosities found in the study ($\eta_c = 1 \times 10^{17}$ Pa s and $\eta_m = 2.2 \times 10^{18}$ Pa s). See color version of this figure at back of this issue.

[47] At about 600 km distance from the 1957 Gobi-Altai rupture, present postseismic velocities reach about 2 mm yr^{-1} (Figure 5). This implies an average tensor shear strain rate of $\sim 2 \times 10^{-9}\ \mathrm{yr}^{-1}$ (in the left-lateral sense when resolved on E-W trending planes) over almost the entire region, a result which is implicit in the 1995–2000 strain rate field (Figure 6). However, the strain rate field exhibits a richer and more variable pattern within about 200 km of the Gobi-Altai rupture. The contribution of current postseismic strain to the GPS strain field ranges from $6 \times 10^{-9}\ \mathrm{yr}^{-1}$ to $3 \times 10^{-8}\ \mathrm{yr}^{-1}$ compared with $\sim 3 - 5 \times 10^{-9}\ \mathrm{yr}^{-1}$ contributed by the background shear component in the southern and southwestern region (Figure 6, 1995–2000 period). Thus postseismic strain rates are substantial in southern Mongolia. They are smaller elsewhere because of the time span since the 1905 Bolnay earthquake.

6. Conclusion

[48] We used GPS measurements and postseismic deformation models to assess the viscosity of the lower crust and upper mantle in the Baikal-Mongolia area. The data can be fit by a "strong" (high upper mantle and lower crust viscosity) or "weak" (low upper mantle and lower crust viscosity) lithospheric model, but favor a weak model, with an upper mantle viscosity of 1×10^{18} to 4×10^{18} Pa s and a lower crust viscosity of 3×10^{16} to 2×10^{17} Pa s.

[49] The presence of a weak mantle beneath Mongolia is consistent with results from independent seismological and petrological studies, that show an abnormally hot upper mantle in that area. The weak lower crust suggested by our models is significantly smaller than the theoretical viscosity derived from the petrological composition and temperature gradient of the lower crust in Mongolia. This may be the result of a transient viscosity of the lower crust, caused either by a non-Newtonian or a biviscous rheology.

[50] We find that the GPS velocity field in the Baikal Mongolia area can be modeled as the sum of (1) a rigid translation and rotation of the whole network, (2) a 3 to 5 mm yr^{-1} simple shear velocity gradient between the Siberian platform to the north and northern China to the south, and (3) the (small, <2 mm yr^{-1}) contribution of postseismic deformation, primarily caused by both the 1905 Bolnay-Tsetserleg sequence and the 1957 Bogd earthquake.

[51] The companion paper by *Pollitz et al.* [2003] uses the rheological parameters found here and a Coulomb stress analysis to investigate the role of the weak upper mantle under western Mongolia on the clustering of large earthquakes in the last century.

[52] **Acknowledgments.** We thank Dmitri Ionov for insightful discussions on the rheology and thermal structure of western Mongolia and for providing his results in advance of publication. We are grateful to Jacques Déverchère, Jean Chéry, and Rodolphe Cattin for insightful discussions on postseismic effects. We thank the anonymous Associate Editor and two anonymous reviewers whose comments helped improve the quality of this paper. This research was supported by INSU-CNRS ("Intérieur de la Terre" program) and the French Ministry for Research ("ACI Catastrophes Naturelles"). UMR Géosciences Azur, CNRS-UNSA contribution 591.

References

Baljinnyam, I., et al., Ruptures of major earthquakes and active deformation in Mongolia and its surroundings, *Mem. Geol. Soc. Am.*, *181*, 62 pp., 1993.

Bayasgalan, A., Active tectonics of Mongolia, Ph.D. thesis, 180 pp., Trinity Coll. Cambridge, Cambridge, U.K., 1999.

Bills, B. G., D. R. Currey, and G. A. Marshall, Viscosity estimates for the crust and upper mantle from patterns of lacustrine shoreline deformation in the eastern Great Basin, *J. Geophys. Res.*, *99*, 22,059–22,086, 1994.

Brace, W. F., and D. L. Kohlstedt, Limits on lithospheric stress imposed by laboratory experiments, *J. Geophys. Res.*, *85*, 6248–6252, 1980.

Brandon, A. D., R. A. Creaser, S. B. Shirey, and R. W. Carlson, Osmium recycling in subduction zones, *Science*, *272*, 861–864, 1996.

Bürgmann, R., P. Segall, M. Lisowski, and J. Svarc, Postseismic strain following the 1989 Loma Prieta earthquake from GPS measurements, *J. Geophys. Res.*, *102*, 4933–4955, 1997.

Bystricky, M., and S. Mackwell, Creep of dry clinopyroxene aggregates, *J. Geophys. Res.*, *106*, 13,443–13,454, 2001.

Calais, E., M. Vergnolle, J. Déverchère, V. San'kov, A. Lukhnev, and S. Amarjargal, Are postseismic effects of the M = 8.4 Bolnay earthquake (July 23, 1905) still influencing GPS velocities in the Mongolia-Baikal area, *Geophys. J. Int.*, *149*, 157–168, 2002.

Calais, E., M. Vergnolle, V. San'kov, A. Luknev, A. Miroshnitchenko, S. Amarjargal, and J. Déverchère, GPS measurements of crustal deformation in the Baikal-Mongolia area (1994–2002): Implications for current kinematics of Asia, *J. Geophys. Res.*, *108*, doi:10.1029/2002JB002373, in press, 2003.

Chen, W. P., and P. Molnar, Focal depth of the intracontinental and intraplate earthquakes and their implications for the thermal and mechanical-properties of the lithosphere, *J. Geophys. Res.*, *88*, 4183–4214, 1983.

Cunningham, W. D., B. F. Windley, D. Dorjnamjaa, G. Badamgarov, and M. Saandar, A structural transect across the Mongolian Altai: Active transpressional mountain building in central Asia, *Tectonics*, *15*, 142–156, 1996a.

Cunningham, W. D., B. F. Windley, D. Dorjnamjaa, G. Badamgarov, and M. Saandar, Late Cenozoic transpression in southwestern Mongolia and the Gobi Altai-Tien Shan connection, *Earth Planet. Sci. Lett.*, *140*, 67–81, 1996b.

Davisdon, C., S. M. Schmid, and L. S. Hollister, Role of melt during deformation in the deep crust, *Terra Nova*, *6*, 133–142, 1994.

Dell'Angelo, L. N., and J. Tullis, Experimental deformation of partially granitic aggregates, *J. Metamorph. Geol.*, *6*, 495–515, 1988.

Delouis, B., J. Déverchère, V. Melnikova, N. Radziminovitch, L. Loncke, C. Larroque, J. F. Ritz, and V. San'kov, A reappraisal of the 1950 (M_w 6.9) Mondy earthquake, Siberia, and its relationship to the strain pattern at the southwestern end of the Baikal rift zone, *Terra Nova*, *14*, 491–500, 2002.

Deng, J., M. Gurnis, H. Kanamori, and E. Hauksson, Viscoelastic flow in the lower crust after the 1992 Landers, California, earthquake, *Science*, *282*, 1689–1692, 1998.

Déverchère, J., F. Houdry, M. Diament, N. V. Solonenko, and A. V. Solonenko, Evidence for a seismogenic upper mantle and lower crust in the Baikal rift, *Geophys. Res. Lett.*, *18*, 1099–1102, 1991.

Déverchère, J., F. Houdry, N. V. Solonenko, A. V. Solonenko, and V. San'kov, Seismicity, active faults and stress field of the north Muya region, Baikal rift: New insights on the rheology of extended continental lithosphere, *J. Geophys. Res.*, *98*, 19,895–19,912, 1993.

Déverchère, J., C. Petit, N. Gileva, N. Radziminovitch, V. Melnikova, and V. San'kov, Depth distribution of earthquakes in the Baikal rift system and its implications for the rheology of the lithosphere, *Geophys. J. Int.*, *146*, 714–730, 2001.

Doser, D. I., Faulting within the western Baikal rift as characterized by earthquake studies, *Tectonophysics*, *196*, 87–107, 1991.

Dziewonski, A. M., and D. L. Anderson, Preliminary reference Earth model, *Phys. Earth Planet. Inter.*, *25*, 297–356, 1981.

Freed, A. M., and J. Lin, Delayed triggering of the 1999 Hector Mine earthquake by viscoelastic stress transfer, *Nature*, *411*, 180–183, 2001.

Freymueller, J. T., S. C. Cohen, and H. J. Fletcher, Spatial variations in present-day deformation, Kenai Peninsula, Alaska, and their implications, *J. Geophys. Res.*, *105*, 8079–8101, 2000.

Friederich, W., The *S*-velocity structure of the East Asian mantle from inversion of shear and surface waveforms, *Geophys. J. Int.*, *153*, 88–102, 2003.

Hirth, G., and D. L. Kohlstedt, Water in the oceanic upper mantle: Implication for rheology, melt extraction and the evolution of the lithosphere, *Earth Planet. Sci. Lett.*, *144*, 93–108, 1996.

Hofton, M. A., and G. R. Foulger, Postrifting anelastic deformation around the spreading plate boundary, north Iceland: 1. Modeling of the 1987–1992 deformation field using a viscoelastic Earth structure, *J. Geophys. Res.*, *101*, 25,403–25,421, 1996.

Huang, J., and W. P. Chen, Source mechanisms of the Mogod earthquake sequence of 1967 and the event of 1974 July 4 in Mongolia, *Geophys. J. R. Astron. Soc.*, *84*, 361–379, 1986.

Ionov, D. A., Spinel peridotite xenoliths from the Shavaryn-Tsaram volcano, northern Mongolia: Petrography, major element chemistry and mineralogy, *Geol. Carpathica*, *37*, 681–692, 1986.

Ionov, D., Mantle structure and rifting processes in the Baikal-Mongolia region: Geophysical data and evidence from xenoliths in volcanic rocks, *Tectonophysics*, *351*, 41–60, 2002.

Ionov, D., S. Y. O'Reilly, and W. L. Griffin, A geotherm and lithospheric section for central Mongolia (Tariat region), in *Mantle Dynamics and Plate Interactions in East Asia*, *Geodyn. Ser.*, vol. *27*, edited by M. J. F. Flower et al., pp.127–153, AGU, Washington, D. C., 1998.

Ivins, E. R., Transient creep of a composite lower crust: 2. A polymineralic basis for rapidly evolving postseismic deformation modes, *J. Geophys. Res.*, *101*, 28,005–28,028, 1996. (Correction to "Transient creep of a composite lower crust: 2. A polymineralic basis for rapidly evolving postseismic deformation modes," *J. Geophys. Res.*, *105*, 3229–3232, 2000.)

Ivins, E. R., and C. G. Sammis, Transient creep of a composite lower crust: 1. Constitutive theory, *J. Geophys. Res.*, *101*, 27,981–28,004, 1996.

Karato, S., and P. Wu, Rheology of the upper mantle—A synthesis, *Science*, *260*, 771–778, 1993.

Kaufmann, G., and F. Amelung, Reservoir-induced deformation and continental rheology in the vicinity of Lake Mead, Nevada, *J. Geophys. Res.*, *105*, 16,341–16,358, 2000.

Kenner, S. J., and P. Segall, Postseismic derformation following the 1906 San Francisco earthquake, *J. Geophys. Res.*, *105*, 13,195–13,209, 2000.

Khilko, S. D., R. A. Kurushin, V. M. Kotchetkov, L. A. Misharina, V. I. Melnikova, N. A. Gileva, S. V. Lastochkin, I. Baljinnyam, and D. Monhoo, Strong earthquakes, paleoseismogeological and macroseismic data, in *Earthquakes and the Base for Seismic Zoning of Mongolia*(in Russian), *Trans. Joint Sov.-Mongolian Res. Geol. Sci. Exped.*, vol. 41, pp.19–83, Nauka, Moscow, 1985.

Kirby, S. H., and A. K. Kronenberg, Rheology of the lithosphere: Selected topics, *Rev. Geophys.*, *25*, 1219–1244, 1987.

Kohlstedt, D. L., B. Evans, and S. J. Mackwell, Strength of the lithosphere: Constraints imposed by laboratory measurements, *J. Geophys. Res.*, *100*, 17,587–17,602, 1995.

Kopylova, M. G., S. Y. O'Reilly, and Y. S. Genshaft, Thermal state of the lithosphere beneath Central Mongolia: Evidence from deep-seated xenoliths from the Shavaryn-Saram volcanic centre in the Tariat depression, Hangai, Mongolia, *Lithos*, *36*, 243–255, 1995.

Krylov, S. V., P. B. Mishenkin, and A. V. Bryskin, Deep-struture of the baikal rift from multiwave seismic explorations, *J. Geodyn.*, *13*, 87–96, 1991.

Kurushin, R. A., A. Bayasgalan, M. Olziybat, B. Enhtuvshin, P. Molnar, C. Bayarsayhan, K. Hudnut, and J. Lin, The surface rupture of the 1957 Gobi-Altay, Mongolia, earthquake, *Spec. Pap. Geol. Soc. Am.*, *320*, 143 pp., 1997.

Mackwell, S. J., M. E. Zimmerman, and D. L. Kohlstedt, Hight-temperature deformation of dry diabase with application to tectonics on Venus, *J. Geophys. Res.*, *103*, 975–984, 1998.

Milne, G. A., J. L. Davis, J. X. Mitrovica, H. G. Scherneck, J. M. Johansson, M. Vermeer, and H. Koivula, Space-geodetic constraints on glacial isostatic adjustment in Fennoscandia, *Science*, *291*, 2381–2385, 2001.

Molnar, P., Mountain building-crust in the mantle overdrive, *Nature*, *358*, 105–106, 1992.

Nolet, G., Upper mantle under eastern-Europe inferred from dispersion of rayleigh modes, *J. Geophys.*, *43*, 265–285, 1977.

Okal, E., A surface-wave investigation of the rupture mechanism of the Gobi-Altai (December 4, 1957) earthquake, *Phys. Earth Planet. Inter.*, *12*, 319–328, 1976.

Okal, E., July 9 and 23, 1905, Mongolian earthquakes: A surface wave investigation, *Earth Planet. Sci. Lett.*, *34*, 326–331, 1977.

Peltzer, G., P. Rosen, F. Rogez, and K. Hudnut, Postseismic rebound in fault step-overs caused by pore fluid flow, *Science*, *273*, 1202–1204, 1996.

Petit, C., J. Déverchère, E. Calais, V. San'kov, and D. Fairhead, Deep structure and mechanical behavior of the lithosphere in the Hangai-Hovsgol region, Mongolia: New constraints from gravity modelling, *Earth Planet. Sci. Lett.*, *7*, 133–149, 2002.

Piersanti, A., Postseismic deformation in Chile: Constraints of the asthenosphereric viscosity, *Geophys. Res. Lett.*, *26*, 3157–3160, 1999.

Pollack, H. N., and D. S. Chapman, On the regional variation of heat flow, geotherms and lithospheric thickness, *Tectonophysics*, *38*, 279–296, 1977.

Pollitz, F. F., Postseismic relaxation theory on the spherical Earth, *Bull. Seismol. Soc. Am.*, *82*, 422–453, 1992.

Pollitz, F. F., Gravitational viscoelastic postseismic relaxation on a layered spherical Earth, *J. Geophys. Res.*, *102*, 17,921–17,941, 1997.

Pollitz, F. F., Transient rheology of the uppermost mantle beneath the Mojave Desert, California, *Earth. Planet. Sci. Lett.*, *215*, 89–104, 2003.

Pollitz, F. F., and T. H. Dixon, GPS measurements across the northern Caribbean plate boundary zone: Impact of postseismic relaxation following historic earthquakes, *Geophys. Res. Lett.*, *25*, 2233–2236, 1998.

Pollitz, F. F., and I. S. Sacks, Modelling of postseismic relaxation following the great 1957 earthquake, southern California, *Bull. Seismol. Soc. Am.*, *82*, 454–480, 1992.

Pollitz, F. F., and I. S. Sacks, Viscosity structure beneath northeast Iceland, *J. Geophys. Res.*, *101*, 17,771–17,793, 1996.

Pollitz, F. F., G. Peltzer, and R. Bürgmann, Mobility of the continental mantle: Evidence from postseismic geodetic observation following the 1992 Landers earthquake, *J. Geophys. Res.*, *105*, 8035–8054, 2000.

Pollitz, F. F., C. Wicks, and W. Thatcher, Mantle flow beneath a continental strike-slip fault: Postseismic deformation after the 1999 Hector Mine earthquake, *Science*, *293*, 1814–1818, 2001.

Pollitz, F. F., M. Vergnolle, and E. Calais, Fault interaction and stress triggering of twentieth century earthquakes in Mongolia, *J. Geophys. Res.*, *108*, doi:10.1029/2002JB002375, in press, 2003.

Presnall, D. C., Phase diagrams of Earth-forming minerals, in *Mineral Physics and Crystallography, A Handbook of Physical Constants*, *AGU Ref. Shelf*, vol. 2, edited by T. J. Ahrens, AGU, Washington, D. C., 1995.

Ranalli, G., and D. C. Murphy, Rheological stratification of the lithosphere, *Tectonophysics*, *132*, 281–295, 1987.

Ritz, J. F., E. T. Brown, D. L. Bourlés, H. Philip, A. Schlupp, G. M. Raisbeck, F. Yiou, and B. Enkhtuvshin, Slip rates along active faults estimated with cosmic-ray-exposure dates: Application to the Bogd fault, Gobi-Altay, Mongolia, *Geology*, *23*, 1019–1022, 1995.

Ritz, J.-F., et al., Late Pleistocene to Holocene slip rates for the Gurvan Bulag thrust fault (Gobi-Altay, Mongolia) estimated with 10Be dates, *J. Geophys. Res.*, *108*(B3), 2162, doi:10.1029/2001JB000553, 2003.

Rudnick, R. L., and D. M. Fountain, Nature and composition of the continental crust: A lower crustal perspective, *Rev. Geophys.*, *33*, 267–309, 1995.

Rydelek, P. A., and I. S. Sacks, Asthenospheric viscosity and stress diffusion: A mechanism to explain correlated earthquakes and surface deformations in the northeast Japan, *Geophys. J. Int.*, *100*, 39–58, 1990.

Rydelek, P. A., and I. S. Sacks, Migration of large earthquakes along the San Jacinto fault; stress diffusion from the 1857 Fort Tejon earthquake, *Geophys. Res. Lett.*, *28*, 3079–3082, 2001.

Savage, J. C., and G. Plafker, Tide-gauge measurements of uplift along the south coast of Alaska, *J. Geophys. Res.*, *96*, 4325–4335, 1991.

Savage, J. C., and J. Svarc, Postseismic deformation associated with the 1992 $M_w = 7.3$ Landers earthquake, southern California, *J. Geophys. Res.*, *102*, 7565–7577, 1997.

Schlupp, A., Néotectonique de la Mongolie Occidentale analysée à partir de données de terrain, sismologiques et satellitaires, Ph.D. thesis, Univ. Louis Pasteur, Strasbourg, France, 1996.

Sibson, R. H., Fault zone models, heat-flow, and the depth distribution of earthquakes in the continental-crust of the United-States, *Bull. Seismol. Soc. Am.*, *72*, 151–163, 1982.

Stein, S., and R. G. Gordon, Statistical test of additional plate boundaries from plate motion inversions, *Earth Planet. Sci. Lett.*, *69*, 401–412, 1984.

Stosch, H. G., D. A. Ionov, I. S. Puchtel, S. J. G. Galer, and A. Sharpouri, Lower crustal xenoliths from Mongolia and their bearing on the nature of the deep crust beneath central Asia, *Lithos*, *36*, 227–242, 1995.

Strehlau, J., and R. Meissner, Estimation of crustal viscosities and shear stress from an extrapolation of experimental steady state flow data, in *The Composition, Structure, and Dynamics of the Lithosphere-Astenosphere System*, *Geodyn. Ser.*, vol. 16, edited by K. Fuchs and C. Froidevaux, pp. 69–86, AGU, Washington, D. C., 1987.

Thatcher, W., Strain accumulation and release after the 1906 San Francisco earthquake, *J. Geophys. Res.*, *80*, 4862–4872, 1975.

Thatcher, W., The earthquake deformation cycle at the nankai trough, southwest Japan, *J. Geophys. Res.*, *89*, 3087–3101, 1984.

Tse, S. T., and J. R. Rice, Crustal earthquake instability in relation to the depth variation of frictional slip properties, *J. Geophys. Res.*, *91*, 9452–9472, 1986.

Vertlib, M. B., Determination of focal depths by the composite method for some regions of Pribaikalie (in Russian), in *Seismic Investigations in East Siberia*, edited by V. A. Rogozhina, pp. 82–88, Nauka, Moscow, 1981.

Villaseñor, A., M. H. Ritzwoller, A. L. Levshin, M. P. Barmin, E. R. Engdahl, W. Spakeman, and J. Trampert, Shear velocity structure of central Eurasia from inversion of surface wave velocities, *Phys. Earth Planet. Inter.*, *123*, 169–184, 2001.

Wallace, P., Water and partial melting in mantle plumes: Inferences from the dissolved H_2O concentrations of Hawaiian basaltic magmas, *Geophys. Res. Lett.*, *25*, 3639–3642, 1998.

Weertman, J., Creep laws for the mantle of the Earth, *Philos. Trans. R. Soc. London, Ser. A*, *288*, 9–26, 1978.

E. Calais, Department of Earth and Atmospheric Sciences, Purdue University, West Lafayette, IN 47907-1397, USA. (ecalais@purdue.edu)

F. Pollitz, U.S. Geological Survey, 345 Middlefield Road, MS 977, Menlo Park, CA 94025, USA. (fpollitz@usgs.gov)

M. Vergnolle, UMR 6526 CNRS Géosciences Azur, University of Nice, 250 rue Albert Einstein, F-06560 Valbonne, France. (vergno@geoazur.unice.fr)

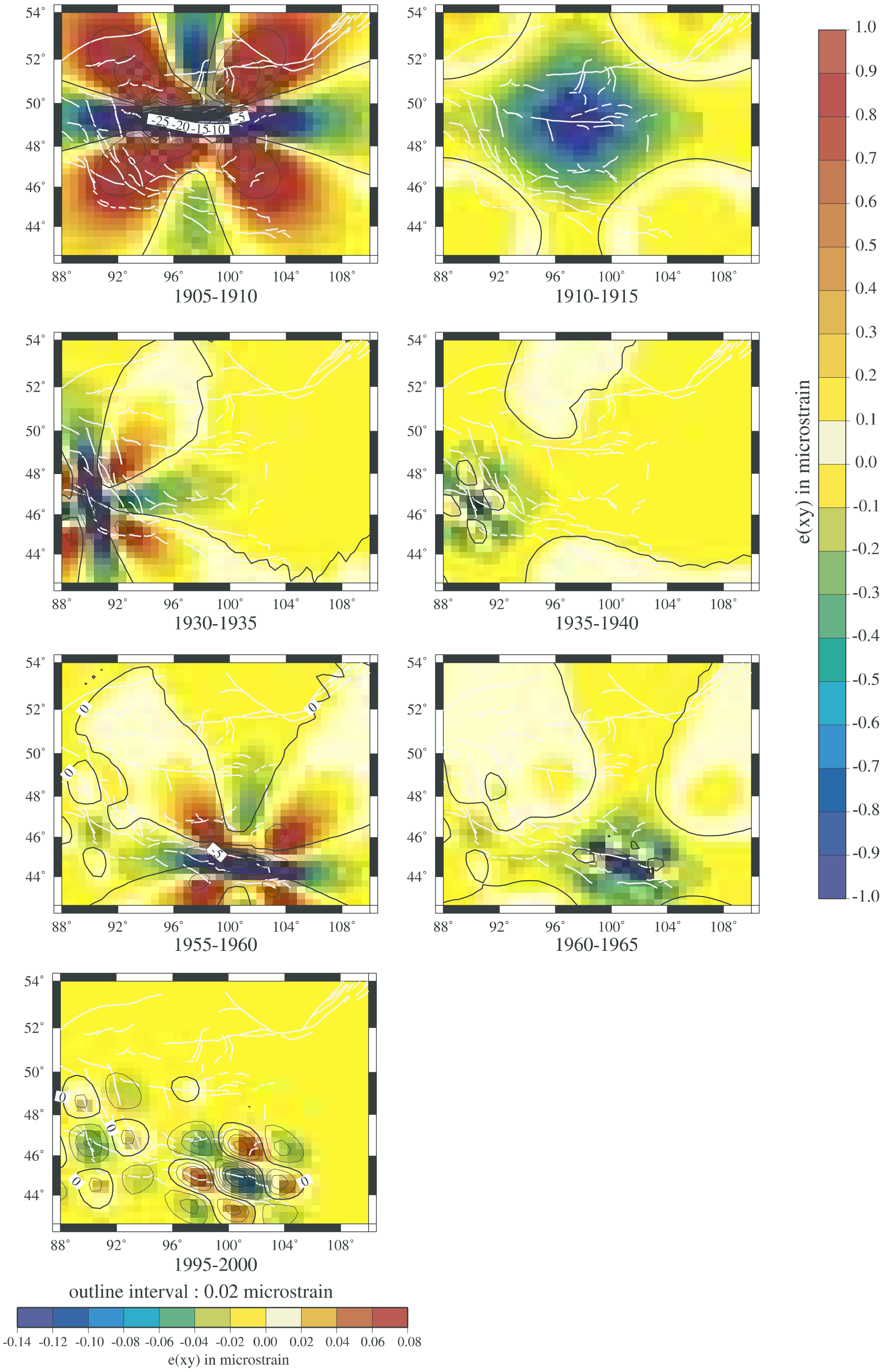

1905-1910

1910-1915

1930-1935

1935-1940

1955-1960

1960-1965

1995-2000

Figure 6. Map of the accumulated postseismic strain within selected 5 year periods during the following 10 years after each major events: Bolnay-Tsetserleg sequence earthquake in 1905, Fu Yun earthquake in 1931, and Bogd earthquake in 1957 and at present (1995–2000). Scale on the right corresponds to the maps on its left side, and isolines on these maps are every microstrain. Scale on the bottom correspond to present period (1995–2000), and isolines on this map are every 0.02 µstrain. The postseismic strain is obtained using the best fit lower crust and upper mantle viscosities found in the study ($\eta_c = 1 \times 10^{17}$ Pa s and $\eta_m = 2.2 \times 10^{18}$ Pa s).

eastern Russia: From Baikal to Chukotka, *Geol. Soc. Am. Abstr. Programs*, *27*(5), 19, 1995.

Gordon, R. G., D. F. Argus, and M. B. Heflin, Revised estimate of the angular velocity of India relative to Eurasia, *Eos Trans. AGU*, *80*(46), Fall Meet. Suppl., F273, 1999.

Heki, K., S. Miyazaki, H. Takahashi, M. Kasahara, F. Kimata, S. Miura, N. F. Vasilenko, A. Ivashchenko, and K. D. An, The Amurian plate motion and current plate kinematics in eastern Asia, *J. Geophys. Res.*, *104*, 29,147–29,155, 1999.

Herring, T. A., J. L. Davis, and I. I. Shapiro, Geodesy by radio interferometry: The application of Kalman filtering to the analysis of very long baseline interferometry data, *J. Geophys. Res.*, *95*, 12,561–12,581, 1990.

Houseman, G., and P. E. England, Finite strain calculations of continental deformation: Method and general results for convergent zones, *J. Geophys. Res.*, *91*, 3651–3663, 1986.

Houseman, G., and P. England, Crustal thickening versus lateral expulsion in the India-Asia continental collision, *J. Geophys. Res.*, *98*, 12,233–12,249, 1993.

Khilko, S. D., R. A. Kurushin, V. M. Kotchetkov, L. A. Misharina, V. I. Melnikova, N. A. Gileva, S. V. Lastochkin, I. Baljinnyam, and D. Monhoo, Earthquakes and the base of the seismogenic zoning of Mongolia (in Russian), in *The Joint Soviet-Mongolian Research Geological Scientific Expedition*, vol. 41, 225 pp., Nauka, Novosibirsk, Russia, 1985.

King, R. W., F. Shen, B. C. Burchfield, L. Royden, E. Wang, Z. Chen, Y. Liu, X. Zhang, J. Zhao, and Y. Li, Geodetic measurement of crustal motion in southwest China, *Geology*, *25*, 179–182, 1997.

Kogan, M. G., et al., Geodetic constraints on thr rigidity and relative motion of Eurasia and North America, *Geophys. Res. Lett.*, *27*, 2041–2044, 2000.

Kong, X., and P. Bird, Neotectonics of Asia: thin-shell finite-element models with faults, in *The Tectonic Evolution of Asia*, edited by A. Yin and T. M. Harrison, pp. 19–34, Cambridge Univ. Press, New York, 1996.

Kurushin, R. A., A. Bayasgalan, M. Olziybat, B. Enhtuvshin, P. Molnar, Ch. Bayarsayhan, K. Hudnut, and J. Lin, The surface rupture of the 1957 Gobi-Altay, Mongolia, earthquake, *Spec. Pap. Geol. Soc. Am.*, *320*, 143 pp., 1997.

Larson, K., R. Brgmann, R. Bilham, and J. Freymueller, Kinematics of the India-Eurasia collision zone from GPS measurements, *J. Geophys. Res.*, *104*, 1077–1093, 1999.

Mazzotti, S., X. LePichon, P. Henry, and S. Miyazaki, Full interseismic locking of the Nankai and Japan-West Kuril subduction zones: An analysis of uniform elastic strain accumulation in Japan constrained by permanent GPS, *J. Geophys. Res.*, *105*, 13,159–13,177, 2000.

Milne, G. A., J. L. Davis, J. X. Mitrovica, H.-G. Scherneck, J. M. Johansson, M. Vermeer, and H. Koivula, Space-geodetic constraints on glacial isostatic adjustment in Fennoscandia, *Science*, *291*, 2381–2385, 2001.

Molnar, P., and Q. Deng, Faulting associated with large earthquakes and the average of deformation in central and eastern Asia, *J. Geophys. Res.*, *89*, 6203–6227, 1984.

Molnar, P., and S. Ghose, Seismic moments of major earthquakes and the rate of shortening across the Tien Shan, *Geophys. Res. Lett.*, *27*, 2377–2380, 2000.

Molnar, P., and J. M. Gipson, A bound on the rheology of continental lithosphere using very long baseline interferometry: The velocity of south China with respect to Eurasia, *J. Geophys. Res.*, *101*, 545–553, 1996.

Molnar, P., B. C. Burchfield, Z. Zhao, K. Liang, S. Wang, and M. Huang, Geologic evolution of northern Tibet: Results of an expedition to Ulugh Muztagh, *Science*, *235*, 299–305, 1987.

Okal, E., The July 9 and 23, 1905, Mongolian earthquakes: A surface wave investigation, *Earth Planet. Sci. Lett.*, *34*, 326–331, 1977.

Parfeevets, A. V., V. A. Sankov, A. I. Miroshnitchenko, and A. V. Lukhnev, Crustal state of stress evolution of Mongolia-Baikal mobile belt (in Russian), *Tikhookeanskaya Geol.*, *21*, 14–28, 2002.

Paul, J., et al., The motion and active deformation of India, *Geophys. Res. Lett.*, *28*, 647–650, 2001.

Peltzer, G., and F. Saucier, Present-day kinematics of Asia derived from geologic fault rates, *J. Geophys. Res.*, *101*, 27,943–27,956, 1996.

Peltzer, G., and P. Tapponnier, Formation and evolution of strike-slip faults, rifts, and basins during the India-Asia collision: An experimental approach, *J. Geophys. Res.*, *93*, 15,085–15,117, 1988.

Prentice, C. S., K. J. Kendrick, K. Berryman, A. Bayasgalan, J. F. Ritz, and J. Q. Spencer, Prehistoric ruptures of the Gurvan Bulag fault, Gobi Altay, Mongolia, *J. Geophys. Res.*, *107*(B12), 2321, doi:10.1029/2001JB000803, 2002.

Ritz, J. F., E. T. Brown, D. L. Bourlès, H. Philip, A. Schlupp, G. M. Raisbeck, F. Yiou, and B. Enkhtuvshin, Slip rates along active faults estimated with cosmic-ray-exposure dates: Application to the Bogd fault, Gobi-Altay, Mongolia, *Geology*, *23*, 1019–1022, 1995.

Ritz, J.-F., et al., Late Pleistocene to Holocene slip rates for the Gurvan Bulag thrust fault (Gobi-Altay, Mongolia) estimated with 10Be dates, *J. Geophys. Res.*, *108*(B3), 2162, doi:10.1029/2001JB000553, 2003.

San'kov, V. A., et al., On the estimation of rates of horizontal Earth crust movements of the Baikal rift system on the basis of GPS geodesy and seismotectonics (in Russian), in *Tectonophysics Today*, edited by V. N. Strakhov and Y. G. Leonov, pp. 120–128, United Inst. of the Phys. of the Earth, Russ. Acad. of Sci., Moscow, 2002.

Savage, J. C., Strain accumulation in western United States, *Annu. Rev. Earth Planet Sci.*, *368*, 11–43, 1983.

Schlupp, A., Néotectonique de la Mongolie Occidentale analysée à partir de données de terrain, sismologiques et satellitaires, Ph.D. thesis, Univ. Louis Pasteur, Strasbourg, France, 1997.

Sella, G. F., T. H. Dixon, and A. Mao, REVEL: A model for Recent plate velocities from space geodesy, *J. Geophys. Res.*, *107*(B4), 2081, doi:10.1029/2000JB000033, 2002.

Shen, Z. K., C. Zhao, A. Yin, Y. Li, D. Jackson, P. Fang, and D. Dong, Contemporary crustal deformation in east Asia constrained by Global Positionning System measurements, *J. Geophys. Res.*, *105*, 5721–5734, 2000.

Solonenko, A. V., N. V. Solonenko, V. I. Melnikova, and E. A. Shteiman, Seismicity and the stress field of the Baikal seismic zone, *Bull. Cent. Rech. Explor. Prod.*, *21*, 207–231, 1997.

Tapponnier, P., and P. Molnar, Active faulting and cenozoic tectonics of China, *J. Geophys. Res.*, *82*, 2905–2930, 1977.

Tapponnier, P., and P. Molnar, Active faulting and Cenozoic tectonics of the Tien Shan, Mongolia and Baikal regions, *J. Geophys. Res.*, *84*, 3425–3459, 1979.

Tapponnier, P., G. Peltzer, A. Y. Le Dain, R. Armijo, and P. Cobbold, Propagating extrusion tectonics in Asia: New insights from simple experiments with plasticine, *Geology*, *10*, 611–616, 1982.

Vergnolle, M., F. Pollitz, and E. Calais, Constraints on the viscosity of the continental crust and mantle from GPS measurements and postseismic deformation models in western Mongolia, *J. Geophys. Res.*, *108*, doi:10.1029/2002JB002374, in press, 2003.

Vertlib, M. B., Determination of focal depths by the composite method for some regions of Pribaikalie (in Russian), in *Seismic Investigations in East Siberia*, edited by V. A. Rogozhina, pp. 82–88, Nauka, Moscow, 1981.

Vilotte, J. P., M. Daignieres, and R. Madariaga, Numerical modeling of intraplate deformation: Simple mehcnical models of continental collision, *J. Geophys. Res.*, *87*, 19,709–19,728, 1982.

Wang, Q., et al., Present-day crustal deformation in China constrained by Global Positioning System measurements, *Science*, *294*, 574–577, 2001.

S. Amarjargal, Research Center for Astronomy and Geophysics, P.O. Box 788, Ulaanbaatar 210613, Mongolia. (amar@csg.mn)

E. Calais, Department of Earth and Atmospheric Sciences, Purdue University, CIVIL 1397, West Lafayette, IN 47907-1397, USA. (ecalais@purdue.edu)

J. Déverchère, UMR CNRS 6538, University Bretagne Occidentale, Technopole Brest-Iroise, Place Nicolas Copernic, F-29280 Plouzané, France. (jacdev@univ-brest.fr)

A. Lukhnev, A. Miroshnitchenko, and V. San'kov, Institute of the Earth's Crust, Siberian Branch of the Russian Academy of Sciences, 128 Lermontova Street, 664033 Irkutsk, Russia. (loukhnev@crust.irk.ru; miroshni@crust.irk.ru; sankov@crust.irk.ru)

M. Vergnolle, UMR CNRS 6526, Université de Nice, 250 Rue A. Einstein, F-06560 Valbonne, France. (vergno@geoazur.unice.fr)

Geophys. J. Int. (2006) doi: 10.1111/j.1365-246X.2006.03147.x

Difference in the GPS deformation pattern of North and Central Zagros (Iran)

A. Walpersdorf,[1,*] D. Hatzfeld,[1] H. Nankali,[3] F. Tavakoli,[3] F. Nilforoushan,[3] M. Tatar,[4] P. Vernant,[2] J. Chéry[2] and F. Masson[2]

[1] *Laboratoire de Géophysique Interne et Tectonophysique, Grenoble, France*
[2] *Laboratoire de Dynamique de la Lithosphère, Montpellier, France*
[3] *National Cartographic Center, Research Department, Tehran, Iran*
[4] *International Institute for Earthquake Engineering and Seismology, Tehran, Iran*

Accepted 2006 July 17. Received 2006 July 7; in original form 2005 July 19

SUMMARY

Measurements on either side of the Kazerun fault system in the Zagros Mountain Belt, Iran, show that the accommodation of the convergence of the Arabian and Eurasian Plates differs across the region. In northwest Zagros, the deformation is partitioned as 3–6 mm yr^{-1} of shortening perpendicular to the axis of the mountain belt, and 4–6 mm yr^{-1} of dextral strike-slip motion on northwest–southeast trending faults. No individual strike-slip fault seems to slip at a rate higher than ~2 mm yr^{-1}. In southeast Zagros, the deformation is pure shortening of 8 ± 2 mm yr^{-1} occurring perpendicular to the simple folded belt and restricted to the Persian Gulf shore. The fact that most of the deformation is located in front of the simple folded belt, close to the Persian Gulf, while seismicity is more widely spread across the mountain belt, confirms the decoupling of the surface sedimentary layers from the seismogenic basement. A comparison with the folding and topography corroborates a southwestward propagation of the surface deformation. The difference in deformation between the two regions suggests that right-lateral shear cumulates on the north–south trending Kazerun strike-slip fault system to 6 ± 2 mm yr^{-1}.

Key words: continental deformation, fault motion, Global Positioning System (GPS), plate convergence, Satellite geodesy, Zagros.

INTRODUCTION

The aim of our GPS surveys is to study (1) the location of superficial deformation in a sedimentary cover decoupled from the basement (case of southeastern Zagros) and (2) the different behaviour of deformation between southeastern and northwestern Zagros. This study will help to answer the following questions: Is the Zagros deformation field distributed or localized on individual faults? Is the transition between pure and oblique shortening, from southeastern to northwestern Zagros, visible in the present-day deformation field? Is there any evidence for strain partitioning in northwestern Zagros? How do the shallow sediments accommodate the present-day deformation and how does this superficial deformation compare with the basement deformation as evidenced by the seismicity?

The tectonic settings of the Zagros are given by the Eurasia–Arabia collision, taking place entirely inside Iran's political borders. The current Eurasia–Arabia convergence rate is estimated to increase from west to east along the Iranian Persian Gulf line from 18 to 25 mm yr^{-1} oriented about 10°N (Fig. 1). This increase is due to the proximity of the Arabia–Eurasia Euler pole situated in North Africa at 27.9 ± 0.5°N, 19.5 ± 1.4 °E with 0.41 ± 0.01 ° Myr^{-1} (Vernant *et al.* 2004, corroborating Euler pole locations of Sella *et al.* 2002; McClusky *et al.* 2000, 2003). The shortening is concentrated on the Iranian territory mainly across two mountain ranges, the Alborz in the north, the Zagros in the south, but slip on several important strike-slip faults that bound non-deforming blocks (e.g. Central Iran, Lut) also accommodate some shortening. At the southeastern margin of the Arabia–Eurasia collision zone, along the Makran, the shortening is absorbed by subduction of oceanic lithosphere beneath southeast Iran at 19.5 mm yr^{-1} (Vernant *et al.* 2004). In the Persian Gulf, no shortening is observed (Tatar *et al.* 2002). The first GPS results indicated that the southeastern Zagros undergoes about 10 mm yr^{-1} of pure shortening (Tatar *et al.* 2002).

The Zagros mountain belt is approximately 1500 km long, 250–400 km wide, and runs from eastern Turkey, where it connects to the North and East Anatolian faults, to the Oman Gulf, where it dies out at the Makran subduction zone (Fig. 1). The belt lies on

---

*Corresponding author: LGIT, Maison des Géosciences, BP 53, 38041 Grenoble Cedex 9, France. E-mail: andrea.walpersdorf@obs.ujf-grenoble.fr.

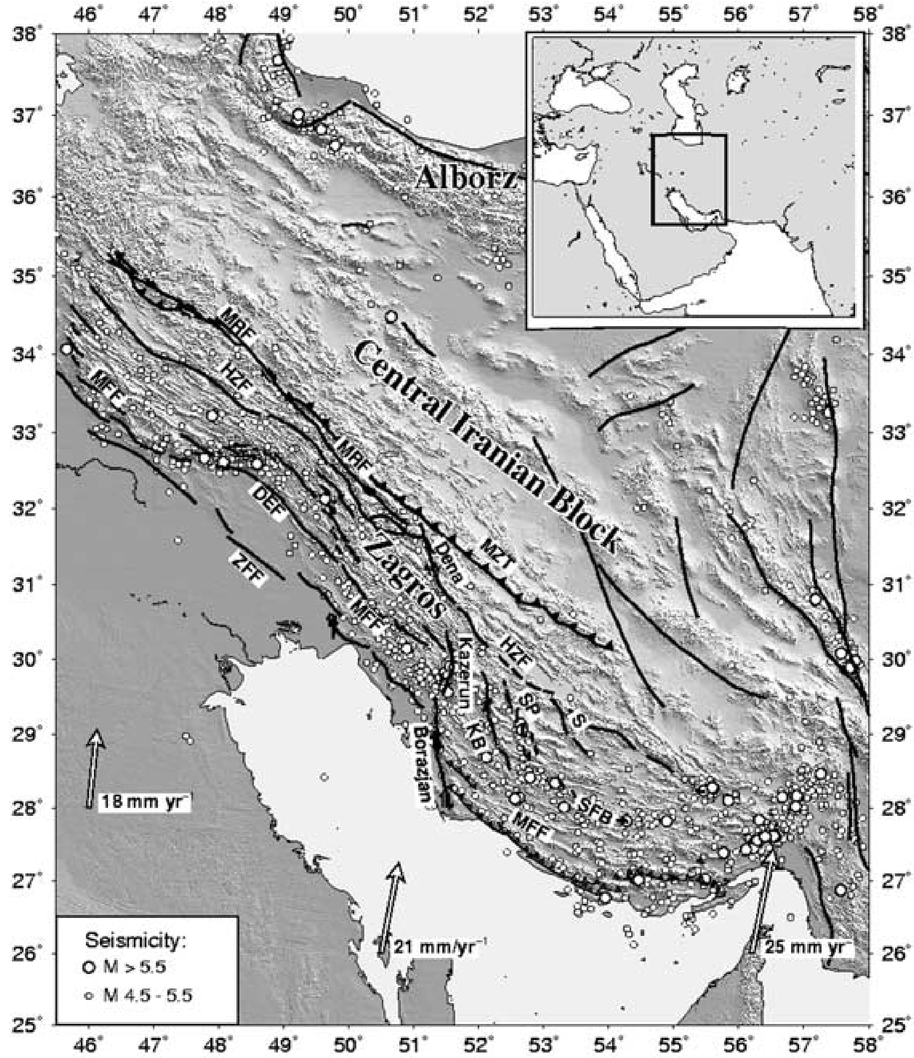

Figure 1. Location of the Zagros major active faults (Berberian 1995) and seismicity (Engdahl *et al.* 1998). The inset displays the global location of Zagros and Iran in the collision zone between the Arabian and Eurasian plates. The velocity vectors indicate the Arabia–Eurasia collision rate according to the rotation pole of Vernant *et al.* (2004). Zagros active faults are reported: MRF: Main Recent Fault; MZT: Main Zagros Thrust; HZF: High Zagros Fault; DEF: Dezful Embayment Fault; MFF: Zagros Mountain Front Fault; ZFF: Zagros Fore deep Fault; Dena fault; Kazerun fault; Borazjan fault; KB: Kareh Bas fault; SP: Sabz Pushan fault; S: Sarvestan fault and SFB: simple fold belt (Berberian 1995).

the former Arabian passive margin that is covered by up to 10 km of Infracambrian to Miocene sediments (e.g. Haynes & McQuillan 1974; Stocklin 1974; Stoneley 1981). These sediments contain several layers of evaporite at different depths that decouple the surface deformation from the basement (Berberian 1981, 1995; Berberian & King 1981). During the Mesozoic, the Zagros underwent a major episode of convergence, mostly accommodated by subduction on the Main Zagros Thrust (MZT) (Stocklin 1974; Stoneley 1981). After the closure of the oceanic basins, a second episode of deformation during the Neogene led to the folding that affected the simple folded belt located between the MZT and the Persian Gulf (Falcon 1974).

The Zagros mountains are affected by the active NS trending Kazerun fault that offsets the folds and the lower Miocene terranes. Maximum and minimum displacement rates on the fault have been inferred from these offsets by Berberian (1981, 1995) and Authemayou *et al.* (2005) to 15 and 4 mm yr^{-1}, respectively. Present-day activity of the Kazerun fault is evidenced by recent earthquakes with right lateral mechanisms located on the fault (Baker *et al.* 1993). The main recent fault (MRF) is an active NW–SE trending right lateral strike-slip fault which runs along the MZT (Berberian 1995) and is observed northwest of the Kazerun fault (Tchalenko & Braud 1974; Ricou *et al.* 1977). The Dorud segment of the MRF is seismically the most active (Tchalenko & Braud 1974; Berberian 1981). A remarkable feature of the Zagros fold belt is that it propagates with time from the MZT towards the Persian Gulf (Falcon 1974; Shearman 1976; Berberian 1995; Hessami *et al.* 2001).

Most of the Zagros deformation seems to be aseismic (North 1974; Jackson *et al.* 1995; Masson *et al.* 2005). The seismicity is located in the basement, probably on reactivated former normal faults, and seems to be concentrated in the west of the mountain belt, in a region with a topography lower than 1000 m (Talebian & Jackson 2004).

Salt layers, present particularly in the southeastern part of Zagros, are suspected to create decoupling of the superficial layers from the basement. If this is the case, the Zagros deformation, as observed by GPS in the southeastern part, represents only the deformation of the sedimentary cover placed on top of the Arabian platform.

Talebian & Jackson (2004) proposed a kinematical description for the present-day deformation of the Zagros mountain belt. The authors compiled earthquake slip vectors related to thrust and strike-slip events and compare them with respect to the overall constraints given by the NUVEL1-A (DeMets *et al.* 1994) or REVEL (Sella *et al.* 2002) plate models. According to the present-day kinematics, the transition from pure shortening in southeast Zagros to oblique shortening in northwest Zagros is accommodated in the region of the Kazerun fault system.

GPS DATA

We have measured two GPS networks in Zagros, the Central Zagros network covering the southeastern part, and the North Zagros network, covering the northwestern part (see site locations on Fig. 3). Data were collected in campaigns during 2001 and 2003 (18 forced antenna centring sites in North Zagros) and 1997, 2000 and 2003 (15 sites with tripod antenna set-up in Central Zagros) using a mixture of Trimble SSI and Ashtech Z-12 receivers and choke ring antennae. Each site was observed for at least 48 hr per campaign. During each campaign, we measured simultaneously some sites from the Iran Global network (KHOS, KSHA for North Zagros, ALIS, ARDA, LAMB for Central Zagros) (Nilforoushan *et al.* 2003; Vernant *et al.* 2004) to connect the different networks. Data from three Iranian permanent stations (AHVA, MASH, TEHR) were used in the campaign analyses when available. We also include the analysis of the GPS measurements (1999 and 2001) from the Iran Global network (Nilforoushan *et al.* 2003; Vernant *et al.* 2004) in the present study.

The data have been analysed with the GAMIT/GLOBK 10.1 software (King & Bock 2002). 32 IGS stations have been included to establish the terrestrial reference frame. Final IGS orbits and corresponding Earth orientation parameters have been used. In the combination of daily solutions with the Kalman filter GLOBK, the continuous time-series of daily SOPAC global solution files (IGS3 network) has been included from 1997 December to 2003 November, covering all measurement epochs presented here.

The precision of the inferred site velocities has been evaluated by (1) the campaign repeatabilities, giving the short term scatter of the site coordinate estimates and (2) velocity residuals on locally inferred rigid tectonic blocks, evaluating long-term uncertainties for the campaign stations (McClusky *et al.* 2000).

The average campaign repeatabilities are given in Table 1. They correspond to the increasing quality of the Central Zagros measurements (longer observation spans and more simultaneous observations by higher number of field teams). For the Central Zagros network, with a mean repeatability of 4 and 1 mm in 1997 and 2003, respectively, on the horizontal components, we could expect velocity uncertainties of 1 mm yr^{-1} over the 6 yr observation time span. Mean horizontal repeatabilities of 2 mm in the 2001 and 2003 North Zagros network yield a 2 mm yr^{-1} precision over the 2 yr time span.

Table 1. Mean repeatabilities on the north, east and vertical baseline components in each of the five campaigns presented in this paper. This statistic is limited on the local North Zagros and Central Zagros network stations with maximum baseline lengths of 3000 km. # bl is the number of measured baselines entering in the statistics.

Repeatabilities [mm]:					
Campaign	Epoch	#bl	N	E	U
C. Zagros	1997.918	25	2.8	3.0	7.4
C. Zagros	2000.096	144	1.7	2.0	5.2
N. Zagros	2001.721	233	1.1	1.7	4.7
N. Zagros	2003.690	231	0.7	1.5	3.2
C. Zagros	2003.885	206	0.9	1.3	2.8

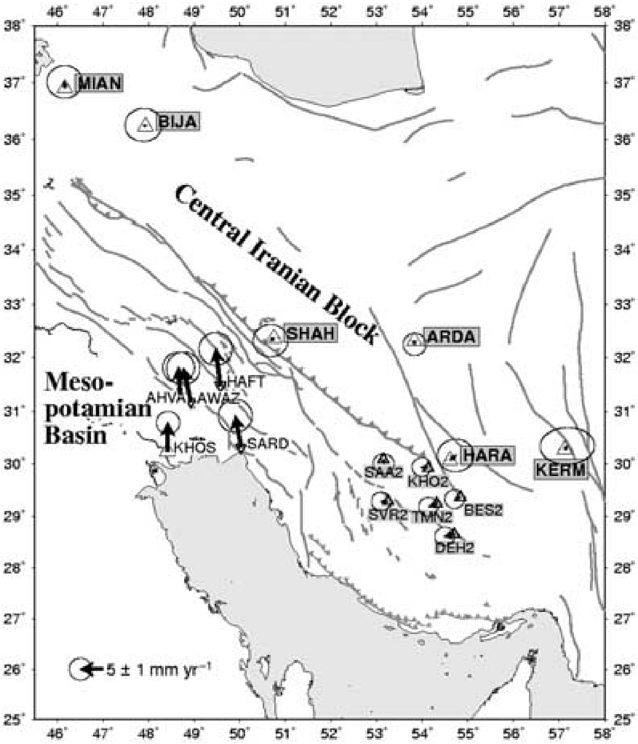

Figure 2. Identification of the two Iranian rigid blocks used for establishing the velocity precisions by evaluating the velocity residuals with respect to rigid block motion: the Central Iranian Block (stations MIAN, BIJA, SHAH, ARDA, HARA, KERM), which can be extended to the northern Central Zagros (stations SAA2, KHO2, SVR2, TMN2, DEH2, BER2), and the Mesopotamian basin (Stations AHVA, AWAZ, HAFT, KHON, SARD).

Systematic errors like tripod set-up (in the Central Zagros network) or antenna phase centre offsets cannot be identified by the repeatability results only. These systematic errors do show up in the comparison of velocities for sites on the same tectonically rigid block. They contribute to the velocity residuals with respect to rigid block motion. Two rigid microblocks represented by several GPS sites can be used in this study to estimate velocity uncertainties (Fig. 2): The larger one is the Central Iranian block (stations MIAN, BIJA, SHAH, ARDA, HARA, KERM, the smaller one the Mesopotamian basin in the south of North Zagros (stations KHOS, AWAZ, AHVA, SARD, HAFT). We estimate horizontal residual velocities of 1.9 mm yr^{-1} on the Central Iranian block similar to Vernant *et al.* (2004). When we include six Central Zagros stations with low residual velocities with respect to Central Iran (SAA2, KHO2, BES2, SVR2, DEH2, TMN2; see Fig. 2), the average residuals with respect to a rigid motion of this block are evaluated to 1.2 mm yr^{-1}. In the Mesopotamian basin, south of North Zagros, the average residuals of the five site velocities KHOS, AWAZ, AHVA, SARD and HAFT are 2.2 mm yr^{-1}. These residuals with respect to a rigid block motion suggest that the uncertainty of the velocity estimates presented in this study is about 2 mm yr^{-1} with slightly smaller values for the Central Zagros measurements due to the 6 yr observation span, in spite of the tripod set-up in this network.

Therefore, 2 mm yr^{-1} seems to be a conservative value for the uncertainties in both the Central and the Northern Zagros. This value will be used as a lower bound on deformation estimates in the tectonic interpretation (see below).

THE ZAGROS VELOCITY FIELD

To focus on the Zagros deformation, we define a reference frame by minimizing the velocities of the stations located on the Central Iranian block (MIAN, BIJA, SHAH, ARDA, HARA and KERM; see Fig. 2) following Vernant *et al.* (2004). The velocity field we obtain on the Zagros networks with respect to the Central Iran block is shown in Table 2 and Fig. 3(a). A general value for the uncertainty of our velocity estimates is 2 mm yr^{-1} as indicated above.

Along the Persian Gulf (stations KHOS, SARD, ALIS, KAN2, OSL2, BMG2, LAMB), velocities of 6–10 mm yr^{-1} are observed representing the eastward increasing motion of the Arabian plate relative to Central Iran. While the eastern site velocities are aligned with the BAHR (Bahrain) velocity vector, the more westerly stations show a rotation to NNW. The transition between pure shortening in the east and oblique shortening in the west is located near the right-lateral Kazerun fault system (Kazerun, Sabs Pushan, Kareh Bas and Sarvestan faults; see Fig. 1 for fault locations). A large northern region of Central Zagros does not deform relative to the Central Iranian block as demonstrated by the low residual velocities of the GPS sites SAA2, KHO2, SVR2, TMN2, BES2 and DEH2. This low deformation suggests that the MZT is inactive in this part of the Zagros and that the deformation in Central Zagros is concentrated further southwest, in the region close to the Persian Gulf shore. A more distributed velocity field is observed in North Zagros with velocities relative to Central Iran decreasing from 6 mm yr^{-1} at the coast to 3 mm yr^{-1} in the centre of the Zagros mountain belt and to zero on the northern side of the MRF.

The Zagros velocity field indicates relative displacement rates of the order of 2 mm yr^{-1} (at the limit of resolution) across several individual faults. In the North Zagros, we find this magnitude of strike-slip activity for the MRF and for the Dena fault, while for the Dezful embayment fault (DEF) and for the Zagros mountain front fault (MFF) the relative motion of 2 mm yr^{-1} is rather transpressive (for fault locations see Fig. 1). In the Central Zagros network, 4–6 mm yr^{-1} of shortening is restricted to the Zagros MFF. The difference in deformation between the two networks suggests 3–6 mm yr^{-1} of right lateral strike-slip motion on the NS trending Kazerun fault system, distributed over the Kazerun, Borazjan, Kareh Bas and Sabz Pushan faults.

The Zagros velocity field is also represented with respect to the Arabian plate as the larger tectonical unit bordering the Zagros deformation belt (Fig. 3b). The Arabian plate reference frame has been established by applying the Arabia–Eurasia rotation pole established by Vernant *et al.* (2004) (27.9°N, 19.5°E, 0.41° Myr^{-1}), to the Zagros velocity field. The BAHR residual velocity is 0.4 mm yr^{-1}, and the residual velocities of the Iranian GPS sites along the Persian Gulf (AHVA, AWAZ, KHOS, SARD, ALIS, KAN2, OSL2, BMO2, LAMB) are evaluated to an average of 2.9 mm yr^{-1} mainly oriented W to WNW with larger values in the centre. The absence of velocity components parallel to the Arabia–Eurasia shortening axis and the velocity amplitudes hardly above the error limit of 2 mm yr^{-1} confirm the absence of shortening in the Persian Gulf.

The velocity field of northern Zagros has been estimated from only two measurements over a 2 yr time span. Therefore, it is probably unreliable to analyse pairs of site velocities to quantify precisely the low (typically 2 mm yr^{-1}) displacement rates along individual faults. However, the analysis of subsets of site velocities (e.g. velocities along transects as shown in the next section) and of strain calculated over the whole velocity field or a subset of stations (as shown later) can be used to average the individual velocity observations and obtain a more significant characterization and quantification of the deformation in the Zagros networks.

The GPS site velocities are interpreted in this paper as constant, interseismic displacement rates. This supposes that no coseismic instantaneous displacement is contained in the displacement rates of the GPS stations, due to earthquakes occurring close to the GPS stations in the time interval covered by the successive measurement campaigns. Seismic catalogues show that no significant earthquake ($Ms > 6$) took place close to the stations in our network in the time between the surveys.

To infer fault slip velocities from GPS displacement rates, a deformation model would be necessary, taking into account the fault emplacements with respect to the GPS sites and the fault mechanisms. Both fault locations and motions are still poorly known for the Zagros, because most of the faults are blind faults (Berberian, 1995), so that in this work we restrict ourselves not to overinterpret single site velocities.

COMPARISON OF THE DEFORMATION BETWEEN CENTRAL ZAGROS AND NORTH ZAGROS

The difference in deformation between Northern and Central Zagros can be highlighted by plotting the velocity distributions on transects (TN1, TN2, TN3 in the North Zagros, TC1 and TC2 in Central Zagros) perpendicular to the Zagros mountain belt (Fig. 4). We project the velocity of the closest stations onto directions parallel and perpendicular to the mountain axis and interpret these two directions as strike-slip and shortening components of active structures parallel to the Zagros mountain axis, with respect to Central Iran. The two velocity components are plotted with respect to the distance between the GPS site and the approximate emplacement of the MRF (Fig. 4).

In order to illustrate (but not to compute) the deformation patterns, we superpose simple mechanical models on top of the velocity observations. For the strike-slip component, we use a model of a locked strike-slip fault in an elastic half-space (Savage & Burford 1973) centred on the MRF or the MZT. This model is evaluated for a locking depth at 10 km. Note that the locking depth is not significant for describing the velocity distribution on the spatial scale of the transects.

In the North Zagros, for TN1 and TN2, located north, most of the strike-slip deformation is associated with the MRF, whereas for TN3, located further south, most of the strike-slip deformation is associated with the Zagros MFF. In the Central Zagros, the strike-slip component is approximately 2 mm yr^{-1} and it is located in the southwestern part of the network, near the Persian Gulf. There is a marked difference between the two parts of Zagros because the total strike-slip velocities vary from 2 mm yr^{-1} in Central Zagros to 4–6 mm yr^{-1} in North Zagros.

For the compressive component we use a model with a uniformly distributed homogeneous strain over the whole Zagros, corresponding to a linear velocity distribution. This simple model is sufficient to analyse the shortening patterns related to the young continental collision taking place throughout the Zagros. In this case of shortening, we fit the model to the velocity observations. While in North Zagros the ensemble of site velocities fit a linear velocity

Table 2. GPS velocity field with respect to the Central Iranian Block (CIB) and with respect to ITRF 2000. Networks: IG: Iran Global; NZ: North Zagros; CZ: Central Zagros; IP: Iran permanent; IGS: International GPS Service.

GPS station velocities [mm yr^{-1}]

	Positions		Velocities w.r.t. Iran Central Block		ITRF2000 velocities		Velocity uncertainties (95 per cent conf. interval	
SITE (net)	long (°E)	lat (°N)	v east	v north	v east	v north	sig v east	sig v north
MIAN (IG)	46.162	36.908	−0.06	1.34	23.87	23.55	1.59	1.46
ILAM (IG)	46.427	33.648	−0.65	3.98	24.14	26.11	1.61	1.47
DELO (NZ)	47.429	32.692	0.02	3.31	25.26	25.44	1.53	1.51
GORI (NZ)	47.739	33.057	−2.05	3.75	23.15	25.93	1.51	1.49
BIJA (IG)	47.930	36.232	−0.46	0.24	24.02	22.39	1.66	1.50
KORA (NZ)	48.175	33.406	0.70	3.44	25.91	25.57	1.50	1.48
KHOS (IG)	48.409	30.246	0.14	6.27	26.16	28.32	1.06	1.02
BORU (NZ)	48.506	33.772	−2.89	1.05	22.32	23.13	1.50	1.48
DEZF (NZ)	48.678	32.657	−2.45	4.58	23.06	26.66	1.50	1.48
AHVA (IP)	48.684	31.340	−0.29	5.56	25.57	27.64	1.42	1.41
AWAZ (NZ)	48.925	31.188	−1.66	7.12	24.23	29.25	1.50	1.48
JOZA (NZ)	48.952	34.256	−1.84	2.71	23.36	24.77	1.50	1.48
SOLE (NZ)	49.328	32.037	−2.19	4.71	23.62	26.84	1.50	1.48
HAFT (NZ)	49.571	31.484	−1.02	7.96	24.97	29.96	1.50	1.48
SHOL (NZ)	49.668	33.073	0.40	0.72	26.10	22.75	1.51	1.49
GHAR (NZ)	49.851	35.140	−0.26	0.28	24.88	22.34	1.51	1.49
SARD (NZ)	50.026	30.325	−1.32	6.88	24.93	28.88	1.52	1.49
CHEL (NZ)	50.098	32.482	−2.80	3.75	23.12	25.81	1.51	1.49
KHON (NZ)	50.458	33.157	−1.82	−0.06	23.96	21.99	1.51	1.49
KRD2 (NZ)	50.531	31.808	−3.25	1.71	22.80	23.76	1.50	1.48
DEDA (NZ)	50.578	30.990	1.05	3.85	27.31	25.63	1.51	1.48
BAHR (IGS)	50.608	26.209	4.83	6.74	31.99	28.76	0.52	0.23
SHAH (IG)	50.748	32.367	−0.79	−0.56	25.22	21.44	1.56	1.45
ALIS (IG)	51.082	28.919	−0.87	8.17	25.92	30.13	1.04	1.00
KSHA (IG)	51.255	34.150	0.21	−0.60	25.94	21.34	1.05	1.02
TEHN (IP)	51.334	35.697	−0.78	−3.02	24.59	18.94	1.39	1.38
TEHR (IG)	51.386	35.747	0.81	−1.27	26.16	20.68	1.65	1.51
SEMI (NZ)	51.430	31.225	−2.93	0.19	23.40	22.21	1.51	1.49
NOSH (IG)	51.768	36.586	−2.10	−3.09	23.17	18.79	1.71	1.50
QOMS (IG)	51.799	32.250	−1.90	0.75	24.32	22.67	1.51	1.48
KAN2 (CZ)	52.056	27.834	0.87	8.10	28.01	30.03	0.88	0.86
FAR2 (CZ)	52.106	28.851	−1.88	5.32	25.08	27.19	0.88	0.85
OSL2 (CZ)	52.607	27.474	0.11	9.16	27.36	30.98	1.63	1.52
QIR2 (CZ)	53.029	28.477	−2.08	1.53	25.11	23.38	0.84	0.83
ISL2 (CZ)	53.066	28.347	−1.42	2.60	25.87	24.40	0.86	0.84
SAA2 (CZ)	53.146	30.087	0.03	−.92	27.03	20.92	0.95	0.88
SVR2 (CZ)	53.244	29.281	−1.48	0.04	25.63	21.94	0.88	0.85
BMG2 (CZ)	53.480	26.970	3.15	5.81	30.67	28.35	1.08	1.08
SEMN (IG)	53.564	35.662	0.15	−5.82	26.07	15.94	1.64	1.48
GOT2 (CZ)	53.631	28.624	−.70	2.42	26.57	24.23	0.99	0.95
BIG2 (CZ)	53.637	27.852	−.56	1.52	26.81	23.37	0.92	0.90
ARDA (IG)	53.822	32.313	0.10	−.75	26.78	21.02	1.02	1.00
LAMB (IG)	54.004	26.883	3.50	7.22	31.14	28.92	1.08	1.01
KHO2 (CZ)	54.126	29.923	−1.42	0.24	25.70	22.02	0.86	0.85
KORD (IG)	54.199	36.860	−0.78	−9.41	24.94	12.04	1.67	1.49
TMN2 (CZ)	54.316	29.239	−1.85	−.67	25.44	21.06	0.86	0.85
LAR2 (CZ)	54.320	27.644	0.59	4.33	28.16	26.07	0.89	0.86
HARA (IG)	54.608	30.079	1.20	0.99	28.41	22.71	1.63	1.47
DEH2 (CZ)	54.700	28.645	−2.15	−.44	25.34	21.31	0.87	0.85
BES2 (CZ)	54.832	29.363	−1.32	−.40	26.08	21.32	0.87	0.85
ROBA (IG)	56.070	33.369	1.56	−4.11	28.45	17.48	1.60	1.46
KHAS (IG)	56.233	26.208	3.32	9.79	31.43	31.31	1.83	1.50
KERM (IG)	57.119	30.277	0.56	0.79	28.22	22.25	2.45	1.66

distribution along the transects (and therefore a homogeneous strain), in Central Zagros the velocity gradients are constrained excluding the stations in the non-deformable part of Central Iran. We observe an increase of the shortening component from North Zagros to Central Zagros (from 2 mm yr^{-1} to 8 mm yr^{-1}) due to the proximity of the relative Arabia–Eurasia rotation pole (e.g. Sella *et al.* 2002; Vernant *et al.* 2004).

With an uncertainty of 2 mm yr^{-1} on our velocity estimates (not including the systematic bias that are not measurable before a third campaign), we will only provide a first-order interpretation of the

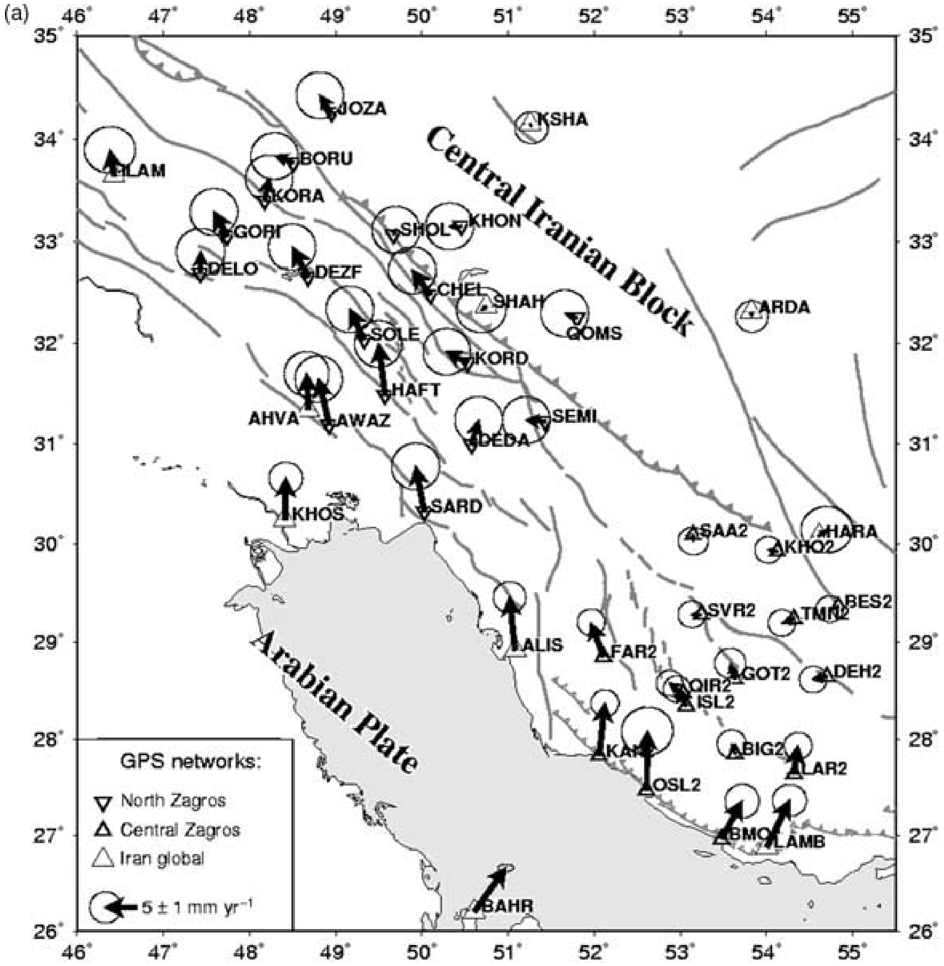

Figure 3. (a) North Zagros and Central Zagros velocity fields with respect to the Central Iranian block. The scale vector corresponds to 5 mm yr^{-1}. The error ellipses indicate formal errors within a 95 per cent confidence interval. The different networks (North Zagros, Central Zagros and Iran Global) are marked with different symbols. We observe a different velocity field on both sides of the Kazerun fault system. (b) North Zagros and Central Zagros velocity fields with respect to the Arabian Plate. Same captions as Fig. 3(a).

tectonics of the region and not try to estimate the strike-slip rates on individual faults of the Zagros folded belt (MRF, High Zagros Fault, Zagros MFF). The fault parallel component (strike-slip motion) in North Zagros increases from north to south (from transect TN1 to TN3) from 4 to 6 mm yr^{-1}. This strike-slip motion is observed along transect TN1 for the stations located on the Zagros folded belt (DELO–ILAM–GORI–DEZF–KORA–BORU) relative to Central Iran (GARA), on TN2 for the stations located south of the Dezful Embayment (AWAZ–HAFT) relative to the Zagros folded belt (SOLE–KORD–CHEL) and Central Iran (SHOL–KHON), and along transect TN3 for the stations located south of the Zagros MFF (ALIS–SARD) relative to the Zagros folded belt (DEDA–SEMI) and Central Iran (QOMS–ARDA).

Shortening is insignificant in the region spanned by the transect TN1 (DELO–GORI–KORA–BORU–JOZA). Further south, on transect TN2, the stations south of the DEF (KHOS–AWAZ–HAFT) converge relative to the Zagros folded belt stations (SOLE–KORD–CHEL–SHOL–SHAH) with a velocity of about 3 ±1 mm yr^{-1} . On transect TN3, the NS trending Kazerun fault marks a place of several mm yr^{-1} of shortening due to its obliqueness with respect to the profile.

For the Central Zagros, a fault parallel motion of 2 ± 1 mm yr^{-1} relative to Central Iran affects the westernmost stations (KAN2–OSL2–FAR2) suggesting that a small amount of strike-slip motion (with respect to the orientation of the MRF/MZT) is accommodated by the Kazerun fault system. On the contrary, the shortening shows a large gradient of up to 8 mm yr^{-1} between stations located on the Persian Gulf shore (KAN2–OSL2 on TC1 and BMG2–LAMB on TC2) and all other stations located further north (SAA2–TMN2–KHO2–HARA on TC1 and DEH2–KERM on TC2). Only the two stations BIG2 and LAR2 located further inland show a slow convergence (3 ± 1 mm yr^{-1}) toward Central Iran. This suggests that most of the shortening (75 per cent) is accommodated by structures located along the Persian Gulf such as the Zagros MFF.

SLIP RATES FOR THE KAZERUN FAULT SYSTEM

As seen in Fig. 1, the Kazerun fault system separates the Zagros into two regions of contrasting deformation systems and, therefore, it should accommodate some differential motion. We can infer velocity estimates on different segments of the Kazerun fault system by comparing the velocity fields in the North and the Central Zagros on each side of the fault system.

The two stations located south of the Zagros MFF (KAN2 and ALIS) on either side of the fault system show similar motion relative

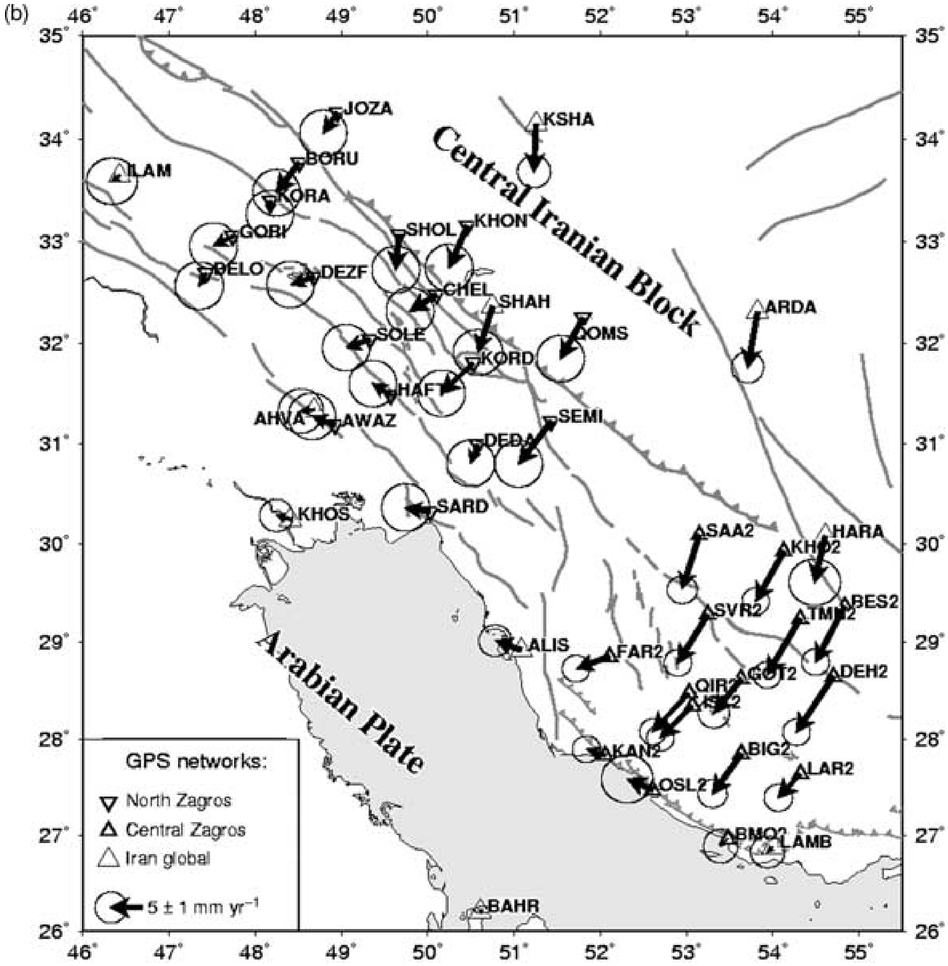

Figure 3. (*Continued.*)

to Central Iran, which suggests that they both belong to the non-deformable part of the Arabian plate. However, going further north, we measure 3 ± 2 mm yr^{-1} of relative NS displacement between ALIS and FAR2, which characterizes the slip rate in the southern part of the Kazerun fault system. We also measure 3 ± 2 mm yr^{-1} between DEDA and SEMI which can be attributed to the Dena fault. The motion on the Karebas and on the Sabz Pushan faults can be estimated from the comparison between FAR2 and QIR2 on one hand and FAR2 and SVR2 on the other hand, suggesting a motion of about 2 ± 2 mm yr^{-1} of the Karebas fault and almost of the same order on Sabz Pushan. Therefore, the cumulated motion accommodated by the total Kazerun strike-slip fault system is of about 6 ± 2 mm yr^{-1}.

THE ZAGROS STRAIN DISTRIBUTION

The strain tensors obtained over 19 stations in the North Zagros and 15 stations in Central Zagros are shown in Fig. 5(a). Over the whole North Zagros network, we see a dominating compressive component oriented perpendicular to the mountain axis. A smaller extensive component is assumed to be due to a strike-slip component present in the overall deformation pattern. In Central Zagros, we notice higher strain rates (25 per cent) on both the compressive and the extensive component with respect to North Zagros. The decrease of the overall deformation rates from Central to North Zagros could be due to two reasons: First, the North Zagros network is larger than the Central Zagros network, so that the velocity differences are spread over larger distances and second, the relative motion between Arabia and Eurasia decreases from east to west according to the Eurasia–Arabia rotation pole (Vernant *et al.* 2004).

In order to compare the distribution of the deformation in both the Northern and Central Zagros, we define several subnetworks (three in the southeast and five in the northwest) of similar sizes to compare strain rates (Fig. 5b). The numerical values are summarized in Table 3. The formal errors of the strain estimates are 10–15 nanostrain yr^{-1}. We conclude that significant deformation can be shown by the present analysis in subnetworks where values of more than 10–15 nanostrain yr^{-1} are obtained. The values observed for two subnetworks being situated in supposedly non-deforming parts of the network, NZ1 in the Mesopotamian basin in the North Zagros, and CZ1 in the northern part of Central Zagros, are of 5–10 nanostrain yr^{-1}. Based on significant strain observations, we note that the strain distribution is different in Central Zagros with respect to North Zagros. In Central Zagros, the compressional axes are parallel to each other and perpendicular to the fold axes and most of the deformation is concentrated in one band along the Persian Gulf coast, in CZ3. In North Zagros, the compressional axes vary in orientation, and two separate zones of significant deformation can be distinguished, NZ2, and NZ4a and NZ4b. This analysis of the strain rates in subnetworks shows that the deformation is not homogeneously distributed but concentrated in zones located near active

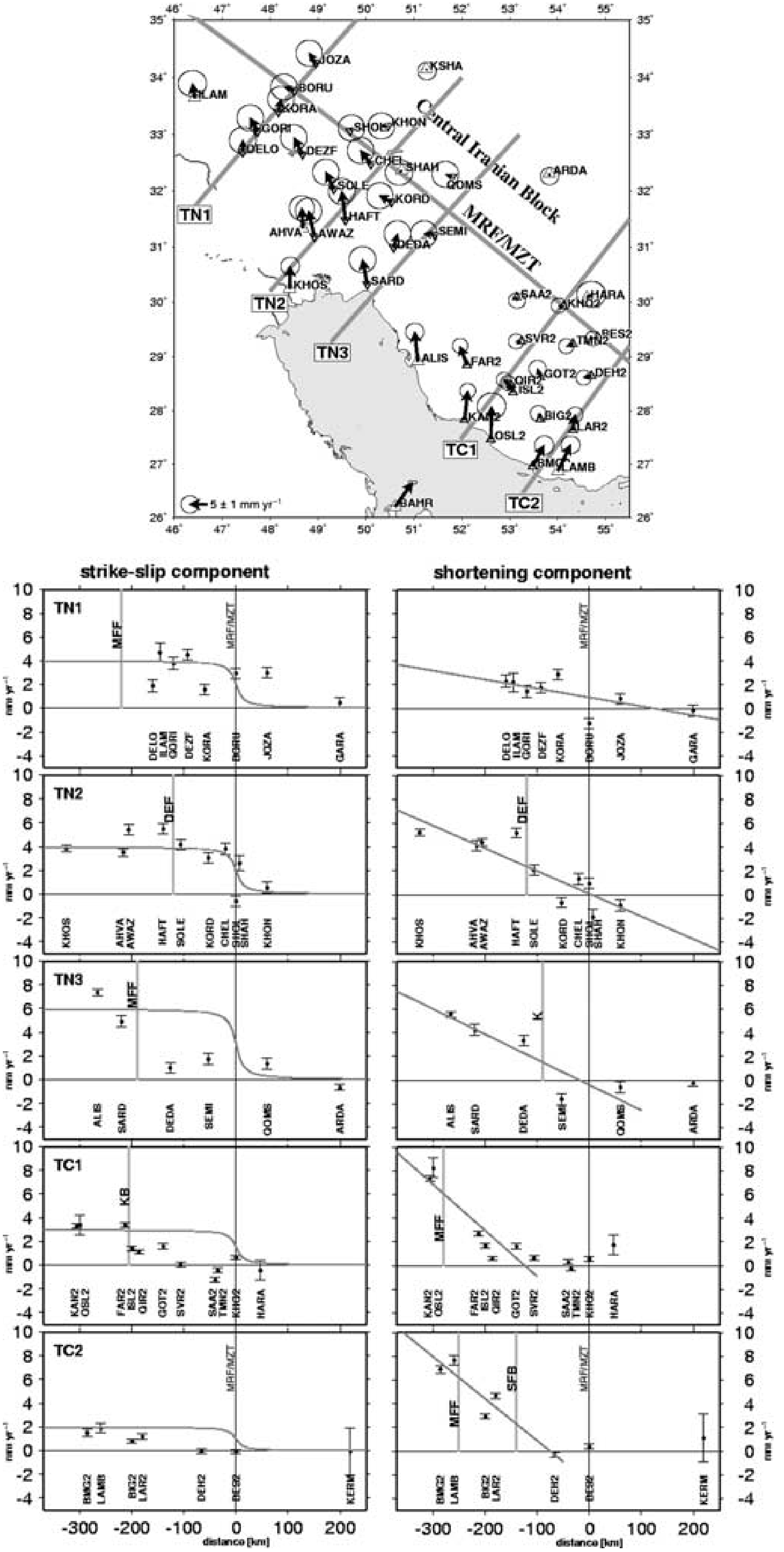

Figure 4. Site velocities (mm yr^{-1}) with respect to the site distance to the main recent fault (MRF)/main Zagros thrust (MZT) (in km, on the *x*-axis) on 5 transects (locations shown on the map), TN1, TN2 and TN3 in the North Zagros, TC1 and TC2 in the Central Zagros, from northwest to southeast. On the left, we display the fault parallel components (strike-slip component), on the right, the fault perpendicular component (shortening). A simple model is superposed on the individual velocities (dark grey lines, for details see text). Modelled total strike-slip velocities vary from 2 to 6 mm yr^{-1}, strain rates from 8 to 39 nanostrain yr^{-1}. Light grey vertical lines indicate fault locations.

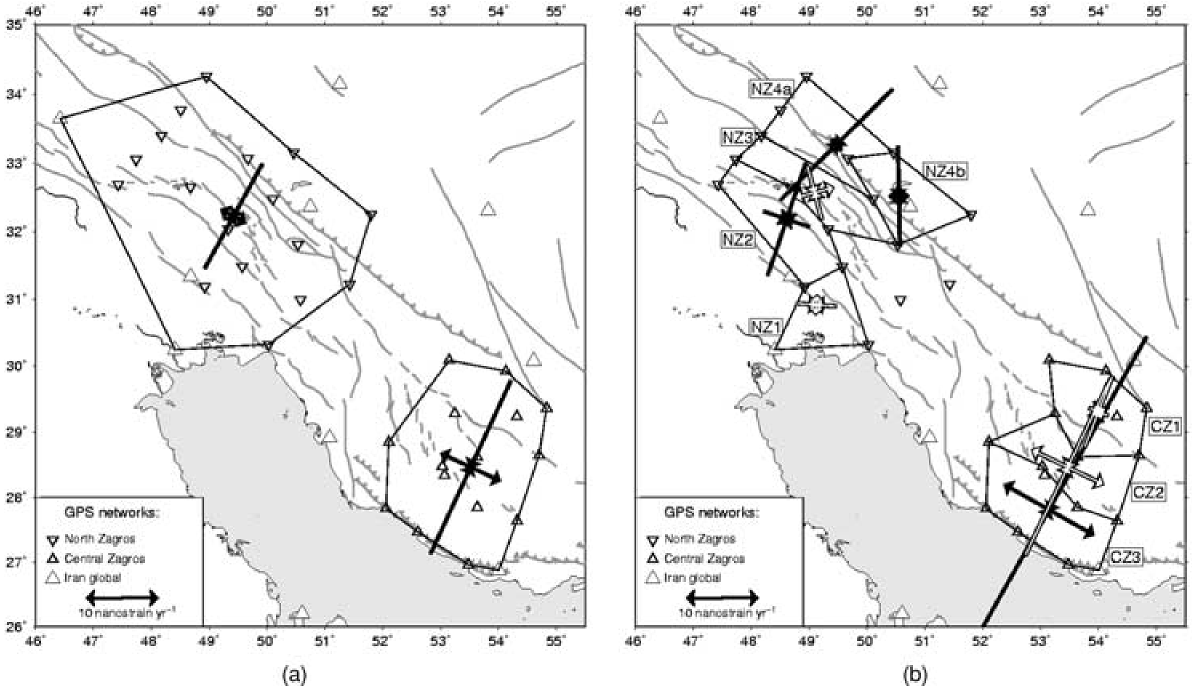

Figure 5. (a) Overall strain rates in the North and Central Zagros networks. Numerical values are indicated in Table 3. (b) Strain rates in subnetworks. Black and white strain crosses distinguish relatively high and low deformation rates, respectively.

Table 3. Strain rate values and their uncertainties for the main networks, for the five North Zagros subnetworks and the three Central Zagros subnetworks. The most significant values in the subnetworks are highlighted. For the localization of the subnetworks refer to Fig. 5(b).

North and central Zagros strain rates in nanostrain yr^{-1}

	North Zagros	Major axis	Sec. axis	Central Zagros	Major axis	Sec. axis
Main networks:	NZ	−16.5 ± 3.0	3.9 ± 2.5	CZ	−27.3 ± 3.0	9.2 ± 2.9
Subnetworks:	NZ1	−5.5 ± 10.8	2.6 ± 9.9	CZ1	−10.7 ± 6.8	−2.6 ± 5.2
	NZ2	**−16.9 ± 14.9**	**−6.8 ± 9.3**	CZ2	−23.4 ± 1.2	11.1 ± 3.8
	NZ3	−7.7 ± 15.1	5.4 ± 15.8	**CZ3**	**−57.0 ± 7.4**	**14.6 ± 3.7**
	NZ4a	**−22.5 ± 14.3**	**2.0 ± 7.8**			
	NZ4b	**−14.2 ± 13.0**	**2.6 ± 11.2**			

faults, such as the MFF (CZ3) in Central Zagros, and the DEF/MFF (NZ2) and the MRF (NZ4a/b) in North Zagros.

COMPARISON WITH SEISMICITY

To compare the shallow deformation with the basement deformation, we have to compare the GPS results with seismicity. Two cross sections across the Zagros (Fig. 6) have been chosen to study the distribution of seismicity with respect to the Zagros topography and the GPS measured surface displacement rates. The topography shows that the width of the belt in North Zagros is much narrower than in Central Zagros (∼200 versus ∼350 km). However, the average altitude of the deforming belt (the simple fold belt) is lower in North Zagros (excluding Mt. Dena which is in a peculiar region) than in Central Zagros, while one expects that comparable deformation over a narrower range would lead to higher altitudes. One explanation for this difference is the additional strike-slip motion present in North Zagros while Central Zagros deformation is dominated by thrusting. This means that, contrary to the Central Zagros, the crust is not trapped in North Zagros but can escape from pure shortening (and therefore folding) by lateral translation along strike-slip faults such as the MRF. A second reason for the lower deformation in North Zagros is the decrease of relative motion in the Arabia–Eurasia collision with respect to Central Zagros.

Talebian & Jackson (2004) showed that larger magnitude seismicity is restricted to the edge of the Zagros fold belt and, therefore, could be associated with only the most recent of the faults proposed by Berberian (1995) in the Zagros. This was even more apparent when considering only the earthquakes of magnitude $Mb > 5$ that are located in regions of low topography. However, microearthquake seismicity is spread on a wider region (Tatar *et al.* 2004). We plotted both the total seismicity available in the ISC catalogue and the relocated earthquakes of magnitude $mb > 5$ (Engdahl *et al.* 1998) in Fig. 6. The superficial deformation of Central Zagros inferred from GPS measurements is much more concentrated along the Persian Gulf coast than shown by the seismicity (Fig. 6, TC1). Models of the Zagros folded deformation are derived from balanced cross sections of the sedimentary cover (i.e. McQuarrie 2004; Sherkaty & Letouzey 2004; Molinaro *et al.* 2005). These models assume that the sedimentary cover folds whereas the basement is affected by active faults. Some of the listed authors assume that every fold is related to an active fault. If the sedimentary cover is totally decoupled from the basement, then there is no need for the surface folds to be located at the same place as the active faults in the basement (Tatar

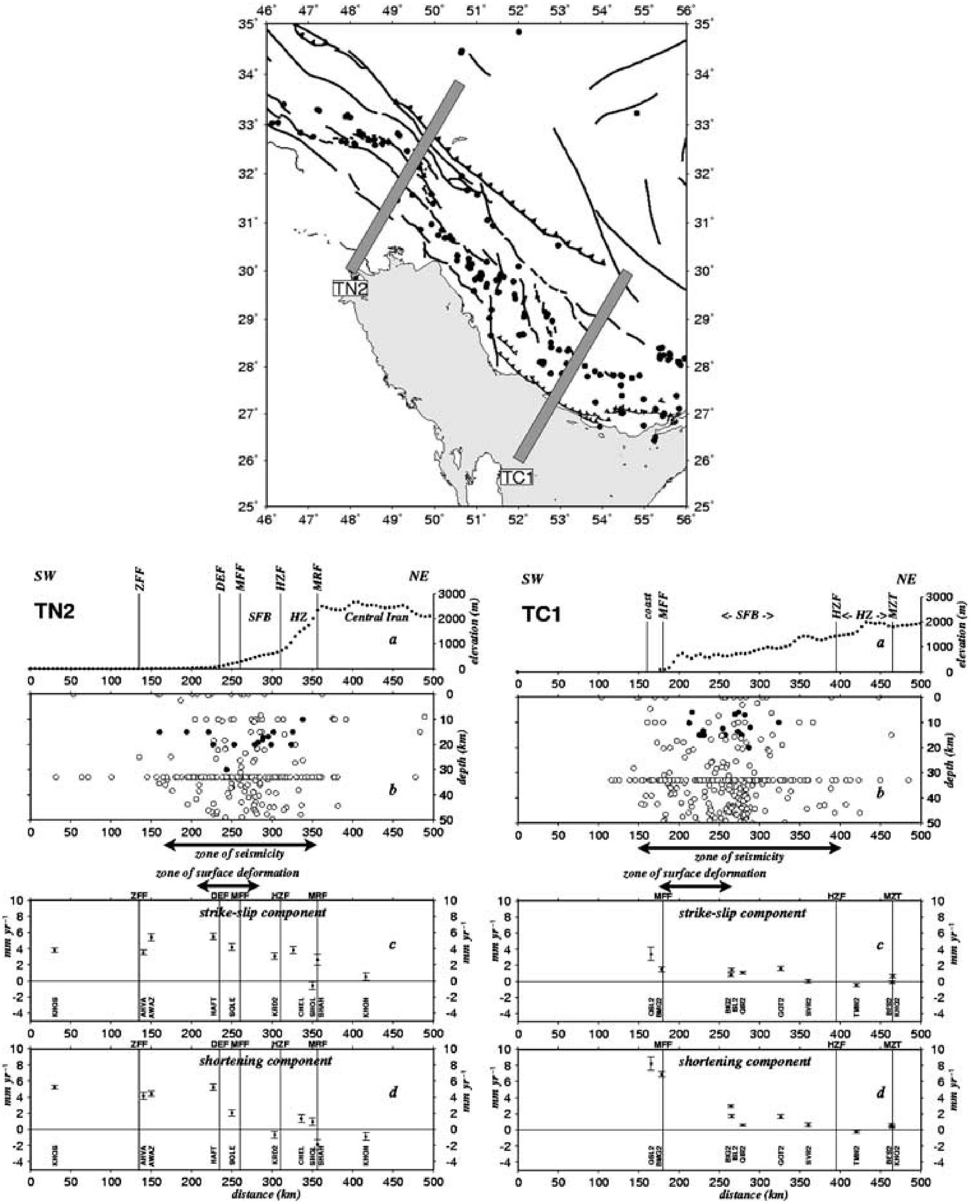

Figure 6. On the two transects TN2 and TC1 we display (a) the topography, (b) the seismicity (open circles: USGS, black circles: Engdahl *et al.* 1998), (c) NW–SE strike-slip motion parallel to MRF/MZT and (d) shortening perpendicular to MRF/MZT. The approximate location of different faults is indicated by vertical lines. Horizontal arrows indicate that the surface deformation evidenced by GPS measurement is concentrated in narrow areas, whereas the basement deformation evidenced by the seismicity is distributed in a larger area, suggesting a decoupling between the two.

et al. 2004). The only constraint is that both the deformation of the basement (seismicity) and of the shallow sedimentary cover (GPS) should be of comparable value. However, the comparison between the brittle deformation evidenced by earthquake activity and the total deformation inferred by strain from GPS measurements shows that only 10 per cent of the total deformation in Zagros is released by earthquakes (North 1974; Jackson & McKenzie 1988; Masson *et al.* 2005).

There are two possible explanations for the relatively aseismic deformation of the Zagros. Firstly, that the amount of deformation of the basement is smaller (by 80 per cent) than the deformation evidenced at surface by GPS. This implies that the Zagros basement underthrusts beneath the Central Iran region to the northeast, as an active subduction. This seems unlikely because we do not observe any seismicity located north of the MZT that acted as the suture of former subduction (Maggi *et al.* 2000; Talebian & Jackson 2004). Secondly, that the mechanical properties do not allow all the deformation to release seismic energy probably because of the unusually large thickness of the sedimentary cover that reduces the thickness of the brittle crust.

CONCLUSIONS

The two GPS surveys in the North Zagros give a consistent velocity field relative to Central Iran. The third survey in Central Zagros increases the precision of the velocity field and allows a comparison with North Zagros. The average velocity uncertainties are evaluated to 2 mm yr^{-1}.

Present-day deformation in the North Zagros is characterized by cumulated 3–6 mm yr^{-1} of shortening and cumulated 4–6 mm yr^{-1} of right-lateral strike-slip, consistent with first estimates from the larger scale Iran Global GPS network (Vernant *et al.* 2004). This strike-slip motion is lower than the 10–17 mm yr^{-1} proposed on only the MRF by Talebian and Jackson (2002). Talebian and Jackson suggested this slip rate based on the assumption that the observed offset of 50 km on the MRF was achieved in 3–5 Ma. If we assume a constant slip rate of at most 4–6 mm yr^{-1} (cumulated slip rate across the whole North Zagros mountain belt), the MRF has formed not earlier than 10 Ma ago. In our study, 2–3 mm yr^{-1} of slip rate have been localized on the MRF, resulting in a fault age of 25 Ma. We can compare these estimates for the MRF with those of the Kazerun fault, as their respective onsets are certainly related. On the Kazerun fault, fault offsets between 12–27 km (minimal values, Authemayou *et al.* 2005) and 140 km (Berberian 1995) have been suggested. The GPS inferred present-day displacement rates we can take into account are 6 ± 2 mm yr^{-1} (maximum value inferred across the whole Kazerun strike-slip fault system) and 2 mm yr^{-1} (restricted to the Kazerun fault *sensu stricto*). Considering fault offsets of around 20 km, the latest onset time is about 3 Ma with a constant displacement rate of 6 ± 2 mm yr^{-1}, the earliest onset time is about 10 Ma with a constant slip rate of 2 mm yr^{-1}. These estimates are lower, but reaching the same order of magnitude as for the MRF. This could evidence a simultaneous onset of both faults. The Kazerun fault offset of 140 km as postulated by Berberian (1995) implies an earliest onset 35 Ma ago and does not seem to correspond to the same tectonical period.

In Central Zagros, 8 mm yr^{-1} of shortening and 2–3 mm yr^{-1} of strike-slip motion are observed, consistent with the first results of Tatar *et al.* (2002). This increase of the rate of shortening in Central Zagros compared to North Zagros is consistent with the location of the Arabia–Eurasia rotation pole which predicts an increase of 4 mm yr^{-1} for the NS component between KHOS and LAMB. We confirm Tatar *et al.*'s (2002) result that the MZT is currently inactive but the Central Zagros velocity field is distributed differently than proposed by Tatar *et al.* (2002). The northern region not deforming relatively to the Central Iranian block is spread over a larger zone, and the shortening is more concentrated along the coast of the Persian Gulf. In both studies, a small strike-slip component is observed in the western part of the network near the Kazerun strike-slip fault system, coherent to Talebian & Jackson's (2004) kinematical description.

The GPS measured deformation of Central Zagros concentrated along the coast is consistent with geomorphological observations (such as growth rates of folds evidenced by terrace uplifts, Vita-Finzi 1987; Oveisi, personal communication, 2005) and supports a model of propagation of the folding deformation to the SW (Shearman 1976; Hessami *et al.* 2001). The comparison between the superficial deformation concentrated along the coastline and the more widely spread seismicity confirms the decoupling of the sedimentary layer from the basement.

The North Zagros velocity field is more complex with the presence of shortening and strike-slip distributed across the belt. The strike-slip motion is likely associated with the MRF and shortening with the DEF but our data do not help to quantify this motion on single faults. No individual fault seems to present slip rates of more than 2 mm yr^{-1}.

Therefore, the deformation occurring in the Central Zagros (pure shortening) is different from that in North Zagros (partitioned between shortening and strike-slip), as is suggested by tectonic and seismological observations (i.e. Ricou *et al.* 1977; Berberian 1995; Talebian & Jackson 2004; Authemayou *et al.* 2006) and the morphology. The two parts of the Zagros are separated by the Kazerun fault system across which right-lateral strike-slip occurs at ∼2–3 mm yr^{-1} on individual fault segments, yielding a cumulated strike-slip rate of 6 ± 2 mm yr^{-1}.

ACKNOWLEDGMENTS

The GPS campaigns have been successful thanks to the help of many colleagues: M. Peyret, M.-N. Bouin, C. Sue, and the field teams of NCC and IIEES in Tehran. This project was financed by the CNRS-INSU 'Intérieur de la Terre' programme, the NCC and the IIEES. HN, FN, MT and FT were partially supported by the French Embassy in Tehran. The GPS receivers were provided by CNRS-INSU and NCC. We benefited from interesting discussions with M. Berberian, J. Jackson, P. Molnar, M. Talebian, C. Vita-Finzi and P. Tregoning, and from a constructive review by V. Regard.

REFERENCES

Authemayou, C., Bellier, O., Chardon, D., Malekzade, Z. & Abassi, M., 2005. Role of the Kazerun fault system in active deformation of the Zagros fold-and-thrust belt (Iran), *Comptes Rendus Geoscience,* **337**(5), 475–547.

Authemayou, C., Chardon, D., Bellier, O., Malekzade, Z., Shabanian, I. & Abbassi, M., 2006. Late Cenozoic Partitioning of oblique plate convergence in the Zagros fault-and-thrust belt (Iran), *Tectonics,* **25,** TC3002, doi:10.1029/2005TC001860, 2006.

Baker, C., Jackson, J. & Priestley, K., 1993. Earthquakes on the Kazerun Line in the Zagros mountains of Iran: strike-slip faulting within a fold-and-thrust belt, *Geophys. J. Int.,* **115,** 41–61.

Berberian, M., 1981. Active faulting and tectonics of Iran, in *Zagros-Hindu-Kush-Himalaya Geodynamic evolution*, **Vol. 3,** pp. 33–69, eds Gupta, H.K. & Delany, F.M., Am. Geophys. Union, Geodyn. Ser.

Berberian, M., 1995. Master blind thrust faults hidden under the Zagros folds: active basement tectonics and surface morphotectonics, *Tectonophysics,* **241,** 193–224.

Berberian, M. & King, G.C.P., 1981. Towards a paleogeography and tectonic evolution of Iran, *Can. J. Earth Sci.,* **18,** 210–265.

DeMets, C., Gordon, R.G., Argus, D.F. & Stein, S., 1994. Effects of recent revisions to the geomagnetic reversal time scale on estimates of current plate motions, *Geophys. Res. Lett.,* **21,** 2191–2194.

Engdahl, E.R., Van der Hilst, R.D. & Buland, R.P., 1998. Global teleseismic earthquake relocation with improved travel times and procedures for depth determination, *Bull. seism. Soc. Am.,* **88,** 722–743.

Falcon, N., 1974. Southern Iran: Zagros Mountains, in *Mesozoic-Cenozoic Orogenic Belts*, **Vol. 4,** pp. 199–211, ed. Spencer, A.M, Spc. Publ. Geol. Soc. London.

Haynes, S.J. & McQuillan, H., 1974. Evolution of the Zagros suture zone, southern Iran, *Bull. geol. Soc. Am.,* **85,** 739–744.

Hessami, K., Koyi, H., Talbot, C.J., Tabasi, H. & Shabanian, E., 2001. Progressive unconformities within and evolving foreland fold-thrust belt, Zagros Mountains, *J. geol. Soc. Lond.,* **158,** 969–981.

Jackson, J. & McKenzie, D., 1988. The relationship between plate motions and seismic moment tensors and the rates of active deformation in the Mediterranean and Middle East, *Geophys. J. R. astr. Soc. Lond.,* **83,** 45–73.

Jackson, J., Haines, J. & Holt, W., 1995. The accommodation of Arabia-Eurasia plate convergence in Iran, *J. geophys. Res.,* **100,** 15 205–15 219.

King, R.W. & Bock, Y., 2002. *Documentation for the GAMIT analysis software*, release 10.1, Massachusetts Institute of Technology, Cambridge, Massachusetts.

Maggi, A., Jackson, J.A., Priestley, K. & Baker, C., 2000. A re-assessment of focal depth distributions in Southern Iran, the Tien Shan and Northern India: do earthquakes really occur in the continental mantle?, *Geophys. J. Int.,* **143,** 629–661.

Masson, F., Chéry, J., Hatzfeld, D., Martinod, J., Vernant, P., Tavakoli, F. & Ghafory-Ashtiani, M., 2005. Seismic versus aseismic deformation in Iran inferred from earthquakes and geodetic data, *Geophys. J. Int.,* **160,** 217–226.

McClusky, S. *et al.*, 2000. Global Positioning System constraints on plate kinematics and dynamics in the eastern Mediterranean and Caucasus, *J. geophys. Res.,* **105,** 5695–5719.

McClusky, S., Reilinger, R., Mahmoud, S., Ben Sari, D. & Tealeb, A., 2003. GPS constraints on Africa (Nubia) and Arabia Plate motions, *Geophys. J. Int.,* **155,** 126–138.

McQuarrie, N., 2004. Crustal scale geometry of the Zagros fold-thrust belt, Iran, *J. Struct. Geol.,* **26,** 519–535.

Molinaro, M., Zeyen, H. & Laurencin, X., 2005. Lithospheric structure underneath the south-eastern Zagros Mountains, Iran: recent slab break-off?, *TerraNova,* **17,** 1–6.

Nilforoushan, F. *et al.*, 2003. GPS network monitors the Arabia-Eurasia collision deformation in Iran, *J. of Geodesy,* **77,** 411–422.

North, R.G., 1974. Seismic slip rates in the Mediterranean and the Middle East, *Nature,* **252,** 560–563.

Ricou, L.E., Braud, J. & Brunn, J.H., 1977. Le Zagros, *Mém. H. Sér. Soc. Géol. Fr.,* **8,** 33–52.

Savage, J. & Burford, R., 1973. Geodetic determination of relative plate motion in Central California, *J. geophys. Res.,* **95,** 4873–4879.

Sella, G.F., Dixon, T.H. & Mao, A., 2002. REVEL: a model for recent plate velocities from space geodesy, *J. geophys. Res.,* **107**(B4), ETG 11-1, 11-32.

Sherkaty, S. & Letouzey, J., 2004. Variation of structural style and basin evolution in the central Zagros (Izeh zone and Dezful Embayment), Iran, *Marine and Petroleum Geology,* **21**(5), p. 535.

Shearman, D.J., 1976. Geological evolution of Southern Iran – report of Iranian Makran Expedition, *Geographical Journal,* **142,** 393–410.

Stocklin, J., 1974. Possible ancient continental margin in Iran, in *Geology of Continental Margins*, pp. 873–877, eds Burke, C. & Drake, C., Springer-Verlag, New York.

Stoneley, R., 1981. The geology of the Kuh-e-Dalneshin area of southern Iran, and its bearings on the evolution of southern Thetys, *J. geol. Soc. Lond.,* **138,** 509–526.

Talebian, M. & Jackson, J., 2002. Offset on the main recent fault of the NW Iran and implications on the late Cenozoic tectonics of the Arabia-Eurasia collision zone, *Geophys. J. Int.,* **150,** 422–439.

Talebian, M. & Jackson, J., 2004. A reappraisal of earthquake focal mechanisms and active shortening in the Zagros mountains of Iran, *Geophys. J. Int.,* **156,** 506–526.

Tatar, M., Hatzfeld, D., Martinod, J., Walpersdorf, A., Ghafori-Ashtiany, M. & Chéry, J., 2002. The present-day deformation of the central Zagros from GPS measurements, *Geophys. Res. Lett.,* **29**(19), 1927.

Tatar, M., Hatzfeld, D. & Ghafory-Ashtiany, M., 2004. Tectonics of the Central Zagros (Iran) deduced from microearthquake seismicity, *Geophys. J. Int.,* **156,** 255–266.

Tchalenko, J.S. & Braud, J., 1974. Seismicity and structure of the Zagros (Iran)—the Main Recent Fault between 33 and 35°N, *Phil. Trans. Roy. Soc. Lond.,,* **277,** 1–25.

Vernant, P. et al., 2004. Present-day crustal deformation and plate kinematics in the Middle East constrained by GPS measurements in Iran and northern Oman, *Geophys. J. Int.,* **157,** 381–398.

Vita-Finzi, C., 1987. 14C deformation chronologies in coastal Iran, Greece and Jordan, *J. geol. Soc. Lond.,* **144,** 553–560.

Available online at www.sciencedirect.com

SCIENCE DIRECT®

Earth and Planetary Science Letters 245 (2006) 365 – 372

EPSL

www.elsevier.com/locate/epsl

Deformation in the Jura Mountains (France): First results from semi-permanent GPS measurements

Andrea Walpersdorf [a,*], Stéphane Baize [b], Eric Calais [c], Paul Tregoning [d], Jean-Mathieu Nocquet [e]

[a] *Laboratoire de Géophysique Interne et Tectonophysique, Joseph Fourier University, Maison des Géosciences, BP 53, 38041 Grenoble Cedex 9, France*
[b] *IRSN-Seismic Hazard Division, France*
[c] *Purdue University, West Lafayette, IND, USA*
[d] *Research School of Earth Sciences, The Australian National University, Canberra, Australia*
[e] *Géosciences Azur, Valbonne, France*

Received 13 May 2005; received in revised form 24 January 2006; accepted 20 February 2006
Available online 11 April 2006
Editor: V. Courtillot

Abstract

New GPS estimates of relative motion across the Jura Mountain Belt with respect to the Eurasian Plate indicate less than 1 mm/yr of convergence, considerably less than previous estimates. Velocity uncertainties have been evaluated by several methods and range from 0.2 to 0.5 mm/yr for the semi-permanent stations. The major, statistically-significant strain feature inferred by the Jura GPS measurements is along-arc extension, compatible with tectonic studies. That the detected deformation is small in magnitude highlights two important issues: previous estimates are over-stated and that the approach of using semi-permanent GPS installations is capable of detecting small tectonic signals. Using the upper bound as the rate of convergence, we estimate that this would generate an earthquake of magnitude 5–5.5 every 15 to 75 yr.

Keywords: GPS; Jura; Alps; slow deformation; seismic hazard; semi-permanent GPS installations

---

1. Introduction

Although France has low to moderate seismotectonic activity, several earthquakes of Ml > 5 are recorded in historical catalogues [1] and by paleoearthquake evidence (e.g. [2]). Most of France behaves as a rigid block with internal deformation of no more than 0.5 mm/yr [3].

The Alpine region is the most deforming part of France, where the kinematics are characterized by a radial extension in the internal Alps and perpendicular compression in the forelands [4]. The velocity field and pattern of deformation are clearly influenced by the vicinity of the Eurasian–African plate boundary but the controlling processes of the strain pattern are still a matter of debate.

The Jura area, located between the alpine orogen and its foreland, is known to have been an active area during the Neogene. Some evidence suggests that this is still the case, but precise knowledge of deformation and slip rates is still unavailable. A local GPS network was installed to

---

[*] Corresponding author. Tel.: +33 4 76 82 81 04; fax: +33 4 76 82 81 01.

E-mail addresses: andrea.walpersdorf@obs.ujf-grenoble.fr (A. Walpersdorf), stephane.baize@irsn.fr (S. Baize).

0012-821X/$ - see front matter © 2006 Elsevier B.V. All rights reserved.
doi:10.1016/j.epsl.2006.02.037

address this issue and to improve the seismic hazard assessment of the region. Here we present deformation estimates from four years of GPS data observed on six semi-permanent sites.

2. Structural and active tectonics settings

The Jura is the youngest external fold-and-thrust belt related to Alpine orogeny, where faulting and folding began during Miocene [5]. The thrusting of the frontal Jura over its foreland (Bresse graben) occurred during Mio–Pliocene and a total shortening of 30 km occurred over the whole Jura [6]. The most prominent feature of the Jura tectonics is the thin-skin style, with faults and folds rooted into a decollement level (Triassic salt layers). The implication of the basement in the deformation is still debated (e.g. [7]). Most of the models refer to various indenters to explain the fan-shape of the stress/strain orientation pattern and the overall shape and the curvature of the belt.

The current stress/strain pattern is similar to that during the Mio–Pliocene [8]. Shortening and mountain building in the Jura still appear active, mainly within the internal zones [7]. Some neotectonic evidence is reported in the Jura [9], such as in La Balme de Sillingy along the Vuache fault. This fault is currently seismically active with focal mechanisms that reveal left-lateral displacements along NW–SE planes (Fig. 1). The last event occurred on July 15, 1996 at Epagny, close to Annecy (Ml = 5.3), at a depth of 2 km [10]. The French historical catalogue includes several destructive earthquakes that also occurred along the Vuache fault (11/08/1839 in Annecy; 17/04/1936 in Frangy, both with similar surface effects and damage). Elsewhere in the southern Jura the seismicity appears more diffuse except on other NW–SE faults, the Culoz fault for example (Fig. 1).

Slip rates on Jura faults are poorly documented. Estimates of the cumulative lateral offset on the Vuache Fault vary from 1 [10] to 12 km [11], inferring a mean slip rate ranging from 0.5 to 4.4 mm/yr, respectively.

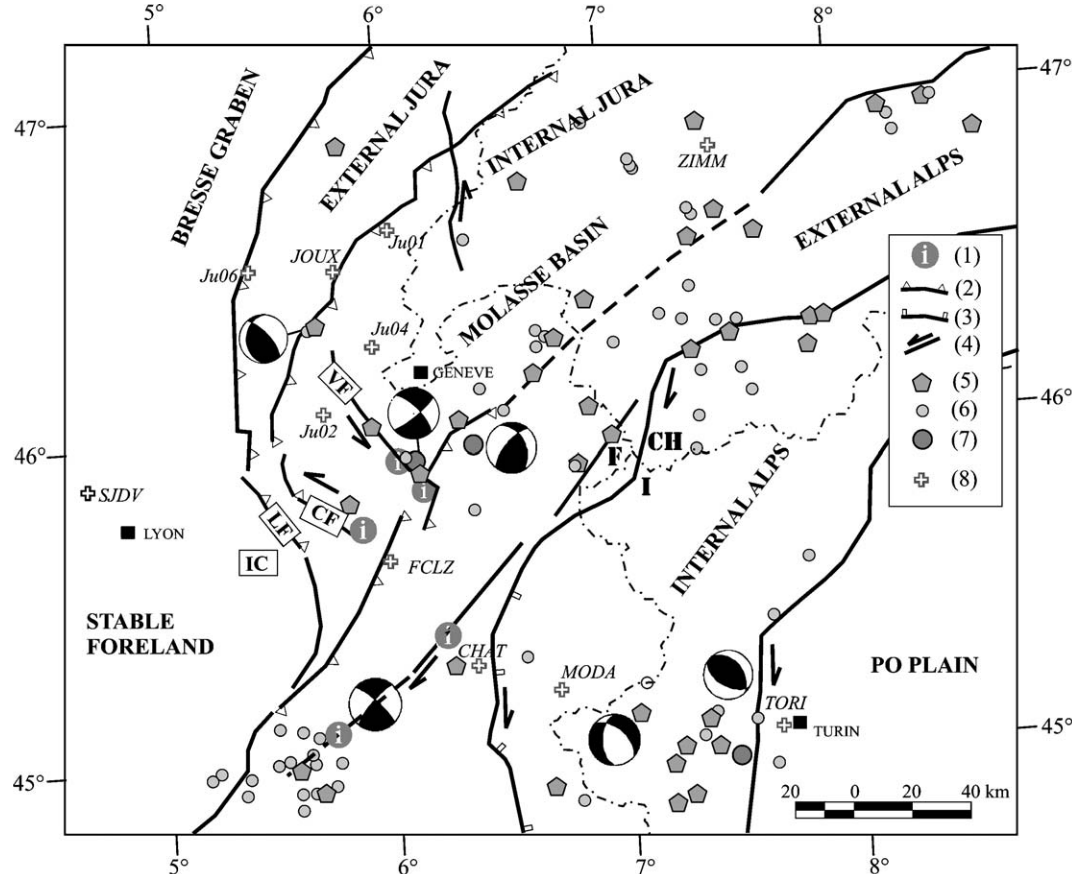

Fig. 1. Active deformation of the Jura Mountains. (1) Reliable neotectonic evidences (see Baize et al., [9] for a synthesis); (2) reverse, (3) normal, (4) strike-slip faulting. (5) Historical epicenters of earthquakes (www.sisfrance.fr). Current seismicity from CEA/LDG (unpublished): (6) 4 < Ml < 5; (7) Ml > 5. VF: Vuache Fault; CF: Culoz Fault; LF: Lagnieu Fault; IC: Ile Crémieu.

Previous geodetic studies using triangulation and GPS data estimated high relative velocities (several mm/yr) within the External Alps and the Jura relative to stable Europe (e.g. [12]), including a drastic shortening in the southern Jura (3–4 mm/yr).

3. GPS processing and results

The 6 semi-permanent sites were each observed over a 10 day period, once or twice per year from May 2000 to August 2004. The sites were selected in order to span 6 tectonic blocks separated by the faults thought to be active (Figs. 1 and 2). The data of these sites are added to those of 18 (in 2000) to 25 (in 2004) sites in the REGAL network (http://kreiz.unice.fr/regal) combined with data from 31 continuously operating sites in western Europe. Site coordinates, orbital parameters, Earth Orientation Parameters, zenith tropospheric delays (13 per day) were estimated using the GAMIT software [13] to generate daily fiducial-free estimates of a polyhedron of sites. These solutions were subsequently combined using GLOBK [14] to estimate a time-evolving polyhedron and time-series of daily site coordinates. Further details of the GPS analysis are given in the Appendix.

We included additional observations on some permanent sites in the REGAL network, commencing in 1997. The additional data prior to the commencement of the Jura network was required in order to obtain stable velocity estimates of the REGAL sites that were consistent with those of Nocquet and Calais [15], derived from REGAL data up to the end of 2001. The Jura velocities

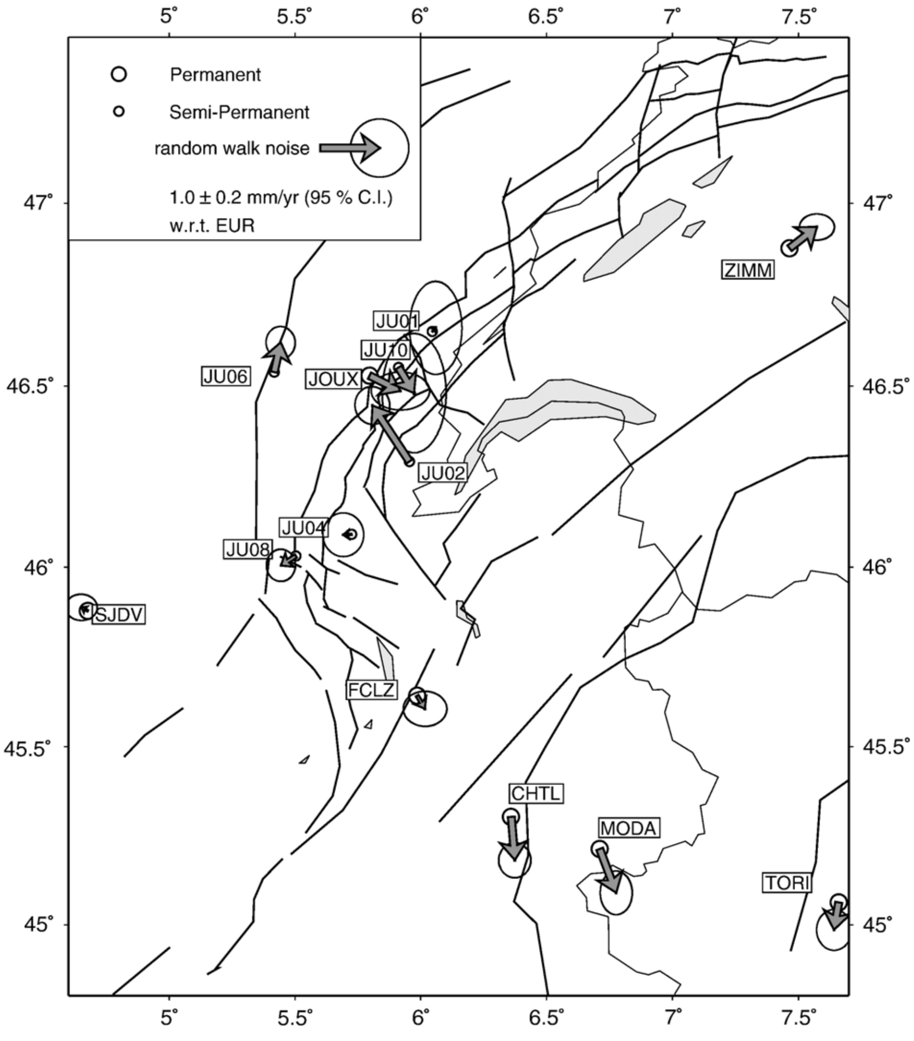

Fig. 2. Velocities of the Jura semi-permanent GPS network relative to the Eurasian Plate. Black lines indicate the faults delimiting the individual tectonical blocks in the region.

(Table 1) were then transformed into a reference frame with respect to stable Eurasia (see Appendix).

Different strategies have been applied to establish realistic estimates of the velocity uncertainties of the semi-permanent stations (see Appendix). These tests suggest that the Jura site velocities have a precision of 0.2–0.5 mm/yr (95% confidence level). The individual velocities in the semi-permanent network show relative motion of 0.1–1.1 mm/yr with respect to stable Eurasia (Table 1) and are barely statistically significant at the 95% confidence level.

4. Discussion

The "tectonic signal" of deformation between the Jura Mountains and the Eurasian reference frame is barely detectable over the noise of the GPS analysis. In addition, there may still be a need for further observations on JU08 and JU10 before the velocity estimates stabilize (see Appendix, Fig. A.3). The uncertainties calculated by applying a site-by-site random-walk noise model are probably realistic and only a few points show relative motion significantly different from zero at the 95% confidence level. Thus, the main result of our analysis is that most of the Jura displacement rates are lower than the present level of uncertainty (0.2–0.5 mm/yr) and that the estimates of 3–4 mm/yr of overall shortening for the Jura Mountains [16,17,12] are too high. This supports the findings of Nocquet and Calais [15].

Strain calculated over the 6 semi-permanent stations and the permanent station JOUX is presented in Table 2 for the solutions with and without random-walk noise. Both solutions show arc-parallel extension but only the solution without random-walk noise shows significant NW–SE compression, compatible with stress measurements [8]. When adding random-walk noise, the major strain feature is the extension along-arc, while the arc-perpendicular compressive component becomes insignificant.

Table 1
Jura site velocities with respect to the Eurasian Plate and in ITRF2000

Eurasia			ITRF2000		Sigma	
(mm/yr)			(mm/yr)		(mm/yr)	
Site	Vel N	Vel E	Vel N	Vel E	Vel N	Vel E
CHTL	−0.73	0.06	14.03	20.45	±0.12	±0.11
FCLZ	−0.22	0.13	14.52	20.37	±0.12	±0.15
JOUX	−0.26	0.52	14.51	20.52	±0.13	±0.20
JU01	0.06	0.06	14.88	20.08	±0.32	±0.18
JU02	0.94	−0.62	15.70	19.50	±0.13	±0.12
JU04	−0.01	−0.14	14.81	19.96	±0.15	±0.14
JU06	0.50	0.11	15.27	19.99	±0.11	±0.11
JU08	−0.16	−0.25	14.68	19.79	±0.11	±0.10
JU10	−0.43	0.26	14.42	20.23	±0.41	±0.22
MODA	−0.74	0.28	14.04	20.79	±0.15	±0.11
SJDV	0.06	−0.11	14.87	19.88	±0.09	±0.11
TORI	−0.46	−0.08	14.22	20.61	±0.14	±0.12

Table 2
Jura strain tensors, with and without random walk noise

Solution	Eps1 [1E-8]	Eps2 [1E-8]	Az (°)
Stochastic	5.6±2.4	−0.2±3.2	111±19
Deterministic	4.3±2.9	−6.2±3.2	148±11

Extension is positive, compression negative and the azimuth given is for the most compressive component.

In the most active part of the Jura (the southern end between the Vuache and Lagnieu faults), the differential displacement of JU02 with respect to JU04 (1 mm/yr to NNW) is consistent with left lateral movement along the NW–SE trending faults (Vuache and Droisy faults).

Assuming that the upper bound GPS estimates of relative motion (1 mm/yr) are correct, and assuming a characteristic total width and length of the active fault of 3 and 30 km, one can calculate, using the Wesnousky [18] model, that the mean recurrence time of a magnitude 5–5.5 characteristic earthquake is 15–75 yr. The historical catalogues show earthquakes with the lower limit magnitude (5), but with a recurrence time clearly longer than 15 yr (~50 yr), indicating either that the true relative motion is significantly lower than 1 mm/yr, or that characteristic earthquakes have magnitudes larger than 5–5.5. An alternative explanation would be that part of the total slip is released aseismically.

5. Conclusion

Relative velocities in the Jura Mountains with respect to the Eurasian Plate are <1 mm/yr, with uncertainties in the range of 0.2–0.5 mm/yr. However, the individual site velocities (with respect to Eurasia) need to be interpreted carefully because the results are barely – if at all – significantly different from zero. Nevertheless, with an upper bound of 1 mm/yr, the present-day convergence in the Jura is considerably less than previously thought. If significant, the major strain feature inferred by the Jura GPS measurements is along-arc extension, compatible with previous tectonic studies but with a significantly reduced rate of convergence.

The Jura semi-permanent GPS network requires additional sites to provide sufficient spatial coverage, with a current absence of sites located in the southern end of the Jura belt, between the Culoz fault and the Ile

Crémieu and also where the indenter is thought to push into the pre-Alps nappes or the sub-alpine molasses where deep-seated thrusts are known. While the estimated rates of convergence are near-zero, we show here that semi-permanent networks are capable of producing such results and therefore present a viable alternative to permanent installations for tectonic studies.

Acknowledgements

We are grateful to the colleagues helping to get the Jura semi-permanent network set up and started: F. Jouanne (LGCA Chambéry), F. Mathieu (CEA) and O. Scotti (IRSN). Many thanks to J.L. Combe (Jura Energie Solaire) who is running the measurements. Thanks to two anonymous reviewers for their comments and encouragements.

Appendix A. Estimation of velocity uncertainties for the semi-permanent GPS network

We have paid particular attention to the precise evaluation of the sub-millimetric velocity estimates in the low deformation area of the Jura. In particular, the velocity uncertainties have been evaluated carefully by a realistic calculation strategy and corroborated by a number of different tests which are presented in this Appendix.

We generated coordinate time series for the permanent and semi-permanent stations from the daily solutions spanning 1997 to 2004 and estimate linear velocities. The maximal differences between these displacement rates for the Jura stations are 1.3 and 1.0 mm/yr in the north and east components, respectively. These values give an upper limit of the differential site motions in the Jura region.

Next, we estimated site velocities for all 62 stations (6 semi-permanent sites, 25 REGAL and 31 other European reference sites) applying coloured noise (in the form of random-walk variation of the site coordinates) to account for the non-Gaussian nature of the noise characteristics of GPS data (e.g. [19,20]). The amount of noise was calculated for each individual station from the noise characteristics of the time series with varying integration times. This strategy helps evaluate realistic velocity uncertainties for the GPS stations according to their different observation spans and measurement environments. The average values applied to the 62 stations are 0.5, 0.3 and 2.8 mm^2/yr for the north, east and vertical components, respectively.

We aligned our network with the ITRF2000 by computing 7-parameter transformations of the coordinates and velocities of 18 well known IGS sites (Fig. A.1) to their ITRF2000 values [21]. The velocities of 23 sites were subsequently inverted to solve for the Euler vector representing motion of the Eurasian Plate with respect to ITRF2000. The residual velocities of these 23 sites are less than 1 mm/yr and are shown in Figs. A.1 and A.2. The estimated Euler vector is comparable to previous

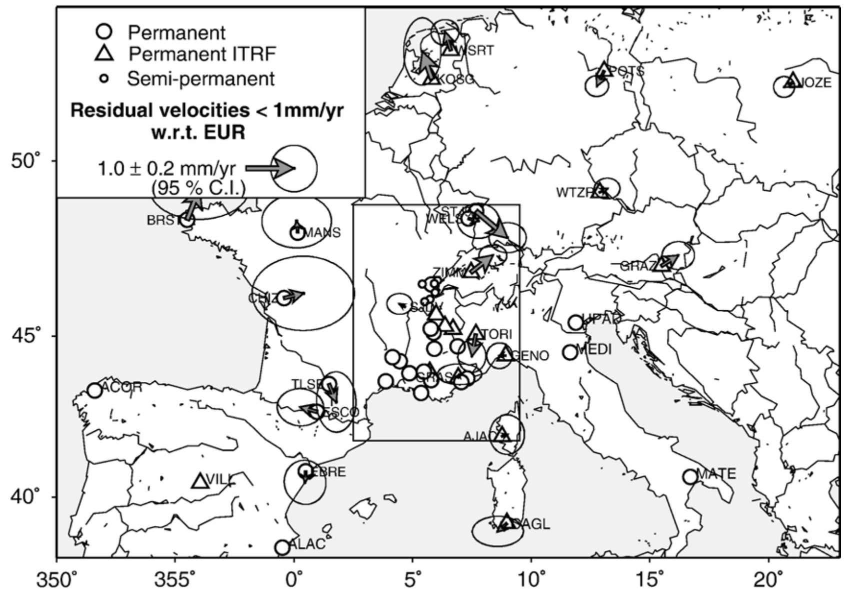

Fig. A.1. GPS stations used in the analysis covering western Europe. Sites used to define the ITRF2000 reference frame are shown by triangles. Velocity vectors are indicated only for stations with residuals of less than 1 mm/yr with respect to the Eurasian Plate, subsequently used to define the Eurasian reference frame. The frame indicates the zoom presented in Fig. A.2.

estimates (Table A.1) and the χ^2 of the inversion for the Euler vector is 1.5.

Following Beavan et al. [23], we computed several velocity solutions with different amounts of random-walk noise applied uniformly to all site coordinates until the χ^2 of the inversion for the Euler vector was close to 1.0. The amount of random-walk noise to be applied to all of the stations to obtain a χ^2 of 1 is 0.5 mm^2/yr for the horizontal coordinates and 3.65×10^3 mm^2/yr on the vertical coordinates (the heights are downweighted in the 7-parameter transformation by a factor 10). The solution without stochastic noise gives a slightly different Euler vector for the Eurasian Plate (Table A.1) from the stochastic solution.

The resulting velocity field with respect to the Eurasian Plate is shown in Fig. A.2 (western Alps), Fig. 2 (zoom on the Jura and environment) and Table 1. The addition of random-walk noise increased the formal uncertainties of the velocity estimates by a factor of 5–10 for continuously recording sites (e.g. SJDV, TORI) but increased the

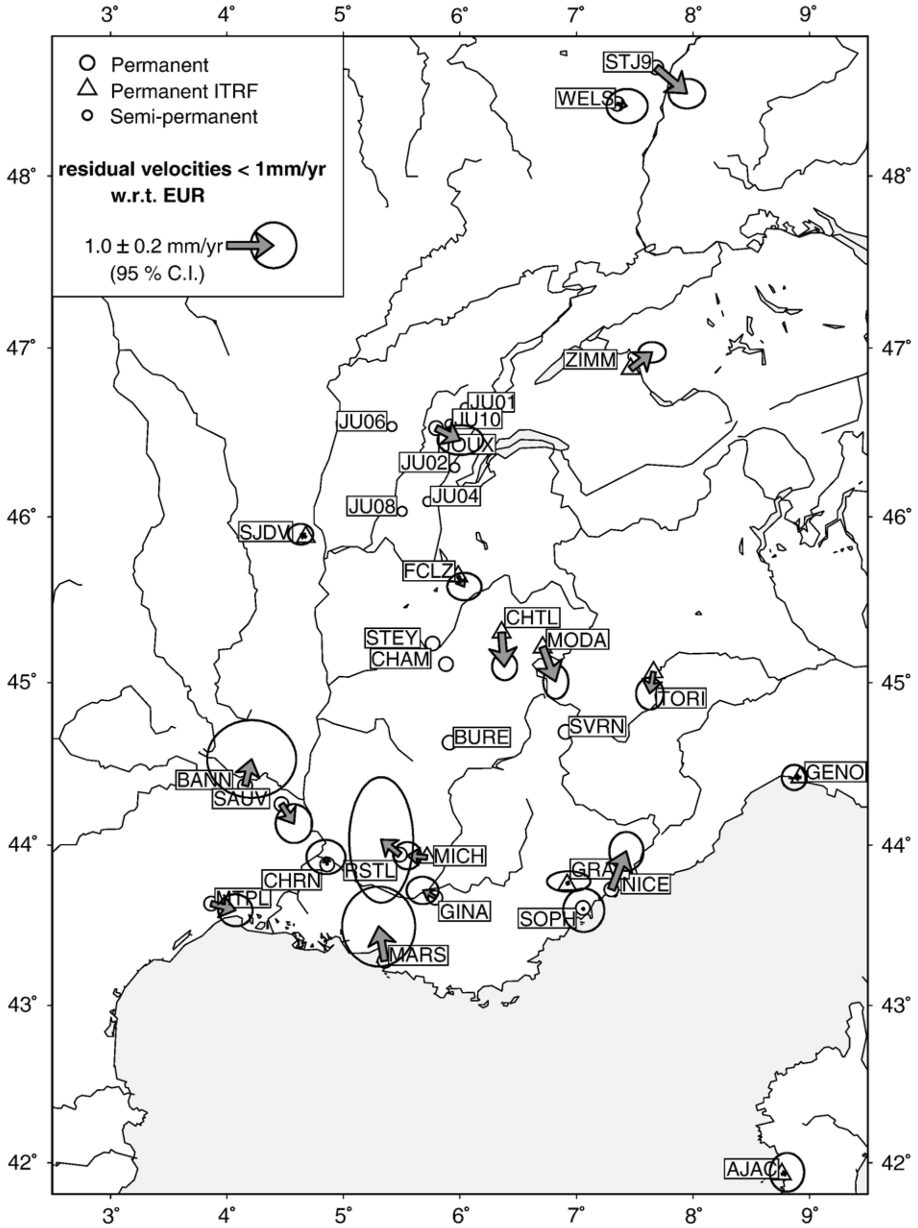

Fig. A.2. Zoom on the western Alps, symbols as in Fig. A.1.

uncertainties of the sites in the Jura region by a factor of 1–3 with respect to the deterministic solution. These increased uncertainties represent a more realistic estimate of the true uncertainties. An average value for the velocity uncertainty of both the semi-permanent and the permanent stations with a span of more than 3 yr is 0.2 mm/yr. The velocity estimates with and without stochastic noise show average differences of 0.2 mm/yr.

What is the effect on the velocity estimates of having campaign-style observations rather than continuous observations? We can explore this by comparing velocity estimates at permanent stations derived using all the data with estimates using only data at the times that Jura sites were observed. Our tests show that the “semi-permanent” velocities for 4 permanent stations differ from the “complete” velocity by less than 0.3 mm/yr (0.24, 0.16, 0.14 and 0.01 mm/yr for FCLZ, GINA, MODA and CHRN respectively). This variation is consistent with our velocity uncertainty estimates derived using coloured noise and can be considered as another estimation of the upper error limit for the true semi-permanent stations. These tests on the formal velocity errors suggest that the uncertainties on horizontal velocities of our semi-permanent stations are between 0.2 and 0.3 mm/yr (95% confidence) after 4 years and up to 8–10 measurement epochs.

Finally, we have checked the stability of the sites velocity estimates as a function of length of observation span. Fig. A.3 shows the evolution of the horizontal velocities of two semi-permanent sites (JU08 and

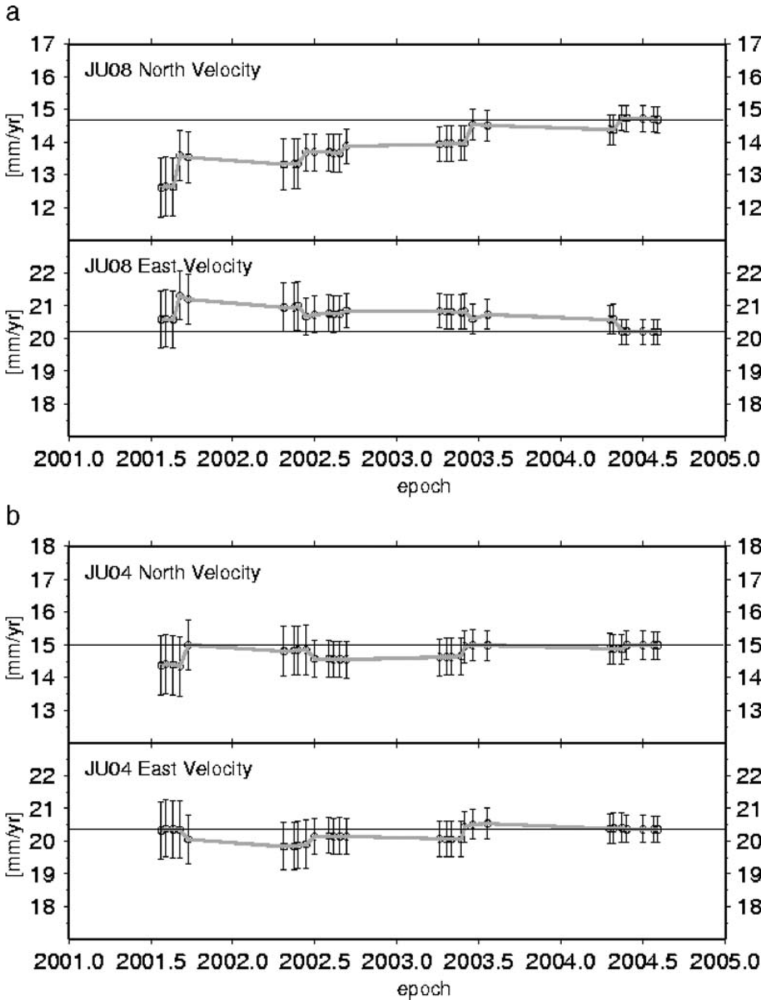

Fig. A.3. Convergence test results for two semi-permanent sites of the Jura network (JU08 and JU04). The dots represent successive estimates of the site velocities, starting from mid-2001 when all sites have been measured at least 3 times. Each new point corresponds to a new measurement epoch of one of the Jura stations. The horizontal line indicates the velocity estimated over the total observation span to the end of 2004. The reference frame is ITRF2000.

JU08) in an ITRF2000 reference frame as more observations are included. The first velocity estimate is shown after three epochs of measurement (epoch 2001.564), each epoch consisting of about 10 24-h GPS measurements. Then, after each new Jura measurement epoch, a new solution was calculated for the whole network. The horizontal line represents the final value in August 2004. The permanent stations SJDV, FCLZ and JOUX, as well as some of the semi-permanent stations (JU02, JU04, JU06) show stable values after epoch 2001.564 at a level of 0.5 mm/yr. JU01 seems to have converged since 2003. However, the semi-permanent sites JU08 and JU10 still have significant rate changes up to the 2004 measurements (in particular for the North component) and their velocity solutions seem to have converged only to a level of 0.5 mm/yr after 4 years of measurement. Clearly, the velocity estimates of some Jura stations (JU01, JU02, JU04, JU06) are more reliable (uncertainties of about 0.2 mm/yr) than others (JU08, JU10, with uncertainties closer to 0.5 mm/yr).

Table A.1
Parameters of the Eurasian Euler pole with respect to ITRF2000

Solution	Lat N (°)	Lon E (°)	Rot. rate (°/My±σ)	Semi-major axis	Semi-minor axis	Azimuth
Stochastic	59.723	−95.492	0.269 ±0.0020	1.09	0.06	69.7
Deterministic	58.040	−99.724	0.262 ±0.0004	0.21	0.02	65.7
Altamimi et al., [21]	57.965	−99.374	0.260			
Sella et al., [22]	58.27	−102.21	0.257			
Nocquet and Calais, [15]	56.0	−101.5	0.25			

References

[1] C. Beauval, O. Scotti, Mapping *b*-values in France using two different magnitude ranges: possible non-power-law model? Geophys. Res. Lett. 30 (17) (2003) 1892, doi: 10.1029/2003GL017576.

[2] M. Sébrier, A. Ghafiri, J.L. Blès, Paleoseismicity in France: fault trench studies in a region of moderate seismicity, J. Geodyn. 24 (1997) 207–217.

[3] J.M. Nocquet, E. Calais, Geodetic measurements of crustal deformation in the western Mediterranean and Europe, Pure Appl. Geophys. 161 (2004), doi: 10.1007/s00024-003-2468-z.

[4] C. Sue, F. Thouvenot, J. Frechet, P. Tricart, Widespread extension in the core of the western Alps revealed by earthquake analysis, J. Geophys. Res. 104 (B11) (1999) 25611–25622.

[5] H.P. Laubscher, Jura kinematics and the Molasse Basin, Eclogae Geol. Helv. 85 (1992) 287–303.

[6] J.L. Mugnier, S. Guellec, G. Ménard, F. Roure, M. Tardy, P. Vialon, Crustal balanced cross-sections through the external Alps deduced from the ECORS profile, in: F. Roure, P. Heitzmann, R. Polino (Eds.), Deep structure of the Alps, Mém. Soc. Géol. France, N. S. n°, vol. 156, 1990, pp. 203–216.

[7] A. Sommaruga, Décollement tectonics in the Jura foreland fold-and-thrust belt, Mar. Pet. Geol. 16 (1999) 111–134.

[8] A. Becker, The Jura Mountains — an active foreland fold-and-thrust belt? Tectonophysics 321 (2000) 381–406.

[9] S. Baize, M. Cushing, F. Lemeille, T. Granier, B. Grellet, D. Carbon, P. Combes, C. Hibsch, Inventaire des indices de rupture affectant le Quarternaire, en relation avec les grandes structures connues, en France métropolitaine et dans les régions limitrophes, Mém. Soc. Géol. Fr. 175 (2002) 142.

[10] F. Thouvenot, J. Fréchet, P. Tapponnier, J.-C. Thomas, B. Le Brun, G. Ménard, R. Lacassin, L. Jenatton, J.R. Grasso, O. Coutant, A. Paul, D. Hatzfeld, The ML 5.3 Épagny (French Alps) earthquake of 1996 July 15: a long-awaited event on the Vuache Fault, Geophys. J. Int. 135 (1998) 876–892.

[11] D. Aubert, Le Risoux, un charriage jurassien de grandes dimensions, Eclogae Geol. Helv. 64 (1971) 151–156.

[12] F. Jouanne, N. Genaudeau, G. Ménard, X. Darmendrail, Estimating present-day displacement fields and tectonic deformation in active mountain belts: an example from the Chartreuse Massif and the southern Jura Mountains, western Alps, Tectonophysics 296 (1998) 403–419.

[13] R.W. King, Y. Bock, Documentation for the GAMIT analysis software, release 10.1, Massachusetts Institute of Technology, Cambridge, MA, 2002.

[14] T.A. Herring, J.L. Davis, I.I. Shapiro, Geodesy by radio interferometry: The application of Kalman filtering to the analysis of very long baseline interferometry data, J. Geophys. Res. 95 (B8) (1990) 12,561–12,581.

[15] J.M. Nocquet, E. Calais, Crustal velocity field of the western Europe from permanent GPS array solutions, 1996–2001, Geophys. J. Int. 154 (2003) 72–88.

[16] J. Martinod, F. Jouanne, J. Taverna, G. Ménard, J.F. Gamond, X. Darmendrail, J.C. Notter, C. Basile, Present-day deformation of the Dauphiné alpine and subalpine massifs (SE France), Geophys. J. Int. 127 (1996) 189–200.

[17] F. Jouanne, G. Menard, D. Jault, Present-day deformation measurements in the French north-western Alps/southern Jura Mountains: data from triangulation comparison, Geophys. J. Int. 119 (1994) 151–169.

[18] S.G. Wesnousky, Earthquakes, quaternary faults, and seismic hazard in California, J. Geophys. Res. 91 (1986) 12587–12631.

[19] A. Mao, C.G.A. Harrison, T.H. Dixon, Noise in GPS coordinate time series, J. Geophys. Res. 104 (1999) 2797–2816.

[20] S.D.P. Williams, Offsets in global positioning system time series, J. Geophys. Res. 108 (B6) (2003) 2310, doi: 10.1029/2002JB002156.

[21] Z. Altamimi, P. Sillard, C. Boucher, ITRF2000: a new release of the International Terrestrial Reference Frame for earth science applications, J. Geophys. Res. 107 (B10) (2002) 2214.

[22] G.F. Sella, T.H. Dixon, A. Mao, REVEL: a model for recent plate velocities from space geodesy, J. Geophys. Res. 107 (B4) (2002) ETG 11-1–ETG 11-32.

[23] J. Beavan, P. Tregoning, M. Bevis, T. Kato, C. Meertens, Motion and rigidity of the Pacific Plate and implications for plate boundary deformation, J. Geophys. Res. 107 (B10) (2002) 2261, doi: 10.1029/2001JB000282.